Prifysgol Abertawe
Swansea University

UGA
Université
Grenoble Alpes

THÈSE

Pour obtenir le grade de

DOCTEUR DE L'UNIVERSITE GRENOBLE ALPES

préparée dans le cadre d'une cotutelle entre la *Communauté Université Grenoble Alpes* et l'*Université de Swansea*

Spécialité : **Matériaux, Mécanique, Génie Civil, Electrochimie**

Arrêté ministériel : le 6 janvier 2005 – 25 mai 2016

Présentée par

Hugo SPIESER

Thèse dirigée par **Julien BRAS** et **David GETHIN**
codirigée par **Aurore DENNEULIN** et **Davide DEGANELLO**

préparée au sein des **Laboratoires Génie des Procédés Papetiers – LGP2, UMR 5518** et **Welsh Centre for Printing and Coating – WCPC**

dans **l'École Doctorale I-MEP2 – Ingénierie – Matériaux, Mécanique, Environnement, Energétique, Procédés, Production**, et le **College of Engineering** de l'**Université de Swansea**

Smart and Safe Packaging

Thèse soutenue publiquement le **20 novembre 2020**
devant le jury composé de :

Pr. Kar Seng TENG
Professeur à Université de Swansea, Président
Pr. Eliane ESPUCHE
Professeur à Université Claude Bernard Lyon 1, Rapportrice
Pr. Long LIN
Professeur à Université de Leeds, Rapporteur
Dr. Davide BENEVENTI
Directeur de Recherche CNRS à Grenoble INP, Examinateur
Dr. Julien BRAS
Maitre de Conférences à Grenoble INP, Directeur de thèse
Pr. David GETHIN
Professeur à Université de Swansea, Co-directeur de thèse
Dr. Aurore DENNEULIN
Maitre de Conférences à Grenoble INP, Co-encadrante de thèse, invitée
Pr. Davide DEGANELLO
Professeur à Université de Swansea, Co-encadrant de thèse, invité

Acknowledgements

As so many people were involved either very closely or from a distance in this achievement, I will try to thank you all here. 2 countries – 3 different labs but also family and friends; the list is very long. Where should I start?

First of all, I would like to thank the members of my jury and especially the external examiners Pr. Eliane Espuche and Pr. Long Lin for accepting the invitation to review this PhD work. My most sincere thanks also go to the internal examiners Pr. Vincent Teng and Dr. Davide Beneventi – thanks to Pr. Teng for accepting to be president of the jury and for your help organising the viva in Swansea. Thanks a lot, to all the jury members for the constructive and relevant discussion both about the manuscript and the PhD defence. I thoroughly enjoyed sharing and discussing my work with you.

I would like to address my deepest thanks to my supervisory team. Thank you, David and Davide, for welcoming me in Swansea. David, you were always there when I needed you – it felt like there were no issues too complex for you to solve and you have been a reassuring presence all the way through. Davide, thanks for your passion and your ideas, also thanks for the discussions and debates that had nothing to do with the PhD work (I needed them). Working with both of you was a pleasure from day one and you two form a great team. Merci au duo français pour m'avoir accompagné tout au long du chemin. Julien, merci pour m'avoir fait confiance et m'avoir guidé durant ces 3 années et quelques – j'ai réellement apprécié travailler avec toi. Merci pour ces discussions scientifiques, pour tous ces conseils, pour ces semaines de conférences, j'ai beaucoup appris auprès de toi. Aurore, merci pour tout. Merci pour ton dévouement et ta présence que ce soit en visio, par mail, sms, téléphone, Whatsapp, pigeon voyageur ou en face à face. Merci de m'avoir accompagné, de m'avoir rassuré, merci pour ces discussions science et celles qui n'avaient rien à voir avec la thèse – j'ai eu beaucoup de chance de t'avoir comme encadrante. Un grand merci à vous tous, je n'aurais pu rêver mieux comme encadrement !

Merci à tout le LGP2. Merci aux collègues et compagnons de galère – euh de thèse. Merci à la team MatBio, aux anciens qui nous ont accueillis et montrés la voie – Fleur, Johanna, Charlène, Erwan, Flavien, Hippo, Manon. Merci Flavien pour m'avoir montré de près à quoi ressemble un spécimen de thésard en rédaction – tu m'auras beaucoup fait rire pendant tes derniers mois. Merci Hippo pour ces discussions microbio, pour ces retours à vélo pendant lesquels j'ai pu vider mon sac, merci pour ces sorties ski et pour ces « quelques » bières le long du chemin. Merci Manon pour avoir toujours été disponible (même après la thèse !!) pour un conseil ou un café, merci au bureau B120 en général pour m'avoir fait une petite place et nourri pendant tout ce temps, on s'y sentait bien.

Merci aux copains avec qui j'ai commencé – Mathieu, Estelle et Gab. Merci Estelle et Gab pour votre amitié, pour ces randos, ces sorties jusqu'au bout de la nuit (et ces lendemains parfois difficiles), ces pauses cafés (et thés), ces 150 000 messages, ces appels et visios, ces soirées jeux en confinement (et sans confinement d'ailleurs), ces voyages, ce canapé toujours prêt à m'accueillir sur Grenoble. Entre Grenoble, Nantes, Alès et Swansea, vous avez toujours été aussi proches malgré la distance et je ne peux vous remercier assez pour ça. Cette victoire au tournoi de pétanque international du LGP2 en 2017 restera peut-être le plus grand succès de ma thèse !
Merci aux nouveaux – Maxime, Lorelei, Eva, Bastien. Merci Maxime pour tous les coups de main sur la sérigraphie, merci Bastien pour ton humour (avoir trois ans de thèse pour apprendre à l'apprécier n'est pas de trop !!). Merci à mes compagnons de bureau – Axelle, Amina, Sudha et Flavien, pour m'avoir supporté et écouté. J'ai été ravi de passer 1 an et demi à vos côtés tous les jours. Merci aux copains de papet' et assimilés, merci aux toulousains (ceux proches et ceux plus loin – même si ceux loin sont toujours aussi proches…) – Régis, Laurie, Nico, Pauline, Arthur, Antoine et le reste de la fine équipe. Sans vous tous, ces trois années auraient été beaucoup plus tristes.

Merci aux collègues non-thésards. Merci Cécile pour ton naturel, ta gentillesse et ta patience – même si je pouvais souvent lire l'angoisse dans ton regard quand je frappais à ta porte (« mais qu'est-ce qu'il a encore fait ? » ou bien « qu'est-ce qu'il va encore me demander celui-là ? »). Je ne compte pas le nombre de fois où j'ai passé la tête dans ton bureau ou pris une chaise pour discuter (parfois bien trop tôt le matin…). Merci Bertine pour ton rire, tes histoires et nos excursions au CMTC, on n'en trouve pas des aussi sympas et drôles que toi au Pays de Galles ! Merci Guillaume, pour ces blagues dans les couloirs et les labos, mais aussi pour tes conseils et ton accompagnement sur la technique et la science derrière ton métier. Merci Karim pour ta franchise et ta porte toujours ouverte (bien souvent à mes risques et périls !). Merci Franck pour avoir plus d'une fois sauvé mon ordinateur et ma thèse même à plus de mille km de ton bureau. Merci au ST, qui m'ont vu débarquer avec toutes sortes de demandes – c'est une chance incroyable pour le labo de vous avoir – Chu, Charlotte, Olivier, Momo et Phillipe (profite de ton repos bien mérité). Merci à Stéphane V., Stéphane D., Laurence, Sylvie, Maxime, Névin, Mikaël, Jessy, Karine, Lydia et les autres permanents pour votre bonne humeur, merci aux enseignants chercheurs pour votre temps. Merci Didier pour ta gestion du labo, humaine, ouverte et plein de gentillesse, même en ces temps difficiles.
Merci à tous pour vos sourires, vos bonjours et quelques mots dans les couloirs qui vous donnent envie de se lever pour aller au labo. « On se s'aperçoit de la valeur de ce que l'on a seulement une fois qu'on l'a perdu » (ou un truc du genre), et j'ai pleinement vécu cette citation en quittant le LGP2 pour le Pays de Galles.

Leaving Grenoble for Swansea in the middle of the PhD was quite a journey. Thanks to all the people who welcomed me in Swansea. Thanks to the WCPC team – Brent, Lorn, Caitlin, David, Alex, Tatyana, Ben, Jon, Sarah-Jane, Chris, David, Davide, James and the others. Thanks for the help in the lab and outside the lab. Thanks Zari for the help on my project. Thanks a lot Thierry for your time, I really appreciated your input. Thanks also to the CNH team – Simon, Mo, Alex, Tom, Mike, Daimei, Olivia, Benoit, Natasha, James, Ryan, Gareth, Sarah, Fi, Jon F., Jon E., Ffi, Owen, Anitha, Ehsaneh, Hina, Paul, Jacob and the others – all of you have been really kind to me. Thanks Alex for using your knowledge of French to make fun of me, but also trying to convince me that rheology is the best part of it all (still not convinced though…). Thanks Tom for the tennis lessons – I might have evacuated the PhD frustration on you, sorry about that! Thanks Mike for the enlightening discussions about so many different subjects. Thank you all three, for the afternoons on the beach, at the pub, at ours or yours, for the laughs and for your friendship. Special thanks also go to the Italo-Americano-French group – Manu, Marti, Carla, Claudia, Rob, Benoît, Andrew. Friday dinner's at Benoît's was a wonderful tradition and I miss it. Thanks for the amazing discussions, food, drinks and parties, it was nice to have fellow expatriates to cry our homes together. Merci Benoît pour la livraison de pain en confinement, pour les super plats vegan et pour ces bons moments passés ensemble.
Wales is an amazing country and I was incredibly lucky to have the opportunity to discover it, from the city life of Swansea and Cardiff, to the beautiful seaside of Gower, Pembrokeshire or Anglesey Peninsula, and to the dramatic landscape of Welsh hills and mountains of Snowdonia or Brecon Beacons. There is still so much I did not have the time to see, and I will definitely come back soon.

Merci aux copains de toujours – Eliot, Alizée, Yacine, Sylvain – merci d'avoir été là durant mes retours en Alsace – vous voir tous quelques fois par an fait du bien dans les périodes difficiles de cette aventure !
Merci à mes parents et mon frérot de m'avoir soutenu, de s'être intéressés à mon quotidien et d'être venus me voir à Grenoble ou à Swansea.

38 merci et 16 thanks plus tard (je gardais le meilleur pour la fin), merci Noémi pour ta présence ces trois dernières années (avec quelques autres en plus avant, et beaucoup à venir). Merci de m'avoir suivi des montagnes Grenobloises jusqu'au fin fond du Pays de Galles, et d'avoir partagé avec moi ces moments incroyables. Merci pour ton soutien et pour avoir été toujours là, que ce soit dans les échecs ou les succès. T'avoir auprès de mois ces derniers mois a été incroyablement bénéfique, sûrement beaucoup plus que tu ne l'imagines et je ne peux t'en remercier assez. J'ai vraiment hâte de vivre la prochaine étape de nos aventures.

Merci à tous !

Hugo Spieser, 2020

General Table of Content

Scientific contributions

Publications in scientific journal

1. Spieser, H., Denneulin, A., Deganello, D., Gethin, D., Koppolu, R., Bras, J. Cellulose nanofibrils and silver nanowires active coatings for the development of antibacterial packaging surfaces. *Carbohydrate Polymers* **240**, 116305 (2020).

2. Spieser, H., Jardin, A., Deganello, D., Gethin. D., Bras, J., Denneulin, A. Rheology of cellulose nanofibrils and silver nanowires for the development of screen-printed antibacterial surfaces. Submitted to *Journal of Materials Science* (2020).

3. Spieser, H., Tehrani, Z., Ali, M., Daghigh Ahmadi, E., Denneulin, A., Bras, J., Deganello, D., Gethin, D. Metal Organic Framework sensors on flexible substrate for ammonia sensing application at room temperature. Submitted to *Journal of Material Chemistry C* (2020).

Oral presentation in international conferences

1. Spieser, H., Denneulin, A., Deganello, D., Gethin, D., Bras, J. An approach to develop smart and safe packaging: antibacterial and printed sensors in *COST FP1405 ActinPak Fair and Final Conference* (2018)

2. Spieser, H., Tehrani, Z., Denneulin, A., Bras, J., Deganello, D., Gethin, D. Printed and flexible gas sensors based on metal organic framework and nano-carbon hybrid systems **accepted for presentation at *8th International Symposium on Sensor Science* (2020) but cancelled due to Covid-19**.

3. Spieser, H., Tehrani, Z., Denneulin, A., Bras, J., Deganello, D., Gethin, D. Printing processes for smart sensors and antibacterial thin films *in IOP PGS* (2020).

Poster presentation in international conferences

1. Spieser, H., Denneulin, A., Deganello, D., Gethin, D., Bras, J. Hybrid coatings based on cellulose nanofibrils/silver nanowires to develop barrier and antimicrobial properties for active packaging applications in *TAPPI International Conference on Nanotechnology for Renewable Materials* (2018)

2. Spieser, H., Denneulin, A., Deganello, D., Gethin, D., Bras, J. Cellulose nanofibrils/silver nanowires suspensions for the development of barrier properties and antibacterial surfaces in *ACS National Meeting & Exposition* (2019)

Abbreviations

Chemicals and materials

Ag NP	Silver nanoparticle
Ag NW	Silver nanowire
CNF	Cellulose nanofibril
T-CNF	TEMPO-oxidised cellulose nanofibril
TEMPO	2,2,6,6-tetramethylpiperidine-N-oxyl
DI water	Deionized water
PET	Polyethylene terephthalate
PLA	Polylactic acid
IS	Isotonic solution
NB	Nutrient broth
PCA	Plate counting agar
CFU	Colony forming unit
DDPH	2, 2-diphenyl-1-picrylhydrazyl
HPMC	Hydroxypropylmethyl cellulose
MOF	Metal Organic Framework
CuBTC	Copper benzene-1,3,5-tricarboxylate
PGrCuBTC	Printed sensor based on carbon-graphene/CuBTC
IDE	Interdigitated electrode

Methods

FEG-SEM	Field-emission gun scanning electron microscopy
ICP-OES	Inductively coupled plasma – optical emission spectroscopy
OTR	Oxygen transmission rate
WVTR	Water vapour transmission rate
RSA	Radical scavenging activity
TEM	Transmission electron microscopy
AFM	Atomic force microscopy

SEM	Scanning electron microscopy
XRD	X-ray diffraction
XPS	X-ray photoelectron spectroscopy
EDX	Energy dispersive X-Ray
FTIR	Fourier-transform infrared
ATR	Attenuated total reflectance
I/V	Current/voltage
MFC	Mass flow controller

General Introduction

General Introduction

In the second half of the 20th century, post-war Europe saw major economic growth due to national reconstructions associated with high employment, industrial mass production and demographic boom. As a consequence, generalised globalisation raised an intensified international flux of goods, services and information. Advancing technology and ever-increasing worldwide goods consumption has led to the age of plastics. Their relatively easy processability and strong physico-chemical properties such as optical, mechanical or barrier properties make them the perfect candidate for many applications in building and construction, automotive, agriculture, electronics, household leisure and sports, appliances, medical furniture and packaging. In 2018, the production of plastic in Europe reached 64.4 million tons and the packaging sector represents the largest sector demands[1]. The market value of the packaging sector was valued at high as 917 billion US dollar in 2019 and is still rising at an annual growth of 2.8%[2].

In the packaging industry, the largest part concerns food packaging[3] and the overall increasing number and movement of food products however also causes an increasing amount of worldwide food waste. Around one third of the globally produced food is wasted according to the estimations of the Food and Agriculture Organization (FAO) of the United Nations[4]. This represents 1.2 billion tons per year which seems outrageous as the FAO also estimated in 2018 that around 800 million people were chronically undernourished in the world. Food waste is a important challenge for mankind as the world population is expected to reach 10 billion people in 2050 and feeding all of them is a great challenge[5] (**Figure 1**).

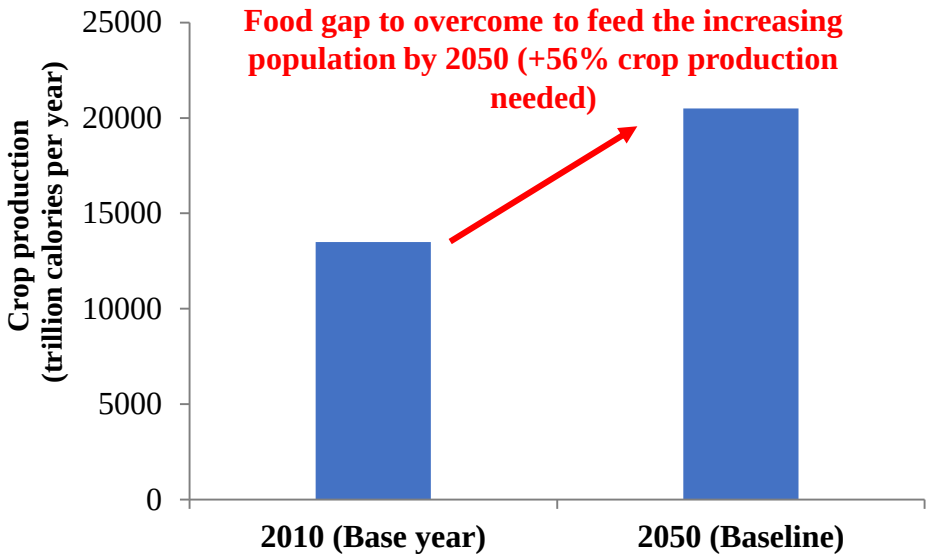

***Figure 1**: Comparative global crop production (trillion calories per year) in 2010 and food gap to overcome compared to the estimative necessary value of crop production in 2050. Data extracted from World Resources Institute. Creating a sustainable food future. (2019)[5].*

Food waste also has huge detrimental impacts on the environment and especially on indicators such as the depletion of limited fossil-based materials, micro-plastic migration in terrestrial and marine environment leading to fauna, flora and human health dangers, and finally to increasing carbon dioxide and greenhouse gas emissions (**Figure 2**).

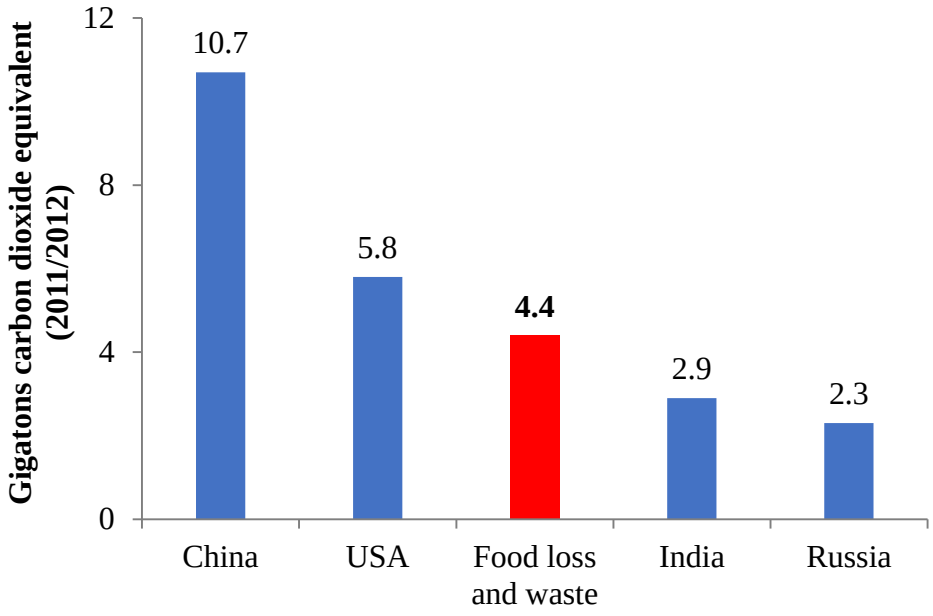

***Figure 2**: Carbon dioxide equivalent of global food waste compared to the highest emitter countries in 2011/2012. Extracted from World Resources Institute. Creating a sustainable food future. (2019)*[5]

The inadequate use of packaging materials leads to food waste and to packaging material waste. Even if continuously increasing, the proportion of recycled plastic for packaging applications only reached 42% in 2019 which corresponds to 7.5 million tons while the rest is either incinerated or disposed in landfills[3]. Several solutions exist to target these issues such as the development of more adequate bio-based materials, a better recyclability or a more efficient and sparing use of packaging materials. The latter could be achieved by developing optimised tailored packaging materials that increase the shelf-life of products and/or give information about the supply chain to identify the critical or malfunctioning steps leading to waste. The development of active and intelligent packaging technologies could then be a tool to fight against the global food and packaging waste.

Active and intelligent packaging technologies aim at controlling and monitoring the packaging atmosphere *via* several mode of actions (**Figure 3**). Active packaging are materials capable of adsorbing or releasing substances within the packaging atmosphere to respond to an internal stimulus, relevant to properties such as antibacterial, antioxidant, carbon dioxide emitters or oxygen/moisture/ethylene scavengers[6]. Intelligent packaging refers to the technologies that can collect, carry and deliver data about the packaging product and contain a wide variety of sensors

and indicators (gas, time/temperature, bacterial) but also interactive system such as radio frequency identification (RFID)[7].

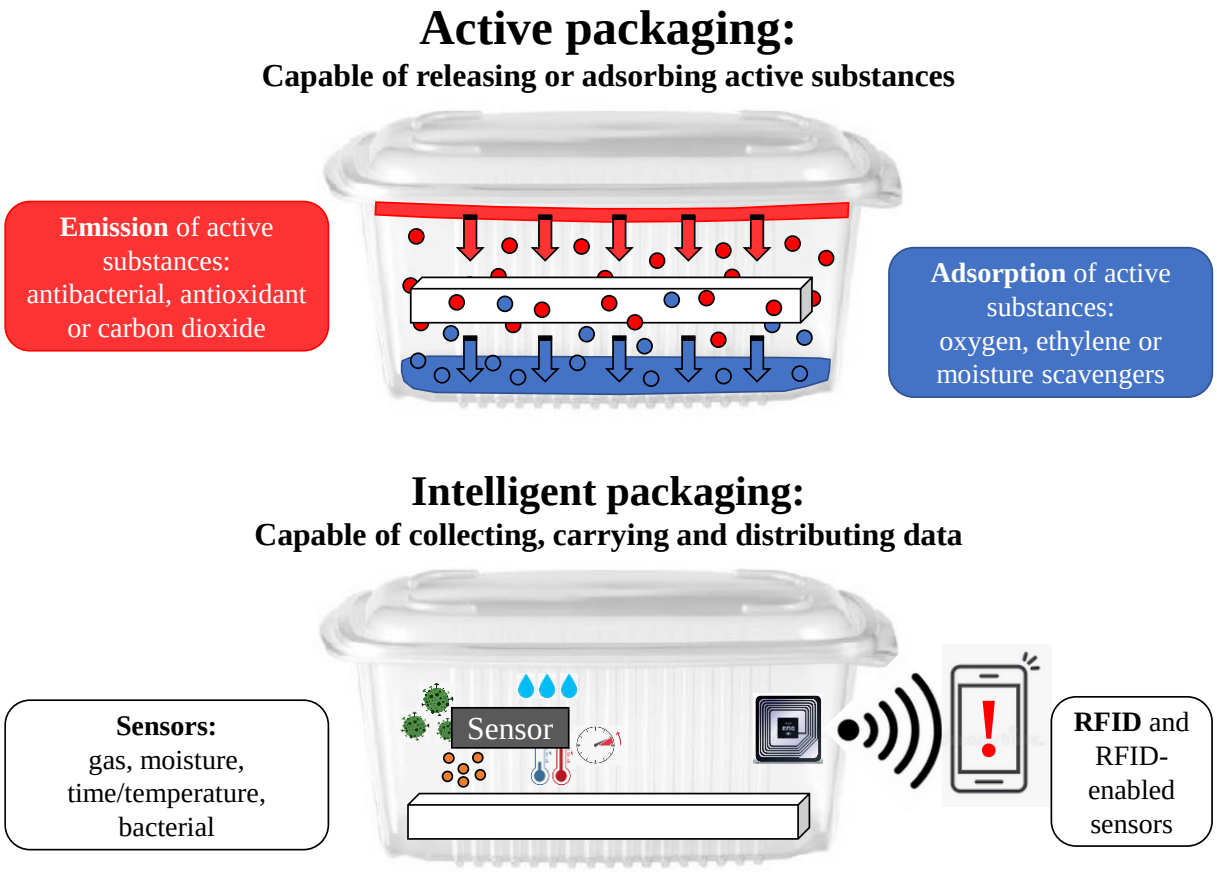

***Figure 3**: Schematic representation of active and intelligent packaging*

Because of the intrinsic nature of packaging materials, one efficient strategy to create active or intelligent properties is to incorporate micro- or nanoparticles (NPs). NPs are usually defined as a particle with at least one of its dimensions at the nano-scale and the term "nanotechnology" was first been used in the 1980s yet the use of NPs by humans can be dated back centuries and even millennia. Indeed metallic NPs were used for a long time in pottery and glass making mainly as coloured pigments[8]. For instance, silver-gold NP alloys were used by the Romans in the 4th century for production of ruby glass and the most known example preserved through time is the Lycurgus cup, bearing remarkable optical properties[9]. However, the study of nanotechnologies as a modern science really started in the 1950s and since Richard Feynman's famous talk "There is plenty of room at the bottom"[10]. Since then, the research and development focused on nanotechnologies has boomed and in the past two decades, led to the commercialisation of a large number of products using nanotechnologies in different field of applications such as electronics, medical and healthcare, waste water treatment and environmental remediation, energy, and also everyday-life materials. The market is still

expanding as the global market for nanotechnologies was valued at 1.055 billion US dollars in 2018 and is expected to reach 2.231 billion US dollars in 2025[11].

Various types of micro- and nanoparticles have been developed in the past decades, including organic, inorganic or hybrid organic-inorganic particles, and also have been introduced in active or smart packaging applications. The wide variety and versatility of micro-nanoparticles enable their tailored use in different applications. For example, metallic nanoparticles (and especially silver) were used extensively due to their antibacterial activity[12] whereas nanocarbon (graphene, carbon nanotubes, etc.) are especially interesting for printed electronics applications mainly because of their electron and thermal conductivity[13]. In the field of organic nanoparticles, nanocellulose is probably one of the more studied materials and includes cellulose nanofibrils or cellulose nanocrystals[14]. Cellulose nanofibrils are produced by mechanical disintegration of a cellulose material and display enhanced optical, mechanical and barrier properties[14] compared to their macro-sized counterpart, making them the perfect candidates for packaging applications[15]. More recently, hybrid organic-inorganic nanoparticles have emerged such as Metal Organic Framework, which present strong potential for analytes separation, adsorption and sensing[16,17]. The research associated with these materials in the packaging field have significantly increased in the past 20 years showing the strong innovation in the sector, as can be seen in **Figure 4**.

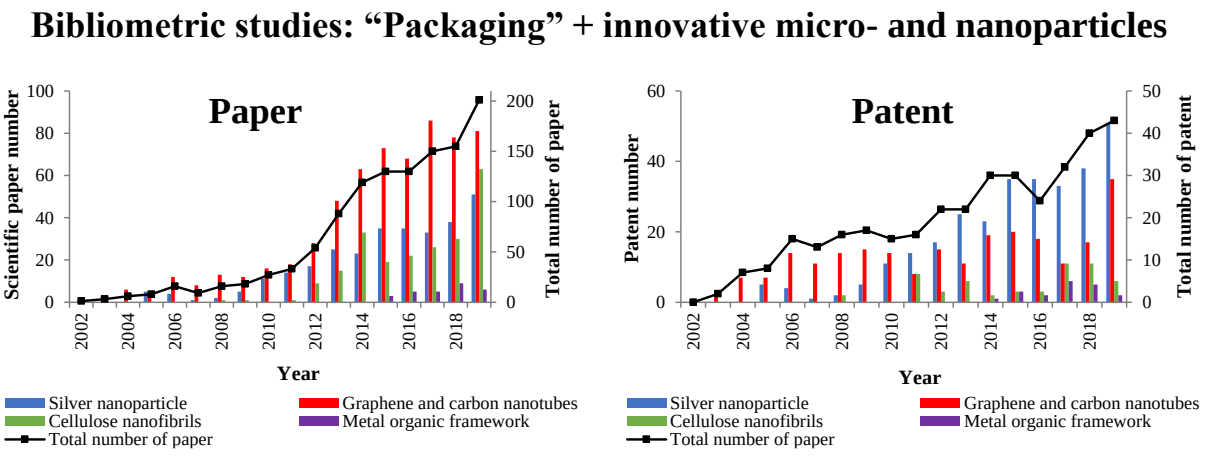

***Figure 4**: Bibliometric studies conducted on **packaging associated with innovative nanoparticle** such as silver nanoparticles, graphene and carbon nanotubes, cellulose nanofibrils and metal organic framework. Extracted from SciFinder with the following descriptors: silver nanoparticle; nanocarbon, graphene, carbon nanotube; cellulose nanofibrils, cellulose microfibrils, nanofibrillated cellulose, microfibrillated cellulose; metal organic framework*

This PhD project called "Smart and Safe Packaging" which started in October 2017 was then dedicated to the development of new active and intelligent packaging technologies based on the use of innovative micro- and nanomaterials. This is a joint project between the Laboratory of Pulp and Paper Science and Graphic Arts (LGP2, Joint Research Unit 5518) of Grenoble (France) and the Welsh Centre for Printing and Coating (WCPC) in the College of Engineering

of Swansea University (United-Kingdom). This project was conducted within the framework of the International Strategic Partnership between the University Grenoble Alpes and Swansea University. Both partners were in constant collaboration and communication to bring their own expertise on active and intelligent packaging technologies to the project.

The aim of the project was to develop new solutions for active and intelligent packaging applications, based on the combination of novel materials. Using these technologies could achieve a better control and extend the shelf-life for the packaged product, the global economic, societal and environmental targets being the reduction of food and materials waste. Specifically, the project was divided into two different approaches on active and intelligent packaging. Firstly, antibacterial packaging materials made of silver nanoparticles and nanocellulose materials were investigated as active packaging technology. Secondly, gas sensors based on Metal Organic Framework materials were developed. The main objectives were to prove the concept and study the feasibility of the developed systems for packaging applications.

This study is then divided into three sections as described in the general scheme (**Figure 5**). **Chapter I** is a literature review that details the general scientific background of the work. The packaging sector is introduced and the existing active and intelligent packaging systems are thoroughly reviewed with a strong emphasis on the technologies and materials relevant to the experimental section of this work, meaning antibacterial packaging and gas sensors.

Chapter II is focused on the development of antibacterial packaging using cellulose nanofibrils and silver nanowires. The first section, **II-1,** is dedicated to the production and characterisation of antibacterial coatings. Several substrates and coating processes, as well as the influence of the coatings on the film properties such as optical, barrier and antibacterial properties, were investigated. Section **II-2** is dedicated to the formulation of inks and their rheological properties for the screen-printing deposition of similar materials, to achieve the localised deposition of antibacterial patterns. Finally, Section **II-3** describes a preliminary investigation of antibacterial (silver migration) and barrier mode of action of the produced materials, modelled at higher scale using the film casting technique.

Chapter III describes the development of gas sensors based on Metal Organic Framework materials and conductive carbon materials. Section **III-1** was especially focused on the preparation of sensors on flexible substrate, and the influence of their formulation on ammonia sensing properties. Section **III-2**, on the other hand, evaluates the capability of the developed sensors to be used to measure humidity.

The manuscript is globally organised in the forms of scientific publications: each sub-section is based on a submitted/accepted scientific publication or presented like one. For a better understanding of the work, additional comments were added in ***grey/italic/bold*** to guide the reader through this thesis.

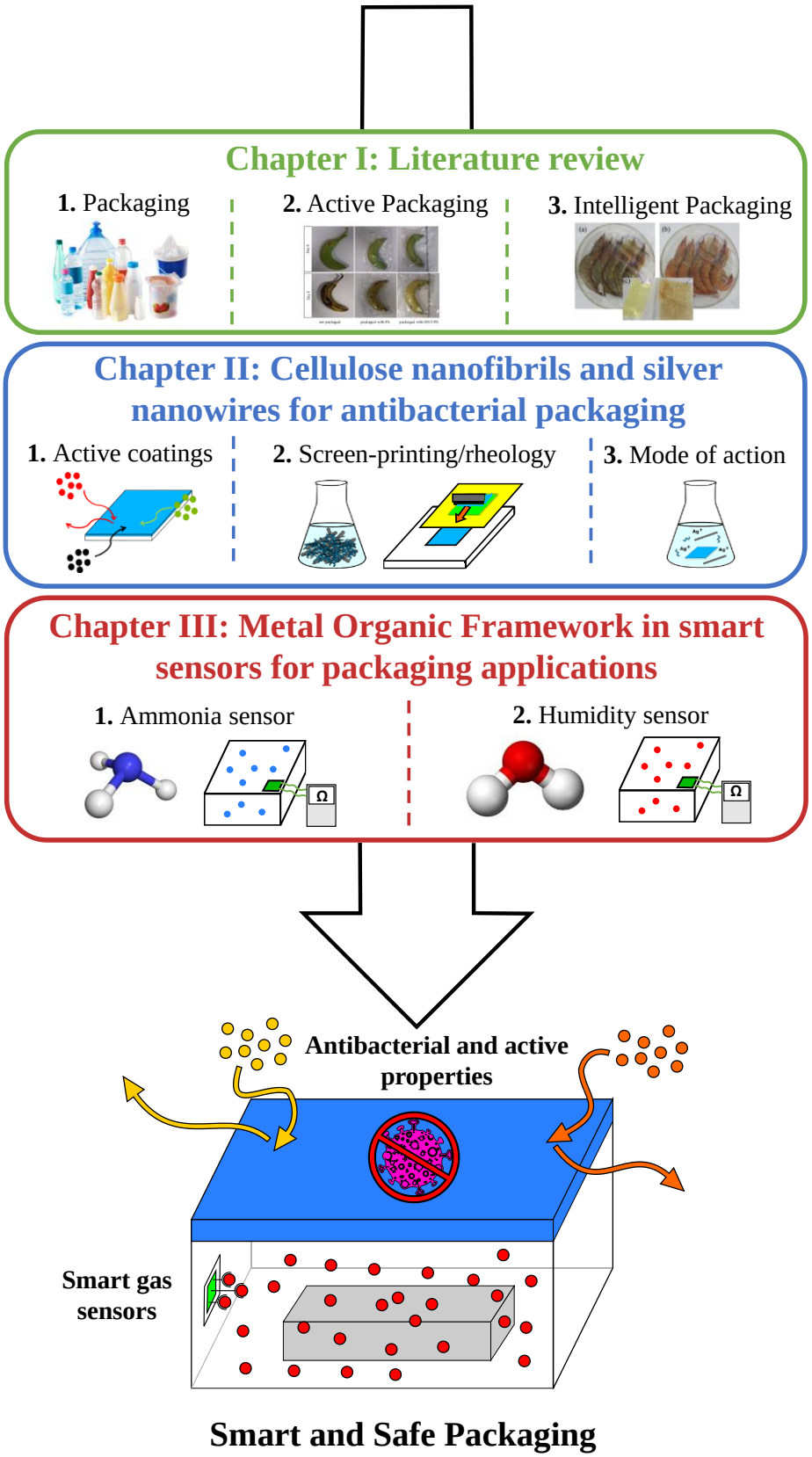

***Figure 5**: Scheme summarising the general organisation of the project. Images respectively reproduced and adapted from www.actu-environnement.com (accessed on 22.04.20), from Tas et al. (2017) with permission from Springer Nature (Copyright 2017)[18] and from Ma et al. (2017) with permission from Elsevier (Copyright 2017)[19]*

References

1. PlasticsEurope. *Plastics - the Facts 2019*.
2. The Future of Global Packaging to 2024. *Strategic forecasts for global packaging to 2024*.
3. All4Pack. *Worldwide packaging*. (2018).
4. Food and Agriculture Organization of the United Nations. *State of food and agriculture 2019: moving forward on food loss and waste reduction.* (2019).
5. World Resources Institute. *Creating a sustainable food future*. (2019).
6. Yildirim, S. *et al.* Active Packaging Applications for Food. *Comprehensive Reviews in Food Science and Food Safety* **17**, 165–199 (2018).
7. Yousefi, H. *et al.* Intelligent Food Packaging: A Review of Smart Sensing Technologies for Monitoring Food Quality. *ACS Sens.* **4**, 808–821 (2019).
8. Colomban, P. The Use of Metal Nanoparticles to Produce Yellow, Red and Iridescent Colour, from Bronze Age to Present Times in Lustre Pottery and Glass: Solid State Chemistry, Spectroscopy and Nanostructure. *JNanoR* **8**, 109–132 (2009).
9. Freestone, I., Meeks, N., Sax, M. & Higgitt, C. The Lycurgus Cup — A Roman nanotechnology. *Gold Bull* **40**, 270–277 (2007).
10. Feynman, R. P. Plenty of Room at the Bottom. (1959).
11. Nanotechnology Market Size, Share and Trend | Industry Forecast -2025. *Allied Market Research* https://www.alliedmarketresearch.com/nanotechnology-market.
12. Tang, S. & Zheng, J. Antibacterial Activity of Silver Nanoparticles: Structural Effects. *Advanced Healthcare Materials* **7**, 1701503 (2018).
13. Saidina, D. S., Eawwiboonthanakit, N., Mariatti, M., Fontana, S. & Hérold, C. Recent Development of Graphene-Based Ink and Other Conductive Material-Based Inks for Flexible Electronics. *Journal of Elec Materi* **48**, 3428–3450 (2019).
14. Dufresne, A. *Nanocellulose: From Nature to High Performance Tailored Materials*. (Walter de Gruyter, 2013).
15. Hubbe, M. A. *et al.* Nanocellulose in Thin Films, Coatings, and Plies for Packaging Applications: A Review. *BioResources* **12**, 2143–2233 (2017).
16. Li, Y. *et al.* Advances of metal–organic frameworks for gas sensing. *Polyhedron* **154**, 83–97 (2018).
17. Li, B. *et al.* Emerging Multifunctional Metal–Organic Framework Materials. *Advanced Materials* **28**, 8819–8860 (2016).
18. Tas, C. E. *et al.* Halloysite Nanotubes/Polyethylene Nanocomposites for Active Food Packaging Materials with Ethylene Scavenging and Gas Barrier Properties. *Food Bioprocess Technol* **10**, 789–798 (2017).
19. Ma, Q., Du, L. & Wang, L. Tara gum/polyvinyl alcohol-based colorimetric NH3 indicator films incorporating curcumin for intelligent packaging. *Sensors and Actuators B: Chemical* **244**, 759–766 (2017).

Chapter I

Literature Review

Table of content – Chapter I

Introduction to Chapter I

This first chapter aims at covering the global context of this PhD project, both for experts and non-experts in the field. An extensive number of references, figures, tables and definitions were consulted and cited to support the different claims. Additional comments are provided in "***grey/bold/italic***" throughout the text to help the readers understand the strategic choices of this literature review as well as to link the different sections to the experimental section of the project.

The first section presents **packaging** in a global way first in terms of historical, economic and social aspects. Innovations in the field, such as active and intelligent packaging as well as the polymeric materials classically used and their surface processing are introduced.

The second section describes **active packaging** technologies such as emitters (antibacterial, antioxidant, carbon dioxide emitter) and scavenger systems (oxygen, ethylene, water). Materials that are relevant to the experimental section of this work (silver nanoparticles and cellulose nanofibrils) are especially reviewed for their properties that are relevant to antibacterial packaging applications.

The last section is focused on the different existing **intelligent packaging** technologies such as sensors, indicators and interactive systems. A specific focus is placed on gas sensors and especially gas sensors based on Metal Organic Frameworks materials that are relevant to the experimental section of this work.

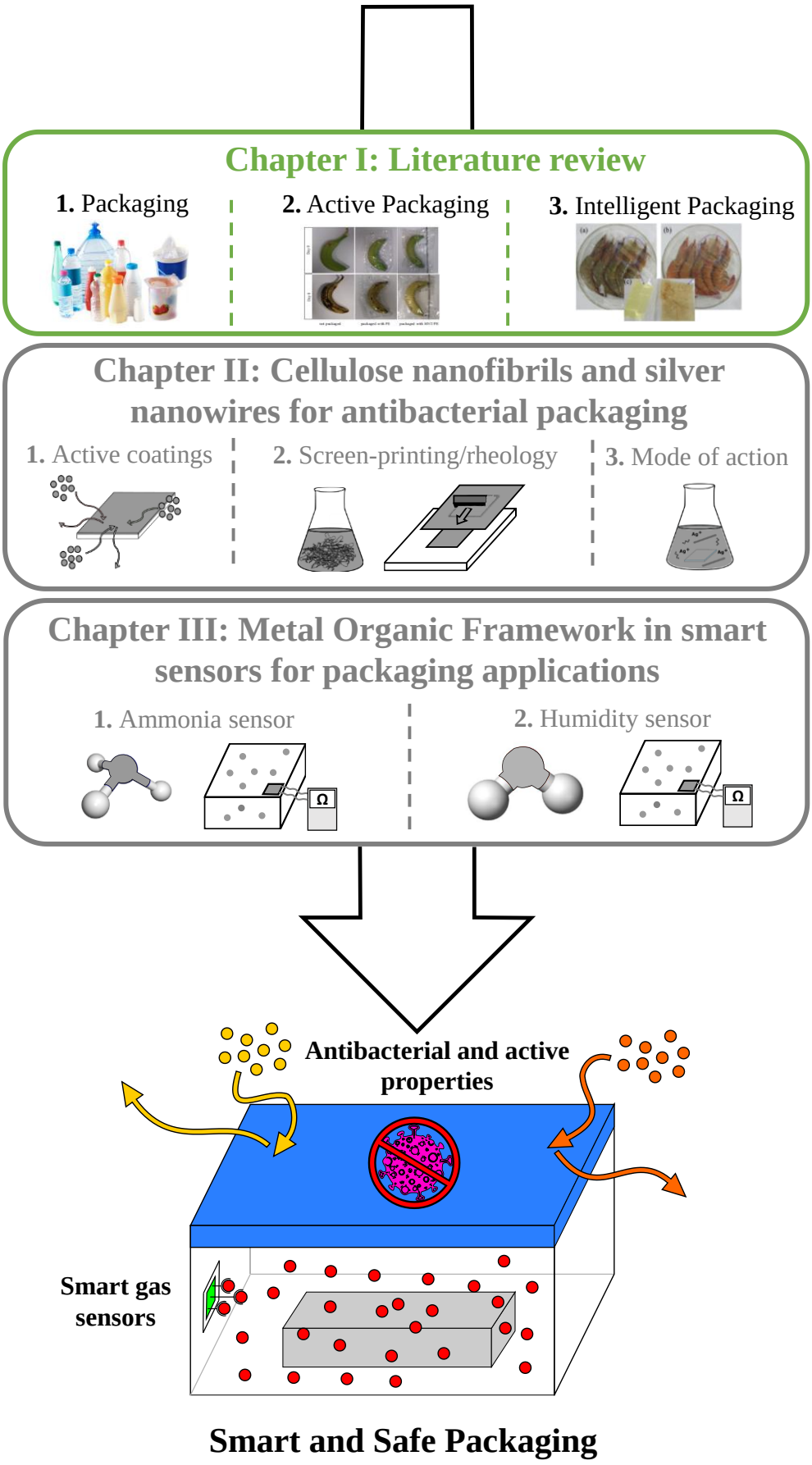
Chapter I: Literature review
1. Packaging
2. Active Packaging
3. Intelligent Packaging
Chapter II: Cellulose nanofibrils and silver nanowires for antibacterial packaging
1. Active coatings
2. Screen-printing/rheology
3. Mode of action
Chapter III: Metal Organic Framework in smart sensors for packaging applications
1. Ammonia sensor
2. Humidity sensor
Ω
Ω
Antibacterial and active properties
Smart gas sensors
Smart and Safe Packaging

1. Introduction to Packaging

This first section discusses the general concepts associated with packaging: a short description of its history and main packaging products used today, society's requirements and needs for packaging materials, and finally the latest innovations in the field. After that, general packaging materials and surface processing technologies are also detailed to introduce the components and processes relevant to the experimental section of this work.

1.1. Packaging context

Throughout the ages, food has always been a vital requirement that has raised critical challenges not only from the collection, production or manufacturing but also from the conservation and transport points of view. Packaging has been used for a long time to help transport and conserve food products longer while still being safe to consume. In China, tree bark for instance was used more than two thousand years ago as flexible packaging technique[1]. Since then, the packaging sector has grown significantly and with today's unstoppable globalisation and online shopping sector, every manufactured product is packaged at some point in its supply chain. The packaging sectors target all different kinds of product and traditionally, packaging materials include glass, metals, paper, cardboard and plastics (**Figure I-1**). Packaging materials are often classified into different categories known as primary, secondary and tertiary packaging. Primary packaging refers to packaging with direct contact with the product whereas secondary packaging refers to packaging which protects individual product units mainly for shelf display. Secondary packaging is also useful for branding and logistics. Finally, tertiary packaging refers to the protection of secondary packaging during storage and transport.

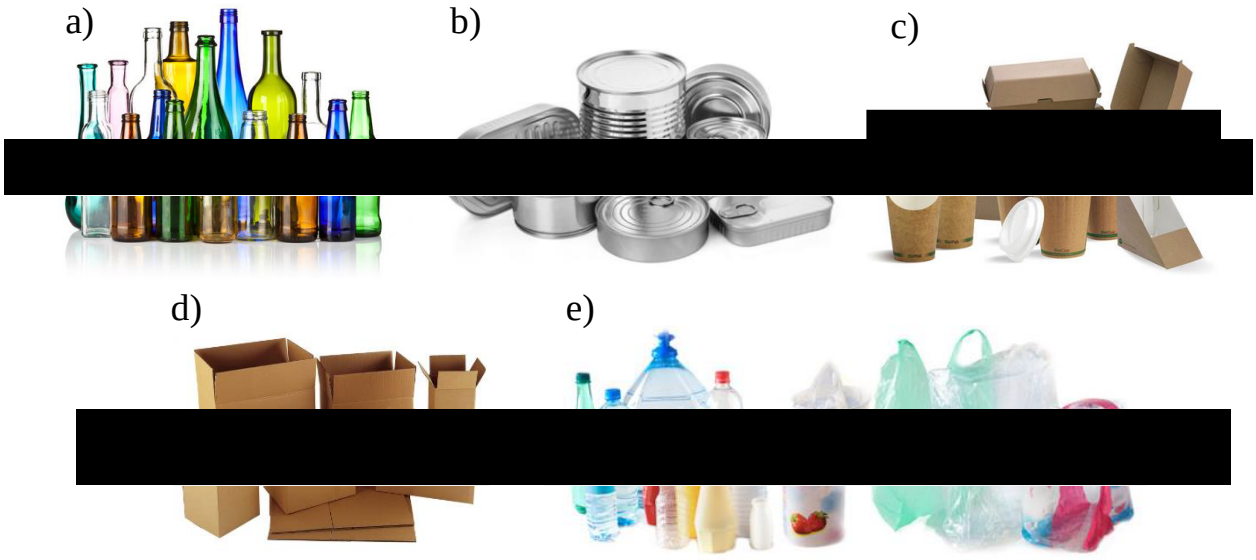

***Figure I-1**: The different types of materials used for packaging applications with a) glass, b) metal, c) paper, d) cardboard and d) plastic packaging. Images respectively extracted from: www.packaginginnovation.com, www.bccourier.com, www.cwpdistributors.com, www. parrs.co.uk, and www.actu-environnement.com. **All web materials in this document were accessed on 22.04.2020**.*

While having been produced for centuries, glass containers have been largely commercially deployed in the 20th century because of innovation in the industrial glass making process enabling their large volume production. They are commonly used for liquid packaging. Metal packaging is another type of rigid packaging that is used today mainly for food packaging applications. The field saw a renewed interest in the 1950s with innovations linked to aluminium-based product such as foil and especially cans. Flexible materials remain the primary choice for packaging applications and are based on polymeric materials. Polymeric materials can either be biobased such as paper and cardboard or from petroleum resources such as classical plastic materials (polyethylene, polypropylene, polyethylene terephthalate, etc.)

The Food and Agriculture Organisation (FAO) of the United-Nations publishes, each year, dreadful statistics about food consumption and agriculture around the world. The overall earth population is ever increasing and expected to reach 10 billion people in 2050[2]. Feeding this ever-increasing population is one of the great challenges that mankind has to face and is already struggling with today. In 2018, 822 million people were considered as chronically undernourished which is almost 40 million more than in 2015[3]. Quality and quantity are not to be confused yet the FAO estimates in the same report that 2 billion people are struggling to get food in sufficient quantity and decent quality. At the same time, global food waste is also growing. Around 15% of the amount of food produced is lost even before reaching the supermarkets and this depends on the global location as for instance this food loss indicator is significantly lower for Australia and New Zealand than for central and southern Asia (**Figure I-2**). This is due to historical and cultural reasons but also the global development stage of the referenced countries. The numbers also depend on the type of food waste explaining the drastic

difference depending on the indicators chosen. By integrating steps after retail corresponding to the consumer purchase and use, it has been estimated that one third of food produced globally is wasted, corresponding to 1.2 billion tons per year[3].

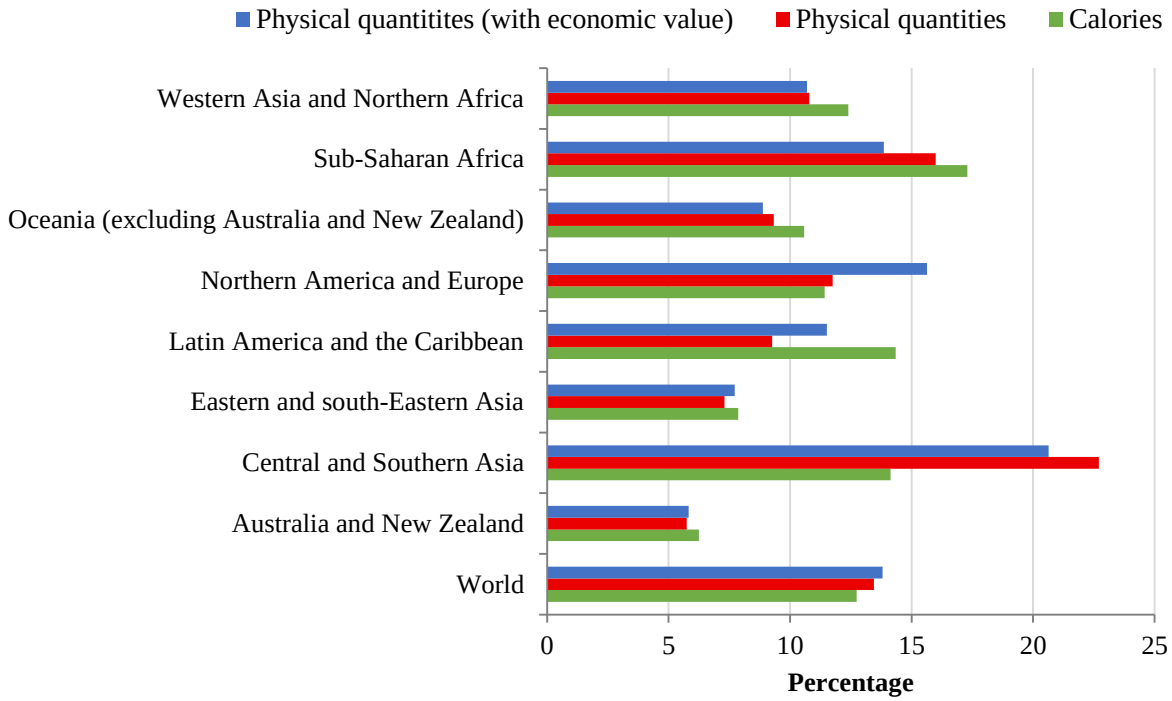

***Figure I-2**: Food loss statistic (%) in the world in 2016 in physical quantity indexed by economic value, physical quantity or by equivalent calories. Data extracted and adapted from Food and Agriculture Organization of the United Nations. State of food and agriculture 2019: moving forward on food loss and waste reduction. (2019)[3]. Accessed online on the 22.04.2020*

A striking metaphor is that if the carbon dioxide emission associated with the global food waste were compared to the carbon emissions of countries, it would be in third place behind China and the United-States[2]. Food waste has detrimental impacts not only on people that do not have access to food products, but also on the environment and economic sectors. The benefits of reducing food waste then includes reducing global emissions and resources use, together with money/resources savings for consumers and producers. One solution to tackle food waste is working on more efficient and tailored packaging for food products. This could also tackle another public issue that is food poisoning by delivering safer food product to the consumers. The main purpose of packaging is indeed to increase the shelf-life of the food products which reduces the amount of global food waste. Moreover, the use of petroleum sourced plastic packaging can have harmful effects on the environment yet it has been shown by Life Cycle Analysis (LCA) that in some cases, the impact of the packaged food product is higher than the packaging[4]. A compromise should then be found between the reduction of food waste by using efficient packaging solution and the environment impacts linked to those packaging technologies.

The packaging industry market value has been estimated at 917 billion US dollar in 2019, is still expanding and is expected to reach 1050 billion by 2024 with an annual growth of 2.8%[5]. Food packaging is by far the most important section of the packaging market. The main role of packaging is to protect its content from the external environment and in many instances, packaging is a sealed container (**Figure I-3**). Damage to the packaged product can first occur via physical interaction such as mechanical stress principally during the storage and delivery step in the supply chains. Chemical interactions also have a detrimental effect on the quality of the packaged product, especially for food packaging where oxidation or moisture absorption linked to a gaseous atmosphere and light-induced process is common. Finally, bacterial contamination and growth can also alter the properties and quality of the packaged product. The boom in the development of plastic materials in the second half of the 20th century also promoted new applications for packaging, especially linked to advertising, brand image and communication. Over the past 20 years, a lot of studies have been dedicated to pushing the properties of packaging materials even further and many of more recent innovations have targeted the field of active and intelligent packaging.

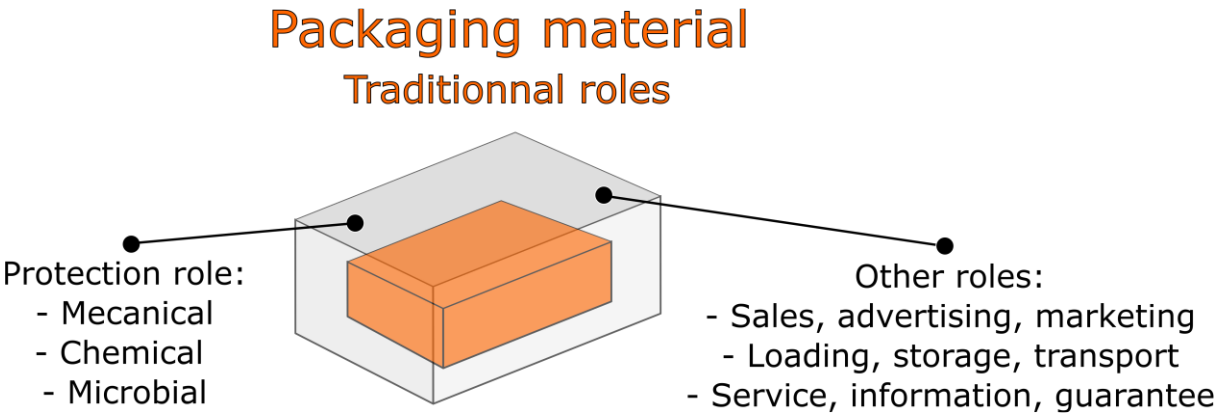

***Figure I-3**: Traditional roles for packaging materials*

The purpose of active and intelligent packaging technologies is to incorporate within the packaging material solutions that offer enhanced quality and safety. Active packaging adsorbs or release substances that can control several parameters in the internal packaging atmosphere such as the odour, aroma, flavour or colour of the packaged products, they can also reduce bacterial contamination and growth or ripening processes. Intelligent packaging aims at acquiring and delivering data that can be beneficial for supply chain or cold chain monitoring with real-time information about the shelf-life of the packaged products. It can also be used for communication purposes to customers and to guarantee authenticity. Various commercial products using active and intelligent packaging technologies are already on the market[6] and the European Regulation (EC) No 1935/2004 concerning food contact materials[7] was supplemented with a specific regulation (EC) No 450/2009 concerning active and intelligent packaging in 2009[8] (**Figure I-4**).

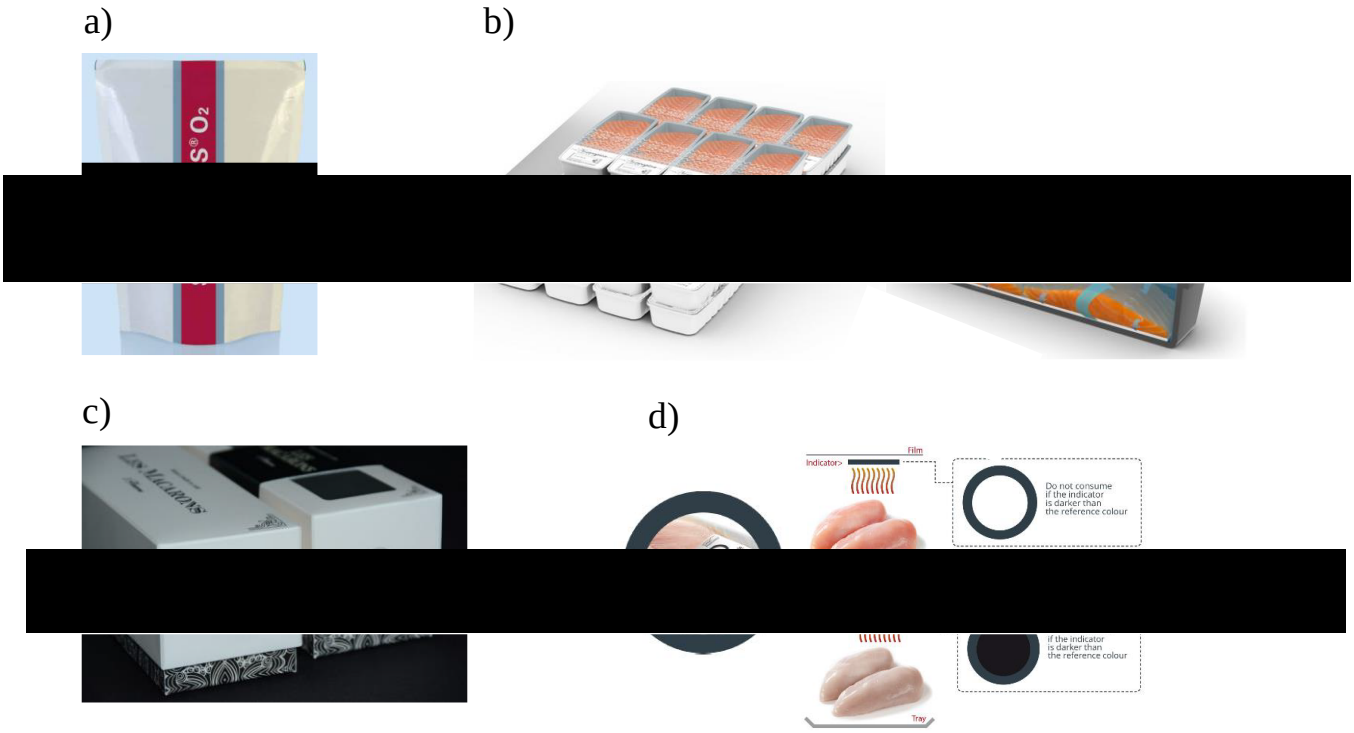

***Figure I-4**: Examples of commercial active packaging technologies with a) Oxygen scavenger SHELFPLUS® O2 (Albis Plastic), b) SuperFresh CO_2 emitter pad (VdP International) and intelligent packaging technologies with c) RFID tags (Stora Enzo) and d) FreshCode freshness indicator (Kao Chimigraf). Images respectively extracted from the companies websites, accessed online on 22.04.2020*

A lot of work has been carried out in the past 10 years to take active and intelligent packaging innovations from academic laboratories into industry, with dedicated initiative such as the European Cooperation in Science and Technology (COST) action called ActInPak[9]. The overall long-term impact of active and intelligent packaging solutions on food waste and food loss indicators still need to be globally assessed.

Today, packaging remains a key player in dealing with the global food waste challenge and has evolved from the sole purpose of physical barrier to multifunctional materials. The next section focuses on polymer-based packaging, the advantage they present and challenges they face both for petroleum-based and bio-based materials.

1.2. Polymer-based packaging materials

Polymer-based packaging materials can be either sourced from natural sources or from petroleum sources. The latter are predominant and often summarised as “plastics”. In the history of packaging materials, plastics are the latest to be discovered. The first experimentation started in the 19th centenary with synthesis of polyvinyl chloride or polystyrene but the real boom happened after the second world war. The term “plastics” usually refers to synthetic polymeric materials prepared from a chemical monomer mainly by polycondensation or polyaddition. The main physicochemical properties of plastics have made them essential in our society and

especially in packaging applications. The packaging sector is the largest market for plastic materials and represents 40% of the plastic converter industry demand[10].

The so-called plastics are indeed easy to shape into the desired form, are flexible, light, resistant to chemical but also of low cost. Such materials are often separated into two different categories which are thermosets and thermoplastics[11]. Thermosets are polymers that when heated undergo an irreversible reaction to take solid form. Once shaped into the desired form, it is very difficult to modify their 3D structure by either heat or pressure. Due to their inherent characteristics, thermoset polymers are commonly not used in packaging applications but more in construction, automotive or energy sector. Thermoset polymers include polyurethane, epoxy resins, unsaturated polyester, vinyl ester, silicon, or acrylic and phenolic resins. Thermoplastics on the other hand soften at high temperature and can easily be shaped to desired forms. They harden when cold but the process can be repeated several times. Thermoplastic polymers include polyethylene (PE) either low-density or high density (LDPE, HDPE), polypropylene (PP), polyvinyl chloride (PVC), polyethylene terephthalate (PET), polystyrene (PS), polyamide (PA) and others. In the packaging field, the most used polymers are PP, PE, PET, and PS which present different properties and can be used in different specific applications (**Table I-1**).

***Table I-1**: Polymers classically used for packaging, their properties and specific applications*

Polymer	Properties	Applications
PP	Good barrier properties to water, transparent, thermal stability	Tubs, microwavable containers
Low-density-PE	Flexible, permeable to gas, sealable, strong, low-cost	Bottles, tubes, bags
High density-PE	Stiff, permeable to gas, strong, low-cost	Bottles, lids
PET	Good barrier properties to gas, good thermal and chemical stability, transparent, light	Containers (bottle, jars, etc.), trays and bag
PS	Hard, brittle, clear	Containers

Plastic packaging materials offers great physicochemical properties. They are however not biodegradable and can cause environmental issues. The main concern linked to the improper disposal of plastics waste is their partial degradation leading to plastic micro- or nanoparticles release in the environment whether terrestrial or aquatic[12,13]. These particles induce environmental concerns linked to detrimental impacts on flora and fauna, but also on human health. Theoretically and by definition, thermoplastics are recyclable. However, packaging products are often complex and made with a combination of different materials of which

separation is, in most of the cases, the principal issue[14]. There were 17.8 million tons of plastics collected post-usage in Europe in 2018, 42% was recycled, 33% was used for energy recovery and 18% was disposed in landfill. This is a positive trend because in 2006, 48% ended up in landfills[15].

Two main strategies have been effective to tilt the balance of these compromises toward the environmentally friendly side: recycling of petroleum-sourced packaging and the use of bio-based packaging technologies. Developing new enzymatic degradation processes is the most promising route for fossil-based polymer recycling[16]. More recently, fully or partially bio-based version of conventional plastic polymers have also been developed such as bio-polyethylene terephthalate (bio-PET), bio-polypropylene (bio-PP) or bio-polyethylene (bio-PE). However, to conclude on the environmental benefits of using such materials, it is important to consider to their full life cycle. They could indeed present greater environmental impacts than their petroleum-based counterparts due to more complex chemical synthesis and lower yields of production. The occupation of arable land for the production of the starting chemicals in the detriment of food production, is also one of the challenges they face.

Historically, bio-based materials used for packaging are based on cellulose and its derivatives. Before the emergence of plastics and in the second part of the 19th century, paper bags with cellulose sourced from wood pulp were developed. From then, corrugated paper and cardboard technologies emerged and started to be produced industrially by the beginning of the 20th century. Paper-based technologies used for packaging applications include Kraft paper (bags for flour, sugar, etc and wrappings), sulphite paper (bags, wrappings but less strong than Kraft paper) and greaseproof or parchment paper (oil-based paper). The demand for paper and cardboard technologies suffered from the boom of plastic but over the past 20 years, new technologies based on cellulosic materials have found great interest in the scientific community. Nanocellulose for instance, defined as cellulose nanoparticles, has shown great promise in packaging applications due to their better barrier properties than regular paper materials[17]. Chemical modifications of cellulose have also been a field of interest in the scientific community principally to increase its processability, such as cellulose ethers (methyl cellulose, carboxymethylated cellulose, hydroxypropyl methyl cellulose, hydroxypropyl cellulose), or cellulose esters (cellulose acetate, cellophane)[18]. Other natural polysaccharides that include starch, alginate, chitosan, or pectin have also been deeply studied for packaging applications and especially for the preparation of edible films for food packaging[19]. Bio-based polymers coming from microbial sourced monomers also display promising properties for packaging applications. Polylactic acid (PLA) and polybutylene succinate (PBS) can be synthesized respectively from lactic acid and succinic acid produced by bacterial fermentation, whereas polyhydroxyalkanoates (PHA, PHB) are directly produced by bacterial fermentation[18]. Finally, even though they are not polymers, natural lipids and proteins such as gluten, gelatin, soy proteins, zein, casein, or whey are also promising bio-based materials for packaging

applications[20]. The different polymer used for packaging applications and reviewed in this section are summarized in the **Figure I-5**.

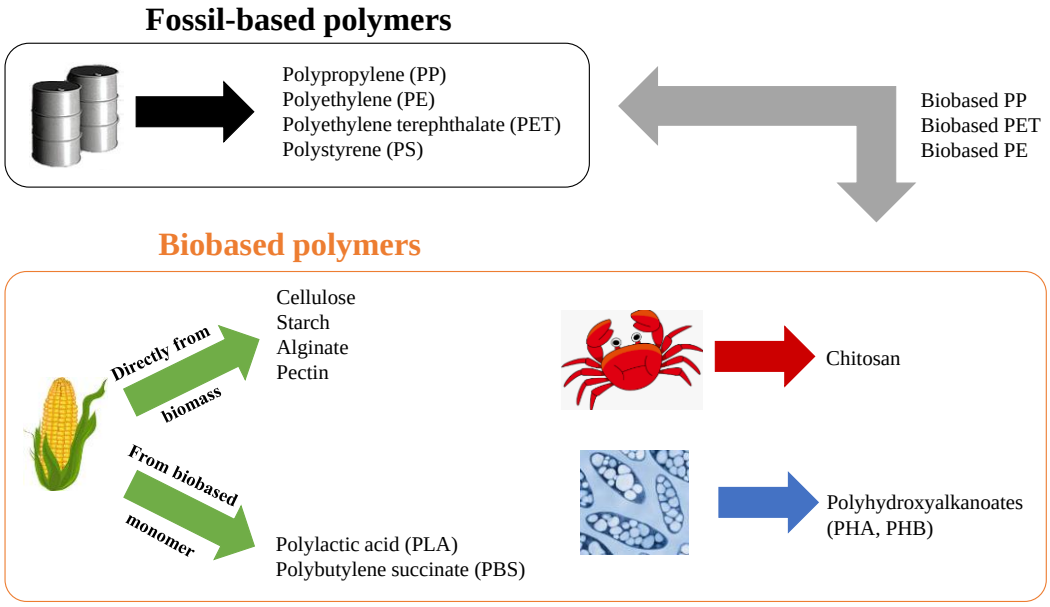

***Figure I-5**: Polymers used for packaging applications classified into biobased and fossil-based*

1.3. Surface processing of packaging materials

The surface of packaging materials, especially films are often processed by printing to offer communication about the products or the brand (logo, nutritional information, technical data, etc.) and for aesthetics reasons. Coating processes are also used to provide a new or reinforced surface function such as optical properties (gloss, shine, UV blocker), enhanced barrier properties (grease- or water-proof) or for active and intelligent packaging applications. The main printing processes used for packaging applications are flexography, offset, gravure, screen and inkjet (**Figure I-6**).

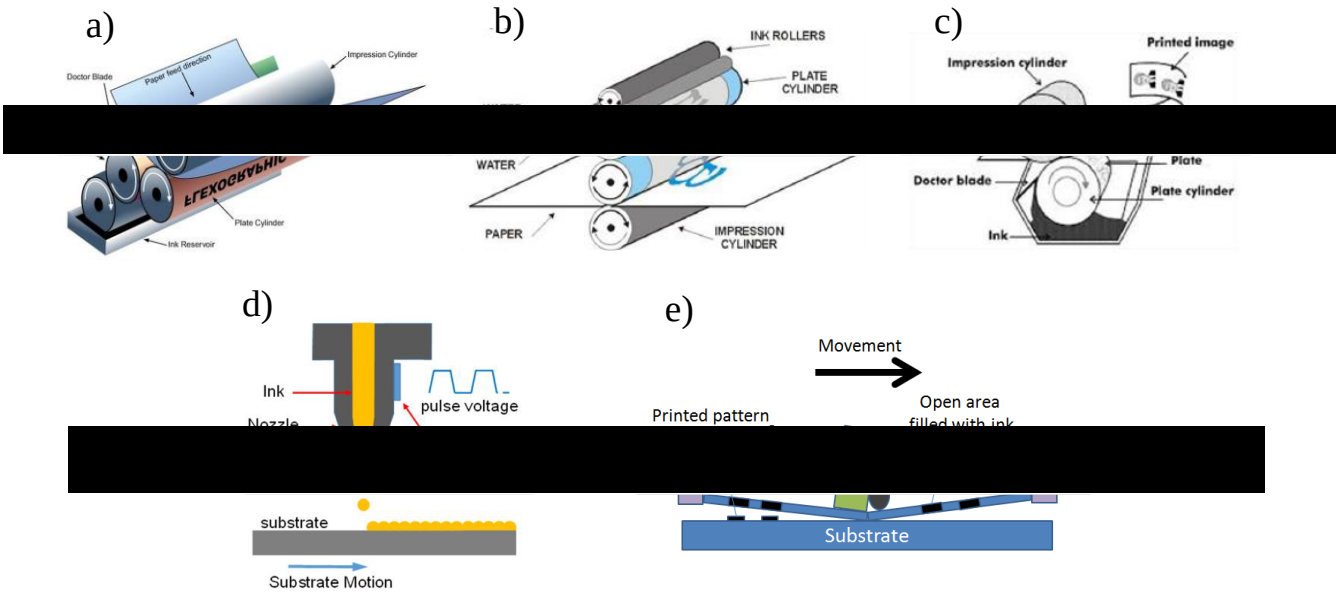

***Figure I-6**: The different printing process used for packaging applications with a) flexography, b) offset printing, c) rotogravure, d) inkjet and d) screen printing. Images respectively extracted from: printsaverepeat.com, www.savanahdesign.com, www.postpressmachines.com, www.helmholtz-berlin.de, and www.emballasjeforeningen.no, accessed online on 22.04.2020*

The concept with conventional high-speed printing processes such as flexography, gravure or off set is the contact involving pressure between the desired substrate and a printing form (or image carrier) which is either an engraved cylinder for gravure, a relief photopolymer cylinder for flexography or a printing plate for offset. For the screen-printing process, the screen mesh is a negative of the pattern to print: the open area corresponds to the design to print. The screen is attached on a frame and the printing is carried out by passage of a squeegee over the screen that forces the ink through the open area only and print on the substrate below. Inkjet is however a printing technique involving no contact between the substrate and the printing head. Droplets are ejected from the printing head either by physically changing the printing head orifice size, or by piezoelectric or thermal excitation and the printing pattern is personalized using digital data. All of these different printing processes have different specifications and requirements and basic print volume/cost/quality. A qualitative comparison is shown in **Table I-2**.

***Table I-2**: Qualitative comparison between the different printing processes used for packaging applications (printing volume, approximate cost per print and print quality)*

	Flexography	**Offset**	**Gravure**	**Screen**	**Inkjet**
Volume	+++	+++	+++	+	+
Cost/print	++	+	+	++	+++
Quality	++	++	+++	++	+++

Coating processes are used to deposit uniformly on the surface of the packaging materials a thin layer of active materials. Classic coating technologies at a small laboratory scale include dip coating, spin coating, slot die, blade coating, and bar coating. In the bar and blade coating process, the solution is deposited on the substrate (in excess) and a bar or blade is passed over the solution to spread it. In the case of the bar coating, different bars are used to deposit different thickness and they are referred as Meyer bar. Meyer bars are wire wound bars and the diameters or the wire winding dictates the quantity deposited. More recently, spin coating has been shown to deposit uniformly very thin layers, by depositing the solution (small volume) on the substrate immobilised on a rotating plate: the centrifugal force then distributes the solution on the substrate. However, this technique is not suitable for large surface and thus not for packaging applications. Dip coating is also considered as a coating process but the concept is even simpler: the object to coat is immersed in the active solution, then retrieved and capillary forces are doing the work. At a larger scale, slot die coating consists of injecting the solution under pressure through a narrow coating head to directly coat on the substrate. **Figure I-7** summarises the different coating processes addressed.

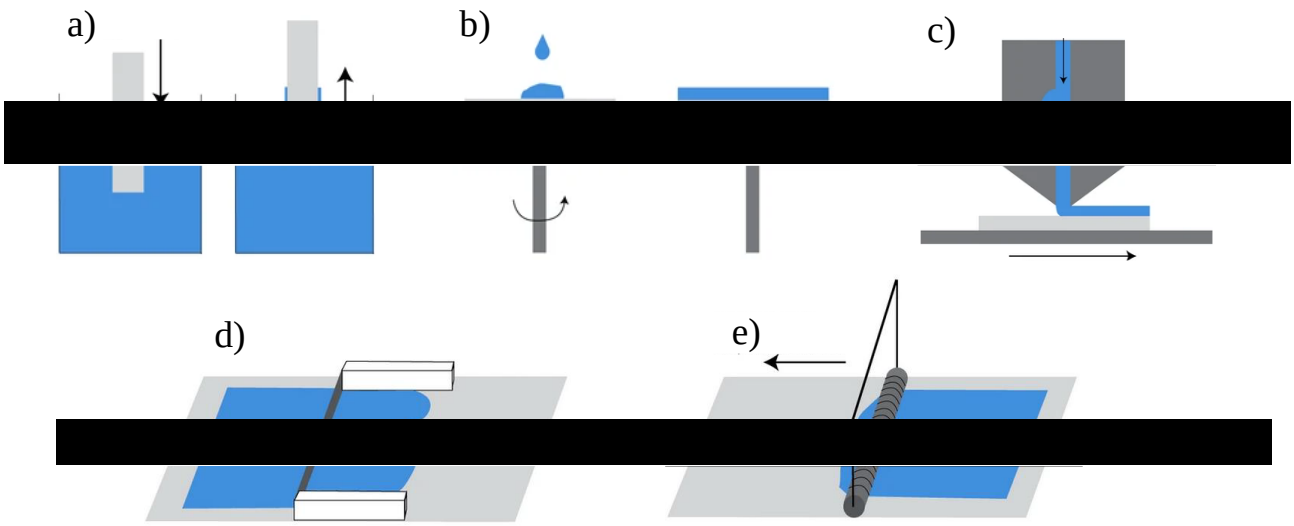

***Figure I-7**: The different coating processes with a) dip coating, b) spin coating, c) slot die, d) blade coating and e) bar coating. Images extracted from www.ossila.com, accessed online on 22.04.2020*

At a larger scale, printing processes may be used to coat packaging materials by adapting the image carrier to deposit a uniform layer.

In the context ok packaging (historical, social, materials, innovations), the polymeric materials used for packaging applications as well as the printing and coating processes involved in the surface modifications of packaging were reviewed in this section. The next section focuses more deeply on active packaging and especially the different technologies commonly used today both in academic research and industrial products.

2. Active packaging

The section reviews the main active packaging technologies and a special focus is placed on antibacterial packaging because a significant part of the experimental study of this work was dedicated to the development of antibacterial packaging using a hybrid system based on silver nanowires and cellulose nanofibrils.

Active packaging refers to the technologies that can interact with the internal atmosphere of the packaging by either emitting or adsorbing various substances. The different technologies are divided into two categories: emitters and scavengers. The purpose of emitters is to release an active substance whether directly in the food product, in the packaging materials or in the internal atmosphere of the packaging. Scavengers aim at eliminating substances that can be unwanted (odour, humidity, gas, etc.) in the internal atmosphere of packaging.

2.1. Emitters

Active packaging emitters technologies include mainly antimicrobial, antioxidant or carbon dioxide release systems.

2.1.1. Antimicrobial

1. General overview

The role of antimicrobial packaging is to fight against food bacterial, viral and fungal contamination to limit the spoilage of the packaged product and to increase their shelf-life. Their activity mainly focuses on bacteria growth inhibition and different classes of antibacterial substances have been used for active packaging applications, such as antibacterial polymer, essential oils or other natural extracts, enzymes or bacteriocin (toxin produced by bacteria), organic acids or nanoparticles. The different categories of antimicrobial materials used for packaging applications are summarised in **Figure I-8**.

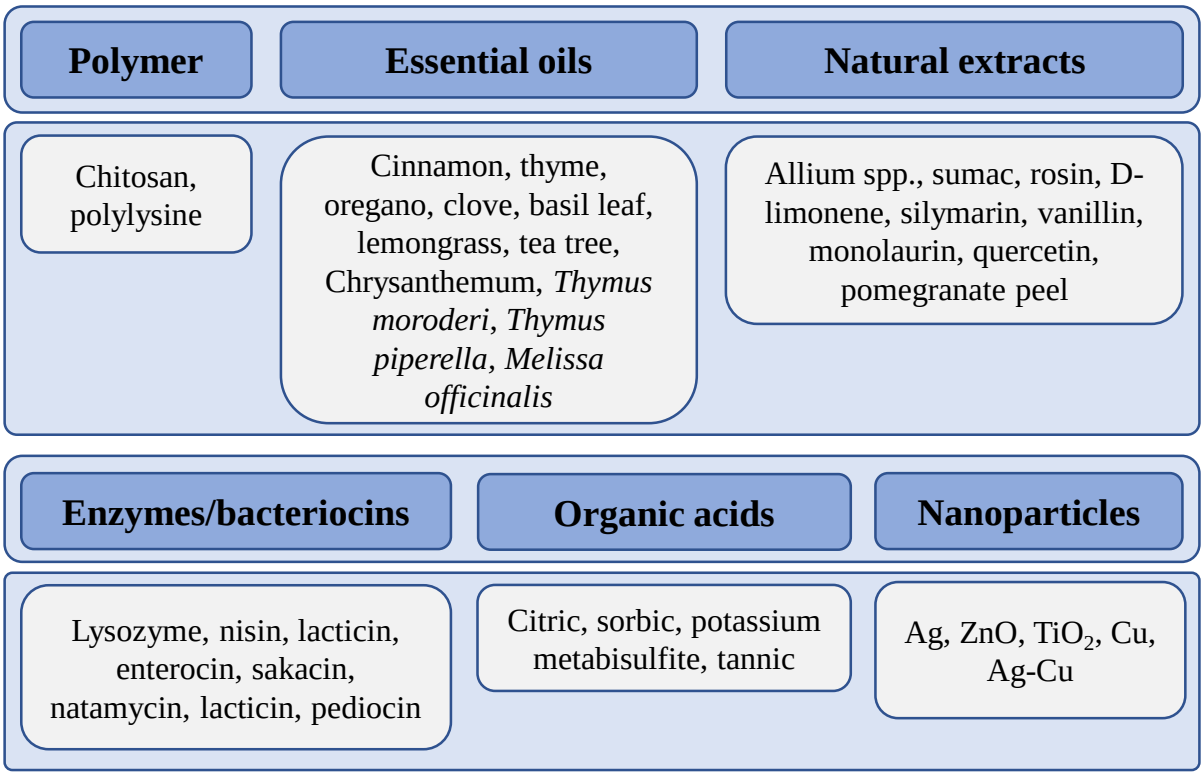

***Figure I-8**: General classification of antimicrobial materials used for packaging applications and specific substances involved*[21–31]

Essential oils (EOs) have been widely used as several exhibit antibacterial activity. They are extracted from aromatic plants and are a complex mixture of a large number of chemical compounds. The antibacterial activity of EOs depend on their nature, but the main established mode of action is toward the bacteria cell membrane. Because of their high hydrophobicity, EOs are able to interact with lipids in cell membrane and modify its permeability[32]. The principal difficulty associated with the use of essential oils in packaging applications is, first, the change in the organoleptic properties of the food that can be induced because of the strong sensory properties of EOs. The high hydrophobicity and the volatility of EOs can also be a serious difficulty to overcome to process them into active packaging technologies[33]. The antibacterial activity and mode of action of natural extracts is close to the one of EOs, only their extraction process being different. Concerning enzymes and bacteriocins used for antibacterial applications, the most common ones are lysozyme and nisin. Lysozyme is a antibacterial enzyme principally extracted from egg white that have preferential interaction with the peptidoglycan layer of Gram-positive bacteria[21], whereas nisin is an antibacterial peptide mainly produced by lactic acid bacteria and its antibacterial mode of action is also linked to their interaction with bacteria membrane[34]. Organic acids are, in most cases, synthetically produced and their antibacterial activity is linked to their acidity. In their dissociated form, the contact with bacteria leads to permeation of H^+ ions through the bacterial cell membrane and elevated acidity inside the cell have several deadly impact such as DNA and protein damage, enzyme inhibition or respiration disruption[35].

A significant part of the experimental section of this work was dedicated to the development of antibacterial packaging based on silver nanoparticles and cellulose nanofibrils. Therefore, a specific focus is placed on reviewing here firstly both materials separately by detailing their production processes and their main properties relevant to the experimental part of this work. Then, the antibacterial properties of hybrid materials made of silver nanoparticles and cellulose nanofibrils are reviewed.

2. Silver nanoparticles

1. Synthesis

Silver is an abundant material mainly found on earth either in the form of bulk metal or soluble salts and more recently it has been processed to give a nanoparticle (NP) state. The properties of silver nanoparticles (Ag NPs) largely depend on several morphological parameters such as their shape, size, crystallinity or the additives used during their synthesis and these parameters can be controlled during the production step to fit the desired application[36]. Different methods exist to synthesise Ag NPs such as chemical, physical or biological processes (**Figure I-9a**).

Chemical processing remains the most classic technique and involves chemical reduction of silver salts into nanoparticles through a nucleation process and growth. Several reduction agents can be used, the more common being polyols, Tollens reagent or sodium borohydride ($NaBH_4$)[37]. The reduced silver atoms then progressively form clusters and then colloidal NPs (**Figure I-9b**). The NPs are usually stabilised in suspensions with the use of capping agents which prevent the aggregation of the NPs during the nucleation and growth steps, leading to narrow and controlled size distribution[38]. The final shape and size is also controlled by other parameters such as reaction time, solvent, precursor nature, concentration and ratio for all chemical used[39] (**Figure I-9c**). The same technique is used for instance for the production of silver nanowires (Ag NWs) by selecting appropriate seed and capping agent for directed growth[40].

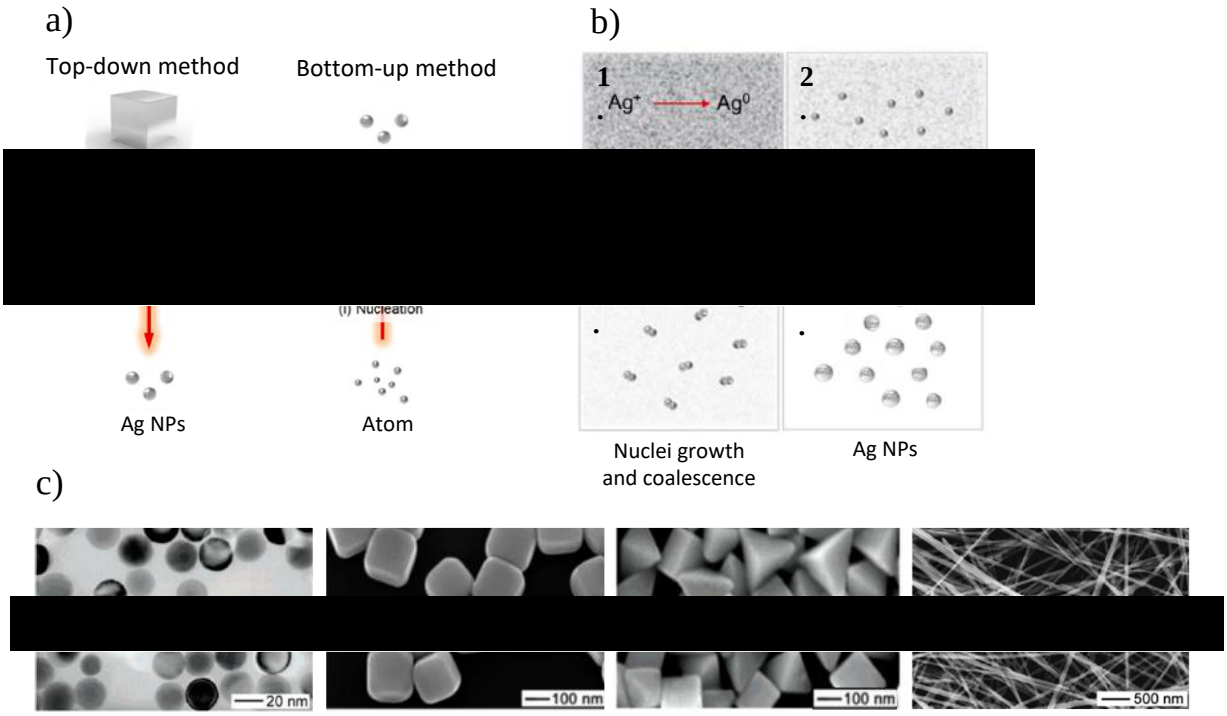

***Figure I-9**: Silver nanoparticles synthesis with a) different synthetic pathways, b) nucleation process for chemical reduction method and c) different shapes. Reproduced and adapted from Lee et al. (2019)*[36]

2. Antibacterial activity

Silver has been known to display antibacterial properties for a very long time now and was used by several civilisations through history for food and water preservation but also medicine and wound-healing[41]. Silver materials were then obviously extensively studied since then and more recently Ag NPs have met a renewed interested in order to fight an ever-increasing concern of antibiotic resistance in pathogenic bacteria[42]. Indeed, since the 1930s, a lot of antibiotics products have been developed and overly and carelessly administrated to patients leading to build up on antibiotic resistance in bacteria and the rise of multi-drug resistant variants[43]. After a non-lethal contact with antibiotics, a resistance acquirement in bacteria can indeed occur via several adaptation processes such as genetic mutation that can then be transferred to a new bacteria generation. Ag NPs have thus been investigated for their activity against multi-drug resistant bacteria and shown to be highly effective against a large range of such resistant-bacteria, including *Methicillin-resistant Staphylococcus aureus* (MRSA), *Methicillin-resistant Staphylococcus Epidermis* (MRSE), or *multi-drug resistant Pseudomonas Aeruginosa*[44–46].

Despite the intensive investigation of the antibacterial properties of Ag NPs, there are still numerous debates among the scientific community about its exact mode of action. A large number of studies have proven that the antibacterial activity of Ag NPs is attributed to the NP and to induced silver ion release[47,48]. Because of their intrinsic chemical nature, both NPs and ions have some common effects on bacteria and the antibacterial activity of Ag NPs is usually believed to happen in several steps. Firstly silver is a Lewis acid and so displays strong

interaction with Lewis bases such as sulphur or phosphorus which elements are predominantly present in the cell wall of bacteria. Because of the nano-scale size of Ag NPs and their high specific surface area, they can adhere and accumulate on the bacterial cell wall, causing severe morphological disruptions such as gaps or pits leading eventually to either penetration inside the cell or directly to cell death[49–52]. Simultaneously, the Ag NPs bound on the bacterial membrane can also interfere with the membrane protein and especially with respiration or proteins leading to the cell respiration inhibition because of degeneration of the proton motive force[53]. This interference with the membrane proteins can also lead to a change in the membrane permeability and cause leaching of the cell content[54]. Secondly, the Ag NPs that accumulate on the bacterial cell wall can penetrate the cell and display a more destructive interaction with the bacterial cell content. The same Lewis acid-base interaction can occur between silver and numerous biomolecules present inside the cell and for instance because of such interaction the Ag NPs can damage the bacterial DNA by disturbing the DNA replication[55].

This interaction between silver and several fundamental biomolecules inside the cell and at the surface can also be attributed to silver ions. Indeed, the accumulation of Ag NPs on the bacterial cell wall and their penetration can also cause silver ions to be released inside the cell[56]. Then, membrane proteins, respiration and transport proteins can also be affected by silver ions because of the same reasons[57,58]. Moreover, silver ions can also display enhanced interaction with cell content and show some specific destructive effects against bacterial contents such as the deactivation of vital enzymes, because of strong interactions with electron donor compounds, such as thiols, carboxylates, or phosphate[59].These combined antimicrobial effects of Ag NPs and silver ions are also linked to the intracellular production of active molecules called reactive oxygen species (ROS) such as hypochlorous acid, hydrogen peroxide but also free radicals such as hydroxyl radical, oxygen singlet or anions superoxide. The synthesis of these molecules inside the cell and their deadly effects are commonly summarised under the term “oxidative stress”. These reactive compounds present a deadly interaction with cell membrane, DNA or diverse cell proteins[60–63].

To summarise, the antibacterial effect of Ag NPs comes from both the NPs and the continuous release of silver ions and takes place either at the surface or inside the bacterial cell. **Figure I-10** outlines the different mechanisms proposed. The exact biological interactions of silver with the cell are diverse and this wide range of effects can probably explain the strong antibacterial activity of such compounds.

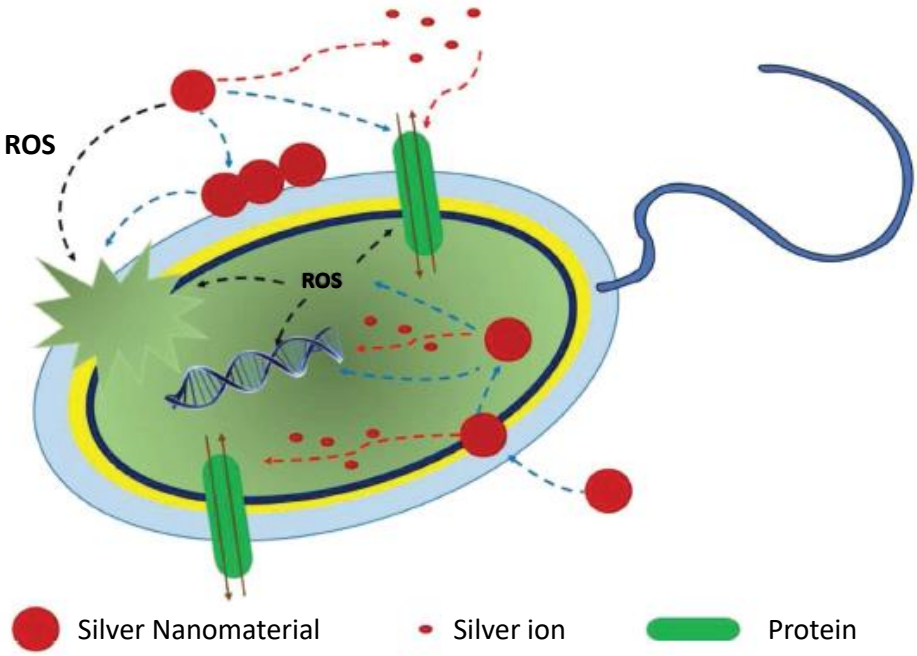

***Figure I-10**: Ag NPs mode of action with the different proposed mechanisms: accumulation on the cell wall and penetration inside the cell, direct damage to the cell membrane, silver ions leaching and damage to membrane, DNA and other enzymes, reactive oxygen species (ROS) production leading to damages toward the membrane, DNA and other enzymes. Reproduced and adapted from Tang et al. (2018) with permission from Wiley (Copyright 2018)*[48]

As previously described, the properties and antibacterial activity of NPs are dependent on several different parameters. Firstly, the antibacterial activity of Ag NPs is linked to their size: the smaller the NPs, the more antibacterial they are[64–66] and it has been suggested that only the smallest Ag NPs can interact spatially with bacteria to bind and penetrate the cell[47]. To go even smaller, silver quantum dots or silver nanoclusters have also been more recently investigated for their antibacterial activity and they show a strong potential, even at very low concentration[67,68]. Secondly, one of the key factors for Ag NPs antibacterial activity is their surface chemistry as this has a major influence on the NPs dispersion and stability. Indeed the role of a wide range of capping agents or post-synthesis polymers grafting and surfactants such as different molecular weight of polyethylene glycol (PEG) and polyvinylpyrrolidone (PVP), Tween 80, anionic sodium dodecyl sulfate (SDS), Brij 35, Brij 58, Brij 97, Brij 98, sodium citrate, mercaptopropionic acid (MPA), mercaptopropionic sulphonic acid (MPS), mercaptohexanoic acid (MHA) has been researched and the results showed that the more dispersed and stable the Ag NPs are, the more antibacterial they are because of greater exposed surface area but also that the capping agents influences the release of silver ions[69,70]. It has also been reported that the surface charge of Ag NPs plays a role in their antibacterial activity and this was investigated by testing negatively- and positively-charged modified Ag NPs after purification by ultrafiltration against Gram-positive bacteria *bacillus*: the authors concluded that the more positively-charged the Ag NPs the higher the antibacterial activity because of enhanced electrostatic attraction between the bacteria surface and the Ag NPs activity[71]. The

shape of the Ag NPs has a strong influence on the antimicrobial activity which increases from nanowire (rod-like), spherical, cubical to truncated triangular. This was explained because of the difference in silver ions release rate (linked to the difference in surface area)[72] but also by different crystalline facet activity and their atom density[47,73,74].

Even though Ag NPs have demonstrated strong antibacterial properties and are now widely researched and used both at the academic and industrial scales, they are still questions raised about their safety and environmental impacts on ecosystems. The most credible scenarios for toxicity towards human are penetration of Ag NPs in the organism by either ingestion of respiration[75]. Ag NPs could have detrimental effects on vital organs due to extensive accumulation but mainly *in vitro* tests have been conducted so far and more work needs to be done on the subject[76]. Environmental concerns linked to Ag NPs are attributed to their toxicity to aquatic organisms and circulation of the food chain, as well as the endangered efficacy of wastewater treatment due to the small size of the NPs, and their potential penetration of the soils of solid-waste treatment plans[77]. More work should be carried out to fully characterize these parameters but Ag NPs release from antibacterial materials and products, as well as recycling and end-of-life should be carefully taken into accounts.

In the experimental section of this work, silver nanoparticle with a rod-like shape also called silver nanowires were used. The particular interest of using silver nanowires over spherical nanoparticles is detailed in the experimental section.

The presented studies concerning the influence of Ag NPs size and shape further explains that the activity of Ag NWs is mainly dictated by their release of silver ions[78]. Several studies have focused on the antibacterial application of Ag NWs based-materials by incorporating the nanowires along with different substrate, matrix or film-forming compounds such as polyethylene naphthalate (PEN)[79,80], polydimethylsiloxane (PDMS)[81], konjac glucomannan (KGM)[82], chitosan[83], polyvinyl alcohol (PVA)[84], cotton[85], graphene oxide[86], polylactic acid (PLA)[87,88], chitosan- hydroxyapatite composite[89], regular fabric[90], mixed-cellulose ester[91], silk fibroin[92], polymethylmethacrylate (PMMA)[93], and polypropylene (PP)-expanded polytetrafluoroethylene (ePTFE)[94]. **Figure I-11** highlights some of these composites and their properties.

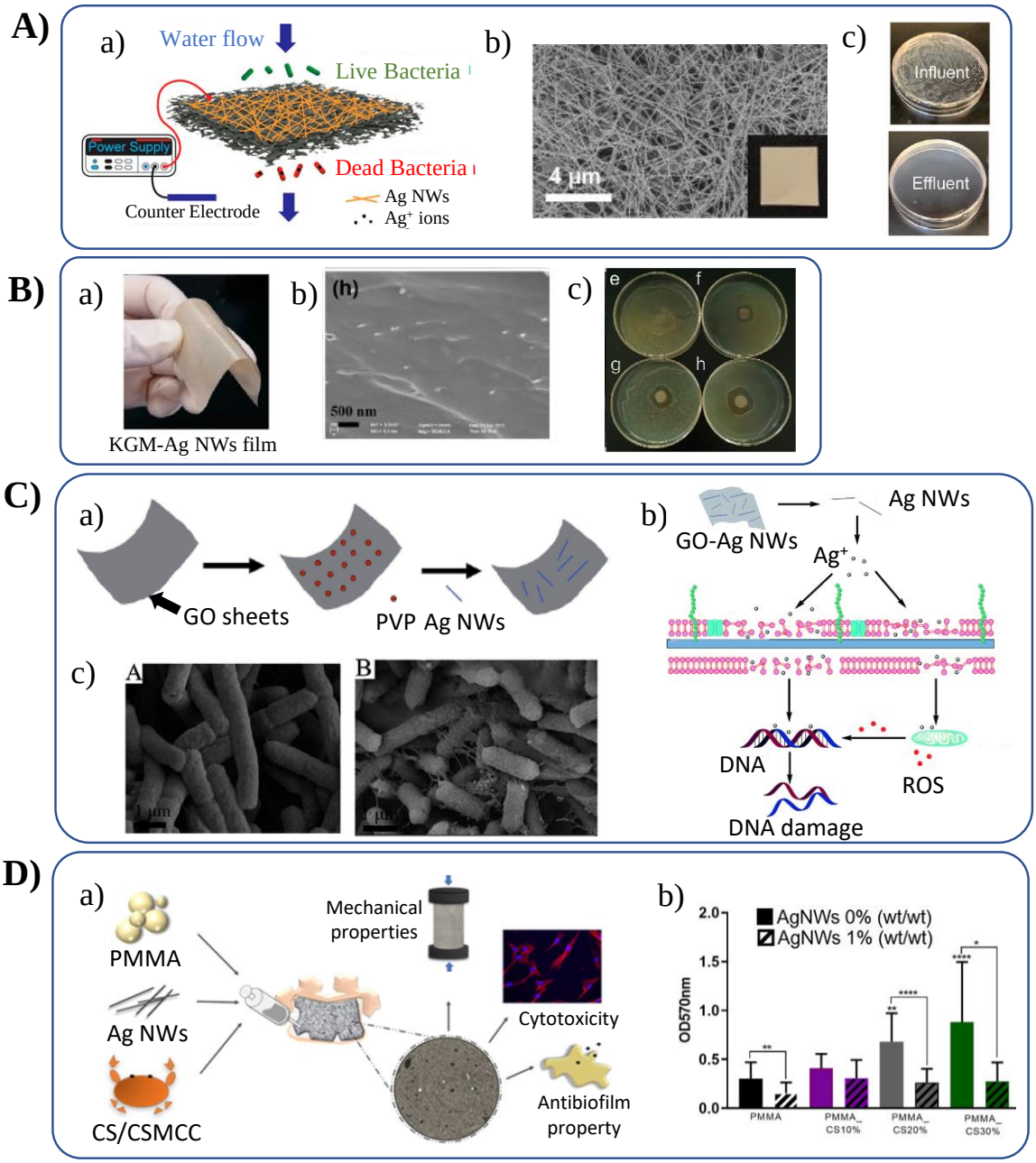

***Figure I-11**: Different examples of antibacterial systems developed with Ag NWs. A) Controllable drinking water filter modified with Ag NWs and using electrochemical cell with a) general schematic, b) Scanning Electron Microscopy (SEM) of the surface of the composite and c) antibacterial testing of the influent and effluent. B) Films prepared from Konjac Glucomannan/Ag NWs systems with a) picture of the film, b) SEM of its surface and c) inhibition zone antibacterial test. C) Graphene oxide sheet wearing Ag NWs with a) general schematic, b) antibacterial mode of action and c) SEM pictures of E. Coli bacterial before (left) and after (right) contact with the active materials. D) Ag NWs composite with chitosan derivatives and PMMA, with a) general schematic and b) bacterial count reduction due to the Ag NWs. Respectively reproduced and adapted from Chen et al. (2019) with permission from the American Chemical Society (Copyright 2019) for A)[91], from Lei et al. (2017) for B)[82], from Cui et al. (2015) with permission from The Royal Society of Chemistry for C)[86], and from De Mori et al. (2019) for D)[93]*

3. Applications of silver nanoparticles for packaging

Due to the extensive work carried out by the scientific community on Ag NPs for the development of active packaging, only the references that focused on real food products are reviewed here. References using other metallic nanoparticles are also mentioned.

While the investigation for nanotoxicity remain scarce, several studies have taken advantages of using micro- and nanoparticle for antibacterial packaging and the most common are inorganic nanoparticles such as silver, zinc oxide, copper, and titanium dioxide nanoparticles (**Table I-3**). In the different references presented, the antibacterial packaging materials is prepared either by coating on a polymeric substrate or by a composite preparation either by casting, extrusion or injection. Casting methods are usually straightforward and Azlin-Hasim et al. (2016) tested a polyvinyl chloride (PVC) composite with low-loading of Ag NPs (0.5% wt) for chicken breast packaging but the results showed no significant antibacterial properties on the meat product yet achieved less meat oxidation and an increased shelf-life[95]. One interesting example of immobilised Ag NPs comes from Wu et al. (2018) who prepared Ag NPs immobilised on a laponite nanodisk and then prepared an antibacterial composite out of it by solvent casting in chitosan[96]. The composite showed a large inhibition zone (IZ) in-vitro against *E. Coli*, *S. Aureus*, *A. Niger*, and *P. Citrinum* in inhibition zone antibacterial tests, and increased the shelf-life of packaged litchi from 5 to 7 days.

Several references relate the preparation of Ag NPs composite by extrusion blowing. Motlagh et al. (2012) used polyethylene (PE) as matrix to load up to 2% wt of Ag NPs and the authors showed a significant reduction in the bacterial cell count of *E. Coli* and *S. Aureus* in dried barberry[97]. Li et al. (2017) prepared similar composites but with extra TiO_2 NPs added in the low-density PE (LDPE) matrix and proved antibacterial properties against *A. Flavus* in rice but only using qualitative Scanning Electron Microscope (SEM) imaging[98]. Similar Ag/TiO_2 materials were however not efficient as antibacterial packaging of orange juice[99]. Combining the antibacterial properties of Ag and ZnO NPs was performed by Panea et al. (2014), who prepared composites with an LDPE matrix by injection-molding[100]. The authors reported a 100% decrease in bacteria count for in-vitro studies against *E. Coli*, *P. Aeruginosa*, and *L. Monocytogenes*, but only a slight decrease in bacteria count present in chicken breast during storage was found. Other preparation techniques were also used, for example Cozmuta et al. (2015) coated an Ag/TiO_2 suspension by a bar coating process on high-density PE (HPDE) and prepared a sandwich-like packaging by overlapping a second HDPE layer. The authors then wrapped fresh bread in the prepared packaging and antibacterial tests revealed that compared to the control, a 35% reduction in bacterial count for yeast and moulds and 43% reduction in bacterial count for *B. Subtilis*, and 30% for *C. Cereus* was achieved after 6 days. Finally Ag NPs/polyvinyl alcohol (PVA) composites were also prepared by Deng et al. (2019) by tape

casting showing antibacterial property against *A. Niger* and less oxidation for grapes packaged with it[101].

***Table I-3**: Metallic nanoparticles-based systems for antibacterial packaging applications (IZ=inhibition zone, SEM=scanning electron microscope)*

Antibacterial agent (% wt)	Polymer matrix or substrate/ process	Bacteria tested	In-vitro antibacterial effect	Food product tested	Impact on food	Reference
Ag (0.5 % wt)	PVC/Film casting	*E. Coli, S. Aureus, B. Cereus, P. Fluorescens*	No-vitro study	Chicken breast	No significant decrease in bacterial count, less oxidation, enhanced shelf-life	Azlin-Hasim et al. (2016)[95]
Ag NPs (not supplied)	PVA/Tape casting	*A. Niger*	Decrease in bacterial count (IZ: 14.4 mm for *A. Niger*)	Grape	Less mass loss, decrease of decay rate, less vitamin degradation	Deng et al. (2019)[101]
Ag NPs (2% wt)	PE/extrusion-blowing	*E. Coli, S. Aureus*	No-vitro study	Barberry	Decrease in bacterial count (after 13 weeks, 2.3 log reduction for mould, 2.8 total bacterial count), less sensory degradation	Motlagh et al. (2013)[97]
Laponite-Ag NPs (2% wt)	Chitosan/Film casting	*E. Coli, S. Aureus, A. Niger, P. Citrinum*	Decrease in bacterial count (IZ: 7.7 mm for *S. Aureus*, 2.8 mm for *E. Coli*, 4.0 mm for *A. Niger*, 3.0 mm for *P. citrinum*)	Litchi	Enhanced shelf-life	Wu et al. (2018)[96]
Ag/TiO_2 (9% wt)	LDPE/extrusion blowing	*A. Flavus*	Qualitative decrease in bacterial count (SEM imaging)	Cooked rice	Less pasting properties degradation, less aging	Li et al. (2017)[98]
Ag/TiO_2	HDPE/ Bar coating	Yeasts, molds, *B. Subtilis, B. Cereus*	No-vitro study	Bread	Decrease in bacterial count (after 6 days: 1.25 log reduction for yeast/mould, 4.6 for *B. Subtilis* and 0.8 for *B. Cereus*), less nutrient degradation, less oxidation,	Cozmuta et al. (2015)[102]
Ag/TiO_2 and ZnO (5% wt and 1% wt)	LDPE/Extrusion blowing	Yeasts and moulds, total aerobic bacteria	No-vitro study	Orange juice	Ag/TiO2 – Small decrease in bacterial count (< 1 log reduction) after 7 days, less oxidation ZnO – Small decrease in bacterial count (<1 log reduction) for 7 days, less oxidation	Emamifar et al. (2010)[99]
Ag/ZnO (5% wt)	LDPE/Injection molding	*E. Coli, P. Aeruginosa, L. Monocytogenes,* Mesophilic, *Enterobacteriaceae, Lactobacillus*	100% decrease in bacterial count	Chicken breast	Small decrease in bacterial count (< 1 log reduction) after 21 days, less oxidation	Panea et al. (2014)[100]
ZnO (11% wt)	Alginate/Film casting	*S. Typhimurium, S. Aureus*	Decrease in bacterial count (IZ: 27.9 mm for *S. Typhimurium*, 30.6 mm for *S. Aureus*)	Poultry meat	100% decrease in bacterial count after 8 days for *S. Typhimuirum* and 6 days for *S. Aureus*	Akbar et al. (2014)[103]
ZnO (3% wt)	Agar/Film casting	*L. Monocytogenes, S.Typhimurium*	Decrease in bacterial count (viable colony method after 9h: 5.8 log reduction for *L. Monocytogenes*, 7.2 for *S. Typhimurium*)	Smoked salmon	Small decrease in bacterial count (< 1 log reduction) after 5 days	Baek et al. (2018)[104]
ZnO (1% wt)	PLA/Film casting	*L. Monocytogenes, E. Coli*	Decrease in bacterial count (viable colony method after 12h: 3.7 log reduction for *L. Monocytogenes*, 6.1 for *E. Coli*)	Minced fish paste	100% decrease in bacterial count after 10 days	Shankar et al. (2018)[105]
TiO_2 (3% wt)	LDPE/Extrusion blowing	*Pseudomonas spp., R. Mucilaginosa,* Mesophilic, yeast	Decrease in bacterial count (after 3h: 2.5 log reduction for *Pseudomonas spp.*, 2 for *R. Mucilaginosa*)	Fresh pears	Decrease in bacterial count (after 17 days: 2 log reduction for Mesophilic, 1.27 for yeast)	Bodaghi et al. (2013)[106]
Cu (not supplied)	PLA/Film casting	*Pseudomonas spp.* (from Fiordilatte cheese)	Decrease in bacterial count (after 24h: 2.1 log reduction)	Fiordilatte cheese	Decrease in bacterial count (after 6 days: 1.9 log reduction), less sensory degradation, enhanced shelf life	Conte et al. (2013)[107]

In the experimental section of this work, silver nanoparticles were used in combination with nanocellulose materials and especially cellulose nanofibrils. A specific care was taken in the next section to review these materials, from their production to their main properties relevant to this work.

3. Cellulose nanofibrils

1. Production

Even if they do not present direct active properties, several types of nanomaterials have been used in combination with antibacterial materials for packaging applications due to their outstanding properties. For instance, nanomaterials coming from cellulose sources have been widely investigated, for different applications such as cosmetics, printed electronics, biomedical, composites, or packaging. Cellulose is a natural polysaccharide present in plant materials and producing nanoparticles out of this bulk material has opened a whole new world of innovations and possibilities because of their promising physico-chemical properties. Cellulose nanoparticles are often referred to as nanocellulose and are usually defined by being a cellulose particle with at least one dimension having a size in the nanoscale range. The cellulose polymer is made of D-glucose monomers linked together by a 1,4-β glucosidic bond and the chain is terminated either with a reducing or non-reducing end (**Figure I-12a**). Nanocellulose materials take principally two distinctive forms, either cellulose nanocrystals (CNC) or cellulose nanofibrils (CNF) (**Figure I-12b**). Their production process and their final properties are both very different and so they are used in different applications.

In the experimental section of this work, only cellulose nanofibrils were used and so mainly this type of nanocellulose materials is reviewed here.

CNF are produced by mechanical disintegration of cellulose fibres whereas CNC are prepared by acid hydrolysis. The physical defibrillation of cellulose microfibrils (separation without physical damage) in the secondary cell wall of wood leads to nano-sized fibrils (diameter ≈ 1-100 nm, length ≈ 500 nm to few μm). The first report of such material production appeared in 1983[108] starting from wood material. The material produced is a whitish viscous gel and the most common processes that are today used for large volume production of CNF are homogenizers (or microfluidizers) and ultrafine friction grinding, yet more processes exist such as extrusion, steam explosion, ball milling or aqueous counter collision[109]. In the last 10 years the overall industrial production of CNF has skyrocketed: the overall production of CNF indeed increased from 4450 kg/day in 2015 to 12000 kg/day in 2018[110,111]. Different commercial products containing CNF can now be found on the market. **Figure I-13** and **Table I-4** give an overview of these available commercial products.

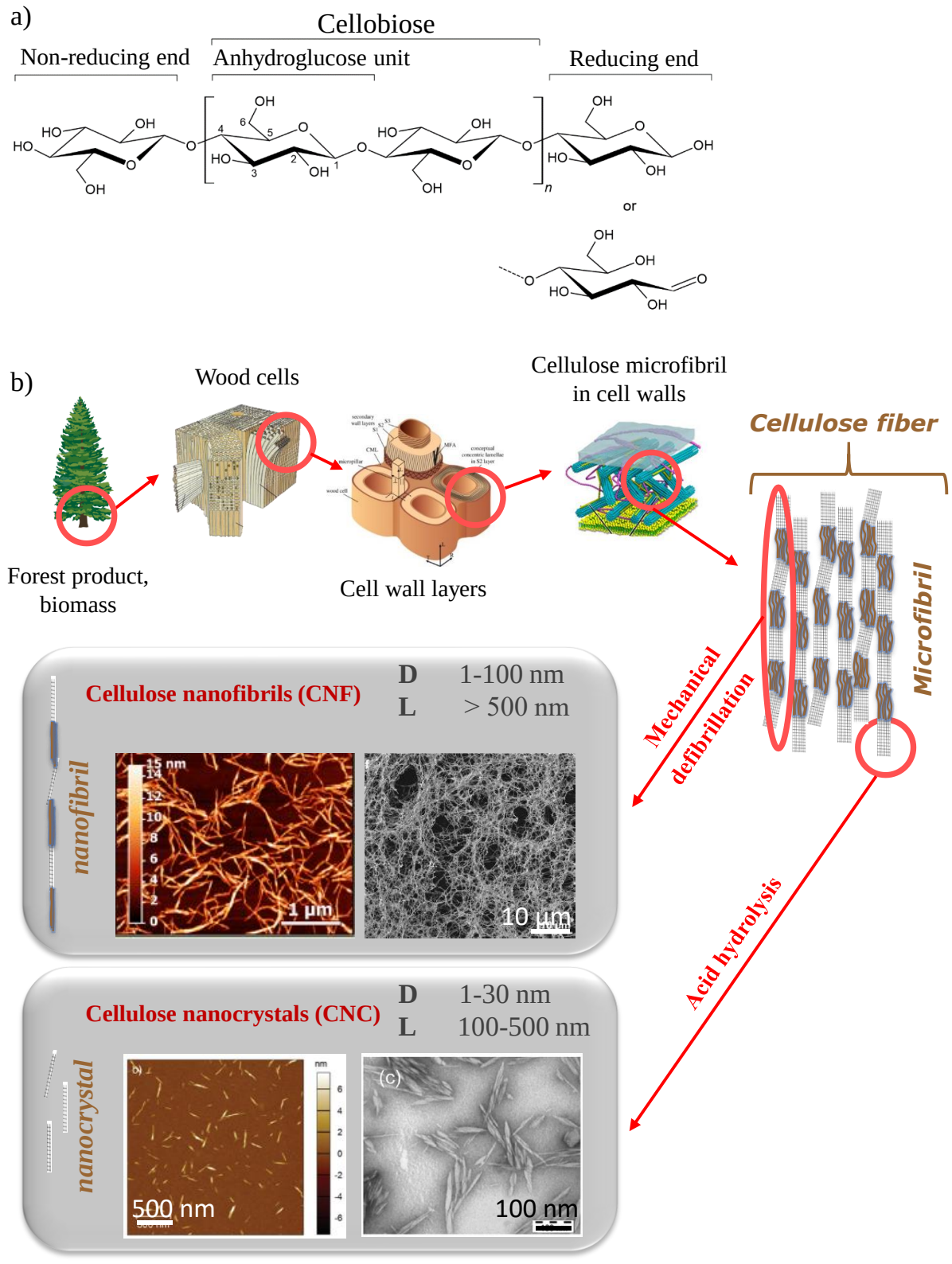

***Figure I-12**: Nanocellulose material with a) chemical formula of cellulose and b) cellulose nanofibrils (CNF) and cellulose nanocrystals(CNC) production schematic. CNF image were reproduced and adapted from Grüneberger et al. (2014) with permission from Springer Nature (Copyright 2014)[112] and from Nechyporchuk et al. (2016) with permission from the American Chemical Society (Copyright 2016)[113]. CNC images were reproduced and adapted from Foster et al. (2018) with permission from The Royal Society of Chemistry[114] and from Mascheroni et al. (2016) with permission from Springer Nature (Copyright 2016)[115]*

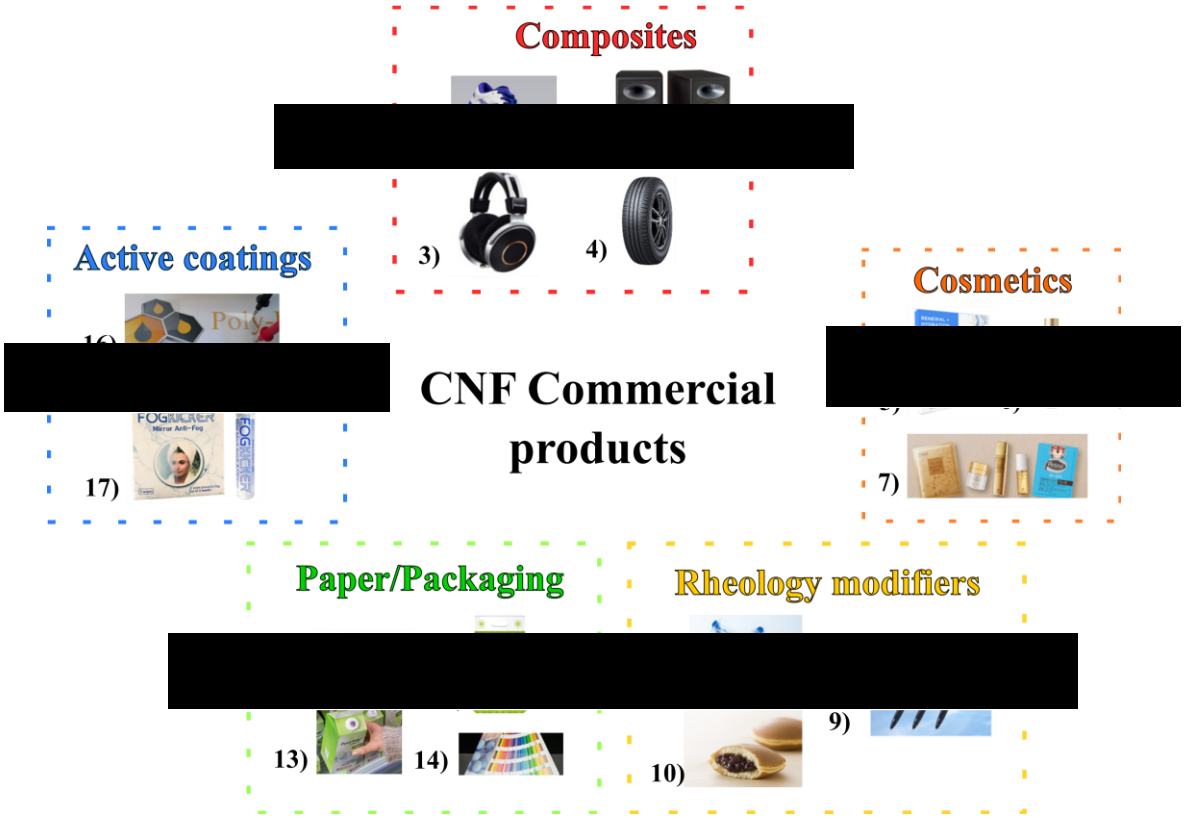

***Figure I-13**: Some examples of commercial product incorporating cellulose nanofibrils. Information about each of them can be found in the Table I-4. Images extracted from the companies websites, accessed online on the 22.04.2020*

***Table I-4**: Some examples of commercial products incorporating cellulose nanofibrils corresponding to the Figure I-13 images*

Product name/Brand	Product info	Launch date	Number in Figure I-13
GEL-KAYANO™ 25/Asics	Shoes (midsole foam)	2018	1
S-PM50 (30) (D)/Onkyo-Pioneer	Speakers	2016	2
SE-MONITOR5/Onkyo-Pioneer	Headphones	2017	3
ENASAVE NEXTIII/Sumitomo Rubber Industries	Tyres	2019	4
RENEWAL+HYDRATION/DeLeón cosmetics	Skin care masks	2019	5
Surisuri/Nippon paper	Cosmetics (lotion)	2018	6
Nanocell-Posoo-White day/ Natural Friend	Various cosmetics	Not supplied	7
Cellink Bioink/Cellink	Ink for bio-3D-printing	2015	8
Uni-Ball Signo 307/ Mitsubishi Pencil	Ink additive	2015	9
Dorayaki/ Tago no Tsuki	Food additive	2018	10
Elleair Kirekira!/ Daio Paper	Toilet wipes	2018	11
Hada Care Acty-Poise/ Nippon paper	Adult diapers (adsorbent sheets)	2015	12
Elopak/Stora Enzo	Milk carton packaging	2017	13
Pro sheet/ Nanopaper	Art storage sheets	Not supplied	14
PolyBioWire/Poly-Ink	Transparent conductive coatings	2015	15
FogKicker/Treaty Biotech	Antifog coatings	2016	16

The energy consumption needed to produce CNF by mechanical fibrillation from pulp suspension is enormous and hindered its industrial development in the early stages[116]: the increasing numbers of commercial CNF materials and products in the last 20 years can be explained by the fact that CNF production has met a revolution in the late 2000s because of the innovations that led a substantial decrease of the energy needed for production. Indeed, new pretreatments have been developed in order to decrease the amount of energy needed during the fibrillation process.

First in 2006, Saito et al. investigated a new pretreatment by using 2,2,6,6-tetramethylpiperidine-N-oxyl (TEMPO) chemical as a cellulose oxidant[117]. This pretreatment is commonly called TEMPO-oxidation and selectively oxidises the primary hydroxyls of cellulose into carboxylic acid and requires a complex mixture of TEMPO/NaBr/NaClO reagents. This oxidation induces electrostatic repulsion that reduces the energy needed for the mechanical process and enables the production of really small dimensions and highly homogeneous CNF. TEMPO-oxidised CNF are usually produced as a highly viscous and transparent gel. Then, in 2007 Pääkkö and al. developed an enzymatic pretreatment to hydrolyse cellulose pulp fibres with endoglucanase enzymes before mechanical treatments to produce CNF[118]. Enzymatic pretreatment is commonly used for industrial production of CNF because of its low price, environmentally friendly aspect and straightforward use. Since then, a lot of research have been focusing on the development of new chemical modification of cellulose such as cationization, phosphorylation, carboxymethylation, sulphoethylation, periodate oxidation, sulphonation or ozonation in order to act as pretreatment for CNF production and has already been reviewed elsewhere[119].

Qualifying one CNF suspension from another is something the scientific community has not yet agreed upon. This can be explained by the fact that CNF suspensions can be very different from one another depending on the cellulose source, the pretreatment used, the mechanical defibrillation process and even the post-treatment (**Figure I-14**). CNF suspensions are also often not a perfectly size distributed materials but rather a heterogeneous mixture made of nanoscale, microscale and sometimes even macroscale cellulose fibres. It then becomes clear that characterising such materials is complex. Some studies have even tried to developed quality indexes in order to judge the quality of a CNF suspension[120].

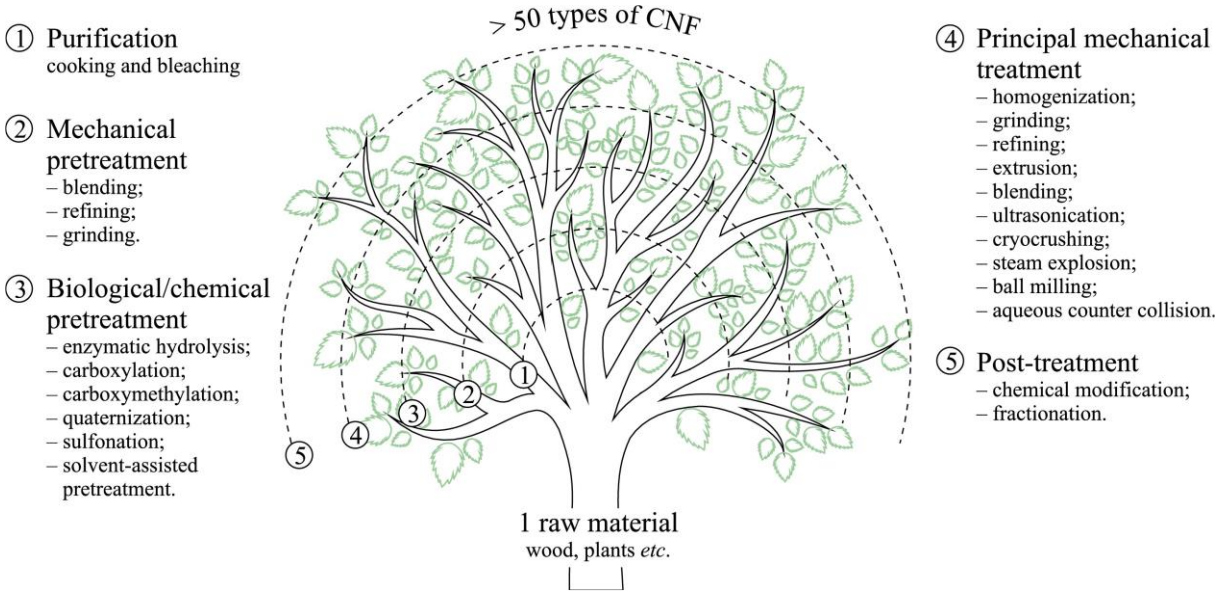

***Figure I-14**: Representation of cellulose nanofibrils diversity based on the preparation steps. Reproduced from Nechyporchuk et al. (2016) with permission from the American Chemical Society (Copyright 2016)*[121]

The other major type of nanocellulose material is cellulose nanocrystals (CNC) that are produced by hydrolysing the amorphous regions of cellulose using mainly sulphuric acid and thus creating small crystalline particles (diameter ≈ 1-30 nm, length ≈ 100-500 nm). This acidic treatment leads to surface enriched with sulphate groups which stabilises the particles in suspension in water[122]. The production of CNC was first reported by Ranby et al. in 1949 starting from wood materials[123] but the applications of CNC today are mainly composites reinforcements, biomedical and rheological additives. Bacterial cellulose is also considered as nanocellulose materials and is synthesised by bacteria leading to pure cellulosic material, exempt of lignin and hemicellulose. Thus, its main research focuses on biomedical applications[124], but this will not be developed further in this literature review.

2. Properties

The main properties of CNF materials outside their biodegradability, biocompatibility and biobased nature come from their nano-size: high specific surface area, enhanced networks of hydrogen bonding and high flexibility and so its capacity to form highly entangled network and high versatility for chemical functionalization. The interests of using CNF materials are then numerous: film forming and self-standing capability, barrier and insulating properties, rheology modifiers and binders, active molecules encapsulation, nanomaterials stabilisation and, templating, composites reinforcement, or optical properties and sensing. The properties and applications of CNF materials depend on the final form of the materials prepared: suspensions, thin films, aerogels, 3D-printed, etc.

In the experimental section of this work, CNF was used as an aqueous suspension to formulate active inks, as well as thin films deposited on packaging materials. Their properties

that are of interest to packaging applications are detailed here. Indeed, a specific care is taken first to review the properties of CNF suspension. Secondly the film characteristics of CNF materials especially optical and barrier properties are reviewed.

As described before, CNF materials are mainly produced in low solid (<5% wt) aqueous suspensions which are gel-like, but at higher mass content, can also look like a paste (**Figure I-15a**, **b** and **c**). CNF suspension displays interesting colloidal properties linked to rheology and particle/emulsion stabilization. CNF suspensions are gel-like materials with a high viscosity even for a low solid content. The morphology of the CNF materials plays a major role in the rheological properties and as a general rule: the higher the aspect ratio the higher the viscosity[125–127]. Different suspensions parameters also influence the rheological properties of CNF suspensions such as the chemical functionalisation (grafting charge)[128], the suspensions pH[118], the presence of adsorbents[129,130], or the suspension concentration[114]. It is also very important to keep in mind that when compared to theoretical rheology laws, that CNF materials are not perfect spherical particles and even not rod-like rigid nanoparticles but rather flexible fibres with various morphology distribution.

CNF materials display shear-thinning behaviour, meaning that the viscosity tends to decrease when exposed to a higher shear rate (**Figure I-15d**). Usually, the shear shinning behaviour is affected by the CNF concentration: the more concentrated the suspension, the more shear thinning it is[128]. Cellulose macrofibrils also display shear-thinning behaviour which is due to the destruction of aggregates[131,132]. The same conclusion can be drawn for CNF suspensions concentrated enough where the alignment of the particles under the shear applied can also explain such behaviour[133]. This shear thinning property is also time-dependent as CNF suspensions usually display thixotropic behaviour: when stabilised at a specific shear rate and then exposed to a higher shear, it takes some time for the viscosity to come back to its initial value when exposed back to the original shear rate. This is due to the fact that exposing the suspension to a high shear rate will untangle the network by aligning the fibrils, and reforming the network after that and is dependent on the networking capability of the CNF material[134].

Because of their gel-like behaviour, viscoelastic properties of CNF are interesting to study using oscillatory rheology in order to characterise the properties of the gel networks. Measuring the storage and loss moduli within the linear viscoelastic regions then helps to characterise the strength of the gel network[113] (**Figure I-15e**) and as for shear viscosity measurements, the systems responses are also affected by CNF functionalisation and grafting charge[135], morphology[136], suspensions ionic strength or pH and presence of charged polymers[137,138].

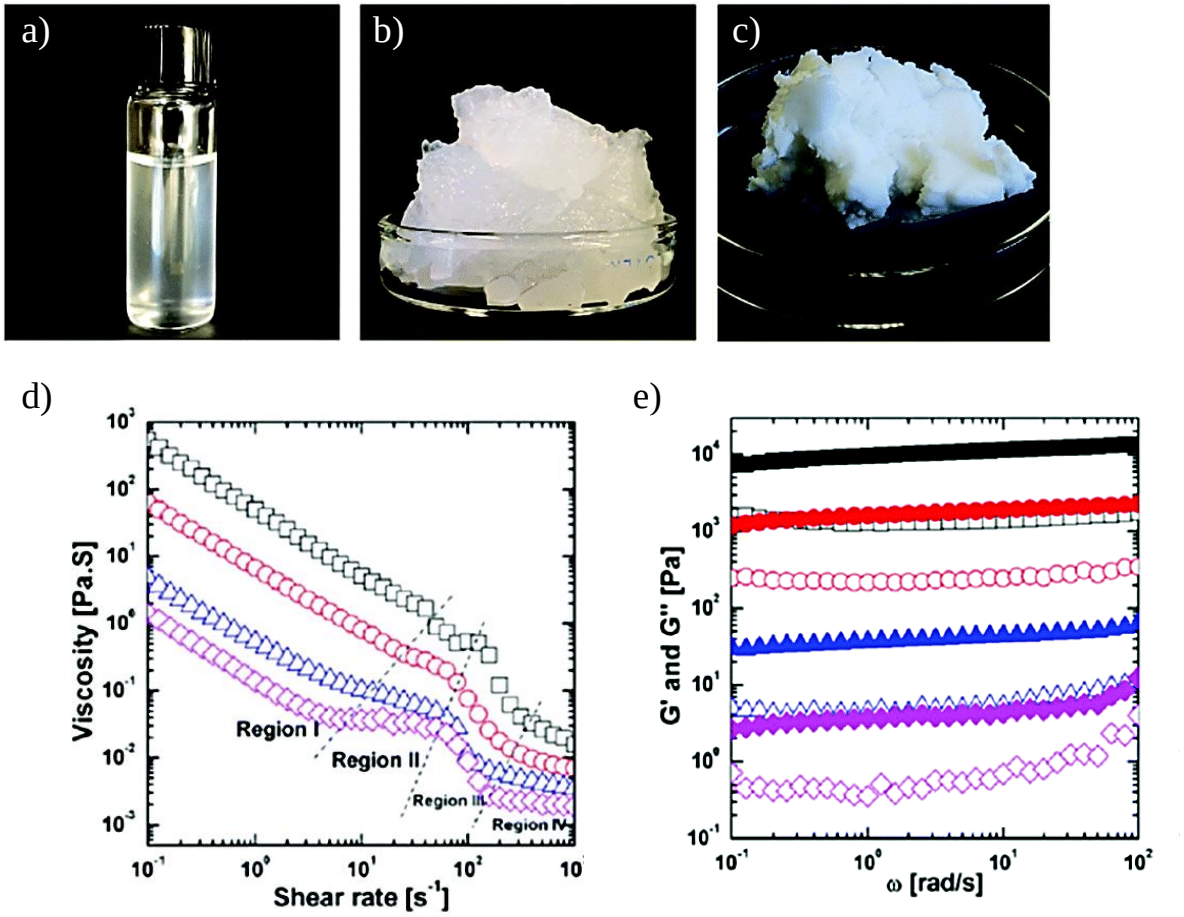

***Figure I-15**: CNF visual aspect with different suspensions forms with a) carboxymethylated-CNF (Innventia) at 0.1% wt, b) CNF (Innventia) at 2% wt and c) CNF (Exilva) at 10% wt, and rheological properties of CNF suspensions with d) flow curve experiments and shear thinning behaviour depending of the mass content for 0.25% wt (magenta diamonds), 0.5% wt (blue triangles), 1% wt (red circles) and 1.5% wt (black squares), e) viscoelastic properties at 1 Hz (G' - solid symbols and G'' open symbols) depending of the mass content for 0.25% wt (magenta diamonds), 0.5% wt (blue triangles), 1% wt (red circles) and 1.5% wt (black squares). Reproduced and adapted from Foster et al. (2018) with permission from The Royal Society of Chemistry for a), b) and c)[114] and from Li et al. (2015) with permission from the American Chemical Society (Copyright 2015) for d) and e)[139]*

The hydrophilic character of CNF makes them relatively easy to disperse in aqueous media. Such character is then an undeniable advantage to prepare composite suspensions and stabilize hydrophobic particles in water. Metallic nanoparticles (or other hydrophobic nanoparticles) are usually dispersed in suspensions using surfactants and producing stable suspensions in aqueous media is challenging. CNF suspensions can then be used as a stabilising agent either during synthesis of other hydrophobic nanoparticles or post-synthesis by simple mixing. Several examples in the literature investigate the stabilisation of non-metallic inorganic nanoparticles by CNF suspensions. Titanium dioxide nanoparticles were for instance successfully incorporated into different nanocomposites with CNF systems for antibacterial applications[140], paper reinforcement[141], or flexible electronics[142]. CNF suspensions are also widely used to stabilise nanocarbons suspensions and an extensive review has already been published including nanocarbons materials such as fullerene, carbon nanotubes, graphene for flexible

electronics, energy, pollutants removal and biomedical[143]. Finally, stabilising metallic nanoparticles remain the most classic use of CNF suspensions. If simple mixing of suspended systems is a straight-forward technique, a better stabilisation and limited release of NPs is often achieved by reducing in-situ metallic salts and a wide range of metallic nanoparticles were investigated such as gold, silver, copper, iron or even cobalt, for applications such as sensors, catalysis, medical or smart materials[144].

CNF also present interesting properties when dried into thin films. The main properties of CNF as thin films are mechanical, optical and barrier properties. Firstly, CNF thin films can be used as free-standing films that can be prepared by several techniques starting with CNF suspensions, such as films casting, filtering or using paper sheet former. Films prepared from a paper sheet former process are usually called nanopaper. Using such a process enables a fast production (compared to time consuming film casting) of large surface with a good homogeneity but need a relatively large amount of CNF suspension[145]. Using coating or printing processes, CNF can also be deposited on the surface of different substrates corresponding to packaging materials such as polymeric materials like polyethylene terephthalate (PET), polylactic acid (PLA), ceramic, polypropylene (PP), polyethylene (PE), polyvinyl chloride (PVC), glass, aluminium, paper, or even directly on food product (vegetable)[146–158].

First of all, films made of CNF also display interesting mechanical properties but will not be reviewed here as this is out of scope of the experimental section of this work[159]. Concerning the optical properties, usually only films or coatings made of small size CNF materials display high transparency because of their dimensions being smaller than the visible light wavelength[160]. Reduced density and larger nanofibrils can create nanopaper with a strong light scattering compared to dense plastic materials. The transparency of such materials is then strongly dependent on the distance between the nanopaper and the light detector[160]. The morphology of the fibres deeply impacts the optical properties of thin films and so do the pretreatment and functionalization[161–164].

Finally, CNF materials present high oxygen barrier properties that can compete with petroleum-based plastic packaging materials. This oxygen barrier properties are commonly accepted to be due to the strongly packed network of hydrogen bonding within the dense CNF matrix which hinder the passage of the target molecule through the film[165–167]. Then the flexibility of the CNF creates strongly entangled networks with high tortuosity. The less permeable section of CNF is their crystalline regions and the flexibility of the CNF can compensate to close the gaps [166,168,169]. That also explains why CNF materials exhibits greater barrier properties than CNC[170]. Based on what has been described, morphological properties and CNF nature (aspect ratio, fibrillation, etc.) plays a major role: the denser and more cohesive the material is then the lower the oxygen permeability[171]. For the same reasons, CNF pretreatments, chemical modifications and surface charge have an impact on the oxygen barrier properties[162,172,173].

As other bio-based polymers, the hydrophilic nature of CNF makes it a relatively poor water barrier material. First of all, the oxygen permeability is strongly dependent on the humidity level and increases significantly when exposed to a high level of humidity[148,166,174]. Then the water vapour transmission rate of CNF films is generally high[175]. To overcome such a sensitivity to water, several techniques can be employed such as using CNF in a multi-layered composite, surface functionalization, thermal treatment or additives such as nanoclay for instance[176–178].

After reviewing separately Ag NPs and CNF, the next section is focused on antibacterial systems made of the combination of these materials.

4. Silver nanoparticles/cellulose nanofibrils for antibacterial materials

Antibacterial composites made of silver nanoparticles and cellulose nanomaterials have been extensively studied by the scientific community over the past 20 years. In most cases, such composites are used in the form of films, are prepared by either solvent casting or by filtration processes and the Ag NPs are prepared by in-situ reduction of silver salts.

Several research groups prepared CNF/Ag NPs by the filtration process and for instance Yan et al. (2020) used commercial CNF and Ag NPs to prepare antibacterial films with a low loading of Ag NPs (0.1% wt) which displayed strong antibacterial properties. The authors filtrated the CNF/Ag NPs suspension over a polylactic acid (PLA) electrospun membranes to create promising antibacterial scaffolds[179]. Li et al. (2019) also prepared antibacterial surface by filtration[180]. They prepared dialdehyde-modified CNF by performing periodate oxidation on TEMPO-oxidised CNF, mixing them with silver salt followed by filtration. No extra reductants were needed to in-situ prepare Ag NPs and antibacterial properties with low and controlled release of silver ions were proven.

Instead of soaking a cellulose membrane into a silver salt solution, or adding it to a CNF suspension, Yan et al. (2016) sprayed a silver nitrate solution onto CNF films prepared by filtration and then prepared Ag NPs by either chemical or UV reduction[181]. With this innovative process, a relatively high Ag loading (3.9% wt) into the films was achieved that showed a significant inhibition zone against *E. Coli*. Ramaraju et al. (2015) used covalent bonding to prepare CNF/Ag NPs composite and reported Ag NPs stabilised with a dendrimer covalently bound on TEMPO-oxidized CNF[182]. They prepared films by filtration and verified the antibacterial activity by using the inhibition zone (IZ) test against *E. Coli* and *S. Aureus*. Bober et al. (2014) prepared polypyrrole/CNF/Ag NPs composite by in-situ polymerisation and in-situ reduction[183]. The composites displayed enhanced film forming ability and small antibacterial effect against *S. Aureus* and *S. Infantis* but no effect against *C. Albicans* and *L. Monocytogenes* measured by the inhibition zone test. Finally, Xiao et al. (2013) produced a complex antibacterial systems with Ag NPs, TiO_2, chitosan and CNF materials[184]. Silver nitrate

solution was filtered over a CNF/TiO_2/Chitosan film produced by layer-by-layer assembly to achieve ultrathin films (< 30 nm), then the silver ions were UV-reduced and the final composite displayed 100% antibacterial effect against *E. Coli* and *S. Aureus*.

Solvent casting (or sometimes also called film casting) is also a common method to prepare CNF/Ag NPs films and for example Yu et al. (2019) demonstrated the antibacterial properties of CNF/Ag NPs films prepared by solvent casting with in-situ Ag NPs preparation using either a chemical reductant or a UV reduction technique[185,186]. The antibacterial properties of the films were investigated in liquid media and the logarithmic reduction in the bacterial count was found to be around 5-6 for *E. Coli*, 1.5 for *S. Aureus* and 3.5 for *L. Monocytogenes*. Several other more complex systems such as a hyperbranched epoxy composite involving triethanol amine-modified CNF and in-situ Ag NPs synthesis, or with the addition of additives to improve film forming properties or give extra antibacterial activity such as latex, citric acid or tannins, were also developed [187–189].

Finally, some authors have reported the antibacterial testing of CNF/Ag NPs in the form of suspension. Thus, Wang et al. (2014) who demonstrated that in-situ produced Ag NPs induced a significant antibacterial effect even in suspension[190]. Xiong et al (2013) also showed that CNF/Ag NPs system can be used in the form of aerogels that display 100% antibacterial activity toward *S. Aureus* and a slow release of silver ions[191]. Uddin et al. (2017) also prepared aerogel using 3 different types of CNF named unmodified, TEMPO-oxidised and cationic-modified CNF and the produced system showed different antibacterial activity[192]. Coating a CNF/Ag NPs system on paper was reported by Martins et al. (2012). The authors prepared the CNF/Ag NPs systems by layer-by-layer electrostatic assembly and then used the composite in a formulation with starch to coat on paper using a size press. The coated paper exhibited a 3.8 logarithmic reduction of bacterial count when compared to the control, by testing in liquid media against *S. Aureus*[193]. **Figure I-16** shows some example of CNF/Ag NPs materials prepared for antibacterial activity and **Table I-5** summarises the key studies found in the literature.

To summarise, most of the examples found in the literature prepared CNF/Ag NPs composites by in-situ reduction of silver salt, using either film casting or filtration processes. While it seems to provide better entrapment of the Ag NPs produced into the CNF matrix, these production methods do not appear to be easily scalable. Only spherical Ag NPs have been introduced into CNF material for antibacterial activity and only few references have investigated the release of silver ions. All the referenced literature shows the antibacterial activity of such compositions to different extents.

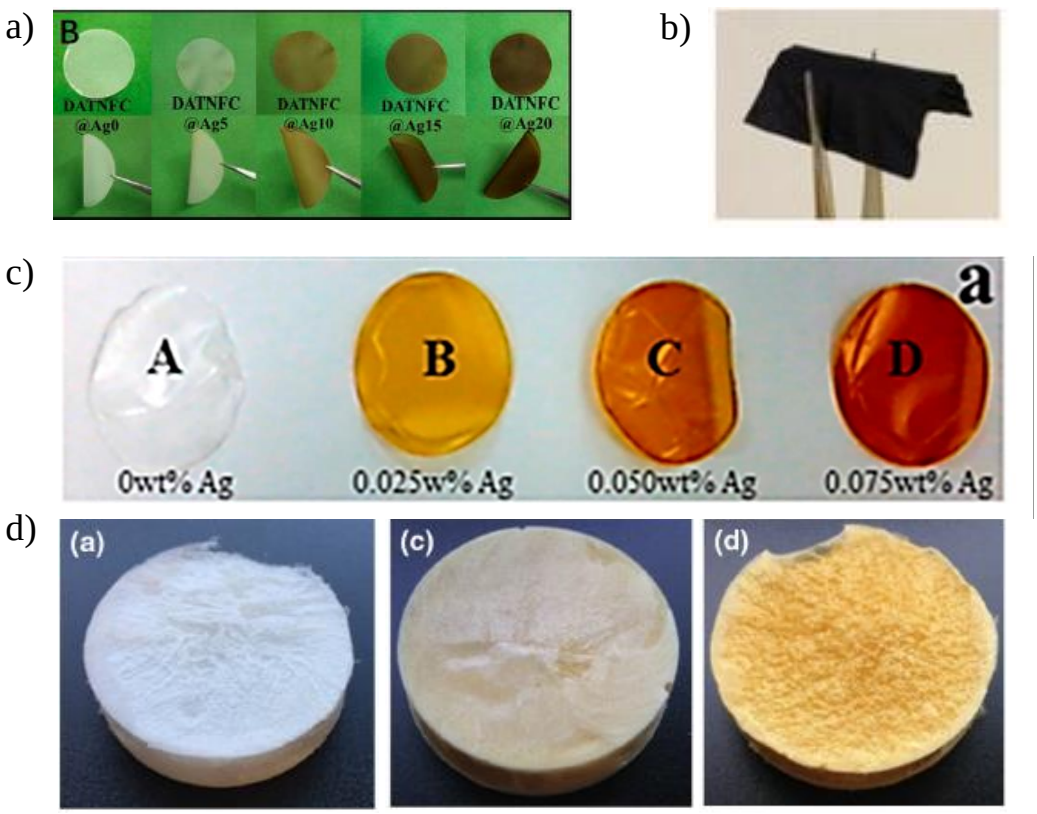

***Figure I-16**: Different examples of antibacterial materials made of CNF/Ag NPs combination, with a) films prepared by filtration containing periodate-modified CNF with different loading of Ag NPs prepared in-situ, b) film prepared by filtration containing TEMPO-oxidized CNF and in-situ synthesized Ag NPs along with polypyrrole, c) films prepared by filtration containing TEMPO-oxidised CNF and different loading of in-situ prepared Ag NPs cross-linked together using a poly(amido amine) dendrimer and d) aerogels prepared by freeze drying with from left to right: unmodified CNF, CNF/Ag NPs prepared in-situ with 0.02 mmol.g^{-1} Ag NO_3 loading and CNF/Ag NPs prepared in-situ with 0.1 mmol.g^{-1} $AgNO_3$ loading. The pictures are respectively reproduced and adapted from Li et al. (2019) with permission from the American Chemical Society (Copyright 2018) for a)[180], from Bober et al. (2014) with permission from the American Chemical Society (Copyright 2014) for b)[183], from Ramaraju et al. (2015) with permission from Elsevier (Copyright 2014) for c)[182] and from Uddin et al. (2017) with permission from Springer Nature (Copyright 2017) for d)[192]*

***Table I-5**: Systems prepared with CNF and Ag NPs materials: raw materials, composite preparation and antibacterial properties (C=commercial, P=produced, 0=non-applicable, av.=average, NM=non-measured, CPM=counting plate method, IZ=inhibition zone, MIC=minimum inhibitory concentration, red.=reduction)*

CNF (Commercial /supplier /type)	Ag NPs (Commercial /supplier /size)	Additive	Form Process	Loading (% wt Ag)	Antibacterial activity			Reference
					Bacteria	Method	Result	
C/Shanghai RanYuan Biotech./not supplied	C/Shanghai Chaowei Nanotech./15nm (av.)	0	Film Filtration on PLA	0.1%	*E. Coli* *S. Aureus*	Liquid (CPM)	> 95% antibacterial activity after 4h	Yan et al. (2020)[179]
P/0/periodate oxidized	P in-situ/0/5-50nm	latex	Film Casting	6% wt CNF/Ag in latex	*E. coli* *E. Faeali* *M. luteus*	IZ	1.2 mm 1.3 mm 1.1 mm	Errokh et al. (2019)[187]
P/0/NaOH and $Ca(OH)_2$ treated	C/TNS Nanotecnologia LTDA/5-20nm	Citric acid + Silane or tannin	Film Casting	1 drop of commercial Ag, 5%wt citric acid	*S. Enteriditis* *L. Monocytogenes*	IZ	*S. Enteriditis*: Silane AgNPs-CNF NaOH 10.25 mm, Tannin AgNPs-CNF NaOH 11.6 mm, Silane AgNPs-CNF $Ca(OH)_2$ 9.25 mm, Tannin AgNPs-CNF $Ca(OH)_2$ 6 mm *L. Monocytogenes*: Silane AgNPs-CNF NaOH 7.1 mm, Tannin AgNPs-CNF NaOH 6.9 mm, Silane AgNPs-CNF $Ca(OH)_2$ 7.5 mm, Tannin AgNPs-CNF $Ca(OH)_2$ 6.8 mm	Scatolino et al. (2019)[188]
C/University of Maine/ not supplied	P in-situ/010-40nm	0	Film Casting	5.2%	*E. Coli* *S. Aureus*	IZ, liquid (CPM)	IZ. 1.5 mm 1.4 mm	Liquid. 6 log red. (6h) 1.5 log red. (6h)	Yu et al. (2019)[185]
C/University of Maine/ not supplied	P in-situ/0/5-15nm	0	Film Casting	3.1%	*E. Coli* *L. Monocytogenes*	Liquid (CPM) (suspension 10mg.ml^{-1})	5 log red. (6h) 3.5 log red. (6h)		Yu et al. (2019)[186]
P/0/periodate oxidised	P in-situ/0/20-40nm	0	Film Filtration	1.8%	*E. Coli* *S. Aureus*	IZ, liquid (CPM)	IZ. 4.3 mm 1.4 mm	Liquid > 98% antibacterial activity for both (24h)	Li et al. (2019)[180]
P/0/TEA modified + epoxy hyperbranched	P in-situ/0/NM	Epoxy hardener	Film Casting	Estimated around 8 (NM)	*S. Aureus* *C. Albicans*	MIC, liquid (absorbance)	MIC. 125 µg.ml^{-1}	Liquid. 0.26 A red. (9h) 0.16 A red (9h)	Gogoi et al. (2018)[189]

(continued)

***Table I-5**: continued*

CNF (Commercial /supplier /type)	Ag NPs (Commercial /supplier /size)	Additives	Form process	Loading (% wt Ag)	Antibacterial activity			Reference
					Bacteria	Method	Result	
P/0/TEMPO	P in-situ/0/5-10nm	0	Film Filtration	3.9%	*E. Coli*	IZ	11 mm	Yan et al. (2016)[181]
P/0/TEMPO (+cross-linked dendrimer-AgNPs)	P mixing/0/2-10nm	poly(amido amine) dendrimer	Film Filtration	0.1%	*E. Coli* *S. Aureus*	IZ	12 mm 17 mm	Ramaraju et al. (2015)[182]
P/0/TEMPO	P in-situ/0/15-20nm	polypyrrole	Film Filtration	25%	*C. Albicans* *S. Aureus* *S. Infantis* *L. Monocytogenes*	IZ (qualitative)	0 mm ≈2 mm 0 mm ≥ 3 mm	Bober et al. (2014)[183]
P/0/TEMPO	P in-situ/0/5-10nm	0	Suspension 0	Estimated around 37% (NM)	*E. Coli*	Liquid (absorbance)	0.3 A red. (18h)	Wang et al. (2014)[190]
P/0/from MCC	P in-situ/0/10-30nm	Fe_3O_4	Aerogel Freeze drying Film Casting	4.7%	*S. Aureus*	IZ (qualitative) Liquid (absorbance)	IZ. Significant compared to control Liquid. 100% A red. for film/aerogel (12h)	Xiong et al. (2013)[191]
P/0/unmodified, TEMPO and cationic	P in-situ/0/10-40nm	0	Aerogel Freeze drying	Estimated around 2% (NM)	*E. Coli* *S. Aureus*	Liquid (CPM)	4 log red. for unmodified/TEMPO and 7.5 log red. for cationic (14h)	Uddin et al. (2017)[192]
C/Shanghai Kayon Bio.Tech./Filter paper MFC	P in-situ/0/5-20nm	titanium-chitosan	Film Filtration	1.25%	*E. Coli* *S. Aureus*	Liquid (CPM)	100% antibacterial activity (24h)	Xiao et al. (2013)[184]
C/Centre Technique du Papier/Enzymatic	C/Colorobia/30-50 nm	Polyelectro-lytes +starch for coating	Suspension 0 Paper coating Layer-by-layer	0.1% 0.0005%	*S. Aureaus* *K. Pneumoniae*	Liquid (CPM)	Suspension: 8 log red. (24h) 8.3 log red. (24h) Paper coating: 3.8 log red. (24h)	Martins et al. (2012)[193]
P/0/Cellulose acetate electrospun	P in-situ/0/av. 3 nm	0	Film Electrospinning	Estimated around 0.05% (NM)	*E. Coli* *S. Aureus* *K. Pneumoniae* *P. Aeruginosa*	Liquid (CPM)	> 99% antibacterial activity (18h)	Son et al. (2004)[194]

In this section about antibacterial packaging, the global context of antibacterial packaging and the relevant materials was first explained. A specific focus was placed on the materials used in the experimental section of this work, first individually and then together. Specifically, silver nanoparticles were first reviewed in terms of production method and antibacterial mode of action. The literature references dealing with packaging materials made of silver nanoparticles and tested against real food products was then investigated. Then, cellulose nanofibrils materials were generally reviewed both in terms of preparation techniques and properties relative to packaging. Finally, the scientific literature dealing with cellulose nanofibrils/silver nanoparticles materials for antibacterial properties was detailed.

Even if not directly used in the experimental section of the work, for completeness, other active packaging technologies are reviewed briefly in the next sections. These include antioxidant and carbon dioxide releaser for emitters categories, together with oxygen, ethylene and moisture scavenging technologies.

2.1.2. Antioxidant

Antioxidant is a very commonly studied active packaging technology. An antioxidant substance is by definition a substance that can inhibit oxidation reaction and especially interact with oxygen reactive species, and is of particular interest when it comes to food products. Indeed, fats contained in food products are particularly prone to oxidation which can lead to rancidity, off-flavour and strong odours. Antioxidant have then been used for a long time as additional preservatives in food products in order to extend their shelf-life. The purpose of such active packaging is to incorporate the antioxidant inside the packaging instead of directly in the food product. Antioxidant can be synthetic such as butylated hydroxytoluene (BHT), butylated hydroxyanisole (BHA) or tert-Butylhydroquinone (TBHQ). However, extensive work has been focused on the last 20 years to develop, extract and use natural antioxidants. Essential oils and natural extracts have shown strong antioxidant properties as well as some micro-nanoparticles. Classic antioxidant agents used in packaging applications are summarised in **Figure I-17**.

The antioxidant capability of a compound can be investigated using several methods and the most used in food packaging applications are the thiobarbituric acid reactive substances assay (TBARS), 2,2-diphenyl-1-picrylhydrazyl (DDPH) test, 2,2'-azino-bis(3-ethylbenzothiazoline-6-sulfonic acid) (ABTS) test, or involve peroxide or pentanal/hexanal/heptanal content measurements[21]. The packaging incorporating nanoparticles are mainly prepared by film casting[195–198], by coating processes[199–201] or composite preparation[202] and are summarised in **Table I-6**. Some examples using antioxidant packaging[203–205] can be found in **Figure I-18**.

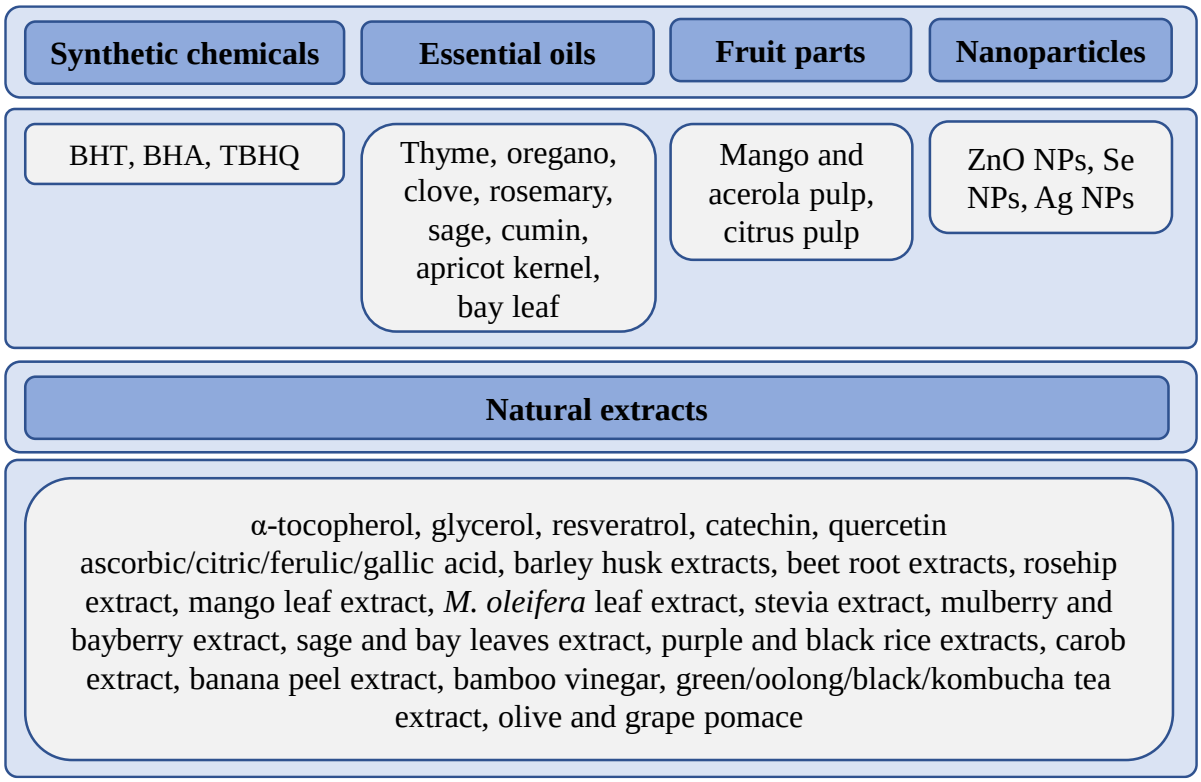

***Figure I-17**: General classification of antioxidant materials used for packaging applications and specific substances involved*[21,200,206–218]

***Table I-6**: Antioxidant packaging systems based on micro- and nanoparticles*

Antioxidant	Form/process	Food target	Antioxidant test/study conclusion	Reference
ZnO NPs	Film/Film casting with bacterial cellulose and polypyrrole	Chicken thighs	DDPH/enhanced antioxidant activity	Pirsa et al. (2019)[195]
ZnO NPs	Film/Film casting with chitosan	Poultry minced meat	TBARS/enhanced antioxidant activity	Souza et al. (2019)[196]
ZnO NPs (+ ginger essential oil)	Film/Film casting with gelatine and glycerol	Pork	Peroxide value/enhanced antioxidant activity	Zhang et al. (2017)[197]
Se NPs	Film coating on PET/laminate PET/adhesive/LDPE	Cooked ham, chicken, ready-to-eat vegetables	Hexanal content, TBARS, fatty acid content/enhanced antioxidant activity	Vera et al. (2018)[199]
Ag NPs, TiO_2 NPs, SiO_2 NPs, attapulgite	Bags/Extrusion blowing	Rice	fatty acid content, lipase activity/enhanced antioxidant activity	Wang et al. (2018)[202]
Ascorbic acid loaded chitosan/tripolyphosphate nanoaggregates	Direct food coating/Dip coating	Mushrooms	Polyphenol oxidase activity, ABTS and DPPH radical scavenging/enhanced antioxidant activity	Ojeda et al. (2019)[201]
gallic acid encapsulated in lentil flour/polyethylene oxide nanofibers	Film coating on PLA/Electrospinning	Walnuts	polyunsaturated fatty acid (PUFA) content, peroxide value/enhanced antioxidant activity	Aydogdu et al. (2019)[200]
Olive pomace MPs	Film/Film casting with chitosan	Walnuts	peroxide index, secondary oxidation compounds, and fatty acids/enhanced antioxidant activity	de Moraes Crizel et al. (2018)[198]

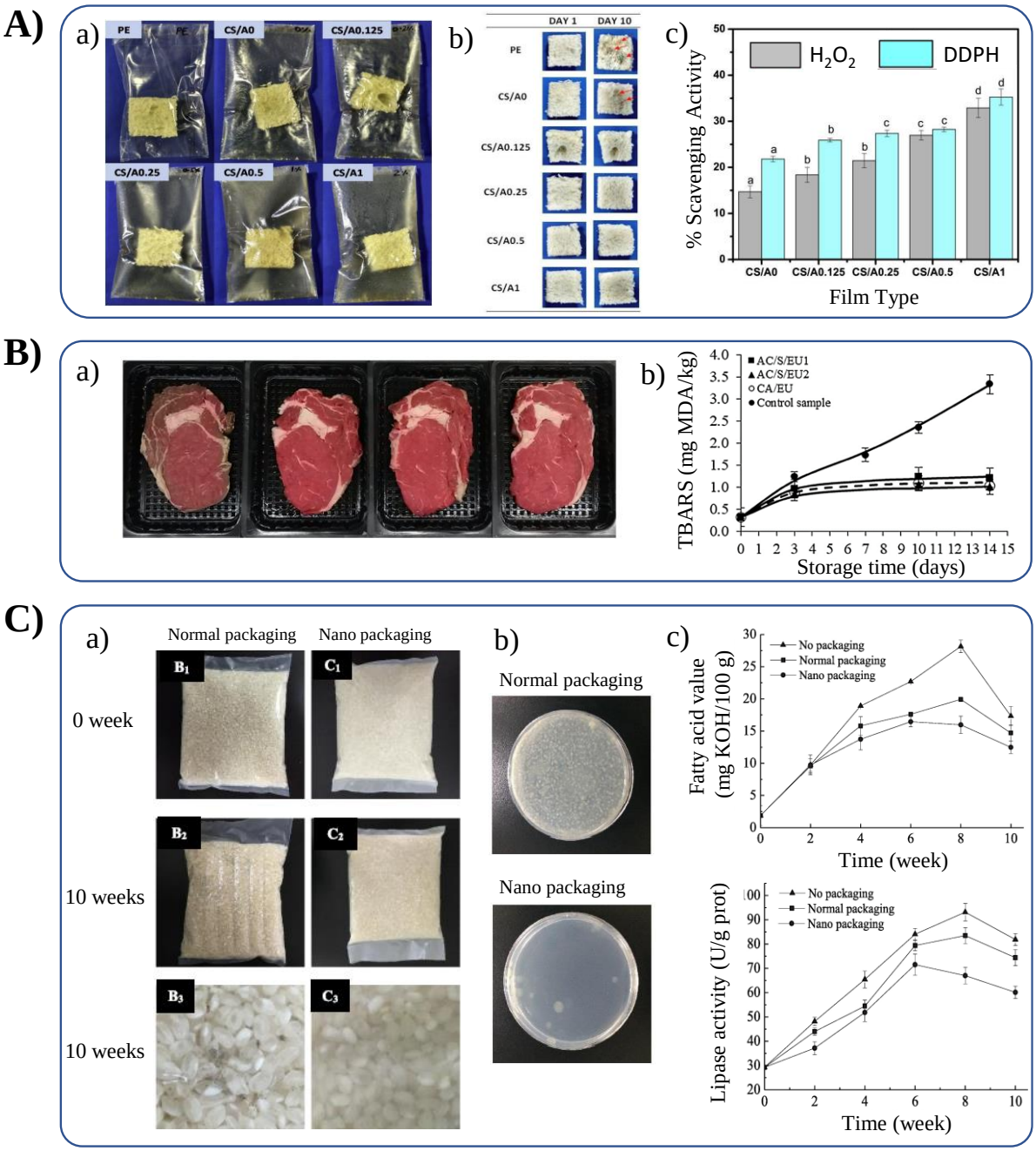

***Figure I-18**: Examples of antioxidant packaging systems. A) apricot kernel essential oil (KEO) incorporated in chitosan films with a) different KEO loading and sliced bread packaging, b) visual aspect of the bread and less mould appearance and c) antioxidant activity of the systems. B) Cellulose acetate- or starch-based coatings containing clove essential oil (CEO) on oriented polypropylene with a) visual aspect of beef packaged with the active film after 14 days of storage (from left to right; control, starch-CEO low loading, starch-CEO high loading and cellulose-acetate-CEO low loading) and b) antioxidant properties of the system assessed by TBARS assay. C) Nanocomposite made of Ag NPs, nano-TiO_2, nanoclays and nanosilicate with a) visual aspect of the composites and rice packaged after 0 and 10 weeks, b) antibacterial testing after 10 weeks for control and nanocomposite and c) antioxidant properties for the nanocomposites investigated by fatty acid value (top) and lipase activity (down). Respectively reproduced and adapted from Priyadarshi et al. (2018) with permission from Elsevier (Copyright 2018) for A)[203], from Navikaite-Snipaitiene et al. (2018) with permission from Elsevier (Copyright 2018) for B)[204] and from Wang et al. (2018) with permission from Elsevier (Copyright 2017) for C)[202].*

2.1.3. Carbon dioxide emitter

A less common but still effective active packaging technology to improve the shelf-life of food products uses carbon dioxide (CO_2) emitters. CO_2 displays antimicrobial activity and slows down microbial growth. Several hypotheses concerning its mechanisms have been suggested which is dependent on the bacteria involved[219]. CO_2 is soluble in water and fat and so can easily interact with bacteria *via* the following proposed modes of actions: internal pH acidification, cell penetration and modification of bacterial membrane permeability, or interference with bacterial enzymes[220]. So, emitting CO_2 inside the packaging helps reduce the overall bacterial contamination of the food products. CO_2 emitters are often used with Modified Atmosphere Packaging (MAP) to keep the internal atmosphere saturated to fight against CO_2 release outside the packaging atmosphere as packaging materials have usually higher CO_2 permeability than O_2. The technology is usually used in sachet forms and several commercial products exist such as Cellsorb-Active (Cellcomb, Sweden), CO_2 Fresh-pads (CO_2 Technologies, USA) or Superfresh (vdP International, The Netherlands). In most of the reported literature, a mixture of sodium bicarbonate and ascorbic acid is used to release CO_2 and several food products have been tested in packaging applications such as fish (cod, salmon)[221,222] and meat (chicken, reindeer, lamb or cooked ham)[223–226]. All of the cited examples showed a bacterial growth reduction and increased shelf-life by using CO_2 emitters.

2.2. Scavengers

The role of scavengers is to interact and capture undesired gas molecules in the inside atmosphere of the packaging. Indeed, gas trapped inside the packaging either during the packaging process or gas produced by the package content can have a negative impact on the shelf-life of the product. The main applications of scavengers are for oxygen, ethylene and humidity scavenging.

2.2.1. Oxygen scavenging

In active food packaging using scavenging technology, oxygen scavenging is the most developed technique. Indeed, gaseous oxygen present in the headspace of packaging is responsible for oxidation of components of the food but also promotes the growth of aerobic microorganisms, leading to nutritional, visual and sensory deterioration of the food products[21]. The oxidation of food products is related to the generation of reactive oxygen species which are highly reactive partially reduced oxygen compounds that cause degradation reaction with proteins and lipids, vitamins, or sugars[227]. Concerning microbial food spoilage, it has been showed that a low concentration of oxygen inhibits the growth of aerobic microorganism[228].

Oxygen scavenging system are often used in combination with Modified Atmosphere Packaging (MAP) or vacuumed packaging to keep the oxygen level very low. Indeed, even with

MAP technology, there is still the possibility of faulty inert gas flushing, physical defects or insufficient oxygen permeability of the packaging material. Oxygen scavengers are mainly contained inside micro-perforated, highly permeable gas sachets that are placed inside the packaging. Such form is however not always very well accepted by the consumers because of potential leaching of active materials. Recently, more efforts have been made in incorporating the scavenger system inside the packaging substrate itself. Oxygen scavenging is not a recent technology and several commercial products exists, such as for instance Ageless® (Mitsubishu Gas Chemical, USA), ATCO® (Laboratoires Standa, France), BestKept® (Chunwang, China) for sachet-like oxygen scavenging and for instance Ageless OMAC® (Mitsubishu Gas Chemical, USA), ShelfPlus® O_2 (Albis Plastic, USA), AMOSORB™ (PolyOne, USA), or ZerO_2™ (Southcorp Packaging, Australia) for film-like oxygen scavengers (**Figure I-19**).

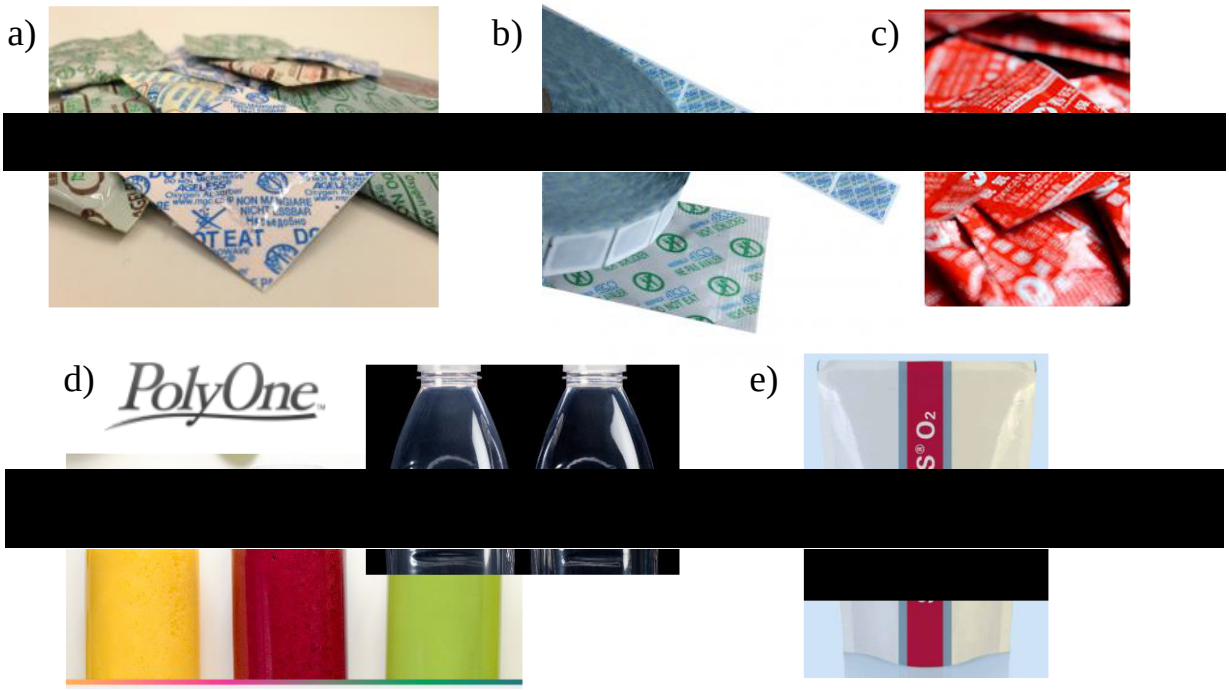

***Figure I-19**: Commercial oxygen scavenger technologies in sachet form from a) Ageless® (Mitsubishu Gas Chemical, USA), b) ATCO® (Laboratoires Standa, France), c) BestKept® (Chunwang, China), and directly incorporated inside the film packaging from d) AMOSORB™ (PolyOne, USA) and e) ShelfPlus® O_2 (Albis Plastic, USA). All pictures are extracted from the companies respective websites, accessed online on the 22.04.2020*

The main technology for oxygen scavenging is based on iron materials, because of their low toxicity and low cost. Most commercial products then use iron derived materials, which works by oxidation of the iron powders Fe(0) into Fe(III) for complete oxidation[229]. Moreover, it has also been shown that iron nanoparticles are capable to achieve higher oxygen scavenging properties than their macro- and micro-counterpart[230]. However, several other systems exist and several studies have investigated the impact of oxygen scavenger on various food item preservation using active chemical such as photosensitive dyes[231,232], ascorbic acid derivatives[233,234], sulphite-based system[235], pyrogallic acid[236], or palladium particles[237]. The

different oxygen scavenging systems reported in the scientific literature for active packaging applications are summarised in **Table I-7**. Finally, promising materials based on biological systems such as bacteria or enzymes have also emerged[238,239].

***Table I-7**: Oxygen scavengers for active packaging applications (OPET= oriented PET, OPA=oriented polyamide, BOPP=biaxially oriented PP, CPP=cast PP, OS=oxygen scavenger, EVOH= ethylene vinyl alcohol, EVA=ethylene vinyl acetate, LLDPE=Linear LDPE, SiOx=silicon oxide)*

Oxygen scavenger	OS form	Food target	Packaging materials	Study conclusion	Reference
Commercial products					
Ageless® (Fe)	Sachet	Chicken thighs	OPET/OPA/CPP	Less lipid/protein oxidation, less bacterial growth	Demirhan et al. (2017)[240]
Ageless® (Fe)	Sachet	Dry sausages	OPET/OPA/CPP	Less colour degradation, less microbial growth	Sahin et al. (2017)[241]
Ageless® (Fe)	Sachet	Wheat flour tortilla	Cryovac®	No improvement	Antunez et al. (2012)[242]
Ageless® (Fe)	Sachet	Ground meat	LDPE/PA/LDPE	Less lipid oxidation, less bacterial growth	Chounou et al. (2012)[243]
BestKept®	Sachet	Sponge cake	Cryovac®	Less textural and colour degradation, less lipid oxidation, less microbial growth	Janjarasskul et al. (2016)[244]
ATCO® (Fe)	Sachet	Strawberries	Microperforated BOPP	Less textural and colour degradation	Kartal et al. (2012)[245]
ATCO® (Fe)	Sachet	Endives	LDPE	Less colour degradation	Charles et al. (2008)[246]
Didai®	Sachet	Lamb loins	Cryovac®	No improvement	Trindade et al. (2013)[247]
Ageless OMAC® (Fe)	Film	Anchovy oil	PET/**OS**/PE/adhesive	Less lipid oxidation, less nutrient degradation (vitamin C and E)	Johnson et al. (2018)[248]
$Fe(OH)_2$ (no brand name)	Film	Meatball	PP/adhesive/EVOH/adhesive/**OS**/PP	Less colour and flavour degradation, less lipid oxidation	Shin et al. (2009)[249]
ABSO2RB (Fe)	Film	Cheese spread	PET/foil/**OS**/PE	Less nutrient degradation (Vitamin C)	Gomes et al. (2009)[250]
SHELFPLUS™O22400 (Fe)	Film	Salami roll	PET/adhesive/foil/adhesive/PE/**OS**	Less colour degradation, less lipid oxidation	Sängerlaub et al. (2012)[251]
ZerO2™	Film	Probiotic yogurt	EVOH/**OS**/EVA/Nupak®	Improved stability of probiotic bacteria	Miller et al. (2003)[252]
ZerO2™	Film	Milk	OPET/EVOH/**OS**/CPP	Less flavour degradation	Perkin et al. (2007)[253]
AMOSORB™	Film	Citrus juice	**OS** mixed with PET	Less colour degradation, less nutrient degradation (Vitamin C)	Baiano et al. (2004)[254]
AMOSORB™	Film	Fresh-cut banana	**OS** mixed with PET	Less colour degradation	Galdi et al. (2011)[255]
Home design					
Fe NPs (+ activated carbon, NaCl, $CaCl_2$)	Sachet	Roasted sunflower seeds and walnuts	Glass containers	Less lipid oxidation	Mu et al. (2013)[230]
Sodium metabisulfite	Sachet	Kimchi	PE/EVA/PE	Less colour degradation, less bacterial and mould growth	Lee et al. (2018)[235]
Sodium l-ascorbate (+ activated carbon)	Sachet	Raw meatloaf	PP	Less microbial growth, less lipid oxidation	Lee et al. (2018)[233]
Ascorbic acid + Fe powder or Zn powder	Film	Buns and bread	**OS** mixed with LLDPE	Less textural and flavour degradation	Matche et al. (2010)[234]
Polyfuryloxirane + photosensitive dyes (eosin/curcumin)	Film	Sunflower oil	**OS** mxide with ethyl cellulose	Less lipid oxidation	Maloba et al. (1996)[231]
Photosensitive dyes	Film	Orange juice	EVOH/**OS**/CPP	Less colour degradation, less nutrient degradation (Vitamin C)	Zerdin et al. (2003)[232]
Pyrogallic acid	Film	Peeled garlic	LDPE/**OS**	Less textural and colour degradation, less bacterial growth	Singh et al. (2019)[236]
Palladium	Film	Cooked cured ham	**OS** coated on PET/SiOx	Less colour change	Hutter et al. (2015)[237]

2.2.2. Ethylene Scavenging

Some fruits including tomatoes, melons or bananas are called climacteric fruits, meaning that their ripening stage is dependent on ethylene production. Ethylene is a plant hormone that controls different physiological mechanisms including the ripening mechanism in a autocatalytic manner: the ripening stage of the fruit triggers ethylene production and the ethylene produced stimulate the ripening by accelerating respiration[256]. Climacteric fruits can then continue the ripening process after they are harvested. Thus, controlling atmospheric ethylene concentration is key in controlling the ripening process and so the shelf-life of these fruits in packaged products. As for oxygen scavenger, technologies that aim at reducing the amount of ethylene inside fruits packaging are either the fine-tuning of the permeability of packaging materials, modified atmosphere packaging (MAP) or ethylene scavenger. Ethylene scavenger can also be found principally inside a permeable sachet, or incorporated inside the packaging materials and several commercial products are available[257].

Very recently, ethylene scavenging for active packaging applications have been thoroughly reviewed[257,258]. The ethylene scavenging mechanism can occur via a chemical route such as oxidation reaction or via a physical route such as adsorption. Oxidation of ethylene is commonly conducted using potassium permanganate however the toxicity of this chemical leads to debate concerning its use it for food packaging application[259–262]. Ethylene scavenging via physisorption can occur using substance such as zeolites[263–265] or clays (kaolin, montmorillonite, halloysite nanotubes)[266–268]. A combination of titanium dioxide and silver nanoparticles systems also showed strong capability to scavenge ethylene in food packaging applications[269–271]. Other systems have been proven to be effective to scavenge ethylene but have not been tested in packaging applications, for instance, activated carbon, substituted diene and triene, oxidising agents such as potassium dichromate, silver nitrate, or iodine pentoxide[258]. Some examples of ethylene scavengers are described in **Figure I-20**. The different examples of ethylene scavenger successfully used in food packaging applications are summarised in **Table I-8**.

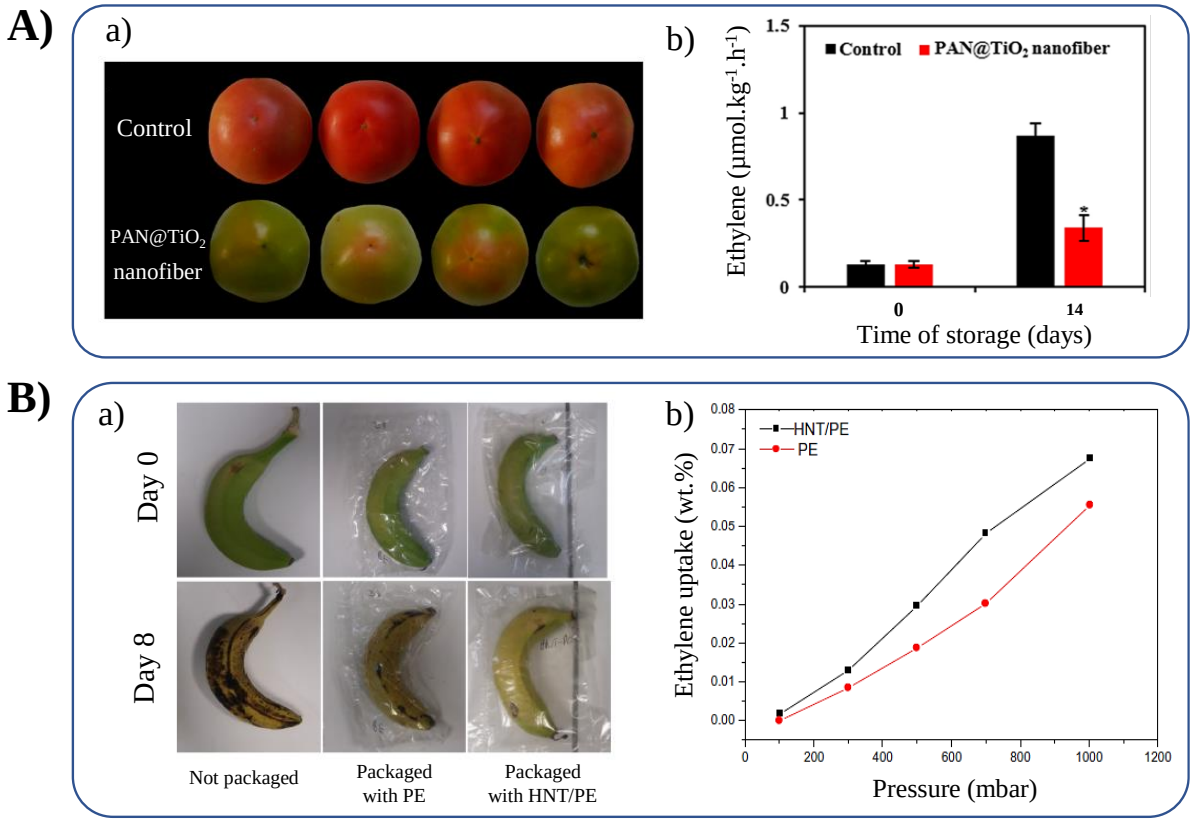

***Figure I-20**: Ethylene scavenging technologies examples. A) Electrospun polyacrylonitrile (PAN) fibers coated with TiO_2 and deposited on polypropylene films for tomato packaging with a) visual pictures of the reduction in ripening process and b) corresponding ethylene production during 14 days of storage. B) Halloysite nanotubes/LDPE composites produced by extrusion blowing for bananas packaging with a) visual pictures of the reduction in ripening process and b) corresponding ethylene uptake. Respectively reproduced and adapted from Zhu et al. (2019) for A)[272] and from Tas et al. (2017) with permission from Springer Nature (Copyright 2017) for B)[267]*

***Table I-8**: Ethylene scavengers for active packaging applications (PAN=polyacrylonitrile, NT=nanotubes)*

Ethylene scavenger	Agent form	Food target	Packaging materials	Study conclusion	Reference
$KMnO_4$	Sachet	Guava fruit	PVC	Less colour and textural degradation, less mould growth	Murmu et al. (2018)[262]
$KMnO_4$ (+ silica/silica gel)	Sachet	Pointed gourd	PP	Less colour, sensory and textural degradation, less microbial and fungal growth	Bhattacharjee and Dhua (2017)[259]
$KMnO_4$ (+ vermiculite)	Sachet	Sapodilla fruit	PVC	Less textural degradation and less nutrient degradation (Vitamin C)	de Souza et al. (2017)[260]
$KMnO_4$ (+ silica crystals)	Sachet	Guava fruit	LPDE	Less colour, sensory and textural degradation	Singh and Giri (2014)[261]
PAN/TiO_2 nanofibers	powder	Tomatoes	PP	Less colour and textural degradation	Zhu et al. (2019)[272]
Ag NPs, TiO_2 NPs, montmorillonite	Film	Kiwi	Mixed with LDPE	Less colour and textural degradation, less nutrient degradation (Vitamin C), less microbial growth	Hu et al. (2011)[266]
Ag NPs, TiO_2, kaolin	Film	Strawberry	Mixed with LDPE	Less colour and textural degradation, less nutrient degradation (Vitamin C), less mould growth	Yang et al. (2010)[270]
Ag NPs, TiO_2 NPs, kaolin	Film	Chinese bayberries	Mixed with PE	Less ripening, less microbial growth	Wang et al. (2010)[268]
Ag NPs, TiO_2 NPs, kaolin	Film	Chinese jujube	Mixed with PE	Less colour and textural degradation, less nutrient degradation (Vitamin C), less microbial growth	Li et al. (2009)[271]
Ag NPs, TiO_2	Film	Tomatoes	Mixed with chitosan	Less colour and textural degradation, less fungal growth	Kaewklin et al. (2018)[269]
ZnO NPs	Film	Apple	Coated on PVC	Less colour change, lower ripening, less oxidation	Li et al. (2011)[273]
Halloysite NT	Film	Strawberry, banana, tomato	Mixed with LDPE	Less colour and textural degradation, less microbial growth	Tas et al. (2017)[267]
Zeolites (mordenite framework inverted)	Film	Mango	Mixed with LDPE-PS block polymer	Less colour, flavour, sensory and textural degradation, less microbial growth	Boonruang et al. (2012)[263]
Zeolites	Film	Broccoli florets	Mixed with LDPE	Less colour, sensory and textural degradation	Esturk et al. (2014)[264]
$KMnO_4$ (+ zeolite NP)	Filter	Peach	No packaging/in fridge	Less textural degradation, less fungal growth	Emadpour et al. (2015)[265]

2.2.3. Moisture Scavenging

The humidity inside a packaging is another key parameter to control as most packaged food products are sensitive to moisture either in a positive or negative way. For some dry products such as nuts, powders (coffee, spices, etc) or biscuits, the moisture level needs to be kept as low as possible to increase shelf-life. For products like meat, fish or vegetables however, the moisture level needs to be controlled: not too low to avoid drying but not too high to avoid enhanced microbial growth and retain an appealing visual aspect for the consumers. Indeed, humidity is an important factor affecting microbial growth as bacteria, mould and yeast depend on water for their growth[274]. The packaged products can also undergo structural degradation linked to unfit moisture level. Thus, in order to optimise the shelf-life of food products, the moisture content of a package needs to be carefully optimised by the manufacturer for a specific food product, taking into account parameters such as the supply chain requirements, specific packaging used together with the moisture content and migration inside the food[275]. Different technologies exist to regulate the humidity inside packaging: fine-tuning of packaging permeability, absorbing pads, Modified Atmosphere Packaging (MAP), or desiccants. Commonly, absorbing pads are used along with MAP packaging. Absorbing pads use highly absorbent materials, placed on the bottom of a packaging containing food products likely to release water yet are not really considered as active packaging materials. Desiccants are mainly used in sachet/bag form as no studies have for now focused on the direct incorporation of the moisture scavenger in the packaging material. A large variety of commercial desiccant products exists[276] and different materials have been investigated against food products, including silica gel, sorbitol, various salts such as NaCl, poly(acrylic acid) sodium salt or multi-components bentonite/sorbitol/$CaCl_2$/KCl systems[277–282]. The mentioned references are summarised in the **Table I-9**. Other materials such as zeolites showed promising moisture scavenging capability.

***Table I-9**: Moisture scavengers for active packaging applications (MS=moisture scavenger)*

Moisture scavenger	Agent form	Food target	Packaging materials	Study conclusion	Reference
Silica gel (+ethylene scavenger)	Sachet	Guava fruit	PVC	Less colour and structural degradation, less mould growth	Murmu et al. (2018)[277]
NaCl	Trays	Mushrooms	PP/**MS**/PP/EVOH/PE	Less colour degradation	Rux et al. (2015)[279]
NaCl	Sachet	Tomatoes	LDPE	Less fungal growth	Shizari et al. (1992)[280]
Poly(acrylic acid) sodium salt	Sachet	Maize grain	Not supplied	Less bacterial growth	Mbuge et al. (2016)[281]
Sorbitol	Sachet	Mushrooms	PVC	Less bacterial growth	Roy et al. (1995)[278]
Bentonite, sorbitol, $CaCl_2$, KCl	Sachet	Mushrooms	PVC	Less colour degradation	Mahajan et al. (2008)[282]
DuPont™ Entira™ AS SD100 (resin) + NaCl	Trays	Strawberries, tomatoes	PE/foam+**MS**/ionomer tray closed with PP lid	Shelf -life extension	Rux et al. (2016)[283]

In this section, active packaging technologies were reviewed and both emitters (antibacterial, antioxidant, carbon dioxide emitter) and scavengers (oxygen, ethylene and moisture) were addressed. A specific care was taken to review the materials used in a significant part of the experimental section of this work named nanocellulose (and especially cellulose nanofibrils) and silver nanoparticles (and especially silver nanowires) first separately with their preparation technique and properties relative to packaging applications, and secondly the composites made of the combination of the materials developed for antibacterial applications.

3. Intelligent packaging

This section reviews the main intelligent packaging technologies and a special focus is placed on gas sensors and indicators because a significant part of the experimental study of this work was dedicated to the development of gas sensors using Metal Organic Frameworks materials.

Intelligent packaging technologies are able to collect, store and distribute information. Two sub-categories are usually distinguished: sensors/indicators and interactive technologies. The sensors and indicators roles are to detect changes in quality indicators measurable in the inside atmosphere of a packaging. Interactive technologies refer to the implementation of devices having the capability to collect, carry and deliver data, which relies predominantly on radio-frequency identification (RFID) tags and RFID-enabled sensors.

3.1. Sensors and Indicators

Sensors and indicators provide information either to the consumer, the manufacturer or any other supply chain actor about the package product. The concept is to detect and/or quantify a physical or chemical change in the internal packaging atmosphere relevant as a quality indicator specific to the packaged product. For food products, for instance, these quality indicators may include oxygen and carbon dioxide gaseous concentration, humidity level, time-temperature parameters or any other specific chemicals presence and/or concentration. Whereas the sensor should enable the quantification of the change in the environmental study, the indicators display qualitative or semi-quantitative information based on a visual change (**Figure I-21**).

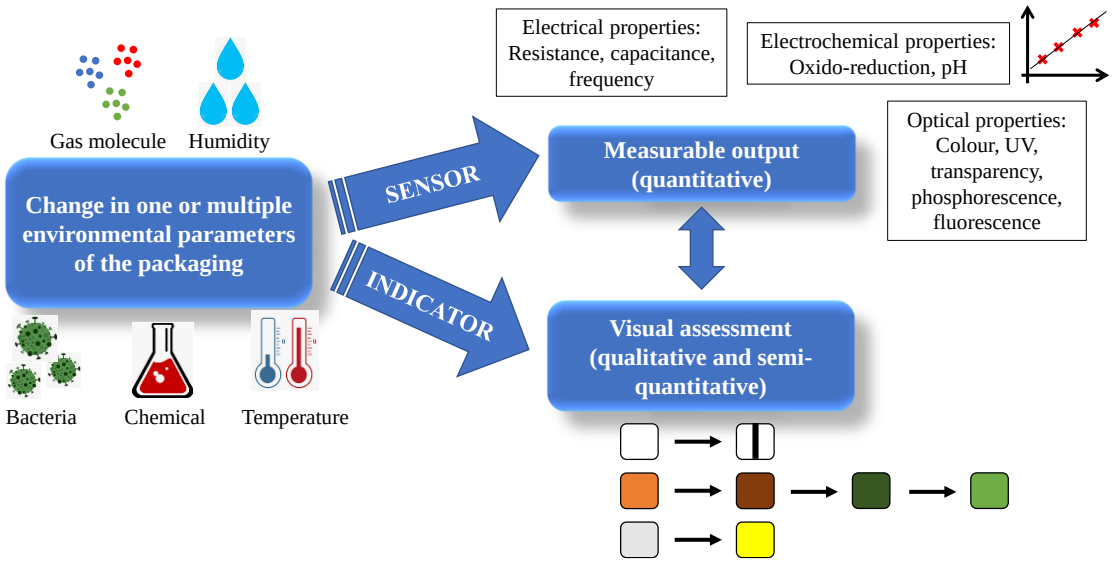

***Figure I-21**: Global schematic about sensors and indicators for intelligent packaging applications*

From a user-friendly perspective, sensors display a precise quantified value but are not always straightforward to read and thus the capability of indicators that can be directly read by the human eye is of more interest.

3.1.1. Gas sensors and Indicators

The internal gas atmosphere of a packaging plays a major role in the shelf-life of a product. The most important gases studied for their influence in for packaging applications are oxygen, carbon dioxide and water (humidity). Their influence and control in active packaging technologies were also already detailed in Sections **2.1.3.**, **2.2.1.** and **2.2.3.**. Other specific gas can also be used as control quality indicators such as for instance ammonia and other volatile amines for seafood freshness.

1. Oxygen

Oxygen gas sensors for packaging applications are mainly based on a photoluminescence (and especially phosphorescence) principle because it can be implemented in a non-destructive, reversible and easy to scale-up approach[284,285]. Photoluminescence is the emission of light induced by prior light emission and in the case of phosphorescence this energy desorption happens through an intermediate excited state. Photoluminescent dyes are usually made of ruthenium or platinum complexes often substituted with porphyrin ligands. The active material is often immobilised inside the packaging in the form of a label[284,286–292], by coating directly on the packaging itself[293,294], or by incorporating inside the packaging film[285] (**Figure I-22**). The quality of food products at the point of sale such as meat, cheese or salad can be detected using this sensor type. Similar devices were tested at the industrial level, enabling the identification of packaging failure through the supply chain[295,296]. Chemiresistive sensor using an iron (II) complex with carbon nanotubes (CNT) prepared by modification of commercial RFID tag has also shown promising results with smartphone compatibility for direct reading[297].

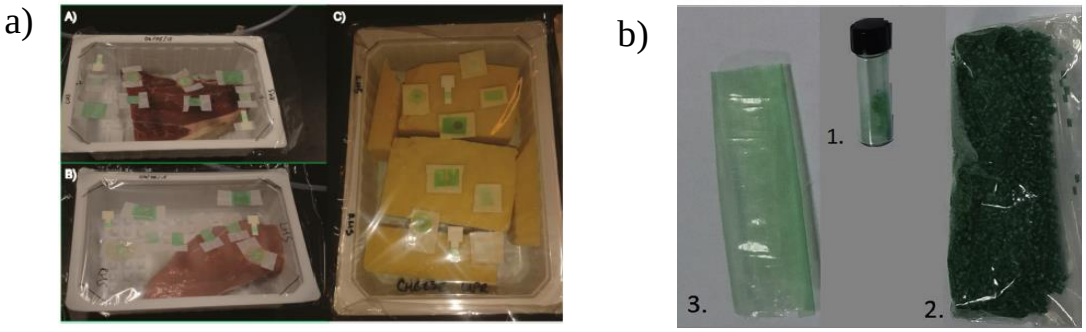

***Figure I-22**: Platinum-porphyrin phosphorescent oxygen sensor: a) prepared from drop-casting on a label which is inserted into meat or cheese packaging or b) preparing a composite by film extrusion with low density polyethylene (LDPE) or polylactic acid (PLA). Respectively reproduced and adapted from Kelly et al. (2018) for a)[292] and from Kelly et al. (2020) with permission from Elsevier (Copyright 2019) for b)[285]*

Oxygen sensors based on luminescence often requires extra equipment to excite the systems and measure the response which cannot be directly checked by human eye. This is why several alternative indicators technology have been developed, using redox systems and colour changes with chemical probes like methylene blue[298–300], but also some less used substances like tetraphenylethene[301], guaiacol[302], zein[303], polyviolene[304] or indigo-tetrasulfonate[305] (**Figure I-23**).

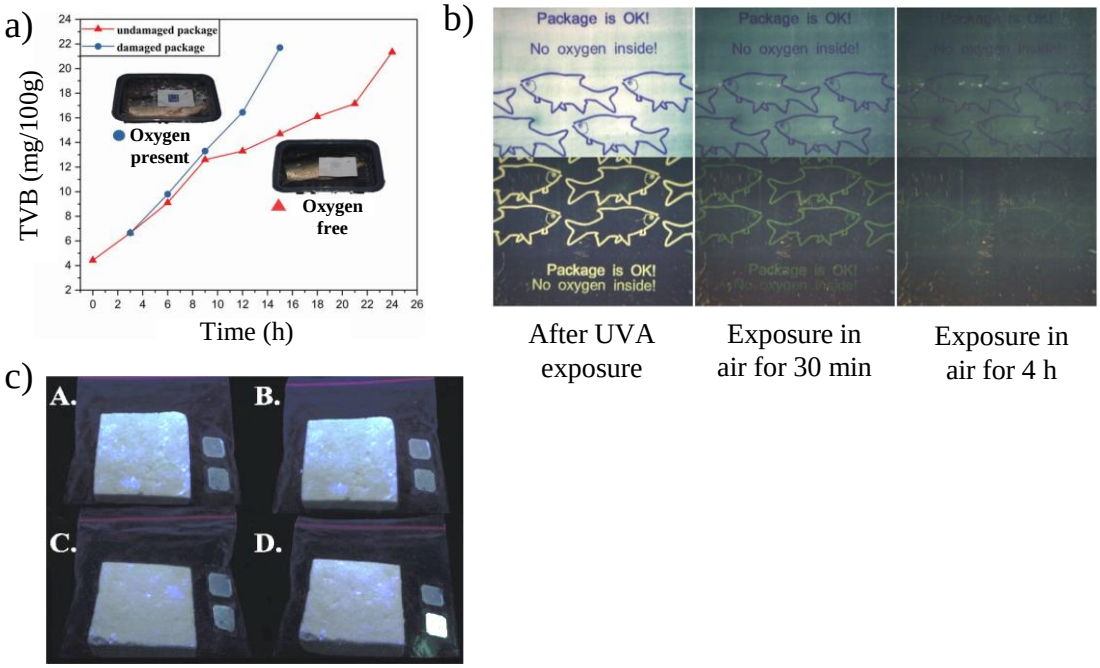

***Figure I-23**: Different oxygen indicators with a) redox sensitive label based on a methylene blue/Ag-TiO_2 system for the detection of oxygen in damaged Modified Atmosphere Packaging (MAP) and corresponding volatile amine measurements to assess fish spoilage, b) redox sensitive system based on methylene blue/TiO_2 printed directly on polymeric substrate by flexography and c) fluorescent label using tetraphenylethene probes (top = control, bottom=probe) for cheese packaging: A.=packaged under N_2 at t=0, B.=under N_2 at t=4 days, C.=under air at t=0 and D.=under air at t=2 days. Respectively reproduced and adapted from Wen et al. (2019) with permission from Wiley (Copyright 2019) for a)[298], from Saarinen et al. (2017) with permission from Wiley (Copyright 2017)[299] and from Rahaman et al. (2019) with permission from The Royal Society of Chemistry for c)[301]*

Adoption from industry for these smart technologies is now starting to develop and oxygen sensors and indicators can already be found commercially with for example OpTech-O_2™ (Ametek Mocon, USA), O_2xydots® (Oxysense, USA), or PSt3 (PreSens, Germany) for sensors and Ageless Eye (Mitsubishi Gas Chemical, USA) for indicators.

2. Carbon dioxide

Due to its importance linked to industrial emission and ecological aspects, carbon dioxide sensors were extensively studied and produced. However, only a few studies have been focusing on the development of carbon dioxide sensors for smart packaging applications[306]. Like oxygen sensors, most of them are optical sensors based on phosphorescence and

fluorescence techniques[307,308]. Some of them have tackled carbon dioxide sensing in Modified Atmosphere Packaging (MAP)[309,310]. However, Bibi et al. (2017) reported the preparation of electrical capacitance-based sensor with wheat gluten as sensing layer on interdigitated electrodes with practical interest for packaging application[311]. Even fewer studies have investigated their performance with real food products. Borchert et al. (2013) for instance prepared CO_2 sensor by drop-casting a platinum porphyrin dye on polyester film[312]. The phosphorescent sensor was then formed into a label and stuck inside a ready-to-eat salad packaging under modified atmosphere conditions. The sensor was sensitive and stable over a 20-day period. More studies have reported the preparation of carbon dioxide indicators, based either on a colorimetric method or transparency method. Colorimetric methods used pH active indicators such as metacresol sodium purple, bromothymol blue, methyl red, bromocresol green or phenol red and have been tested against pork, chicken meat and industrial egg-based dessert[313–316]. CO_2 sensors and indicators are mainly produced in the form of sticker/label, however Nopwinyuwong et al. (2010) and Rukchon et al. (2014) directly coated their indicators on PE films (**Figure I-24**). Transparency indicator are based on indicators in suspension in a sachet, using systems such as chitosan/2-amino 2-methyl 1-propanol, chitosan/blue dye or whey protein isolate[317–319].

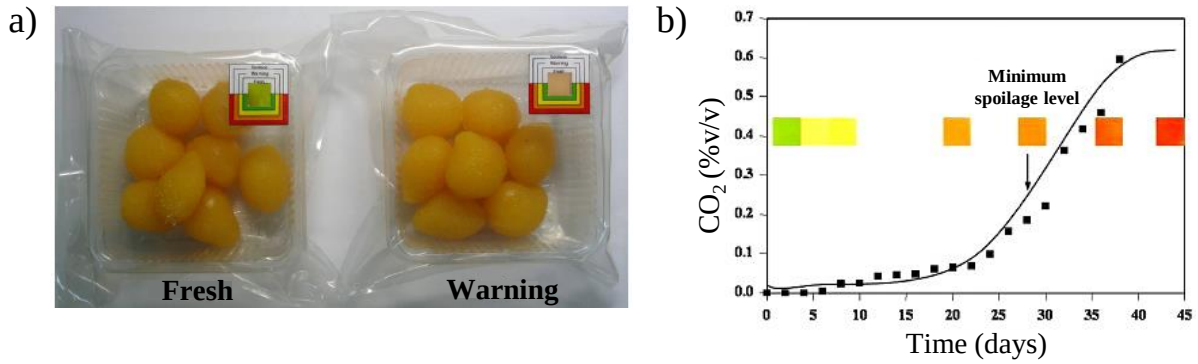

***Figure I-24**: pH sensitive CO_2 indicator label based on bromothymol blue and methyl red with a) application on "golden drop" desserts spoilage detection and b) corresponding CO_2 content versus time and equivalent colours of the indicator. Reproduced and adapted from Nopwinyuwong et al. (2010) with permission from Elsevier (Copyright 2010)[313]*

3. Water

Humidity sensing is of great interest in several applications (industrial equipment, agriculture, indoor environment control) and the reported references are too numerous to count. Humidity sensors are mainly based on active materials that include graphene and other carbon materials, ceramics, luminescent dyes, conductive polymers, organic and inorganic nanoparticles, semiconductor and metal oxides, metal organic frameworks, etc. However, few studies have implemented humidity sensors for intelligent packaging applications and the main reported studies are focusing on using sensors coupled with RFID technology for food products packaging such as mushrooms, cereal, fish or rice[320–322]. However, diverse examples of

humidity sensor developed using promising flexible platforms that could be easily adapted for packaging applications were also reported. Nanocarbons for instance were used for resistive flexible humidity sensors applications using systems such as reduced graphene oxide/poly(diallyldimethylammonium chloride) (PDDA) polymer on polyimide (PI) films, or CNT on paper substrate[323,324]. Rao et al. (2019) also used mechanical sensing methods by embedding graphene oxide into a film made of quaternized-hemicelluloses[325]. Zinc oxide can also be used as a humidity probe, and Reyes et al. (2013) prepared surface acoustic wave sensor with ZnO as active layer deposited on polyimide films[326]. Finally, organic materials could be used for humidity sensing such as cellulose nanofibrils (CNF) and Syrovy et al. (2019) reported impedance sensors based on CNF/polyethylene glycol free standing films[327]. Innovative colorimetric indicators that could be adapted to food packaging were also developed, based on technologies such as redox indicator supported in ionic liquid membrane[328], graphene oxide chip[329], cellulose nanocrystals iridescent film[330] or methylene blue/thiazines luminescent dyes encapsulated in hydroxypropyl cellulose[331].

Other gas have been shown to act as food quality indicators and so their quantification can be beneficial to intelligent packaging applications, for instance, ammonia and volatile amines, ethanol, hydrogen sulphide, or ethylene. In the experimental section of this work, flexible ammonia sensors were developed and so only ammonia and volatiles amines sensors for smart packaging applications will be reviewed here in addition of oxygen, carbon dioxide and water.

4. Ammonia

Volatile amines that include ammonia, trimethylamine and dimethylamine are known to be indicators of spoilage of fresh fish and seafood[332,333]. This is usually monitored by measuring the Total Volatile Basic Nitrogen (TVBN) which is a destructive and time-consuming method. Other biogenic amines were also identified as food spoilage indicators in food products such as meat or cheese[334]. Smart packaging using ammonia or other volatile amine sensor are then of interest for the detection of microbial spoilage principally for fish or seafood products. Nguyen et al. (2019) tested the application of an optical sensor based on polyacetylene vesicles, stabilised with cellulose nanocrystal and chitosan[335]. The sensor was a film prepared by solvent casting and later adapted for a smart label for meat spoilage detection. In another example, Kuswandi et al. (2012) developed an optical sensor based on a polyaniline (PANI) film and the measured ammonia concentration was well correlated with microbial analysis[336]. The authors also successfully implemented their system in a smart label with colorimetric freshness indicator. Promising resistive ammonia sensor based on a CNF aerogel loaded with hydroxyapatite were also developed by Narwade et al. (2019) but were not yet tested against real food products[337]. Other studies have also used commercial sensor and coupled it with RFID technologies to monitor fish spoilage[338]. For a direct transmission of the information, several

colorimetric indicators were also prepared mainly based on pH sensitive materials like sulphonephtalein dyes, purple sweet potato anthocyacin, cinamil and quinoxaline, curcumin and other classic colorimetric dyes such as bromophenol blue, bromocresol green, etc.[339–346]. Finally, ammonia sensing is also interesting in other type of applications like healthcare or industry and so different types of ammonia sensors have been developed by the scientific community. These devices includes printed and flexible sensors that could be adapted for packaging applications, mainly based on nanocarbons (graphene, graphene oxide, CNT) or conductive polymers (PANI, polyporryle, poly(3,4-ethylenedioxythiophene) polystyrene sulfonate (PEDOT/PSS)[347,348]. Examples of these NH_3 and volatiles amines indicators are summarised in **Figure I-25**. **Table I-10** summarises the different gas sensors or indicators developed for intelligent packaging applications.

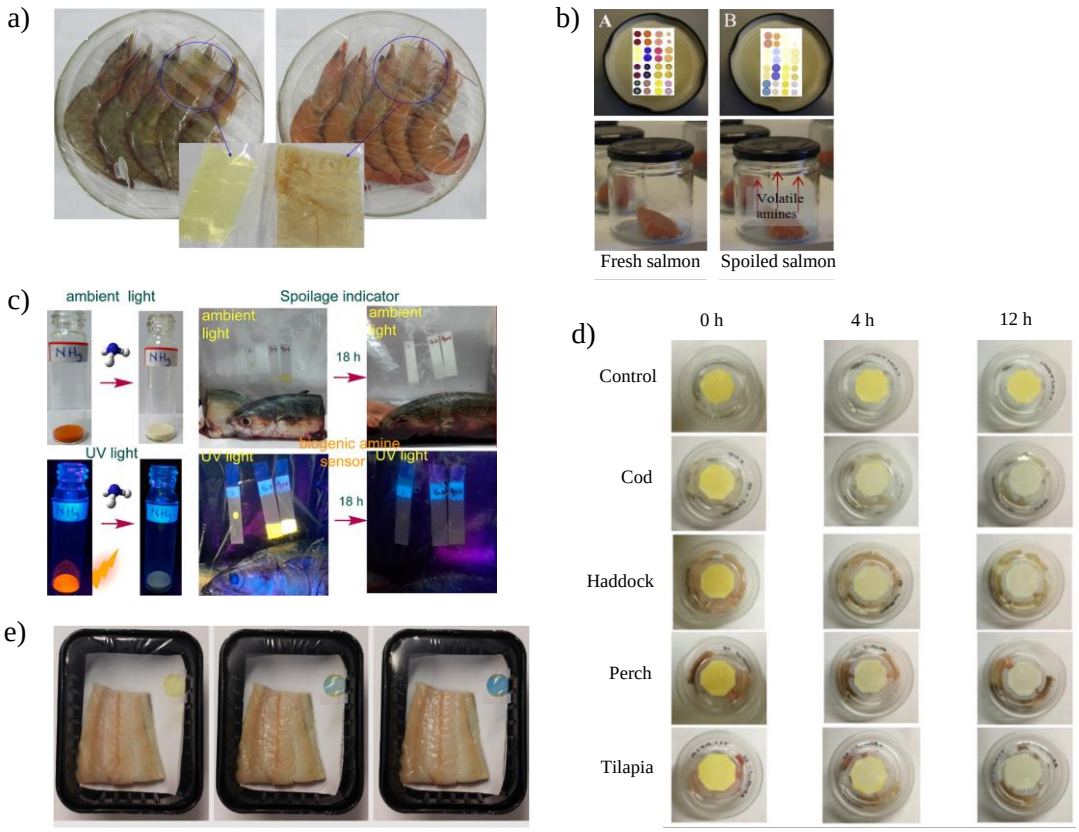

***Figure I-25**: NH_3 and volatile amine indicators for fish and seafood spoilage detection with a) pH sensitive film made of curcumin/tara gum/PVA and colour change before (left) and after spoilage (right), b) pH sensitive label with an array of 16 different colorimetric dyes and colour change after exposure to fresh (left) and spoiled salmon (right), c) fluorescent label based on pyrylium salts and colour change under UV light for unspoiled (left) and spoiled (right) specimen, d) pH sensitive label made by drop-casting quinoxaline on cellulose paper and colour at 0, 4 and 12 hours (from left to right) of storage at room temperature for control, cod, haddock, perch, tilipia (from top to bottom) and e) pH sensitive film using bromophenol blue extruded with LDPE and respective change of colour after storage at room temperature (from left to right: 0, 24 and 48 hours). Respectively reproduced and adapted from Ma et al. (2017) with permission from Elsevier (Copyright 2017) for a)[345], from Morsy et al. (2016) with permission from Elsevier (Copyright 2015) for b)[346], from Basavaraja et al. (2020) with permission from the American Chemical Society (Copyright 2020) for c)[339], from Luo et al. (2019)[343] for d) and from Wells et al. (2019) with permission from Elsevier (Copyright 2018) for e)[342]*

***Table I-10**: Gas sensors and indicators for smart packaging technologies (MB=methylene blue, PAA=porous anodic aluminium)*

Gas	Sensing method	Active material	Sensor form/Process	Food target	Reference
O_2	Phosphorescence	Platinum porphyrin dye	Label/Drop-casting on filter paper; Dip-coating and drop-casting on PP or PS; commercial Optech™ O_2	Beef and chicken meat, smoked fish, sliced ham, bread, cheese, salad	Papkovsky et al. (2000), Fitzegerald et al. (2001), Smiddy et al. (2002), O'Mahony et al. (2006), Hempel et al. (2012), Hempel et al. (2013), O'Callaghan et al. (2016), Kelly et al. (2018), Kelly et al. (2020)[286–292,295,296,349,350]
	Phosphorescence	Platinum porphyrin dye	Film/Drop-casting on PE	Beef lasagna	O'Mahony et al. (2004)[351]
	Phosphorescence	Platinum porphyrin dye	Film/Extrusion + lamination with PLA and LDPE	Beef meat, cheese	Kelly et al. (2020)[285]
	Chemiresistor	Fe(II) complex-CNT	Commercial RFID tag adapted	Vegetables	Zhu et al. (2017)[297]
CO_2	Phosphorescence	Platinum porphyrin dye	Label/Drop-casting on Mylar foil	Salad	Borchert et al. (2013)[312]
H_2O	Resistor	Ag NPs	RFID tag on chip	Mushroom	Le et al. (2016)[321]
	LC resonance	Paper	RFID tag printed on paper	Cereal	Tan et al. (2007)[322]
NH_3	Colorimetric	PANI	Film/Solvent casting	Fish	Kuswandi et al. (2012)[336]
	Colorimetric	Polydiacetylene vesicles	Film/Solvent casting	Beef meat	Nguyen et al. (2019)[335]

Gas	Colorimetric indicating concept	active material	Indicator form/Process	Food target	Reference
O_2	Redox	MB (+TiO_2)	Label/Drop-casting on glass	Meat	Mills and al. (2005)[305]
	Redox	MB (+TiO_2)	Label/Flexography and reverse gravure coating on PET or paper	Fish	Saarinen et al. (2017)[299]
	Fluorescence	Tetraphenylethene	Label/Dip-coating of filter paper	Cheese	Rahaman et al. (2019)[301]
	Redox	MB (+Ag-TiO_2)	Label/Screen-printing on PET	Fish	Wen et al. (2019)[298]
CO_2	pH	Metacresol sodium purple	Label/Solvent casting on Mylar foil	Pork meat	Pérez de Vargas-Sansalvador et al. (2010)[314]
	pH	Bromothymol blue, methyl red, bromocresol green, phenol red	Film/Coating on LLDPE	Industrial dessert, chicken meat	Nopwinyuwong et al. (2010), Rukchon et al. (2014)[315,313]
	Transparency	Chitosan/blue dye	Sachet/Indicator in LDPE sachet	Kimchi	Meng et al. (2014)[317]
	pH	Anthocyanins (+Lysine, ε-polylysine)	Label/Solvent casting on PET	Chicken meat	Saliu et al. (2018)[316]
NH_3	pH	16 different colorimetric dyes	Label/Drop-casting on silica plates	Fish	Morsy et al. (2016)[346]
	pH	Bromocresol green	Label/Dip-coating of PAA membrane	Fish	Mo et al. (2017)[344]
	pH	Curcumin	Film with tara gum/PVA	Shrimp	Ma et al. (2017[345]

In the experimental section of this work, gas sensors were developed using Metal Organic Framework active materials. Even if they have not yet been reported for gas sensing in smart packaging applications, the next section reviews these materials: their synthesis, processability and their gas sensing properties

5. Metal Organic Framework

Metal Organic Framework (MOF) is a relatively recent class of porous and crystalline materials, produced by coordinating organic ligands on metallic ionic centres. By using multifunctional ligands, it is possible to bridge the metallic ions and the organic ligands together, creating an 3D, organised and crystalline network. The precise shape and network organisation is dependent on the geometry and the coordination capability of the ligands/metal couple (**Figure I-26a**). This network organisation also enables the rational building of MOF materials with tunable properties (**Figure I-26b**). The first report of such organic-inorganic material is attributed to Yaghi et al. (1995) who developed a system based on cobalt centres coordinated with benzenetricarboxylate (BTC) ligands[352]. The authors designed the MOF based on metal-carboxylate synthesis and by choosing carefully the ligands, they found out that the synthesis led to a pink crystal insoluble in neither water nor organic ligands. They also showed that it was possible to entrap pyridine molecules inside the porous network. Since then, research focusing on Metal Organic Framework have boomed and a lot of different ligand-metal combinations have been developed for different types of applications such as catalysis, biomedical, gas separation-adsorption-sensing.

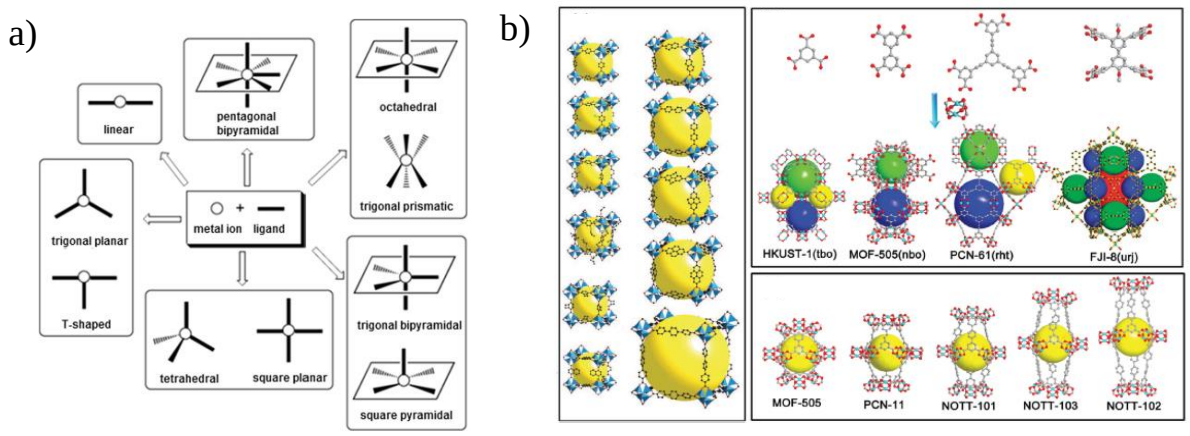

***Figure I-26**: MOF general overview with a) commonly accepted metal-ligand coordination geometries and b) examples of crystalline MOF structures: different isoreticular MOF with chemical formula $Zn_4O[R(COO)_2]_3$ (left), different copper-based MOF with their ligands (top right) and nbo-type MOF (bottom right). The coloured spheres highlight the pore size. Respectively reproduced and adapted from Gangu et al. (2016) with permission from Elsevier (Copyright 2016) for a)[353] and from Li et al. (2016) with permission from Wiley (Copyright 2016) for b)[354]*

1. Synthesis

MOF materials can be synthesised using different procedures and the most classic is the hydro(solvo) thermal process. This process requires high pressure and temperature in the presence of water (hydro) or solvent (solvo) to generate the MOFs. The material precursors are dissolved together in the desired solvent in an autoclave (or any pressured closed vessel). The reaction temperature should then be set higher than the boiling point of the solvent to reach increased pressure which will initiate the heterogeneous reaction between the precursors. Several solvents have already been used in studies reported in scientific literature such as ethanol, methanol, dimethyformamide (DMF), acetonitrile, 1-methyl-2-pyrrolidone (NMP), toluene, etc. This technique is often used because it is relatively easy to operate and it leads to a high yield of MOF production, yet it needs a precise control of several parameters such as temperature and reaction time, solvents and precursors solubility, pH and viscosity of the reaction media, as well as additional reactants such as mineraliser or surfactant[355]. Another technique to produce MOFs which is relatively similar to solvothermal method is to assist the reaction by either microwave or sonication. These green alternatives enable the MOF production by increasing local energy either by electric current or increased Brownian movements for sonication, or either by cavitation phenomenon for microwaves[353]. Other techniques to produce MOFs also exist such as an electrochemical method in which metallic plates were used as electrodes and the ligands precursors dissolved in a solvent while applying a relatively high voltage, precipitating the MOF materials[356]. This synthesis technique is fast, reliable and leads to MOF with high purity[357]. Finally, rarer methods to produce MOFs include a solvent-free mechanochemical procedure, ionothermal synthesis or diffusion techniques[353].

2. Processability

New MOFs structure are designed and synthesised almost every day, however the handling and processing of these materials is not that straightforward. MOFs are mainly synthesised in the form of fine powders, which are not soluble in solvents and very brittle. These powders usually need to be deposited on a substrate as a thin film in order to use the full potential of MOF materials. The most straightforward technique to produce such thin films is first of all the casting process. To do so, the MOF material is suspended in solvent, dispersed and casted on the desired surface. Such a technique is easy to implement and does not require complex equipment but the control of the deposited thickness is difficult. The references using such deposition techniques are too numerous to quote. Other more complicated techniques have been used to deposit MOFs previously synthesised and suspended in solvent such as spin-coating[358–362], electrospraying[363,364], or electrospinning with extra polymeric binders[365]. The 3D-printing process has also been extensively studied[366–368] and other printing processes have been used to deposit MOFs such as screen-printing or inkjet. For instance, Ahmann et al. (2009) and Pohle et al. (2011) used the screen printing processes to produces gas sensors[369,370]. More recently,

Sue and al. (2016) used inkjet printing to deposit MOF materials on Indium Tin Oxide (ITO) for electrocatalytic active surface development whereas da Luz et al. (2015) used the same process to print photoluminescent MOF for anti-counterfeiting applications. Zhuang et al. (2013) used an inkjet process where the authors printed MOF precursors to in-situ synthesise MOF on textile, plastic and paper substrates[371]. MOFs can also be grown in-situ onto the desired surface and several techniques exists that will not be detailed here such as for instance (not exhaustive) electrochemical deposition, chemical vapor deposition, atomic layer deposition, liquid-phase epitaxy, interface synthesis, etc[372]. These in-situ techniques usually enable the deposition of very thin films and often with a precisely controlled orientation for the crystal growth.

In the experimental section of this work, one MOF in particular was used for its gas sensing property, named Copper-benzene-1,3,5-tricarboxylate MOF. The next paragraph summarizes its main properties.

3. Copper-benzene-1,3,5-tricarboxylate

Copper-benzene-1,3,5-tricarboxylate MOF, also called CuBTC (or HKUST-1) is one of the more commonly used MOF today and was first synthesised in 1999 by Chui al[373] using the solvothermal technique. The authors reported that the architecture of the MOF was based on a dimeric copper-copper state with a $[Cu_3(BTC)_2(H_2O)_3]_n$ structure. The produced materials display a good BET (Brunauer, Emmett and Teller) surface area of 692 $m^2.g^{-1}$ and a calculated accessible porosity of 41%. Since then, BET surface area of produced CuBTC MOF has been increased to around 2000 $m^2.g^{-1}$ [354]. The crystallographic structure of such materials is complex resulting in a face-centred cubic crystal presenting 9Å by 9Å porosity. Moreover this specific BET crystallinity was found to be given by another octahedral secondary building unit (SBU) as it is often the case for MOF materials, leading to some other extra porosity yet with smaller apertures (tetrahedral windows of 5 Å and triangular shaped aperture of around 3.5 Å)[374,375] (**Figure I-27a** and **b**). This porosity is also dependent on the hydration state of the MOF materials[376].

There are then 32 Cu-Cu dimers (often described as paddlewheels) for each cubic crystallographic unit and 12 weakly coordinated water molecules (**Figure I-27c**). As previously described, water molecules complete the coordination sphere of each copper dimer, yet can be removed by moderate heating leading to uncoordinated copper sites. The crystals are of square bipyramidal shape in the micro-size range and the colour of the complex then changes from light/turquoise blue (non-activated) to dark blue/dark violet (activated)[377] (**Figure I-27d**). It is important to note that both activated and un-activated CuBTC MOF are stable structures but their physical properties and performances for different applications are impacted by their activation state.

Because the CuBTC MOF presents hydrophilic character and is weakly coordinated water molecules, such a MOF is sensitive to water[378]. CuBTC is unstable in liquid water as Doan et al. (2019) showed that the crystalline structure of CuBTC changes and collapses after immersion for a day[379]. This MOF is also sensitive to water in the gas phase and it was established that 90% of relative humidity was the maximum that the CuBTC MOF can withstand when exposed to water vapour[380]. Water molecule can indeed accumulated on the copper centre and induce a decoordination of the BTC ligand leading to the MOF decomposition because of the collapse of the crystalline structure[379]. CuBTC MOF is however thermally stable until around 250-300°C depending on the reference[377,381].

CuBTC is probably the most widely studied MOF and the performances of CuBTC systems were evaluated for a lot of applications including gas separation, gas sensors, catalysis, or environmental remediation[382] and because of such enthusiasm from the scientific community, this material is now commercially available from different companies such as BASF, ACS Material®, Nanoshel®, novoMOF, or MOF Technologies.

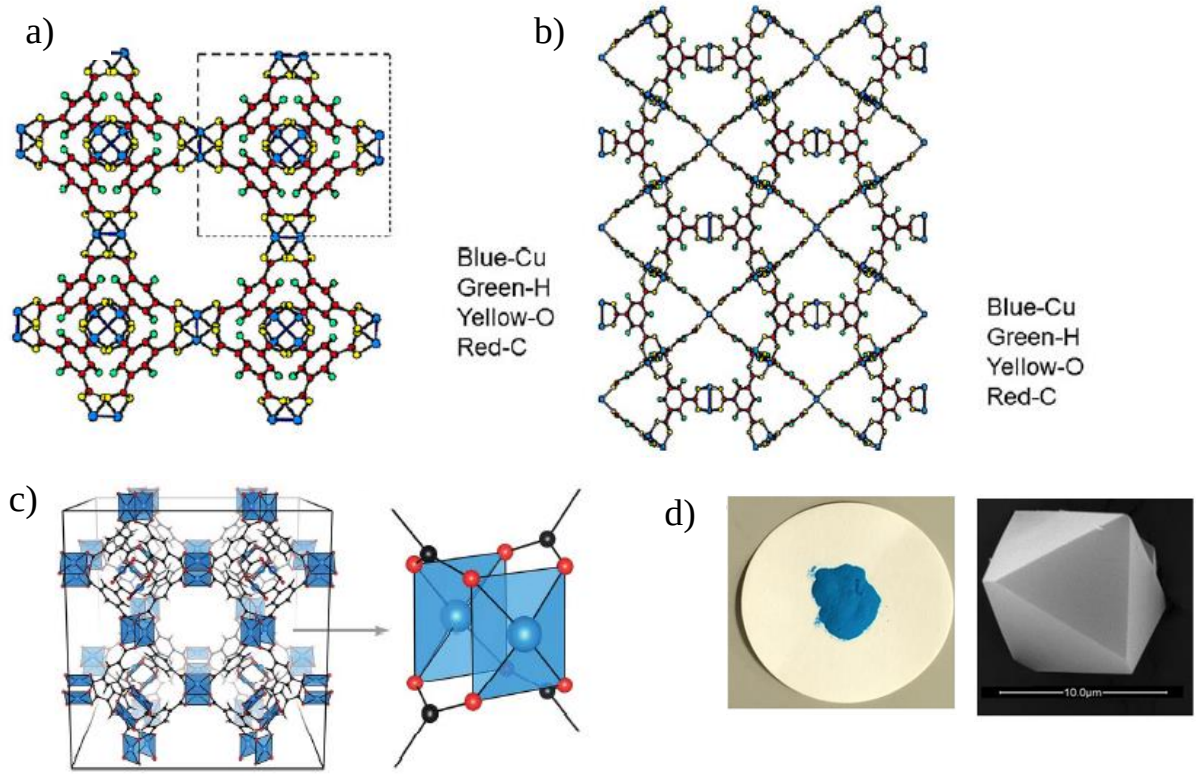

***Figure I-27**: Crystalline structure of CuBTC MOF with a) schematic view along the [100] direction, b) schematic view after 45° rotation along the [100] direction, c) cubic space unit cell (left) and Cu-Cu paddlewheel (right) and d) picture of CuBTC blue powder (left) and SEM image of one crystal (right, 10 µm size). Respectively reproduced and extracted from Wong-Ng et al. (2015) for a) and b)[374], Hendon et al. (2015) for c)[382] and from Al-Janabi et al. (2016) with permission from the American Chemical Society (Copyright 2016) for d)[383]*

4. Gas sensing

Because of the intrinsic nature of MOFs, there is almost an infinite possibility to design such materials and as they present highly ordered structure, it is also possible to rationally design MOFs for specific target applications based on the geometry of the ligand and the coordination capability of the metallic center[384]. Moreover, as previously described, the main properties of MOF materials are linked to their highly crystalline and porous nature. One of the key parameters of MOFs materials is also that they are highly versatile and functional materials. Indeed, the functionality of MOFs for a target application is carried out not only by the metallic centre but also by the organic ligand and even by some hypothetic molecules trapped inside the pores. MOFs are then promising materials for gas adsorption, separation and sensing applications

However, the main drawbacks of MOF materials are their poor stability, low conductivity and low selectivity for adsorption applications. Most of MOFs are indeed insulating materials due to their organic-inorganic nature and electronics applications are hindered by such property. Several techniques exist to dope their conductivity mainly linked to the design in the first place of the MOF but also to charge carrier doping inside. Also, a lot of work has been carried out on the development of new conductive MOF over the past 10 years[385]. MOF devices can be operated using different sensing types such as mechanical techniques (microcantilever, surface wave acoustic, quartz crystal microbalance), optical techniques (interferometry, luminescence, fluorescence, localised surface plasmon resonance) or electrical (capacitance, impedance, resistance, work function)[386].

Due to MOF promising gas sensing and adsorption properties, there is a high-volume scientific production on the subject. So only gas sensors prepared from MOF materials and using a concept similar to the experimental section of this work are reviewed. More precisely, only electrical gas sensors technologies are detailed.

Several authors have reported electrical gas sensing using MOFs. Achmann et al. (2009) were pioneers in the field of electrical gas sensing and especially impedimetric sensors using different commercially available MOF such as Al-terephthalate (AlBDC), Cu- and Fe-1,3,5-benzenetricarboxylate (CuBTC and FeBTC) and their corresponding Lithium-doped MOF against different gas targets (CO_2, O_2, NO, H_2, ethanol, propane, methanol, and humidity)[370]. The authors purchased the MOF either in the form of pellet or powder. The pellets were connected by metal discs on both sides whereas the MOF powders were formulated into printable slurry and then screen printed on top of gold interdigitated electrode (IDE). The impedance of the sensors was followed against gas concentration. In the end only FeBTC was proven to be effective for the sensing of humidity, ethanol and methanol. Using the same device preparation, Pohle et al. in 2011 described the production of a Kelvin probe gas sensor[369].

Mainly two different techniques are classically used to prepare sensors based on MOFs: pellet preparation or coating of MOF slurry onto interdigitated electrodes (IDE). In-situ growing of MOF crystals directly onto the desired electrodes or devices is also an effective option. When using pellets, the sides are usually coated with conductive materials to form electrodes then electrical properties are compared to gas input.

Indeed impedimetric humidity sensors were for example developed by Zhang et al. (2013) using titanium based NH_2-MIL-125 MOF[387]. The sensors were prepared by coating methanol MOF slurry on a silver-palladium IDE and measuring the impedance of the devices. In 2014, Chen et al. used ZIF-67 MOF for formaldehyde sensing by coating ethanol slurry on a silver-palladium IDE and measuring its resistance *vs* gas concentration[388]. For NH_3 sensing, Travlou et al. (2015) prepared a composite made of CuBTC MOF and graphite oxide processed it into a DMF slurry and blade spread in into gold IDE[389]. The actual sensing was made by following the resistance change compared to gas input. For the same application Campbell et al. (2015) built a conductivity sensor based on $Cu_3(HITP)_2$ MOF by preparing an acetone slurry and drop-casting it on gold IDE[390]. The same team prepared a more complicated device the same year: Campbell et al. (2015) used different MOF named $Cu_3(HHTP)_2$, $Cu_3(HITP)_2$, and $Ni_3(HITP)_2$ to prepare a conductivity sensing array for several volatile organic compound (VOC) sensing. The authors prepared acetone slurry for each MOF and drop-cast them onto a gold IDE[391]. Cui et al. (2018) reported the preparation of hybrid MOF/metal oxide slurry in ethanol/terpineol mixture followed by coating on a silver-palladium IDE[392]. The researchers encapsulated zinc oxide micro-rods in the MOF architecture which decreased the working temperature of the devices up to 50°C when compared to zinc oxide only sensors; they showed the successful sensing of their devices for hydrogen target gas at 125°C. CO_2 sensors were developed by Tchalala et al. (2019) using a fluorinated MOF. The developed devices were complex as the authors incorporated two transduction types inside, by spin-coating acetone/ethanol MOF slurry onto titanium-gold capacitive IDE for CO_2 sensing and onto a quartz crystal microbalance for humidity sensing[393].

Even if MOF slurry preparation and use for deposition onto a substrate is classic, there are not many reports of using aqueous slurry and Yin et al. (2018) is the only example for gas sensor preparation. Indeed the authors dispersed Cd(TMA)(DPP) MOF in water and coated it on silver-palladium IDE, measuring the resistance of the device at room temperature versus humidity rate[394]. In 2019, Meng et al. also proved very low detection limit sensors for various gas target (NH_3, H_2S, NO) using naphthalocyanine-based MOF by depositing a water slurry on gold IDE[395].

MOF slurry can also be deposited on substrates other than those carrying an IDE such as alumina or ceramics substrates. Tian et al. (2016) for instance developed a complex system based on a zinc oxide/ZIF-8 MOF core-shell structure for the resistance sensing of

formaldehyde[396]. The authors prepared a slurry with the ZnO/ZIF-8 component along with adhesive, and spin-coated this system on an alumina tube with gold electrodes and platinum wires attached. Several other studies have reported ZnO/ZIF-8 for similar sensing applications[397,398]. Still using MOF slurry deposition, another type of sensing was used by Sachdeva et al. (2017) with a NH_2-MIL-53/Matrimid polymer composite[399]. The composite was made into a THF slurry and drop casted onto a planar transducer sensor for capacitive change measurement. Homayoonia et al. (2016) also drop-casted CuBTC MOF slurry but on a parallel plate capacitance electrode[400]. Finally, Mohan Reddy et al. (2020) drop-casted ZIF-8, Zn(NA), Zn(INA) MOFs on a glass substrate connected with silver paste for resistive sensing of formaldehyde, ammonia and ethanol[401].

The summary of this literature review on electrical gas sensing based on MOF materials, either by slurry deposition on IDE and directly through a pellet, is displayed in **Table I-11**. Some examples are illustrated in **Figure I-28**. Another interesting way to produce a sensor based on MOF is to grow the MOF crystals directly onto the sensing electrode or devices. For instance, Yassine et al. (2016) grew fumarate-based MOF onto an IDE[402]. This enabled the capacitive change measurements that were tested for CH_4, NO_2, H_2, toluene, and H_2S gas. Hosseini et al. (2016) electrochemically grew CuBTC crystals onto a copper substrate for the same type of sensing, but applied to ethanol/methanol gas[403]. Using the same ZnO/ZIF-8 structure previously described, Wu et al. (2017) prepared a H_2 sensing device by growing the complex structure onto a platinum electrode measuring the resistance versus the gas input[404]. In 2019, Yuan et al. prepared capacitive sensors by growing Mg-MOF-74 on a micrometric IDE for CO_2 and benzene detection. The authors showed that it was possible to tune the selectivity of the sensors by using post-synthesis modification of the MOF[405].

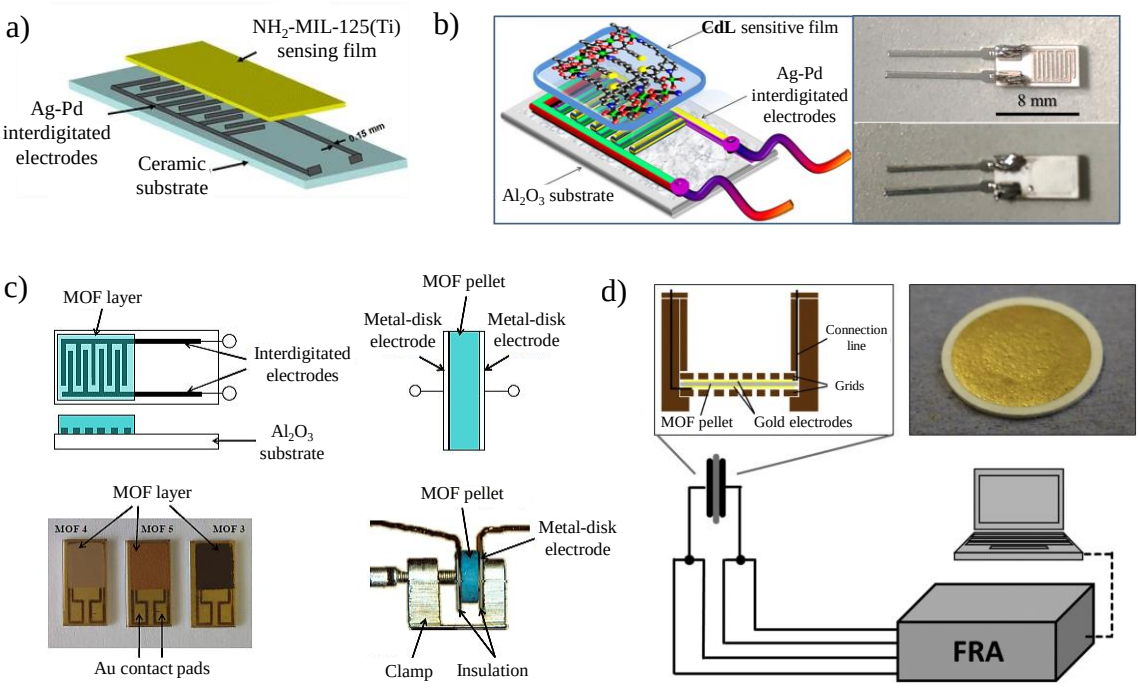

***Figure I-28**: Examples of gas sensors based on MOF materials with a) humidity impedance sensor using NH_2-MIL-125(Ti) MOF drop-casted on Ag-Pd IDE, b) schematic of humidity impedance sensor using Cd(TMA)(DPP) MOF (CdL) drop-casted on Ag-Pd IDE (left) and corresponding picture before (top right) and after coating (bottom right), c) different gas targets (CO_2, O_2, NO, H_2, ethanol, propane, methanol, and humidity) impedance sensors prepared either from screen-printed Al-, Fe- or CuBTC MOF on Au IDE (top and bottom left) or by pressed pellet (top and bottom right), and d) humidity capacitance sensor using CAU-10 MOF pressed into a pellet and insert into gold electrodes. Respectively reproduced and adapted from Zhang et al. (2013) with permission from Springer Nature (Copyright 2013) for a)[387], from Yin et al. (2018) with permission from Elsevier (Copyright 2018) for b)[394], from Achmann et al. (2009) for c)[370] and from Weiss et al. (2016) with permission from Elsevier (Copyright 2015) for d)[406]*

***Table I-11**: Review of electrical gas sensors based on MOF active materials prepared either by pellet use or by coating onto IDE (VOC=volatile organic compound, CVD= chemical vapour deposition, RT=room temperature)*

Target gas	MOF	Device preparation	Sensing (Temperature)	Reference
CO_2	CDMOF-2	Pellet: conductive silver epoxy and copper wire coatings	proton conductivity (RT)	Gassensmith et al. (2014)[407]
CO_2	Co-MOF-74	Direct pellet use	Conductivity (RT)	Strauss et al. (2019)[408]
Humidity	Cu_3TCPP	Pellet: gold paste and gold wire coatings	Capacitance EIS (RT)	Tian et al. (2016)[409]
Humidity	different modification of CAU-10	Pellet: gold electrodes coatings by CVD	Capacitance EIS (RT)	Weiss et al (2015)[410] Weiss et al. (2016)[406]
NH_3	Trimesic acid derived MOF (Ba, Cd, Pb, and Zn)	Pellet: carbon tape on both sides	Conductivity (RT)	Sel et al. (2015)[411]
Hydrocarbons	$Cu[Ni(pdt)_2]$	Direct pellet use	Resistance (RT)	Aubrey et al. (2019)[412]
SO_2, NO_2 and CO_2	NH_2-UiO-66	Pellet: silver conductive adhesive paste coatings	Resistance (150°C)	DMello et al. (2019)[413]
Humidity	NH_2-MIL-125	Coating methanol slurry on Ag-Pd IDE	Impedance (RT)	Zhang et al. (2013)[387]
Humidity	Cd(TMA)(DPP)	Coating water slurry on Ag-Pd IDE	Impedance (RT)	Yin et al. (2018)[394]
NH_3	$Cu_3(HITP)_2$	Drop-casting acetone slurry onto Au IDE	Conductivity (RT)	Campbell et al. (2015)[390]
NH_3	Cu-BTC/graphite oxide	Blade spreading DMF slurry onto Au IDE	Resistance (RT)	Travlou et al. (2015)[389]
NH_3, H_2S, NO	Metallophthalocyanines-based MOF	Drop-casting water slurry Au IDE	Conductance (RT)	Meng et al. (2019)[414]
NH_3, formaldehyde, ethanol	ZIF-8, Zn(NA), Zn(INA)	Drop-casting ethanol slurry on glass contacted with Ag paste	Resistance (RT)	Mohan Reddy et al. (2020)[401]
Formaldehyde	ZIF-67	Coating ethanol slurry onto Ag-Pd IDE	Resistance (150°C)	Chen et al. (2014)[388]
Different VOCs	$Cu_3(HHTP)_2$, $Cu_3(HITP)_2$ $Ni_3(HITP)_2$	Drop-casting acetone slurry onto Au IDE	Conductivity (RT)	Campbell et al. (2015)[391]
H_2	ZIF-8 (+ZnO)	Coating ethanol/terpineol on Ag-Pd IDE	Resistance (125°C)	Cui et al. (2018)[392]
CO_2	AlFFIVE-1-Ni and NbOFFIVE-1-Ni	Spin-coating of acetone/ethanol slurry on Ti/Au IDE	Capacitance (RT)	Tchalala et al. (2019)[393]

To overcome their weak electrical properties, MOFs can be used alongside electrically active materials such as conductive polymer, nanocarbon such as graphene or carbon nanotubes, metallic nanoparticles or metal oxides materials[389,397,415–419]. For instance, it has been shown that MOF/graphene composites present several enhanced properties such as synergetic electrochemical and conductivity properties, better MOF dispersion and a positive impact on the porous structure[420–422].

A panorama of the different systems existing for gas sensing used for smart packaging applications has been set out in this section, as well with the different requirements that are needed for such systems. Even though they have not yet been reported for intelligent packaging gas sensing applications, a specific focus was applied on Metal Organic Framework and their use as gas sensors as relative to the experimental work in this project. Finally, even if not directly used in the experimental section of the work, for completeness, other intelligent packaging technologies are reviewed briefly in the next sections, named Time/Temperature indicators, bacterial sensors and RFID-based technologies.

3.1.2. Time/temperature indicators

Controlling the temperature of a packaged product throughout its supply chain seems today a basic and obvious consideration. The possibility to measure the temperature and record it through time is then an interesting diagnostic for the safety of packaged products whether for food or medical packaging applications. Time/Temperature indicators (TTIs) are devices that can record changes in temperature of a packaged product through time, and display its results to any actors of the supply chain, in a user-friendly manner.

TTIs can be divided into several categories based on the indicating concept: enzymatic, physical, microbial, chemical or using nanoparticles. Enzymatic TTIs are probably the most studied TTIs, were extensively reviewed elsewhere and are based on enzymatic hydrolysis reaction associated with specific dyes using a large variety of enzymes such as laccase, amylase, lipase, glucosidase, etc.[423]. Chemical TTIs involve the change of colour of a chemical linked to its chemical state (redox, pH) with chemicals like anthracene, fructose/glycine, lysine/xylose, or anthraquinone[424–427]. Other chemical TTIs can also use the properties of stimuli responsive polymer such as polydiacetylene[428]. Physical systems are based on the irreversible change in the physical properties of polymer: by entrapping dyes inside the polymer, and releasing it due to physical change such as for instance change of the surface area (contraction/expansion)[429] or thermal transition[430].

More complex systems recently emerged based on a microfluidics concept[431]. Microbial TTIs associated the growth of microorganism to specific dyes changing colour with some bacterial growth indicators and use microorganisms such as *L. Sakei*, *W. Cibari*a or *Janthinobacterium sp.*[432–435]. Finally, systems that employ nanoparticles are also widely used. They mainly use

gold or gold-silver hybrid nanoparticles and are based on the following principle: time and temperature influence the shape and size of the NPs which then affects their plasmonic surface resonance and so their colour[436–438]. This technology has already been adopted by some packaging industrials and TTIs can already be found on the market commercialised by companies such as Vitsab® (Sweden), TEMPIX (Finland), Fresh-check® (USA), and others[439]. Examples of TTIs can be found in **Figure I-29**.

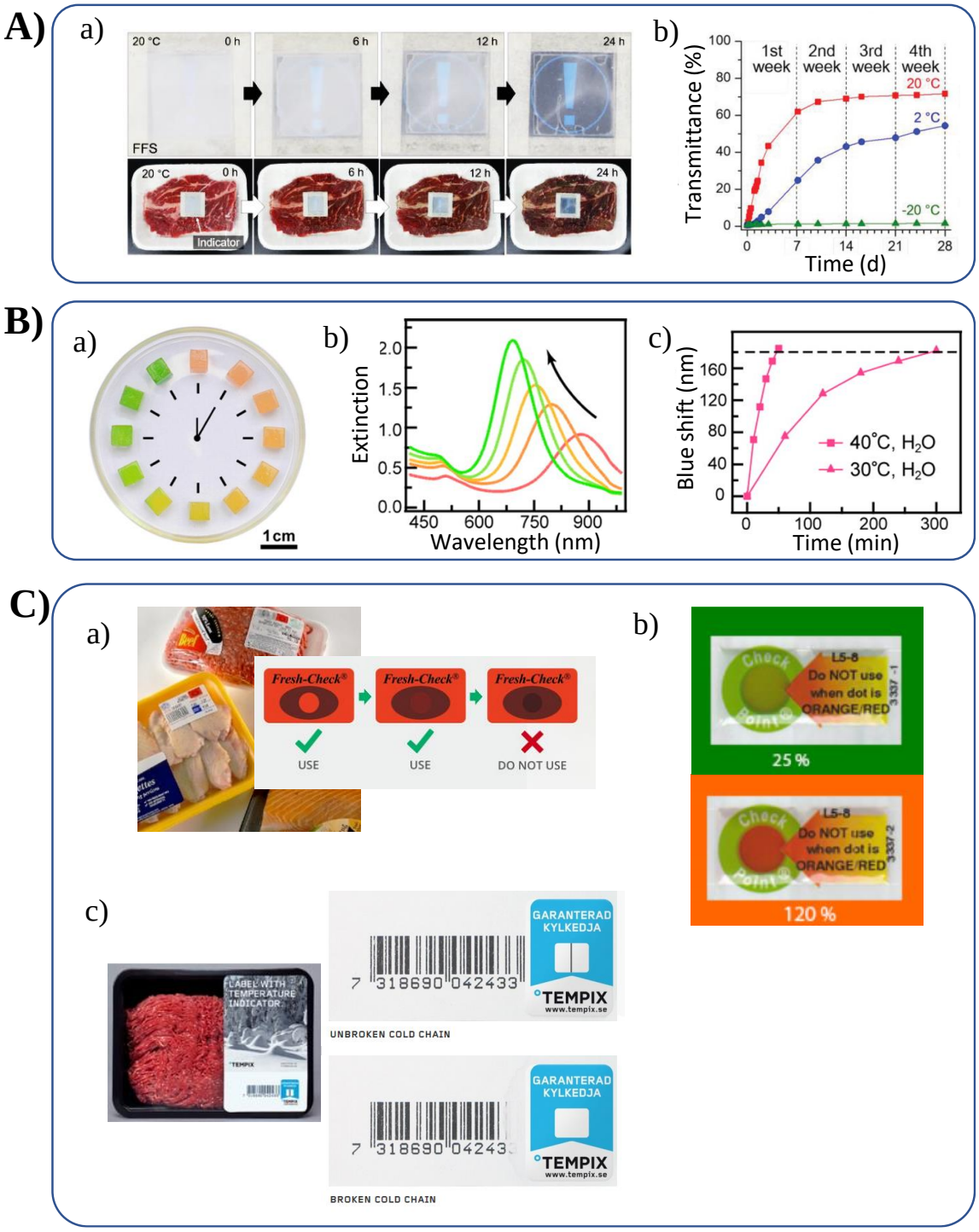

***Figure I-29**: Examples of Time/Temperature Indicators (TTIs) technologies. A) TTI based on a self-healing polyurethane polymer with a) visual evolution at 20°C of the indicator in meat packaging and b) change in the optical properties of the indicator over time at different temperatures. B) TTI based on Ag-Au core shell nanorods that changes colour over time with a) pictures of aerogels at different timeframe, b) evolution of plasmonic surface resonance at different timeframe and c) measured blue shift for time/temperature parameters. C) Commercial TTIs with a) Fresh-check® (USA), b) Vitsab® (Sweden) before (top) and after (bottom) breakage of the cold-chain and c) TEMPIX (TEMPIX AB, Finland). Respectively reproduced and adapted from Choi et al. (2020) with permission from Wiley (Copyright 2020) for A)[429], from Zhang et al. (2013) with permission from the American Chemical Society (Copyright 2013) for B)[438] and extracted from the companies website (accessed online on the 22.04.2020) for C)*

3.1.3. Bacterial indicators

Biosensors can be adapted to be interesting tools for intelligent packaging applications. Biosensors can indeed directly detect the presence of bacteria instead of measuring indirect indicators of bacterial contamination (gas, pH, etc.). The concept of bacterial indicator is similar to the other indicators already detailed: to incorporate within the packaging a label that indicated the presence of bacteria and thus avoiding to use time-consuming and expensive technique to investigate bacterial spoilage. A classic example is to use specific antibodies to detect the presence of bacteria by immobilising the antibodies on functionalised nanoparticles, like gold or palladium[440,441]. Other interesting techniques include electrochemical detection that can be coupled or not with microfluidic devices[442,443]. Bacterial indicators are mainly developed for medical applications yet Yousefi et al. (2018) developed a promising platforms for bacteria detection in food packaging applications[444]. The active substance was DNA oligonucleides capable of sensing bacteria presence by displaying fluorescence. The active molecules were printed on transparent and flexible polymer packaging by the inkjet printing process and successfully applied to the detection of *E. Coli* bacteria in meat and apple samples (**Figure I-30**).

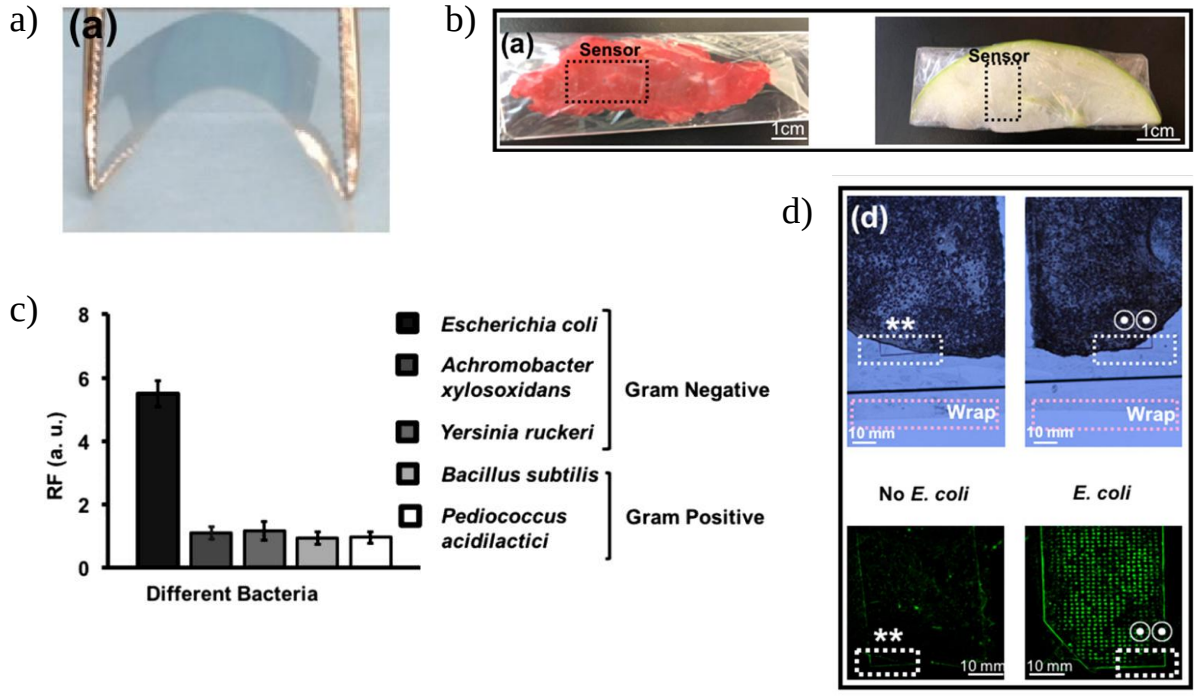

***Figure I-30**: Bacterial indicators system based on DNA oligonucleides and working by fluorescence with a) inkjet printed on flexible transparent cyclo-olefin polymer, b) indicators incorporated in meat and apple slices packaging, c) specificity toward E. Coli bacteria and d) detection of E. Coli in the meat and apple samples. Reproduced and adapted from Yousefi et al. (2018) with permission from the American Chemical Society (Copyright 2018)*[444]

3.2. Interactive technologies (RFID, RFID enabled sensors)

RFID means radio-frequency identification and RFID devices are mainly developed in the form of a tag that can transfer data through a reading device via electromagnetic waves. They have been implemented in packaging application and regarded as the upgraded version of barcodes. One of the key advantages of RFID tags over barcodes is that there is no need to have a direct visual contact between the reader and the tag because it does not use optical signal but electromagnetic ones. Thus, the RFID tags can be directly incorporated inside the packaging materials, still without any direct contact with the food product, ensuring consumer safety. The classic use of RFID tags is to carry data like barcodes and enabling enhanced traceability, control and security for products all throughout their supply chain[445]. However, more innovative systems are combining RFID with other types of smart packaging devices and especially sensors. The concept is then to be able to easily store, recover and transfer the data that was acquired by the sensor. Then, all the different electrical technologies that were reviewed in this section could be adapted to be used along RFID technology. Today's RFID enabled sensors are indeed numerous and include TTIs[446], oxygen sensor/indicator[447,448] (**Figure I-31**), humidity sensor/indicator[449–452] or ammonia sensor/indicator[453] but also other specific chemicals[445].

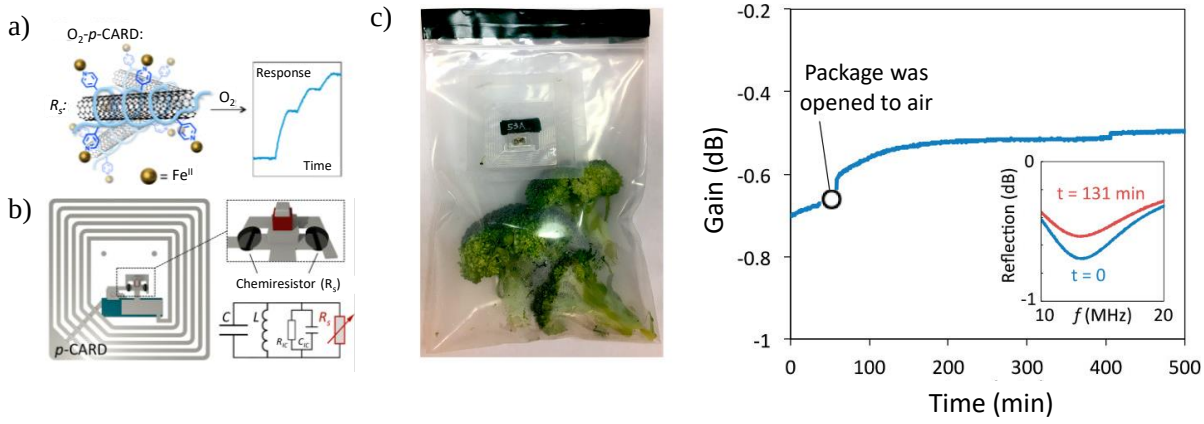

***Figure I-31**: RFID-enabled oxygen sensor example with a) combination of Fe(II) complex and carbon nanotubes as active materials, b) deposited on a commercial adapted RFID tag for and c) wireless detection of the presence of oxygen in broccoli MAP packaged under N_2. Reproduced and adapted from Zhu et al. (2017) with permission from the American Chemical Society (Copyright 2017)*[297]

In this section, intelligent packaging technologies were reviewed for both sensors and indicators technologies (gas, time/temperature, bacterial) but also interactive technologies. A specific care was taken to review the materials used in a significant part of the experimental section of this work named Metal Organic Framework and their properties associated to gas sensing.

Conclusions of Chapter I

This chapter, specifically dedicated to literature review, was divided into three sections. The global context of the packaging sector presented in the first section showed the economic, social and ecological importance of packaging in today's society.

The second section was dedicated to active packaging technologies, separated as emitter (antibacterial, antioxidant, carbon dioxide emitter) and scavenger systems (oxygen, ethylene, water). The review highlighted the diversity of technologies both used in academic research or commercial products. A specific care was taken to review technologies relevant to the experimental section of this work, and especially antibacterial packaging composed of cellulose nanofibrils and silver nanowires. Cellulose nanofibrils were also reviewed for their properties linked to the packaging field and silver nanoparticles antibacterial properties was deeply detailed. The critical challenges identified concerning these materials for antibacterial packaging application were their processability, up-scaling and the leaching of active materials. As for now, there are indeed no or few reports in the scientific literature about the preparation of cellulose nanofibrils/silver nanoparticle materials for packaging applications, that involves a direct route (no chemical synthesis) with a high versatility and adaptability of the solution either for different processes or different process levels. Moreover, they is no report of using silver nanoparticles other than those of spherical shape.

The last section targeted intelligent packaging applications ranging from sensors and indicators to RFID technology. An in-depth review of gas sensors and indicators for packaging applications was specifically conducted. Moreover, as relevant to the experimental section of the work, Metal Organic Framework materials were reviewed, from the production and synthesis to their active properties. The versatility and efficiency of such materials were established, however the review also showed that they are for now principally used in complex systems and that there is no report implementing such gas sensors for packaging applications. Only few references also reported gas sensors made of MOFs materials, with a straight-forward and easy production steps on flexible substrate.

The literature review enabled the definition and precision of the experimental scope of this work. The following experimental chapters are then dedicated to the use the reviewed materials for active and intelligent technologies and tackling the identified challenges they face. Especially, the experimental work will be dedicated on two different strategies. Firstly, the preparation and characterization of antibacterial packaging made of cellulose nanofibrils and silver nanowires will be carried out, with a specific focus on their active properties but also their processability and adaptability to different deposition techniques. Secondly, the preparation and characteristics of smart sensors based on Metal Organic Frameworks will be investigated.

References of Chapter I

1. Berger, K. R. A Brief History of Packaging. *1* **2003**, (2003).
2. World Resources Institute. *Creating a sustainable food future*. (2019).
3. Food and Agriculture Organization of the United Nations. *State of food and agriculture 2019: moving forward on food loss and waste reduction.* (2019).
4. Büsser, S. & Jungbluth, N. The role of flexible packaging in the life cycle of coffee and butter. *Int J Life Cycle Assess* **14**, 80–91 (2009).
5. The Future of Global Packaging to 2024. *Strategic forecasts for global packaging to 2024*.
6. Showcase Archive - Actinpak. http://www.actinpak.eu/showcase/.
7. *Regulation (EC) No 1935/2004 of the European Parliament and of the Council of 27 October 2004 on materials and articles intended to come into contact with food and repealing Directives 80/590/EEC and 89/109/EEC*. *OJ L* vol. 338 (2004).
8. *Commission Regulation (EC) No 450/2009 of 29 May 2009 on active and intelligent materials and articles intended to come into contact with food (Text with EEA relevance)*. *OJ L* vol. 135 (2009).
9. Actinpak – COST ACTION FP1405. *Actinpak* http://www.actinpak.eu/.
10. PlasticsEurope. *Plastics - the Facts 2019*. (2019).
11. Fakirov, S. *Fundamentals of Polymer Science for Engineers*. (Wiley-VCH Verlag GmbH & Co. KGaA, 2017). doi:10.1002/9783527802180.
12. Xu, B. *et al.* Microplastics in the soil environment: Occurrence, risks, interactions and fate – A review. *Critical Reviews in Environmental Science and Technology* **0**, 1–48 (2019).
13. Kögel, T., Bjorøy, Ø., Toto, B., Bienfait, A. M. & Sanden, M. Micro- and nanoplastic toxicity on aquatic life: Determining factors. *Science of The Total Environment* **709**, 136050 (2020).
14. Wang, H., Zhang, Y. & Wang, C. Surface modification and selective flotation of waste plastics for effective recycling——a review. *Separation and Purification Technology* **226**, 75–94 (2019).
15. PlasticsEurope. *Plastics - the Facts 2019*.
16. Wei, R. & Zimmermann, W. Microbial enzymes for the recycling of recalcitrant petroleum-based plastics: how far are we? *Microbial Biotechnology* **10**, 1308–1322 (2017).
17. Ferrer, A., Pal, L. & Hubbe, M. Nanocellulose in packaging: Advances in barrier layer technologies. *Industrial Crops and Products* **95**, 574–582 (2017).
18. Helanto, K. E., Matikainen, L., Talja, R. & Rojas, O. J. Bio-based Polymers for Sustainable Packaging and Biobarriers: A Critical Review. *BioResources* **14**, 4902–4951 (2019).
19. Cazón, P., Velazquez, G., Ramírez, J. A. & Vázquez, M. Polysaccharide-based films and coatings for food packaging: A review. *Food Hydrocolloids* **68**, 136–148 (2017).
20. Chen, H. *et al.* Application of Protein-Based Films and Coatings for Food Packaging: A Review. *Polymers* **11**, 2039 (2019).
21. Yildirim, S. *et al.* Active Packaging Applications for Food. *Comprehensive Reviews in Food Science and Food Safety* **17**, 165–199 (2018).
22. Cui, H., Bai, M., Rashed, M. M. A. & Lin, L. The antibacterial activity of clove oil/chitosan nanoparticles embedded gelatin nanofibers against Escherichia coli O157:H7 biofilms on cucumber. *International Journal of Food Microbiology* **266**, 69–78 (2018).

23. Hager, J. V., Rawles, S. D., Xiong, Y. L., Newman, M. C. & Webster, C. D. Edible Corn-zein-based Coating Incorporated with Nisin or Lemongrass Essential Oil Inhibits Listeria monocytogenes on Cultured Hybrid Striped Bass, Morone chrysops × Morone saxatilis, Fillets During Refrigerated and Frozen Storage. *Journal of the World Aquaculture Society* **50**, 204–218 (2019).
24. Lin, L., Mao, X., Sun, Y., Rajivgandhi, G. & Cui, H. Antibacterial properties of nanofibers containing chrysanthemum essential oil and their application as beef packaging. *International Journal of Food Microbiology* **292**, 21–30 (2019).
25. Mojaddar Langroodi, A. *et al.* Effects of sumac extract dipping and chitosan coating enriched with Zataria multiflora Boiss oil on the shelf-life of meat in modified atmosphere packaging. *LWT* **98**, 372–380 (2018).
26. Li, F. *et al.* Bifunctional Reinforcement of Green Biopolymer Packaging Nanocomposites with Natural Cellulose Nanocrystal–Rosin Hybrids. *ACS Appl. Bio Mater.* (2020) doi:10.1021/acsabm.9b01100.
27. Lan, W. *et al.* Developing poly(vinyl alcohol)/chitosan films incorporate with d-limonene: Study of structural, antibacterial, and fruit preservation properties. *International Journal of Biological Macromolecules* **145**, 722–732 (2020).
28. Tsai, Y.-H., Yang, Y.-N., Ho, Y.-C., Tsai, M.-L. & Mi, F.-L. Drug release and antioxidant/antibacterial activities of silymarin-zein nanoparticle/bacterial cellulose nanofiber composite films. *Carbohydrate Polymers* **180**, 286–296 (2018).
29. Lotfi, M. *et al.* Nanostructured chitosan/ monolaurin film: Preparation, characterization and antimicrobial activity against Listeria monocytogenes on ultrafiltered white cheese. *LWT* **92**, 576–583 (2018).
30. He, T. *et al.* Natural Quercetin AIEgen Composite Film with Antibacterial and Antioxidant Properties for in Situ Sensing of Al3+ Residues in Food, Detecting Food Spoilage, and Extending Food Storage Times. *ACS Appl. Bio Mater.* **1**, 636–642 (2018).
31. Pirsa, S., Sani, I. K., Pirouzifard, M. K. & Erfani, A. Smart film based on chitosan/Melissa officinalis essences/ pomegranate peel extract to detect cream cheeses spoilage. *Food Additives & Contaminants: Part A* **37**, 634–648 (2020).
32. Nazzaro, F., Fratianni, F., De Martino, L., Coppola, R. & De Feo, V. Effect of Essential Oils on Pathogenic Bacteria. *Pharmaceuticals* **6**, 1451–1474 (2013).
33. Burt, S. Essential oils: their antibacterial properties and potential applications in foods—a review. *International Journal of Food Microbiology* **94**, 223–253 (2004).
34. Santos, J. C. P. *et al.* Nisin and other antimicrobial peptides: Production, mechanisms of action, and application in active food packaging. *Innovative Food Science & Emerging Technologies* **48**, 179–194 (2018).
35. Mousavi Khaneghah, A., Hashemi, S. M. B., Eş, I., Fracassetti, D. & Limbo, S. Efficacy of Antimicrobial Agents for Food Contact Applications: Biological Activity, Incorporation into Packaging, and Assessment Methods: A Review. *Journal of Food Protection* **81**, 1142–1156 (2018).
36. Lee, S. H. & Jun, B.-H. Silver Nanoparticles: Synthesis and Application for Nanomedicine. *International Journal of Molecular Sciences* **20**, 865 (2019).
37. Abbasi, E. *et al.* Silver nanoparticles: Synthesis methods, bio-applications and properties. *Critical Reviews in Microbiology* **42**, 173–180 (2016).
38. Ajitha, B., Reddy, Y. A. K., Reddy, P. S., Jeon, H.-J. & Ahn, C. W. Role of capping agents in controlling silver nanoparticles size, antibacterial activity and potential application as optical hydrogen peroxide sensor. *RSC Adv.* **6**, 36171–36179 (2016).

39. Pillai, Z. S. & Kamat, P. V. What Factors Control the Size and Shape of Silver Nanoparticles in the Citrate Ion Reduction Method? *J. Phys. Chem. B* **108**, 945–951 (2004).
40. Nekahi, A., Marashi, S. P. H. & Fatmesari, D. H. High yield polyol synthesis of round- and sharp-end silver nanowires with high aspect ratio. *Materials Chemistry and Physics* **184**, 130–137 (2016).
41. Ebrahiminezhad, A., Raee, M. J., Manafi, Z., Sotoodeh Jahromi, A. & Ghasemi, Y. Ancient and Novel Forms of Silver in Medicine and Biomedicine. *Journal of Advanced Medical Sciences and Applied Technologies* **2**, 122–128 (2016).
42. Rai, M. k., Deshmukh, S. d., Ingle, A. p. & Gade, A. k. Silver nanoparticles: the powerful nanoweapon against multidrug-resistant bacteria. *Journal of Applied Microbiology* **112**, 841–852 (2012).
43. van Duin, D. & Paterson, D. Multidrug Resistant Bacteria in the Community: Trends and Lessons Learned. *Infect Dis Clin North Am* **30**, 377–390 (2016).
44. Panáček, A. *et al.* Silver Colloid Nanoparticles: Synthesis, Characterization, and Their Antibacterial Activity. *J. Phys. Chem. B* **110**, 16248–16253 (2006).
45. Nanda, A. & Saravanan, M. Biosynthesis of silver nanoparticles from Staphylococcus aureus and its antimicrobial activity against MRSA and MRSE. *Nanomedicine: Nanotechnology, Biology and Medicine* **5**, 452–456 (2009).
46. Lara, H. H., Ayala-Núñez, N. V., Ixtepan Turrent, L. del C. & Rodríguez Padilla, C. Bactericidal effect of silver nanoparticles against multidrug-resistant bacteria. *World J Microbiol Biotechnol* **26**, 615–621 (2010).
47. Morones, J. R. *et al.* The bactericidal effect of silver nanoparticles. *Nanotechnology* **16**, 2346 (2005).
48. Tang, S. & Zheng, J. Antibacterial Activity of Silver Nanoparticles: Structural Effects. *Advanced Healthcare Materials* **7**, 1701503 (2018).
49. M, Raffi & M. Raffi, F. H. Antibacterial Characterization of Silver Nanoparticles against E. Coli ATCC-15224. **材料科学与技术** **24**, 192–196 (2009).
50. Cho, K.-H., Park, J.-E., Osaka, T. & Park, S.-G. The study of antimicrobial activity and preservative effects of nanosilver ingredient. *Electrochimica Acta* **51**, 956–960 (2005).
51. Li, W.-R. *et al.* Antibacterial activity and mechanism of silver nanoparticles on Escherichia coli. *Appl Microbiol Biotechnol* **85**, 1115–1122 (2010).
52. Sondi, I. & Salopek-Sondi, B. Silver nanoparticles as antimicrobial agent: a case study on E. coli as a model for Gram-negative bacteria. *Journal of Colloid and Interface Science* **275**, 177–182 (2004).
53. Lok, C.-N. *et al.* Proteomic Analysis of the Mode of Antibacterial Action of Silver Nanoparticles. *J. Proteome Res.* **5**, 916–924 (2006).
54. Rajesh, S., Dharanishanthi, V. & Kanna, A. V. Antibacterial mechanism of biogenic silver nanoparticles of Lactobacillus acidophilus. *Journal of Experimental Nanoscience* **10**, 1143–1152 (2015).
55. Yang, W. *et al.* Food storage material silver nanoparticles interfere with DNA replication fidelity and bind with DNA. *Nanotechnology* **20**, 085102 (2009).
56. Reidy, B., Haase, A., Luch, A., Dawson, K. A. & Lynch, I. Mechanisms of Silver Nanoparticle Release, Transformation and Toxicity: A Critical Review of Current Knowledge and Recommendations for Future Studies and Applications. *Materials* **6**, 2295–2350 (2013).

57. Jung, W. K. *et al.* Antibacterial Activity and Mechanism of Action of the Silver Ion in Staphylococcus aureus and Escherichia coli. *Appl. Environ. Microbiol.* **74**, 2171–2178 (2008).
58. Holt, K. B. & Bard, A. J. Interaction of Silver(I) Ions with the Respiratory Chain of Escherichia coli: An Electrochemical and Scanning Electrochemical Microscopy Study of the Antimicrobial Mechanism of Micromolar Ag+. *Biochemistry* **44**, 13214–13223 (2005).
59. Liau, S. Y., Read, D. C., Pugh, W. J., Furr, J. R. & Russell, A. D. Interaction of silver nitrate with readily identifiable groups: relationship to the antibacterialaction of silver ions. *Letters in Applied Microbiology* **25**, 279–283 (1997).
60. Rinna, A. *et al.* Effect of silver nanoparticles on mitogen-activated protein kinases activation: role of reactive oxygen species and implication in DNA damage. *Mutagenesis* **30**, 59–66 (2015).
61. Foldbjerg, R. *et al.* PVP-coated silver nanoparticles and silver ions induce reactive oxygen species, apoptosis and necrosis in THP-1 monocytes. *Toxicology Letters* **190**, 156–162 (2009).
62. Ivask, A. *et al.* Toxicity Mechanisms in Escherichia coli Vary for Silver Nanoparticles and Differ from Ionic Silver. *ACS Nano* **8**, 374–386 (2014).
63. Xu, H. *et al.* Role of reactive oxygen species in the antibacterial mechanism of silver nanoparticles on Escherichia coli O157:H7. *BioMetals* **25**, 45–53 (2012).
64. Martínez-Castañón, G. A., Niño-Martínez, N., Martínez-Gutierrez, F., Martínez-Mendoza, J. R. & Ruiz, F. Synthesis and antibacterial activity of silver nanoparticles with different sizes. *J Nanopart Res* **10**, 1343–1348 (2008).
65. Choi, O. & Hu, Z. Size Dependent and Reactive Oxygen Species Related Nanosilver Toxicity to Nitrifying Bacteria. *Environ. Sci. Technol.* **42**, 4583–4588 (2008).
66. Carlson, C. *et al.* Unique cellular interaction of silver nanoparticles: size-dependent generation of reactive oxygen species. *J Phys Chem B* **112**, 13608–13619 (2008).
67. Jin, J.-C. *et al.* Ultrasmall silver nanoclusters: Highly efficient antibacterial activity and their mechanisms. *Biomater. Sci.* **5**, 247–257 (2017).
68. Li, F., Lee, C.-S. & Meng, X. Mono-disperse silver quantum dots modified formvar film. *J Nanosci Nanotechnol* **11**, 7937–7939 (2011).
69. Kvítek, L. *et al.* Effect of Surfactants and Polymers on Stability and Antibacterial Activity of Silver Nanoparticles (NPs). *J. Phys. Chem. C* **112**, 5825–5834 (2008).
70. Long, Y.-M. *et al.* Surface ligand controls silver ion release of nanosilver and its antibacterial activity against Escherichia coli. *IJN* **Volume 12**, 3193–3206 (2017).
71. El Badawy, A. M. *et al.* Surface Charge-Dependent Toxicity of Silver Nanoparticles. *Environ. Sci. Technol.* **45**, 283–287 (2011).
72. Helmlinger, J. *et al.* Silver nanoparticles with different size and shape: equal cytotoxicity, but different antibacterial effects. *RSC Adv.* **6**, 18490–18501 (2016).
73. Pal, S., Tak, Y. K. & Song, J. M. Does the Antibacterial Activity of Silver Nanoparticles Depend on the Shape of the Nanoparticle? A Study of the Gram-Negative Bacterium Escherichia coli. *Appl. Environ. Microbiol.* **73**, 1712–1720 (2007).
74. Hong, X., Wen, J., Xiong, X. & Hu, Y. Shape effect on the antibacterial activity of silver nanoparticles synthesized via a microwave-assisted method. *Environ Sci Pollut Res* **23**, 4489–4497 (2016).

75. Ferdous, Z. & Nemmar, A. Health Impact of Silver Nanoparticles: A Review of the Biodistribution and Toxicity Following Various Routes of Exposure. *Int J Mol Sci* **21**, (2020).
76. Korani, M., Ghazizadeh, E., Korani, S., Hami, Z. & Mohammadi-Bardbori, A. Effects of silver nanoparticles on human health. *European Journal of Nanomedicine* **7**, 51–62 (2015).
77. Yu, S., Yin, Y. & Liu, J. Silver nanoparticles in the environment. *Environ. Sci.: Processes Impacts* **15**, 78–92 (2012).
78. Visnapuu, M. *et al.* Dissolution of Silver Nanowires and Nanospheres Dictates Their Toxicity to Escherichia coli. *BioMed Research International* **2013**, 1–9 (2013).
79. Polívková, M. *et al.* Surface characterization and antibacterial response of silver nanowire arrays supported on laser-treated polyethylene naphthalate. *Materials Science and Engineering: C* **72**, 512–518 (2017).
80. Kaimlová, M. *et al.* Optimization of silver nanowire formation on laser processed PEN: Surface properties and antibacterial effects. *Applied Surface Science* **473**, 516–526 (2019).
81. Jiang, S. & Teng, C. P. Fabrication of silver nanowires-loaded polydimethylsiloxane film with antimicrobial activities and cell compatibility. *Materials Science and Engineering: C* **70**, 1011–1017 (2017).
82. Lei, J. *et al.* High-Strength Konjac Glucomannan/Silver Nanowires Composite Films with Antibacterial Properties. *Materials* **10**, 524 (2017).
83. Kiran Shahzadi *et al.* Preparation and characterization of bio-based hybrid film containing chitosan and silver nanowires. *Carbohydrate Polymers* **137**, 732–738 (2016).
84. Zhang, Z. *et al.* Electrospinning of Ag Nanowires/polyvinyl alcohol hybrid nanofibers for their antibacterial properties. *Materials Science and Engineering: C* **78**, 706–714 (2017).
85. Nateghi, M. R. & Shateri-Khalilabad, M. Silver nanowire-functionalized cotton fabric. *Carbohydrate Polymers* **117**, 160–168 (2015).
86. Cui, J. & Liu, Y. Preparation of graphene oxide with silver nanowires to enhance antibacterial properties and cell compatibility. *RSC Adv.* **5**, 85748–85755 (2015).
87. Satoungar, M. T., Fattahi, S., Azizi, H. & Mehrizi, M. K. Electrospinning of Polylactic Acid/silver nanowire biocomposites: Antibacterial and electrical resistivity studies. *Polymer Composites* **39**, E65–E72 (2018).
88. Bayraktar, I. *et al.* 3D printed antibacterial silver nanowire/polylactide nanocomposites. *Composites Part B: Engineering* **172**, 671–678 (2019).
89. De Mori, A. *et al.* Sustained Release from Injectable Composite Gels Loaded with Silver Nanowires Designed to Combat Bacterial Resistance in Bone Regeneration Applications. *Pharmaceutics* **11**, 116 (2019).
90. Doganay, D., Kanicioglu, A., Coskun, S., Akca, G. & Unalan, H. E. Silver-nanowire-modified fabrics for wide-spectrum antimicrobial applications. *Journal of Materials Research* **34**, 500–509 (2019).
91. Chen, W. *et al.* Silver Nanowire-Modified Filter with Controllable Silver Ion Release for Point-of-Use Disinfection. *Environ. Sci. Technol.* **53**, 7504–7512 (2019).
92. Xue, J. *et al.* Bioinspired Unidirectional Silk Fibroin–Silver Compound Nanowire Composite Scaffold via Interface-Mediated In Situ Synthesis. *Angewandte Chemie International Edition* **58**, 14152–14156 (2019).
93. De Mori, A. *et al.* Antibacterial PMMA Composite Cements with Tunable Thermal and Mechanical Properties. *ACS Omega* **4**, 19664–19675 (2019).

94. Mirjalili, S. H., Nateghi, M. R. & Kalantari-Fotooh, F. Preparation of silver nanowire/expanded polytetrafluoroethylene and polypropylene nanocomposites via all solution process method for antibacterial applications. *The Journal of The Textile Institute* **111**, 139–147 (2020).
95. Azlin-Hasim, S. *et al.* The Potential Application of Antimicrobial Silver Polyvinyl Chloride Nanocomposite Films to Extend the Shelf-Life of Chicken Breast Fillets. *Food Bioprocess Technol* **9**, 1661–1673 (2016).
96. Wu, Z., Huang, X., Li, Y.-C., Xiao, H. & Wang, X. Novel chitosan films with laponite immobilized Ag nanoparticles for active food packaging. *Carbohydrate Polymers* **199**, 210–218 (2018).
97. Motlagh, N. V., Mosavian, M. T. H. & Mortazavi, S. A. Effect of Polyethylene Packaging Modified with Silver Particles on the Microbial, Sensory and Appearance of Dried Barberry. *Packaging Technology and Science* **26**, 39–49 (2013).
98. Li, L. *et al.* Effect of stable antimicrobial nano-silver packaging on inhibiting mildew and in storage of rice. *Food Chemistry* **215**, 477–482 (2017).
99. Emamifar, A., Kadivar, M., Shahedi, M. & Soleimanian-Zad, S. Evaluation of nanocomposite packaging containing Ag and ZnO on shelf life of fresh orange juice. *Innovative Food Science & Emerging Technologies* **11**, 742–748 (2010).
100. Panea, B., Ripoll, G., González, J., Fernández-Cuello, Á. & Albertí, P. Effect of nanocomposite packaging containing different proportions of ZnO and Ag on chicken breast meat quality. *Journal of Food Engineering* **123**, 104–112 (2014).
101. Deng, J. *et al.* Nano-silver-containing polyvinyl alcohol composite film for grape fresh-keeping. *mat express* **9**, 985–992 (2019).
102. Cozmuta, A. M. *et al.* Active Packaging System Based on Ag/TiO2 Nanocomposite Used for Extending the Shelf Life of Bread. Chemical and Microbiological Investigations. *Packaging Technology and Science* **28**, 271–284 (2015).
103. Akbar, A. & Anal, A. K. Zinc oxide nanoparticles loaded active packaging, a challenge study against Salmonella typhimurium and Staphylococcus aureus in ready-to-eat poultry meat. *Food Control* **38**, 88–95 (2014).
104. Baek, S.-K. & Song, K. B. Development of Gracilaria vermiculophylla extract films containing zinc oxide nanoparticles and their application in smoked salmon packaging. *LWT* **89**, 269–275 (2018).
105. Shankar, S., Wang, L.-F. & Rhim, J.-W. Incorporation of zinc oxide nanoparticles improved the mechanical, water vapor barrier, UV-light barrier, and antibacterial properties of PLA-based nanocomposite films. *Materials Science and Engineering: C* **93**, 289–298 (2018).
106. Bodaghi, H. *et al.* Evaluation of the photocatalytic antimicrobial effects of a TiO2 nanocomposite food packaging film by in vitro and in vivo tests. *LWT - Food Science and Technology* **50**, 702–706 (2013).
107. Conte, A. *et al.* A novel preservation technique applied to fiordilatte cheese. *Innovative Food Science & Emerging Technologies* **19**, 158–165 (2013).
108. Turbak, A. F., Snyder, F. W. & Sandberg, K. R. Microfibrillated Cellulose, a New Cellulose Product: Properties, Uses, and Commercial Potential. *J. Appl. Polym. Sci.: Appl. Polym. Symp.; (United States)* **37**, (1983).
109. Nechyporchuk, O., Yu, J., Nierstrasz, V. A. & Bordes, R. Cellulose Nanofibril-Based Coatings of Woven Cotton Fabrics for Improved Inkjet Printing with a Potential in E-Textile Manufacturing. *ACS Sustainable Chem. Eng.* **5**, 4793–4801 (2017).

110. Jack Miller. *Nanocellulose - State of the industry 2015*. www.tappinano.org (2015).

111. Jack Miller. *2018 - Cellulose nanomaterials production update*. www.tappinano.org (2018).

112. Grüneberger, F., Künniger, T., Zimmermann, T. & Arnold, M. Rheology of nanofibrillated cellulose/acrylate systems for coating applications. *Cellulose* **21**, 1313–1326 (2014).

113. Nechyporchuk, O., Belgacem, M. N. & Pignon, F. Current Progress in Rheology of Cellulose Nanofibril Suspensions. *Biomacromolecules* **17**, 2311–2320 (2016).

114. Foster, E. J. *et al.* Current characterization methods for cellulose nanomaterials. *Chem. Soc. Rev.* **47**, 2609–2679 (2018).

115. Mascheroni, E. *et al.* Comparison of cellulose nanocrystals obtained by sulfuric acid hydrolysis and ammonium persulfate, to be used as coating on flexible food-packaging materials. *Cellulose* **23**, 779–793 (2016).

116. Eriksen, Ø., Syverud, K. & Gregersen, Ø. The use of microfibrillated cellulose produced from kraft pulp as strength enhancer in TMP paper. *Nordic Pulp & Paper Research Journal* **23**, 299–304 (2008).

117. Saito, T., Kimura, S., Nishiyama, Y. & Isogai, A. Cellulose nanofibers prepared by TEMPO-mediated oxidation of native cellulose. *Biomacromolecules* **8**, 2485–2491 (2007).

118. Pääkkö, M. *et al.* Enzymatic hydrolysis combined with mechanical shearing and high-pressure homogenization for nanoscale cellulose fibrils and strong gels. *Biomacromolecules* **8**, 1934–1941 (2007).

119. Rol, F., Belgacem, M. N., Gandini, A. & Bras, J. Recent advances in surface-modified cellulose nanofibrils. *Progress in Polymer Science* **88**, 241–264 (2019).

120. Desmaisons, J., Boutonnet, E., Rueff, M., Dufresne, A. & Bras, J. A new quality index for benchmarking of different cellulose nanofibrils. *Carbohydrate Polymers* **174**, 318–329 (2017).

121. Nechyporchuk, O., Belgacem, M. N. & Bras, J. Production of cellulose nanofibrils: A review of recent advances. *Industrial Crops and Products* **93**, 2–25 (2016).

122. Reid, M. S., Villalobos, M. & Cranston, E. D. Benchmarking Cellulose Nanocrystals: From the Laboratory to Industrial Production. *Langmuir* **33**, 1583–1598 (2017).

123. Rånby, B. G., Banderet, A. & Sillén, L. G. Aqueous Colloidal Solutions of Cellulose Micelles. *Acta Chem. Scand.* **3**, 649–650 (1949).

124. Bacakova, L. *et al.* Versatile Application of Nanocellulose: From Industry to Skin Tissue Engineering and Wound Healing. *Nanomaterials* **9**, 164 (2019).

125. Albornoz-Palma, G., Betancourt, F., Mendonça, R. T., Chinga-Carrasco, G. & Pereira, M. Relationship between rheological and morphological characteristics of cellulose nanofibrils in dilute dispersions. *Carbohydrate Polymers* **230**, 115588 (2020).

126. Moberg, T. *et al.* Rheological properties of nanocellulose suspensions: effects of fibril/particle dimensions and surface characteristics. *Cellulose* **24**, 2499–2510 (2017).

127. Iwamoto, S., Lee, S.-H. & Endo, T. Relationship between aspect ratio and suspension viscosity of wood cellulose nanofibers. *Polym J* **46**, 73–76 (2014).

128. Lasseuguette, E., Roux, D. & Nishiyama, Y. Rheological properties of microfibrillar suspension of TEMPO-oxidized pulp. *Cellulose* **15**, 425–433 (2008).

129. Missoum, K., Bras, J. & Belgacem, M. N. Organization of aliphatic chains grafted on nanofibrillated cellulose and influence on final properties. *Cellulose* **19**, 1957–1973 (2012).

130. Quennouz, N., Hashmi, S. M., Choi, H. S., Kim, J. W. & Osuji, C. O. Rheology of cellulose nanofibrils in the presence of surfactants. *Soft Matter* **12**, 157–164 (2015).

131. Mongruel, A. & Cloitre, M. Shear viscosity of suspensions of aligned non-Brownian fibres. *Rheol. Acta* **38**, 451–457 (1999).

132. Switzer, L. H. & Klingenberg, D. J. Rheology of sheared flexible fiber suspensions via fiber-level simulations. *Journal of Rheology* **47**, 759–778 (2003).

133. Hubbe, M. A. *et al.* Rheology of Nanocellulose-rich Aqueous Suspensions: A Review. *BioResources* **12**, 9556–9661 (2017).

134. Naderi, A. & Lindström, T. A comparative study of the rheological properties of three different nanofibrillated cellulose systems. *Nordic Pulp & Paper Research Journal* **31**, 354–363 (2016).

135. Benhamou, K., Dufresne, A., Magnin, A., Mortha, G. & Kaddami, H. Control of size and viscoelastic properties of nanofibrillated cellulose from palm tree by varying the TEMPO-mediated oxidation time. *Carbohydrate Polymers* **99**, 74–83 (2014).

136. Saarinen, T., Lille, M. & Seppälä, J. Technical aspects on rheological characterization of microfibrillar cellulose water suspensions. *Annual Transactions of the Nordic Rheology Society* 121–128 (2009).

137. Lowys, M.-P., Desbrières, J. & Rinaudo, M. Rheological characterization of cellulosic microfibril suspensions. Role of polymeric additives. *Food Hydrocolloids* **15**, 25–32 (2001).

138. Tanaka, R. *et al.* Viscoelastic Properties of Core–Shell-Structured, Hemicellulose-Rich Nanofibrillated Cellulose in Dispersion and Wet-Film States. *Biomacromolecules* **17**, 2104–2111 (2016).

139. Li, M.-C. *et al.* Cellulose Nanoparticles: Structure–Morphology–Rheology Relationships. *ACS Sustainable Chem. Eng.* **3**, 821–832 (2015).

140. Yu, Z. *et al.* Preparation of cellulose nanofibril/titanium dioxide nanoparticle nanocomposites as fillers for PVA-based packaging and investigation into their intestinal toxicity. *International Journal of Biological Macromolecules* (2019) doi:10.1016/j.ijbiomac.2019.11.153.

141. Zhao, Y. *et al.* Fabrication of mechanically robust and UV-resistant aramid fiber-based composite paper by adding nano-TiO2 and nanofibrillated cellulose. *Cellulose* **25**, 3913–3925 (2018).

142. Bardet, R., Belgacem, M. N. & Bras, J. Different strategies for obtaining high opacity films of MFC with TiO2 pigments. *Cellulose* **20**, 3025–3037 (2013).

143. Bacakova, L. *et al.* Applications of Nanocellulose/Nanocarbon Composites: Focus on Biotechnology and Medicine. *Nanomaterials* **10**, 196 (2020).

144. Pinto, R. J. B., Neves, M. C., Neto, C. P. & Trindade, T. Composites of Cellulose and Metal Nanoparticles. *Nanocomposites - New Trends and Developments* (2012) doi:10.5772/50553.

145. Sehaqui, H., Liu, A., Zhou, Q. & Berglund, L. A. Fast Preparation Procedure for Large, Flat Cellulose and Cellulose/Inorganic Nanopaper Structures. *Biomacromolecules* **11**, 2195–2198 (2010).

146. Qi, Z.-D., Saito, T., Fan, Y. & Isogai, A. Multifunctional Coating Films by Layer-by-Layer Deposition of Cellulose and Chitin Nanofibrils. *Biomacromolecules* **13**, 553–558 (2012).

147. Aulin, C., Karabulut, E., Tran, A., Wågberg, L. & Lindström, T. Transparent Nanocellulosic Multilayer Thin Films on Polylactic Acid with Tunable Gas Barrier Properties. *ACS Appl. Mater. Interfaces* **5**, 7352–7359 (2013).

148. Cozzolino, C. A., Campanella, G., Türe, H., Olsson, R. T. & Farris, S. Microfibrillated cellulose and borax as mechanical, O2-barrier, and surface-modulating agents of pullulan biocomposite coatings on BOPP. *Carbohydrate Polymers* **143**, 179–187 (2016).

149. Hoeng, F., Denneulin, A., Krosnicki, G. & Bras, J. Positive impact of cellulose nanofibrils on silver nanowire coatings for transparent conductive films. *J. Mater. Chem. C* **4**, 10945–10954 (2016).

150. Vähä-Nissi, M. *et al.* Cellulose nanofibrils in biobased multilayer films for food packaging. *Journal of Applied Polymer Science* **134**, (2017).

151. Virtanen, S., Jämsä, S., Talja, R., Heikkinen, H. & Vuoti, S. Chemically modified cellulose nanofibril as an additive for two-component polyurethane coatings. *Journal of Applied Polymer Science* **134**, (2017).

152. Pacaphol, K. & Aht-Ong, D. The influences of silanes on interfacial adhesion and surface properties of nanocellulose film coating on glass and aluminum substrates. *Surface and Coatings Technology* **320**, 70–81 (2017).

153. Vartiainen, J., Pasanen, S., Kenttä, E. & Vähä-Nissi, M. Mechanical recycling of nanocellulose containing multilayer packaging films. *Journal of Applied Polymer Science* **135**, 46237 (2018).

154. Pacaphol, K., Seraypheap, K. & Aht-Ong, D. Development and application of nanofibrillated cellulose coating for shelf life extension of fresh-cut vegetable during postharvest storage. *Carbohydrate Polymers* **224**, 115167 (2019).

155. Nechyporchuk, O., Yu, J., Nierstrasz, V. A. & Bordes, R. Cellulose Nanofibril-Based Coatings of Woven Cotton Fabrics for Improved Inkjet Printing with a Potential in E-Textile Manufacturing. *ACS Sustainable Chem. Eng.* **5**, 4793–4801 (2017).

156. Hoeng, F., Denneulin, A., Reverdy-Bruas, N., Krosnicki, G. & Bras, J. Rheology of cellulose nanofibrils/silver nanowires suspension for the production of transparent and conductive electrodes by screen printing. *Applied Surface Science* **394**, 160–168 (2017).

157. Koga, H. *et al.* Transparent, Conductive, and Printable Composites Consisting of TEMPO-Oxidized Nanocellulose and Carbon Nanotube. *Biomacromolecules* **14**, 1160–1165 (2013).

158. Pras, O., Beneventi, D., Chaussy, D., Piette, P. & Tapin-Lingua, S. Use of microfibrillated cellulose and dendritic copper for the elaboration of conductive films from water- and ethanol-based dispersions. *J Mater Sci* **48**, 6911–6920 (2013).

159. Benítez, A. J. & Walther, A. Cellulose nanofibril nanopapers and bioinspired nanocomposites: a review to understand the mechanical property space. *J. Mater. Chem. A* **5**, 16003–16024 (2017).

160. Hu, L. *et al.* Transparent and conductive paper from nanocellulose fibers. *Energy Environ. Sci.* **6**, 513–518 (2013).

161. Liu, Y., Yu, S.-H. & Bergström, L. Transparent and Flexible Nacre-Like Hybrid Films of Aminoclays and Carboxylated Cellulose Nanofibrils. *Advanced Functional Materials* **28**, 1703277 (2018).

162. Shimizu, M., Saito, T., Fukuzumi, H. & Isogai, A. Hydrophobic, Ductile, and Transparent Nanocellulose Films with Quaternary Alkylammonium Carboxylates on Nanofibril Surfaces. *Biomacromolecules* **15**, 4320–4325 (2014).

163. Tang, H., Butchosa, N. & Zhou, Q. A Transparent, Hazy, and Strong Macroscopic Ribbon of Oriented Cellulose Nanofibrils Bearing Poly(ethylene glycol). *Advanced Materials* **27**, 2070–2076 (2015).

164. Yang, W. *et al.* High wet-strength, thermally stable and transparent TEMPO-oxidized cellulose nanofibril film via cross-linking with poly-amide epichlorohydrin resin. *RSC Adv.* **7**, 31567–31573 (2017).

165. Lagaron, J. M., Catalá, R. & Gavara, R. Structural characteristics defining high barrier properties in polymeric materials. *Materials Science and Technology* **20**, 1–7 (2004).

166. Aulin, C., Gällstedt, M. & Lindström, T. Oxygen and oil barrier properties of microfibrillated cellulose films and coatings. *Cellulose* **17**, 559–574 (2010).

167. Hansen, N. M. L., Blomfeldt, T. O. J., Hedenqvist, M. S. & Plackett, D. V. Properties of plasticized composite films prepared from nanofibrillated cellulose and birch wood xylan. *Cellulose* **19**, 2015–2031 (2012).

168. Saxena, A., Elder, T. J., Kenvin, J. & Ragauskas, A. J. High Oxygen Nanocomposite Barrier Films Based on Xylan and Nanocrystalline Cellulose. *Nano-Micro Lett.* **2**, 235–241 (2010).

169. Syverud, K. & Stenius, P. Strength and barrier properties of MFC films. *Cellulose* **16**, 75 (2008).

170. Belbekhouche, S. *et al.* Water sorption behavior and gas barrier properties of cellulose whiskers and microfibrils films. *Carbohydrate Polymers* **83**, 1740–1748 (2011).

171. Dufresne, A. *Nanocellulose: From Nature to High Performance Tailored Materials*. *Nanocellulose* (De Gruyter, 2013).

172. Naderi, A. *et al.* Phosphorylated nanofibrillated cellulose: production and properties. *Nordic Pulp & Paper Research Journal* **31**, 20–29 (2016).

173. Chinga-Carrasco, G. & Syverud, K. On the structure and oxygen transmission rate of biodegradable cellulose nanobarriers. *Nanoscale Research Letters* **7**, 192 (2012).

174. Österberg, M. *et al.* A Fast Method to Produce Strong NFC Films as a Platform for Barrier and Functional Materials. *ACS Appl. Mater. Interfaces* **5**, 4640–4647 (2013).

175. Nair, S. S., Zhu, J., Deng, Y. & Ragauskas, A. J. High performance green barriers based on nanocellulose. *Sustainable Chemical Processes* **2**, 23 (2014).

176. Aulin, C., Salazar-Alvarez, G. & Lindström, T. High strength, flexible and transparent nanofibrillated cellulose–nanoclay biohybrid films with tunable oxygen and water vapor permeability. *Nanoscale* **4**, 6622–6628 (2012).

177. Honorato, C. *et al.* Transparent nanocellulose-pigment composite films. *J Mater Sci* **50**, 7343–7352 (2015).

178. Hubbe, M. A. *et al.* Nanocellulose in Thin Films, Coatings, and Plies for Packaging Applications: A Review. *BioResources* **12**, 2143–2233 (2017).

179. Yan, D. *et al.* Surface modified electrospun poly(lactic acid) fibrous scaffold with cellulose nanofibrils and Ag nanoparticles for ocular cell proliferation and antimicrobial application. *Materials Science and Engineering: C* **111**, 110767 (2020).

180. Li, J. *et al.* Controlled Release and Long-Term Antibacterial Activity of Dialdehyde Nanofibrillated Cellulose/Silver Nanoparticle Composites. *ACS Sustainable Chem. Eng.* **7**, 1146–1158 (2019).

181. Yan, J., Abdelgawad, A. M., El-Naggar, M. E. & Rojas, O. J. Antibacterial activity of silver nanoparticles synthesized In-situ by solution spraying onto cellulose. *Carbohydrate Polymers* **147**, 500–508 (2016).

182. Ramaraju, B., Imae, T. & Destaye, A. G. Ag nanoparticle-immobilized cellulose nanofibril films for environmental conservation. *Applied Catalysis A: General* **492**, 184–189 (2015).

183. Bober, P. *et al.* Biocomposites of Nanofibrillated Cellulose, Polypyrrole, and Silver Nanoparticles with Electroconductive and Antimicrobial Properties. *Biomacromolecules* **15**, 3655–3663 (2014).

184. Xiao, W., Xu, J., Liu, X., Hu, Q. & Huang, J. Antibacterial hybrid materials fabricated by nanocoating of microfibril bundles of cellulose substance with titania/ chitosan /silver-nanoparticle composite films. *Journal of Materials Chemistry B* **1**, 3477–3485 (2013).

185. Yu, Z. *et al.* Antimicrobial effect and toxicity of cellulose nanofibril/silver nanoparticle nanocomposites prepared by an ultraviolet irradiation method. *Colloids and Surfaces B: Biointerfaces* **180**, 212–220 (2019).

186. Yu, Z., Wang, W., Kong, F., Lin, M. & Mustapha, A. Cellulose nanofibril/silver nanoparticle composite as an active food packaging system and its toxicity to human colon cells. *International Journal of Biological Macromolecules* **129**, 887–894 (2019).

187. Errokh, A., Magnin, A., Putaux, J.-L. & Boufi, S. Hybrid nanocellulose decorated with silver nanoparticles as reinforcing filler with antibacterial properties. *Materials Science and Engineering: C* **105**, 110044 (2019).

188. Scatolino, M. V. *et al.* Tannin-stabilized silver nanoparticles and citric acid added associated to cellulose nanofibrils: effect on film antimicrobial properties. *SN Appl. Sci.* **1**, 1243 (2019).

189. Gogoi, B., Barua, S., Sarmah, J. K. & Karak, N. In situ synthesis of a microbial fouling resistant, nanofibrillar cellulose-hyperbranched epoxy composite for advanced coating applications. *Progress in Organic Coatings* **124**, 224–231 (2018).

190. Wang, M. S., Jiang, F., Hsieh, Y.-L. & Nitin, N. Cellulose nanofibrils improve dispersibility and stability of silver nanoparticles and induce production of bacterial extracellular polysaccharides. *J. Mater. Chem. B* **2**, 6226–6235 (2014).

191. Xiong, R., Lu, C., Wang, Y., Zhou, Z. & Zhang, X. Nanofibrillated cellulose as the support and reductant for the facile synthesis of Fe3O4/Ag nanocomposites with catalytic and antibacterial activity. *J. Mater. Chem. A* **1**, 14910–14918 (2013).

192. Uddin, K. M. A. *et al.* Retention of lysozyme activity by physical immobilization in nanocellulose aerogels and antibacterial effects. *Cellulose* **24**, 2837–2848 (2017).

193. Martins, N. C. T. *et al.* Electrostatic assembly of Ag nanoparticles onto nanofibrillated cellulose for antibacterial paper products. *Cellulose* **19**, 1425–1436 (2012).

194. Son, W. K., Youk, J. H., Lee, T. S. & Park, W. H. Preparation of Antimicrobial Ultrafine Cellulose Acetate Fibers with Silver Nanoparticles. *Macromol. Rapid Commun.* **25**, 1632–1637 (2004).

195. Pirsa, S. & Shamusi, T. Intelligent and active packaging of chicken thigh meat by conducting nano structure cellulose-polypyrrole-ZnO film. *Materials Science and Engineering: C* **102**, 798–809 (2019).

196. Souza, V. G. L. *et al.* Eco-Friendly ZnO/Chitosan Bionanocomposites Films for Packaging of Fresh Poultry Meat. *Coatings* **10**, 110 (2020).

197. Zhang, L. *et al.* Characterisation of microemulsion nanofilms based on Tilapia fish skin gelatine and ZnO nanoparticles incorporated with ginger essential oil: meat packaging application. *International Journal of Food Science & Technology* **52**, 1670–1679 (2017).

198. de Moraes Crizel, T. *et al.* Active food packaging prepared with chitosan and olive pomace. *Food Hydrocolloids* **74**, 139–150 (2018).

199. Vera, P., Canellas, E. & Nerín, C. New Antioxidant Multilayer Packaging with Nanoselenium to Enhance the Shelf-Life of Market Food Products. *Nanomaterials* **8**, 837 (2018).

200. Aydogdu, A. *et al.* Enhancing oxidative stability of walnuts by using gallic acid loaded lentil flour based electrospun nanofibers as active packaging material. *Food Hydrocolloids* **95**, 245–255 (2019).

201. Ojeda, G. A., Sgroppo, S. C., Martín-Belloso, O. & Soliva-Fortuny, R. Chitosan/tripolyphosphate nanoaggregates enhance the antibrowning effect of ascorbic acid on mushroom slices. *Postharvest Biology and Technology* **156**, 110934 (2019).

202. Wang, F., Hu, Q., Mugambi Mariga, A., Cao, C. & Yang, W. Effect of nano packaging on preservation quality of Nanjing 9108 rice variety at high temperature and humidity. *Food Chemistry* **239**, 23–31 (2018).

203. Priyadarshi, R. *et al.* Chitosan films incorporated with Apricot (Prunus armeniaca) kernel essential oil as active food packaging material. *Food Hydrocolloids* **85**, 158–166 (2018).

204. Navikaite-Snipaitiene, V. *et al.* Development of antioxidant food packaging materials containing eugenol for extending display life of fresh beef. *Meat Science* **145**, 9–15 (2018).

205. Wang, L. *et al.* Effect of nano-SiO2 packing on postharvest quality and antioxidant capacity of loquat fruit under ambient temperature storage. *Food Chemistry* **315**, 126295 (2020).

206. Gantner, M. *et al.* Antioxidant effect of sage (Salvia officinalis L.) extract on turkey meatballs packed in cold modified atmosphere. *CyTA - Journal of Food* **16**, 628–636 (2018).

207. Oudjedi, K., Manso, S., Nerin, C., Hassissen, N. & Zaidi, F. New active antioxidant multilayer food packaging films containing Algerian Sage and Bay leaves extracts and their application for oxidative stability of fried potatoes. *Food Control* **98**, 216–226 (2019).

208. Rodríguez, G. M., Sibaja, J. C., Espitia, P. J. P. & Otoni, C. G. Antioxidant active packaging based on papaya edible films incorporated with Moringa oleifera and ascorbic acid for food preservation. *Food Hydrocolloids* **103**, 105630 (2020).

209. Tayengwa, T. *et al.* Dietary citrus pulp and grape pomace as potential natural preservatives for extending beef shelf life. *Meat Science* **162**, 108029 (2020).

210. Priyadarshi, R., Sauraj, Kumar, B. & Negi, Y. S. Chitosan film incorporated with citric acid and glycerol as an active packaging material for extension of green chilli shelf life. *Carbohydrate Polymers* **195**, 329–338 (2018).

211. Go, E.-J. & Song, K. B. Antioxidant Properties of Rye Starch Films Containing Rosehip Extract and Their Application in Packaging of Chicken Breast. *Starch - Stärke* **71**, 1900116 (2019).

212. Karagöz, Ş. & Demirdöven, A. Effect of chitosan coatings with and without Stevia rebaudiana and modified atmosphere packaging on quality of cold stored fresh-cut apples. *LWT* **108**, 332–337 (2019).

213. Liu, Y. *et al.* Preparation of pH-sensitive and antioxidant packaging films based on κ-carrageenan and mulberry polyphenolic extract. *International Journal of Biological Macromolecules* **134**, 993–1001 (2019).

214. Yun, D. *et al.* Development of active and intelligent films based on cassava starch and Chinese bayberry (Myrica rubra Sieb. et Zucc.) anthocyanins. *RSC Adv.* **9**, 30905–30916 (2019).

215. Yong, H. *et al.* Antioxidant and pH-sensitive films developed by incorporating purple and black rice extracts into chitosan matrix. *International Journal of Biological Macromolecules* **137**, 307–316 (2019).

216. Goulas, V. *et al.* Valorization of Carob Fruit Residues for the Preparation of Novel Bi-Functional Polyphenolic Coating for Food Packaging Applications. *Molecules* **24**, 3162 (2019).

217. Zhang, W., Li, X. & Jiang, W. Development of antioxidant chitosan film with banana peels extract and its application as coating in maintaining the storage quality of apple. *International Journal of Biological Macromolecules* (2019) doi:10.1016/j.ijbiomac.2019.10.275.

218. Zhang, H., He, P., Kang, H. & Li, X. Antioxidant and antimicrobial effects of edible coating based on chitosan and bamboo vinegar in ready to cook pork chops. *LWT* **93**, 470–476 (2018).

219. Dixon, N. M. & Kell, D. B. The inhibition by CO2 of the growth and metabolism of micro-organisms. *Journal of Applied Bacteriology* **67**, 109–136 (1989).

220. Daniels, J. A., Krishnamurthi, R. & Rizvi, S. S. H. A Review of Effects of Carbon Dioxide on Microbial Growth and Food Quality. *J. Food Prot.* **48**, 532–537 (1985).

221. Hansen, A. Å., Mørkøre, T., Rudi, K., Olsen, E. & Eie, T. Quality Changes during Refrigerated Storage of MA-Packaged Pre-rigor Fillets of Farmed Atlantic Cod (Gadus morhua L.) Using Traditional MAP, CO2 Emitter, and Vacuum. *Journal of Food Science* **72**, M423–M430 (2007).

222. Hansen, A. Å., Mørkøre, T., Rudi, K., Langsrud, Ø. & Eie, T. The combined effect of superchilling and modified atmosphere packaging using CO2 emitter on quality during chilled storage of pre-rigor salmon fillets (Salmo salar). *Journal of the Science of Food and Agriculture* **89**, 1625–1633 (2009).

223. Holck, A. L., Pettersen, M. K., Moen, M. H. & Sørheim, O. Prolonged Shelf Life and Reduced Drip Loss of Chicken Filets by the Use of Carbon Dioxide Emitters and Modified Atmosphere Packaging. *J Food Prot* **77**, 1133–1141 (2014).

224. Pettersen, M. K., Hansen, A. Å. & Mielnik, M. Effect of Different Packaging Methods on Quality and Shelf Life of Fresh Reindeer Meat. *Packaging Technology and Science* **27**, 987–997 (2014).

225. Trindade, M. A., Villanueva, N. D. M., Antunes, C. V. & Freire, M. T. de A. Active packaged lamb with oxygen scavenger/carbon dioxide emitter sachet: physical-chemical and microbiological stability during refrigerated storage. *Brazilian Journal of Food Technology* **16**, 216–225 (2013).

226. Chen, J. & Brody, A. L. Use of active packaging structures to control the microbial quality of a ready-to-eat meat product. *Food Control* **30**, 306–310 (2013).

227. Choe, E. & Min, D. B. Chemistry and Reactions of Reactive Oxygen Species in Foods. *Critical Reviews in Food Science and Nutrition* **46**, 1–22 (2006).

228. *Food Packaging and Shelf Life: A Practical Guide*. (CRC Press, 2009).

229. Yam, K. L. *The Wiley Encyclopedia of Packaging Technology*. (John Wiley & Sons, 2010).

230. Mu, H. *et al.* A nanosised oxygen scavenger: Preparation and antioxidant application to roasted sunflower seeds and walnuts. *Food Chemistry* **136**, 245–250 (2013).

231. Maloba, F. W., Rooney, M. L., Wormell, P. & Nguyen, M. Improved oxidative stability of sunflower oil in the presence of an oxygen-scavenging film. *J Am Oil Chem Soc* **73**, 181–185 (1996).

232. Zerdin, K., Rooney, M. L. & Vermuë, J. The vitamin C content of orange juice packed in an oxygen scavenger material. *Food Chemistry* **82**, 387–395 (2003).

233. Lee, J.-S. *et al.* Ascorbic Acid-Based Oxygen Scavenger in Active Food Packaging System for Raw Meatloaf. *Journal of Food Science* **83**, 682–688 (2018).

234. Matche, R. S., Sreekumar, R. K. & Raj, B. Modification of linear low-density polyethylene film using oxygen scavengers for its application in storage of bun and bread. *J. Appl. Polym. Sci.* **122**, 55–63 (2011).

235. Lee, J.-S., Jeong, S., Lee, H.-G., Cho, C. H. & Yoo, S. Development of a Sulfite-Based Oxygen Scavenger and its Application in Kimchi Packaging to Prevent Oxygen-mediated Deterioration of Kimchi Quality. *Journal of Food Science* **83**, 3009–3018 (2018).

236. Singh, S., Gaikwad, K. K. & Lee, Y. S. Development and application of a pyrogallic acid-based oxygen scavenging packaging system for shelf life extension of peeled garlic. *Scientia Horticulturae* **256**, 108548 (2019).

237. Hutter, S., Rüegg, N. & Yildirim, S. Use of palladium based oxygen scavenger to prevent discoloration of ham. *Food Packaging and Shelf Life* **8**, 56–62 (2016).

238. Gohil, R. M. & Wysock, W. A. Designing Efficient Oxygen Scavenging Coating Formulations for Food Packaging Applications: MANAGEMENT OF OXYGEN ATMOSPHERE IN FOOD PACKAGES. *Packag. Technol. Sci.* **27**, 609–623 (2014).

239. Anthierens, T. *et al.* Use of endospore-forming bacteria as an active oxygen scavenger in plastic packaging materials. *Innovative Food Science & Emerging Technologies* **12**, 594–599 (2011).

240. Demirhan, B. & Candoĝan, K. Active packaging of chicken meats with modified atmosphere including oxygen scavengers. *Poultry Science* **96**, 1394–1401 (2017).

241. Şahin, A., Çarkcıoğlu, E., Demirhan, B. & Candoğan, K. Chitosan edible coating and oxygen scavenger effects on modified atmosphere packaged sliced sucuk. *Journal of Food Processing and Preservation* **41**, e13213 (2017).

242. Antunez, P. D., Botero Omary, M., Rosentrater, K. A., Pascall, M. & Winstone, L. Effect of an Oxygen Scavenger on the Stability of Preservative-Free Flour Tortillas. *Journal of Food Science* **77**, S1–S9 (2012).

243. Chounou, N. *et al.* Shelf life extension of ground meat stored at 4 °C using chitosan and an oxygen absorber. *Int J Food Sci Technol* **48**, 89–95 (2013).

244. Janjarasskul, T., Tananuwong, K., Kongpensook, V., Tantratian, S. & Kokpol, S. Shelf life extension of sponge cake by active packaging as an alternative to direct addition of chemical preservatives. *LWT - Food Science and Technology* **72**, 166–174 (2016).

245. Kartal, S., Aday, M. S. & Caner, C. Use of microperforated films and oxygen scavengers to maintain storage stability of fresh strawberries. *Postharvest Biology and Technology* **71**, 32–40 (2012).

246. Charles, F., Guillaume, C. & Gontard, N. Effect of passive and active modified atmosphere packaging on quality changes of fresh endives. *Postharvest Biology and Technology* **48**, 22–29 (2008).

247. Trindade, M. A., Villanueva, N. D. M., Antunes, C. V. & Freire, M. T. de A. Active packaged lamb with oxygen scavenger/carbon dioxide emitter sachet: physical-chemical and microbiological stability during refrigerated storage. *Brazilian Journal of Food Technology* **16**, 216–225 (2013).

248. Johnson, D. R., Inchingolo, R. & Decker, E. A. The ability of oxygen scavenging packaging to inhibit vitamin degradation and lipid oxidation in fish oil-in-water emulsions. *Innovative Food Science & Emerging Technologies* **47**, 467–475 (2018).

249. Shin, Y., Shin, J. & Lee, Y. S. Effects of oxygen scavenging package on the quality changes of processed meatball product. *Food Science and Biotechnology* **18**, 73–78 (2009).

250. Gomes, C. *et al.* Effect of Oxygen-Absorbing Packaging on the Shelf Life of a Liquid-Based Component of Military Operational Rations. *Journal of Food Science* **74**, E167–E176 (2009).

251. Sängerlaub, S. *et al.* Compensation of Pinhole Defects in Food Packages by Application of Iron-based Oxygen Scavenging Multilayer Films: COMPENSATION OF PINHOLE DEFECTS USING IRON-BASED OS. *Packag. Technol. Sci.* **26**, 17–30 (2013).

252. Miller, C. W., Nguyen, M. H., Rooney, M. & Kailasapathy, K. The control of dissolved oxygen content in probiotic yoghurts by alternative packaging materials. *Packag. Technol. Sci.* **16**, 61–67 (2003).

253. Perkins, M. L., Zerdin, K., Rooney, M. L., D'Arcy, B. R. & Deeth, H. C. Active packaging of UHT milk to prevent the development of stale flavour during storage. *Packag. Technol. Sci.* **20**, 137–146 (2007).

254. Baiano, A., Marchitelli, V., Tamagnone, P. & Nobile, M. A. D. Use of Active Packaging for Increasing Ascorbic Acid Retention in Food Beverages. *Journal of Food Science* **69**, E502–E508 (2006).

255. Galdi, M. R. & Incarnato, L. Influence of composition on structure and barrier properties of active PET films for food packaging applications. *Packaging Technology and Science* **24**, 89–102 (2011).

256. Barry, C. S. & Giovannoni, J. J. Ethylene and Fruit Ripening. *J Plant Growth Regul* **26**, 143 (2007).

257. Gaikwad, K. K., Singh, S. & Negi, Y. S. Ethylene scavengers for active packaging of fresh food produce. *Environ Chem Lett* (2019) doi:10.1007/s10311-019-00938-1.

258. Sadeghi, K., Lee, Y. & Seo, J. Ethylene Scavenging Systems in Packaging of Fresh Produce: A Review. *Food Reviews International* **0**, 1–22 (2019).

259. Bhattacharjee, D. & Shankar Dhua, R. Ethylene Absorbents Improve the Shelf Life of Pointed Gourd (Trichosanthes dioica Roxb.) Fruits. *Int. J. Pure App. Biosci.* **5**, 64–71 (2017).

260. de Souza Freitas, W. E. *et al.* Potassium permanganate effects on the quality and post-harvest conservation of sapodilla (Manilkara zapota (L.) P.Royen) fruits under modified atmosphere. *Acta Agronómica* **66**, 331–337 (2017).

261. Singh, R. & Giri, S. K. Shelf-life study of Guava (Psidium guajava L.) under active packaging: An experiment with potassium permanganate salt as ethylene absorbent. *Arch. Lebensmittelhyg* **65**, 32–39 (2014).

262. Murmu, S. B. & Mishra, H. N. Selection of the best active modified atmosphere packaging with ethylene and moisture scavengers to maintain quality of guava during low-temperature storage. *Food Chemistry* **253**, 55–62 (2018).

263. Boonruang, K., Chonhenchob, V., Singh, S. P., Chinsirikul, W. & Fuongfuchat, A. Comparison of Various Packaging Films for Mango Export. *Packaging Technology and Science* **25**, 107–118 (2012).

264. Esturk, O., Ayhan, Z. & Gokkurt, T. Production and Application of Active Packaging Film with Ethylene Adsorber to Increase the Shelf Life of Broccoli (Brassica oleracea L. var. Italica). *Packaging Technology and Science* **27**, 179–191 (2014).

265. Emadpour, M., Ghareyazie, B., Kalaj, Y. R., Entesari, M. & Bouzari, N. Effect of the potassium permanganate coated zeolite nanoparticles on the quality characteristic and shelf

life of peach and nectarine. *International Journal of Agricultural Technology* **11**, 1411–1421 (2015).

266. Hu, Q., Fang, Y., Yang, Y., Ma, N. & Zhao, L. Effect of nanocomposite-based packaging on postharvest quality of ethylene-treated kiwifruit (Actinidia deliciosa) during cold storage. *Food Research International* **44**, 1589–1596 (2011).
267. Tas, C. E. *et al.* Halloysite Nanotubes/Polyethylene Nanocomposites for Active Food Packaging Materials with Ethylene Scavenging and Gas Barrier Properties. *Food Bioprocess Technol* **10**, 789–798 (2017).
268. Wang, K. *et al.* A combination of hot air treatment and nano-packing reduces fruit decay and maintains quality in postharvest Chinese bayberries. *Journal of the Science of Food and Agriculture* **90**, 2427–2432 (2010).
269. Kaewklin, P., Siripatrawan, U., Suwanagul, A. & Lee, Y. S. Active packaging from chitosan-titanium dioxide nanocomposite film for prolonging storage life of tomato fruit. *International Journal of Biological Macromolecules* **112**, 523–529 (2018).
270. Yang, F. M. *et al.* Effect of Nano-Packing on Preservation Quality of Fresh Strawberry (Fragaria ananassa Duch. cv Fengxiang) during Storage at 4 °C. *Journal of Food Science* **75**, C236–C240 (2010).
271. Li, H. *et al.* Effect of nano-packing on preservation quality of Chinese jujube (Ziziphus jujuba Mill. var. inermis (Bunge) Rehd). *Food Chemistry* **114**, 547–552 (2009).
272. Zhu, Z. *et al.* Preparation of PAN@TiO2 Nanofibers for Fruit Packaging Materials with Efficient Photocatalytic Degradation of Ethylene. *Materials* **12**, 896 (2019).
273. Li, X. *et al.* Effect of nano-ZnO-coated active packaging on quality of fresh-cut 'Fuji' apple. *International Journal of Food Science & Technology* **46**, 1947–1955 (2011).
274. Hamad, S. H. Factors Affecting the Growth of Microorganisms in Food. in *Progress in Food Preservation* 405–427 (John Wiley & Sons, Ltd, 2012). doi:10.1002/9781119962045.ch20.
275. Labuza, T. P. & Hyman, C. R. Moisture migration and control in multi-domain foods. *Trends in Food Science & Technology* **9**, 47–55 (1998).
276. Gaikwad, K. K., Singh, S. & Ajji, A. Moisture absorbers for food packaging applications. *Environ Chem Lett* **17**, 609–628 (2019).
277. Murmu, S. B. & Mishra, H. N. Selection of the best active modified atmosphere packaging with ethylene and moisture scavengers to maintain quality of guava during low-temperature storage. *Food Chemistry* **253**, 55–62 (2018).
278. Roy, S., Anantheswaran, R. C. & Beelman, R. B. Sorbitol Increases Shelf Life of Fresh Mushrooms Stored in Conventional Packages. *J Food Science* **60**, 1254–1259 (1995).
279. Rux, G. *et al.* Application of humidity-regulating tray for packaging of mushrooms. *Postharvest Biology and Technology* **108**, 102–110 (2015).
280. Shirazi, A. & Cameron, A. C. Controlling Relative Humidity in Modified Atmosphere Packages of Tomato Fruit. *HortScience* **27**, 336–339 (1992).
281. Mbuge, D. O. *et al.* Application of superabsorbent polymers (SAP) as desiccants to dry maize and reduce aflatoxin contamination. *J Food Sci Technol* **53**, 3157–3165 (2016).
282. Mahajan, P. V., Rodrigues, F. A. S., Motel, A. & Leonhard, A. Development of a moisture absorber for packaging of fresh mushrooms (Agaricus bisporous). *Postharvest Biology and Technology* **48**, 408–414 (2008).
283. Rux, G. *et al.* Humidity-Regulating Trays: Moisture Absorption Kinetics and Applications for Fresh Produce Packaging. *Food Bioprocess Technol* **9**, 709–716 (2016).

284. Kelly, C. A., Santovito, E., Cruz-Romero, M., Kerry, J. P. & Papkovsky, D. P. Application of O2 sensor technology to monitor performance of industrial beef samples packaged on three different vacuum packaging machines. *Sensors and Actuators B: Chemical* **304**, 127338 (2020).

285. Kelly, C. *et al.* Extruded phosphorescence based oxygen sensors for large-scale packaging applications. *Sensors and Actuators B: Chemical* **304**, 127357 (2020).

286. Fitzgerald, M. *et al.* Nondestructive Monitoring of Oxygen Profiles in Packaged Foods Using Phase-Fluorimetric Oxygen Sensor. *Journal of Food Science* **66**, 105–110 (2001).

287. Papkovsky, D. B., Papkovskaia, N., Smyth, A., Kerry, J. & Ogurtsov, V. I. Phosphorescent Sensor Approach for Non-Destructive Measurement of Oxygen in Packaged Foods: Optimisation of Disposable Oxygen Sensors and their Characterization Over a Wide Temperature Range. *Analytical Letters* **33**, 1755–1777 (2000).

288. Smiddy, M., Papkovskaia, N., Papkovsky, D. B. & Kerry, J. P. Use of oxygen sensors for the non-destructive measurement of the oxygen content in modified atmosphere and vacuum packs of cooked chicken patties; impact of oxygen content on lipid oxidation. *Food Research International* **35**, 577–584 (2002).

289. O'Mahony, F. C., O'Riordan, T. C., Papkovskaia, N., Kerry, J. P. & Papkovsky, D. B. Non-destructive assessment of oxygen levels in industrial modified atmosphere packaged cheddar cheese. *Food Control* **17**, 286–292 (2006).

290. Hempel, A. W., Gillanders, R. N., Papkovsky, D. B. & Kerry, J. P. Detection of cheese packaging containment failures using reversible optical oxygen sensors. *International Journal of Dairy Technology* **65**, 456–460 (2012).

291. Hempel, A. W., O'Sullivan, M. G., Papkovsky, D. B. & Kerry, J. P. Assessment and Use of Optical Oxygen Sensors as Tools to Assist in Optimal Product Component Selection for the Development of Packs of Ready-to-Eat Mixed Salads and for the Non-Destructive Monitoring of in-Pack Oxygen Levels Using Chilled Storage. *Foods* **2**, 213–224 (2013).

292. Kelly, C. A., Cruz-Romero, M., Kerry, J. P. & Papkovsky, D. B. Stability and Safety Assessment of Phosphorescent Oxygen Sensors for Use in Food Packaging Applications. *Chemosensors* **6**, 38 (2018).

293. López-Carballo, G., Muriel-Galet, V., Hernández-Muñoz, P. & Gavara, R. Chromatic Sensor to Determine Oxygen Presence for Applications in Intelligent Packaging. *Sensors* **19**, 4684 (2019).

294. Suman, Gaur, V., Kumar, P. & Jain, V. K. Nanomaterial-based opto-electrical oxygen sensor for detecting air leakage in packed items and storage plants. *Journal of Experimental Nanoscience* **7**, 608–615 (2012).

295. O' Callaghan, K. A. M., Papkovsky, D. B. & Kerry, J. P. An Assessment of the Influence of the Industry Distribution Chain on the Oxygen Levels in Commercial Modified Atmosphere Packaged Cheddar Cheese Using Non-Destructive Oxygen Sensor Technology. *Sensors* **16**, 916 (2016).

296. Kelly, C. A., Cruz-Romero, M., Kerry, J. P. & Papkovsky, D. P. Assessment of Performance of the Industrial Process of Bulk Vacuum Packaging of Raw Meat with Nondestructive Optical Oxygen Sensing Systems. *Sensors* **18**, 1395 (2018).

297. Zhu, R., Desroches, M., Yoon, B. & Swager, T. M. Wireless Oxygen Sensors Enabled by Fe(II)-Polymer Wrapped Carbon Nanotubes. *ACS Sens.* **2**, 1044–1050 (2017).

298. Wen, J. *et al.* Visible Colorimetric Oxygen Indicator Based on Ag-Loaded TiO2 Nanotubes for Quick Response and Real-Time Monitoring of the Integrity of Modified Atmosphere Packaging. *Advanced Materials Technologies* **4**, 1900121 (2019).

299. Saarinen, J. J. *et al.* Large-Scale Roll-to-Roll Patterned Oxygen Indicators for Modified Atmosphere Packages. *Packaging Technology and Science* **30**, 219–227 (2017).

300. Mihindukulasuriya, S. D. F. & Lim, L.-T. Oxygen detection using UV-activated electrospun poly(ethylene oxide) fibers encapsulated with TiO2 nanoparticles. *J Mater Sci* **48**, 5489–5498 (2013).

301. Rahaman, S. A., Mondal, D. K. & Bandyopadhyay, S. Formation of disulphide linkages restricts intramolecular motions of a fluorophore: detection of molecular oxygen in food packaging. *Chem. Commun.* **55**, 3132–3135 (2019).

302. Won, K., Jang, N. Y. & Jeon, J. A Natural Component-Based Oxygen Indicator with In-Pack Activation for Intelligent Food Packaging. *J. Agric. Food Chem.* **64**, 9675–9679 (2016).

303. Vu, C. H. T. & Won, K. Novel water-resistant UV-activated oxygen indicator for intelligent food packaging. *Food Chemistry* **140**, 52–56 (2013).

304. Roberts, L., Lines, R., Reddy, S. & Hay, J. Investigation of polyviologens as oxygen indicators in food packaging. *Sensors and Actuators B: Chemical* **152**, 63–67 (2011).

305. Mills, A. Oxygen indicators and intelligent inks for packaging food. *Chem. Soc. Rev.* **34**, 1003–1011 (2005).

306. Puligundla, P., Jung, J. & Ko, S. Carbon dioxide sensors for intelligent food packaging applications. *Food Control* **25**, 328–333 (2012).

307. Borisov, S. M., Waldhier, M. Ch., Klimant, I. & Wolfbeis, O. S. Optical Carbon Dioxide Sensors Based on Silicone-Encapsulated Room-Temperature Ionic Liquids. *Chem. Mater.* **19**, 6187–6194 (2007).

308. Schutting, S. *et al.* NIR optical carbon dioxide sensors based on highly photostable dihydroxy-aza-BODIPY dyes. *J. Mater. Chem. C* **3**, 5474–5483 (2015).

309. McEvoy, A. K. *et al.* Optical sensors for application in intelligent food-packaging technology. in *Opto-Ireland 2002: Optics and Photonics Technologies and Applications* vol. 4876 806–815 (International Society for Optics and Photonics, 2003).

310. Bültzingslöwen, C. von *et al.* Sol–gel based optical carbon dioxide sensor employing dual luminophore referencing for application in food packaging technology. *Analyst* **127**, 1478–1483 (2002).

311. Bibi, F., Guillaume, C., Gontard, N. & Sorli, B. Wheat gluten, a bio-polymer to monitor carbon dioxide in food packaging: Electric and dielectric characterization. *Sensors and Actuators B: Chemical* **250**, 76–84 (2017).

312. Borchert, N. B., Kerry, J. P. & Papkovsky, D. B. A CO2 sensor based on Pt-porphyrin dye and FRET scheme for food packaging applications. *Sensors and Actuators B: Chemical* **176**, 157–165 (2013).

313. Nopwinyuwong, A., Trevanich, S. & Suppakul, P. Development of a novel colorimetric indicator label for monitoring freshness of intermediate-moisture dessert spoilage. *Talanta* **81**, 1126–1132 (2010).

314. Perez de Vargas-Sansalvador, I. M., Erenas, M. M., Diamond, D., Quilty, B. & Capitan-Vallvey, L. F. Water based-ionic liquid carbon dioxide sensor for applications in the food industry. *Sensors and Actuators B: Chemical* **253**, 302–309 (2017).

315. Rukchon, C., Nopwinyuwong, A., Trevanich, S., Jinkarn, T. & Suppakul, P. Development of a food spoilage indicator for monitoring freshness of skinless chicken breast. *Talanta* **130**, 547–554 (2014).

316. Saliu, F. & Della Pergola, R. Carbon dioxide colorimetric indicators for food packaging application: Applicability of anthocyanin and poly-lysine mixtures. *Sensors and Actuators B: Chemical* **258**, 1117–1124 (2018).

317. Meng, X., Lee, K., Kang, T.-Y. & Ko, S. An irreversible ripeness indicator to monitor the CO2 concentration in the headspace of packaged kimchi during storage. *Food Sci Biotechnol* **24**, 91–97 (2015).

318. Jung, J., Puligundla, P. & Ko, S. Proof-of-concept study of chitosan-based carbon dioxide indicator for food packaging applications. *Food Chemistry* **135**, 2170–2174 (2012).

319. Lee, K. & Ko, S. Proof-of-concept study of a whey protein isolate based carbon dioxide indicator to measure the shelf-life of packaged foods. *Food Sci Biotechnol* **23**, 115–120 (2014).

320. Cao, X.-T. & Chung, W.-Y. Range-extended wireless food spoilage monitoring with a high energy efficient battery-free sensor tag. *Sensors and Actuators A: Physical* **299**, 111632 (2019).

321. Le, G. T., Tran, T. V., Lee, H.-S. & Chung, W.-Y. Long-range batteryless RF sensor for monitoring the freshness of packaged vegetables. *Sensors and Actuators A: Physical* **237**, 20–28 (2016).

322. Tan, E. L., Ng, W. N., Shao, R., Pereles, B. D. & Ong, K. G. A Wireless, Passive Sensor for Quantifying Packaged Food Quality. *Sensors* **7**, 1747–1756 (2007).

323. Zhang, D., Tong, J. & Xia, B. Humidity-sensing properties of chemically reduced graphene oxide/polymer nanocomposite film sensor based on layer-by-layer nano self-assembly. *Sensors and Actuators B: Chemical* **197**, 66–72 (2014).

324. Han, J.-W., Kim, B., Li, J. & Meyyappan, M. Carbon Nanotube Based Humidity Sensor on Cellulose Paper. *J. Phys. Chem. C* **116**, 22094–22097 (2012).

325. Rao, J., Gao, H., Guan, Y., Li, W. & Liu, Q. Fabrication of hemicelluloses films with enhanced mechanical properties by graphene oxide for humidity sensing. *Carbohydrate Polymers* **208**, 513–520 (2019).

326. Reyes, P. I. *et al.* ZnO Surface Acoustic Wave Sensors Built on Zein-Coated Flexible Food Packages. *sens lett* **11**, 539–544 (2013).

327. Syrový, T. *et al.* Wide range humidity sensors printed on biocomposite films of cellulose nanofibril and poly(ethylene glycol). *Journal of Applied Polymer Science* **136**, 47920 (2019).

328. Bridgeman, D., Corral, J., Quach, A., Xian, X. & Forzani, E. Colorimetric Humidity Sensor Based on Liquid Composite Materials for the Monitoring of Food and Pharmaceuticals. *Langmuir* **30**, 10785–10791 (2014).

329. Chi, H., Liu, Y. J., Wang, F. & He, C. Highly Sensitive and Fast Response Colorimetric Humidity Sensors Based on Graphene Oxides Film. *ACS Appl. Mater. Interfaces* **7**, 19882–19886 (2015).

330. Bumbudsanpharoke, N., Kwon, S., Lee, W. & Ko, S. Optical response of photonic cellulose nanocrystal film for a novel humidity indicator. *International Journal of Biological Macromolecules* **140**, 91–97 (2019).

331. Mills, A., Hawthorne, D., Burns, L. & Hazafy, D. Novel temperature-activated humidity-sensitive optical sensor. *Sensors and Actuators B: Chemical* **240**, 1009–1015 (2017).

332. LeBlanc, R. J. & Gill, T. A. Ammonia as an Objective Quality Index in Squid. *Canadian Institute of Food Science and Technology Journal* **17**, 195–201 (1984).

333. Monique, E. Volatile amines as criteria for chemical quality assessment. 22 (2005).

334. Doeun, D., Davaatseren, M. & Chung, M.-S. Biogenic amines in foods. *Food Sci Biotechnol* **26**, 1463–1474 (2017).

335. Nguyen, L. H., Naficy, S., McConchie, R., Dehghani, F. & Chandrawati, R. Polydiacetylene-based sensors to detect food spoilage at low temperatures. *J. Mater. Chem. C* **7**, 1919–1926 (2019).

336. Kuswandi, B. *et al.* A novel colorimetric food package label for fish spoilage based on polyaniline film. *Food Control* **25**, 184–189 (2012).

337. Narwade, V. N., Anjum, S. R., Kokol, V. & Khairnar, R. S. Ammonia-sensing ability of differently structured hydroxyapatite blended cellulose nanofibril composite films. *Cellulose* **26**, 3325–3337 (2019).

338. Chung, W.-Y., Le, G. T., Tran, T. V. & Nguyen, N. H. Novel proximal fish freshness monitoring using batteryless smart sensor tag. *Sensors and Actuators B: Chemical* **248**, 910–916 (2017).

339. Basavaraja, D., Thodi F. Salfeena, C., Panda, M. K. & Somappa, S. B. Rapid Visual Detection of Amines by Pyrylium Salts for Food Spoilage Taggant. *ACS Appl. Bio Mater.* **3**, 772–778 (2020).

340. Jiang, G. *et al.* Preparation and characterization of indicator films from carboxymethyl-cellulose/starch and purple sweet potato (Ipomoea batatas (L.) lam) anthocyanins for monitoring fish freshness. *International Journal of Biological Macromolecules* **143**, 359–372 (2020).

341. Luo, X. & Lim, L.-T. An inkjet-printed sulfonephthalein dye indicator array for volatile amine detection. *Journal of Food Science* **85**, 442–454 (2020).

342. Wells, N., Yusufu, D. & Mills, A. Colourimetric plastic film indicator for the detection of the volatile basic nitrogen compounds associated with fish spoilage. *Talanta* **194**, 830–836 (2019).

343. Luo, X. & Lim, L.-T. Cinnamil- and Quinoxaline-Derivative Indicator Dyes for Detecting Volatile Amines in Fish Spoilage. *Molecules* **24**, 3673 (2019).

344. Mo, R. *et al.* An Intelligent Label for Freshness of Fish Based on a Porous Anodic Aluminum Membrane and Bromocresol Green. *ChemistrySelect* **2**, 8779–8784 (2017).

345. Ma, Q., Du, L. & Wang, L. Tara gum/polyvinyl alcohol-based colorimetric NH3 indicator films incorporating curcumin for intelligent packaging. *Sensors and Actuators B: Chemical* **244**, 759–766 (2017).

346. Morsy, M. K. *et al.* Development and validation of a colorimetric sensor array for fish spoilage monitoring. *Food Control* **60**, 346–352 (2016).

347. Alrammouz, R., Podlecki, J., Abboud, P., Sorli, B. & Habchi, R. A review on flexible gas sensors: From materials to devices. *Sensors and Actuators A: Physical* **284**, 209–231 (2018).

348. Dai, J. *et al.* Printed gas sensors. *Chem. Soc. Rev.* **49**, 1756–1789 (2020).

349. Hempel, A., O'Sullivan, M. G., Papkovsky, D. B. & Kerry, J. P. Nondestructive and Continuous Monitoring of Oxygen Levels in Modified Atmosphere Packaged Ready-to-Eat Mixed Salad Products Using Optical Oxygen Sensors, and Its Effects on Sensory and Microbiological Counts during Storage. *Journal of Food Science* **78**, S1057–S1062 (2013).

350. Hempel, A. W., Papkovsky, D. B. & Kerry, J. P. Use of Optical Oxygen Sensors in Non-Destructively Determining the Levels of Oxygen Present in Combined Vacuum and Modified Atmosphere Packaged Pre-Cooked Convenience-Style Foods and the Use of Ethanol Emitters to Extend Product Shelf-Life. *Foods* **2**, 507–520 (2013).

351. O'Mahony, F. C. *et al.* Assessment of oxygen levels in convenience-style muscle-based sous vide products through optical means and impact on shelf-life stability. *Packaging Technology and Science* **17**, 225–234 (2004).

352. Yaghi, O. M., Li, G. & Li, H. Selective binding and removal of guests in a microporous metal–organic framework. *Nature* **378**, 703 (1995).

353. Gangu, K. K., Maddila, S., Mukkamala, S. B. & Jonnalagadda, S. B. A review on contemporary Metal–Organic Framework materials. *Inorganica Chimica Acta* **446**, 61–74 (2016).

354. Li, B. *et al.* Emerging Multifunctional Metal–Organic Framework Materials. *Advanced Materials* **28**, 8819–8860 (2016).

355. Huang, C.-W. *et al.* Metal–organic frameworks: preparation and applications in highly efficient heterogeneous photocatalysis. *Sustainable Energy Fuels* **4**, 504–521 (2020).

356. Mueller, U. *et al.* Metal–organic frameworks—prospective industrial applications. *J. Mater. Chem.* **16**, 626–636 (2006).

357. Müller, U. *et al.* Method for Electrochemical Production of a Crystalline Porous Metal Organic Skeleton Material. (2005).

358. Cheng, Y. *et al.* Ultrathin mixed matrix membranes containing two-dimensional metal-organic framework nanosheets for efficient CO2/CH4 separation. *Journal of Membrane Science* **539**, 213–223 (2017).

359. Hu, Z., Tao, C., Wang, F., Zou, X. & Wang, J. Flexible metal–organic framework-based one-dimensional photonic crystals. *J. Mater. Chem. C* **3**, 211–216 (2014).

360. Burmann, P., Zornoza, B., Téllez, C. & Coronas, J. Mixed matrix membranes comprising MOFs and porous silicate fillers prepared via spin coating for gas separation. *Chemical Engineering Science* **107**, 66–75 (2014).

361. Mandemaker, L. D. B. *et al.* Nanoweb Surface-Mounted Metal–Organic Framework Films with Tunable Amounts of Acid Sites as Tailored Catalysts. *Chemistry – A European Journal* **26**, 691–698 (2020).

362. Kim, R. *et al.* Surface-enhanced infrared detection of benzene in air using a porous metal-organic-frameworks film. *Korean J. Chem. Eng.* **36**, 975–980 (2019).

363. Khoshaman, A. H. & Bahreyni, B. Application of metal organic framework crystals for sensing of volatile organic gases. *Sensors and Actuators B: Chemical* **162**, 114–119 (2012).

364. Wahiduzzaman, Allmond, K., Stone, J., Harp, S. & Mujibur, K. Synthesis and Electrospraying of Nanoscale MOF (Metal Organic Framework) for High-Performance CO2 Adsorption Membrane. *Nanoscale Research Letters* **12**, 6 (2017).

365. Dou, Y., Zhang, W. & Kaiser, A. Electrospinning of Metal–Organic Frameworks for Energy and Environmental Applications. *Advanced Science* **7**, (2020).

366. Li, R. *et al.* 3D Printing of Mixed Matrix Films Based on Metal–Organic Frameworks and Thermoplastic Polyamide 12 by Selective Laser Sintering for Water Applications. *ACS Appl. Mater. Interfaces* **11**, 40564–40574 (2019).

367. Pei, R. *et al.* 3D-Printed metal-organic frameworks within biocompatible polymers as excellent adsorbents for organic dyes removal. *Journal of Hazardous Materials* **384**, 121418 (2020).

368. Lawson, S., Snarzyk, M., Hanify, D., Rownaghi, A. A. & Rezaei, F. Development of 3D-Printed Polymer-MOF Monoliths for CO2 Adsorption. *Ind. Eng. Chem. Res.* (2019) doi:10.1021/acs.iecr.9b05445.

369. Pohle, R., Tawil, A., Davydovskaya, P. & Fleischer, M. Metal Organic Frameworks as Promising High Surface Area Material for Work Function Gas Sensors. *Procedia Engineering* **25**, 108–111 (2011).

370. Achmann, S. *et al.* Metal-Organic Frameworks for Sensing Applications in the Gas Phase. *Sensors* **9**, 1574–1589 (2009).

371. Zhuang, J.-L., Ar, D., Yu, X.-J., Liu, J.-X. & Terfort, A. Patterned Deposition of Metal-Organic Frameworks onto Plastic, Paper, and Textile Substrates by Inkjet Printing of a Precursor Solution. *Advanced Materials* **25**, 4631–4635 (2013).

372. Liu, J. & Wöll, C. Surface-supported metal–organic framework thin films: fabrication methods, applications, and challenges. *Chem. Soc. Rev.* **46**, 5730–5770 (2017).

373. Chui, S. S.-Y., Lo, S. M.-F., Charmant, J. P. H., Orpen, A. G. & Williams, I. D. A Chemically Functionalizable Nanoporous Material [Cu3(TMA)2(H2O)3]n. *Science* **283**, 1148–1150 (1999).

374. Wong-Ng, W. *et al.* Reference diffraction patterns, microstructure, and pore-size distribution for the copper (II) benzene-1,3,5-tricarboxylate metal organic framework (Cu-BTC) compounds. *Powder Diffraction* **30**, 2–13 (2015).

375. Vishnyakov, A., Ravikovitch, P. I., Neimark, A. V., Bülow, M. & Wang, Q. M. Nanopore Structure and Sorption Properties of Cu−BTC Metal−Organic Framework. *Nano Lett.* **3**, 713–718 (2003).

376. Dantas, S., Sarkisov, L. & Neimark, A. V. Deciphering the Relations between Pore Structure and Adsorption Behavior in Metal–Organic Frameworks: Unexpected Lessons from Argon Adsorption on Copper–Benzene-1,3,5-tricarboxylate. *J. Am. Chem. Soc.* **141**, 8397–8401 (2019).

377. Schlichte, K., Kratzke, T. & Kaskel, S. Improved synthesis, thermal stability and catalytic properties of the metal-organic framework compound Cu3(BTC)2. *Microporous and Mesoporous Materials* **73**, 81–88 (2004).

378. Tan, K. *et al.* Water interactions in metal organic frameworks. *CrystEngComm* **17**, 247–260 (2014).

379. Doan, H. V., Sartbaeva, A., Eloi, J.-C., A. Davis, S. & Ting, V. P. Defective hierarchical porous copper-based metal-organic frameworks synthesised via facile acid etching strategy. *Sci Rep* **9**, (2019).

380. Al-Janabi, N. *et al.* Mapping the Cu-BTC metal–organic framework (HKUST-1) stability envelope in the presence of water vapour for CO2 adsorption from flue gases. *Chemical Engineering Journal* **281**, 669–677 (2015).

381. Mu, B. & Walton, K. S. Thermal Analysis and Heat Capacity Study of Metal–Organic Frameworks. *J. Phys. Chem. C* **115**, 22748–22754 (2011).

382. Hendon, C. H. & Walsh, A. Chemical principles underpinning the performance of the metal–organic framework HKUST-1. *Chem. Sci.* **6**, 3674–3683 (2015).

383. Al-Janabi, N. *et al.* A Facile Post-Synthetic Modification Method To Improve Hydrothermal Stability and CO_2 Selectivity of CuBTC Metal–Organic Framework. *Ind. Eng. Chem. Res.* **55**, 7941–7949 (2016).

384. Zhang, M., Bosch, M., Iii, T. G. & Zhou, H.-C. Rational design of metal–organic frameworks with anticipated porosities and functionalities. *CrystEngComm* **16**, 4069–4083 (2014).

385. Sun, L., Campbell, M. G. & Dincă, M. Electrically Conductive Porous Metal–Organic Frameworks. *Angewandte Chemie International Edition* **55**, 3566–3579 (2016).

386. Li, Y. *et al.* Advances of metal–organic frameworks for gas sensing. *Polyhedron* **154**, 83–97 (2018).

387. Zhang, Y. *et al.* A novel humidity sensor based on NH2-MIL-125(Ti) metal organic framework with high responsiveness. *J Nanopart Res* **15**, 2014 (2013).

388. Chen, E.-X., Yang, H. & Zhang, J. Zeolitic Imidazolate Framework as Formaldehyde Gas Sensor. *Inorg. Chem.* **53**, 5411–5413 (2014).

389. Travlou, N. A., Singh, K., Rodríguez-Castellón, E. & Bandosz, T. J. Cu–BTC MOF–graphene-based hybrid materials as low concentration ammonia sensors. *J. Mater. Chem. A* **3**, 11417–11429 (2015).

390. Campbell, M. G., Sheberla, D., Liu, S. F., Swager, T. M. & Dincă, M. Cu3(hexaiminotriphenylene)2: An Electrically Conductive 2D Metal–Organic Framework for Chemiresistive Sensing. *Angewandte Chemie International Edition* **54**, 4349–4352 (2015).

391. Campbell, M. G., Liu, S. F., Swager, T. M. & Dincă, M. Chemiresistive Sensor Arrays from Conductive 2D Metal–Organic Frameworks. *J. Am. Chem. Soc.* **137**, 13780–13783 (2015).

392. Cui, F. *et al.* Fabrication of ZIF-8 encapsulated ZnO microrods with enhanced sensing properties for H2 detection. *J Mater Sci: Mater Electron* **29**, 19697–19709 (2018).

393. Tchalala, M. R. *et al.* Concurrent Sensing of CO2 and H2O from Air Using Ultramicroporous Fluorinated Metal–Organic Frameworks: Effect of Transduction Mechanism on the Sensing Performance. *ACS Appl. Mater. Interfaces* **11**, 1706–1712 (2019).

394. Yin, Y.-Y. *et al.* A 3D pillared-layer cadmium (II) metal-organic framework for chemiresistive humidity sensing with high performance. *Inorganic Chemistry Communications* **97**, 49–55 (2018).

395. Meng, Z., Aykanat, A. & Mirica, K. A. Welding Metallophthalocyanines into Bimetallic Molecular Meshes for Ultrasensitive, Low-Power Chemiresistive Detection of Gases. *Journal of the American Chemical Society* (2018) doi:10.1021/jacs.8b11257.

396. Tian, H., Fan, H., Li, M. & Ma, L. Zeolitic Imidazolate Framework Coated ZnO Nanorods as Molecular Sieving to Improve Selectivity of Formaldehyde Gas Sensor. *ACS Sens.* **1**, 243–250 (2016).

397. Nair, S. S. *et al.* ZnO@ZIF-8: Gas sensitive core-shell hetero-structures show reduced cross-sensitivity to humidity. *Sensors and Actuators B: Chemical* **304**, 127184 (2020).

398. Tian, L. *et al.* Porous ZIF-8 Thin Layer Coating on ZnO Hollow Nanofibers for Enhanced Acetone Sensing. *ChemistrySelect* **5**, 2401–2407 (2020).

399. Sachdeva, S. *et al.* Gas Phase Sensing of Alcohols by Metal Organic Framework–Polymer Composite Materials. *ACS Appl. Mater. Interfaces* **9**, 24926–24935 (2017).

400. Homayoonnia, S. & Zeinali, S. Design and fabrication of capacitive nanosensor based on MOF nanoparticles as sensing layer for VOCs detection. *Sensors and Actuators B: Chemical* **237**, 776–786 (2016).

401. Mohan Reddy, A. J., Katari, N. K., Nagaraju, P. & Manabolu Surya, S. ZIF-8, Zn(NA) and Zn(INA) MOFs as chemical selective sensors of ammonia, formaldehyde and ethanol gases. *Materials Chemistry and Physics* **241**, 122357 (2020).

402. Yassine, O. *et al.* H2S Sensors: Fumarate-Based fcu-MOF Thin Film Grown on a Capacitive Interdigitated Electrode. *Angewandte Chemie International Edition* **55**, 15879–15883 (2016).

403. Hosseini, M. S., Zeinali, S. & Sheikhi, M. H. Fabrication of capacitive sensor based on Cu-BTC (MOF-199) nanoporous film for detection of ethanol and methanol vapors. *Sensors and Actuators B: Chemical* **230**, 9–16 (2016).

404. Wu, X., Xiong, S., Mao, Z., Hu, S. & Long, X. A Designed ZnO@ZIF-8 Core–Shell Nanorod Film as a Gas Sensor with Excellent Selectivity for H2 over CO. *Chemistry – A European Journal* **23**, 7969–7975 (2017).

405. Yuan, H. *et al.* On-Chip Tailorability of Capacitive Gas Sensors Integrated with Metal–Organic Framework Films. *Angewandte Chemie International Edition* **58**, 14089–14094 (2019).

406. Weiss, A., Reimer, N., Stock, N., Tiemann, M. & Wagner, T. Screening of mixed-linker CAU-10 MOF materials for humidity sensing by impedance spectroscopy. *Microporous and Mesoporous Materials* **220**, 39–43 (2016).

407. Gassensmith, J. J. *et al.* A Metal–Organic Framework-Based Material for Electrochemical Sensing of Carbon Dioxide. *J. Am. Chem. Soc.* **136**, 8277–8282 (2014).

408. Strauss, I. *et al.* Metal–Organic Framework Co-MOF-74-Based Host–Guest Composites for Resistive Gas Sensing. *ACS Appl. Mater. Interfaces* **11**, 14175–14181 (2019).

409. Tian, M., Fu, Z.-H., Nath, B. & Yao, M.-S. Synthesis of large and uniform Cu3TCPP truncated quadrilateral nano-flake and its humidity sensing properties. *RSC Adv.* **6**, 88991–88995 (2016).

410. Weiss, A., Reimer, N., Stock, N., Tiemann, M. & Wagner, T. Surface-modified CAU-10 MOF materials as humidity sensors: impedance spectroscopic study on water uptake. *Phys. Chem. Chem. Phys.* **17**, 21634–21642 (2015).

411. Sel, K., Demirci, S., Ozturk, O. F., Aktas, N. & Sahiner, N. NH3 gas sensing applications of metal organic frameworks. *Microelectronic Engineering* **136**, 71–76 (2015).

412. Aubrey, M. L. *et al.* Chemiresistive Detection of Gaseous Hydrocarbons and Interrogation of Charge Transport in Cu[Ni(2,3-pyrazinedithiolate)2] by Gas Adsorption. *Journal of the American Chemical Society* (2019) doi:10.1021/jacs.9b00654.

413. DMello, M. E., Sundaram, N. G., Singh, A., Singh, A. K. & Kalidindi, S. B. An amine functionalized zirconium metal–organic framework as an effective chemiresistive sensor for acidic gases. *Chem. Commun.* **55**, 349–352 (2019).

414. Meng, Z., Aykanat, A. & Mirica, K. A. Welding Metallophthalocyanines into Bimetallic Molecular Meshes for Ultrasensitive, Low-Power Chemiresistive Detection of Gases. *J. Am. Chem. Soc.* **141**, 2046–2053 (2019).

415. Jafari, N., Zeinali, S. & Shadmehr, J. Room temperature resistive gas sensor based on ZIF-8/MWCNT/AgNPs nanocomposite for VOCs detection. *J Mater Sci: Mater Electron* **30**, 12339–12350 (2019).

416. Surya, S. G. *et al.* A silver nanoparticle-anchored UiO-66(Zr) metal–organic framework (MOF)-based capacitive H2S gas sensor. *CrystEngComm* **21**, 7303–7312 (2019).

417. Bhardwaj, S. K., Mohanta, G. C., Sharma, A. L., Kim, K.-H. & Deep, A. A three-phase copper MOF-graphene-polyaniline composite for effective sensing of ammonia. *Analytica Chimica Acta* **1043**, 89–97 (2018).

418. Yin, Y. *et al.* Inducement of nanoscale Cu–BTC on nanocomposite of PPy–rGO and its performance in ammonia sensing. *Materials Research Bulletin* **99**, 152–160 (2018).

419. Khudiar, A. I., Elttayef, A. K., Khalaf, M. K. & Oufi, A. M. Fabrication of ZnO@ZIF-8 gas sensors for selective gas detection. *Mater. Res. Express* **6**, 126450 (2020).

420. Hao, X., Jin, Z., Yang, H., Lu, G. & Bi, Y. Peculiar synergetic effect of MoS2 quantum dots and graphene on Metal-Organic Frameworks for photocatalytic hydrogen evolution. *Applied Catalysis B: Environmental* **210**, 45–56 (2017).

421. Huang, Z.-H., Liu, G. & Kang, F. Glucose-Promoted Zn-Based Metal–Organic Framework/Graphene Oxide Composites for Hydrogen Sulfide Removal. *ACS Appl. Mater. Interfaces* **4**, 4942–4947 (2012).

422. Jabbari, V., Veleta, J. M., Zarei-Chaleshtori, M., Gardea-Torresdey, J. & Villagrán, D. Green synthesis of magnetic MOF@GO and MOF@CNT hybrid nanocomposites with high adsorption capacity towards organic pollutants. *Chemical Engineering Journal* **304**, 774–783 (2016).

423. Jaiswal, R. K., Mendiratta, S. K., Talukder, S., Soni, A. & Saini, B. L. Enzymatic time temperature indicators: A review. *The Pharma Innovation Journal* **7**, 643–647 (2018).

424. Toivola, R. *et al.* Highly sensitive thermal damage sensors for polymer composites: time temperature indicator based on thermochromic fluorescence turn-on response. *Smart Mater. Struct.* **26**, 085039 (2017).

425. Uddin, Z. & Boonsupthip, W. Development and characterization of a new nonenzymatic colored time–temperature indicator. *Journal of Food Process Engineering* **42**, e13027 (2019).

426. Hu, B. *et al.* Development of a novel Maillard reaction-based time–temperature indicator for monitoring the fluorescent AGE content in reheated foods. *RSC Adv.* **10**, 10402–10410 (2020).

427. Galagan, Y. & Su, W.-F. Fadable ink for time–temperature control of food freshness: Novel new time–temperature indicator. *Food Research International* **41**, 653–657 (2008).

428. Nopwinyuwong, A., Boonsupthip, W., Pechyen, C. & Suppakul, P. Preparation of Polydiacetylene Vesicle and Amphiphilic Polymer as Time-Temperature Indicator. *AMR* **506**, 552–555 (2012).

429. Choi, S. *et al.* A Self-Healing Nanofiber-Based Self-Responsive Time-Temperature Indicator for Securing a Cold-Supply Chain. *Advanced Materials* **32**, 1907064 (2020).

430. Lee, B.-S. & Shin, H.-S. Polymer-based time-temperature indicator for high temperature processed food products. *Food Sci Biotechnol* **21**, 1483–1487 (2012).

431. Jafry, A. T., Lim, H., Sung, W.-K. & Lee, J. Flexible time–temperature indicator: a versatile platform for laminated paper-based analytical devices. *Microfluid Nanofluid* **21**, 57 (2017).

432. Vaikousi, H., Biliaderis, C. G. & Koutsoumanis, K. P. Development of a Microbial Time/Temperature Indicator Prototype for Monitoring the Microbiological Quality of Chilled Foods. *Appl. Environ. Microbiol.* **74**, 3242–3250 (2008).

433. Vaikousi, H., Biliaderis, C. G. & Koutsoumanis, K. P. Applicability of a microbial Time Temperature Indicator (TTI) for monitoring spoilage of modified atmosphere packed minced meat. *International Journal of Food Microbiology* **133**, 272–278 (2009).

434. Mataragas, M., Bikouli, V. C., Korre, M., Sterioti, A. & Skandamis, P. N. Development of a microbial Time Temperature Indicator for monitoring the shelf life of meat. *Innovative Food Science & Emerging Technologies* **52**, 89–99 (2019).

435. Kim, E., Choi, D. Y., Kim, H. C., Kim, K. & Lee, S. J. Calibrations between the variables of microbial TTI response and ground pork qualities. *Meat Science* **95**, 362–367 (2013).

436. Lim, S., Gunasekaran, S. & Imm, J.-Y. Gelatin-Templated Gold Nanoparticles as Novel Time–Temperature Indicator. *Journal of Food Science* **77**, N45–N49 (2012).

437. Wang, Y.-C., Lu, L. & Gunasekaran, S. Biopolymer/gold nanoparticles composite plasmonic thermal history indicator to monitor quality and safety of perishable bioproducts. *Biosensors and Bioelectronics* **92**, 109–116 (2017).

438. Zhang, C. *et al.* Time–Temperature Indicator for Perishable Products Based on Kinetically Programmable Ag Overgrowth on Au Nanorods. *ACS Nano* **7**, 4561–4568 (2013).

439. Janjarasskul, T. & Suppakul, P. Active and intelligent packaging: The indication of quality and safety. *Critical Reviews in Food Science and Nutrition* **58**, 808–831 (2018).

440. Tominaga, T. Enhanced sensitivity of lateral-flow test strip immunoassays using colloidal palladium nanoparticles and horseradish peroxidase. *LWT* **86**, 566–570 (2017).

441. Ramos, A. C. *et al.* Evaluation of a rapid immunochromatographic test for detection of distinct variants of Klebsiella pneumoniae carbapenemase (KPC) in Enterobacteriaceae. *Journal of Microbiological Methods* **142**, 1–3 (2017).

442. Basu, P. K. *et al.* Graphene based E. coli sensor on flexible acetate sheet. *Sensors and Actuators B: Chemical* **190**, 342–347 (2014).

443. Altintas, Z., Akgun, M., Kokturk, G. & Uludag, Y. A fully automated microfluidic-based electrochemical sensor for real-time bacteria detection. *Biosensors and Bioelectronics* **100**, 541–548 (2018).

444. Yousefi, H., Ali, M. M., Su, H.-M., Filipe, C. D. M. & Didar, T. F. Sentinel Wraps: Real-Time Monitoring of Food Contamination by Printing DNAzyme Probes on Food Packaging. *ACS Nano* **12**, 3287–3294 (2018).

445. Bibi, F., Guillaume, C., Gontard, N. & Sorli, B. A review: RFID technology having sensing aptitudes for food industry and their contribution to tracking and monitoring of food products. *Trends in Food Science & Technology* **62**, 91–103 (2017).

446. Windl, R. *et al.* Reactivable passive radio-frequency identification temperature indicator. *Journal of Applied Physics* **117**, 17C125 (2015).

447. Martínez-Olmos, A. *et al.* Screen Printed Flexible Radiofrequency Identification Tag for Oxygen Monitoring. *Anal. Chem.* **85**, 11098–11105 (2013).

448. Eom, K., Lee, W., Shin, J., Lee, H. & Won, K. Integration of an oxygen indicator sensor with a passive UHF band RFID tag. *ces* **9**, 889–896 (2016).

449. Borgese, M., Dicandia, F. A., Costa, F., Genovesi, S. & Manara, G. An Inkjet Printed Chipless RFID Sensor for Wireless Humidity Monitoring. *IEEE Sensors Journal* **17**, 4699–4707 (2017).

450. Gonçalves, R. *et al.* RFID-Based Wireless Passive Sensors Utilizing Cork Materials. *IEEE Sensors Journal* **15**, 7242–7251 (2015).

451. Fernández-Salmerón, J., Rivadeneyra, A., Rodríguez, M. A. C., Capitan-Vallvey, L. F. & Palma, A. J. HF RFID Tag as Humidity Sensor: Two Different Approaches. *IEEE Sensors Journal* **15**, 5726–5733 (2015).

452. Oprea, A. *et al.* Capacitive Humidity Sensors on Flexible RFID Labels. in *TRANSDUCERS 2007 - 2007 International Solid-State Sensors, Actuators and Microsystems Conference* 2039–2042 (2007). doi:10.1109/SENSOR.2007.4300564.

453. Espinosa, E. *et al.* Drop-coated sensing layers on ultra low power hotplates for an RFID flexible tag microlab. *Sensors and Actuators B: Chemical* **144**, 462–466 (2010).

Chapter II

Cellulose nanofibrils and silver nanowires for antibacterial packaging

Table of content – Chapter II

Introduction to Chapter II

Chapter I described the different existing technologies for active and intelligent packaging associated with the relevant benefits and challenges they face. This PhD project focused specifically on two different technologies, one for active packaging application detailed in **Chapter II** and one for intelligent packaging application developed in **Chapter III**. More precisely, **Chapter II** focuses on the development of antibacterial packaging applications based on the combination of two innovative nanomaterials namely cellulose nanofibrils and silver nanowires. The first challenge in this chapter was to prove the concept of this new antibacterial packaging material, by investigating different deposition process. Controlling and understanding the processability and the active properties of the designed materials were also a key challenge.

Section **II-1** targeted the proof of concept of the antibacterial surface developed using coating processes on polymeric substrate such as polyethylene terephthalate (PET) and polylactic acid (PLA). The layers, achieved firstly with laboratory-scale bar coating process, were tested for different active properties mainly antibacterial activity and barrier properties. Secondly, a roll-to-roll reverse gravure coating was also tested to assess the possibility to up-scale the production of such active packaging materials.

Section **II-2** showed the preparation of antibacterial localised patterns using similar cellulose nanofibrils/silver nanowires hybrid systems and the screen-printing process. Firstly, the rheological properties of the inks were investigated based on mass content, raw materials sources and ratios and additives to fit the requirement of the screen-printing process. The quality of the print and the antibacterial activity of the layers were also assessed.

Section **II-3** reports a preliminary study that aimed at investigating the antibacterial and barrier mode of action of materials made of cellulose nanofibrils and silver nanowires. Specifically, film cast composites was used as a larger scale system to model the deposition of thin layers developed in the previous sections. The leaching of active materials as well as the barrier properties of the produced films were investigated.

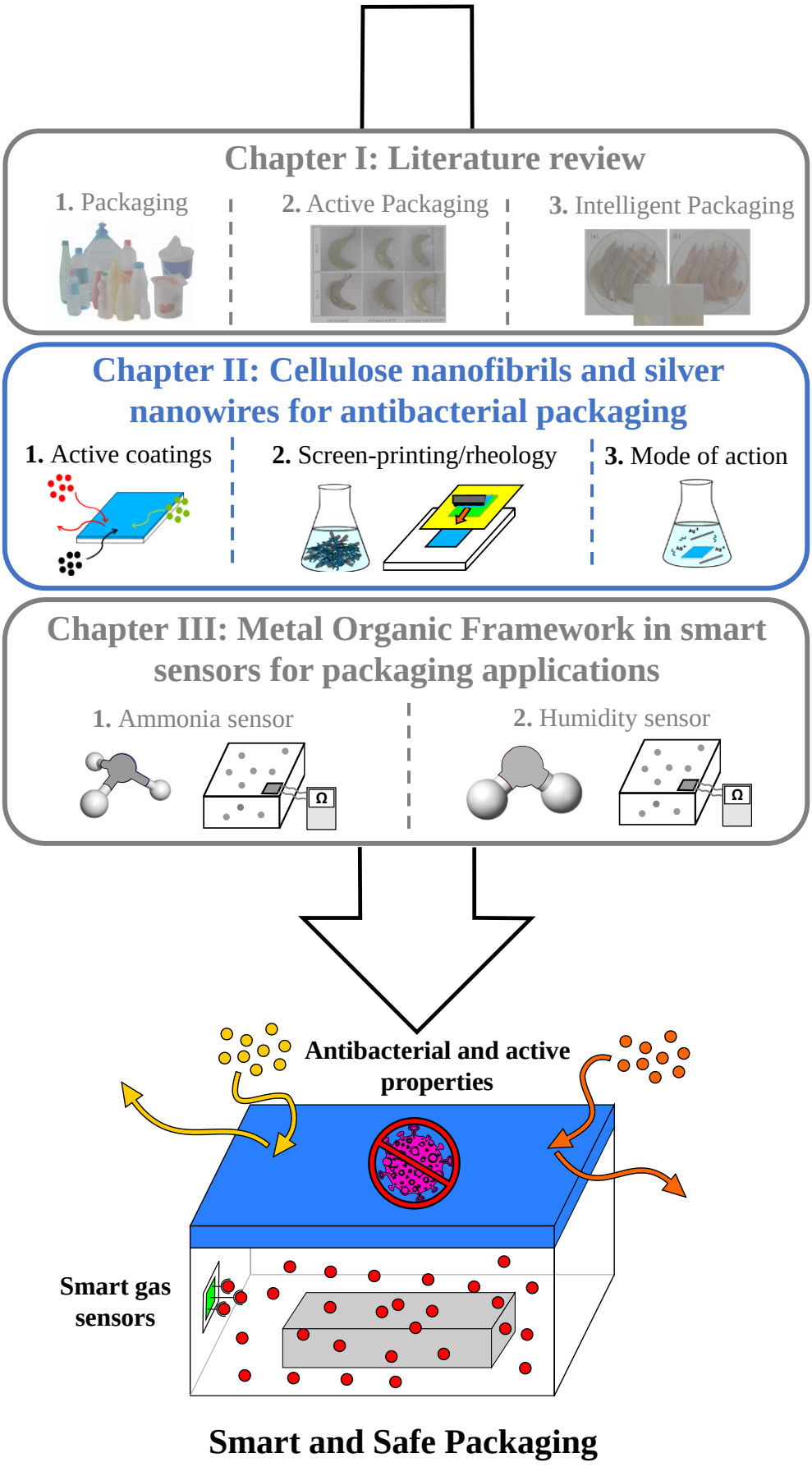

Smart and Safe Packaging

1. Cellulose nanofibrils and silver nanowires transparent coatings for the development of enhanced packaging surfaces

This section is adapted from and expands on Spieser, H. et al. Cellulose nanofibrils and silver nanowires active coatings for the development of antibacterial packaging surfaces. Carbohydrate Polymers 240, 116305 (2020).

Abstract:

An active ink composed of cellulose nanofibrils and silver nanowires was deposited on flexible and transparent polymer films using the bar coating process, achieving controlled thicknesses ranging from 200 nm up to 2 µm. For 350 nm thick coating on polyethylene terephthalate films, high transparency (75.6% transmittance) and significant reduction of bacterial growth equal to 89.3% and 100% was noted respectively against Gram-negative *Escherichia Coli* and Gram-positive *Staphylococcus Aureus* bacteria using AATCC contact active standard test. Retained antibacterial activity was found with films produced by reverse gravure roll-to-roll process, showing the promising capability of this antibacterial solution to be deployed industrially. Finally, the same ink was also deposited on polylactic acid substrate to investigate barrier properties: for 350 nm thick coating, a reduction of 49% of oxygen transmission rate (dry conditions) and 47% reduction of water vapour transmission rate was noted, proving the enhanced barrier properties of the coatings.

Keywords:

cellulose nanofibrils, silver nanowires, transparent coatings, antibacterial activity, barrier properties, up-scaling

1.1. Introduction

In a high consumption society, production and global movement of food products is considerable and increasing continuously[1]. Food products are exposed to harsh conditions throughout all of the supply chain stages and packaging is today expected to meet more and more requirements (mechanical strength, light, low-cost, sustainability, etc.). Recent innovation has focused on the development of active packaging, which refers to the ability of a package to respond to an external stimulus (change in the gaseous atmosphere, oxidation, bacterial breakthrough, etc.)[2]. Within this framework, active packaging aims at increasing the shelf-life of a product by optimising the condition inside the package, thus improving food quality and reducing food waste.

Antimicrobial food packaging has been studied extensively over the past 20 years and aspires to reduce pathogenic contamination against bacteria, fungus or viruses[3] with a preferred mode of action working by contact for consumer safety and environmental concern[4]. Silver nanoparticles (Ag NPs) have recently attracted a lot of attention since they display strong antibacterial activity and can help by fighting against the increasing antibiotic resistance in pathogens[5]. It has been established that the antibacterial effect of Ag NPs is attributed to the nanoscale of the particle itself along with the continuous release of silver ions[6]. The morphology of Ag NPs plays a major role on their antimicrobial activity: the smaller the nanoparticle (the higher surface area) the more active they are against bacteria[7]. The shape of the nanoparticle is also important and the antibacterial activity decreases on progression from pyramids, cubes, spheres, to wire-like shape[8,9]. Different parameters also influence the antibacterial activity of Ag NPs such as surface charge, the presence of residual synthesis surfactants or capping agent, and Ag NPs crystallinity[10–12].

One way to use Ag NPs in packaging applications is to incorporate them into a nanocomposite to limit nanoparticle migration. Ag NPs have been recognised as potentially hazardous for health as studies have focused on evaluating their toxicity against in vivo and in vitro studies. There is still a lack of information and knowledge concerning the global health hazard on humans, but Ag NPs are suggested to be mainly dangerous by oral and inhalation adsorption and silver accumulation in different organs leading to specific malfunctions[13]. The potent activity of Ag NPs is dependent on a lot of factors such as size, surface chemistry, shape, etc. and more research is needed to have a full overview of the toxicity of Ag NPs toward the human body. It then appears obvious that the leaching of Ag NPs in antibacterial composite for food packaging application is an important parameter to address. Nanocellulose materials are biobased, biodegradable and biocompatible nanomaterials that are defined as cellulose particles with a nano-scale size for at least one of their dimensions. One of the established class of nanocellulose are cellulose nanofibrils (CNF) which come from the mechanical fibrillation of pulp suspension[14,15]. CNF have been of particular interest because they display interesting

properties for packaging applications: high oxygen barrier property, vast chemical functionalisation possibilities and good mechanical properties. CNF can be used either alone as a free standing film or as a coating on classic plastic packaging or paper substrates for its reinforcement properties[16–18] and also display good matrix properties that can be used successfully to immobilise nanoparticles.

Combinations of Ag NPs and nanocellulose composites have been investigated extensively by the scientific community[19] and different composite preparation techniques exist. In the most common in-situ synthesis methods, CNF serve as a template matrix for adsorption of silver salts, followed by in-situ chemical reduction[20,21]. Covalent bonding is another option, yet to our knowledge, the only reported example comes from Ramaraju et al. (2015), who reported the immobilisation of Ag NPs stabilised with a dendrimer by covalently bonding the NH_2-terminated dendrimer on TEMPO (2,2,6,6-tetramethylpiperidine-N-oxyl)-oxidised CNF[22]. Finally, the physical mixing approach is just mixing separately produced components. To our knowledge, the only example of simple mixing of CNF materials with Ag NPs for antibacterial applications has been reported by Martins et al. (2012) who prepared CNF/Ag NPs composites based on a polyelectrostatic assembly for antibacterial coating on a paper substrate[23]. Simple mixing is a straightforward easily up-scalable procedure, however immobilisation of the Ag NPs on cellulose materials is relatively poor[24], leading to reduced life-time of the system and possible non-desired release of Ag NPs.

This work presents the development of antibacterial packaging based on a combination of silver nanoparticles and nanocellulose materials. To our knowledge, no studies have reported the use of CNF and silver nanowires (Ag NWs) to develop antibacterial materials, and as described before, CNF/Ag NPs composites are usually not prepared in a straight-forward and versatile manner. Based on the precedent literature review, it was then hypothesised that combining silver nanowires with cellulose nanofibrils could achieve easy-to-process systems that can be deposited on flexible substrate to achieve contact killing antibacterial mode of action along with improved barrier properties. In this study, the technical challenges were firstly to straightforwardly produce a transparent and antibacterial coating on plastic polymer sheets. Secondly, the objectives were to prepare similar active coatings on biobased polymer sheets and to evaluate the enhancement of their barrier property. Finally, the challenge of preparing active surfaces with a roll-to-roll process for up-scaling purposes was addressed.

To tackle the three core challenges, a hybrid ink composed of TEMPO-oxidised cellulose nanofibrils and silver nanowires was firstly deposited on polyethylene terephthalate substrates using a laboratory-scale bar coating process. Thickness and transparency of the coatings were investigated and they were tested against bacterial contamination. The same technique was used to deposit the active ink on bio-based polylactic acid sheets and the barrier properties of the produced films were characterised. Finally, a new lower cost active ink was specifically

formulated by the authors to assess the up-scaling possibility by using a reverse gravure roll-to-roll coating process

Compared to the published work "Spieser, H. et al. Cellulose nanofibrils and silver nanowires active coatings for the development of antibacterial packaging surfaces. Carbohydrate Polymers 240, 116305 (2020)", some additional content is proposed in this section. Precisely, the Inductively Coupled Plasma – Optical Emission Spectroscopy (ICP-OES) leaching assay (in section 1.2.4. and 1.3.1.), the Figure II-1 and the section "Additional film surface and transmission characteristics" (1.2.6. and 1.3.3.) were not part of the published work. The modifications only concern the presentation of additional data and figures, for an enriched and better understanding of the work.

1.2. Materials and methods

1.2.1. Materials

A polyethylene terephthalate (PET) sheet substrate (Melinex® ST726 – 175 µm) and polylactic acid (PLA) substrate (Earthfirst® BCWC – 75 µm) was respectively purchased from Dupont (France) and Sidaplax (Belgium). A hybrid ink system composed of silver nanowires (Ag NWs) and TEMPO oxidised-cellulose nanofibrils (T-CNF) in water (PolyBioWire® 9830C) was supplied by Poly-Ink (France) with an approximate 1% wt total mass and 1:1 ratio given by the supplier. However to investigate a roll-to-roll semi-industrial deposition process, a new specific formulation was prepared, using T-CNF suspension (CNF-A13) from Betulium (Finland) with approximately length of 50-400 nm and diameter of 5-15 nm, at 5 %wt (charge density of 1.6 ± 0.1 $mmol.g^{-1}$, estimated aspect ratio of 22.5) and using 2.5% wt Ag NWs aqueous suspension (NGAP NF Ag-3170) from NanoGap (USA) with estimated length 10-50 µm, diameter 50-100 nm (and so with an estimated aspect ratio of 400).

Escherichia Coli ATCC 8739 and Staphylococcus Aureus ATCC 6538 were purchased from Microbiologics (USA). PCA (Plate Counting Agar) was purchased from BD Difco (USA) and contains beef extract ($3g.l^{-1}$), peptone ($5g.l^{-1}$), agar ($15g.l^{-1}$). Standard nutrient broth 1 was purchased from Roth (Germany) and contains beef extract ($3g.l^{-1}$), peptone ($15g.l^{-1}$), sodium chloride ($6g.l^{-1}$) and glucose ($1g.l^{-1}$). Sodium thiosulphate (>99%), L-histidine (>98.5%), potassium dihydrogen phosphate (>99%), Tween®80 and calcium chloride (>96%) were also obtained from Roth (Germany). L α-phosphatidyl choline (>99%) was purchased from Sigma Aldrich (France). All materials were used as received.

1.2.2. Production of active layer by bar coating process

Coated films were first prepared using the supplied T-CNF/Ag NWs ink and using the bar coating process (KCC101, Erichsen, Germany). Prior to coating, the surface of the films was treated using a corona treatment (Klwar Calvatron SG2, Germany): 2 passes, 90° rotation between the pass. The coatings were then oven-dried and different thickness were achieved using different threaded rod diameter (**Table II-1**).

***Table II-1**: Equivalence between bar coating rod thread diameter and manufacturer estimation of deposited wet thickness*

Threaded rod diameter (mm)	0.15	0.31	0.51	1.27
Estimated wet thickness (µm)	12	24	40	100

Coatings, corona treatment and drying step parameters were optimised through extensive research with visual observation of possible defects, transparency and sheet resistance

measurements. Optimised corona treatment settings are the following: 2.9 $m.min^{-1}$ speed and 330 mA intensity for PET substrate, 3.5 $m.min^{-1}$ speed and 150 mA intensity for PLA substrate. Optimised coatings and drying parameters are the following: coating speed of 5.4 $m.min^{-1}$ for both PET and PLA coatings, oven-drying step at 120°C for 60s for PET and at room temperature overnight for PLA coatings. Each coating was performed at least three times to assess consistency and reproducibility of the process.

1.2.3. Structural and quality characterisation

Field-Emission Gun Scanning Electron Microscope (FEG-SEM) was used to investigate the hybrid nanostructure after 2 nm-coating of Gold /Palladium, at 5.4 mm working distance and 3 kV accelerating voltage. A cross-section through the coated samples was prepared using a LEICA UC6 (Germany) ultramicrotome apparatus equipped with a diamond knife, at room temperature and with a cutting speed of 1 $mm.s^{-1}$. The thickness of the coatings was then estimated by image analysis using FIJI software[25,26]. At least 6 measurements in three different positions in the films were considered.

Transmittance (%) was measured on a UV-spectrophotometer (Shimadzu Manufacturing Inc., USA), using the photometric mode. Six different measurements were conducted on each sample at 550 nm wavelength. Sheet resistance (Ω/sq) of the coated layer was measured by a four-probe system (Jandel Universal, USA). The measurement was repeated at six positions on the film and the average computed along with associated standard deviation.

1.2.4. Antibacterial characterisation

Prior to antibacterial testing, a leaching assay was performed by putting a 2 × 2 cm specimen of coating (24 µm estimated wet thickness) in 10 ml of deionised water (DI water), under agitation (100 rotation per minute - RPM) at 37°C. After 72 hours, the liquid media was recovered and full UV-vis spectra (300-700 nm wavelength, 1 nm scan rate) were recorded on a UV-spectrophotometer (Shimadzu Manufacturing Inc., USA), and compared with the T-CNF/Ag NWs reference suspension diluted in DI water to reach a final Ag NWs concentration of 0.005% wt. An additional leaching assay was also performed using the Inductively Coupled Plasma – Optical Emission Spectroscopy (ICP-OES) technique. The equipment used was the ICP-OES 5100 model from Agilent Technologies (USA) and the tests were performed following the ISO 11885 standard[27]. The ICP-OES analysis was conducted after microwave digestion of the samples in a mixture of nitric acid and oxygen peroxide, using an ETHOS ONE system from Milestone (Italy) following the NF EN 15587-1 standard[28]. The same experimental conditions as before were used (2 × 2 cm specimen of coating at 24 µm estimated wet thickness, 10 ml of DI water as liquid media, 100 RPM, 37°C). The leaching times that were tested are 1, 2, 4, 8 and 24 hours and the experiment was conducted once, but each liquid media extracted was analysed by ICP-OES in duplicate.

All the glassware, consumables, tools and solutions used for the antibacterial characterisation were sterilised prior to use in an autoclave for 20 min at 120°C and 1.034 bar.

Antibacterial activity was assessed initially using an inhibition zone qualitative test following a modified AFNOR EN 1104 standard[29]. To exaggerate the antibacterial activity of the samples, the test was carried out on multilayer coating (10 layers) prepared with the same parameters as single layer coating (threaded rod with 1.27 diameter – 100 µm estimated wet thickness). Ag NWs only coating was used as control and prior to deposition, the starting suspension was diluted to 0.5% wt in DI water and dispersed using an Ultra Turrax high shear disperser (30s, 10000 RPM). The samples produced were cut into 5 cm × 5 cm specimens and dry-sterilised for 24 hours at 60°C. 10 ml of pre-inoculated PCA at 10^5 CFU.ml^{-1} (Colony Forming Unit) was poured in a petri dish and, after cooling, the samples were put on top with the coated side facing the agar. The incubation period was 72 hours at 37°C and the inhibition zone was assessed visually after incubation.

Quantitative tests were performed on single layer coatings with different thickness using the AATCC TM100-1998 standard[30]. The samples were cut into 2 cm × 2 cm specimens and dry-sterilised for 24 hours at 60°C. 200 µl of bacterial suspension at 5.10^5 CFU.ml^{-1} in 20% nutrient broth (5 g.l^{-1} nutrient broth, 6.8 g.l^{-1} sodium chloride) were deposited on the samples specimen and incubated at 37°C for 24 hours. After incubation, the bacterial suspension was recovered by washing with a prepared neutralising solution (3 g.l^{-1} of L-α-phosphatidyl choline, 5 g.l^{-1} of sodium thiosulphate, 1 g.l^{-1} of L-histidine, 30 g.l^{-1} of Tween 80, 10 ml of potassium dihydrogen phosphate at 0.0425 g.l^{-1}, controlled pH of 7.2 ± 0.2) and the final concentration was determined by the plate counting numbering method. The antibacterial activity (AA, %) of the samples was compared quantitatively using Equation **II-1**:

$$AA\ (\%) = \frac{BC_{reference} - \mathrm{BC}_{sample}}{BC_{reference}} \times 100 \quad \textbf{(II-1)}$$

Where $\mathrm{BC}_{\mathrm{reference}}$ (log CFU) is the remaining bacterial concentration on the PET substrate with no coating and $\mathrm{BC}_{\mathrm{sample}}$ (log CFU) is the remaining concentration on the tested sample. The tests were conducted at least three times and the average is presented with standard deviation. The **Figure II-1** summarised the different steps of the standard test.

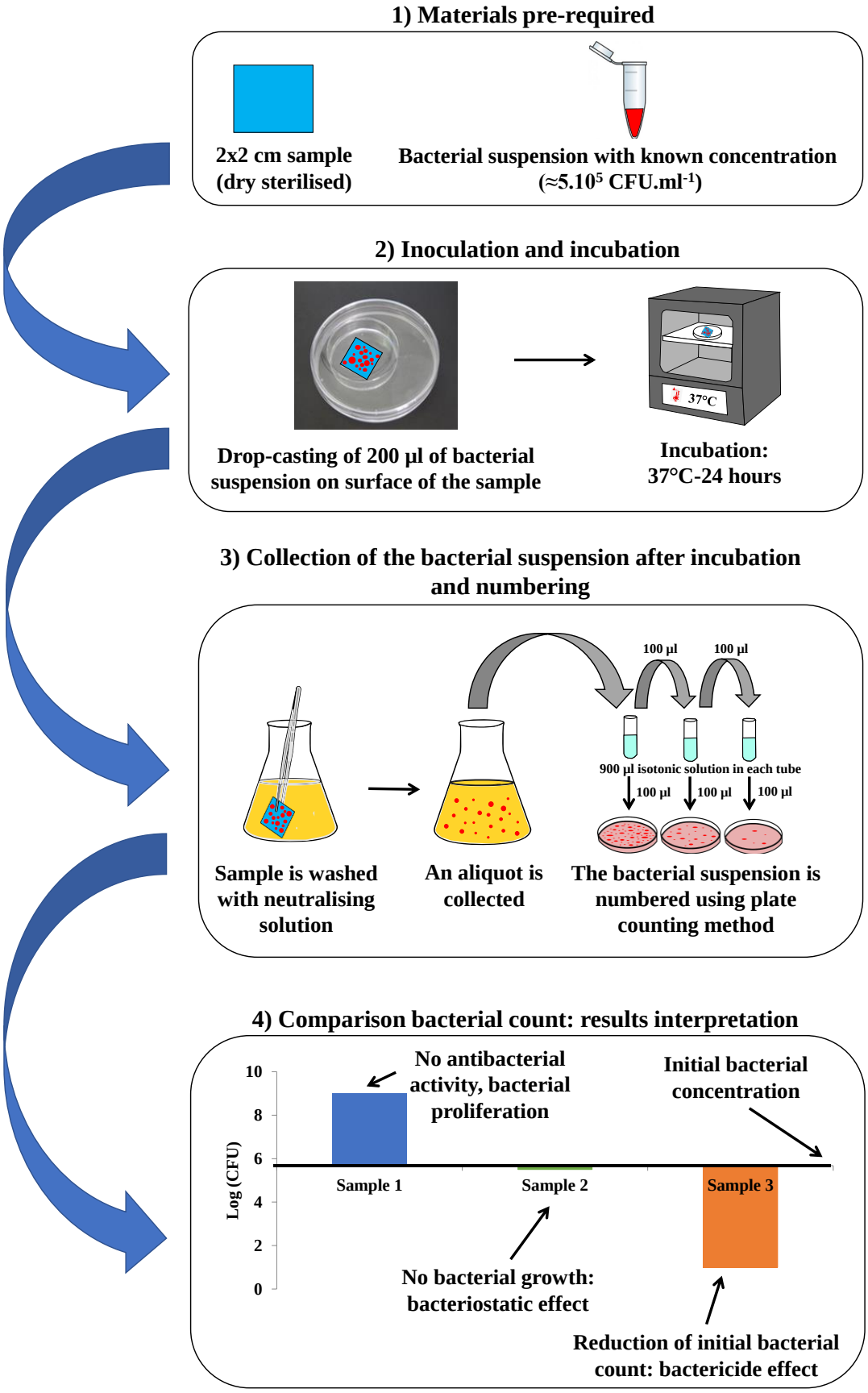

***Figure II-1**: AATCC TM100-1998 standard summarized in a 4-step scheme with 1) prerequired materials, 2) inoculation and incubation steps, 3) collection and numbering and 4) the different possible scenario*

1.2.5. Barrier properties characterisation

The Oxygen Transmission Rate (OTR) of the coated samples was measured at 0, 50 and 80 % relative humidity following the ASTM-F 1927-98 standards[31] on a Systech Illinois Permeation Analyser (USA) equipped with a coulometric detector. The tests were conducted at 23°C and with a 6.15 cm^2 exchange surface. At least 3 different samples for each coating were tested and an average is computed along with the associated standard deviation.

Water Vapour Transmission Rate (WVTR) was also measured on the same samples following a slightly modified T 448 om-09 standard[32]. Around 30 g of anhydrous calcium dichloride salt was placed in a metal cup covered by the test sample and closed by a rubber gasket and screw-down cap. The test was conducted at a regulated temperature (23°C) and relative humidity (50 %). The water-uptake of the anhydrous salt through the tested sample was monitored by weighing at least twice a day for at least one week. The WVTR value was calculated using Equation **II-2**:

$$WVTR\ (g.m^{-2}.day^{-1}) = \frac{24 \times \Delta m}{\Delta t \times S} \quad \textbf{(II-2)}$$

Where Δt (h) is the time between two measurements, Δm (g) the corresponding weigh-uptake and S (m^2) is the exposed surface (6.15 cm^2). Three different samples were tested and the average is presented along with corresponding standard deviation.

1.2.6. Additional film surface and transmission characteristics

The PET and/or PLA coated layers were also tested for antioxidant properties, UV-barrier, anti-fog properties and the potential of performing multi-layer coating was also investigated.

Radical Scavenging Activity (RSA) of the PET coated films was investigated using 2, 2-diphenyl-1-picrylhydrazyl (DDPH) as a free and stable radical. 4 cm^2 of sample was prepared along with 10 ml of DDPH in ethanol at 50 $mg.l^{-1}$, and put under agitation at 100 RPM in a glass vial. Absorbance at 515 nm was tracked during 27 hours using an UV-spectrophotometer (Shimadzu, USA). This was achieved by taking out 3 ml of the solution for and placing it back after the measurement in order to maintain the 10 ml volume. The absorbance of a 10 ml DDPH containing 4 cm^2 of PET film was followed as a reference. Samples were covered in aluminium foil and remained in darkness over the duration of characterisation. When the absorbance measured over time was stable, the RSA (%) was calculated using Equation **II-3**:

$$RSA(\%) = 100 - \frac{A_{reference} - A_{coating}}{A_{reference}} \times 100 \quad \textbf{(II-3)}$$

Where $A_{reference}$ is the absorbance of the PET reference containing solution and $A_{coating}$ the absorbance of the sample solution. The experiments were conducted twice and the average is presented with corresponding standard deviation.

The UV-barrier properties of the PET and PLA references, PET coated samples and PLA coated samples were measured by recording spectra from 200-700 nm at 1 nm scan step on a UV-spectrophotometer (Shimadzu Manufacturing Inc., USA). The general transmittance associated to UV-A (315-400 nm) and UV-B (280-315 nm) was calculated with Equations **II-4** and **II-5**:

$$T(UVA,\%) = \frac{\int_{315}^{400} T_\lambda \times d\lambda}{\int_{315}^{400} d\lambda} \quad \textbf{(II-4)}$$

$$T(UVB,\%) = \frac{\int_{280}^{315} T_\lambda \times d\lambda}{\int_{280}^{315} d\lambda} \quad \textbf{(II-5)}$$

Where T(%) is the transmittance as the associated wavelength λ (nm). The reduction of this parameter compared to the reference substrate was calculated using Equation **II-6**:

$$Reduction\ UVX(\%) = 100 \times \frac{T(UVX,\ \%)_{reference} - T(UVX,\ \%)_{coating}}{T(UVX,\ \%)_{reference}} \quad \textbf{(II-6)}$$

Where $T(UVX, \%)_{coating}$ is the general transmittance (either UV-A, or UV-B) calculated using Equations **II-4** or **II-5** for the coated sample and $T(UVX, \%)_{reference}$ the corresponding value for uncoated reference substrate. Three full UV-vis scans were performed at three different locations of the films and the average values of the reduction of UVX (%) are presented with standard deviation.

The anti-fog properties of the PET coated samples were investigated by visual examination. The sample was put on the top of an Erlenmeyer containing 20 ml of boiling water with the coated layer facing the water vapour. Pictures were taken at 1 min intervals and the film was recovered after 5 min to visually assessed the anti-fog properties. The same procedure was performed with PET reference film. The static contact angle experiments on the PET coatings was performed using an OCA40 (DataPhysics Instruments GmbH, Germany) apparatus. The contact angle values were taken after 5 min of contact with a 5 µl drop of DI water and the measurement was repeated at least 5 times at different location on the films.

1.2.7. Specific ink formulation and characterisation for up-scaling test

A specific, lower cost and in bigger volume formulation was prepared using T-CNF suspension (Betulium) and Ag NWs suspension (NanoGap) redispersed together at 1% wt total mass with a mass ratio of 1:1 using an Ultra Turrax high shear disperser (30 s, 10000 RPM).

T-CNF was imaged using a Philips CM 200/FEI (USA) Transmission Electron Microscope (TEM) equipped with a TemCam F216 from TVIPS (Germany), at 200 kV acceleration voltage.

A diluted suspension of T-CNF was drop-cast on a copper grid with an amorphous carbon coating and uranyl acetate (2%) dye was deposited on the drop-cast sample. AFM images were recorded on a Veeco NanoScope-V apparatus (Canada). Ag NWs suspension was drop-cast on a Mica susbtrate and dried overnight. A tapping mode with an OTESPA Bruker (USA) silicon cantilever was used covering a 3.3 µm × 3.3 µm surface area.

The sedimentation evolution of the formulated ink was characterised by putting 10 ml of ink into a cylindrical glass vial of 29 mm diameter section and measuring the sediment height after a fixed time. The sediment height (S, %) was calculated using Equation **II-7**:

$$S = \frac{H}{H_0} \times 100 \quad \textbf{(II-7)}$$

Where H (mm) is the measured sediment height and H_0 (mm) the total liquid height.

The rheological studies were performed on a rotational rheometer (MCR302, Antonn Paar) at a set temperature of 20°C with a cone-plate geometry (1.013° angle, 50 mm diameter and 55 µm truncate) along with a set gap of 0.108 mm. Flow curve experiments were performed with increasing shear rate ranging from 0.1 to 1000 s^{-1}.

Reverse gravure coating was conducted using a Mini-Labo™ apparatus from MIRWEC Film, Inc./ Yasui Seiki company (USA). Coating was applied at a speed of 1 $m.min^{-1}$ and dried using infrared heaters. Two different coating weights were produced using two different gravure rolls: roll 30 (estimated surface volume of 150 $cm^3.m^{-2}$, estimated transfer fraction of 0.33 and estimated approximate wet coat thickness of 30-45 µm), and roll 120 (estimated surface volume of 34.7 $cm^3.m^{-2}$, estimated transfer fraction of 0.28 and estimated approximate wet coat thickness of 5-11 µm).

1.3. Results and discussions

1.3.1. Bar coating deposition on PET and antibacterial properties

The active ink was bar coated at 4 different thicknesses on PET sheets and the dry thickness was determined from a cross section captured by FEG-SEM imaging (**Figure II-2**). For the thicker coatings, the results demonstrated a higher standard deviation because the ultramicrotome cuts damaged the coated layer.

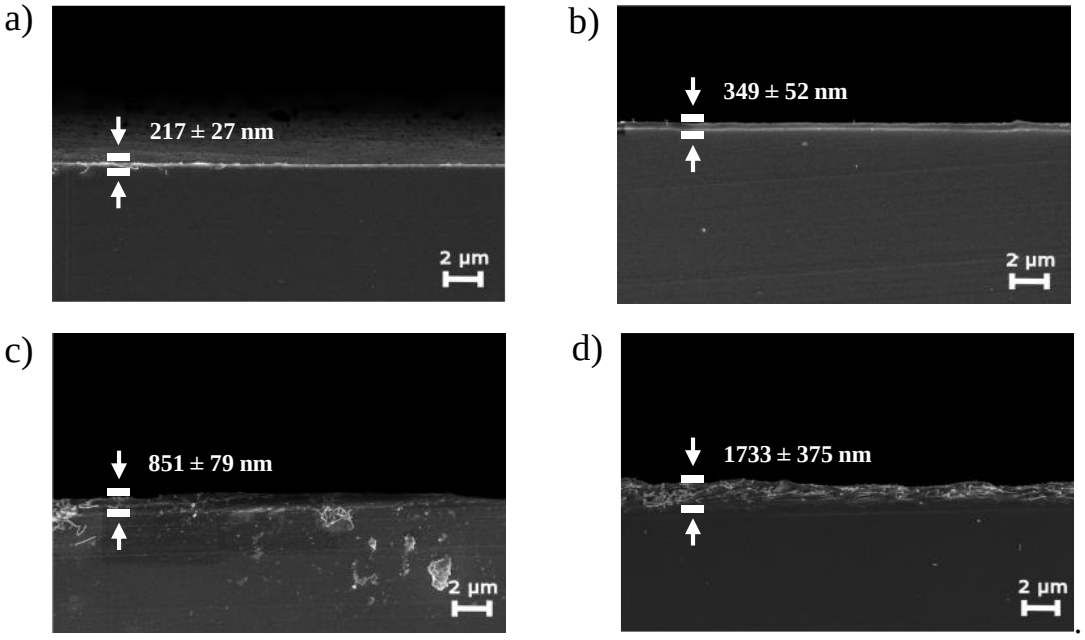

Figure II-2: FEG-SEM cross section images of a) 12 µm wet estimated thickness coating b) 24 µm wet estimated thickness coating c) 40 µm wet estimated thickness coating d) 100 µm wet estimate thickness coating

The measured average thicknesses are respectively 217 ± 27, 349 ± 52, 851 ± 79 and 1733 ± 375 nm. A good linear correlation was found between wet and dry values (**Figure II-3a**) proving a controlled thickness deposition and accurate measurement. Consequently, in this study, the samples will be designated T-CNF/Ag NWs 200, T-CNF/Ag NWs 350, T-CNF/Ag NWs 850, T-CNF/Ag NWs 1750, referring to their dry thickness.

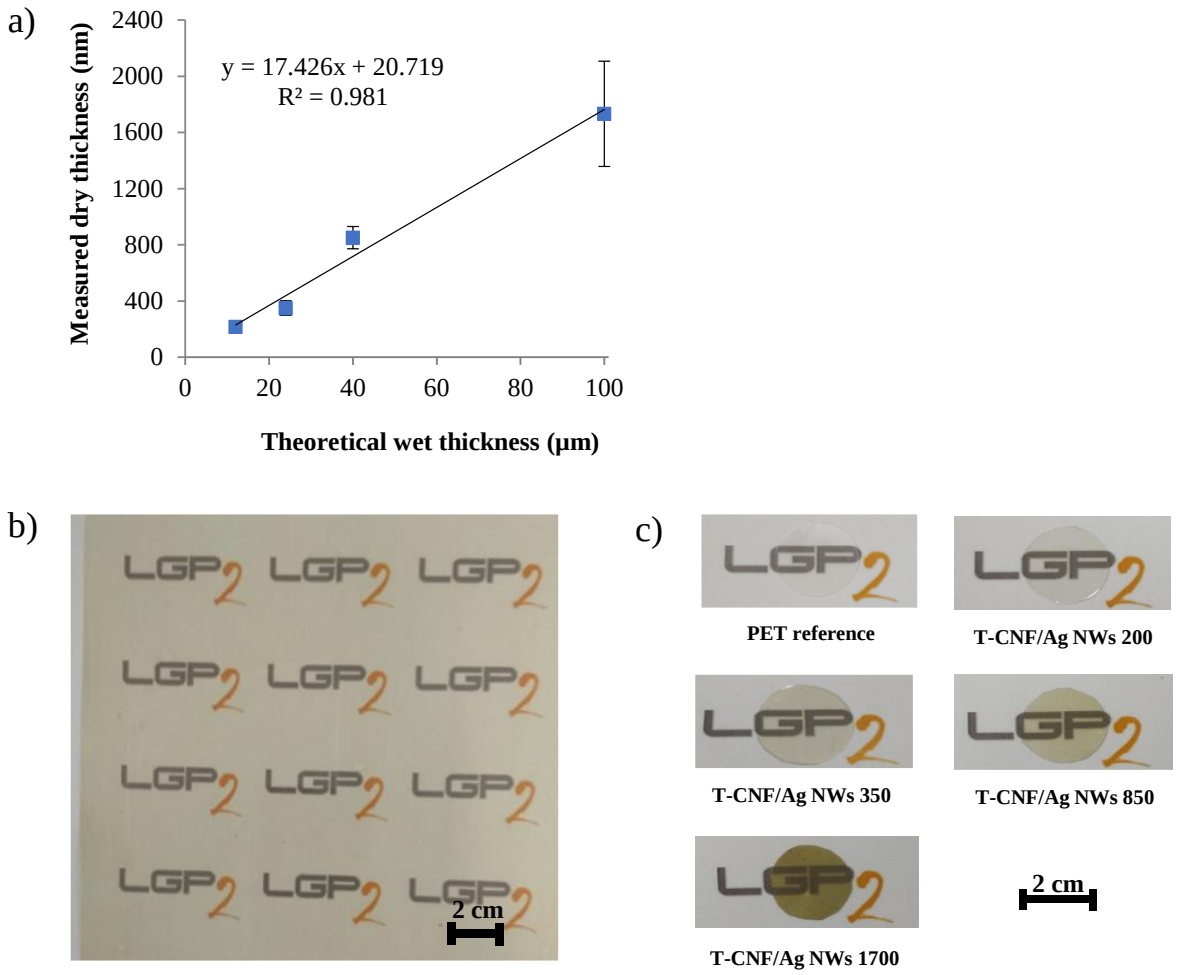

***Figure II-3**: Coating quality investigated by a) measured dried thickness (nm) vs theoretical wet thickness (µm), b) qualitative picture of 15 cm × 15 cm large area of T-CNF/Ag NWs 350 sample and c) qualitative picture of reduced area of all produced samples (2 cm diameter) and scale bar.*

From a macroscopic point of view, the coatings were observed to be uniform with no local uncoated patches (**Figure II-3b**). For packaging applications, one of the key parameters for active coatings is to retain transparency for the purpose of aesthetics and product display. The coatings were found to be relatively transparent as the LGP2 logo is clearly visible under the different samples displayed in **Figure II-3c**. The transmittance at 550 nm was measured at 83.3, 75.6, 67.3 and 34.5% respectively for T-CNF/Ag NWs 200, T-CNF/Ag NWs 350, T-CNF/Ag NWs 850 and T-CNF/Ag NWs 1750 samples, when compared to the 89.8% reference uncoated PET. Coating quality may also be determined by measuring conductivity[33] and except for T-CNF/Ag NWs 200, the produced coatings display high conductivity (low sheet resistance) with a very low standard deviation, providing further confirmation of coating uniformity (**Figure II-4b**).

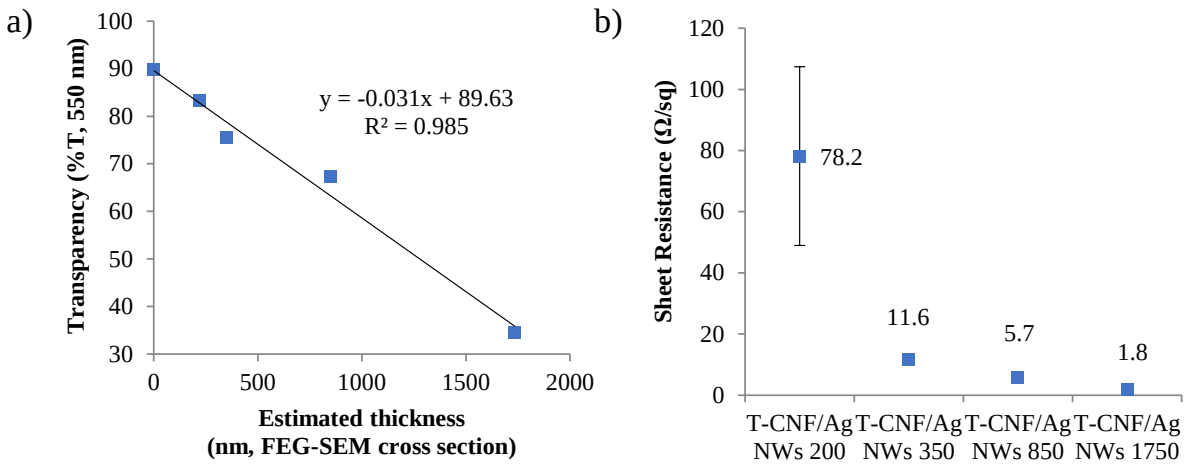

***Figure II-4**: Coatings quality assessment using a) transparency measurement (%T, 550 nm) vs estimated dry thickness (nm) and b) sheet resistance measurements by 4-probe system (Ω /sq)*

The morphology of the coated layer was also investigated using electron microscopy imaging (**Figure II-5**) and the coated layer was found to be highly organised in a dense network, yet not aggregated, with an orientation of the Ag NWs toward the direction of shearing during the bar coating process. A slight porosity was noted at the T-CNF/Ag NWs interface, attributed to some minor degradation of the T-CNF at this sensitive location.

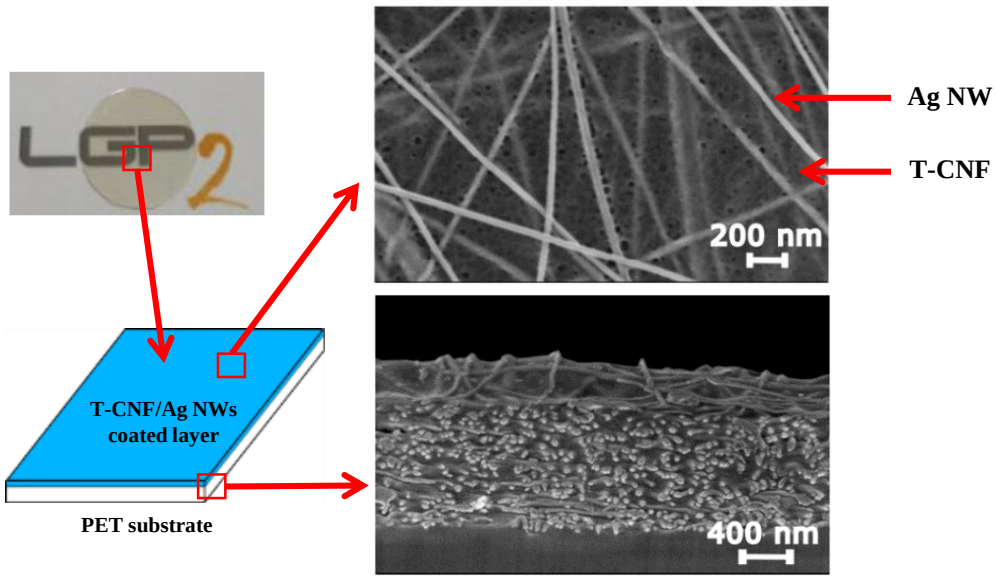

***Figure II-5**: Schematic view of the T-CNF/Ag NWs 850 coated samples and FEG-SEM pictures of surface and cross-section*

A preliminary leaching study was performed prior to antibacterial characterization. The test showed that no peaks corresponding to Ag NWs could be seen after recording UV-vis spectra of the recovered liquid media after the leaching assay (**Figure II-6**). It can then be concluded that there is only limited leaching of Ag NWs when measured by this technique. Moreover, a more precise leaching test was conducted using Inductively Coupled Plasma - Optical Emission

Spectrometry (ICP-OES) technique. The leaching assays were performed on a similar T-CNF/Ag NWs 350 sample (chosen because preliminary studies - not shown - indicating its promising antibacterial activity) using the same experimental conditions (liquid media, volume, temperature and sample weight), respectively after 1, 2, 4, 8 and 24 hours. For all leaching times, the measured total Ag concentration was below the detection limit of 0.5 $mg.l^{-1}$ (or 0.5 ppm), meaning that there was less than 5 µg of Ag release for 4 cm^2 of sample after 24 hours in 10 ml of deionized water. This proves that the prepared system presents a very limited release of active silver materials, both nanoparticles and silver ions.

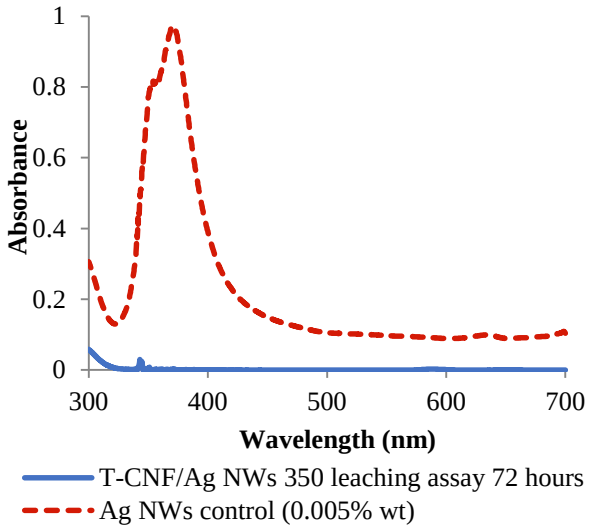

***Figure II-6**: UV-vis spectra (300-700 nm) of liquid media recovered after leaching assay (2 × 2 cm T-CNF/Ag NWs 350 in 10 ml of deionized water under 100 RPM agitation and 37°C for 72 hours) and Ag NWs control suspension (0.005% wt)*

The antibacterial activity of the active coatings was then investigated with a qualitative inhibition zone test (**Figure II-7a**). For the sample coated only with Ag NWs, a broad inhibition zone is visible proving the antibacterial activity of Ag NWs. The antibacterial activity of Ag NWs was established to be mainly due to the release of silver ions because of their lower surface area and thus lower adhesion with bacteria cell walls compared to spherical or cubic silver nanoparticles[9,34]. It can then be assumed that the broad inhibition zone of the sample is due to the release of silver ions into the media. For the sample coated with the mixture of both T-CNF and Ag NWs, no inhibition zone can be seen which suggests that physically entrapping the Ag NWs within the T-CNF matrix leads to a contact killing mode of action with no or minimal release of active material.

To quantitatively verify the activity of the sample the AATCC standard method was performed against both Gram-positive *Staphylococcus Aureus* and Gram-negative *Escherichia Coli* (**Figure II-7b**). The T-CNF/Ag NWs 200 sample show a surprising activity: it displays no impact against *E. Coli* whereas for *S. Aureus*, a strong reduction of 6.3 log of colony forming unit compared to the uncoated reference sample was noted, which corresponds to a 86.5%

activity. Indeed, the bacterial activity in the presence of silver nanoparticles is usually higher for *E. Coli* than *S. Aureus*[35]. This is explained by the difference in the bacteria cell wall: Gram-positive bacteria display a more permeable layer made of peptidoglycan only whereas Gram-negative bacteria have a thinner yet more impermeable lipopolysaccharide layer coupled to a thin peptidoglycan layer[36]. The difference in activity observed when compared with the literature could be explained by the very thin coating layer for T-CNF/Ag NWs 200 which is probably close to the antibacterial activity limit of the coating. The T-CNF/Ag NWs 350 and T-CNF/Ag NWs 850 coatings displayed more or less the same performance respectively 89.3% *vs E.Coli*/100% *vs S. Aureus* and 87.6% *vs E.Coli*/100% *vs S. Aureus*, showing that a 350 nm thick coating is enough to achieve almost 100% antibacterial activity.

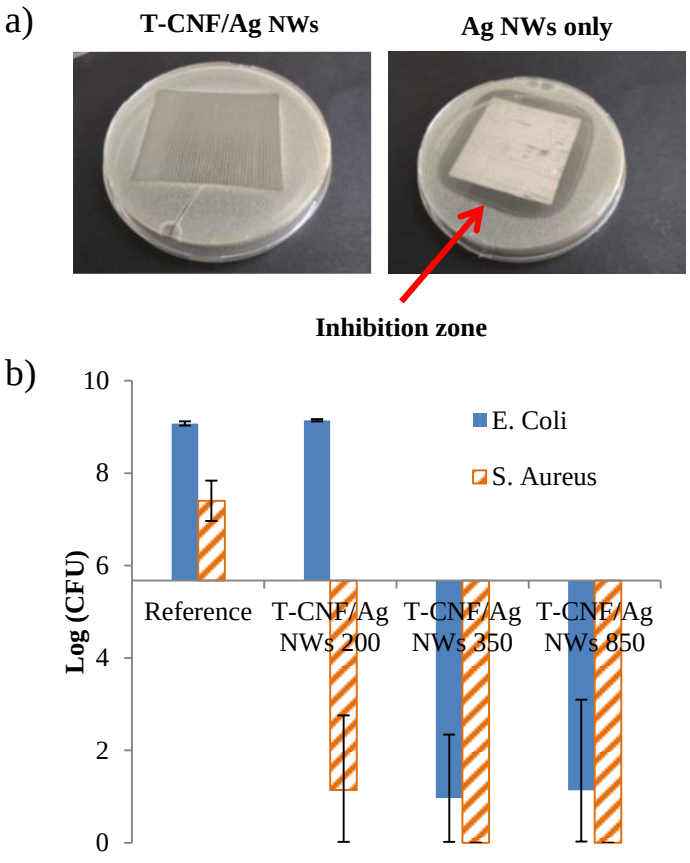

***Figure II-7**: Antibacterial characterization of the coated samples by a) inhibition qualitative analysis for E. Coli bacteria strain b) qualitative analysis using AATCC standard method 100-1998 vs E. Coli and S. Aureus with results expressed in log of colony forming unit*

1.3.2. Bar coating on PLA and barrier properties

In order to explore a bio-based substrate, the same ink was also deposited on polylactic acid (PLA) films using the bar coating process. The coatings were found to be homogeneous, with no uncoated patches and no visual defects (**Figure II-8a**). The different deposited thickness for the PLA coatings were estimated to be relatively close to the ones for the PET coatings. Indeed,

the decrease of the transparency of the reference films due to the coating are approximatively the same for both the PET and PLA coatings (**Figure II-8b**). The samples were then named with the same code, for instance T-CNF/Ag NWs 350 PLA corresponds to the T-CNF/Ag NWs coating on PLA with an approximated thickness of 350 nm.

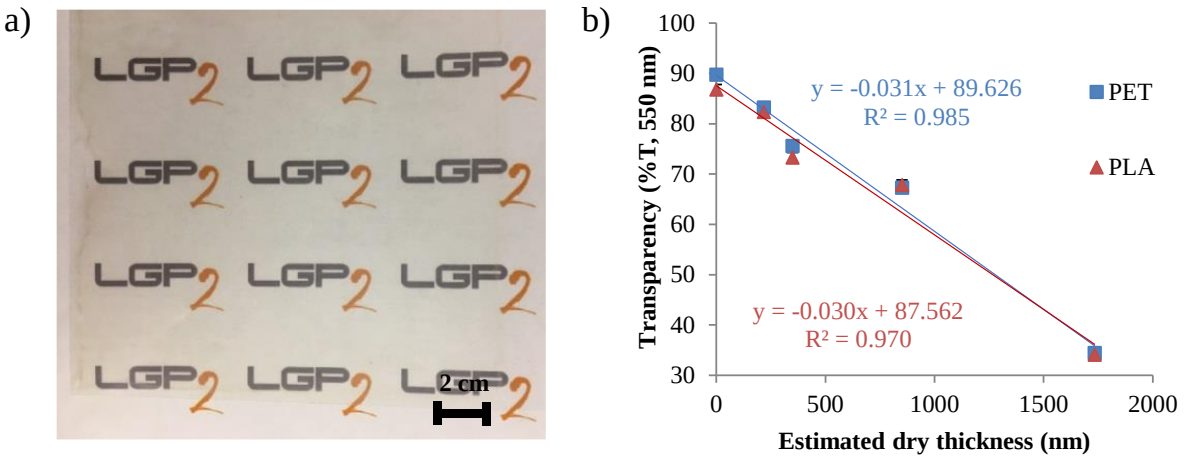

***Figure II-8**: T-CNF/Ag NWs coating on PLA quality assessment with a) picture of 15 cm × 15 cm large area of T-CNF/Ag NWs 350 sample and b) transparency (%T, 550nm) measurements and comparison with coatings on PET*

CNF are often used in packaging application for their interesting barrier properties[37] and so the barrier properties of the coated PLA was investigated. Under dry conditions, the oxygen transmission rate (OTR) of the produced films was significantly decreased achieving more than 90% reduction for an estimated 1750 nm thick coatings but the measured values are however higher than those classically found in the literature for a T-CNF coating[17,38] (**Figure II-9a**). Surprisingly in this study, coating T-CNF material only was not possible due to high dewetting and so it was not possible to compare T-CNF/Ag NWs coatings to T-CNF coating only. A stronger surface treatment may be required to achieve T-CNF only coatings. CNF performance as a barrier layer is generally explained first by the large specific surface area and dense network of hydrogen bonding within the material which makes it difficult for any molecules to pass through[37]. The CNF network also presents high tortuosity due to the impermeable crystalline regions and strong entanglement of the flexible fibres presenting a capability to seal any gaps within the network[39–41]. Adding larger and rigid Ag NWs into the T-CNF matrix probably led to a physical disruption of the sealed network and thus explaining the difference between the measured properties and the ones described in the literature.

As expected from using CNF materials, the OTR measurement is humidity dependent (**Figure II-9b**) and at high humidity (80%) the OTR values of the different coatings are close to the uncoated PLA reference. The different coatings also showed a significant improvement in the WVTR values (**Figure II-9c**) which is relatively similar (around 50% reduction) for all of the samples. This is interesting as coating CNF on polymer substrate usually leads to unchanged or

slightly reduced water vapor permeability[42,43], due to the hydrophilic nature and low water resistance of such materials[44].

Coatings on biopolymer PLA sheets were successfully conducted and the coatings were found to be homogeneous with no uncoated patches and no visual defects. The deposited layers were found to be relatively similar to the coatings on PET and significant decrease for both the oxygen transmission rate and water vapour transmission rate was noted, proving the enhanced barrier properties.

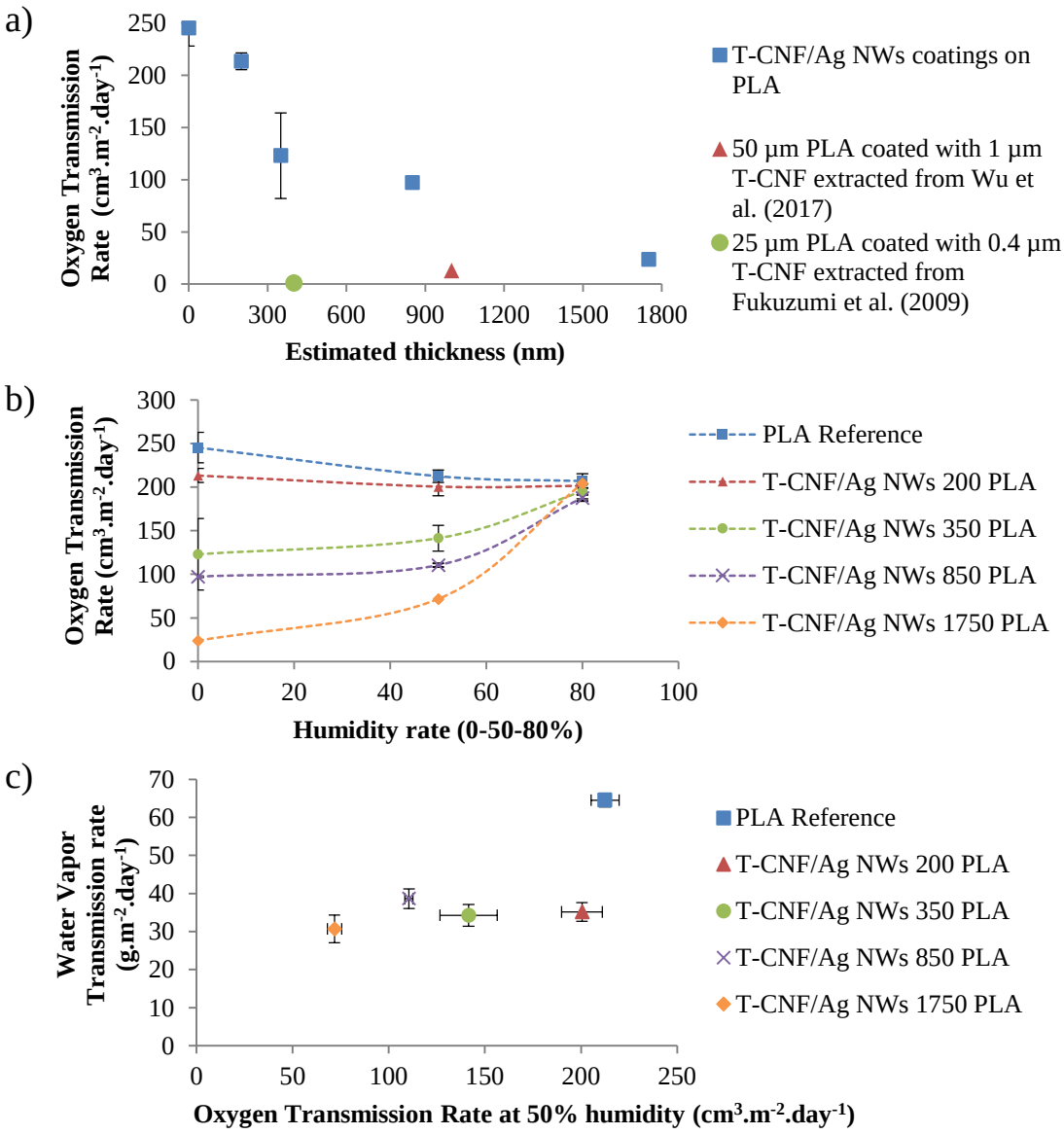

***Figure II-9**: PLA coatings barrier properties characterizations with a) Oxygen Transmission Rate ($cm^3.m^{-2}.day^{-1}$) measurements in dry conditions vs estimated coating thickness (nm) and comparison with literature data, b) Oxygen Transmission Rate ($cm^3.m^{-2}.day^{-1}$) measurements at different humidity rate (0-50-80%) and c) Water Vapour Transmission Rate ($g.m^{-2}.day^{-1}$) vs Oxygen Transmission Rate ($cm^3.m^{-2}.day^{-1}$) at 50% of humidity*

1.3.3. Additional film surface and transmission characteristics

The PET and PLA coatings were also tested for antioxidant, UV-barrier and anti-fog properties to show the multifunctional enhanced surface characteristics. Firstly, the antioxidant properties of the coatings on PET were investigated using the 2, 2-diphenyl-1-picrylhydrazyl (DDPH) assay normalized to the PET reference. In this test, the quenching of free DDPH radical by the antioxidant is followed over time by monitoring the absorbance at 515 nm. After 27 hours of experiments, the activity plateau was reached, and this value was taken as representative of the antioxidant activity of the coated samples (**Figure II-10a**). The antioxidant properties of the films are thickness dependent with a good linear correlation (R^2=0.98) but they have low performances (>90 RSA%) which could be explained by the low loading of Ag NWs and limited access to the entrapped Ag NWs surface (**Figure II-10b**). The antioxidant properties of Ag NPs are usually ascribed to the different oxidation states of silver ions and so their capability to quench free radicals, the best systems' performances due to residual compounds such as flavonoids, terpenes or polyphenol after biosynthesis using plant extracts[45].

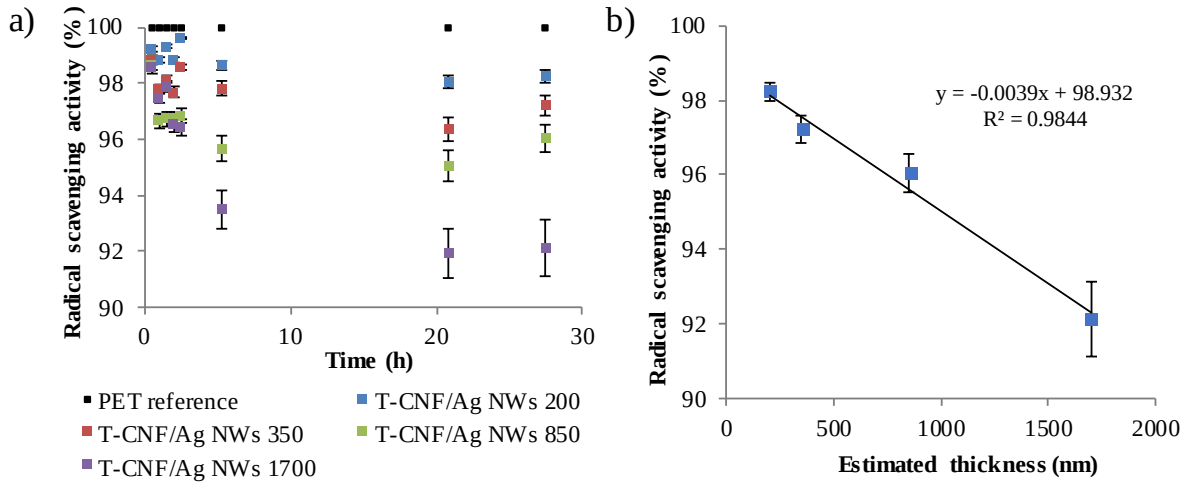

***Figure II-10**: DDPH antioxidant test with a) evolution of the radical scavenging activity (%) of the different coated samples vs the PET reference over time and b) radical scavenging activity (%) vs estimated thickness (nm)*

UV-light can have a detrimental effect on packaged food product as food oxidation is catalysed by light. Several food components are sensitive to light and to high energy UV emissions and especially saturated and unsaturated fats but also nutrient such as vitamins[46]. So, UV shielding properties of packaging can enhance the shelf-life of food products together with their nutritional quality. UV-shielding properties are mainly achieved by using semi-conductor metal oxides (ZnO, TiO_2, CeO_2, etc) materials due to their high scattering effect and band gap properties, but also organic materials such as phenolic compounds, oxanilides or cyanoacrylates or natural materials such as natural extracts[46]. However, silver nanoparticles present an absorption band in the UV region around 350-450 nm because of its localised surface plasmon resonance (LSPR). Due to the symmetry and shape of Ag NWs, the LSPR takes the form of

two interconnected peaks dependent on their aspect ratios[33]. In the case of transparent coatings typically presented in this work, this absorption capability then reduces the amount of UV-light passing through the films, and so presents UV barrier properties. The UV-vis spectra (from 200 to 700 nm) of the different coatings both for PET and PLA were compared to the reference films (**Figure II-11a** and **b**). The reduction in UV-transmittance for the different regions compared to the reference substrates were calculated and can be found in **Figure II-11c** and **d**. Compared to the PLA reference, the PET reference films already present full blocking capability in the UV-B region. Overall, the reduction of the transmitted UV light is thickness dependent with the higher UV reduction being for T-CNF/Ag NWs 1750 and T-CNF/Ag NWs 1750 PLA, respectively 89.56% for UVA, and 83.61%/79.38% for UVA/UVB.

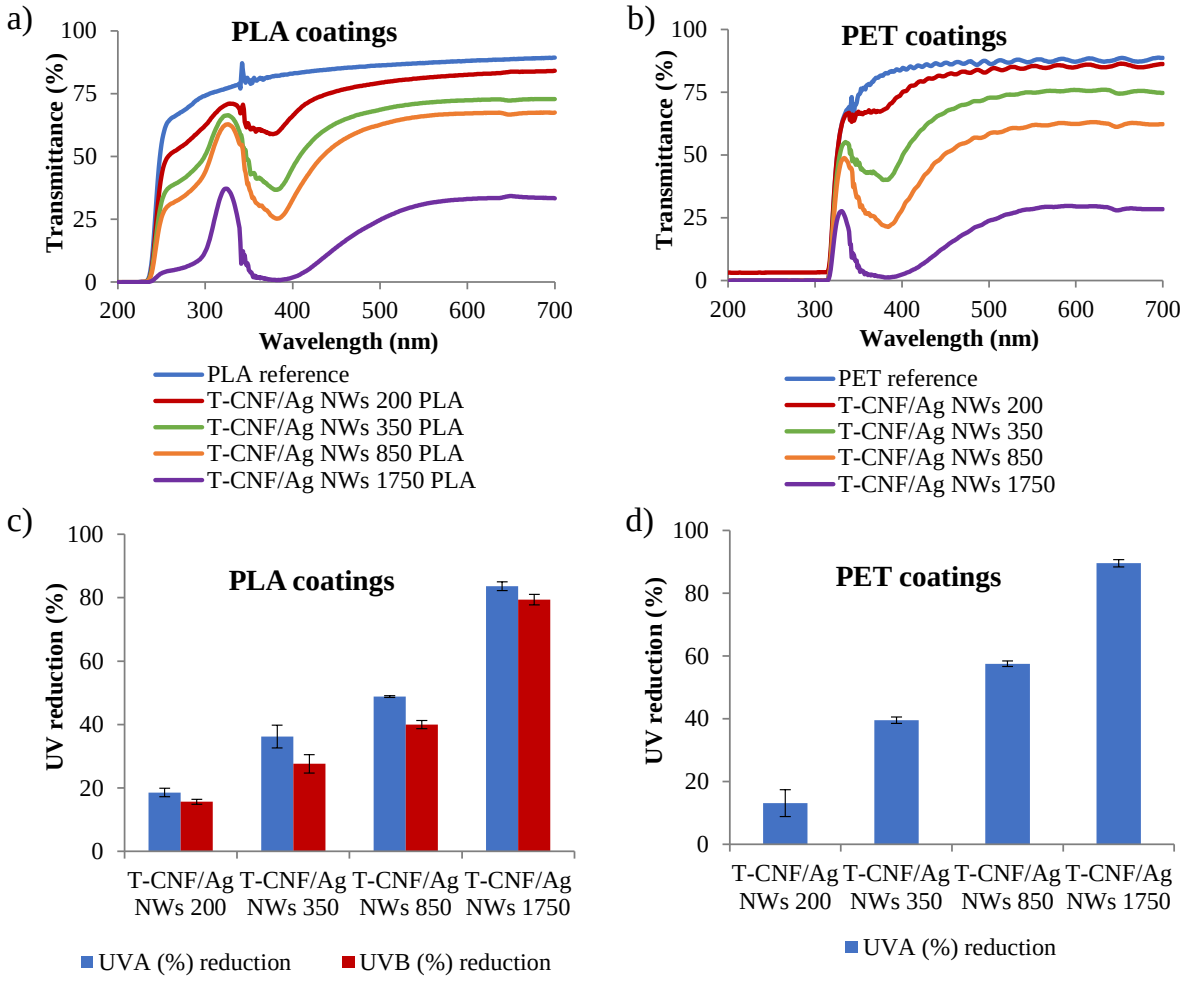

***Figure II-11**: UV-shielding properties of the active coatings with a) Full UV-vis spectra of the different PLA coatings and PLA reference, b) Full UV-vis spectra of the different PET coatings and PET reference, c) extracted UVA and UVB reduction (%) for PLA coatings compared to PLA reference and d) extracted UVA reduction (%) for PET coatings compared to PET reference*

Due to the modification of the packaging internal atmosphere coupled with storage conditions, condensation from the internal water can arise on the film surface and can modify the optical properties of the packaging films. This can induce a lack of visibility of the inside of the

packaging and reduce the attractiveness of the product for the consumer. Anti-fog solutions that reduce this condensation and its consequences are then expected for fresh packaged products. This fog is due to the formation of microdroplets on the surface of the packaging leading to light scattering and coating with a hydrophilic/hygroscopic polymer has been shown to be an efficient solution to the issue as the water vapour will spread evenly over the surface thus retaining the optical properties[47,48]. For instance, coatings with nanocellulose materials can prevent droplets forming on the film when exposed to water vapour[49]. As it can be seen from **Figure II-12** that the film coated with T-CNF/Ag NWs displays less condensation than the un-coated film after a short exposure (5 min) to boiling water, proving its promising anti-fog properties.

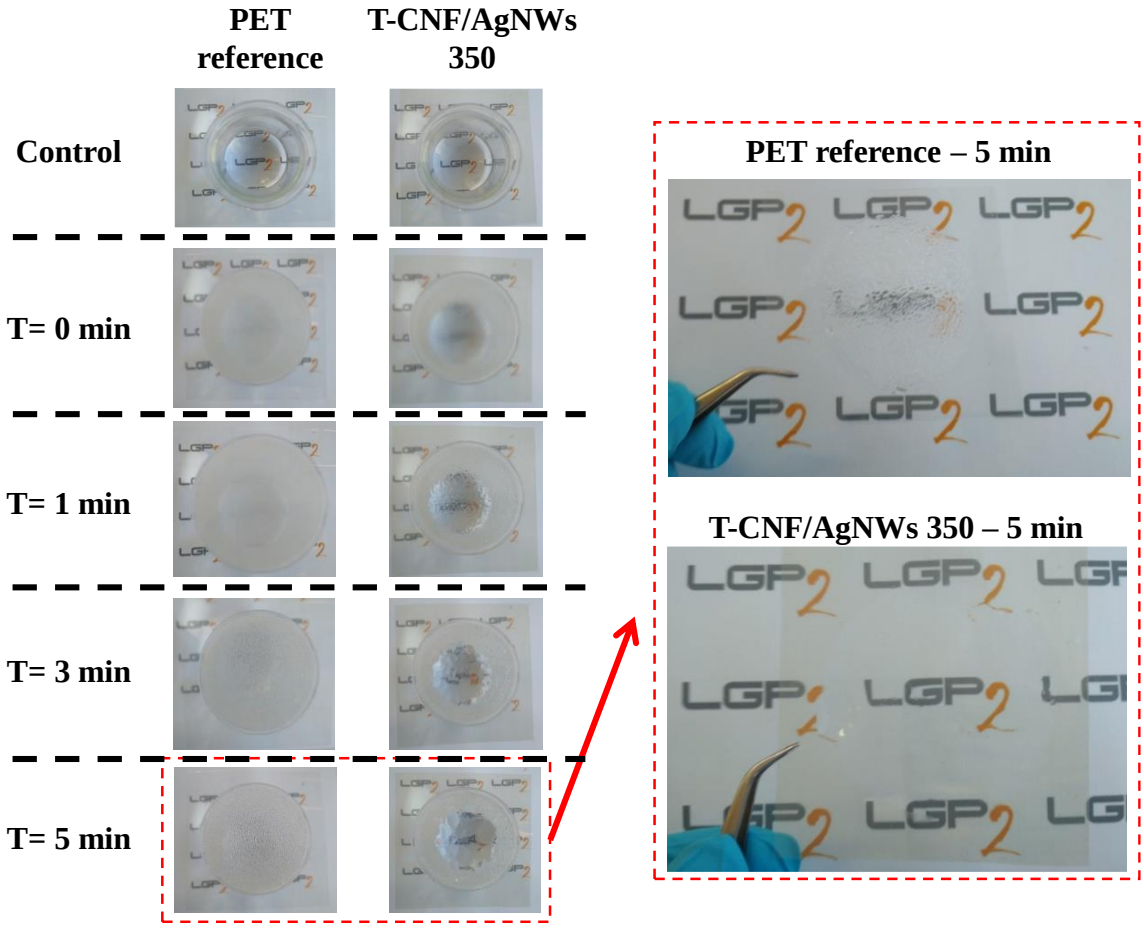

***Figure II-12**: Anti-fog properties of T-CNF/Ag NWs 350 coating compared to PET reference film*

The hydrophilicity of the coatings was investigated by the static water contact angle measurement (**Figure II-13a)**. The T-CNF/Ag NWs 200, 350 and 850 present relatively similar values (around 34-35°) while the T-CNF/Ag NWs 1750 sample present a very low contact angle toward water (14.40°) compared to the PET reference (71.53°). Qualitative pictures of the water drop on the surface of the coatings can be seen on **Figure II-13b**. These results indicate the strong modifications of the surface properties of the films toward water. However, the contact angle measurements cannot be directly linked to the anti-fog properties of the films. Indeed, the

exposure during a short time to a large volume of liquid (5 µl) differs from exposure to water vapour over a longer time period.

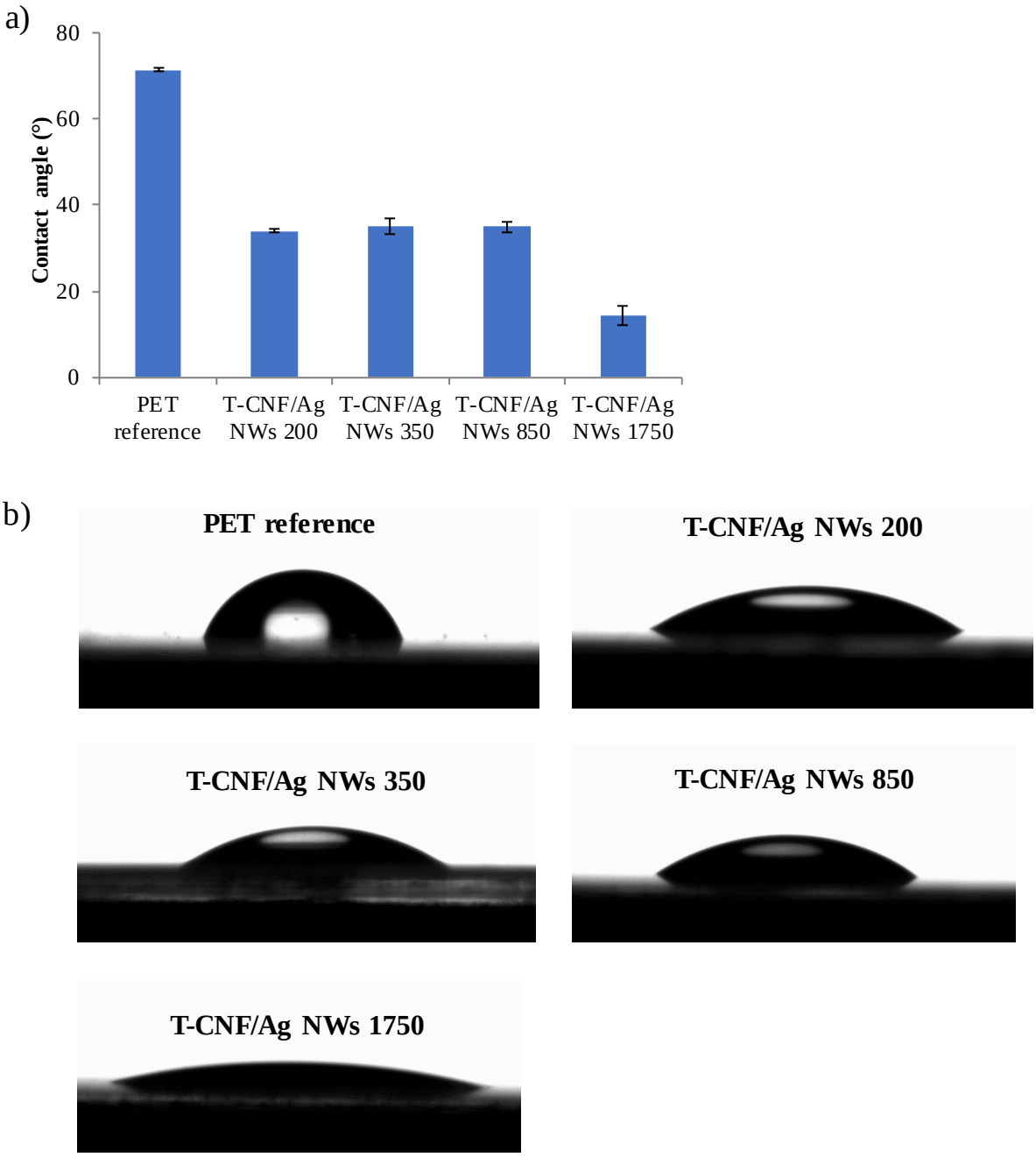

***Figure II-13**: Hydrophilic character of the PET coatings with a) water contact angle (°) and b) qualitative picture of the water drops on the surface of the coatings*

1.3.4. Up-scaling

As a more direct route and from a more economical point of view, a similar antibacterial ink was specifically formulated by simple mixing and redispersion of the separately supplied components T-CNF and Ag NWs in deionised water (see *Materials and methods* section). The purchased T-CNF possess small dimensions (approximatively length 50-400 nm, diameter: 5-

15 nm) and are rather rigid, as shown in the TEM images in **Figure II-14**. The silver nanowires dimensions were approximately one order of magnitude higher than the T-CNF: estimated length 10-50 µm, diameter 50-100 nm (**Figure II-14b** and **c**).

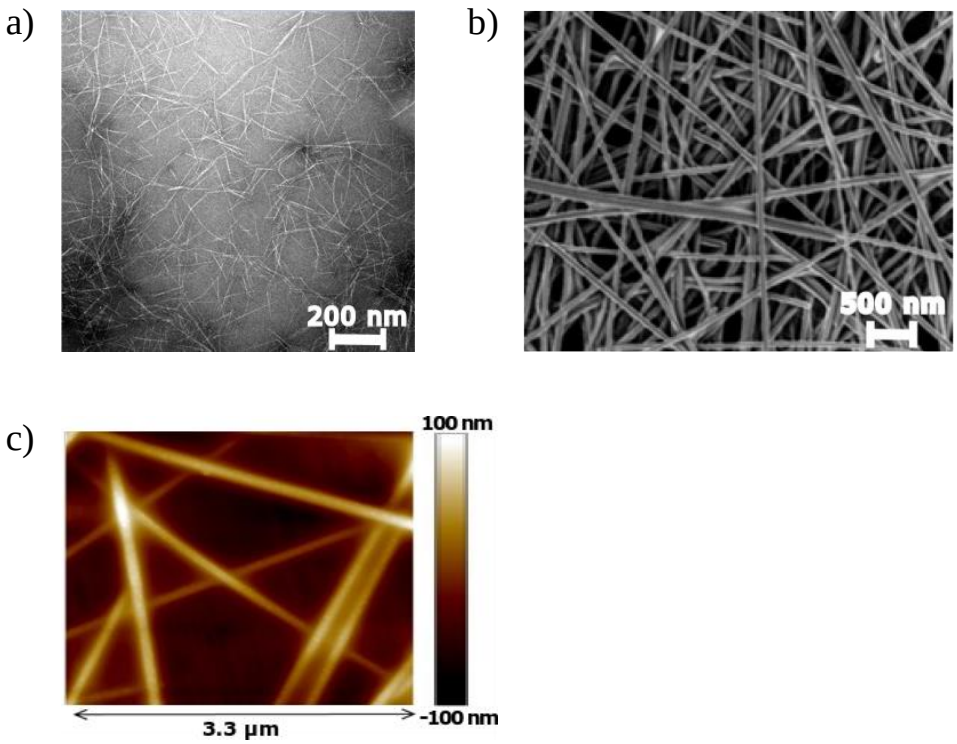

Figure II-14*: Raw materials microscopy imaging for a) TEM images of T-CNF b) SEM images of silver nanowires and c) AFM images of silver nanowires*

As it has already been described elsewhere[50], the T-CNF/Ag NWs ink is relatively stable over time and exhibits a very low sedimentation rate, for example 75% sedimentation height after 8 months of testing, as compared to the Ag NWs suspension without T-CNF, that sedimented completely after 4 days (**Figure II-15a**). Flow curve rheology experiments were performed to assess the possibility to use coating process for ink deposition and both materials and the final formulation display classic strong shear thinning behaviour[15,51] (**Figure II-15b**). These behaviours can be explained by the high aspect ratio of the nanoparticles in these colloidal suspensions and the induced alignment of the particles at high shear rate, thus decreasing the viscosity. Ink viscosity at high shear rate was found to be in line with the expectations for the bar coating process. It was found that for the different tested shear rate, the viscosity of T-CNF suspension was one order of magnitude higher than Ag NWs. T-CNF dictates the viscosity in the T-CNF/Ag NWs ink by acting as a rheological modifier which has already been shown in the literature for other aqueous CNF suspension coatings[52].

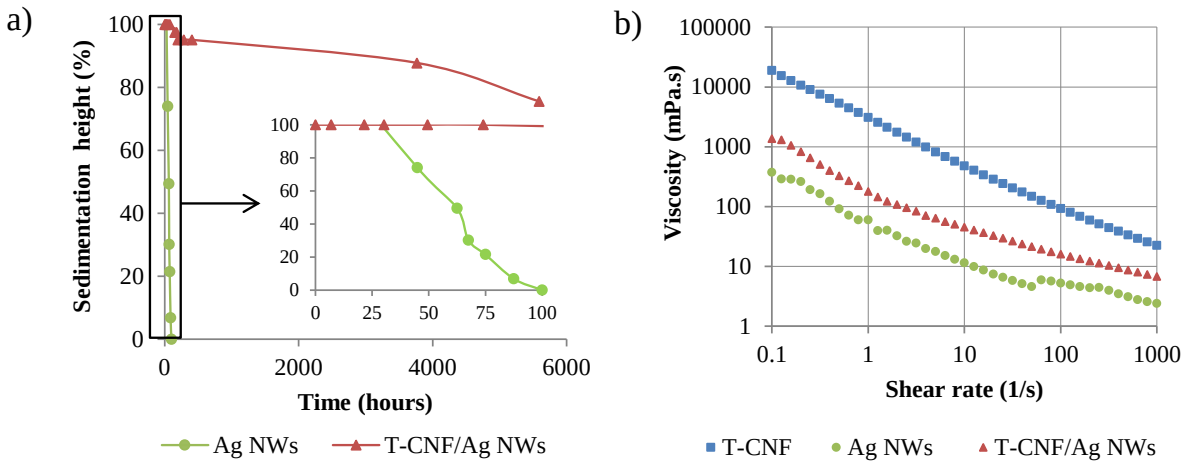

***Figure II-15**: Ink formulation characterisation compared to raw materials with a) sedimentation height measurement (%) and b) rheological flow curves. All formulations are at 1% wt total mass concentration*

1.3.5. Roll-to-roll process deposition

The potential for this formulation to be applied to an industrial-like roll-to-roll coating process was also investigated using a reverse gravure coating process. Reverse gravure coating is interesting for packaging applications because of the wide range of inks and substrate that can be used and was also chosen because of the versatility of the process and the possibility to deposit low coat weights with a uniform and controlled thickness[53,54]. Two different coating thicknesses were investigated and designated after their estimated wet thickness and previously established wet thickness/dry thickness relationship for the bar-coated samples. In other words, T-CNF/Ag NWs 850RR for the coating using the roll 30 (wet coat thickness of 30-45 µm), and T-CNF/Ag NWs 200RR for the coating using roll 120 (wet coat thickness of 5-11 µm). The coatings were found to be visually of high quality at the macroscale with no uncoated patches, no visual defects and good uniformity (**Figure II-16a**). The antibacterial properties of the T-CNF/Ag NWs 200RR are relatively low whereas T-CNF/Ag NWs 850RR displays a strong antimicrobial effect (**Figure II-16b**). The T-CNF/Ag NWs 850RR sample showed a strong and significant bactericidal effect, precisely 7.22 log reduction corresponding to 77.9% calculated antibacterial activity against *E. Coli* and 100% against *S. Aureus*. On the other hand, the T-CNF/Ag NWs 200RR sample showed no activity at all against *S. Aureus* whereas it showed a 7.57 log reduction corresponding to 81.7% activity against *E. Coli*. The measured antibacterial activity for the roll-to-roll coated samples using the up-scaled ink formulation were found to be in line with the results for the bar coated samples and thus the proposed solution for antibacterial packaging could hence be easily adapted to an industrial scale.

a)

b)

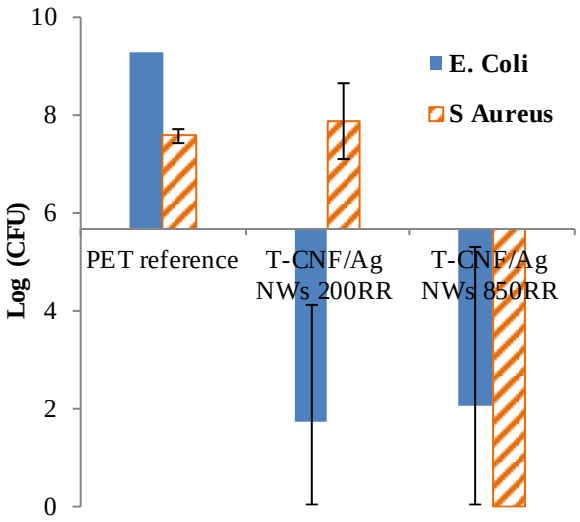

***Figure II-16**: Roll-to-roll coatings with a) visual aspect of the coatings and b) AATCC qualitative method for antibacterial activity assessment*

1.4. Conclusion

This work demonstrated the antibacterial activity of a hybrid system composed of TEMPO-oxidised cellulose nanofibrils and silver nanowires, coated as thin layers on different flexible polymeric substrate. The controlled thickness of the coatings on PET ranged from 200 to 1750 nm with a high relative transparency superior to 65%. The antibacterial activity was suggested to work by an active contact killing mode of action and for the 350 nm thick coating, a significant AATCC standard antibacterial activity of 89.3% and 100% was noted respectively against Gram-negative *Escherichia Coli* and Gram-positive *Staphylococcus Aureus* bacteria. Leaching assay using both UV-vis and ICP-OES techniques showed a very limited release (<0.5 ppm) of active silver compounds. Moreover, the same ink was also deposited on PLA sheets with similar estimated thickness and quality. After coating, oxygen and water vapour permeability of the PLA substrate was significantly reduced, respectively 49% of oxygen transmission rate (dry conditions) and 47% reduction of water vapour transmission rate for 350 nm thick coating. Other active properties were also proven for the developed coatings, such as UV-shielding property achieving a reduction in the UV transmittance as high as 39.5% for UVA, and 36.2%/27.6% for UVA/UVB respectively for 350 thick coating on PET and PLA, when compared to uncoated reference substrate. Anti-fog properties were also qualitatively demonstrated. However, only a very small antioxidant effect (DDPH assay) was measured for this 350 nm thick coating (97.2% radical scavenging activity). Finally, a similar ink with lower cost materials was specifically formulated for up-scaling purposes and producing active surfaces using a roll-to-roll process was proved using the reverse gravure process, showing a strong retained antibacterial activity.

Perspectives for a future work would be investigation of the migration of silver ions within the cellulose nanofibrils matrix and the influence of matrix surface chemistry. The possibility to have a localised deposition of the developed antibacterial layer by a printing process could also be of interest to limit the cost of the solution, but also for some specific applications as detailed in the coming section (**II-2**).

2. Rheology of cellulose nanofibrils and silver nanowires inks for the development of screen-printed antibacterial patterns

This section is adapted and expands on Hugo Spieser, Alexandre Jardin, Davide Deganello, David Gethin, Julien Bras, Aurore Denneulin. Rheology of cellulose nanofibrils and silver nanowires for the development of screen-printed antibacterial surfaces, submitted in Journal of Materials Science (2020).

Abstract:

TEMPO (2,2,6,6-tetramethylpiperidine-N-oxyl)-oxidised cellulose nanofibrils (T-CNF) and silver nanowires (Ag NWs) were formulated as active inks. Their rheological properties were investigated to design suitable conditions for processing by the screen-printing process, with the aim of preparing antibacterial patterns. Different sources of raw materials were first tested and selected based on their standard shear rheology. Rheological experiments mimicking the screen-printing process were then applied to different ink formulations to investigate their thixotropic and viscosity properties. The experiments conducted at 1% wt total mass content and different ratios of T-CNF/Ag NWs showed that the recovery (%), the recovery time and the viscosity are formulation dependent. A ratio higher than 1:1 (T-CNF:Ag NWs) was suggested to be necessary for screen-printing applications, because of a higher recovery time (> 10 s) and sufficient recovery (> 80%). Higher mass content T-CNF formulation (from 1 to 2% wt) were also tested and based on the findings, an suitable ratio 2:1 (T-CNF:Ag NWs) and total mass content of 2.5% wt was then selected to prepare an ink suitable for screen printing. Printing defects were corrected by addition of water-soluble polymer hydroxypropyl methylcellulose (HPMC). The printed pattern with the optimised ink formulation displays a 67.4% antibacterial activity against *E. Coli* in a standard contact active test, with a high transparency (>70%). The antibacterial activity was slightly impacted by the HPMC additive, proving the promising features of the developed solution for active packaging applications.

Keywords:

cellulose nanofibrils, silver nanowires, rheology, screen-printing, antibacterial activity

2.1. Introduction

The packaging industry is facing new challenges in today's world and new innovations in packaging solutions have emerged like active and intelligent packaging. Active packaging is usually defined as a technology able to respond to a stimulus either from the internal and external atmosphere of the packaging, by either releasing or adsorbing active substances. Several categories of active packaging can be distinguished such as gas scavengers, antioxidants or antibacterial packaging[2]. Antibacterial packaging is a common way to fight against bacterial contamination and so an interesting technique to enhance the shelf-life of packaged product especially for food applications.

Different active agents have been used for antibacterial packaging applications such as essential oils, organic acids, natural extract or nanoparticles. Silver nanoparticles (Ag NPs) demonstrate a strong antibacterial activity: its mode of action and the influence of different parameters on its activity have been thoroughly reviewed in the scientific literature[55]. Examples of Ag NPs activity against bacterial contamination in real food products have also been reported, for instance cooked cereal or fruit[56,57]. The use of Ag NPs or silver microparticles have been studied deeply in the field of printed electronics due to their high electronic and thermal conductivity properties. Notably, the properties of silver nanoparticles with a high aspect ratio and rod-like aspect called silver nanowires have been studied because of their capability to form percolated networks[33]. Silver nanowires have also been studied for antibacterial applications adaptable to packaging applications and especially with polymeric substrate or composite such as polyethylene naphthalate (PEN)[58], polyvinyl alcohol (PVA)[59] or polypropylene/polytetrafluoroethylene systems (PP/ePTFE)[60], but also bio-based solution such as konjac glucomannan[61], chitosan[62] or PLA materials[63].

More recently, silver nanoparticles have been used in composites with cellulose and nanocellulose materials[19]. Composites with cellulose nanofibrils (CNF) present several advantages such as to entrap the silver nanoparticles within the CNF network, to stabilise the Ag NPs and to control its dispersion as the produced systems are prepared by in-situ Ag NPs synthesis[20,64].

Because of the inherent activity of antibacterial packaging, active materials are mainly directly inserted inside or at the surface of the packaging film. For instance, using a coating or printing process to functionalise the surface of polymeric materials is an interesting way to produce antibacterial packaging by taking advantages of the versatility and flexibility of the deposition processes. Printing processes enable the deposition of a specific localised pattern when compared to surface deposition such as coatings. This localised deposition implies economy of materials and so the development of cost-effective solutions. Printing processes also enable the production of tailored solutions to a specific problem, and have been used in the field of active

and intelligent packaging for the development of smart detectors, such as gas and humidity indicators/sensors and microbial sensors/indicators[65–68].

Only few references have reported the use of hybrid ink made of CNF and active materials for deposition by printing techniques. For instance, Koga et al. (2013) reported inkjet printing of TEMPO-oxidised CNF and carbon nanotubes for printed electronics applications[69]. Choi et al. (2016) also inkjet-printed CNF as a pre-layer on paper to improve the deposition of supercapacitors made of carbon nanotubes and a solid-state electrolyte. Another cellulosic substrate was used by Nechyporchuk et al. (2017), who printed regular pigment and silver nanoparticle conductive inks on cotton fabric[70]. Screen-printing was also used by El Baradai et al. (2015) to print a mixture of microfibrillated cellulose, graphite and carboxymethyl cellulose for the production of an electrode in lithium ion batteries[71]. Hoeng et al. (2017) reported the use of TEMPO-oxidised cellulose nanofibrils (T-CNF) and silver nanowires (Ag NWs) for printed electronics application[51]. The authors prepared inks fit for screen-printing requirement using the thickening characteristic and the shear-thinning properties of the T-CNF. The ink optimisation was based solely on the ink viscosity and the authors showed the need to add a water-soluble polymer named hydroxypropyl methylcellulose to modify the thixotropic and viscoelastic properties of the ink. No in-depths characterisation of the impact of the T-CNF/Ag NWs ratios and ink composition on the thixotropic behaviour of the inks were performed, and the study was mainly a proof of concept focused on electrical properties. Cellulose nanofibrils in ink formulation are interesting due to their good properties as a dispersing agent, rheology modifier or film forming capability. Other examples using printing processes with cellulose nanofibrils mainly include 3D printing[72] or the use of nanocellulose materials as a substrate[73].

Printing processes include a wide range of techniques, the most common used for packaging applications being flexography, offset, gravure, screen and inkjet. Each process requires a specific ink behaviour, that needs to be tailored to fit the process requirement. Screen-printing consists of a squeegee pushing ink through a patterned screen mesh with open areas. It is one of the more versatile printing techniques and was selected in this study because it is easy to use, low cost (low quantity of ink necessary) and accepts a wide range of ink viscosity (around 10 to 200 Pa.s at 1 s^{-1} shear rate). The ink requires shear-thinning behaviour and adequate viscoelastic properties. CNF materials then present interesting rheological properties for such a process as they present strong shear thinning behaviour attributed to alignment of particles under shear and to the destruction of local entanglements (particle aggregates)[74]. This entangled network also promotes the thixotropic behaviour of CNF materials and appropriate viscoelastic properties[75]. TEMPO-oxidised CNF has met a strong interest since its development because of major energy savings during the mechanical fibrillated process and the low dimensions and highly charged fibrils that are produced[76]. The rheological properties of such materials are also strongly dependent on factors such as pH, electrolytes, surfactants, co-solvents, temperature or concentration[77–81].

In this work, the rheology properties of different sources of TEMPO-oxidised cellulose nanofibrils and silver nanowires were first investigated. After selection of the appropriate source, different inks were prepared at 1% wt total mass content and different ratios of T-CNF/Ag NWs. The thixotropic and viscosity properties of the inks were then measured using a shear-induced rheological model, which mimics the screen-printing process. Higher mass content inks, as well as the influence of the hydroxypropyl methylcellulose (HPMC) additive, were also investigated. This optimisation step led to the preparation of an ink fit for screen-printing. The topography of the prints was assessed and the influence of HPMC additives was correlated with the print quality and the antibacterial activity of the produced pattern.

Several examples in the literature have reported the production of composite made of nanocellulose and silver nanoparticles, but to our knowledge, this work is the first example of printing a combination of cellulose nanofibrils and silver nanowires for the development of antibacterial surfaces. Only Martins et al. (2012) used a coating process to deposit a starch-based mixture of cellulose nanofibrils and silver nanoparticles on paper substrate to develop an antibacterial substrate[23]. An investigation of the rheological properties of inks made of cellulose nanofibrils and silver nanoparticles has been reported by Hoeng et al. (2017) who did not fully investigate the impact of the component's ratios and mass content on the thixotropic properties of the suspensions[51].

2.2. Materials and Methods

2.2.1. Materials

The active inks were prepared using TEMPO-oxidised cellulose nanofibrils (T-CNF) and silver nanowires (Ag NWs) from different sources. The aqueous suspension of T-CNF were provided by University of Maine (USA, TOCN, 1.8% wt, 1.11 ± 0.1 mmol.g^{-1} measured charge density) and by Betulium (Finland, CNF-A13, 5% wt, 1.63 ± 0.1 mmol.g^{-1} measured charge density). Two aqueous suspension of silver nanowires (Ag NWs) were purchased from NanoGap (USA) referenced under the tradename NGAP NF Ag-3170 (2.6% wt) and NGAP NF Ag-3140 (3.2% wt). The polyethylene terephthalate (PET) substrate used for the printing test was provided by Dupont (France) (Melinex® ST726 – 175 µm). Deionised water (DI water) was used for all experiments. Hydroxypropyl methylcellulose (HPMC) was purchased from ThermoFisher Scientific (US) with the following specifications: 27.0-30.0% wt methoxy content and 7.0-12.0% wt hydroxypropoxy content. Hydrochloric acid (>99%) and sodium hydroxide (>99%) were acquired from Sigma Aldrich (US).

The following chemicals were used for the antibacterial tests: Escherichia Coli ATCC 8739 (Microbiologics, USA), L α-phosphatidyl choline (Sigma Aldrich, France, >99%), L-histidine (Roth, Germany, >98.5%), Tween®80 (Roth, Germany), potassium dihydrogen phosphate (Roth, Germany, >99%), sodium thiosulphate (Roth, Germany, >99%). The nutrient broth (NB, Roth, Germany) presents the following composition: 15 g.l^{-1} peptone, 6 g.l^{-1} sodium chloride, 3 g.l^{-1} beef extract, 1 g.l^{-1} glucose. The plate counting agar (PCA, BD Difco, USA) presents the following composition: 15 g.l^{-1} agar, 5 g.l^{-1} peptone and 3 g.l^{-1} beef extract. The materials were used as received. Isotonic solution (IS) was prepared by dissolving calcium chloride in DI water at 8.5 g.l^{-1}. A neutralising solution was prepared by dissolving the following chemicals in 1 l of DI water: 3 g of L α-phosphatidyl choline, 1 g of L-histidine, 30 g of Tween®80, 10 g of potassium dihydrogen phosphate, 4.10^{-4} g of sodium thiosulphate and the pH was controlled between 7 and 7.2.

2.2.2. Raw material characterisation

The two sources of T-CNF were imaged by Transmission Electronic Microscope (TEM) on a CM 200 equipment from FEI/Phillips (Japan) with a TemCam F216 camera from TVIPS (Germany). Prior to imaging, the T-CNF was diluted, drop-casted on a copper grid and dyed with uranyl acetate. The acceleration voltage was set at 200 kV. The diameter and thickness of the T-CNF was measured using the FIJI software[25,26] and 10 nanofibrils were measured on each image and the measurements were conducted on 10 different images. The average and associated standard deviation are presented.

Charge density (mmol.g^{-1}) of the T-CNF was measured following a standard procedure. A suspension at approximately 250 mg.ml^{-1} was prepared and the pH was set to pH<3.5 with hydrochloric acid (0.1 mol.l^{-1}). After 15 min of magnetic stirring, the mixture was titrated with sodium hydroxide (0.01 mol.l^{-1}) by recording conductivity. Equivalent volumes were calculated by intersection of the linearly correlated curves: the first volume corresponds to the titration of the hydrochloric acid whereas the second corresponds to the titration of the T-CNF carboxylic acid function. Charge density (X) was calculated using Equation **II-8**:

$$X\ (mmol.g^{-1}) = \frac{C_{NaoH} \times V_{2eq}}{m} \quad \textbf{(II-8)}$$

Where X (mmol.g^{-1}) is the charge density, C_{NaOH} (mmol.l^{-1}) is the sodium hydroxide concentration, V_{2eq} (l) is the second equivalent volume corresponding to the carboxylic acid function titration volume and m (g) the dry mass of T-CNF titrated. Three titrations were conducted for each sample and the average is presented with the standard deviation.

The turbidity of the T-CNF suspensions at 0.1% wt was assessed using a portable turbidimeter that measures the scattered light at 90° angle compared to the incident light. The experiments were performed at least 6 times and average is presented with standard deviation.

2.2.3. Suspensions preparation

All suspensions prepared throughout this work were redispersed in water at the desired mass content and ratio between T-CNF and Ag NWs using an Ultra Turrax high shear disperser for 30 s at 10 000 rotation per minute (RPM), that is based on laboratory good practice experience (proper dispersion but no physical damage). Throughout this work, the suspensions concentration (%) is mass concentration (% wt) and the solvent was deionised water. Several suspensions with T-CNF mass content ranging from 0 to 2% wt and Ag NWs mass content ranging from 0 to 1% wt were prepared and **Figure II-17** shows the compositions of the different formulated ink.

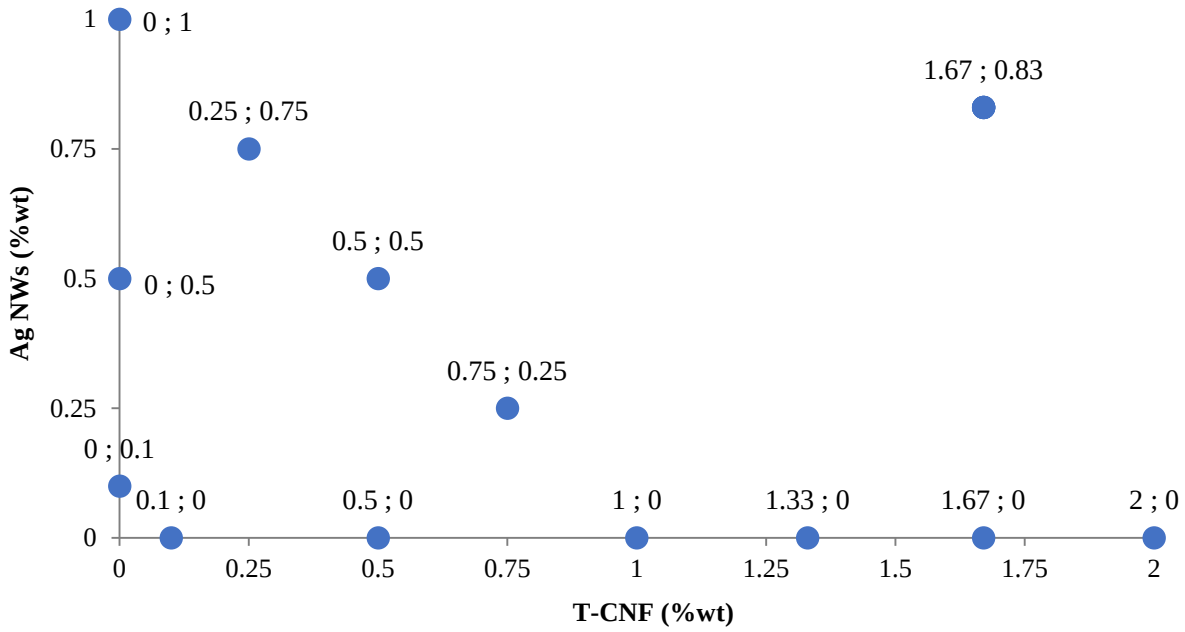

***Figure II-17**: The different inks formulated and their T-CNF/Ag NWs composition (% wt)*

The suspensions based on T-CNF/Ag NWs (1.66% wt/0.83% wt) and HPMC additives (0, 3, 5 and 8% wt) were prepared with the following protocol: the desired mass of T-CNF and Ag NWs were weighed with the desired amount of water, and the desired mass of HPMC was added slowly at 60°C under several steps of high shear dispersion (30 s, 10000 RPM) until the HPMC was uniformly dissolved (2-3 min).

2.2.4. Rheology and suspension properties

All rheological tests were conducted on a MCR302 rotational rheometer from Anton Paar (Germany). All the tests were performed at 20°C with a set gap of 0.108 mm and using a cone on plate geometry with the following characteristics: diameter of 50 mm, truncate of 55 µm and angle of 1.013°. To perform the flow curve experiments, the shear rate was increased from 0.1 to 1000 s^{-1} with a logarithmic ramp of 40 different steps and a 60 s duration for each. Different concentrations of the different sources of material were tested and especially, 0.1, 0.5 and 1 % wt. To test reproducibility, the 0.1 and 0.5% wt concentration for T-CNF from Betulium, and the 0.1% wt concentration for Ag NWs 31-70 were each tested twice and the tests were found to be reproducible. The other flow curves were therefore performed only once for reason of material saving.

Rheological events occurring during the screen-printing process were simulated using a protocol adapted from Neidert et al (2008)[82] (**Figure II-21** and **Figure II-25**). The first step simulates the ink at rest on the screen by applying a 2 s^{-1} shear rate for 150 s (Step 1). The second step simulates the squeegee passing over the screen and transferring the ink to the substrate by applying a 1000 s^{-1} shear rate during 15 s (Step 2). The last step simulates the ink

at rest on the substrate after printing by applying a 2 s^{-1} shear rate for 150 s (Step 3). The following parameters were extracted from the experimental data: viscosity (mPa.s), the recovery (%) and recovery time (s) and their calculation is detailed in the results and discussion section. The three-step rheological experiment was performed three times for the formulation at 1% wt total mass and found to be reproducible. The other formulations were tested once and the extracted parameters were in line with expected results.

The shear rate of Step 2 was also later changed to 200 and 500 s^{-1} to investigate the impact of the shear rate of the high shear rate step of the model on the extracted parameters.

Finally, the viscoelastic properties were investigated by preliminary experiments, performed once following laboratory practice that has been found to be robust. Firstly, a strain sweep measurement from 1 to 200% at a fixed frequency of 10 Hz was performed. At the same frequency, a three-step model was also performed with a first step at 2% strain for 150 s, followed by a second step at 200% for 15 s and a third step at 2% for 150 s.

The surface tension of the prepared inks was also evaluated using the Du Noüy ring method on a Sigma 700 tensiometer from Attension (UK) with at least 20 measurements on each suspension.

2.2.5. Screen-printing

The screen-printing experiments were conducted on a Dek Horizon 03i printer (ASM Pacific Technology, Singapore) with the following optimised parameters: 1 mm print gap, 120 $mm.s^{-1}$ forward speed, 80 $mm.s^{-1}$ reverse speed, and 7 kg pressure. The polyester screen mesh used presents the following specifications: 120 $thread.cm^{-1}$ mesh count, 34 µm thread diameter, 12 µm emulsion thickness and 45° screen angle. The resulting prints were dried at 120°C for 1 min in an oven and each formulation was printed at least 3 times to assess the reproducibility of the process. The quality of the print was verified by scanning them on a black background and performing image analysis using the FIJI software: the images were formatted into 8-bits, a grey histogram distribution was recovered from the printed area and its standard deviation extracted from the software. For a straightforward representation, the histogram distributions were smoothed and drawn as curves.

2.2.6. Print surface characterisation

The thickness (nm) and surface roughness (µm) of the deposited layer was measured on a Veeco Wyco NT9300 white light interferometer with the following parameters: 1.2 × 0.93 mm measured area, 736 × 480 pixels resolution, ×5 magnification. To measure the thickness, a specific focus was made on the edge area of the printed layer. The height differences between the substrate and the ink layer was measured by excluding the printing edge which can present irregularities. The surface roughness was measured on the whole scanned area. At least 5

measurements were taken on 3 different printed squares for each formulation. To enhance the 3D visualisation of the printed surfaces, the missing data were automatically corrected by the software using the "data restore" function and the contrast was enhanced using the "max contrast" function.

The transparency of the printed pattern was investigated by measuring the transmittance at 550 nm wavelength on a UV-spectrophotometer (Shimadzu Manufacturing Inc., USA). At least 5 measurements were conducted on 3 different printed squares for each reference. The average is presented with standard deviation.

2.2.7. Antibacterial properties

Prior to testing, all the desired solutions, glassware and tools were sterilised in an autoclave for 20 min at 120°C and 1.034 bar. The antibacterial properties of the screen-printed layers toward *E. Coli* bacteria were evaluated by performing the AATCC TM100-1998 standard[30] test. The test has already been detailed in the previous **II-1** section along with a scheme of the different steps. To summarise the technique, a bacterial suspension with a known concentration was deposited on the surface of the samples and the concentration was measured again after 24 hours of contact to assess the activity of the prints. For each sample, a 2 cm × 2 cm surface of a print was cut and dry-sterilised at 60°C for 16 h in an oven prior to the experiments. *E. Coli* bacterial suspension was diluted at 10^5 CFU.ml^{-1} in 20% NB (1 volume NB, 4 volume IS) and 200 µl was drop-casted in microdroplet form on the surface of the sample. The systems were then incubated at 37°C for 24 h. The samples were then recovered, washed with 50 ml of the neutralising solution and the remaining bacterial concentration was measured by a plate counting method using plate counting agar (PCA). Antibacterial activity (AA, %) was calculated with Equation **II-9**:

$$AA\ (\%) = \frac{BC_{PET\ ref} - \mathrm{BC}_{print}}{BC_{PET\ ref}} \times 100 \quad \textbf{(II-9)}$$

Where $BC_{PET\ ref}$ (log CFU) is the bacterial concentration on PET substrate after 24 h of incubation, BC_{print} (Log CFU) the equivalent on the printed sample. Three different samples were tested for each formulation and the average is presented with associated standard deviation.

2.3. Results and discussions

2.3.1. Raw material characterisation

In the first part of this study, two sources of each raw materials were investigated. For the TEMPO-oxidised CNF (T-CNF) sources, suspensions from two different suppliers named Betulium (Finland) and University of Maine (USA) were used, respectively called CNF Betu and CNF Maine. The prepared suspensions are highly homogeneous as indicated by their low turbidity (respectively 18.9 ± 1.8 NTU for CNF Betu and 6.2 ± 0.8 NTU for CNF Maine) and optical microscopy images (not shown) confirmed that there are no macro/micro scaled fibres in both cases. TEM imaging was conducted on the T-CNF suspensions to assess their morphological parameters (**Figure II-18**) and the average size and diameter of the nanofibrils were measured by image analysis software (**Table II-2**). For both sources, the dimensions were found to be relatively close to one another. Due to coloration and entanglement, measurements were complex to perform, however errors were managed through a suitable sample size of nanofibrils, typically 100 for each source of T-CNF. The oxidation charge however was higher for CNF Betu than for CNF Maine.

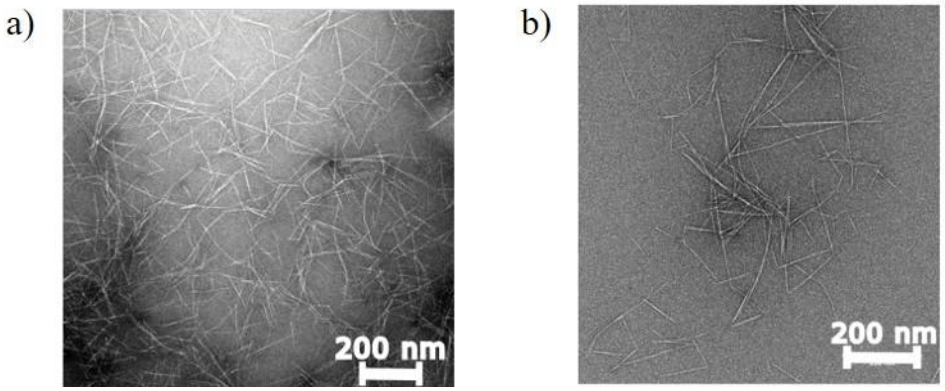

***Figure II-18**: TEM imaging of T-CNF suspensions from different sources with a) CNF Betu and b) CNF Maine*

***Table II-2**: Length (nm) and diameter (nm) of the T-CNF suspensions measured by image analysis of TEM pictures, corresponding calculated average aspect ratio and oxidation charge (µmol.g^{-1}) measured by conductimetric titration*

T-CNF source	Length (nm)	Diameter (nm)	Average calculated aspect ratio	Oxidation charge (µmol.g^{-1})
CNF Betu	297 ± 133	8 ± 4	37	1630 ± 93
CNF Maine	356 ± 164	5 ± 2	71	1111 ± 107

Two different morphologies of Ag NWs from the same supplier called Ag NWs 31-70 and Ag NWs 31-40 were tested, and their length and diameter supplied by the manufacturer is summarised in **Table II-3**.

***Table II-3**: Length (µm) and diameter (nm) of the Ag NWs supplied from the manufacturer and calculated average aspect ratio*

Ag NWs source	Length (µm)	Diameter (nm)	Average calculated aspect ratio
Ag NWs 31-40	14 ± 10	37 ± 5	378
Ag NWs 31-70	28 ± 23	72 ± 21	389

2.3.2. Rheological properties of raw materials suspensions

Flow curve rheology experiments were conducted for individual suspensions of T-CNF and Ag NWs and the influence of the sources and the concentration (0.1, 0.5 and 1% wt in water) of the raw materials was evaluated (**Figure II-19**). The Herschel–Bulkley model was fitted to the experimental shear stress data using Equation **II-10**:

$$\sigma = \sigma_0 + k\gamma^n \quad \textbf{(II-10)}$$

Where σ is the shear stress (Pa), σ_0 the yield stress (Pa), γ the shear rate (s^{-1}), k the consistency ($Pa.s^n$) and n the flow index. The extracted parameters of the model can be found in **Table II-4**. This model was used as it has been used previously to describe relatively well the non-Newtonian yield stress material behaviour of T-CNF[74,83,84].

Firstly, and as expected, all of the different T-CNF suspensions exhibit strong shear shinning behaviour (**Figure II-19a**). This behaviour is essential for the formulated ink to properly flow and cover the desired surface when used in a deposition process that induces a strong shear that is characteristic of screen-printing. As expected, the viscosity is also concentration dependent: the higher the mass content, the higher the viscosity[85]. The experimental data fits the Herschel–Bulkley model relatively well and the different parameters extracted (consistency, flow index and yield stress) are formulation and source dependent. An increase in the mass content of T-CNF led to a decrease in the flow index, an increase in the consistency and an increase in the yield stress. These findings are consistent with previous reports, and are attributed to a stronger, more entangled and denser CNF networks at higher concentration[86–88].

Comparing the results obtained for CNF Betu 0.5% wt and CNF Maine 0.5% wt led to the following conclusion: if their viscosity is relatively different at 0.1 s^{-1}, their viscosity is quite similar at 1000 s^{-1}. The morphological properties of the different sources of T-CNF are relatively similar yet the calculated aspect ratio is almost two times higher for the CNF Maine, which could explain its higher viscosity due to promoted entanglement[89,90]. The difference in viscosity could also be explained by the difference in oxidation charge. A higher oxidation charge implies a weaker hydrogen bonding network and better dispersion because of enhanced electrostatic repulsion at neutral pH and so a lower viscosity[91]. These conclusions also fit well

with the higher consistency, lower flow index and higher yield stress for CNF Maine 0.5% wt compared to CNF Betu 0.5% wt. However, there are also external factors that could explain the difference in rheological properties of these two commercial T-CNF suspensions, such as the cellulose sources or the fibrillation process.

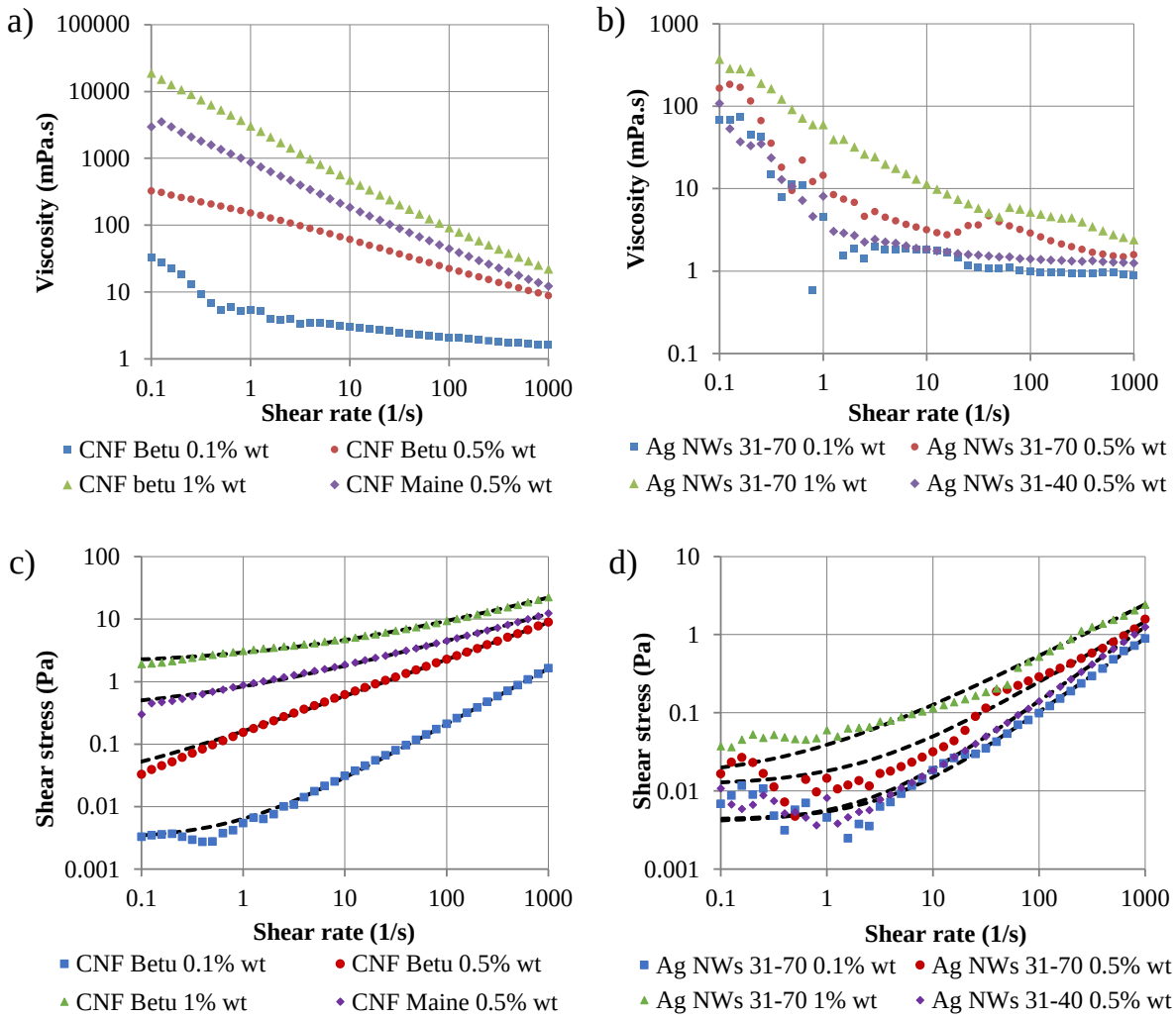

***Figure II-19**: Flow curve experiment for the raw materials and influence of concentration and sources with viscosity dependence on shear rate for a) T-CNF and b) Ag NWs suspensions and shear stress dependence on shear rate (dotted lines represent the fitting to the Herschel-Bulkley model) for c) T-CNF and d) Ag NWs suspensions*

The Ag NWs suspensions also display a shear thinning behaviour (**Figure II-19b**). This is due to the high aspect ratio of the nanoparticles (average calculated aspect ratio of 378 and 389, respectively for Ag NWs 31-40 and 31-70) and so their consequent orientation when exposed to a high shear rate which decreases the suspensions viscosity[92,93]. The same trend as for T-CNF can be seen concerning the concentration of the suspension: the higher the concentration, the higher the viscosity.

***Table II-4**: Herschel–Bulkley law fitting and extracted consistency (k, Pa.sn), flow index (n) and yield stress (σ_0, Pa)*

	Consistency (k, Pa.s^n)	**Flow index (n)**	**Yield stress (σ_0, Pa)**
CNF Maine 0.5% wt	0.523	0.451	0.316
CNF Betu 0.1% wt	0.003	0.894	0.003
CNF Betu 0.5% wt	0.146	0.592	0.015
CNF Betu 1% wt	1.020	0.432	1.895
Ag Nws 31-40 0.5% wt	0.002	0.958	0.004
Ag Nws 31-70 0.1% wt	0.001	0.960	0.004
Ag Nws 31-70 0.5% wt	0.006	0.790	0.012
Ag Nws 31-70 1% wt	0.024	0.667	0.015

The Ag NWs suspensions do not fit well with the model used, and the flow curves present a slightly erratic behaviour. This might be correlated with the fact that the Ag NWs are rod-like rigid nanoparticle with low colloidal stability especially at these low concentrations, and also with the working limits of the rheometer. Even if not flexible as T-CNF, the high aspect ratio of the Ag NWs could explain the similar results concerning the parameters extracted from the model. Indeed, a higher Ag NWs concentration implies a higher consistency, a lower flow index and a higher yield stress consistent with a stronger interconnected Ag NWs network and more particle-particle interaction[93]. Concerning the source of the Ag NWs, the Ag NWs 31-70 suspension is slightly more viscous, which might be explained by the bigger size of the nanoparticles both for the diameter and the length.

As the rheological properties of the two different sources of CNF are rather similar, the CNF Betu was finally chosen to be the main focus of this study because of their higher oxidation charge which predicts a better dispersion. Concerning the choice of the Ag NWs source, the Ag NWs 31-70 and Ag NWs 31-40 display relatively close viscosity independently of the shear rate and so the Ag NWs 31-70 was chosen to be the main focus of the study because of their larger dimensions and so lower expected release when entrapped in the T-CNF matrix. For the rest of this study, T-CNF refers to CNF Betu and Ag NWs to Ag NWs 31-70.

The flow curves properties of T-CNF 0.5% wt, Ag NWs 0.5% wt and their combination showed that as expected from the independent viscosity of the raw materials, the T-CNF in the ink will predominate and determine the viscosity of the system. Indeed, the viscosity of the T-CNF/Ag NWs 1:1 1% wt suspension is close to the viscosity of the T-CNF 0.5% wt suspension (**Figure II-20**).

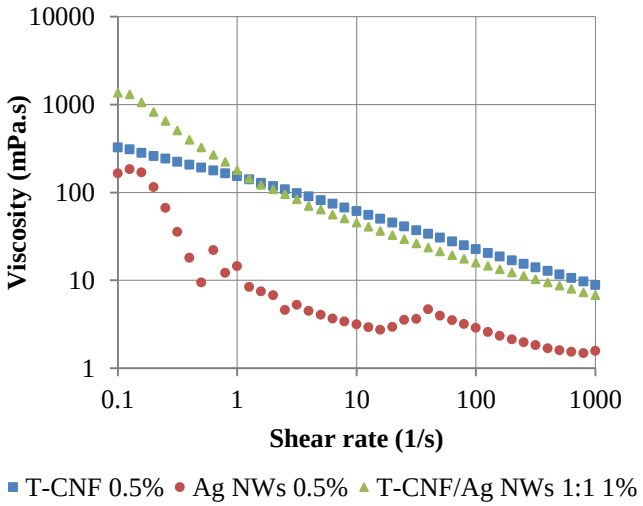

***Figure II-20**: Flow curve experiment for T-CNF 0.5%, Ag NWs 0.5% and T-CNF/Ag NWs 1:1 1%*

2.3.3. Model of high shear deposition process

During a deposition process that involves high shear rate, the ink structure undergoes strong physical changes and this is particularly true for inks composed of high aspect ratio nanoparticles. The thixotropic rheological component of these inks needs to be determined to obtain the desired behaviour when deposited on the substrate. To investigate the thixotropy of formulations based of T-CNF and Ag NWs, a 3-step experiment was applied to model the high shear deposition process. For these experiments, the total mass content was fixed at 1% wt and ratio between the two components was varied between 0 and 1. The results are displayed in **Figure II-21** with the overview of the three steps (**Figure II-21a**) and a zoomed in view on the step three (**Figure II-21b**). Relevant parameters (recovery time, recovery, viscosity) were extracted from this experimental data and are summarized in **Table II-5**.

The viscosity (Step 1, Step 2 or Step 3) is the viscosity measured at the end of the corresponding step. The recovery (%) is the ratio of the viscosity at the end of Step 1 and at the end of Step 3 as calculated from Equation **II-11**:

$$Recovery\ (\%) = 100 \times \frac{\eta_{end\ Step\ 1}}{\eta_{end\ Step\ 3}} \quad \textbf{(II-11)}$$

Where η_{end} Step 1 (Pa.s) and η_{end} Step 3 (Pa.s) are the viscosity for Steps 1 and 3, respectively.

The recovery time was estimated by fitting the first order stretch exponential model to the last step of the experiment (Step 3), as classically used to characterise the build-up recovery structure of thixotropic fluid, using the assumption that the recovery process is due to the re-orientation of the system during the transition steps [87,93,94] (Equation **II-12**):

$$\eta\ (Pa.s) = \eta_{\infty} + (\eta_0 - \eta_{\infty})(1 - e^{-\left(\frac{t}{\tau}\right)^r}) \quad \textbf{(II-12)}$$

Where η (Pa.s) is the viscosity, η_{∞} (Pa.s) the viscosity for an infinite shearing time, η_0 (Pa.s) the viscosity at the beginning of the shear step, t (s) is the time, τ (s) a time constant and r a constant (dimensionless). In the specific case of our study, Equation **II-12** was adapted to yield Equation **II-13**:

$$\eta\ (Pa.s) = \eta_{end\ Step\ 3} + (\eta_{start\ Step\ 3} - \eta_{end\ Step\ 3})(1 - e^{-\left(\frac{t}{\tau}\right)}) \quad \textbf{(II-13)}$$

Where η (Pa.s) is the viscosity, $\eta_{\text{end Step 3}}$ (Pa.s) the viscosity at the end of the Step 3, $\eta_{\text{start Step 3}}$ (Pa.s) the viscosity at the start of the Step 3 (taken 1 s after the switch from Step 2 to Step 3, to limit inertia interferences), t (s) is the time and τ (s) is the recovery time. The r constant was assumed to be equal to 1. The recovery time (s) was found by fitting the experimental data to equation **II-13** above, using the least-squares method.

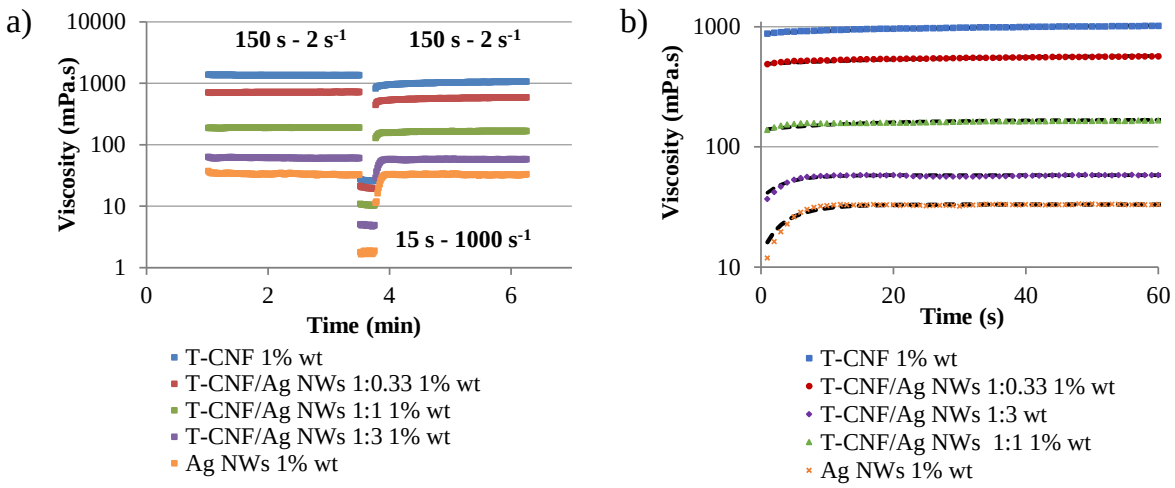

***Figure II-21**: 3-step rheological model of shear-induced deposition process for T-CNF/Ag NWs suspensions at 1% wt and ratios varying from 0 and 1 with a) overview of the viscosity vs time response and b) zoom on step 3 build-up curves in the first 60 s (dotted lines represent the fitting with the stretch exponential model)*

***Table II-5**: Recovery time (s), recovery (%) and viscosity (mPa.s) extracted from the 3-step model, compared to the T-CNF content*

	Ag NWs 1% wt	T-CNF/Ag NWs 1% wt 1:3	T-CNF/Ag NWs 1% wt 1:1	T-CNF/Ag NWs 1% wt 1:0.33	T-CNF 1% wt
% T-CNF	0	25	50	75	100
Recovery time (s)	3.9 ± 0.5	4.0 ± 0.9	13.8 ± 1.8	37.8 ± 2.2	44.2 ± 2.2
Recovery (%)	91.7 ± 13.1	94.0 ± 2.7	88.1 ± 0.4	81.0 ± 1.0	79.6 ± 6.6
Viscosity (mPa.s) Step 1	42.6 ± 13.8	63.0 ± 1.8	190.1 ± 4.5	745.8 ± 20.2	1234.8 ± 103.1
Viscosity (mPa.s) Step 2	2.0 ± 0.2	4.9 ± 0.1	10.4 ± 0.2	19.8 ± 0.4	24.9 ±1.3
Viscosity (mPa.s) Step 3	38.1 ± 7.1	59.2 ± 1.9	167.4 ± 4.8	603.9 ± 13.2	981.4 ± 98.6

In the previous section, it was established that the rheological behaviour is predominantly dictated by the T-CNF in the T-CNF/Ag NWs suspensions. For this reason, the viscosity for all three steps, the recovery (%) and the recovery time were drawn against the concentration of T-CNF inside the suspensions (**Figure II-23**).

As expected, the viscosity for all three steps is dependent on the concentration of T-CNF: the higher the concentration, the higher the viscosity (**Figure II-23a**) as previously described. From Steps 1 and 3, the viscosity differs for the same composition. This is highlighted in **Figure II-23b** which shows that the recovery (%) is dependent on the T-CNF concentration: the higher the T-CNF concentration the lower the recovery, which may be due to a permanent disruption of the more entangled network.

The recovery time was also impacted by the ink composition. The recovery time indeed increases with an increasing T-CNF content. It is below 10 s from 0 to 50% wt of T-CNF in the ink (**Figure II-23b**), and reaches 42.1 s for T-CNF 1%. The same plausible explanation could apply for the changes in recovery (%): the higher amount of T-CNF, the more permanent the disruption of the network is by the high shear step, and the longer it takes to recover to an equilibrium state. For the suspension made only with Ag NWs, a high recovery (91.7 %) is obtained with relatively low recovery time (3.9 s). This can be explained by the rigid and stiff structure of the Ag NWs that do not present a highly entangled network like T-CNF.

If highly charged CNF such as T-CNF are not expected to display major flocculation behaviour, the impact of high shear rate on the T-CNF network is important[95]. High shear rate is expected to break down the gel structure and lead to the alignment, deformation and gradient of concentration at the microscale level[86,96]. Moreover, the impact of the Ag NWs and their

equilibrium with silver ions is unclear, but could also play a role in the charged structure of the network[74,97]. The **Figure II-22** presents a schematic of either high or low ratio of T-CNF/Ag NWs situations, and suggests how the hybrid network is impacted by the high shear process. Even though previous studies have probed the rheological behaviour of T-CNF/Ag NWs systems, this is the first time that, such an investigation of the thixotropic and viscosity behaviour of T-CNF/Ag NWs suspensions under a high shear screen-printing model, is reported[51].

For screen printing, the optimum target for the recovery would be close to 100% to allow a maximum print resolution. The time necessary for the ink to recover its viscosity is also an important parameter. The ideal situation would be to have a recovery fast enough to achieve a homogenous levelling (> ca. 10 s) but not long to avoid extensive slumping (< ca. 200 s)[51,98,99]. All of the different formulations display a high enough recovery (%) for a printing with high resolution. However, in the 0 to 50% wt of T-CNF range, the recovery times are rather short (< 10 s) and these characteristic times could be too small for an even spreading of the ink on the substrate[51,98]. This seems to indicate that the optimal rheological conditions are a higher mass content ink with a T-CNF content higher than 50% wt. The increasing recovery times with the increasing T-CNF content is promising for screen-printing applications. Another parameter to consider is the substrate/ink interaction and a higher content of T-CNF led to a higher surface tension (**Figure II-23c**). Although there is no surface tension target for screen-printing, the surprinsingly high values measured can lead to unsatisfactory substrate/ink interaction.

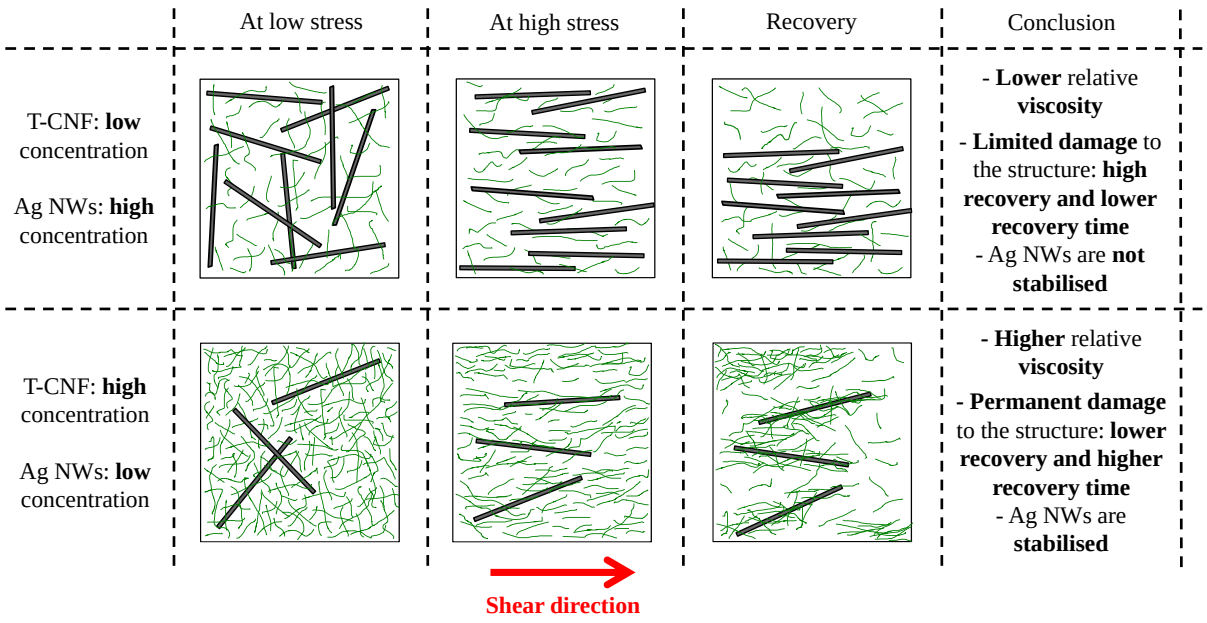

***Figure II-22**: Schematic representation (cross-section) of two separate formulation (high or low ratio of T-CNF/Ag NWs) under different situation (low or high shear stress, recovery) and impact on its network*

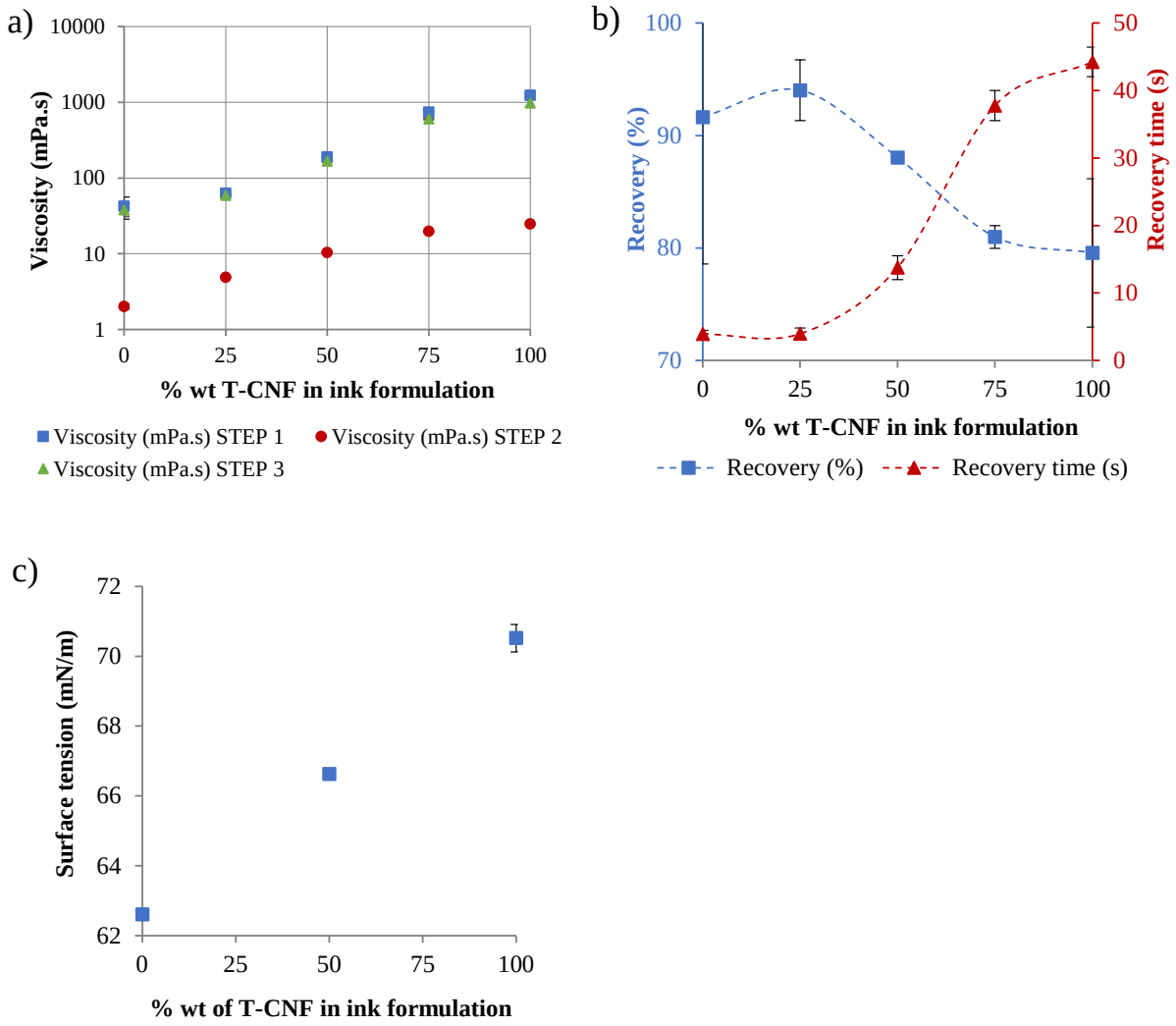

***Figure II-23**: Rheological parameters extracted from the 3-step model compared to the T-CNF content of the suspensions with a) the viscosity (mPa.s) at the end of each step, b) the recovery (%) and the recovery time (s) and other ink properties with d) measured surface tension ($mN.m^{-1}$)*

As discussed above, T-CNF has a strong impact on viscosity and in order to fit more closely with the screen-printing process requirements, the same experiments were performed using only T-CNF at higher concentration (respectively at 1.33, 1.6 and 2 % wt) to provide higher viscosity ranges more aligned with the screen-printing process, and the corresponding values can be found in **Table II-6**.

***Table II-6**: Recovery time (s), recovery (%) and viscosity (mPa.s) extracted from the 3-step model for T-CNF 1% wt, 1.33% wt, 1.66% wt and T-CNF 2% wt*

	T-CNF 1%	**T-CNF 1.33%**	**T-CNF 1.66%**	**T-CNF 2%**
Recovery time (s)	44.2 ± 2.2	41.9	40.4	37.3
Recovery (%)	79.6 ± 6.6	55.8	64.7	83.9
Viscosity (mPa.s) Step 1	1234.8 ± 103.1	4598.3	8691	15054
Viscosity (mPa.s) Step 2	24.9 ±1.3	4.9376	10.396	19.58
Viscosity (mPa.s) Step 3	981.4 ± 98.6	2567.1	5627.3	12631

The extracted recovery times are relatively similar between 1 and 2% wt of T-CNF. The recovery (%) of the different tested formulation ranges from approximately 55 to 85%. The recovery (%) for T-CNF 1.33% wt, T-CNF 1.66% wt and T-CNF 2% wt are high enough for a good printing resolution (>50%), and their recovery time also seem to be in line with the expected requirements. The T-CNF 1.66% wt was then selected as a good compromise between viscosity and thixotropic properties. Based on the findings about the rheological behaviour of T-CNF/Ag NWs inks (and the cost of Ag NWs), a 2:1 (T-CNF:Ag NWs) ratio was selected to provide the antibacterial properties. In combination, this gives a total mass concentration of 2.5% wt. However, when the selected ink was screen-printed on the PET substrate, it displayed a bead forming defect as shown in **Figure II-24**.

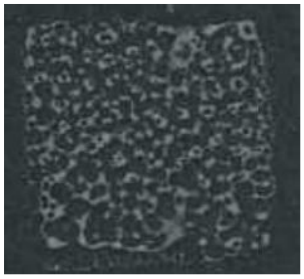

***Figure II-24**: Picture of the printed square on PET substrate with T-CNF/Ag NWs 2.5% wt 2:1*

This could be due to a range of factor such as viscoelastic properties or poor wetting dynamics leading to reticulation. Previous work on similar systems has shown the positive impact of the addition of water-soluble polymer such as hydroxypropyl methylcellulose (HPMC)[51], impacting mainly the viscoelastic properties and recovery time of the formulated inks. So, different amounts (3, 5 and 8% wt) were added in the T-CNF/Ag NWs 2.5% wt 2:1. The same rheological investigation was then performed.

To simplify the notation in the following section, the inks will be named only after their HPMC content as described in **Table II-7**.

Table II-7*: Ink formulated with different HPMC content and detailed composition*

Ink name	T-CNF (% wt)	Ag NWs (% wt)	HPMC (%, wt)
0% HPMC	1.66	0.84	0
3% HPMC	1.66	0.84	3
5% HPMC	1.66	0.84	5
8% HPMC	1.66	0.84	8

2.3.4. Additive and rheological properties

The same three step rheological model was applied to the HPMC formulations (**Figure II-25**), and the same parameters linked to viscosity and recovery were extracted (**Table II-8**). The reference 0% HPMC displays a recovery (72.4%) slightly higher than the T-CNF 1.66% wt formulation (64.7%) showing that the addition of Ag NWs also impacts the recovery (%), whereas the recovery time was relatively similar for both formulations (respectively 39.6 s for 0% HPMC and 37.3 s for T-CNF 1.66% wt).

The viscosity drastically increases with the concentration of HPMC, going from 8.2 Pa.s for HPMC 0% to 57.4 Pa.s for HPMC 8%, due to the thickening effect of the water-soluble cellulose derivative[51]. With an increasing amount of HPMC, the recovery (%) drops from 72.4% for HPMC 0% to 59.2% for HPMC 3%. It is not too much impacted for HPMC 5% and HPMC 8% (respectively 59.1 and 65.5%). The recovery time however decreases with an increasing content of HPMC, reaching 13.6 s for 8% HPMC compared to 29.2 s for 5% HPMC or 33.6 s for 3% HPMC.

The recovery parameters (time and %) are promising for 0% HPMC but its viscosity is in the low range of what is classically expected for screen-printing inks. The 5% HPMC formulation is selected to be a good compromise between recovery and viscosity parameters.

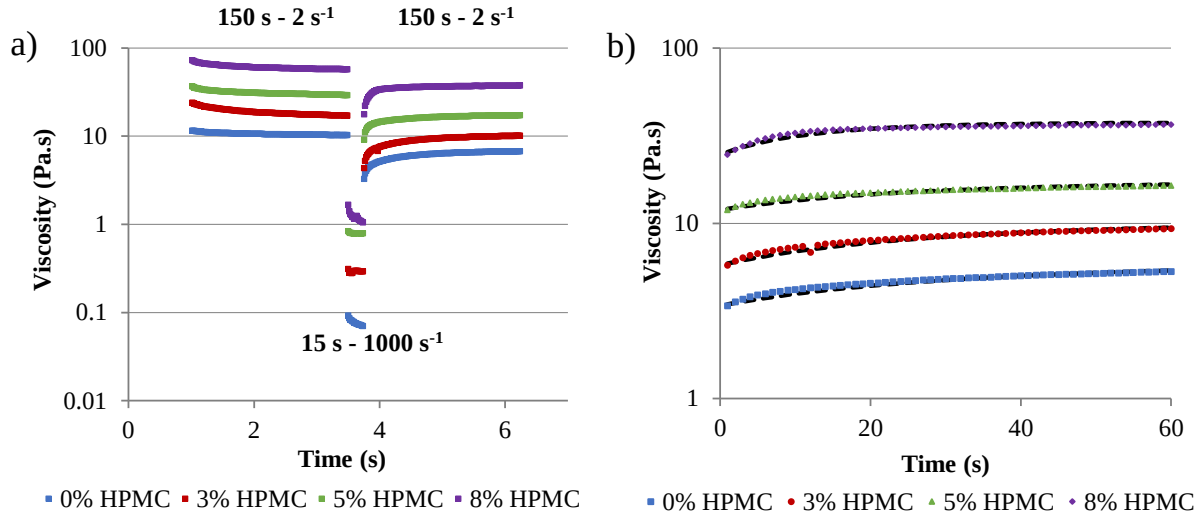

***Figure II-25**: 3-step rheological model of shear-induced deposition process for the formulations T-CNF/Ag NWs 2.5% wt 2:1 plus different HPMC content (0, 3, 5 and 8% wt) with a) overview of the viscosity vs time response and b) zoom on step 3 build-up curves in the first 60 s (dotted lines represent the fitting with the stretch exponential model)*

***Table II-8**: Recovery time (s), recovery (%) and viscosity (mPa.s) extracted from the 3-step model for the formulations with different HPMC content*

	0% HPMC	3% HPMC	5% HPMC	8% HPMC
Recovery time (s)	39.6	33.6	29.2	13.6
Recovery (%)	72.4	59.2	59.1	65.5
Viscosity (mPa.s) Step 1	8209	17229	29341	57426
Viscosity (mPa.s) Step 2	72	293	795	1057
Viscosity (mPa.s) Step 3	5945	10193	17344	37607

The impact of the shear rate of the high shear step (Step 2) was also investigated on the 0% HPMC reference by testing at 200, 500 and 1000 s^{-1} and comparing the extracted parameters in terms of recovery time and recovery (%) (**Figure II-26**). It was found that both parameters are shear rate dependent: the recovery time increase with an increasing shear rate and the recovery (%) decreases with an increasing shear rate. The higher the shear rate, the stronger the deformation and so with higher shear rate, the entangled network of T-CNF/Ag NWs is more impacted in an irreversible manner: the systems do not go back entirely to their original state and it takes longer time to reach the equilibrium state.

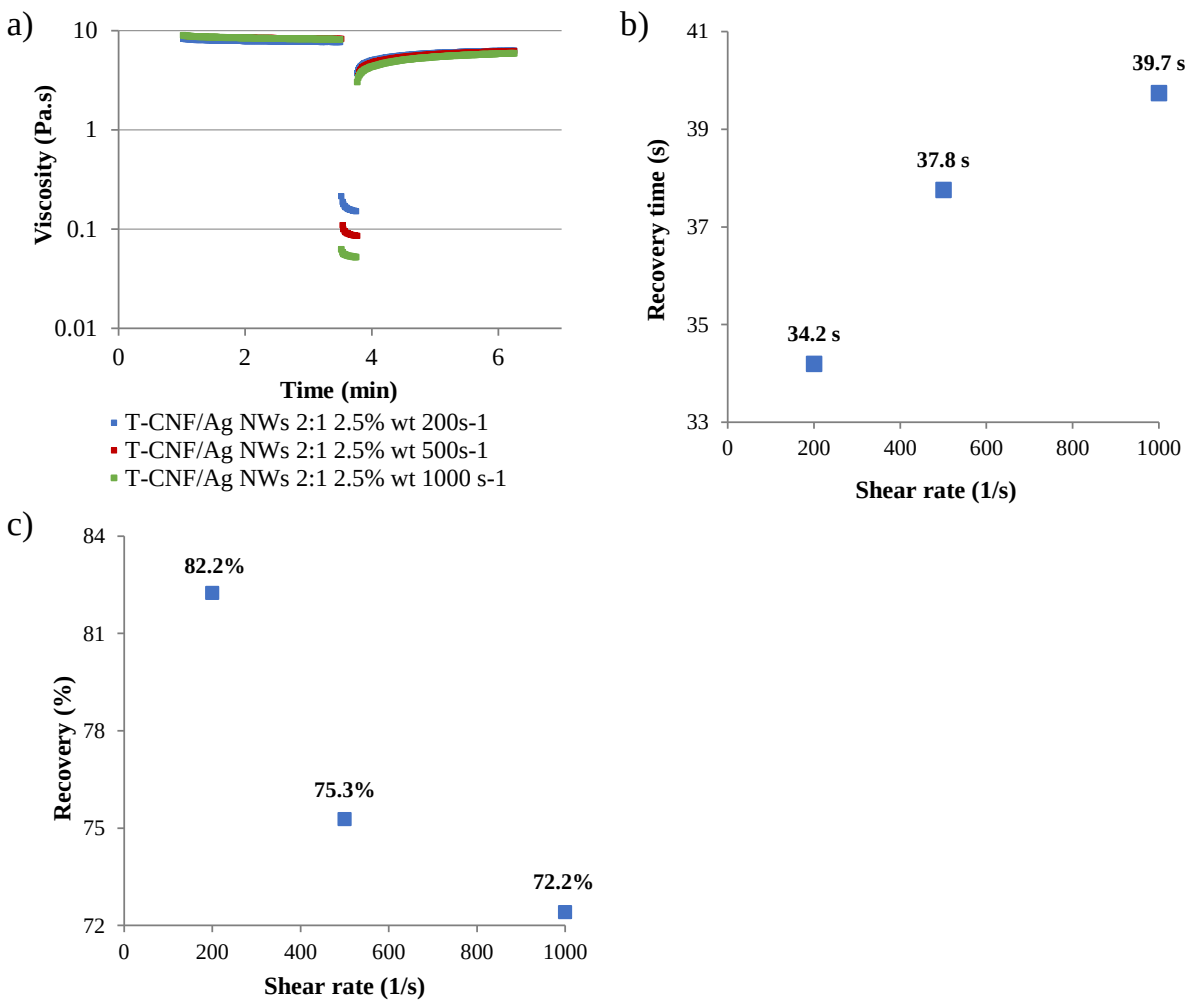

***Figure II-26**: 3-step rheological model of shear-induced deposition process with different shear rate for the step 2 (200, 500 or 1000 s^{-1}) for the formulation T-CNF/Ag NWs 2.5% wt 2:1 with a) overview of the viscosity vs time response b) recovery time (s) vs shear rate (s^{-1}) and c) recovery (%) vs shear rate (s^{-1})*

Preliminary investigation of the viscoelastic properties of the ink were also performed. A three-steps oscillatory experiment was conducted at a fixed frequency of 10 Hz and by modelling the low shear steps by a 2% deformation for 150 s and the high shear step with a 200% deformation for 15 s (**Figure II-27**).

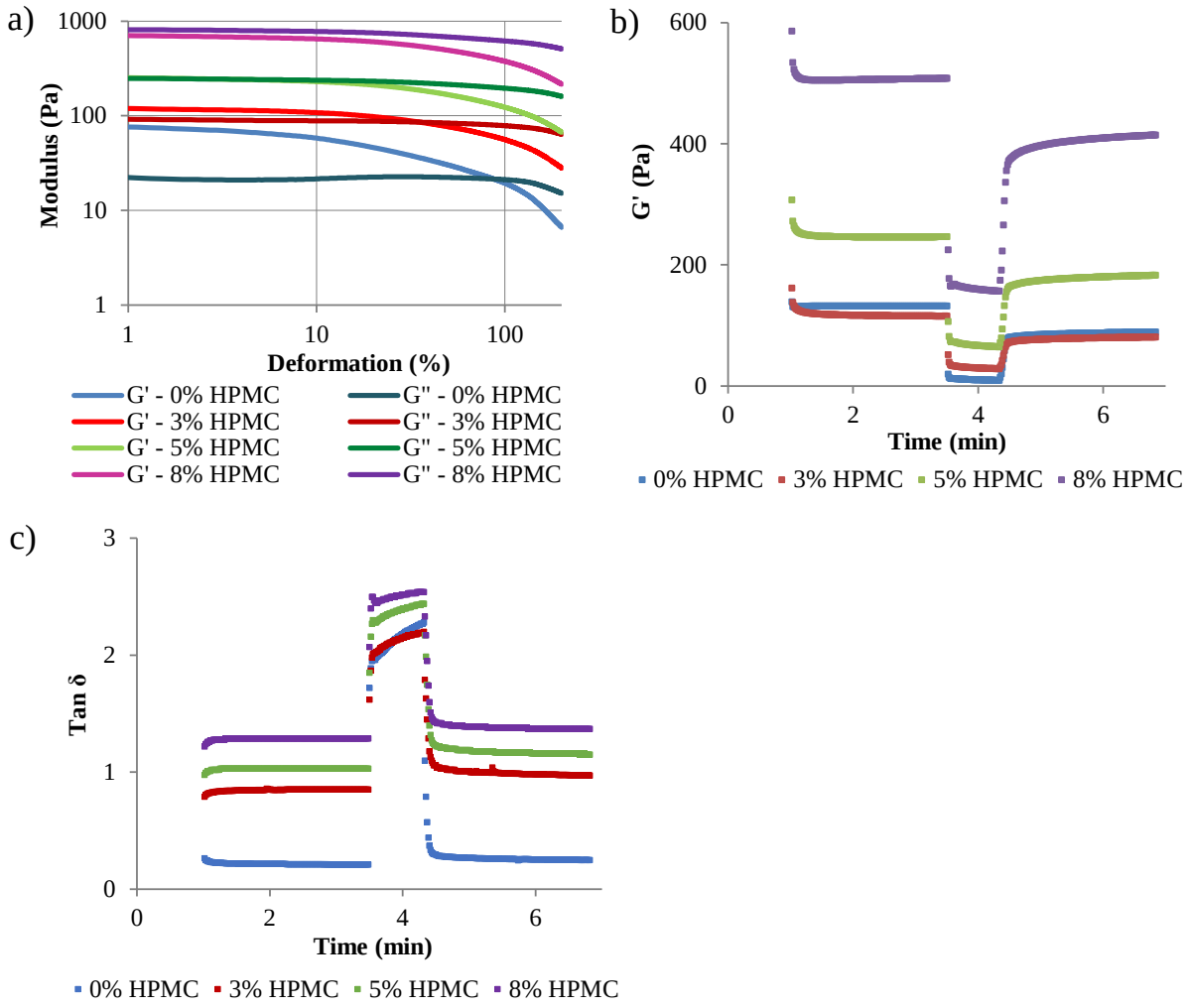

***Figure II-27**: Viscoelastic properties of the ink formulation with different content of HPMC with a) sweep measurement from 1 to 200% deformation at 10 Hz, b) G' (Pa) extracted from the 3-step model, c) tan (δ) extracted from the 3-step model*

The linear viscoelastic region (LVE) was estimated for each formulation by a strain sweep for 1 to 200% deformation. It was found that, for all formulations, the storage (G') and loss modulus (G") were not dependent on the strain amplitude for low values (<10%), proving the strong 3D structure (**Figure II-27a**). For most samples (except 8% HPMC) and at these low amplitudes, G' is higher than G" and so the formulation presents a classic elastic behaviour. At higher strain, all formulation (except 8% HPMC) displays a transition from elastic to viscous behaviour as G' decreases and G" increases. This corresponds to the destruction of the gel-like behaviour into a liquid behaviour. The concentration of HPMC in the ink influences the viscoelastic properties: the higher the HPMC concentration, the higher the G' (**Figure II-27a** and **b**). This indicates an increased gel stiffness and mechanical resistance. Surprisingly, the higher the concentration of HPMC, the lower the critical strain for the elastic/viscous transition. 8% HPMC even display a viscous behaviour even at 1% strain.

Based on the results of the strain sweep experiment, it was hypothesised that for the different samples, a 2% deformation should lie within the LVE whereas a 200% deformation should lie outside of the LVE. The 3-step model also highlights a surprising trend: passing from 2% to 200% leads to an increase of the loss factor for all formulation yet it is already above 1 at the rest modelled step (2% strain) for 8% HPMC (**Figure II-27c**). These preliminary results are not sufficient to conclude on the viscoelastic properties of the system. The tested deformation and frequency range might not be completely adapted, and should be expanded to fully characterise the viscoelastic properties of the inks as more experimental work is required.

For high surface charge and small dimensions, the gel structure of T-CNF suspension is dominated by the immobilisation of water molecules insides the network[36]. Adding HPMC is supposed to influence the rheological properties of the CNF suspension because of a flocculation by depletion mechanism. Non-ionic polymer is not adsorbed on the charged T-CNF and this induces attraction between the T-CNF and so a stronger gel network follows. At the high T-CNF and HPMC concentration tested, the change in the viscoelastic properties could then be due to the destabilisation of the immobilised water molecules.

The optimal screen-process viscoelastic desired requirements could be expressed as a loss factor below 1 for the step in which the ink is at rest on the screen and on the substrate (solid-like behaviour) and a loss factor superior to one during the high shear printing step showing the ink flowing through the screen (liquid-like behaviour). This tends to indicate that the viscoelastic properties of 0% HPMC are ideal for printing whereas the addition of HPMC disrupts these requirements. However, correlating rheological properties and print quality is still a complex challenge today.

2.3.5. Image consistency and antibacterial properties

The formulation with different content of HPMC were printed and the resulting patterns can be found in **Figure II-28**. The print quality is greatly enhanced with the addition of 5% wt or 8% wt of HPMC. This is mostly coherent with the previous rheological parameters extracted from the experiments but not entirely, showing that the rheological test can only give a general guidance for prevision of the print quality.

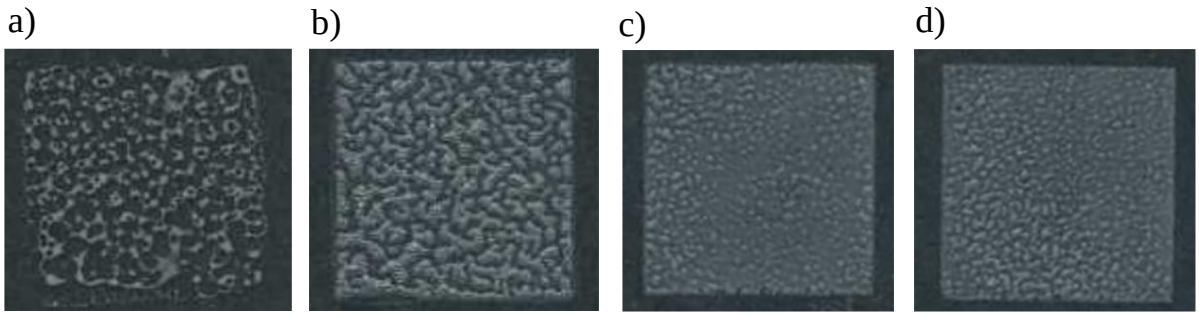

***Figure II-28**: Picture of the printed square on PET substrate with T-CNF/Ag NWs 2.5% wt 2:1 and different amount of HPMC with a) 0% wt, b) 3% wt, c) 5% wt and d) 8% wt*

The quality of the print was estimated by image analysis using FIJI software. Adding HPMC reduces the statistical dispersion of the grey histogram and the graphs shifted from the black background to higher intensity meaning a better coverage of the surface and less mottling defect that makes the substrate appear under the print (**Figure II-29**). There is not much difference in the prints from 5 to 8% of HPMC and this was confirmed by the extracted standard deviation of the grey histogram distribution (**Table II-9**).

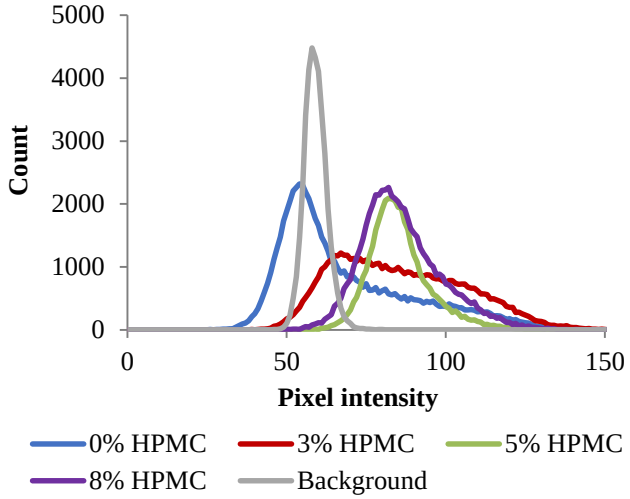

***Figure II-29**: Grey histogram distribution for the different formulation printed and comparison with the black background*

***Table II-9**: Characterisation of the prints as function of the HPMC content in the ink with grey histogram standard deviation, thickness (nm) and surface roughness (nm) (N/A=not applicable)*

HPMC content (%)	0	3	5	8
Grey histogram standard deviation	20.8	20.2	9.6	12.7
Thickness (nm)	N/A	269 ± 138	622 ± 140	811 ± 276
Roughness (nm)	N/A	450 ± 106	482 ± 134	549 ± 137
Transparency (T_{550nm}, %)	82.4 ± 1.8	75.2 ± 1.1	73.3 ± 0.9	68.0 ± 1.9

The topography of the print was also assessed by white light interferometry by measuring the thickness and surface roughness of the prints (**Table II-9**). For the reference formulation without any HPMC (0% HPMC), the quality of the print was not sufficient to measure reliable topographic parameters. For all other samples, the measured dry thickness is less than 1 µm which might be surprising for screen printing process but consistent with the very low mass content of the ink compared to conventional screen-printing inks. The measured thicknesses increased with an increasing content of HPMC and range from 269 to 811 nm. The measured thicknesses are relatively close to the one measured for the bar coating process as described in the Section **1** of this chapter. For all samples, the surface roughness is relatively similar to each sample and very high compared to the deposited thickness, which could be explained by the heterogeneity of the print and the presence of defects even for a high content of HPMC. The patterns transparency was measured to range from 82.4 for 0% HPMC to 68.0% for 8% HPMC. These values are also relatively similar to the one obtained using coating process as shown in Section **II-1**. This indicates that adding HPMC in the formulation does not alter the high retained transparency too much, which is a key feature of the developed solution for active packaging application.

The 3D images extracted from white light interferometry highlight the surface aspect of the prints (**Figure II-30**).

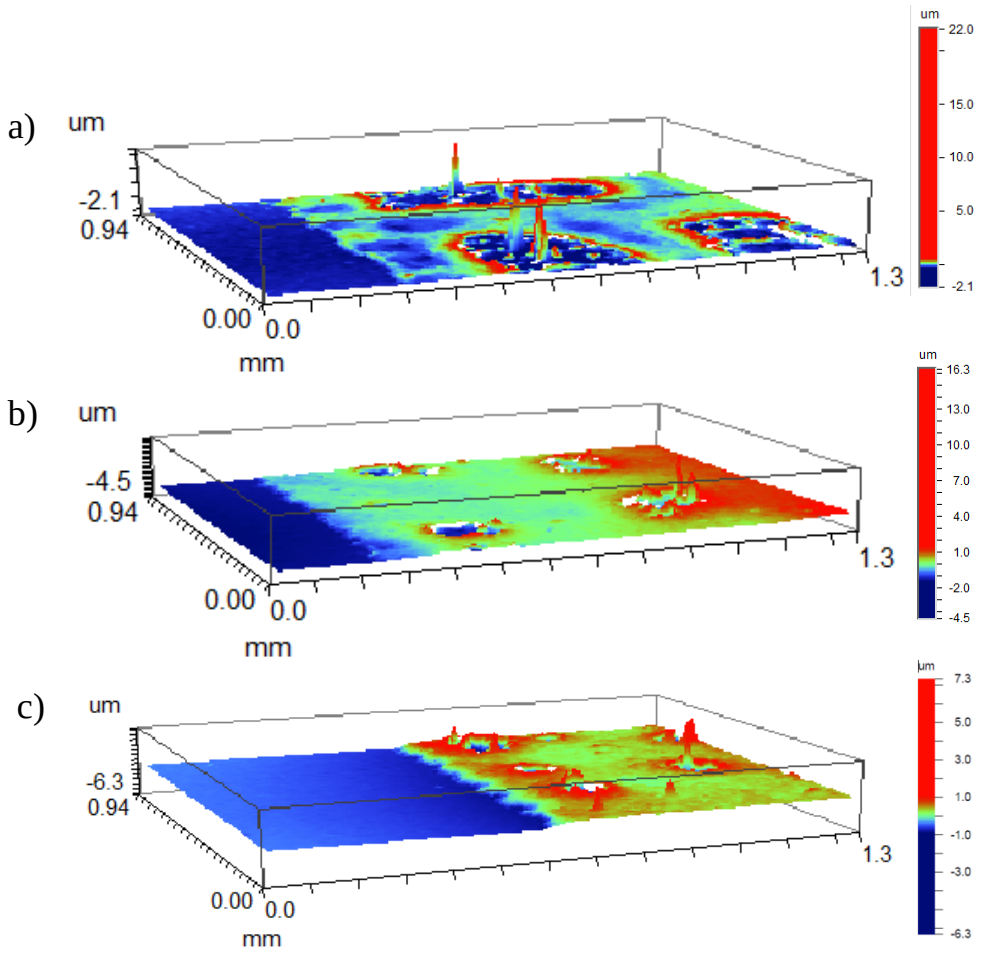

***Figure II-30**: 3D surface pictures of the prints extracted from white light interferometry with a) 3% HPMC, b) 5% HPMC and c) 8% HPMC*

Finally, the HPMC 0% and HPMC 5% prints were tested against *E. Coli* bacterial contamination using the AATCC TM100-1998 standard designed for active surfaces (**Figure II-31**). This test is adapted for contact active surface and is performed by drop-casting a bacterial suspension (known volume and known concentration) on top of the tested surface. After 24 hours of contact in an incubator (37°C, 100 RPM), the bacterial suspension is recovered, numbered and compared with the starting concentration. In the **Figure II-31**, the horizontal line represents the starting bacterial concentration and the histograms represent the final concentration of the bacterial suspension after contact with either the PET reference film (untreated), or the printed samples HPMC 0% and HPMC 5%. The antibacterial activity was calculated comparing the bacterial concentration at the end of the test, between the PET reference and the different samples.

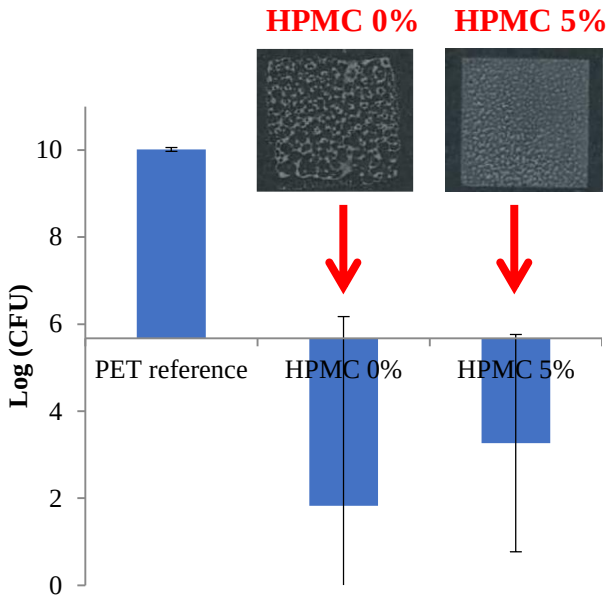

***Figure II-31**: Qualitative analysis of the antibacterial activity of PET reference, HPMC 0% and HPMC 5% samples, using AATCC TM100-1998 standard vs E. Coli with results expressed in log of colony forming units (log CFU)*

Despite the low thickness of the deposited layers, the prints present a bactericidal activity toward *E. Coli* with a calculated antibacterial activity of 81.8% and 67.4% for HPMC 0% and HPMC 5% respectively. The measured antibacterial activity is relatively similar with the results obtained for reverse gravure coating in Section **1** of this chapter. As previously described, the print quality is greatly enhanced from HPMC 0 to HPMC 5% and only a small loss in the antibacterial activity is registered between the two formulations, which probably corresponds to a deeper entrapment of the Ag NWs due to the HPMC addition and consequent lower accessibility of Ag NWs and lower silver ions release rate (**Figure II-32**). This is a significant result that proves the versatility of the formulation that can be adapted to fit the process requirements, even at a high concentration of additives (5% wt) compared to the loading of the

antibacterial silver nanowires (0.84% wt). The high standard deviation shown in **Figure II-31** can be attributed to the heterogenous surface due to the printing defects.

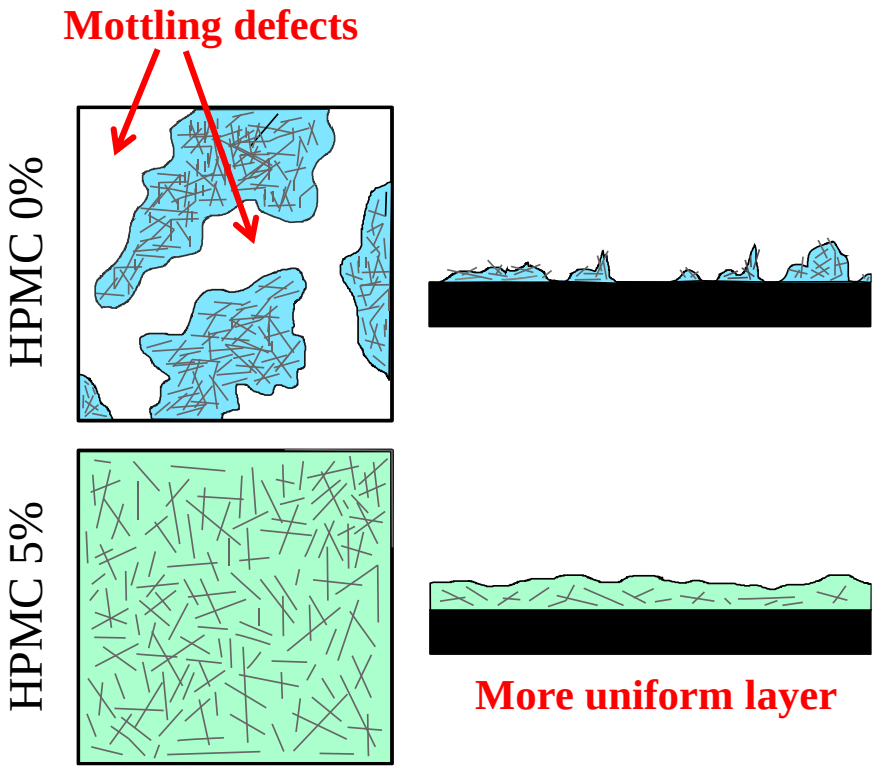

***Figure II-32**: Schematic representation of printed samples HPMC 0% and HPMC 5% and the benefits of adding HPMC into the ink formulation*

2.4. Conclusion

The rheological properties of ink formulations based on TEMPO-oxidised cellulose nanofibrils and silver nanowires were investigated in a systematic, step-by-step manner. Different sources of TEMPO-oxidised cellulose nanofibrils and silver nanowires were first tested using flow curve shear viscosity experiments and the selected materials were then formulated together at different ratios. The viscosity and thixotropic behaviour of the inks were found to be highly dependent on the formulation and higher content screen-printing inks were then prepared based on the optimal formulation. Hydroxypropyl methylcellulose was included as an additive which improved the print quality and the rheological properties of the mixture were investigated with a 3-step screen-printing model. The quality of the print (image analysis, surface roughness and thickness) were correlated to the rheological findings and the antibacterial activity of the prints was established, which proves the potential application to use such a formulation for patterned antibacterial packaging applications.

Demonstration

The possibility to introduce localised antibacterial pattern deposition is interesting for all sorts of packaging applications (food or medical packaging lids or seals for example). It also promotes materials economy as well as the efficient design of tailored antibacterial solutions when compared to full surface coating. Using antibacterial pattern was for instance imagined for the development of a smart label that helps the consumer (or at any another level of the supply chain) to identify microbial breakthrough in packaged product. In this concept, the idea was first of all to print the word “SAFE” using conventional graphic ink on a transparent label. Next to it, the letters “UN” are printed using the T-CNF/Ag NWs transparent solutions and a thin layer of nutritive medium is put on the top. The label is stuck inside the packaging material and the nutritive media is put in contact with the packaged food. If there is a microbial breakthrough, a whitish veil will appear on the nutritive media, revealing by transparency the letter “UN” because of the antimicrobial activity of the transparent T-CNF/Ag NWs pattern deposited. The concept of this technology is imaged in **Figure II-33a** and **b** and a first proof of concept was performed by drop casting the pattern “UN” instead of screen-printing (**Figure II-33c**). This could be another application for the developed solution toward intelligent packaging applications.

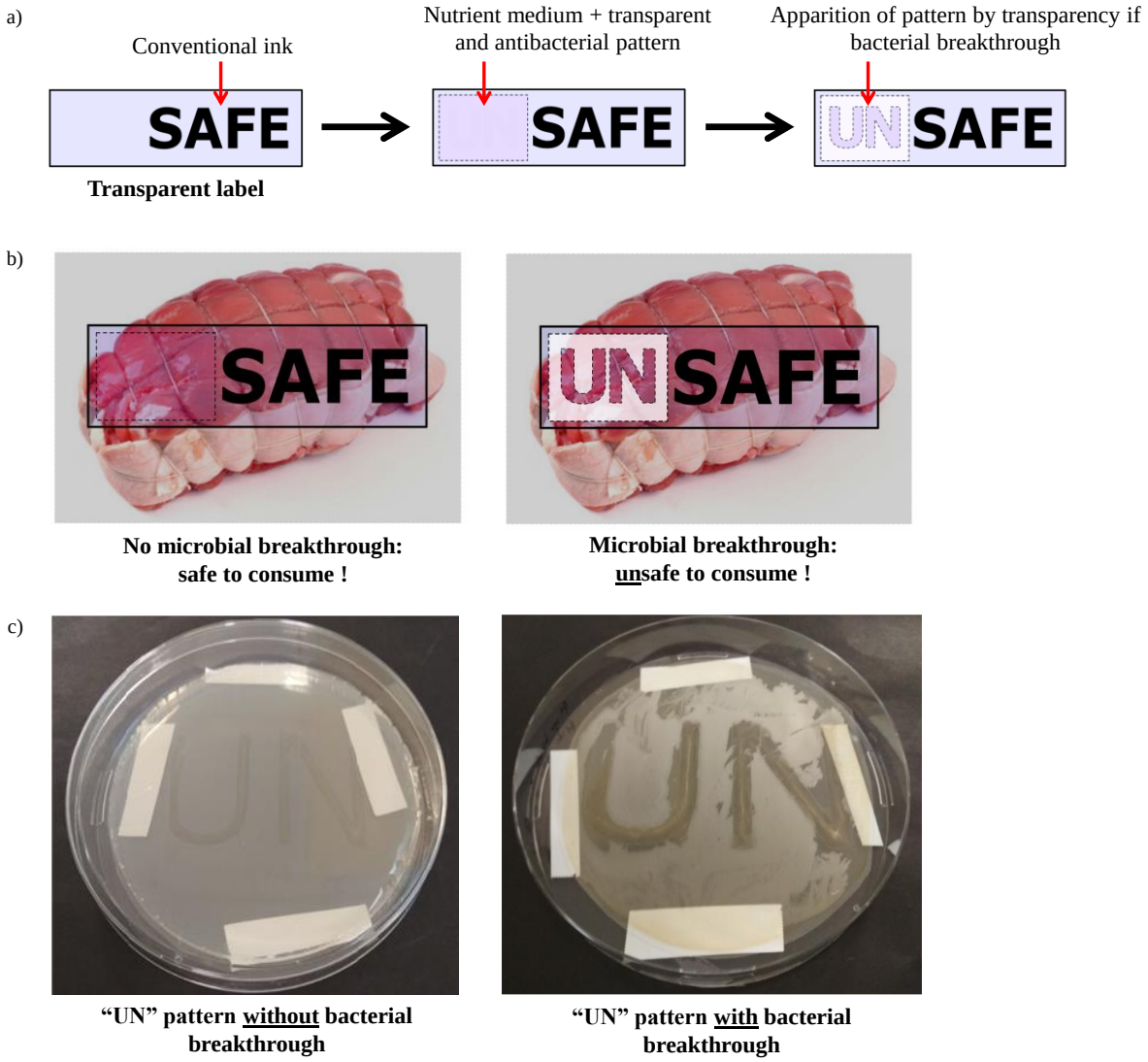

***Figure II-33**: Concept of smart packaging application imagined using the localized deposition of transparent antibacterial pattern with a) schematic of the smart label, b) smart label in action without bacterial breakthrough (left) and with bacterial breakthrough (right) in the scenario of meat package and c) proof of concept by drop casting the pattern "UN" on inoculated agar (E. Coli)*

3. Antibacterial mode of action and barrier properties of cellulose nanofibrils and silver nanowires cast films

Abstract:

The antibacterial activity and barrier properties of thin layers made of TEMPO-oxidised cellulose nanofibrils and silver nanowires have been previously demonstrated. However, their precise mode of action is still under investigation and is relatively complex because of the very thin layers deposited (< 2 µm). Larger scale models of the active coatings and prints developed in the previous sections were then prepared by the film casting method. The high silver loading films were found to be homogenous and around 20 µm thick as measured by microscopy analysis. Firstly, the absence of Ag NWs leaching from the film was verified by a spectroscopic method. Then, the quantity of silver ions being leached from the film castings were investigated by an easy-to-use and low-cost potentiometry technique, using different experimental setups. The quantity of silver ions leaching from the films was measured to be around 12.3 ppm after 1 hour of test with a significant standard deviation. However, a control test was performed under similar conditions using the ICP-OES technique, which indicated that only 0.76 ppm of total silver was released. This might indicate that the potentiometric analytical technique is not well adapted for the leaching assay of silver ions from cellulose nanofibrils/silver nanowires film-cast composites. Finally, the barrier properties of the films were measured and compared with cellulose nanofibrils control films, to assess the impact of the nanowires. Relatively similar results were obtained for both water and oxygen transmission rate, proving that the antibacterial silver nanowires do not hinder the cellulose nanofibrils barrier properties.

Keywords:

cellulose nanofibrils, silver nanowires, film casting, silver ion leaching, barrier properties

3.1. Introduction

The innovative field of active packaging consists of materials that can either release (generally called emitters) or absorb active substances (generally called scavengers) to modify the packaging atmosphere depending on the requirements[2]. Most common active emitters are classified into different categories such as antibacterial, antioxidant or carbon dioxide emitters. Antibacterial materials are the most commonly studied and this category includes materials such as essential oils, natural extract, organic acids or metallic nanoparticles. Silver nanoparticles (Ag NPs) for instance have been deeply studied because of their strong antibacterial activity and potential to fight against bacteria's antibiotic resistance[5]. The antibacterial mode of action is based on both the nanoparticle itself and the continuous release of silver ions[6,55] and includes damage to membrane protein[100,101] or disruption of DNA replication[102] or increased oxidative stress[103,104]. Several parameters influence the antibacterial activity of the Ag NPs such as the size, the shape, the ion release rate or the stability and surface chemistry[7,34,105,106].

Because of the inherent mode of action of active packaging based on emitter technologies, one of the key parameters to control is the migration of the active substance into the food product. To reach the market, active packaging technologies have to comply with the (EC) No 450/2009 regulation dealing with active and intelligent packaging[107] in addition to the (EC) No 1935/2004 food contact materials regulation[108]. The European Food Safety Authority (EFSA) is responsible for publishing advice and reports on food contact materials to help the development of such active packaging technologies while respecting the health and safety for the consumer. Ag NPs are not considered as safe to consume and their migration is considered as a primary concern for the development of active packaging based on Ag NPs. That is why studies focusing on Ag NPs for food packaging applications have mainly produced composites by casting or extrusion methods to limit this migration. For instance, casting with polyvinyl chloride (PVC), polyvinyl chloride (PVA) or chitosan[57,109,110] and extrusion-blowing or injection-moulding with polyethylene (PE) have been reported[111,112]. Ag NPs can also be embedded into cellulose based materials and Ag NPs/cellulose or Ag NPs/nanocellulose composites have been deeply studied in the scientific literature[19].

Cellulose and Ag NPs composites films for antibacterial applications are mainly prepared by solvent casting with silver nanoparticles incorporated by in-situ reduction of silver salts. This enables the entrapment of the silver nanoparticles but is not convenient for large scale synthesis. Silva et al. (2014) investigated the ionic release from different cellulose/Ag NPs matrix[113]. The authors compared the kinetics of silver ions leaching from different sources of cellulose such as eucalyptus fibres, bacterial cellulose and enzymatic cellulose nanofibrils (CNF). It was shown that the silver ion release from CNF was lower than for eucalyptus fibres and bacterial cellulose, and that the diffusion of ions through the matrix was the limiting kinetic step. Li et

al. (2019) employed dialdehyde modified CNF as the reduction agent for in-situ green synthesis of Ag NPs with strong antibacterial properties[114]. The release of silver ions was linear with the time of immersion and the authors proved a sustained and very long release of silver ions up to 320 days. Interestingly, Yu et al. (2019) showed that when preparing a CNF/Ag NPs composite with in-situ chemical synthesis, the release of silver ions was dependent on the media tested and especially that the release was higher in phosphate buffer solution that in pure water[21]. Both reached a plateau respectively after 6 and 24 hours. Xiong et al. (2013) also showed that the ion release is dependent on the form of the composite, proving that the same suspension processed in aerogel form implies a higher release rate than film cast systems[115]. No plateau was observed even after 48 hours of experiments. Finally, Errokh et al. (2019) produced a periodate oxidised CNF/Ag NPs composites by in-situ reaction using Tollens reagent, and the composite was reinforced with an acrylic matrix. The resulting materials showed a very small release of silver ions (ppb).

It has been proven that the antibacterial activity of silver nanowires (Ag NWs) worked mainly by the release of silver ions because of their size and specific surface area[34]. So, the concept of Ag NWs/T-CNF antibacterial materials developed all throughout **Chapter II**, is to physically entrap the Ag NWs within the T-CNF network, to act as a contact active surface. This aims to stop any Ag NWs to be released outside of the prepared active layer while permitting the local controlled release of silver ions. Some previous examples have indeed reported the leaching of spherical Ag NPs when used in a CNF matrix[116,117]. Compared to spherical Ag NPs (diameter typically < 100 nm), Ag NWs anisotropic morphology and larger dimensions (diameter typically < 100 nm, length typically > tens of µm) are less prone to be released from an entangled network such as a CNF matrix. This is highly beneficial for active packaging applications because of the safety issues of NPs consumption, while silver ions have been proven to be less toxic and authorised (within a fixed limit) to be used in food contact materials by the European Food Safety Agency[118]. This is also an interesting for the environmental concern of releasing Ag NPs into the ecosystems. Moreover, in the discussed scientific literature, there is no reference to our knowledge of the investigation of the release of silver ions from a CNF/Ag NPs system with non-spherical Ag NPs. The high loading of Ag NWs in the presented work could then act as a reservoir of silver ions and enable a long-term antibacterial activity through continuous silver ion leaching. This concept of using such a CNF/Ag NWs network compared to most common spherical Ag NPs is highlighted on **Figure II-34**.

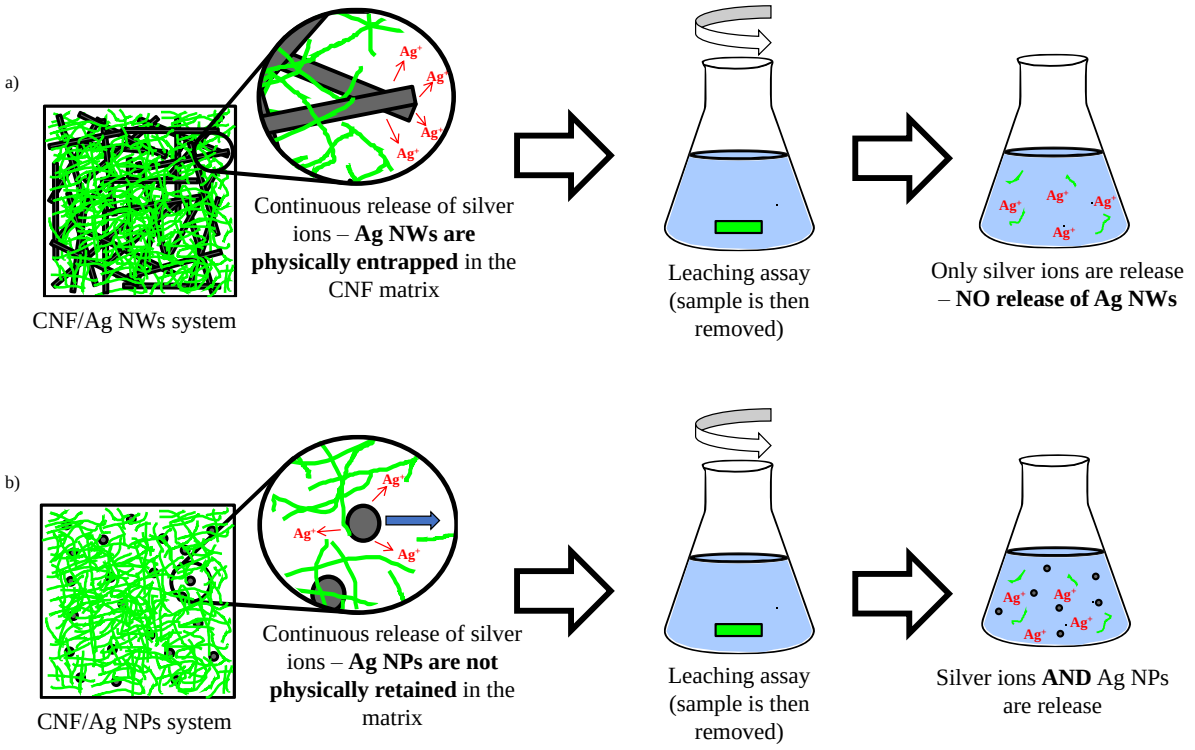

***Figure II-34**: Schematic representation of the concept of the CNF/Ag NPs network and associated leaching behaviour of a) CNF/Ag NWs and b) CNF/spherical Ag NPs*

In the previous **II-1** and **II-2** sections of this work, active surfaces prepared either by coating or printing processes were proven to be highly antibacterial. However, the layers deposited were very thin (< 2 µm). In the case of the active coatings described in Section **II-1** for instance, the quantity of silver deposited per square cm is estimated to range from few µg to tens of µg and the silver ions release was measured to be below 0.5 ppm by the Inductively Coupled Plasma – Atomic Emission Spectroscopy (ICP-OES) technique. This very small amount makes it very complex to adequately measure the release of silver ions using easy-to-access and non-expensive experimental techniques such as potentiometry, which complicate a full-scale analysis of silver ions leaching. It was then decided to model the deposited layers at a higher scale by enlarging the quantity of silver used to make the measurements easier and especially using film casting technique.

In this preliminary study, TEMPO-oxidised cellulose nanofibrils and silver nanowires composites were then prepared by a film casting process. The non-leaching of Ag NWs was verified by spectroscopic measurement and the silver ions leaching was investigated by potentiometry. A control measurement was also performed by the ICP-OES analytical technique. The production of these films also provided an opportunity to investigate the impact of silver nanowires on the barrier properties of the cellulose nanofibrils matrix.

3.2. Materials and methods

3.2.1. Materials

The silver nanowires NGAP NF Ag-31-70 (mass content of 2.6% wt) were acquired from nanogap (USA) and the TEMPO-oxidised cellulose nanofibrils CNF-A13 from Betulium (Finland) (mass content of 5%, 1.6 mmol.g^{-1} measured charge density). Silver nitrate (>99%) was purchased from Sigma Aldrich, (France). All suspensions and solutions were prepared with deionized water (DI water).

3.2.2. Preparation of films by casting method

Film casting was prepared by weighing 0.25 g dry of T-CNF and 0.05 g dry of Ag NWs in 50 ml of DI water and suspended using the high-shear disperser Ultra-turrax for 3 min at 7200 rotation per minute (RPM). Then, 1 hour of magnetic stirring followed by 3 min in the ultrasonic bath were applied to limit air bubbles. The suspensions were then cast into a plastic petri dish (8.9 cm diameter and 62.21 cm² surface) and dried overnight at 40°C. The films were recovered the next day. Control films with only T-CNF were also prepared by dispersing 0.25 g dry of T-CNF in 50 ml of DI water and following the same procedure.

3.2.3. Imaging and release measurements

The surface and cross section of the films were imaged by Scanning Electron Microscopy (SEM) with a 10 nm carbon metallisation on an ESEM Quanta 200 equipment from FEI (Japan). The cross section was performed with a razor blade. The images were taken at 10 kV and 9.8 mm working distance.

Prior to any silver ions release measurement, the leaching of Ag NWs was investigated by a spectroscopic method. The test was performed by cutting a square surface (2 cm × 2 cm), which was deposited on a metal grid, and agitated (100 RPM) in 10 ml of DI water in a closed container, at 37°C. After 1 hour, the liquid was sampled and analysed using a UV spectrometer (Shimadzu Manufacturing Inc., USA) with the following parameters: 300-700 nm range, 1 nm scan rate. The full spectra obtained was compared with Ag NWs only control suspension diluted to 0.005% wt. The **Figure II-35** summarises the experimental strategy for the assessment of Ag NWs leaching.

The silver ion release was conducted using a similar procedure. A 2 cm × 2 cm sample was immersed in 10 ml of DI water on a metal grid, in a closed container and put at 37°C under 100 RPM agitation. Two different strategies of characterisation were performed. In the first, the liquid media was recovered after one hour and analysed by potentiometry (**Figure II-35**). This test was performed 3 times and the average is presented with standard deviation.

In the second strategy, for material economy and to investigate the successive leaching behaviour of the sample, the liquid media was changed after 10 min and the test was continued. The liquid media was successively changed 4 times (each time at 10 min interval) and at each step, the concentration of silver ions in the recovered media was measured. This procedure was performed twice to present an average with standard deviation. Compared to the strategic pathway described in **Figure II-35**, the successive test uses the extracted sample after Step 3 in another liquid media and the action is repeated repeatedly, each extracted liquid media being tested for silver ions content.

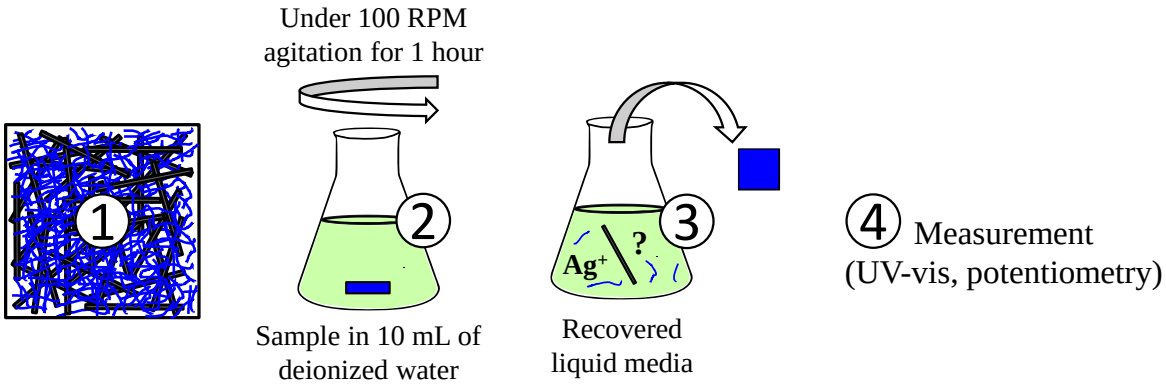

***Figure II-35**: Experimental setups for silver leaching with schematic of the concept of the release test for a non-successive experiment (either for Ag NWs or silver ions)*

For the potentiometric studies, the recovered liquid was mixed with 5 ml of KNO_3 at 1 $mol.l^{-1}$ (ionic strength buffer) and diluted to 100 ml in DI water. The potential between a silver electrode and a calomel reference was measured. A calibration curve was previously performed with known concentration of prepared silver nitrate (2 repeats for each concentration, 2 potential measurements for each concentration) ranging from 10^{-2} to 10^{-7} $mol.l^{-1}$. The calibration curve presents 3 sections (**Figure II-36**): the Nernstian section where measured potential *vs* silver concentration is linear (blue), the non-sensitive section where the measured potential is independent of the silver ions concentration (red) and in between is the linear extrapolation section (green). The detection limit is calculated by the intersection of the Nernstian and non-sensitive section and the values in between are extrapolated. The detection limit was calculated as 3.3×10^{-6} $mol.l^{-1}$.

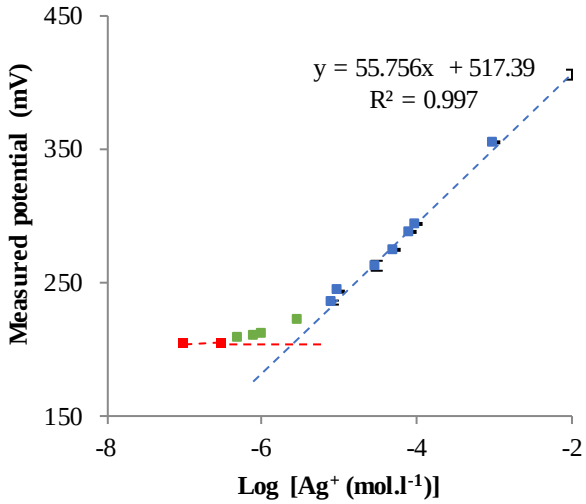

***Figure II-36**: Calibration curve for the potentiometric measurement of silver ions concentration with the measured potential (mV) between the silver electrode and the saturated calomel reference vs the silver ions concentration (mol.l^{-1}) in logarithmic scale*

The total silver leaching was also controlled using the Inductively Coupled Plasma – Optical Emission Spectroscopy (ICP-OES) technique, with the same leaching test procedure as for the potentiometry in the direct strategy (2 × 2 cm sample, 1 hour, 10 ml DI water, 100 RPM, 37°C). The equipment used was the ICP-OES 5100 model from Agilent Technologies (USA). The test were performed following the ISO 11885 standard[27]. The ICP-OES analysis were conducted after microwave digestion of the samples in a mixture of nitric acid and oxygen peroxide, using an ETHOS ONE system from Milestone (Italy) following the NF EN 15587-1 standard[28]. The leaching assay was performed only once, but the ICP-OES analytical measurement was done in duplicate.

3.2.4. Barrier properties

The barrier properties of the cast films prepared were investigated and compared between T-CNF/Ag NWs and T-CNF reference to measure the impact of the Ag NWs.

UV-vis full spectra of the prepared films were performed on a Shimadzu Manufacturing Inc. (USA) equipment, from 200 to 700 nm with 1 nm scan rate.

The Water Vapour Transmission Rate (WVTR) of the cast films was quantified using a slightly modified T 448 om-09 standard[32]. Approximately 30 g of calcium dichloride anhydrous salt was deposited at the bottom of a metal cup that was sealed with the film casting sample, using rubber gaskets and a screw-down cap. The prepared devices were kept in a climatic chamber for 7 days at 50% relative humidity (RH) and 23°C, and weighed twice a day to record the water-uptake of the hygroscopic salt within the metal cup, transmitted through the film samples (2.01 cm² exposed surface). Finally, the WVTR was calculated using the following Equation **II-14** when the mass-uptake was stabilised:

$$WVTR\ (g.m^{-2}.day^{-1}) = \frac{24 \times \Delta m}{\Delta t \times S} \quad \textbf{(II-14)}$$

Where Δt (day) is the time interval between measurements, Δm (g) the mass-uptake in the time interval and S (cm^2) the surface of sample exposed. 4 different samples were tested for each film reference and average is presented with standard deviation.

The Oxygen Transmission Rate (OTR) of the films (with a 2.01 cm^{-1} exchange surface) was measured on an OX-TRAN 2/21 ML equipment from AMETEK MOCON (USA), following the ASTM F1927 standard[31]. The tests were performed at 23°C and carried out in duplicates (average is presented with standard deviation), both at 0 and 50% of relative humidity (RH). Due to a technical incident, the OTR of T-CNF sample at 50% RH was performed only once.

3.3. Results and discussions

To prepare composites with a larger size than for coatings and prints developed in previous experimental chapters, films made of T-CNF/Ag NWs were prepared by casting method. Because of the large quantity of materials required and the cost of silver nanowires, a mass ratio of T-CNF/Ag NWs of 5:1 was selected. The films prepared then achieved a theoretical loading of around 800 µg.cm^{-2}. The films were found to be homogeneous by Scanning Electron Microscope (SEM) imaging with a measured thickness around 20 µm (**Figure II-37**).

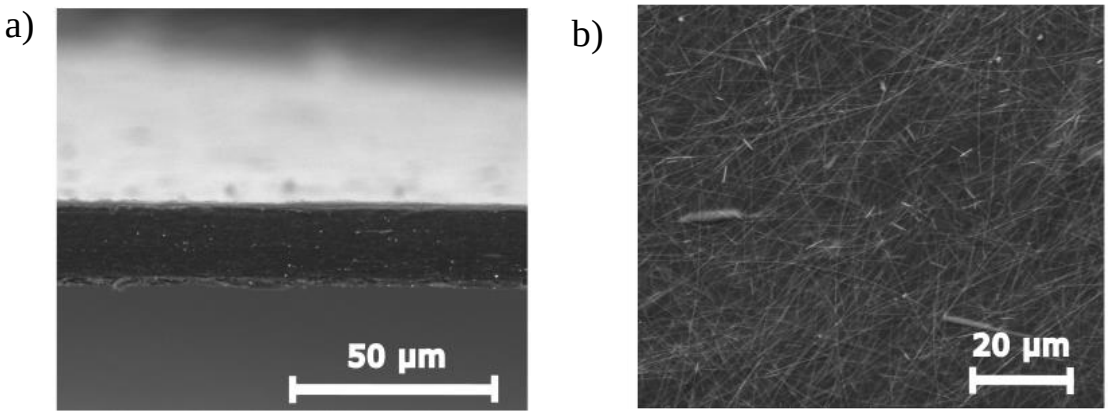

***Figure II-37**: Scanning Electron Microscopy pictures of the films casting samples with a) cross section, b) surface*

First of all, the film casting prepared were checked for Ag NWs release. After one hour of agitation in water, the film casting sample was extracted and the recovered liquid media was analysed by UV-vis method. No sharp peaks corresponding to the Ag NWs could be seen in the recovered liquid media compared to Ag NWs reference suspension, which indicate that there is no detectable release of Ag NWs when measured by this technique (detection limit estimated around 0.5 mg.l^{-1}) (**Figure II-38**).

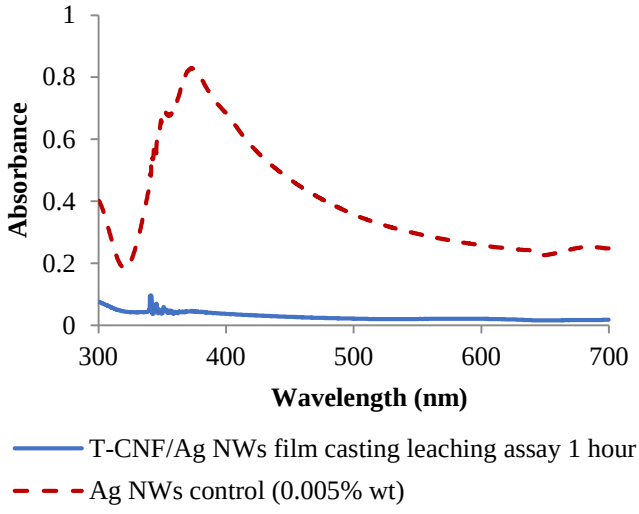

***Figure II-38**: Ag NWs leaching analysis by UV-vis (2 x 2 cm of film casting in 10 ml of DI water during 1 hour at 100 RPM-37°C) compared to Ag NWs control suspension at 0.005% wt*

The leaching of silver ions was then investigated, either directly after 1 hour or by a successive assay by changing several times the liquid media after 10 min. The successive tests were carried out from an economy of materials point of view. However, because of the poor mechanical strength of the wet T-CNF/Ag NWs film, only four successive data points could be extracted before destruction of the film occured. After 40 min, the cumulative silver ion concentration released was measured as 39.2 ppm (**Figure II-39a**). This was significantly higher than the direct release after one hour, which may be explained by a disruption in the release equilibrium induced by the liquid media change or potential mechanical damages to the film, and so an enhanced release. In the direct strategy, 12.3 ppm of silver ions were released after one hour (**Figure II-39b**). A high standard deviation was noted and these values seemed rather high when compared to the literature.

A control test was then performed using the Inductively Coupled Plasma – Optical Emission Spectroscopy (ICP-OES) technique. The test conducted by ICP-OES showed that using a direct strategy and after 1 hour of test, the total silver concentration of the liquid media was measured as 0.76 ppm (**Figure II-39**). This is significantly lower than the results obtained with potentiometric studies. This suggests that the potentiometric studies are over-evaluating the silver ions quantity released from the matrix. Another explanation could be that the measured silver ions concentration by the potentiometric method are too close to the detection limit of the technique, or that the presence of charged T-CNF in the media is interfering with the potentiometric method. All of the different silver ions quantity release in the different tests are however higher than the minimum inhibitory concentration (MIC) of silver nitrate toward *Escherichia Coli* taken here as reference bacteria (around 3.5 ppm)[119].

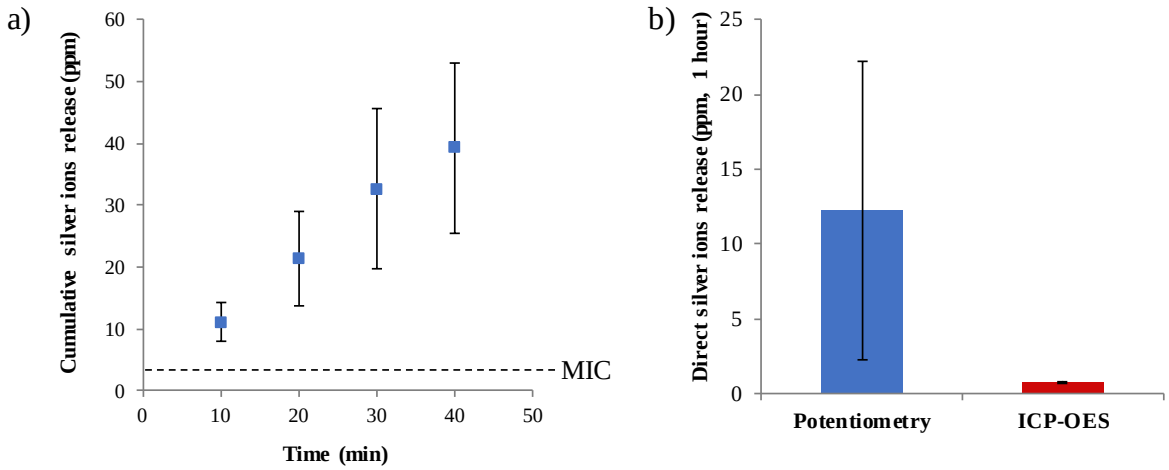

***Figure II-39**: Silver ions release measurements with a) cumulated silver ion release (ppm) after 40 min (the dotted line represents the minimum inhibitory concentration extracted from Greulich et al.*

(2012)[119]) and b) direct silver ion release (ppm) after 1 hour comparing potentiometry and ICP-OES technique (total silver content)

The European Food Safety Agency (EFSA) recommends a total migration of silver ions below 0.05 mg/kg of food[118], which is a number based on the human no-observed-adverse-effect level (NOAEL). The World Health Organization (WHO) indeed stated a NOAEL estimated around 10 g of silver for a total lifetime intake concerning drinking water. The EFSA recommendation is then based on the assumption that 1 kg of food is consumed in a day per person. Supposing that it takes 20 cm × 20 cm of flexible film to prepare the lid of some meat packaging for example, that means 400 cm². The value of silver leaching obtained after 1 hour using the ICP-OES measurement was 7.6 µg, for a 4 cm² sample. Assuming the silver ions is directly proportional to the sample surface, the silver leaching for a 400 cm² surface could be approximated to 0.76 mg. This value is over the EFSA recommendation, which suggests that the T-CNF/Ag NWs composites should not be used in the form of film casting but rather in thin film coatings such as those developed in studies reported in Section **II-1**.

If we consider that the silver ion release from T-CNF/Ag NWs systems is directly proportional to the silver loading, then the results obtained in this section can help us extrapolate the theoretical value for the coatings obtained in section **II-1**. Following this assumption based on silver loading, then the theoretical silver ions release from the 350 nm coating developed in Section **II-1** (T-CNF/Ag NWs 350 sample) should be 67 times lower (as the theoretical loading of silver in the coatings is 67 times lower than in the film cast). It could then be estimated that a 400 cm² packaging lid made of 350 nm T-CNF/Ag NWs coating releases 0.011 mg of silver after one hour, which is lower than the EFSA recommendation. A leaching analysis over a longer time period and in the exact conditions of food packaging must however be conducted to conclude on the complete safety aspect of the developed solution for food packaging applications.

The literature references presented in the introduction, that studied the release of silver ions from CNF/Ag NPs composites are summarised in **Table II-10**. For each reference, the extracted values of the ascending slope of silver ion release before reaching a plateau (after one hour or normalised to one hour) were normalised to the mass of sample used for the test and the silver loading inside the composite.

***Table II-10**: Summary of the literature examples that investigated silver ions release from CNF/Ag NWs matrix (P=prepared, C=commercial, MCC=microcrystalline cellulose, App.=approximatively)*

CNF	Ag NPs (preparation/size)	Matrix (process/additive)	Silver loading (%)	Ag release	Ag release ($ppm.g^{-1}.\%silver^{-1}.hour^{-1}$)	Reference
From MCC	P in-situ/10-30 nm	Freeze drying/Fe_3O_4 NPs (aerogel) and casting/Fe_3O_4 NPs (films)	4.7	0.1 ppm for film/0.25 for aerogel after 1 hour. 0.34 ppm for film/0.66 for aerogel for 48 hours	0.425	Xiong et al. (2013)[115]
Enzymatic	P in-situ/10-30 nm	Film (lyophilized)	2.8	7-8 µg for 1 hour. 18-26 µg for 48 hours	1.664	Silva et al. (2014)[113]
Periodate oxidised	P in-situ/5-50 nm	Film (casting)/latex	App. 1	0.5 ppb/g of sample for 1 hour. 1.5 ppb/g of sample for 24 hours.	0.003	Errokh et al. (2019)[120]
Dialdehyde modified	P in-situ/20-40 nm	Film (filtration)	1.8	0.2% after 2 days. 3.6% after 32 days	0.008	Li et al. (2019)[114]
Not provided	P in-situ/5-15 nm	Film (casting)	3.1	1-3.2 mg/m^2 for 6 hours. 2-3 mg/m^2 for 48 hours	0.003	Yu et al. (2019)[21]

The ICP-OES control demonstrated that after 1 hour, the silver ions release was equal to 0.76 ppm. Considering the sample mass, this also equals to 38 $ppm.g^{-1}$ of $sample.hour^{-1}$. Then, considering the 5:1 ratio T-CNF:Ag NWs, which corresponds to a 16.7% wt loading of Ag NWs, the normalised release rate of silver ions from the composite prepared in this work was finally calculated as 2.275 $ppm^{-1}.g^{-1}.\%silver^{-1}.hour^{-1}$. This is higher than the release rate found in the literature and is surprising as it has previously been shown that the dissolution rate of Ag NWs is usually lower that spherical Ag NPs due to lower specific surface area (similar diameter but larger length for Ag NWs)[34,106].

This higher release of silver ions in this work than in the presented literature example could be explained by of several reasons. First of all, only a limited timeframe of silver ions release has been investigated and there was no sign of a stabilisation in the quantity release during the performed test. That means that the complete silver leaching behaviour is still unknown. The high silver ions release could also be due to the high silver loading, that may induce a local saturation of the T-CNF carboxyl adsorption sites and so a higher quantity of free silver ions. The origin of the NPs can also be responsible for the higher leaching quantity. Because the NPs were not produced by in-situ reduction, the Ag NWs suspension that was added into the T-CNF suspensions was already ion rich as part of the equilibrium between Ag NWs and ions when stored in suspensions (and used unwashed contrary to in-situ produced Ag NPs). This might be responsible for a high starting concentration of silver ions.

The barrier properties of the films casting systems prepared were also investigated in order to verify the impact of the Ag NWs on well-known barrier properties of the T-CNF matrix[17,18].

First of all, it can be seen in **Figure II-40a**, that the T-CNF film presents a high transparency that is completely lost by the addition of the Ag NWs. The T-CNF/Ag NWs film is however a 100% barrier to UV-light, which could be an interesting feature for packaging applications, as the UV-light catalyses the oxidation and so leads to deterioration of food products.

The water vapour barrier properties of the film casting were tested both against oxygen and water vapour. It was found that there is no major difference in the oxygen transmission rate between 0 and 50% of relative humidity (RH), as well as no major difference in the water vapour transmission rate (**Figure II-40b**, **c** and **d**). This is a significant result that shows that adding the Ag NWs into the T-CNF matrix does not hinder their good barrier properties.

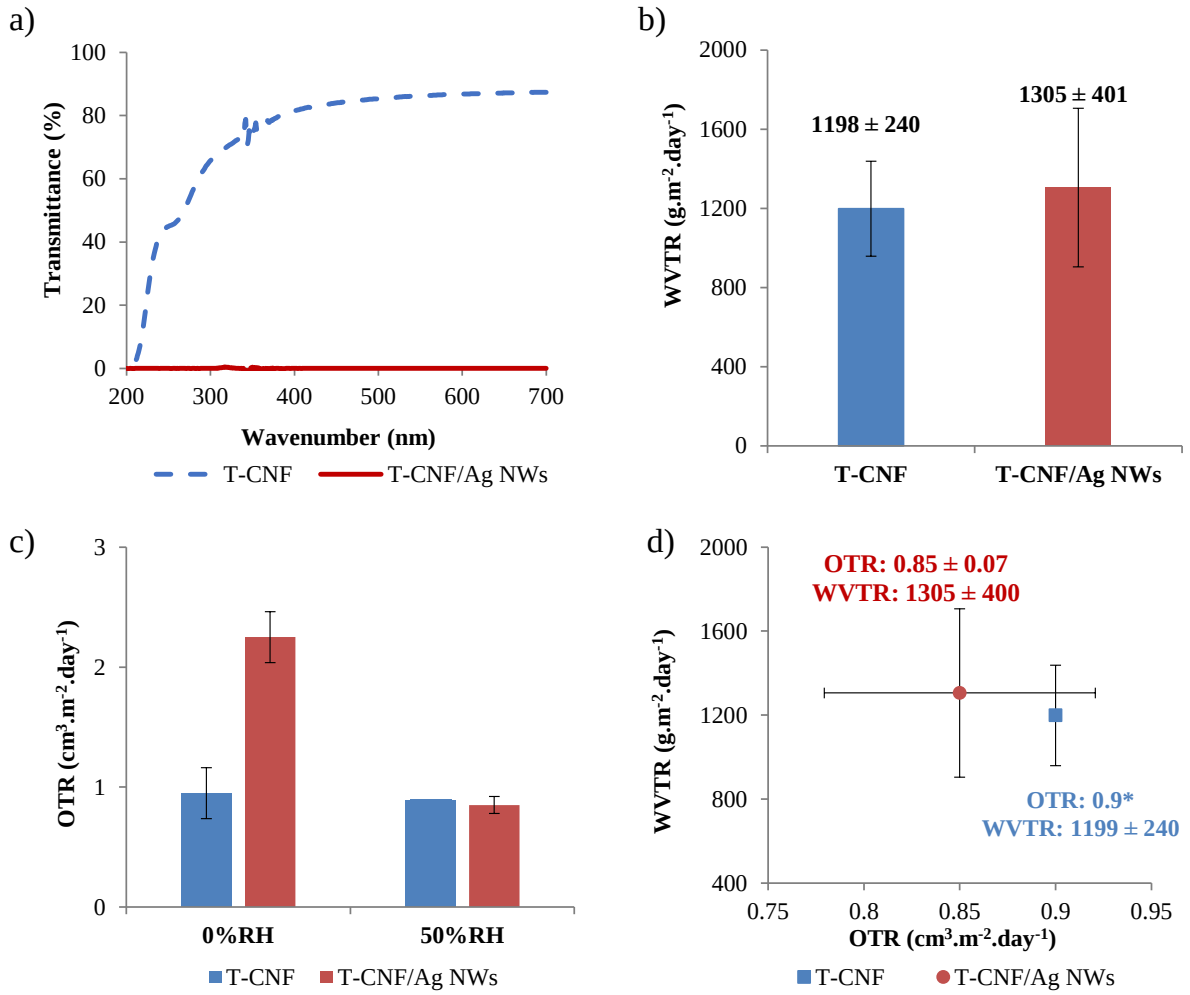

***Figure II-40**: Barrier and optical properties of the T-CNF and T-CNF/Ag NWs film with a) UV-vis full spectra and b) Water Vapour Transmission Rate (WVTR, $g.m^{-2}.day^{-1}$), c) Oxygen Transmission Rate (OTR, $m^{-3}.m^{-2}.day^{-1}$) at 0 and 50% RH and d) WVTR vs OTR at 50% RH (*due to a technical incident, the OTR of T-CNF at 50% RH was performed only once)*

3.4. Conclusion

TEMPO-oxidised cellulose nanofibrils and silver nanowires materials were prepared using a film casting technique. The prepared films were homogenous and were tested for silver ions leaching as a high loading model of the coated or printed layers investigated in Sections **II-1** and **II-2.** Silver ion leaching was measured by a potentiometric method and controlled by ICP-OES technique. The results obtained with the ICP-OES (0.76 ppm after 1 hour) were significantly lower than those from the potentiometric studies, which suggests that the potentiometry technique is not suited to this application. Extrapolating the obtained results to the coatings reported in Section **II-1**, showed that the ions release could be below the European Food Safety Agency recommendation within the tested timeframe, for food packaging applications. The investigation of the barrier properties of the cast films showed that the silver nanowires did not significantly impact the good properties of the cellulose nanofibrils matrix, both for oxygen and water vapour gas analytes. This preliminary study paves the way for a more precise and complete study: longer leaching times as well as tests under real food packaging conditions should be performed. Investigating the impact of different cellulose nanofibrils matrix (different sources or chemical modification) on the leaching properties is also an interesting perspective.

Conclusions of Chapter II

The goal of the studies reported in **Chapter II** was to develop antibacterial packaging based on the combination of active nanomaterials named cellulose nanofibrils and silver nanowires. Different formulations and processes were investigated and materials with antibacterial activity suitable for active packaging applications were achieved.

In Section **II-1**, active inks were coated on flexible polymeric substrates. Laboratory-scale bar coating was first shown to enable the successful controlled thickness deposition with high retained transparency. Strong antibacterial activity (90-100%) for both Gram-positive and Gram-negative bacteria was proven for 350 nm thick coating with a mode of action working by contact (limited release of active materials). Enhanced barrier properties toward water vapour and oxygen was also proven and other active properties such as UV-barrier, antioxidant or antifog properties were verified. A similar system was also developed for roll-to-roll reverse gravure coating that showed a retained antibacterial activity, proving the up-scaling potential of such a solution for antibacterial and transparent coating.

In Section **II-2,** the rheological properties of similar inks made with different content, sources and ratio of the raw materials were investigated. The thixotropic and viscosity properties of the inks were found to be dependent on ratios and solid content which was optimised for higher mass content screen-printing inks. A water-soluble polymer additive (hydroxypropylmethyl cellulose, HPMC) was added to the ink at 5% wt to improve the quality of the print. Rheological parameters were also found to be highly dependent on the HPMC content yet correlation between the rheology and the print quality was complex to established. An antibacterial activity > 65% was found for the print and only a minor loss of antibacterial activity occurred due to the addition of HPMC, and all printed patterns displayed high transparency. The obtained results emphasised the potential of such solution to be deployed for localised deposition of antibacterial pattern for packaging applications.

In Section **II-3**, larger scale models of the previously thin deposited layers were prepared by films casting. The release of silver ions from the samples was tested using different experimental setups and techniques. It was found that potentiometric studies are not suited for such applications, as the silver ions quantity was found to be well below the control performed by Inductively Coupled Plasma – Optical Emission Spectroscopy technique. The results were extrapolated toward the coatings reported in Section **II-1**, which showed the promising possibility of these systems to comply with the European Food Safety Agency regulations (within the tested timeframe), however a more complete experimental campaign is needed. The films prepared were also tested for their barrier properties both water vapour and oxygen, that proved that the silver nanowires do not significantly impact the strong barrier properties of the cellulose nanofibrils matrix.

References of Chapter II

1. Food and Agriculture Organization of the United Nations. *World food and agriculture: statistical pocketbook 2019.* (2019).
2. Yildirim, S. *et al.* Active Packaging Applications for Food. *Comprehensive Reviews in Food Science and Food Safety* **17**, 165–199 (2018).
3. Sofi, S. A. *et al.* A Comprehensive Review on Antimicrobial Packaging and its Use in Food Packaging. *Current Nutrition & Food Science* **14**, 305–312 (2018).
4. Kaur, R. & Liu, S. Antibacterial surface design – Contact kill. *Progress in Surface Science* **91**, 136–153 (2016).
5. Rai, M. k., Deshmukh, S. d., Ingle, A. p. & Gade, A. k. Silver nanoparticles: the powerful nanoweapon against multidrug-resistant bacteria. *Journal of Applied Microbiology* **112**, 841–852 (2012).
6. Morones, J. R. *et al.* The bactericidal effect of silver nanoparticles. *Nanotechnology* **16**, 2346 (2005).
7. Carlson, C. *et al.* Unique cellular interaction of silver nanoparticles: size-dependent generation of reactive oxygen species. *J Phys Chem B* **112**, 13608–13619 (2008).
8. Pal, S., Tak, Y. K. & Song, J. M. Does the Antibacterial Activity of Silver Nanoparticles Depend on the Shape of the Nanoparticle? A Study of the Gram-Negative Bacterium Escherichia coli. *Appl. Environ. Microbiol.* **73**, 1712–1720 (2007).
9. Hong, X., Wen, J., Xiong, X. & Hu, Y. Shape effect on the antibacterial activity of silver nanoparticles synthesized via a microwave-assisted method. *Environ Sci Pollut Res* **23**, 4489–4497 (2016).
10. El Badawy, A. M. *et al.* Surface Charge-Dependent Toxicity of Silver Nanoparticles. *Environ. Sci. Technol.* **45**, 283–287 (2011).
11. Kvítek, L. *et al.* Effect of Surfactants and Polymers on Stability and Antibacterial Activity of Silver Nanoparticles (NPs). *J. Phys. Chem. C* **112**, 5825–5834 (2008).
12. Smetana, A. B., Klabunde, K. J., Marchin, G. R. & Sorensen, C. M. Biocidal Activity of Nanocrystalline Silver Powders and Particles. *Langmuir* **24**, 7457–7464 (2008).
13. Korani, M., Ghazizadeh, E., Korani, S., Hami, Z. & Mohammadi-Bardbori, A. Effects of silver nanoparticles on human health. *European Journal of Nanomedicine* **7**, 51–62 (2015).
14. Turbak, A. F., Snyder, F. W. & Sandberg, K. R. Microfibrillated Cellulose, a New Cellulose Product: Properties, Uses, and Commercial Potential. *J. Appl. Polym. Sci.: Appl. Polym. Symp.; (United States)* **37**, (1983).
15. Herrick, F. W., Casebier, R. L., Hamilton, J. K. & Sandberg, K. R. Microfibrillated Cellulose: Morphology and Accessibility. *J. Appl. Polym. Sci.: Appl. Polym. Symp.; (United States)* **37**, (1983).
16. Afra, E., Mohammadnejad, S. & Saraeyan, A. Cellulose nanofibils as coating material and its effects on paper properties. *Progress in Organic Coatings* **101**, 455–460 (2016).
17. Fukuzumi, H., Saito, T., Iwata, T., Kumamoto, Y. & Isogai, A. Transparent and High Gas Barrier Films of Cellulose Nanofibers Prepared by TEMPO-Mediated Oxidation. *Biomacromolecules* **10**, 162–165 (2009).
18. Rodionova, G. *et al.* Mechanical and oxygen barrier properties of films prepared from fibrillated dispersions of TEMPO-oxidized Norway spruce and Eucalyptus pulps. *Cellulose* **19**, 705–711 (2012).

19. Xu, Y., Li, S., Yue, X. & Lu, W. Review of Silver Nanoparticles (AgNPs)-Cellulose Antibacterial Composites. *BioResources* **13**, 2150-2170–2170 (2017).
20. Uddin, K. M. A. *et al.* Retention of lysozyme activity by physical immobilization in nanocellulose aerogels and antibacterial effects. *Cellulose* **24**, 2837–2848 (2017).
21. Yu, Z., Wang, W., Kong, F., Lin, M. & Mustapha, A. Cellulose nanofibril/silver nanoparticle composite as an active food packaging system and its toxicity to human colon cells. *International Journal of Biological Macromolecules* **129**, 887–894 (2019).
22. Ramaraju, B., Imae, T. & Destaye, A. G. Ag nanoparticle-immobilized cellulose nanofibril films for environmental conservation. *Applied Catalysis A: General* **492**, 184–189 (2015).
23. Martins, N. C. T. *et al.* Electrostatic assembly of Ag nanoparticles onto nanofibrillated cellulose for antibacterial paper products. *Cellulose* **19**, 1425–1436 (2012).
24. Ilić, V. *et al.* The influence of silver content on antimicrobial activity and color of cotton fabrics functionalized with Ag nanoparticles. *Carbohydrate Polymers* **78**, 564–569 (2009).
25. Schindelin, J. *et al.* Fiji: an open-source platform for biological-image analysis. *Nat Methods* **9**, 676–682 (2012).
26. Schneider, C. A., Rasband, W. S. & Eliceiri, K. W. NIH Image to ImageJ: 25 years of image analysis. *Nat. Methods* **9**, 671–675 (2012).
27. ISO Standard. *ISO 11885 -Water quality, Determination of selected elements by inductively coupled plasma optical emission spectrometry (ICP-OES)*. (ISO/TC 147/SC 2, 2007).
28. AFNOR standard. *NF EN ISO 15587-1 - Digestion pour la détermination de certains éléments dans l'eau - Partie 1 : digestion à l'eau régale*. (AFNOR Association, La Plaine Saint-Denis, France, 2002).
29. AFNOR standard. *NF EN 1104 - Papier et carton destinés à entrer en contact avec les denrées alimentaires : Détermination du transfert des constituants antimicrobiens*. (AFNOR Association, La Plaine Saint-Denis, France, 2005).
30. AATCC standard. *TM100 - Test Method for Antibacterial Finishes on Textile Materials: Assessment of Antibactrial Textile*. (AATCC, Research Triangle Park, NC, 1998).
31. ASTM standard. *F1927, 14 - Test Method for Determination of Oxygen Gas Transmission Rate, Permeability and Permeance at Controlled Relative Humidity Through Barrier Materials Using a Coulometric Detector*. (ASTM International, West Conshohocken PA, 2014).
32. TAPPI Standard. *T 448 om-09 - Water vapor transmission rate of paper and paperboard at 23°C and 50% RH*. (Technical Association of the Pulp and Paper Industry, New York, 2009).
33. Fahad, S. *et al.* Recent progress in the synthesis of silver nanowires and their role as conducting materials. *J Mater Sci* **54**, 997–1035 (2019).
34. Visnapuu, M. *et al.* Dissolution of Silver Nanowires and Nanospheres Dictates Their Toxicity to Escherichia coli. *BioMed Research International* **2013**, 1–9 (2013).
35. Chernousova, S. & Epple, M. Silver as Antibacterial Agent: Ion, Nanoparticle, and Metal. *Angew. Chem. Int. Ed.* **52**, 1636–1653 (2013).
36. Slavin, Y. N., Asnis, J., Häfeli, U. O. & Bach, H. Metal nanoparticles: understanding the mechanisms behind antibacterial activity. *Journal of Nanobiotechnology* **15**, 65 (2017).
37. Ferrer, A., Pal, L. & Hubbe, M. Nanocellulose in packaging: Advances in barrier layer technologies. *Industrial Crops and Products* **95**, 574–582 (2017).

38. Wu, B. *et al.* Preparation and characteristics of TEMPO-oxidized cellulose nanofibrils from bamboo pulp and their oxygen-barrier application in PLA films. *Front. Chem. Sci. Eng.* **11**, 554–563 (2017).
39. Lagaron, J. M., Catalá, R. & Gavara, R. Structural characteristics defining high barrier properties in polymeric materials. *Materials Science and Technology* **20**, 1–7 (2004).
40. Syverud, K. & Stenius, P. Strength and barrier properties of MFC films. *Cellulose* **16**, 75 (2008).
41. Belbekhouche, S. *et al.* Water sorption behavior and gas barrier properties of cellulose whiskers and microfibrils films. *Carbohydrate Polymers* **83**, 1740–1748 (2011).
42. Vartiainen, J., Laine, C., Willberg-Keyriläinen, P., Pitkänen, M. & Ohra-aho, T. Biobased mineral-oil barrier-coated food-packaging films. *Journal of Applied Polymer Science* **134**, (2017).
43. Aulin, C., Karabulut, E., Tran, A., Wågberg, L. & Lindström, T. Transparent Nanocellulosic Multilayer Thin Films on Polylactic Acid with Tunable Gas Barrier Properties. *ACS Appl. Mater. Interfaces* **5**, 7352–7359 (2013).
44. Nair, S. S., Zhu, J., Deng, Y. & Ragauskas, A. J. High performance green barriers based on nanocellulose. *Sustainable Chemical Processes* **2**, 23 (2014).
45. Bedlovičová, Z., Strapáč, I., Baláž, M. & Salayová, A. A Brief Overview on Antioxidant Activity Determination of Silver Nanoparticles. *Molecules* **25**, (2020).
46. Kwon, S. *et al.* A Short Review of Light Barrier Materials for Food and Beverage Packaging. *KOREAN JOURNAL OF PACKAGING SCIENCE & TECHNOLOGY* **24**, 141–148 (2018).
47. Nuraje, N., Asmatulu, R., Cohen, R. E. & Rubner, M. F. Durable Antifog Films from Layer-by-Layer Molecularly Blended Hydrophilic Polysaccharides. *Langmuir* **27**, 782–791 (2011).
48. Introzzi, L. *et al.* 'Wetting enhancer' pullulan coating for antifog packaging applications. *ACS Appl Mater Interfaces* **4**, 3692–3700 (2012).
49. Li, F., Biagioni, P., Bollani, M., Maccagnan, A. & Piergiovanni, L. Multi-functional coating of cellulose nanocrystals for flexible packaging applications. *Cellulose* **20**, 2491–2504 (2013).
50. Hoeng, F., Denneulin, A., Krosnicki, G. & Bras, J. Positive impact of cellulose nanofibrils on silver nanowire coatings for transparent conductive films. *Journal of Materials Chemistry C* **4**, 10945–10954 (2016).
51. Hoeng, F., Denneulin, A., Reverdy-Bruas, N., Krosnicki, G. & Bras, J. Rheology of cellulose nanofibrils/silver nanowires suspension for the production of transparent and conductive electrodes by screen printing. *Applied Surface Science* **394**, 160–168 (2017).
52. Grüneberger, F., Künniger, T., Zimmermann, T. & Arnold, M. Rheology of nanofibrillated cellulose/acrylate systems for coating applications. *Cellulose* **21**, 1313–1326 (2014).
53. *Handbook of Print Media: Technologies and Production Methods*. (Springer-Verlag, 2001). doi:10.1007/978-3-540-29900-4.
54. Vak, D. *et al.* Reverse gravure coating for roll-to-roll production of organic photovoltaics. *Solar Energy Materials and Solar Cells* **149**, 154–161 (2016).
55. Tang, S. & Zheng, J. Antibacterial Activity of Silver Nanoparticles: Structural Effects. *Advanced Healthcare Materials* **7**, 1701503 (2018).
56. Li, L. *et al.* Effect of stable antimicrobial nano-silver packaging on inhibiting mildew and in storage of rice. *Food Chemistry* **215**, 477–482 (2017).

57. Wu, Z., Huang, X., Li, Y.-C., Xiao, H. & Wang, X. Novel chitosan films with laponite immobilized Ag nanoparticles for active food packaging. *Carbohydrate Polymers* **199**, 210–218 (2018).
58. Kaimlová, M. *et al.* Optimization of silver nanowire formation on laser processed PEN: Surface properties and antibacterial effects. *Applied Surface Science* **473**, 516–526 (2019).
59. Zhang, Z. *et al.* Electrospinning of Ag Nanowires/polyvinyl alcohol hybrid nanofibers for their antibacterial properties. *Materials Science and Engineering: C* **78**, 706–714 (2017).
60. Mirjalili, S. H., Nateghi, M. R. & Kalantari-Fotooh, F. Preparation of silver nanowire/expanded polytetrafluoroethylene and polypropylene nanocomposites via all solution process method for antibacterial applications. *The Journal of The Textile Institute* **111**, 139–147 (2020).
61. Lei, J. *et al.* High-Strength Konjac Glucomannan/Silver Nanowires Composite Films with Antibacterial Properties. *Materials* **10**, 524 (2017).
62. Kiran Shahzadi *et al.* Preparation and characterization of bio-based hybrid film containing chitosan and silver nanowires. *Carbohydrate Polymers* **137**, 732–738 (2016).
63. Satoungar, M. T., Fattahi, S., Azizi, H. & Mehrizi, M. K. Electrospinning of Polylactic Acid/silver nanowire biocomposites: Antibacterial and electrical resistivity studies. *Polymer Composites* **39**, E65–E72 (2018).
64. Yan, J., Abdelgawad, A. M., El-Naggar, M. E. & Rojas, O. J. Antibacterial activity of silver nanoparticles synthesized In-situ by solution spraying onto cellulose. *Carbohydrate Polymers* **147**, 500–508 (2016).
65. Saarinen, J. J. *et al.* Large-Scale Roll-to-Roll Patterned Oxygen Indicators for Modified Atmosphere Packages. *Packaging Technology and Science* **30**, 219–227 (2017).
66. Wen, J. *et al.* Visible Colorimetric Oxygen Indicator Based on Ag-Loaded TiO2 Nanotubes for Quick Response and Real-Time Monitoring of the Integrity of Modified Atmosphere Packaging. *Advanced Materials Technologies* **4**, 1900121 (2019).
67. Tan, E. L., Ng, W. N., Shao, R., Pereles, B. D. & Ong, K. G. A Wireless, Passive Sensor for Quantifying Packaged Food Quality. *Sensors* **7**, 1747–1756 (2007).
68. Yousefi, H., Ali, M. M., Su, H.-M., Filipe, C. D. M. & Didar, T. F. Sentinel Wraps: Real-Time Monitoring of Food Contamination by Printing DNAzyme Probes on Food Packaging. *ACS Nano* **12**, 3287–3294 (2018).
69. Koga, H. *et al.* Transparent, Conductive, and Printable Composites Consisting of TEMPO-Oxidized Nanocellulose and Carbon Nanotube. *Biomacromolecules* **14**, 1160–1165 (2013).
70. Nechyporchuk, O., Yu, J., Nierstrasz, V. A. & Bordes, R. Cellulose Nanofibril-Based Coatings of Woven Cotton Fabrics for Improved Inkjet Printing with a Potential in E-Textile Manufacturing. *ACS Sustainable Chem. Eng.* **5**, 4793–4801 (2017).
71. El Baradai, O. *et al.* Microfibrillated Cellulose Based Ink for Eco-Sustainable Screen Printed Flexible Electrodes in Lithium Ion Batteries. *Journal of Materials Science & Technology* **32**, 566–572 (2016).
72. Espinosa, E., Filgueira, D., Rodríguez, A. & Chinga-Carrasco, G. Nanocellulose-Based Inks—Effect of Alginate Content on the Water Absorption of 3D Printed Constructs. *Bioengineering* **6**, 65 (2019).
73. Syrový, T. *et al.* Wide range humidity sensors printed on biocomposite films of cellulose nanofibril and poly(ethylene glycol). *Journal of Applied Polymer Science* **136**, 47920 (2019).
74. Hubbe, M. A. *et al.* Rheology of Nanocellulose-rich Aqueous Suspensions: A Review. *BioResources* **12**, 9556–9661 (2017).

75. Naderi, A. & Lindström, T. A comparative study of the rheological properties of three different nanofibrillated cellulose systems. *Nordic Pulp & Paper Research Journal* **31**, 354–363 (2016).
76. Saito, T., Nishiyama, Y., Putaux, J.-L., Vignon, M. & Isogai, A. Homogeneous suspensions of individualized microfibrils from TEMPO-catalyzed oxidation of native cellulose. *Biomacromolecules* **7**, 1687–1691 (2006).
77. Alves, L. *et al.* Tuning rheology and aggregation behaviour of TEMPO-oxidised cellulose nanofibrils aqueous suspensions by addition of different acids. *Carbohydrate Polymers* **237**, 116109 (2020).
78. Fukuzumi, H., Tanaka, R., Saito, T. & Isogai, A. Dispersion stability and aggregation behavior of TEMPO-oxidized cellulose nanofibrils in water as a function of salt addition. *Cellulose* **21**, 1553–1559 (2014).
79. Calabrese, V. *et al.* Understanding heat driven gelation of anionic cellulose nanofibrils: Combining saturation transfer difference (STD) NMR, small angle X-ray scattering (SAXS) and rheology. *Journal of Colloid and Interface Science* **535**, 205–213 (2019).
80. Silva, M. A. da *et al.* Alcohol induced gelation of TEMPO-oxidized cellulose nanofibril dispersions. *Soft Matter* **14**, 9243–9249 (2018).
81. Quennouz, N., Hashmi, S. M., Choi, H. S., Kim, J. W. & Osuji, C. O. Rheology of cellulose nanofibrils in the presence of surfactants. *Soft Matter* **12**, 157–164 (2015).
82. Neidert, M., Zhang, W., Zhang, D. & Kipka, A. Screen-printing simulation study on solar cell front side AG paste. in *2008 33rd IEEE Photovoltaic Specialists Conference* 1–4 (2008). doi:10.1109/PVSC.2008.4922793.
83. Martoïa, F., Dumont, P. J. J., Orgéas, L., Belgacem, M. N. & Putaux, J.-L. Micro-mechanics of electrostatically stabilized suspensions of cellulose nanofibrils under steady state shear flow. *Soft Matter* **12**, 1721–1735 (2016).
84. Koponen, A. I. The effect of consistency on the shear rheology of aqueous suspensions of cellulose micro- and nanofibrils: a review. *Cellulose* **27**, 1879–1897 (2020).
85. Saito, T., Kimura, S., Nishiyama, Y. & Isogai, A. Cellulose nanofibers prepared by TEMPO-mediated oxidation of native cellulose. *Biomacromolecules* **8**, 2485–2491 (2007).
86. Lasseuguette, E., Roux, D. & Nishiyama, Y. Rheological properties of microfibrillar suspension of TEMPO-oxidized pulp. *Cellulose* **15**, 425–433 (2008).
87. Shao, Y., Chaussy, D., Grosseau, P. & Beneventi, D. Use of Microfibrillated Cellulose/Lignosulfonate Blends as Carbon Precursors: Impact of Hydrogel Rheology on 3D Printing. *Ind. Eng. Chem. Res.* **54**, 10575–10582 (2015).
88. Iotti, M., Gregersen, Ø. W., Moe, S. & Lenes, M. Rheological Studies of Microfibrillar Cellulose Water Dispersions. *J Polym Environ* **19**, 137–145 (2011).
89. Albornoz-Palma, G., Betancourt, F., Mendonça, R. T., Chinga-Carrasco, G. & Pereira, M. Relationship between rheological and morphological characteristics of cellulose nanofibrils in dilute dispersions. *Carbohydrate Polymers* **230**, 115588 (2020).
90. Iwamoto, S., Lee, S.-H. & Endo, T. Relationship between aspect ratio and suspension viscosity of wood cellulose nanofibers. *Polym J* **46**, 73–76 (2014).
91. Besbes, I., Alila, S. & Boufi, S. Nanofibrillated cellulose from TEMPO-oxidized eucalyptus fibres: Effect of the carboxyl content. *Carbohydrate Polymers* **84**, 975–983 (2011).
92. Li, W., Yang, S. & Shamim, A. Screen printing of silver nanowires: balancing conductivity with transparency while maintaining flexibility and stretchability. *npj Flex Electron* **3**, 1–8 (2019).

93. Hemmati, S., Barkey, D. P. & Gupta, N. Rheological behavior of silver nanowire conductive inks during screen printing. *J Nanopart Res* **18**, 249 (2016).
94. Barnes, H. A. Thixotropy—a review. *Journal of Non-Newtonian Fluid Mechanics* **70**, 1–33 (1997).
95. Nechyporchuk, O., Belgacem, M. N. & Pignon, F. Current Progress in Rheology of Cellulose Nanofibril Suspensions. *Biomacromolecules* **17**, 2311–2320 (2016).
96. Martoïa, F. *et al.* Heterogeneous flow kinematics of cellulose nanofibril suspensions under shear. *Soft Matter* **11**, 4742–4755 (2015).
97. Fall, A. B., Lindström, S. B., Sprakel, J. & Wågberg, L. A physical cross-linking process of cellulose nanofibril gels with shear-controlled fibril orientation. *Soft Matter* **9**, 1852–1863 (2013).
98. Faddoul, R., Reverdy-Bruas, N. & Blayo, A. Formulation and screen printing of water based conductive flake silver pastes onto green ceramic tapes for electronic applications. *Materials Science and Engineering: B* **177**, 1053–1066 (2012).
99. Elen, K. *et al.* Screen-printing of flexible semi-transparent electrodes and devices based on silver nanowire networks. *Nanotechnology* **29**, 425201 (2018).
100. Lok, C.-N. *et al.* Proteomic Analysis of the Mode of Antibacterial Action of Silver Nanoparticles. *J. Proteome Res.* **5**, 916–924 (2006).
101. Rajesh, S., Dharanishanthi, V. & Kanna, A. V. Antibacterial mechanism of biogenic silver nanoparticles of Lactobacillus acidophilus. *Journal of Experimental Nanoscience* **10**, 1143–1152 (2015).
102. Yang, W. *et al.* Food storage material silver nanoparticles interfere with DNA replication fidelity and bind with DNA. *Nanotechnology* **20**, 085102 (2009).
103. Rinna, A. *et al.* Effect of silver nanoparticles on mitogen-activated protein kinases activation: role of reactive oxygen species and implication in DNA damage. *Mutagenesis* **30**, 59–66 (2015).
104. Xu, H. *et al.* Role of reactive oxygen species in the antibacterial mechanism of silver nanoparticles on Escherichia coli O157:H7. *BioMetals* **25**, 45–53 (2012).
105. Long, Y.-M. *et al.* Surface ligand controls silver ion release of nanosilver and its antibacterial activity against Escherichia coli. *IJN* **Volume 12**, 3193–3206 (2017).
106. Helmlinger, J. *et al.* Silver nanoparticles with different size and shape: equal cytotoxicity, but different antibacterial effects. *RSC Adv.* **6**, 18490–18501 (2016).
107. *Commission Regulation (EC) No 450/2009 of 29 May 2009 on active and intelligent materials and articles intended to come into contact with food (Text with EEA relevance)*. *OJ L* vol. 135 (2009).
108. *Regulation (EC) No 1935/2004 of the European Parliament and of the Council of 27 October 2004 on materials and articles intended to come into contact with food and repealing Directives 80/590/EEC and 89/109/EEC*. *OJ L* vol. 338 (2004).
109. Azlin-Hasim, S. *et al.* The Potential Application of Antimicrobial Silver Polyvinyl Chloride Nanocomposite Films to Extend the Shelf-Life of Chicken Breast Fillets. *Food Bioprocess Technol* **9**, 1661–1673 (2016).
110. Deng, J. *et al.* Nano-silver-containing polyvinyl alcohol composite film for grape fresh-keeping. http://www.ingentaconnect.com/content/asp/me/2019/00000009/00000009/art00001;jsessionid=1ipaax7v6kirq.x-ic-live-02 (2019) doi:info:doi/10.1166/mex.2019.1592.

111. Motlagh, N. V., Mosavian, M. T. H. & Mortazavi, S. A. Effect of Polyethylene Packaging Modified with Silver Particles on the Microbial, Sensory and Appearance of Dried Barberry. *Packaging Technology and Science* **26**, 39–49 (2013).

112. Panea, B., Ripoll, G., González, J., Fernández-Cuello, Á. & Albertí, P. Effect of nanocomposite packaging containing different proportions of ZnO and Ag on chicken breast meat quality. *Journal of Food Engineering* **123**, 104–112 (2014).

113. Silva, F. M., Pinto, R. J. B., Daniel-da-Silva, A. L. & Trindade, T. Cationic release behaviour of antimicrobial cellulose/silver nanocomposites. *Cellulose* **21**, 3551–3560 (2014).

114. Li, J. *et al.* Controlled Release and Long-Term Antibacterial Activity of Dialdehyde Nanofibrillated Cellulose/Silver Nanoparticle Composites. *ACS Sustainable Chem. Eng.* **7**, 1146–1158 (2019).

115. Xiong, R., Lu, C., Wang, Y., Zhou, Z. & Zhang, X. Nanofibrillated cellulose as the support and reductant for the facile synthesis of Fe3O4/Ag nanocomposites with catalytic and antibacterial activity. *J. Mater. Chem. A* **1**, 14910–14918 (2013).

116. Yu, Z. *et al.* Antimicrobial effect and toxicity of cellulose nanofibril/silver nanoparticle nanocomposites prepared by an ultraviolet irradiation method. *Colloids and Surfaces B: Biointerfaces* **180**, 212–220 (2019).

117. Gogoi, B., Barua, S., Sarmah, J. K. & Karak, N. In situ synthesis of a microbial fouling resistant, nanofibrillar cellulose-hyperbranched epoxy composite for advanced coating applications. *Progress in Organic Coatings* **124**, 224–231 (2018).

118. Scientific Opinion on the safety evaluation of the substance, silver zeolite A (silver zinc sodium ammonium alumino silicate), silver content 2 – 5 %, for use in food contact materials. *EFSA Journal* **9**, 1999 (2011).

119. Greulich, C. *et al.* The toxic effect of silver ions and silver nanoparticles towards bacteria and human cells occurs in the same concentration range. *RSC Adv.* **2**, 6981–6987 (2012).

120. Errokh, A., Magnin, A., Putaux, J.-L. & Boufi, S. Hybrid nanocellulose decorated with silver nanoparticles as reinforcing filler with antibacterial properties. *Materials Science and Engineering: C* **105**, 110044 (2019).

Chapter III

Intelligent sensors based on Metal Organic Frameworks for packaging applications

Table of content – Chapter III

Introduction to Chapter III

Chapter I presented a detailed literature review on the different Active and Intelligent packaging solutions currently existing. The **Chapter II** discussed an antibacterial active packaging system whereas **Chapter III** is focused on the development of smart sensors for intelligent packaging application. The gas sensors were developed based on a combination of active materials such as Metal Organic Frameworks (MOF) and conductive carbon compounds. The key challenges in the studies reported in this chapter were to prepare sensors using the described materials and to investigate their performances for gas sensing applications.

Section **III-1** details the preparation of resistive ammonia sensors using copper benzene-1,3,5-tricarboxylate (CuBTC) MOF associated with conductive carbon-graphene ink. Thus, inks with different compositions were formulated and deposited on polyethylene terephthalate flexible polymeric substrate, carrying screen printed silver interdigitated electrodes. The relationship between formulation composition, electrical, morphological and chemical properties were first investigated. Secondly, the gas sensing performances of the devices were assessed (response, sensitivity, characteristic times, etc.) and its mechanism researched using spectroscopic methods.

Section **III-2** researched how the optimised formulation stated in Section **III-1** could be adapted for a different gas target application. The prepared sensors were tested as humidity sensors using different experimental setups, and their performances compared to the carbon-graphene only control.

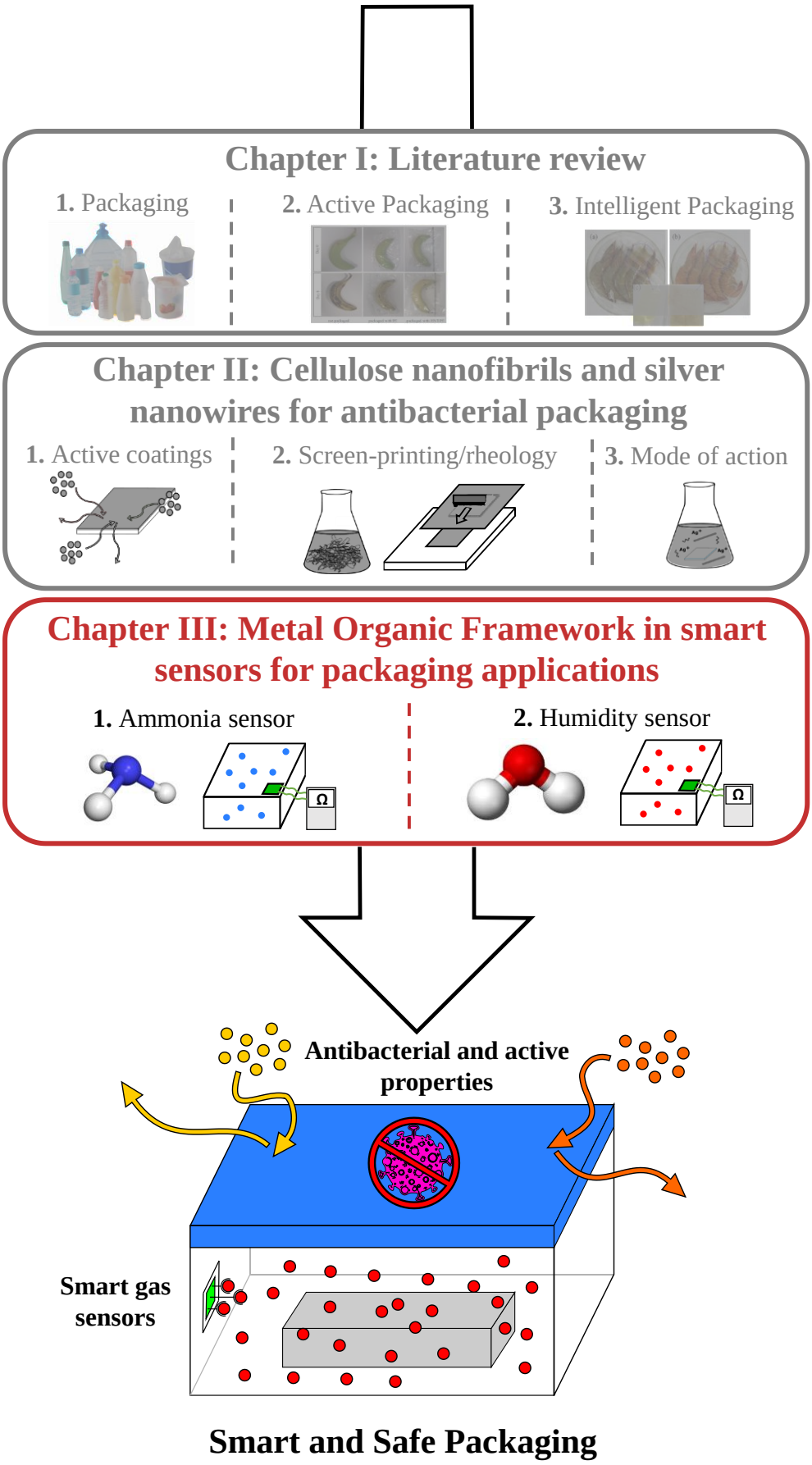

Smart and Safe Packaging

1. Ammonia sensors based on Metal Organic Framework on flexible substrate

This section is adapted from Hugo Spieser, Zari Tehrani, Muhammad Ali, Ehsaneh Daghigh Ahmadi, Aurore Denneulin, Julien Bras, Davide Deganello, David Gethin. Metal Organic Framework sensors on flexible substrate for ammonia sensing application at room temperature, submitted in Journal of Materials Chemistry C (2020).

Abstract:

The application of sensitive gas sensors manufactured in high volume at low cost has great interest due to an extensive array of potential applications. Such areas include industrial processing, biotechnology and intelligent food packaging. This work reports a straightforward and versatile technique using screen-printing and drop-casting processes, to produce gas sensors on a flexible plastic substrate, based on a combination of metal organic framework and graphene-carbon materials. We demonstrate a sensitive and stable ammonia sensor (4.6% maximal response) over a range from 20 to 100 ppm. The response and sensitivity of the optimized formulation are respectively 36 and 45 times higher than a carbon-graphene only sensor and makes the developed devices suitable for intelligent packaging. The sensors production process is fast, reliable and low-cost and so there is a strong potential for the process principles to be adapted industrially for a different gas target or application.

Keywords:

gas sensor, ammonia detection, metal organic framework, screen-printing, conductive carbon, low-cost manufacturing

1.1. Introduction

The capability to adsorb, separate or sense gas molecules in our environment remains nowadays a great challenge in several fields of applications to tackle social issues such as greenhouse gas emission or human health and safety. Different 3D porous materials have been investigated for gas sensor applications, including Metal Organic Frameworks (MOFs). MOFs are crystalline and microporous materials based on the coordination of metallic centres with organic ligands[1]. They display very large surface areas, high porosity and offer almost infinite possibilities in terms of designing and building architecture[2].

Electrical gas sensors based on MOFs technology are mainly prepared either using in-situ growing of MOF crystals onto electrodes[3,4], by preparing pressed pellets[5–7] or by coating a MOF slurry onto electrodes with different processes such as spin-coating, drop-casting, or even screen printing[8–10]. However, despite MOFs promising gas adsorption properties, a lot of application in electronics are still challenging due to their poor conductivity[11]. Indeed, MOFs are mainly described as insulators and their conductivity is usually lower than 10^{-10} $S.cm^{-1}$ as they do not present any low energy charge transport pathway. To solve this issue, MOFs can be mixed and used along with conducting nano- or micro-materials and especially conductive carbon materials as shown recently[12].

Up to now, the reported sensing target gases for such MOFs/micro- and nano-carbon composites are different volatile organic compounds (VOCs), hydrogen, or ammonia. Fardindoost et al. (2017) researched a combination of graphene oxide and cobalt-base MOF produced by in-situ synthesis for promising selective hydrogen sensing[13]. Different VOC sensing was conducted recently by Jafari et al. (2019) using Zeolitic Imidazolate Framework-8 (ZIF-8) and ZIF-67 MOF with carbon nanotubes and silver nanoparticles[14]. Several studies also reported the use of MOF-derived oxides along with nano-carbon materials for acetone, ethanol or sulphur dioxide sensing[15–18]. The different MOF derived-oxides tested showed sensitive, selective, fast, and stable sensing characteristics.

Ammonia is an industrial by-product and is a toxic gas even at very low concentration and thus there is a need for efficient ammonia sensors. Travlou et al. (2015) was the first group to report resistance change ammonia sensing featuring a combination of graphene derivatives and MOF[19]. Copper benzene-1,3,5-tricarboxylate (abbreviated CuBTC or HKUST-1 with BTC being 1,3,5-benzenetricarboxylate ligand) MOF was synthesised in-situ with aminated-graphite oxide, processed into the slurry in dimethylformamide (DMF) and blade-spread on gold interdigitated electrodes (IDE). The prepared sensors were working at room temperature, with a 100-500 ppm sensing range and 4.0% response at 100 ppm. A similar system was investigated by Yin et al. (2018)[20] but using reduced graphene oxide (rGO) coated with polypyrrole nanofiber (PPy–rGO). After in-situ synthesis of CuBTC with PPy–rGO, the composite was

prepared into the ink in DMF and drop coated on Indium tin oxide (ITO) substrate. The sensors displayed selective (compared to hydrogen sulphur, ethanol, hydrogen, methane, acetone) and reversible sensing range from 10 to 150 ppm at room temperature with 12.4% response for 50 ppm ammonia concentration. Bhardwaj et al. (2018) also took advantages of adding a conductive polymer into MOF/graphene derivative systems and prepared a three-component composite with rGO, silica coated CuBTC and polyaniline (PANI)[21]. CuBTC was prepared in situ with tetraethyl orthosilicate to form silica coated CuBTC particles to improve aqueous stability, mixed with rGO and aniline was finally polymerised in-situ with the rGO/silica coated CuBTC mixture. The sensors were prepared by drop-casting ethanol slurry onto a 4-probe chromium electrode. The performances of the sensors at room temperature were found to be very interesting with a low detection limit (1 ppm) and a strong gas response (10% at 1 ppm) for a 1-100 ppm linear window. Finally, Ko et al. (2017) investigated sensors based on graphite and different hexahydroxytriphenylene (HHTP) derived MOFs, achieving response around 4% at 80 ppm with a 5-80 ppm linear range[22]. The innovation of their research was the sensor production process which was mechanical abrasion on a paper substrate. **Table III-1** summarises a global literature review concerning MOFs and ammonia sensing, including MOF/graphene derivatives combination.

The MOF/micro- and nano-carbon systems investigated in the literature requires in-situ and complex chemical synthesis[19–21], or use MOFs that are not commercially available[22]. A significant research challenge using these MOF/micro- and nano-carbon systems, is the development of facile and straightforward preparation of sensors, with strong sensing characteristics (sensitivity, selectivity, stability, fast response and recovery). In this work, a composite CuBTC/carbon-graphene ink was prepared by simple mixing of the commercially supplied components, and requires no small batch complex chemical synthesis. This straightforward preparation from the particulate supplied active materials has significant benefits in terms of industrialisation up-scaling or commercialisation. Moreover, it provided the opportunity to prepare the devices on a flexible polymer substrate. Only a few recent examples (2019) in the literature has reported the use of flexible polymer substrates for electrical gas sensors based on MOF materials, and none for the detection of ammonia[14,17].

Inks with different ratios of CuBTC/carbon-graphene were formulated and drop-casted on screen-printed silver interdigitated electrodes. The surface properties of the sensors were investigated as well as their electrical gas sensing (sensitivity, stability, kinetics) capability using a custom-built gas rig capable of achieving controlled gas concentration down to ppm levels[23]. Finally, an investigation of the surface chemical properties of the devices was also performed before and after exposure to ammonia to provide insight into the sensing mechanisms.

***Table III-1**: Literature review of ammonia sensing technology based on MOF: preparation, performances and operating parameters (IDE=interdigitated electrode, RT=room temperature, RH=relative humidity, N/A=not applicable)*

Sensor material	Sensing type	Device preparation (substrate)	Response (%, ppm)	Response calculation	Concentration range (ppm)	Response time/Recovery time (min)	Operating conditions	Commercial materials/ commercially available	Reference
MOF									
$Cu_3(HITP)_2$	Conductance	Drop-casting suspension on Au IDE (ceramic)	0.81%/5 ppm 0.87%/5 ppm 0.70%/5 ppm 0.70%/5 ppm	$100*\Delta G/G_0$	0.5-10	N/A	RT/dry N_2 RT/dry air RT/N_2 60%RH RT/air 60%RH	No/No	Campbell et al. 2015[24]
ZnO/ZIF-8 ZnO/ZIF-71	Conductance	Direct solvothermal growth (ceramic)	37%/100 ppm 35%/100 ppm	$100*\Delta I/I_0$	10-200	N/A	250°C/dry air	No/Yes	Zhou et al. 2018[25]
$Cu_3(HHTP)_2$	Resistive	Spray layer-by-layer on Au IDE (glass)	129%/100 ppm	$100*\Delta R/R_0$	1-100	1.36/9.11	RT/dry air	No/No	Yao et al. 2017[26]
SNNU-88	Resistive	Direct solvothermal growth on Ag-Pd IDE (ceramic)	2.3/50 ppm	R_0/R	5–100	1.45/2.12	25°C/air	No/No	Li et al. 2018[27]
ZIF8 Zn(INA) Zn(NA)	Resistive	Drop-casting suspension (glass)	9/100 ppm 139/100 ppm 220/100 ppm	R_0/R	10-100	1.12/0.9 1.5/2.35 0.77/3.33	RT/dry air	No/Partially	Mohan et al. 2020[28]
Cu-TCPP on Cu-HHTP Zn-TCPP on Cu-HHTP	Resistive	Layer by layer spray on Au IDE (sapphire)	230%/100 ppm 70%/100 ppm	$100*\Delta R/R_0$	1-100	N/A N/A	RT/dry air	No/No	Yao et al. 2019[29]
NiPc-Cu NiPc-Ni	Resistive	Drop-casting suspension on Au IDE (glass)	30%/80 ppm 14.5%/80 ppm	$100*\Delta G/G_0$	2-80	N/A	RT/dry N_2	No/No	Meng et al. 2019[30]
$Ba(o\text{-}CbPhH_2IDC)(H_2O)_4]_n$	Impedance	Pressed pellets	27%/25 ppm 148%/25 ppm 198%/25 ppm 243%/25 ppm	$100*\Delta Z/Z_0$	5-25	8/N/A 10/N/A 12/N/A 13/N/A	30°C/air 75%RH 30°C/air 85%RH 30°C/air 93%RH 30°C/air 98%RH	No/No	Guo et al. 2018[31]
$\{Na[Cd(MIDC)]\}_n$	Impedance	Pressed pellets	363%/30 ppm 662%/30 ppm 1379%/30 ppm	$100*\Delta Z/Z_0$	0.05 -30	N/A N/A N/A	25°C/air 68%RH 25°C/air 85%RH 25°C/air 98%RH	No/No	Liu et al. 2018[32]
$[Cu(p\text{-}IPhHIDC)]_n$	Impedance	Pressed pellets	8620%/130 ppm 3900%/130 ppm 3231%/130 ppm 1824%/130 ppm 569%/130 ppm 484%/130 ppm	$100*\Delta Z/Z_0$	2-130	N/A N/A N/A N/A N/A N/A	25°C/air 68%RH 40°C/air 68%RH 25°C/air 85%RH 40°C/air 85%RH 25°C/air 98%RH 40°C/air 98%RH	No/No	Sun et al. 2018[33]

(Continued)

***Table III-1**: Continued*

Sensor material	Sensing type	Device preparation (substrate)	Response (%, ppm)	Response calculation	Concentration range (ppm)	Response time/Recovery time (min)	Operating conditions	Commercial materials/ commercially available	Reference
NDC-Y-fcu-MOF	Capacitive	Direct solvothermal growth on Au IDE (silicon wafer)	25%/100 ppm	10^{-4}*100*ΔC/C	1-100	4.17/N/A	RT/dry N_2	No/No	Assen et al. 2017[34]
Eu^{3+}@Ga(OH)bpydc	luminescence	Suspension spin coating (quartz)	0.33/100 ppm	$1-I/I_0$	10-500	N/A	RT/NH_3 [aq] vapor	No/No	Hoa et Yan. 2016[35]
MIL-124@Eu3+	luminescence	Direct solvothermal growth (ceramic)	0.07/100 ppm	$1-I/I_0$	100-1350	N/A	0-60°C/air 0-100%RH	No/No	Zhang et al. 2017[36]
FJU-56	Absorbance	MOF powder	1.051/10 ppm	A/A_0	0-10	N/A	RT/NH_3 [aq] vapor	No/No	Zhang et al. 2018[37]
ZA-MPTMS-Eu-UiO-67	Fluorescence	Suspension precipitation (glass)	0.73/80 ppm	I/I_0	40-200	N/A	RT/ NH_3 [aq] vapor	No/No	Ma et Yan 2019[38]
MR-MOF-Eu	Fluorescence	MOF deposition (glass)	0.75/100 ppm	I/I_0	50-300	N/A	30C°C/NH_3 [aq] vapor	No/No	Mal et al. 2020[39]
MOF/Graphene									
CuBTC/graphite oxide	Resistive	Coating suspension on Au IDE (ceramic)	4/100 ppm	R/R_0	100-500	N/A	RT/dry air	No/Yes	Travlou et al. 2015[19]
SiO_2 coated Cu-BTC/rGO/Pani	Resistive	Drop-casting suspension on 4 probe Cr electrode (not supplied)	144%/100 ppm	$100*\Delta R/R_0$	1-100	0.58/0.28	RT/NH_3 [aq] vapor	No/Yes	Bhardwaj et al. 2018[21]
CuBTC/PPy–rGO	Resistive	Drop-casting suspension between copper foil strips (ITO)	12.4%/50 ppm	$100*\Delta R/R_0$	10-150	0.22/0.27	25°C/air 50%RH	No/Yes	Yin et al. 2018[20]
Graphite/$Cu_3(HHTP)_2$ Graphite/$Co_3(HHTP)_2$ Graphite/$Fe_3(HHTP)_2$ Graphite/$Ni_3(HHTP)_2$	Conductance	Abrasion on Au IDE (paper)	4.6%/80 ppm 4.2%/80 ppm 4.0%/80 ppm 2.9%/80 ppm	$-100*\Delta G/G_0$	5-80	N/A N/A N/A	RT/dry N_2	No/No	Ko et al. 2017[22]

1.2. Materials and methods

1.2.1. Materials

For a substrate, 175 µm Melinex ® 339 polyester film was purchased from DuPont Teijin Films (USA), the AST 6025 silver ink and the C2171023D1 carbon-graphene ink from Sun Chemicals (USA), the copper benzene-1,3,5-tricarboxylate (CuBTC) Metal Organic Framework (MOF) from MOF Technologies (UK) having a BET surface area of 1781 $m^2.g^{-1}$ and mean pore diameter of 1.5069 nm as supplied by the manufacturer and analytical reagent grade n-butyl acetate from Fisher Scientific (UK). The materials were used as received.

1.2.2. Gas sensor fabrication

The gas sensors were prepared in three different steps (**Figure III-1**). First interdigitated electrodes (IDE) were prepared using the screen-printing process and a silver paste. Then, an active ink was prepared by the combination of CuBTC Metal Organic Framework and carbon-graphene materials dispersed in butyl acetate solvent. Finally, the active ink was drop-casted on the interdigitated electrodes and oven-dried.

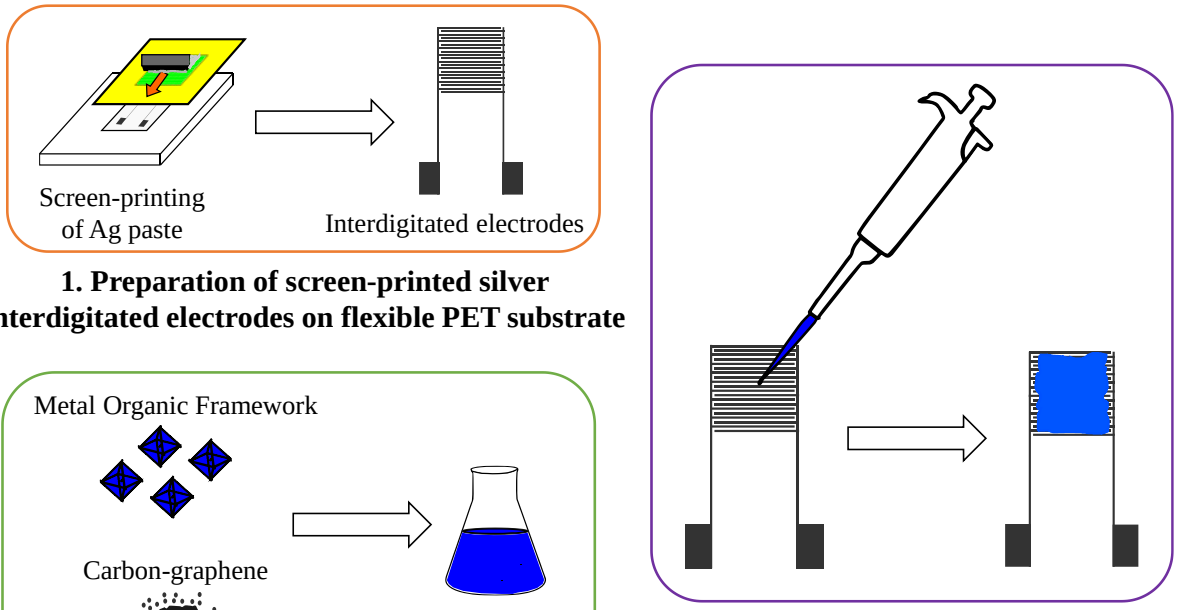

***Figure III-1**: Schematic representation of the preparation of the gas sensors in several steps*

1. Fabrication of electrode by screen-printing

An interdigitated electrode (IDE) design was used to optimise the total conductive sensing surface[40,41], and the design is shown in **Figure III-2**.

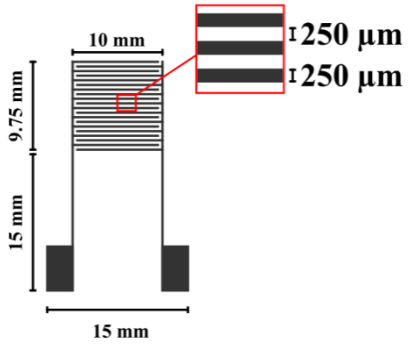

***Figure III-2**: Schematic representation of the interdigitated design and associated metrics*

The silver IDEs were printed using an R29 series screen printer from Reprint using the following parameters: 50 $mm.s^{-1}$ forward speed, 10 $mm.s^{-1}$ reverse speed, 5.0 kg front squeegee pressure and 2.0 mm print gap. The printed IDEs were oven-dried for 30 min at 100°C. Polyester screen with a 120-34 mesh was used and based on its specification (**Table III-2**), the expected target wet thickness was 15 µm. The screen printing process was chosen because of the high reproducibility and manufacturing scale-up potential for printed electronics applications[42,43].

***Table III-2**: Summary of screen specifications used for screen-printing of the interdigitated electrode*

Mesh count (threads per cm)	120
Wire diameter (µm)	34
Emulsion over mesh (OEM) thickness (µm)	12
Screen angle (°)	22.5

2. Ink formulation

Inks suitable for drop casting were prepared by weighing the desired mass of the two components and mixing them in butyl acetate solvent to reach the final desired concentration. A vortex mixing technique at room temperature was used three times for 30 s because it was found to visually disperse the materials properly to make the ink for deposition. All of the inks were based on a 200 $mg.ml^{-1}$ concentration of MOF with the corresponding dry carbon-graphene (35% mass content commercial ink) mass added to reach inks with different ratios. The first control ink (MOF only) was prepared by dispersing 200 $mg.ml^{-1}$ of MOF dry powder in butyl acetate with the same mixing procedure and the second control ink (carbon-graphene

only) was prepared by dispersing 54 mg.ml^{-1} dry of the commercial ink in butyl acetate. Within this work, the sensors produced are referred to as PGrCuBTC X with X as the dry mass percentage of graphene in the ink, for instance: PGrCuBTC 21.25 is the ink with 21.25%wt carbon-graphene/78.75%wt MOF. The composition of each ink is detailed in **Table III-3**.

***Table III-3**: Summary of the composition of the different CuBTC/carbon-graphene ink formulations for 1 ml of butyl acetate solvent*

Formulation name (PGrCuBTC) %	Carbon-Graphene dry (mg)	CuBTC MOF (mg)
0 (control): CuBTC	0	200
20	50.0	200
21.25	54.0	200
22.5	58.1	200
25	66.7	200
30	85.7	200
50	200.0	200
100 (control): carbon-graphene	54.0	0

3. Deposition of active material on the electrode

8 µl of the ink formulated was drop-casted on the printed IDE with a micropipette, aiming to cover the electrodes completely, followed by oven-drying at 100°C for 30 min. At least four devices using the same ink formulation were prepared. The deposited mass was measured and average is presented with standard deviation (**Table III-4**).

***Table III-4**: Mass (mg) of CuBTC/carbon graphene ink deposited on screen printed IDE for each formulation (NM=not measurable)*

Formulation name (PGrCuBTC) %	Mass of ink drop-cast (mg)
0 (control): CuBTC	1.70 ± 0.53
20	1.65 ± 0.21
21.25	2.37 ± 0.42
22.5	1.77 ± 0.32
25	1.85 ± 0.50
30	1.30 ± 0.34
50	1.90 ± 0.90
100 (control): carbon-graphene	NM

The quantity of ink deposited on the electrodes is relatively similar for each formulation and with expected standard deviation considering the small amount deposited and the manual drop-casting deposition technique.

1.2.3. Characterisation techniques

The pristine IDE was characterised using a White light Interferometer Veeco Wyco NT9300 at ×5 magnification and 736 × 480 pixels resolution with a 1.2 mm × 0.93 mm measured area. The thickness was measured by the difference between the substrate while excluding the print edges. At least 20 different samples were tested with four measurements on each, and the average results along with standard deviation are summarised in **Table III-5**. The obtained thickness is close to the target (15 µm), and the lines show very good consistency: the deviation from the target geometry is a well-known characteristic of the process that may be compensated for if necessary[44].

***Table III-5**: Summary of the pristine IDE morphology parameters measured by White Light Interferometry*

Digit thickness (µm)	Digit widths (µm)	Interspacing (µm)
14.7 ± 1.1	275.6 ± 19.0	227.0 ± 19.3

The same measurement parameters were used to investigate the drop-casted layers and the thicknesses were measured by the difference between substrate and deposited layer measured between the silver lines. The average surface roughness (Sa) of the samples was also measured at three different locations on the drop cast surface and four different sensors were tested. The average is presented along with the standard deviation in **Table III-7** and discussed in the Results and Discussions section.

X-ray diffraction (XRD) spectra were obtained on a Bruker D8 Discover apparatus equipped with Cu source (α=1.5406 Å). A Kratos Axis Supra XPS equipped with an Al Kα X-Ray monochromatic source was used to conduct the X-ray photoelectron spectroscopy (XPS) experiments at 15 mA emission current, with a pass energy of 20 eV.

Scanning electron microscopy (SEM) pictures were recorded on a Hitachi S4800 with 2.5 kV acceleration voltage, 20 µA emission current and a working distance of 11.9 mm. The atomic force microscopy (AFM) experiments were performed on a JPK NanoWizards II equipment (Dimension-3100 Multimode) from Bruker. A non-contact AFM tip (radius 8 nm) was used at 320 Hz using a spring constant of 40 N/m on AC mode. The SEM equipment coupled with an Energy Dispersive X-Ray analyzer (EDX) X-MAX 50mm² from Oxford Instrument to measure the atomic weight distribution (%) for each element was used, and the measurements were

performed on images taken at the same parameters settings as the SEM imaging above with 120 s collection.

Fourier-transform infrared (FTIR) measurements were conducted at room temperature on Bruker Alpha P equipment using Universal attenuated total reflectance (ATR) detector from 400 to 4000 cm^{-1} at a 2 cm^{-1} resolution and a total of 16 accumulated scans. Three spectra were recorded for each reference at different locations on the sample, to assess reproducibility. The Raman measurements were performed on a Renishaw apparatus coupled with a 532 nm wavelength excitation laser at 0.03 mW power and acquisition time of 20 s for PGrCuBTC 0 and PGrCuBTC 21.25 at 0.15 mW power and acquisition time of 10 s for PGrCuBTC 100. Three spectra were recorded for each reference at different locations on the sample, to assess reproducibility. For both FTIR and Raman measurements, no baseline correction and no normalisation was conducted, but the different spectra were shifted along the Y-axis to facilitate the reading and interpretation.

Current-voltage (I/V) curves were recorded using a two-probe SemiProbe I/V (SemiProbe MA-8005 manipulator) connected to a 2612B Keithley source meter: a sweeping mode from -1.0 to 1.0 volts with 100 measurements point was used and the source limit and source range was adjusted between 10 µA and 1 A depending on the devices. The resistance was calculated by measuring the corresponding I/V curve slope. At least five devices were tested and average is presented with corresponding standard deviation.

The gas sensing experiments were conducted at room temperature (ca. 20-22°C) and under dry conditions, and using pure Nitrogen 293679-L (>99.9995%) and pure Oxygen 284915-V (>99.999%) from BOC as carrier gas, mixed with a ratio 4:1 to model air composition independently of the total flow rate used. 298610-AK-B dry ammonia (H_20 < 200 ppm according to manufacturer) from BOC was used as the gas target. The gas sensing system was built up using Sandvik 3R60 tubes with 6.25 × 0.89 mm 1/4" ×20 dimensions and a flow chart of the whole system is displayed in **Figure III-3a**. The gas bottles were connected to ASCO (UK) SCG256B404VMS solenoid valves in order to close and open the desired section of the system. The lines were then connected to GFC17 mass flow controller (MFC) from Aalborg in order to control the desired flow of gas inside the lines. The different lines then meet in the gas chamber and the gases are extracted through an exhaust line. In order to prepare the printed sensors for the gas sensing experiments, the following procedure was conducted. Crocodile clip connectors 65801-005LF from Farnell were clipped through the printed silver pads on the devices. Classic electrical wires were soldered onto in the crocodile clips and the other end was soldered on the metal connection of the feedthrough. Pictures of the prepared devices can be seen in **Figure III-3b**. The sensor was placed in the gas flow and connected via the feedthrough to a Keithley 6487 meter which measure the resistance set to a resolution of 0.01 Ohm. The system is fully automated and it is possible to program different sensing steps and to control

the following parameters: opening and closing of the relays, flow rate of the MFC and acquisition time.

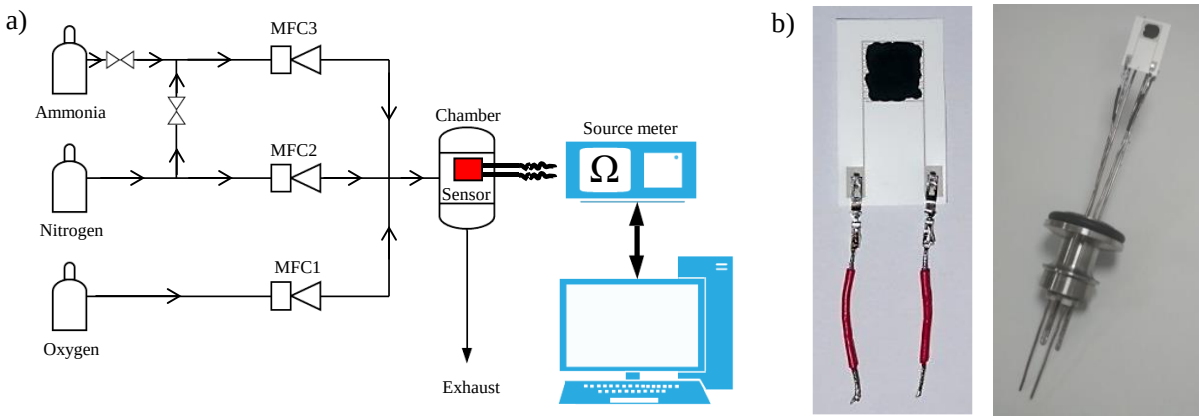

***Figure III-3**: Gas sensing system with a) schematic flow chart system of the custom-built gas rig and b) Picture of the printed sensors with connection for gas sensing (crocodile clips and soldered electrical wires) and the whole system soldered on the gas chamber feedthrough*

Only the response to dry ammonia concentration was investigated under dry atmosphere and the tests were carried out with two different sets of parameters (high and low range) to fit the linear range of the sensors. For both sets of parameters, acquisition time was set at 1 s. The sensors were first flashed with a stabilisation step to stabilise their resistance under dry airflow and then successively exposed to dry ammonia and dry air with an increasing ammonia concentration. The different parameters used are summarised in **Table III-6**.

***Table III-6**: Summary of the experimental parameters used during the gas sensing tests*

	Concentration (ppm)	**Increment (ppm)**	**Steps time in/out (min)**	**Total flow (sccm)**	**Stabilisation step time/flow (min/sccm)**
High range	50-500	50	60/60	200	120/1000
Low range	20-100	20	30/30	1000	60/1000

The sensors response (%) was calculated for each step of the experiment using Equation **III-1**:

$$Response\ (\%) = 100 \times \frac{R_p - R_0}{R_0} \quad \textbf{(III-1)}$$

Where R_0 (Ω) is the resistance of the device at the beginning of ammonia input for the desired step and R_p (Ω) is the resistance of the device on the plateau (averaged for 600 s for the High range and 300 s for the Low range). For each step, the response time (s) was calculated as the time during the NH_3 input to reach 90% of the plateau resistance and recovery time (s) as the time during the NH_3 output necessary to recover 90% of the baseline resistance value. Finally,

the sensitivity of the sensor was defined by the slope of the response (%)/concentration (ppm) calculated by the linear fitting. At least two sensors from each formulation were tested and the average along with standard deviation is presented.

1.3. Results and discussions

1.3.1. Characterisation of carbon-graphene electrode with CuBTC (PGrCuBTC)

1. Surface topography and electrical properties

Different ink formulations were prepared and drop-casted on the screen-printed silver interdigitated electrodes. Within this work, the ratio between CuBTC and carbon-graphene component was varied and the sensors produced are referred as PGrCuBTC X with X the mass percentage of graphene in the ink, for instance: PGrCuBTC 21.25 is the ink with 21.25%wt carbon-graphene/78.75%wt MOF. The drop-casting process is straightforward and was used because of the small volume necessary for the formulation and thus the economy of materials. A typical example of the prepared devices can be seen in **Figure III-4a** along with a display of the flexibility of the sensor (**Figure III-4b**).

a) b)

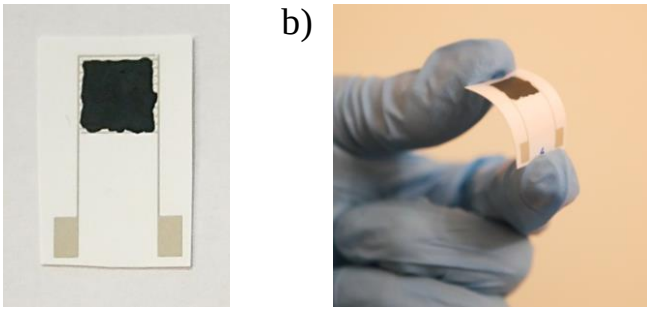

Figure III-4*: Representation of the prepared devices with a) picture of one PGrCuBTC sensor prepared by drop-casting CuBTC/carbon-graphene ink on silver interdigitated electrode b) evidence of device flexibility*

The thickness and the surface roughness of the sensors was then measured (**Table III-7**).

***Table III-7**: Summary of the thickness (µm) and surface roughness (Sa, µm) measured by White Light Interferometry for the different sensors prepared*

Formulation name (PGrCuBTC) %	Electrode thickness (µm)	Electrode roughness (Sa, µm)
0 (control): CuBTC	45.79 ± 2.56	15.68 ± 3.16
20	32.62 ± 0.90	10.47 ± 2.26
21.25	31.95 ± 3.04	9.25 ± 1.95
22.5	36.19 ± 5.64	12.58 ± 3.48
25	27.15 ± 6.99	6.01 ± 2.16
30	34.94 ± 5.91	7.09 ± 3.55
50	24.82 ± 10.18	8.27 ± 4.62
100 (control): carbon-graphene	3.05 ± 0.28	4.62 ± 0.46

PGrCuBTC 0 (only CuBTC) displays the largest thickness and roughness and an increasing quantity of carbon-graphene in the ink formulation reduces the thickness and also the roughness. The mechanisms that influence this are not clear, but it could be suggested based on previous work that adding carbon-graphene into the formulation reduces the CuBTC aggregation because of enhanced dispersive forces[45] and so leading to a reduced thickness and roughness. However, as shown in **Figure III-6c**, PGrCuBTC 21.25 retains some elements of surface roughness when compared with PGrCuBTC 100 and this is important in sensing application as it effectively increases the surface area available for sensing. The measured roughness is relatively high compared to the measured thickness which could indicate that the dispersion of the materials on the surface of the IDE is not optimal and especially of micro-sized CuBTC crystals, probably because of the drop-casting process.

The carbon-graphene added into the formulation is necessary to confer conductivity to the deposited layer, because of the insulating nature of the CuBTC. The ratio of the raw materials in the ink was then modified to optimise the electric properties of the sensors as a compromise between the absorption capability of the MOF and layer conductivity to detect the change in electrical signal of the CuBTC layer when exposed to the target. The resistance of the sensors was measured and found to be strongly formulation dependent (**Figure III-5a**). Beyond 50% wt of carbon-graphene in the formulation, the resistance of the devices is around 6-7 Ω and does not vary with the concentration attributed to saturation of the percolating network formed by the carbon-graphene content. Also, the sensors are not conductive below 20% wt of carbon-graphene (>50 MΩ) which is now attributed to the concentration being below the percolation threshold. Surprisingly, the evolution of resistance is not linear and the resistance change is significant at the carbon-graphene concentration in the 21.25-25% wt range. Indeed, the

resistance of PGrCuBTC 21.25 is 68 times higher than PGrCuBTC 22.5. Also, the lower the concentration of carbon-graphene inside the ink, the more difficult it is to prepare sensors in a reproducible manner due to high sensitivity of resistance to carbon-graphene content. PGrCuBTC 21.25 was then chosen to be most appropriate because of the lower content of carbon-graphene within the ink while retaining a measurable conductivity i.e the carbon-graphene does not mask the MOF detection capability. The dispersion of the raw materials could also play a role in the electrical properties of the sensors. Finally, the current/voltage curve of PGrCuBTC 21.25 shows its ideal resistor behaviour makes it fit for reliable sensing independently of the voltage applied (**Figure III-5b**).

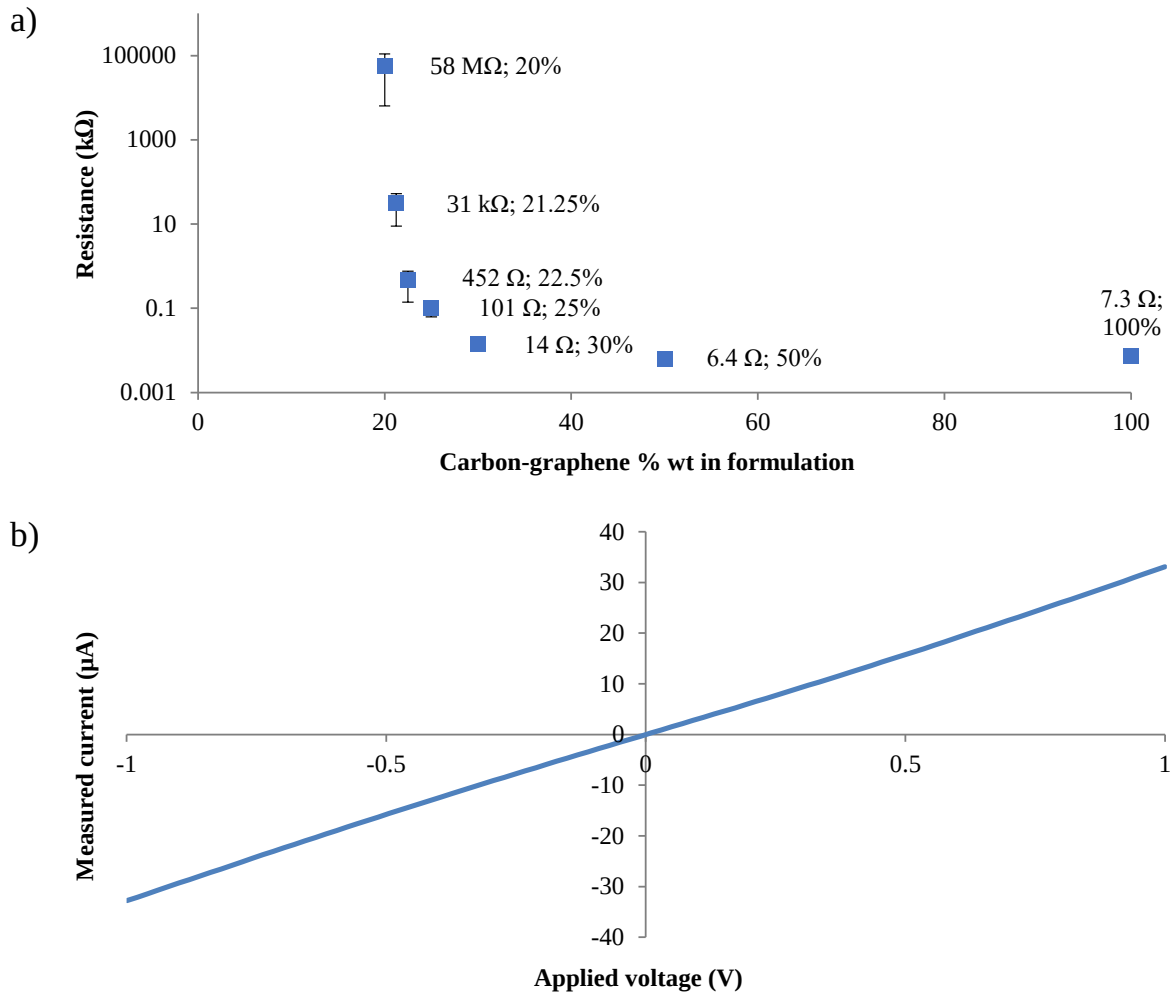

***Figure III-5**: Electrical properties of the sensors with a) resistance (Ω) of the sensors compared to the mass percentage of carbon-graphene in the ink formulation and b) Current/Voltage curve of PGrCuBTC 21.25*

2. Microscale topography

On the Scanning Electron Microscope (SEM) images of the surface of PGrCuBTC 21.25, it is possible to distinguish the population of CuBTC crystals due to their distinctive shape (**Figure III-6a**). **Figure III-6b** shows a zoomed in view of one specific crystal sitting on the graphitic

platelet, confirming the spatial interaction between the two materials. The surface of the controls and PGrCuBTC 21.25 were also imaged by Atomic Force Microscopy (AFM) and for PGrCuBTC 0 (MOF only), it appears random and heterogeneous (**Figure III-6c**). This might be due to some CuBTC aggregation that leads to a more heterogeneous surface. The surface of PGrCuBTC 100 also appears rough but with a small maximum height due to the small size of the carbon particles. On the other hand, the surface of PGrCuBTC 21.25 is smoother with a higher maximum height compared to PGrCuBTC 100. This is consistent with the addition of micro-particles such as MOF crystallites.

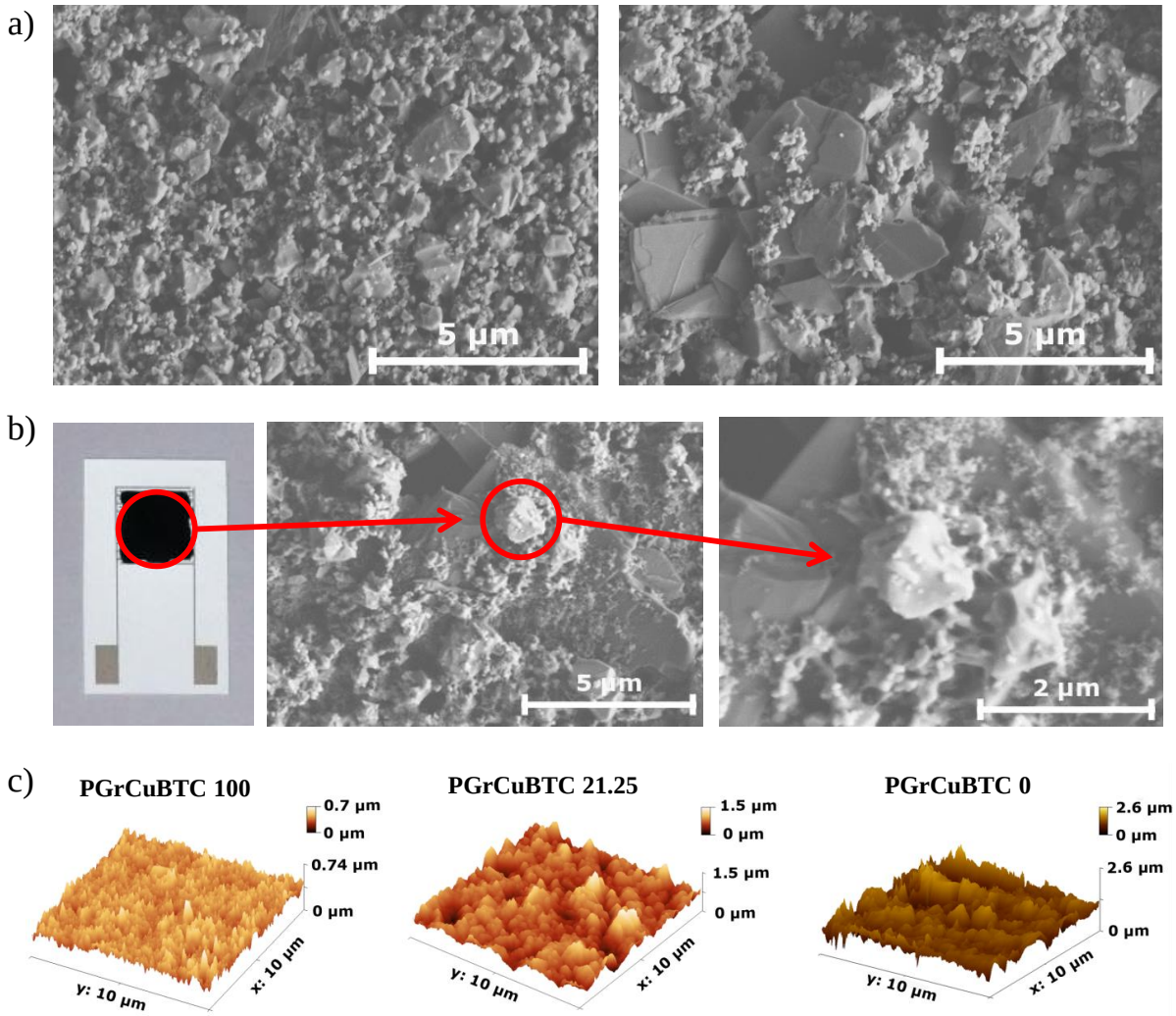

***Figure III-6**: Surface topography of the prepared sensors with a) SEM picture of the surface of PGrCuBTC 21.25, b) SEM picture of the surface of PGrCuBTC 21.25 with zoom on one CuBTC crystallite and c) AFM images of the surface of PGrCuBTC 0, PGrCuBTC 21.25 and PGrCuBTC 100*

3. Surface chemistry

X-ray Diffraction (XRD) was performed on the surface of the PGrCuBTC 0 and PGrCuBTC 21.25 (**Figure III-7**). The characteristic peaks of CuBTC at small angle can be seen on PGrCuBTC 0 in the 6-18° region as described in the literature[46–48] which indicates that

dispersing CuBTC into butyl acetate and drop-casting on the screen-printed silver IDE does not impact its crystallinity. Moreover, the spectrum of PGrCuBTC 21.25 is similar to PGrCuBTC 0 which also indicates that mixing with the carbon-graphene component does not alter the crystallinity of the MOF. This proves that the crystalline structure of the CuBTC, which is a key factor for its gas sensing properties, is not affected by the sensor preparation.

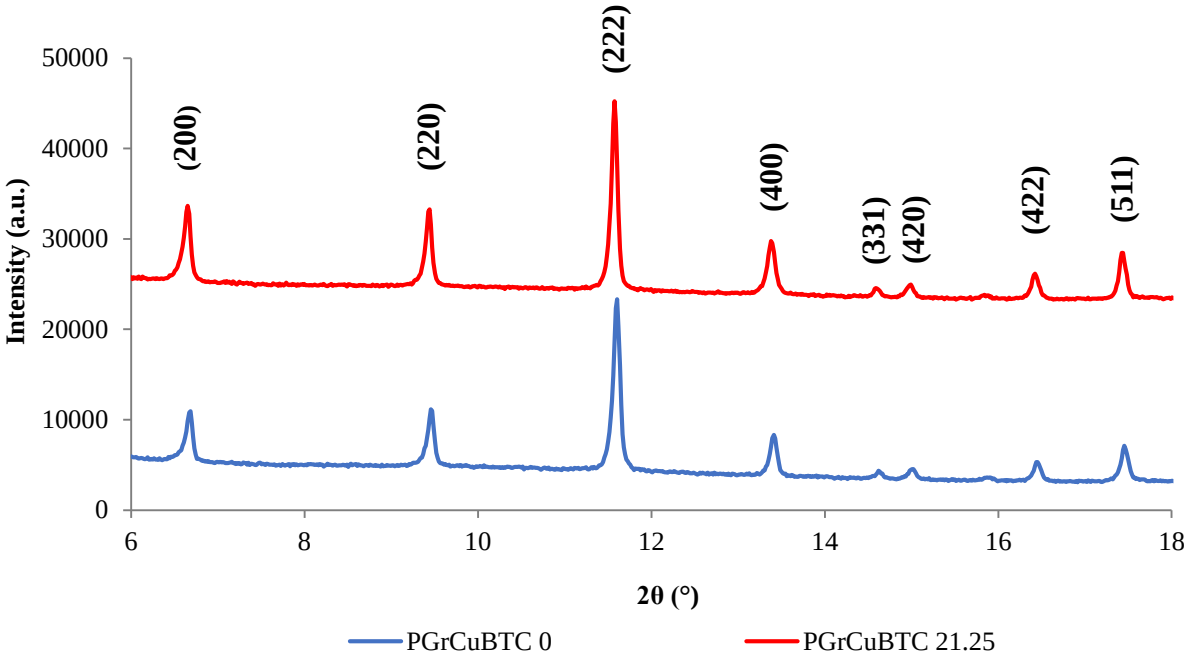

***Figure III-7**: X-ray Diffraction of the surface of PGrCuBTC 0 and 21.25*

The surface chemistry of the devices was then investigated using first Fourier-transform infrared (FTIR), Raman spectroscopy and SEM coupled with an Energy Dispersive X-Ray (SEM-EDX) mapping measurements (**Figure III-8** and **Figure III-9**). Concerning FTIR results (**Figure III-8a**), the PGrCuBTC 0 display the classic peaks of CuBTC[49–51]: the Cu-O stretching band at 490 cm^{-1}, the aromatic C-H (out of plane) deformation bands at 730 cm^{-1} and 761 cm^{-1}, the C-H aromatic stretching band at 1112 cm^{-1}, the COO symmetric stretching band at 1372 cm^{-1}, and the corresponding asymmetric bands at 1448 cm^{-1} and 1648 cm^{-1}. The peaks at 1709 cm^{-1}, 1280 cm^{-1} and the slight shoulder at 1618 cm^{-1} and 1254 cm^{-1} could indicate the presence of a small quantity of free benzene-1,3,5-tricarboxylic acid ligand[52,53]. As expected only small and not well-defined signals can be seen on the PGrCuBTC 100 spectrum as carbon and graphene materials have high refractive index which is relatively close to the diamond value thus making ATR FTIR difficult[54]. The PGrCuBTC 21.25 spectrum is the superposition of the PGrCuBTC 0 and PGrCuBTC 100 spectra in proportions, confirming the proper mixing and dispersion of the materials at the surface of the devices. On the Raman spectra of PGrCuBTC 0, the following CuBTC characteristic peaks can be noted (**Figure III-8b**)[55,56]: the Cu-Cu dimer stretching band at 177 cm^{-1}, the Cu-O stretching bands at 283 cm^{-1}, 449 cm^{-1} and 507 cm^{-1}, the

aromatic C-H out of place deformation bands at 746 cm^{-1} and 829 cm^{-1}, the C=C aromatic stretching bands at 1009 cm^{-1}, 1549 cm^{-1}, and 1618 cm^{-1}, the COO symmetric stretching at 1391 cm^{-1} and the corresponding asymmetric band at 1468 cm^{-1}. For the PGrCuBTC 100 sample, the 1360 cm^{-1} band can be attributed to the D band, the 1575 cm^{-1} to the G band and the slight shoulder on the latter to the D' band. Finally, a small 2D band can be found at 2710 cm^{-1}. The obtained spectrum is typical of a mixture of carbon and graphene materials[57,58]. As for the FTIR spectra, the PGrCuBTC 21.25 is the superposition of the PGrCuBTC 0 and 100; leading to the same conclusion.

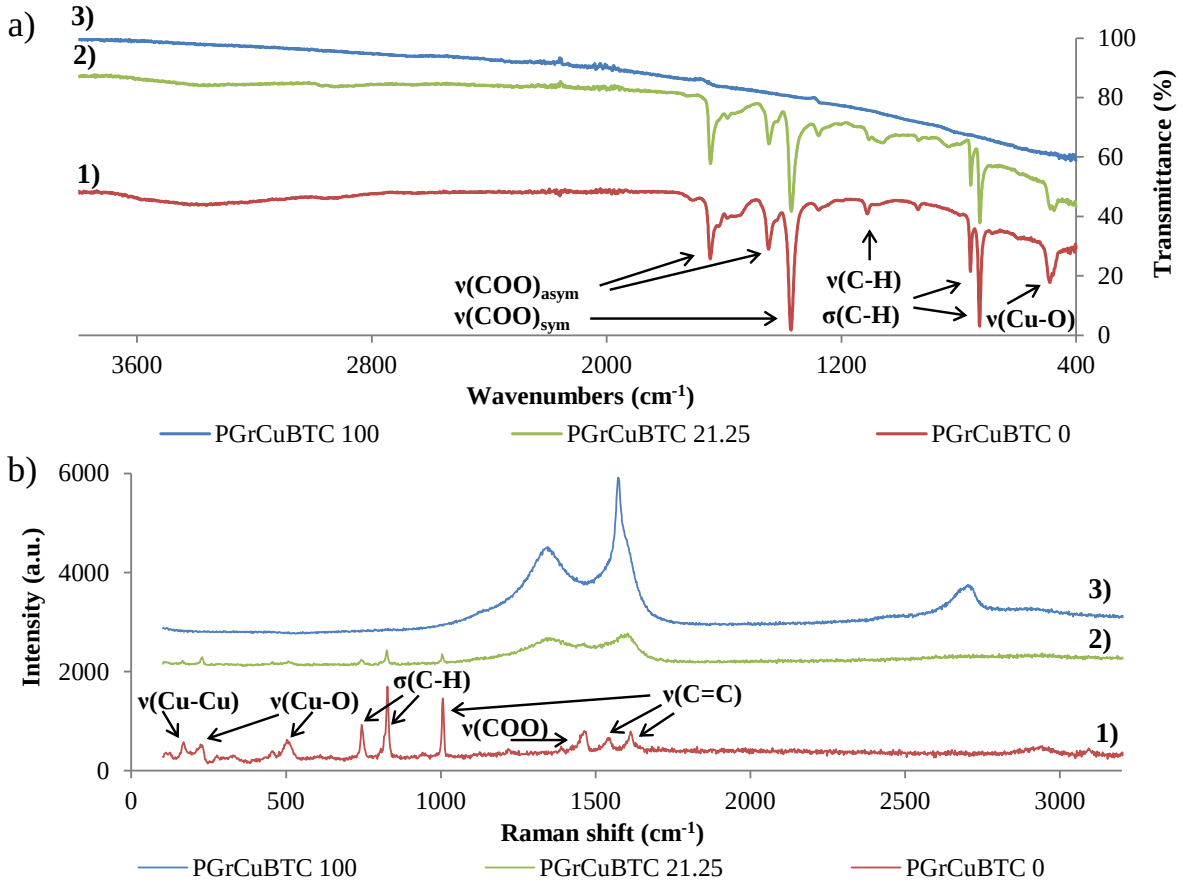

***Figure III-8**: Surface chemistry investigation of the produced sensors with a) FTIR spectra of the PGrCuBTC 0 (1), 21.25 (2) and 100 (3) samples, b) Raman spectra of the PGrCuBTC 0 (1), 21.25 (2) and 100 (3) samples*

The SEM-EDX mapping indicates that the different elements are relatively well dispersed in the scanned areas, which tend to suggest that the CuBTC is well dispersed at the surface of the devices. An example for PGrCuBTC 21.25 is provided in **Figure III-9a**, **b, c** and **d**. The SEM-EDX mapping was also performed for the sensors prepared with the different formulations (**Figure III-9e)**. The surface atomic weight (%) measured by SEM-EDX for carbon, oxygen and copper elements was found to be formulation dependent, showing that as expected, the formulation impacts the surface chemical properties of the devices. The linear correlation between the surface atomic weight (%) and the ink formulation shows the good dispersion of

the ink components during the formulation and deposition on the electrodes, as well as the reproducibility of the device's preparation.

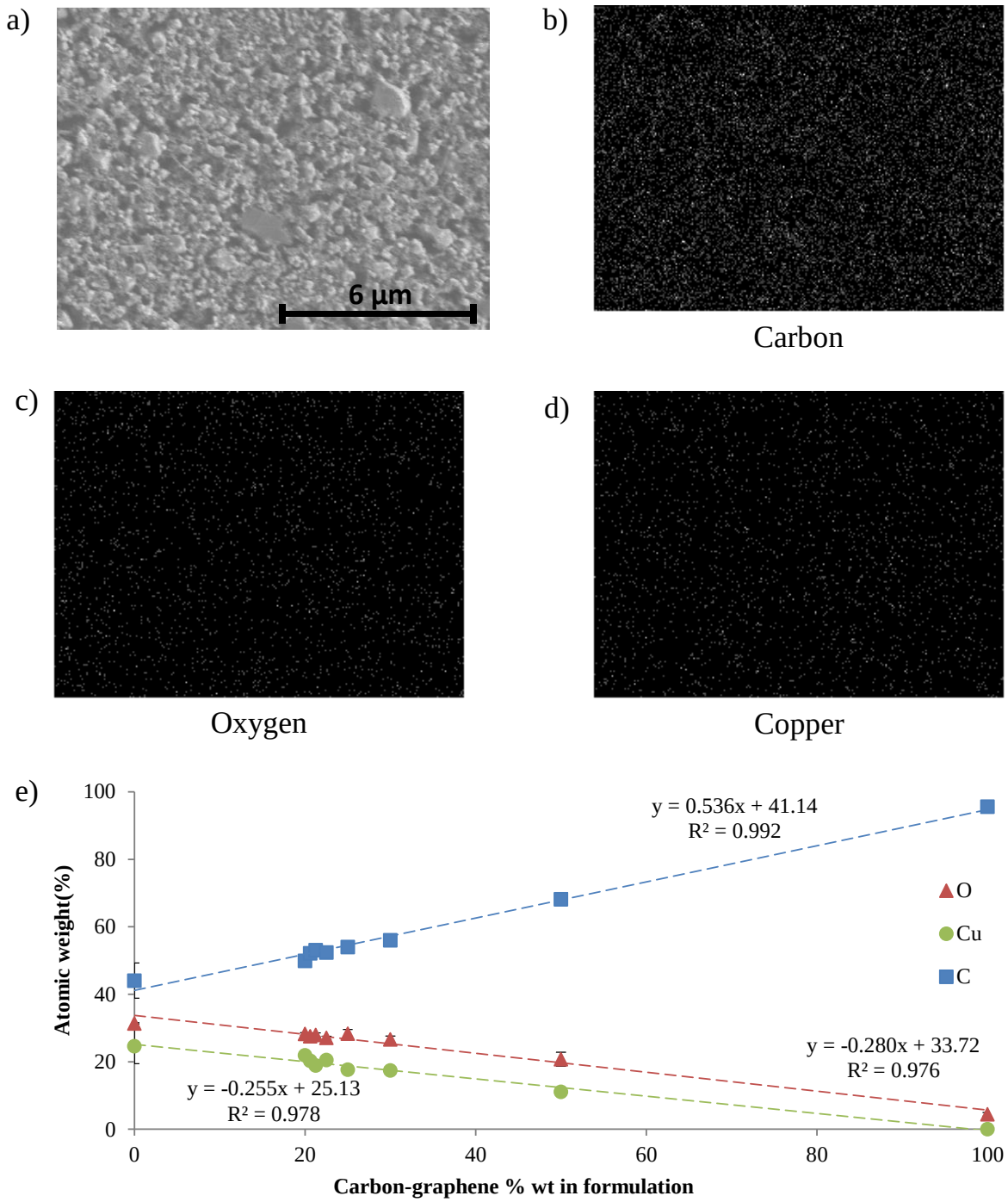

***Figure III-9**: SEM-EDX of the surface of PGrCuBTC 21.25 with a) corresponding SEM image, b) mapping for carbon, c) mapping for oxygen, d) mapping for copper and e) mapping for the devices prepared with the different formulation, with extracted atomic weight (%) of the carbon, oxygen and copper elements drawn against the carbon-graphene % wt in the ink formulation*

To confirm this trend, X-ray photoelectron spectroscopy (XPS) experiments were also performed on PGrCuBTC 0, 21.25 and 100. The survey scans are available in **Figure III-10** and the atomic regions in **Figure III-11**.

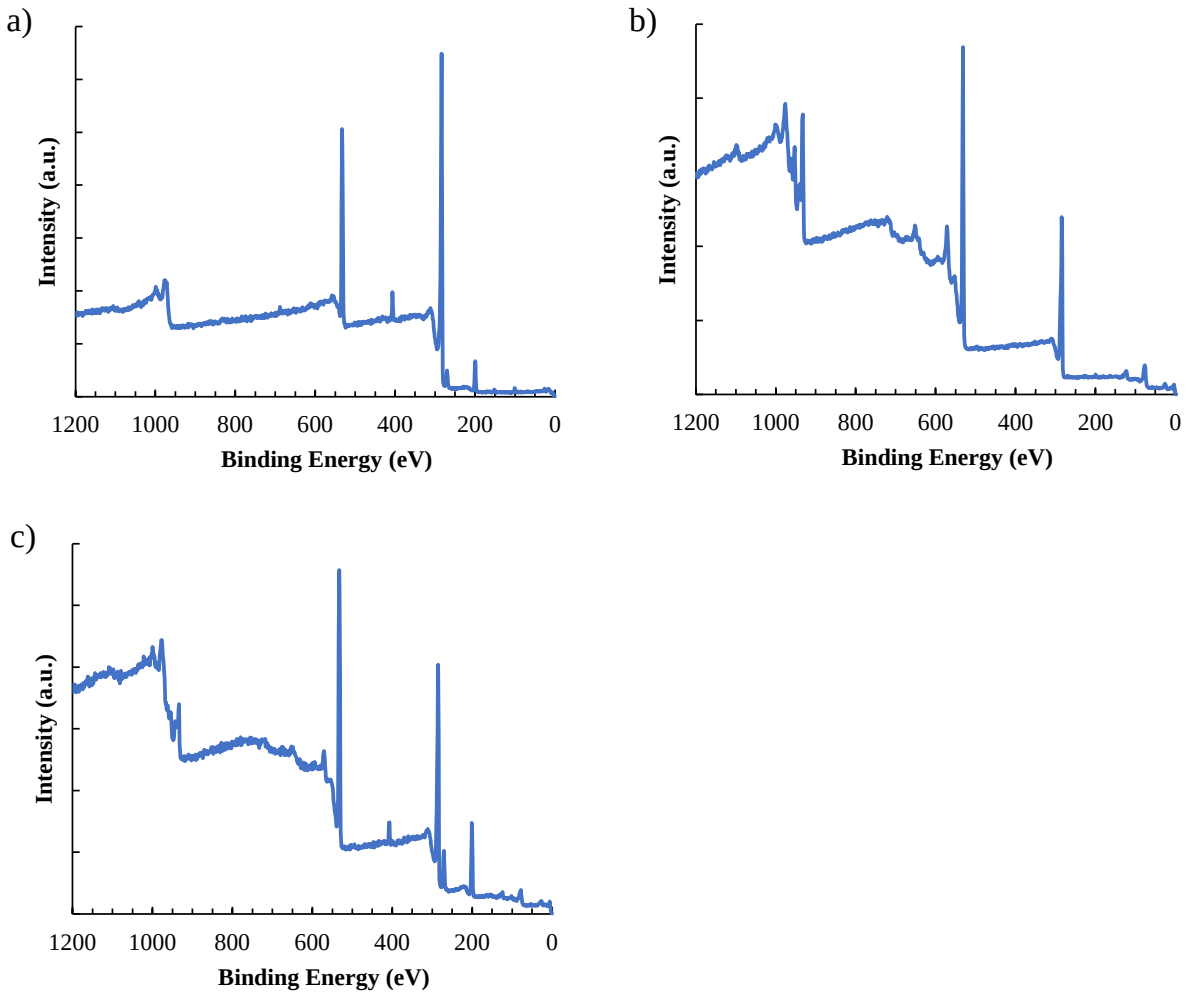

***Figure III-10**: Survey scans of X-ray photoelectron spectroscopy of a) PGrCuBTC 100, b) PGrCuBTC 0 and c) PGrCuBTC 21.25*

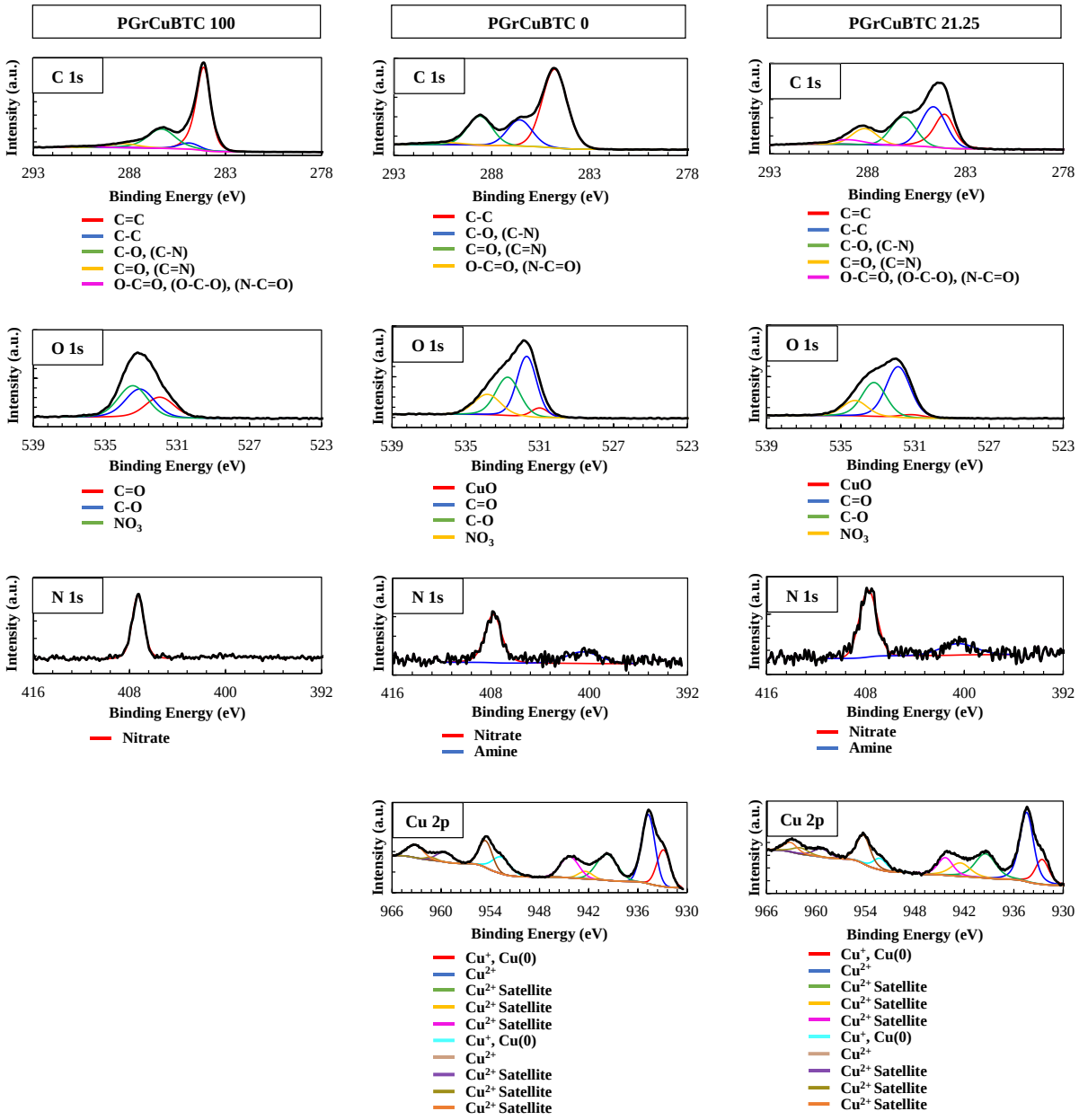

***Figure III-11**: Atomic regions of X-ray photoelectron spectroscopy of PGrCuBTC 100, 0 and 21.25 with the detected atoms, the measured response and fitting of the attributed peaks*

The elemental concentration for each device matches the expected elements, meaning mainly carbon and oxygen for PGrCuBTC 100, and carbon, oxygen and copper for PGrCuBTC 0 and 21.25 (**Table III-8**). A relatively low amount of chlorine was found in all samples which was attributed to environment contamination whereas residual nitrogen was attributed to additives present in the carbon-graphene materials[59] and residual nitrate from CuBTC synthesis.

***Table III-8**: Elemental concentration (atomic %) measured by X-ray photoelectron spectroscopy (XPS) for PGrCuBTC 100, 0 and 21.25*

Sample name	Element	Atomic Concentration (%)
PGrCuBTC 100	O 1s	17.48 ± 0.14
	N 1s	2.02 ± 0.08
	C 1s	78.33 ± 0.16
	Cl 2p	2.17 ± 0.02
PGrCuBTC 0	Cu 2p	6.18 ± 0.04
	O 1s	33.73 ± 0.14
	N 1s	1.33 ± 0.21
	C 1s	58.58 ± 0.18
	Cl 2p	0.18 ± 0.04
PGrCuBTC 21.25	Cu 2p	2.48 ± 0.03
	O 1s	27.50 ± 0.14
	N 1s	1.02 ± 0.19
	C 1s	66.54 ± 0.20
	Cl 2p	2.46 ± 0.04

PGrCuBTC 100 spectra fit well with the corresponding literature and especially in the C1s spectra: C-C (59.58%), C=C (6.55%), C=O (26.85%), C-O (5.38%) and O-C=O (1.64%) peaks respectively at 284.09, 284.89, 286.3, 288.28 and 290.4 eV, are common attribution for graphene and carbon materials[59–62]. These are reflected in the O1s spectra as C=O (25.76%) and C-O (35.35) peaks respectively present at 531.98 and 533.08 eV and a peak at 533.47 was attributed to the NO_3 (38.88%) bond relative to the nitrocellulose additive in the commercial ink[63]. In the C1s region of the PGrCuBTC 0, C-C (57.32%), C-O (19.12%) and C=O (21.09%) peaks respectively at 284.79, 286.57 and 288.61 eV are the main attributions for CuBTC materials as described previously[64,65]. A smaller peak relative to O-C=O (2.47%) bond can be found at 290.59 eV which could be attributed to a low amount of free BTC ligand[66]. In the O1s spectra, the C-O (32.80%) and C=O (42.41%) peaks (respectively 532.73 and 531.70 eV) match the C1s spectra whereas a NO_3 (19.02%) was found at 533.83 eV, associated with nitrate-based impurities. Finally, a small peak at 531.00 eV attributed to the CuO (5.77%) bond showed that the CuBTC contains impurities linked to its synthesis which is further confirmed by the presence of nitrate peak (68.24%) in the N1s spectra at 407.81 eV[67]. The Cu 2p region is also in accordance with literature, showing mainly Cu(II) peaks at 934.73 and 954.57 eV

N(respectively 26.35% and 10.08%) and minor presence of Cu(0) and Cu(I) at 932.88 and 952.67 eV (respectively 14.01 and 8.63%)[68,69]. The detailed peaks attribution, binding energy and atomic concentration can be found in the **Table III-9**, **Table III-10** and **Table III-11**.

***Table III-9**: Peak attribution, corresponding bonding energy position (eV) and atomic concentration (%) measured by X-ray photoelectron spectroscopy for PGrCuBTC 100*

PGrCuBTC 100			
Element	**Component**	**Binding Energy Position (eV)**	**Atomic Conc. (%)**
C1s	C=C	284.09	59.58
	C-C	284.89	6.55
	C-O, (C-N)	286.33	26.85
	C=O, (C=N)	288.28	5.38
	O-C=O, (O-C-O), (N-C=O)	290.40	1.64
N1s	Nitrate	407.29	100.00
O1s	C=O	531.98	25.76
	C-O	533.08	35.35
	NO_3	533.47	38.88

***Table III-10**: Peak attribution and corresponding bonding energy position (eV) and atomic concentration (%) measured by X-ray photoelectron spectroscopy (XPS) for PGrCuBTC 0*

PGrCuBTC 0			
Element	**Component**	**Binding Energy Position (eV)**	**Atomic Conc. (%)**
C1s	C-C	284.79	57.32
	C-O, (C-N)	286.57	19.12
	C=O, (C=N)	288.61	21.09
	O-C=O, (N-C=O)	290.59	2.47
N1s	Nitrate	407.81	68.24
	Amine	400.53	31.76
O1s	CuO	531.00	5.77
	C=O	531.70	42.41
	C-O	532.73	32.80
	NO_3	533.83	19.02
Cu 2p	Cu^+, Cu(0)	932.88	14.01
	Cu^{2+}	934.73	26.35
	Cu^{2+} Satellite	939.77	15.53
	Cu^{2+} Satellite	942.41	3.01
	Cu^{2+} Satellite	944.32	11.00
	Cu^+, Cu(0)	952.67	8.63
	Cu^{2+}	954.57	10.08
	Cu^{2+} Satellite	959.57	4.57
	Cu^{2+} Satellite	961.22	0.88
	Cu^{2+} Satellite	963.16	5.94

***Table III-11**: Peak attribution and corresponding bonding energy position (eV) and atomic concentration (%) measured by X-ray photoelectron spectroscopy (XPS) for PGrCuBTC 21.25*

PGrCuBTC 21.25			
Element	**Component**	**Binding Energy Position (eV)**	**Atomic Conc. (%)**
C1s	C=C	284.00	24.73
	C-C	284.63	33.40
	C-O, (C-N)	286.17	23.59
	C=O, (C=N)	288.15	13.23
	O-C=O, (O-C-O), (N-C=O)	289.03	5.05
N1s	Nitrate	407.78	74.36
	Amine	400.52	25.64
O1s	CuO	531.17	3.25
	C=O	531.90	49.19
	C-O	533.21	32.80
	NO_3	534.23	14.76
Cu 2p	Cu^+, Cu(0)	932.56	10.60
	Cu^{2+}	934.45	29.47
	Cu^{2+} Satellite	939.43	15.54
	Cu^{2+} Satellite	942.50	8.23
	Cu^{2+} Satellite	944.31	8.22
	Cu^+, Cu(0)	952.23	4.87
	Cu^{2+}	954.23	12.05
	Cu^{2+} Satellite	959.33	4.09
	Cu^{2+} Satellite	961.90	3.02
	Cu^{2+} Satellite	963.10	3.93

Finally, the PGrCuBTC 21.25 spectra for all detected elements are in accordance with the mixing of both CuBTC 0 and 100 with the applied ratio. The XPS experiments proved the presence and chemical structure of the expected carbon-graphene and CuBTC materials corresponding to relevant literature, as well as suggesting the uniform distribution of the raw materials at the surface of the electrodes.

To summarise this section, it was first found that adding more carbon-graphene materials to the CuBTC materials reduces the thickness and roughness of the produced sensors, probably because it improves the dispersion of CuBTC and thus reducing aggregation of crystals. The electrical properties of the devices were then found to be highly formulation-dependent and PGrCuBTC 21.25 was chosen as the optimised formulation because of the lowest carbon-graphene content while being still conductive enough for reliable measurements. For this formulation, SEM imaging showed the interaction of CuBTC crystal with carbon-graphene materials and AFM measurements confirmed the macro-scale morphological investigation. XRD experiments also showed that the crystalline structure of CuBTC was retained through the formulation and deposition on the substrate. The surface chemistry of the sensors was investigated and using SEM-EDX mapping, the atomic weight (%) of carbon, oxygen and copper was found to be linearly correlated with the composition of the formulation which means that the dispersion of the materials is good. FTIR and Raman spectroscopy showed that PGrCuBTC 21.25 spectra are the superposition of PGrCuBTC 0 and 100 spectra adding further confirmation that there is proper dispersion and good mixing between the two components. Finally, XPS experiments also proved that the chemical structure of the sensors is correlated with the materials used in accordance with appropriate literature.

1.3.2. Gas sensing

The different sensors produced were tested against ammonia sensing in dry conditions, initially from 50 to 500 ppm (high range). A typical example of the change of resistance of the sensors with the increasing input of ammonia for PGrCuBTC 25 can be found in **Figure III-12a**. As an example, the resistance for this device switched from around 91.5Ω when stabilized under the carrier gas mixture, to around 92.7Ω when exposed to 500 ppm of ammonia. **Figure III-12b** also shows that the response for each step is nonlinear with the ammonia concentration. The PGrCuBTC 21.25 displayed a higher standard deviation than the other devices (small standard deviations, not visible on the graph). Moreover, the difference in response comparing PGrCuBTC 21.25 and PGrCuBTC 22.5 is significant, which could be explain by a similar argument than for their electrical properties: the PGrCuBTC 21.25 reached the percolation threshold of the carbon-graphene materials, thus enabling a better charge transport and so a higher measured response. This graph can be differentiated into two sections having a breakpoint at 150 ppm, which suggests the saturation of the sensors. That is why the responses of the sensors were investigated in more details over the range 20-100 ppm (low range) and an example result is presented for PGrCuBTC 25 in **Figure III-12c**. The slight difference is response at 100 ppm for the two ranges could be explained by the significant change in the flow rate used. The PGrCuBTC 25, 22.5 and 21.25 all displayed good linear fitting in the 40-100 ppm range (**Figure III-12d**). Surprisingly PGrCuBTC 21.25 is the only sensor to achieve good sensing at 20 ppm. PGrCuBTC 50 displayed no proper response because of the resistance

stabilization due to carbon content being more dominant than the sensing response attributable to the MOF. The sensing results for each sensor are summarised in **Table III-12**, for parameters including sensitivity (%.ppm^{-1}), and response (%) at 100 ppm and the coefficient of determination for linear fit from either 20 to 100 ppm for PGrCuBC 21.25 and 40 to 100 ppm for all other sensors.

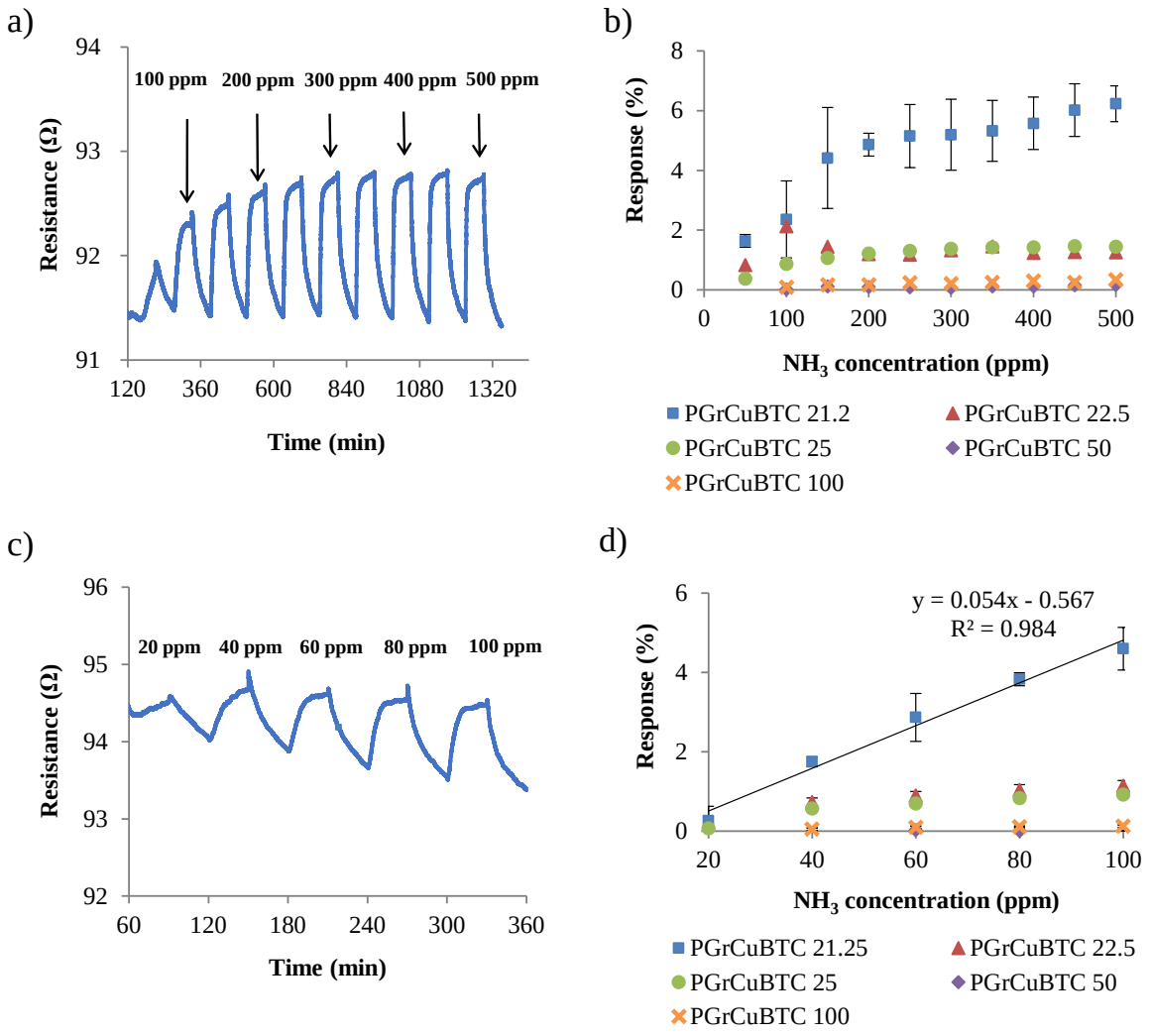

***Figure III-12**: Gas sensing experiments with a) example of results of PGrCuBTC 25 (resistance vs time) for the high range (50-500 ppm NH_3), b) summary of the response (%) for the different sensors for the high range (50-500 ppm NH_3), c) example of results of PGrCuBTC 25 (resistance vs time) for the low range (20-100 ppm NH_3) and d) summary of the response (%) for the different sensors for the low range (20-100 ppm NH_3)*

***Table III-12**: Summary of the sensing parameters for all PGrCuBTC sensors for the 20-100 ppm range*

Formulation name PGrCuBTC	**21.25**	**22.5**	**25**	**50**	**100 (control)**
Sensitivity (%.ppm^{-1})	**0.0538**	0.0068	0.0060	-	0.0012
Coefficient of determination R^2	**0.984**	0.993	0.993	-	0.912
Response at 100 ppm (%)	**4.60 ± 0.54**	1.14 ± 0.14	0.92 ± 0.1	-	0.12 ± 0.03

PGrCuBTC 21.25 displayed the highest response (4.6%) and compared with PGrCuBTC 100 (only carbon-graphene), this is 36 times higher at 100 ppm, proving that the CuBTC is responsible for the gas sensing properties. Moreover, PGrCUBTC 21.25 shows a sensitivity of 0.054 %.ppm^{-1}, which is 45 times more than for PGrCuBTC 100. Only a small change can be seen between the performances of PGrCUBTC 22.5 and PGrCUBTC 25. The sensors characteristic times (response and recovery) were also extracted from the gas sensing results and are summarised in **Figure III-13**, but the graphs only show PGrCuBTC 21.25, PGrCuBTC 22.5 and PGrCuBTC 25 because PGrCuBTC 50 and 100 results were found to be erratic.

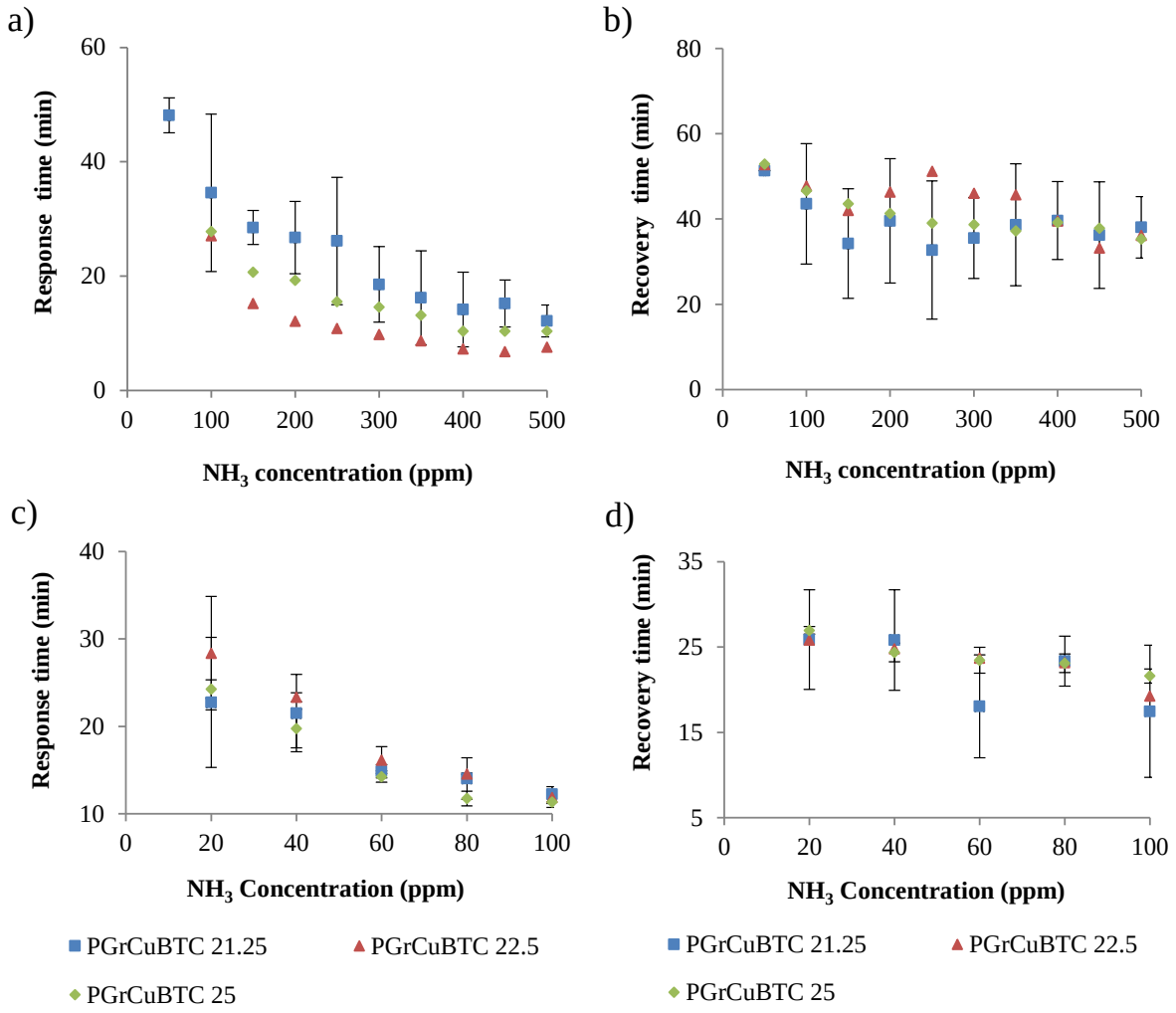

***Figure III-13**: Sensing kinetics of the PGrCuBTC 21.25, 22.5 and 25 sensors with a) response time (min) for the high range (50-500 ppm NH_3), b) recovery time (min) for the high range (50-500 ppm NH_3), c) response time (min) for the low range (20-100 ppm NH_3) and d) recovery time (min) for the low range (20-100 ppm NH_3)*

For all sensors, recovery and response times are lower for the low range because of the increased flow rate during the experiments. The recovery time is nearly independent of the concentration of gas and is relatively similar for each sensor for either the low or high range. The response time, however, is concentration dependent: the higher the concentration, the lower the response time, and this is true for all PGrCuBTC 21.25, 22.5 and 25 sensors. Similar results have been reported and attributed to enhanced diffusion and reaction rate at higher gas concentration[70–72]. Finally, the stability of the sensor was also evaluated by investigating PGrCuBTC 21.25 response after five successive cycles at 500 ppm, and the result is displayed in **Figure III-14**. The tested sensor was stable over 5 cycles with only a 7% response loss which could be due to irreversible ammonia adsorption or residual humidity in the sensor. The stability over several successive cycles of exposure to ammonia could indicate the reusability of the devices. However, more work should be carried out to understand the impact of humidity on the sensing performances, as it is a major parameter to control for practical packaging applications.

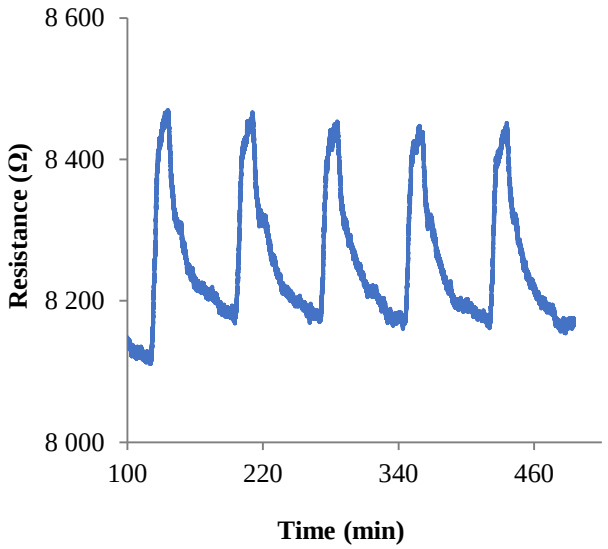

***Figure III-14**: Stability of the PGrCuBTC 21.25 sensor investigated by five successive cycles of 500 ppm NH_3 input and relaxation*

In summary, as expected from the electrical properties of the different sensors produced, the PGrCuBTC 21.25 showed the best gas sensing performances. For the first 50-500 ppm range tested, this sensor showed a response as high as 6.24% for 500 ppm. However, the behaviour of the sensor over this range was not linear, and a smaller 20 to 100 ppm range was tested. In this range, the sensors displayed a linear behaviour and with a response of 4.6% for 100 ppm for PGrCuBTC 21.25. The kinetics of the sensing was also investigated, and response time was found to be concentration-dependent, whereas recovery time was not. Finally, the stability of the sensor was proved to be good, showing only a minor performance loss through 5 consecutive ammonia input cycle. All these results showed the strong potential of such a device for reliable ammonia sensing under dry conditions with a low detection limit and excellent stability.

Table III-13 summarises the literature review discussed in the introduction and is focused only on MOF/micro- and nano-carbon systems. The performances of the system developed in this work is in accordance with the literature yet on the low side of the range. However, compared to the literature, the straightforward formulation of active inks by simple mixing of commercially supplied components and its deposition onto flexible polymeric substrate for the development of sensitive and stable sensors is the key challenge addressed in this work. The results obtained in the work then show the strong potential of the developed solution to be industrially up-scaled.

***Table III-13**: Literature review of ammonia sensors based on MOF/micro- and nano-carbon systems*

Sensor material	Material preparation	Device preparation (substrate)	Response (%, ppm)	Concentration range (ppm)	Ref.
Cu-BTC/graphite oxide	In-situ MOF synthesis	Coating suspension on Au IDE (ceramic)	4/100	100-500	[19]
SiO_2 coated Cu-BTC/rGO/PANI	Synthesis of silica-coated CuBTC and in-situ aniline polymerization with graphene	Drop-casting suspension on 4 probe Cr electrode (not supplied)	144/100	1-100	[21]
Cu–BTC/PPy–rGO	In-situ MOF synthesis	Drop-casting suspension between copper foil strips (ITO)	20.3/100	10-150	[20]
Graphite/$Cu_3(HHTP)_2$ Graphite/$Co_3(HHTP)_2$ Graphite/$Fe_3(HHTP)_2$ Graphite/$Ni_3(HHTP)_2$	MOF synthesis and ball-milling with graphite powder	Abrasion on Au IDE (paper)	4.6/80 4.2/80 4.0/80 2.9/80	5-80	[22]
Cu-BTC/carbon-graphene	**Simple mixing of commercial MOF and carbon-graphene**	**Drop-casting suspension on screen printed Ag IDE (PET)**	**4.6/100**	**20-100**	**This work**

1.3.3. Sensing mechanism

To investigate the sensing mechanisms, FTIR and Raman spectroscopy were performed before and after exposure to 100 ppm of ammonia for 30 min for PGrCuBTC 0, 21.25 and 100. No change could be seen on the Raman spectra and they are displayed in **Figure III-15**. However, some changes can be seen on FTIR spectra before and after sensing (**Figure III-16**) and especially for PGrCuBTC 0 (**Figure III-16c**). The major changes on the FTIR spectra of PGrCuBTC 0 before and after sensing are a significant increase in the intensity of already present peaks. Indeed, there is a sharp increase of intensity for the characteristic peaks of free benzene-1,3,5-tricarboxylate (BTC) ligand at 1618 cm^{-1}, for the one at 1648 cm^{-1} and 1254 cm^{-1}. However, no increase in the free acidic peak at 1709 cm^{-1} can be seen. This indicates that there is a change in the coordination of the BTC ligand but not corresponding to free BTC ligands. This tends to indicate a chemical reaction between ammonia and the BTC ligand, leading to $BTC(NH_4)_3$. So this analysis suggests that the mechanism of ammonia interacting

with CuBTC is working by gas adsorption on the copper metallic centre with a partial reaction between BTC ligand and ammonia, and this is in agreement with previous literature on the subject[73–76]. However, the experimental techniques used cannot conclude on the sensing mechanism of the CuBTC/carbon-graphene composite, even though previous work have suggested that the synergetic effect of CuBTC/graphene derivatives enables the creation of a charge transfer mechanism, through electron donation and the depletion of charge carrier when exposed to ammonia vapour[19,77].

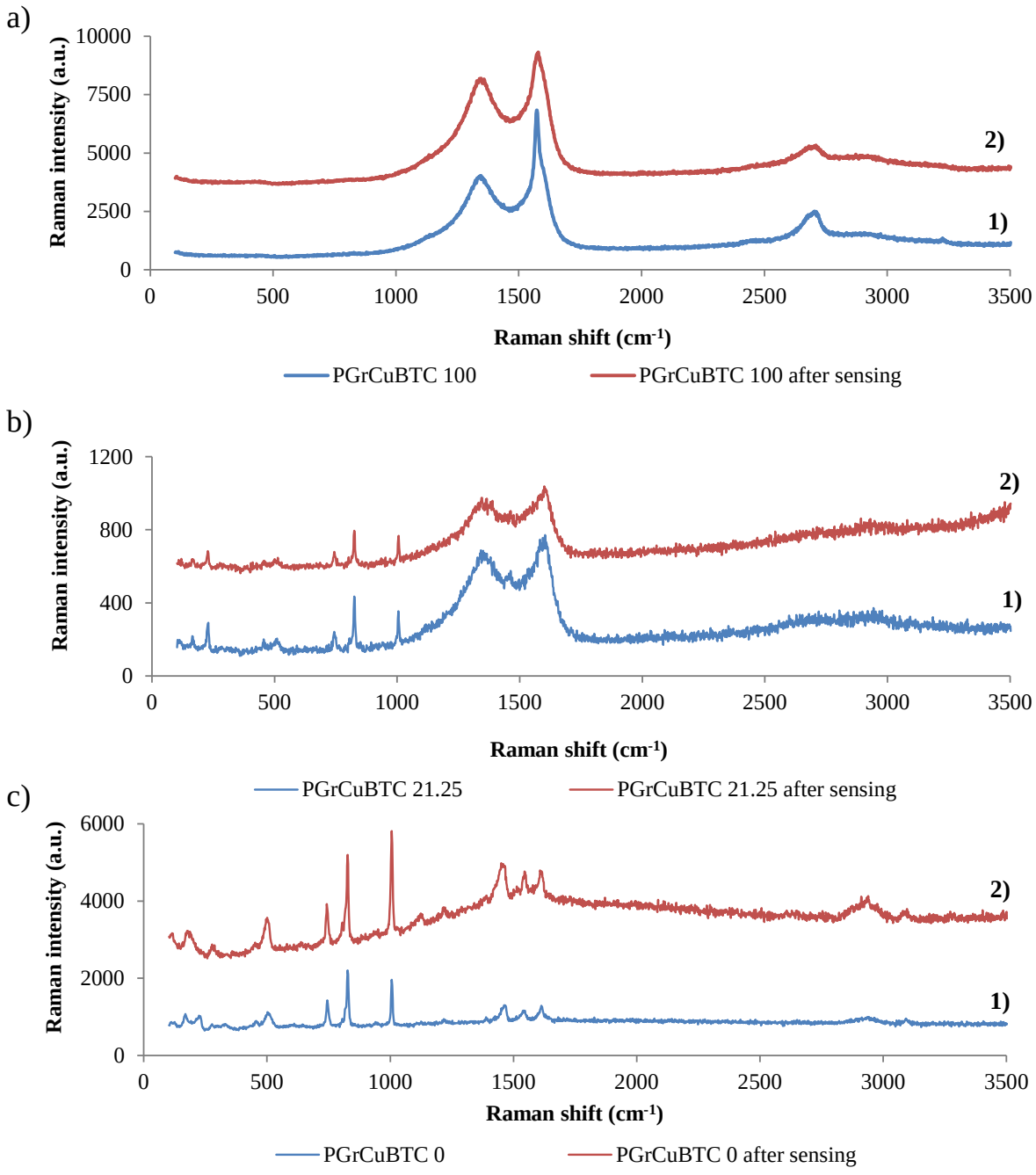

***Figure III-15**: Raman spectra before (1) and after (2) exposure to 100 ppm of NH_3 for 30 min for a) PGrCuBTC 100, b) PGrCuBTC 21.25 and c) PGrCuBTC 0*

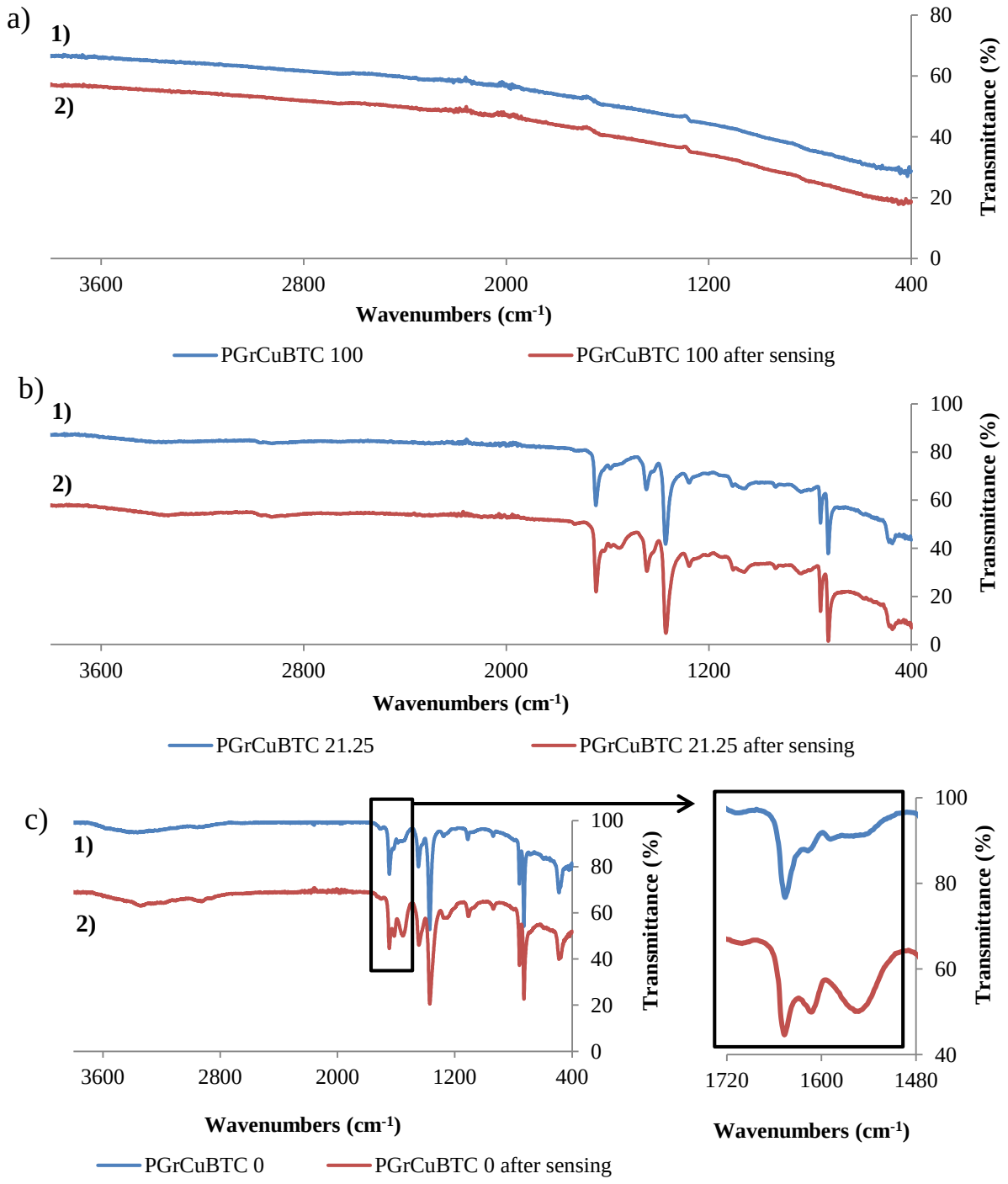

***Figure III-16**: FTIR spectra before (1) and after (2) exposure to 100 ppm of NH_3 for 30 min for a) PGrCuBTC 100, b) PGrCuBTC 21.25 and c) PGrCuBTC 0 with a zoom on the 1480-1720 cm^{-1} region*

1.4. Conclusion

In this work, gas sensors were produced using metal organic framework and conductive carbon-graphene materials. Copper-based CuBTC metal organic framework and carbon-graphene conductive materials were formulated with different ratios and drop-casted on screen-printed silver interdigitated electrodes. Morphological analyses, microscale topography and surface chemistry investigation proved the consistency of the formulation and deposition process. The electrical properties of the sensors were highly formulation-dependent and the optimised devices were tested against ammonia gas sensing in dry conditions. The optimised devices displayed a low detection limit (20 ppm) and a linear range from 20 to 100 ppm. The sensor response was found to be as high as 4.6% (100 ppm) with the optimised formulation which is 36 times higher than the only carbon-graphene blank sensor. The developed sensors also showed consistent results in stability tests. Compared to previous studies, this work proposes the development of sensitive and stable ammonia sensors, based on the straightforward formulation of active inks by simple mixing of commercially available materials followed by their deposition on flexible polymeric substrate. These research outputs highlight the potential industrial and commercial scale-up of the developed solutions. Noting MOF response to water, further investigations can be conducted to assess the behaviour of the sensor in humid environmental conditions and also to increase the sensitivity of the devices through investigation of other nanocarbon systems. While the sensors were not responsive to a nitrogen/oxygen atmosphere, selectivity to other gas analytes is another key challenge that could be researched and improved if necessary using overprinting of suitable selective overlays.

2. Humidity sensors based on Metal Organic Framework on flexible substrate

Abstract:

Humidity sensors were successfully developed using CuBTC Metal Organic Framework (MOF) and carbon-graphene materials. The sensors present a good correlation between relative humidity (RH) and resistance in the 30 to 80% RH tested range. A reproducible response as high as 54.2% for 80% RH was established for under flow experiments, and the devices display a response and a recovery time less than 20 min for all the tested range. Under vacuum experiments concluded on the fact that the response is solely due to humidity change. Finally, the interest of using CuBTC MOF for such sensing applications was proven as the optimised formulation response to humidity change was significantly higher than carbon-graphene control. The versatile, easy-to-produce and low-cost sensors is promising for several applications including intelligent packaging.

Keywords:

humidity sensor, metal organic framework, screen-printing, conductive carbon, low-cost manufacturing

2.1. Introduction

Detection and quantification of environmental humidity is a key factor in several fields of applications such as in weather forecast, industry (machine control, health and safety, packaging, etc.) or agricultural control. Humidity sensors are traditionally prepared from several types of active materials that include ceramics, semi-conductors and polymers[78]. More recently, micro- and nanomaterials such as graphene or Metal Organic Frameworks (MOFs) have met a strong interest in the scientific community for humidity sensing applications[79,80].

MOF are crystalline materials built by bridging multifunctional organic ligands with metallic centres. Since the late 90s and the first appearance of the term "MOF", thousands of structures have been developed because of the rational design possible due to the inherent nature of these materials[1,81]. MOFs are highly porous, versatile and multifunctional materials that are of high interest in various types of applications including gas sensing[82,83]. Humidity sensing using MOFs are based on several different sensing techniques such as quartz-crystal microbalance (QCM), Surface Acoustic Wave (SAW), and various optical or electronical devices. The copper-benzene-1,3,5-tricarboxylate (CuBTC) MOF is historically one of the first and most studied MOF[46] and has been widely investigated for humidity sensing as its physical properties are dependent on its hydration state[84,85].

For instance, Kosuru et al. (2016) reported the proof of concept of QCM sensors based on CuBTC which were sensitive between 22 and 69% relative humidity (RH)[86]. Chappanda et al. (2018) also showed that CuBTC synthesised with carbon nanotubes (CNT) display increased sensitivity compared to plain CuBTC when used in QCM sensors[87]. The authors proved a similar or higher sensitivity than for other reported QCM sensors in the literature at the time, while testing them between 5 and 75% RH. SAW sensors were prepared by Robinson et al. (2012) using layer by layer technique to grow CuBTC thin films sensitive for water vapour concentration as low as 3 ppm[88].

One of the first humidity sensors based on CuBTC was developed by Lu et al. (2011) and related to optical sensors technology, prepared by growing CuBTC crystals on silica nanospheres[89]. Near-infrared extinction spectra showed that the photonic band gap of the materials undergo a red shift when exposed to water vapour, which was correlated to the amount of water vapour adsorbed. The developed sensor was however also sensitive to several other analytes such as ethanol or carbon disulphide. A system based on fibre optic technology was investigated by Ohira et al. (2015) who simply correlated the visible change of colour of CuBTC when exposed to different levels of humidity[90]. The prepared system was very sensitive (as low as 40 ppb), reversible and with fast response (around 20 s). Ullman et al. (2018) also used a similar colorimetric concept to prepare sensors by spin-coating CuBTC on either rigid or flexible substrate[91]. The reflectance of the devices was well correlated with the humidity level over a

low humidity range (1-5% RH) and polystyrene was coated on the top of the devices for higher humidity levels (> 10% RH) to enable time-dependent qualitative measurements by slowing down the water molecule transport.

Several types of electrical sensors using CuBTC were also developed by the scientific community. Capacitive sensors were first prepared by Liu et al. (2011) by in-situ growth of CuBTC onto a copper plate, which showed a reversible capacitance change in the 11-85 % RH range with relatively short characteristic times (around 20 s for both response and recovery time)[92]. Sapsanis et al. (2015) grew CuBTC on gold interdigitated electrodes (IDE) using liquid phase epitaxy technique and the sensors were successfully operated from 30 to 90 % RH[93]. Finally, Hosseini et al. (2019) also prepared capacitive sensors, but using electrochemical growth on a copper plate electrode assisted with an imidazolium ionic liquid[3]. The sensors were operated between 20 and 100 ppm with a measured detection limit of 5.5 ppm and sensitivity studies showed that the sensors were not sensitive toward nonpolar analytes.

Only one recent example prepared a resistive sensor by drop-casting a combination of graphene oxide and CuBTC on a silver IDE on a glass substrate, which achieved a very high response (6200% at 85%RH)[94]. Other types of sensing such as techniques using Kelvin probes or organic thin film transistor technology have also been reported[95,96]. Finally, other MOFs have also been proved to be effective as humidity sensor including MIL-96, MIL-100, MIL-101, MIL-125 or CAU-10[97–101]. The different literature examples are summarised in the **Table III-14**.

The sensor preparation technique of this work, including the screen-printing of silver interdigitated electrode and the drop-casting of the CuBTC/carbon-graphene hybrid ink, was optimised in Section **III-1**. In Section **III-1**, the electrical properties were found to be strongly formulation dependent because of the insulating nature of CuBTC and the high electrical conductivity for the carbon-graphene materials. The composition was then optimised to obtain the highest CuBTC/carbon-graphene ratio with a measurable and reproducible conductivity. This optimised formulation called PGrCuBTC 21.25 displayed the highest sensitivity to ammonia sensing and so it was selected to be tested here for humidity sensing. As reported for the ammonia sensing application in Section **III-1**, the innovation of this work lies in straightforward preparation of the devices, prepared by simple mixing of the commercial materials into an ink formulation, and drop-casting onto a flexible plastic substrate. Only a few examples have reported the use of flexible substrates for humidity sensors based on MOF materials[91,102]. The sensing response of the sensors was tested using different experimental setups and compared with carbon-graphene only control devices.

***Table III-14**: Literature review of humidity sensing technology based on MOF: sensing type, preparation and operating range*

Sensor material	Sensing type	Device preparation (substrate)	Range (% RH)	Reference
MIL-96 (Al)	Capacitive	Langmuir-Blodgett thin film deposition on Ti-Au IDE (Si wafer)	0.2-20	Andres et al. (2020)[97]
MIL-101-NH_2-SO_3H	Impedance	Drop-casting on Ag-Pd Ide (ceramic)	11-95	Ru et al. (2019)[98]
MIL-100 (Fe)	Impedance	Pellet	11-97	Seo et al. (2019)[100]
Basoviv M050 (Mg) (+ Au NPs, KOH)	Impedance	Coating on Au IDE (PET)	20-90	Su et al. (2018)[102]
Cd(TMA)(DPP)	Impedance	Coating on Ag-Pd IDE (ceramic)	11-97	Yin et al. (2018)[103]
MIL-101 (Cr)	Impedance	Coating on Ag-Pd IDE (ceramic)	33-95	Zhang et al. (2017)[104]
CAU-10 modified	Impedance/dielectric properties	Pellet	10-90	Weiss et al. (2015-2016)[101,105]
NH2-MIL-125 (Ti)	Impedance	Coating on Ag-Pd IDE (ceramic)	11-95	Zhang et al. (2013)[99]
FeCl3-NH2-MIL-125 (Ti)	Impedance	Coating on Ag-Pd IDE (ceramic)	11-95	Zhang et al. (2014)[106]
LiCl/UiO-66-NH_2	Impedance	Coating on Ag-Pd IDE (ceramic)	11-95	Zhang et al. (2020)[107]
$\{[Eu_2(L)_3\cdot(H_2O)_2\cdot(DMF)_2]\cdot 16H_2O\}_n$	Luminescence	Powder direct use	33-85	Wang et al. (2016)[108]
$[Cu_3L_2(H_2O)_{2.75}]\cdot 0.75H_2O\cdot 1.75DMA$	QCM	Dip-coating of QCM Ag electrodes (not supplied)	17-98	Zhou et al. (2017)[109]
CuBTC				
CuBTC (+CNT)	QCM	Spin-coating on QCM Au electrodes (quartz)	5-75	Chappanda et al. (2018)[87]
CuBTC	QCM	Drop-casting on QCM Au electrodes (quartz)	22-69	Kosuru et al. (2016)[86]
CuBTC	SAW	Layer-by-layer coating on SAW device (quartz)	0.01-59	Robinson et al. (2012)[88]
CuBTC (+silica colloidal crystal thin fil)	Optical	In-situ growth on colloidal silica crystals (glass)	4-48	Lu et al. (2011)[89]
CuBTC	Optial (fiber optic)	Filtration through PTFE filter	0.0002-0.4	Ohira et al. (2015)[90]

(Continued)

***Table III-9**: Continued*

Sensor material	Sensing type	Device preparation (substrate)	Range (% RH)	Reference
CuBTC	Optical	Spin-coating (glass)	0.1-5	Ullman et al. (2018)[91]
CuBTC (+poly(3-hexylthiophene-2,5-diyl)	OTFT based sensor	Spin-coating on Au electrodes (Si wafer)	0-30	Jang et al. (2018)[95]
CuBTC	CS-FET sensor (work function)	Layer-by-layer growth on Kelvin probe (Si wafer)	0-47	Gardner et al. (2019)[96]
CuBTC	Capacitive	Electrochemical in-situ growth on copper parallel plate (copper)	0.08-0.4	Hosseini et al. (2019)[3]
CuBTC	Capacitive	In-situ growth on copper plate (copper)	11-85	Liu et al. (2011)[92]
CuBTC	Capacitive	In-situ growth on Au IDE (Si wafer)	30-90	Sapsanis et al. (2015)[93]
CuBTC (+GO)	Resistive	Drop-casting on Ag IDE (glass)	11-85	Zhang et al. (2018)[94]

2.2. Materials and Methods

2.2.1. Materials

Copper benzene-1,3,5-tricarboxylate (CuBTC) was supplied by MOF Technologies (UK). The screen-printing inks named silver AST 6025 and carbon-graphene C2171023D1 were supplied by Sun Chemicals (USA). N-butyl acetate (analytical reagent grade) was supplied by Fisher Scientific (UK). The polyethylene terephthalate (PET) substrate (175 µm Melinex ® 339) was supplied by DuPont Teijin Films (USA). All products were used as received.

2.2.2. Sensor preparation

The interdigitated structure of the sensors was prepared using the same technique as for the ammonia sensors reported in Section **III-1** (and with the same dimensions), by screen-printing the silver ink on the PET substrate. To summarise, the printing was conducted on a R29 series Reprint equipment with forward parameters set at 5.0 kg pressure and 50 $mm.s^{-1}$ speed. The printing gap was set at 2.0 mm. The printer was equipped with a polyester screen with the following parameters: 120 $thread.cm^{-1}$ mesh count, 34 µm thread diameter, 12 µm emulsion over mesh thickness and 22.5° screen angle. After printing the devices were dried in an oven at 100°C for 30 min.

The formulation named PGrCuBTC 21.25 presenting the best response toward ammonia sensing reported in Section **III-1** was selected for the response toward humidity. To summarise, the active suspension was prepared by mixing 200 mg and 54 mg respectively of CuBTC and dry carbon-graphene materials (35% mass content commercial ink) in 1 ml of butyl acetate solvent. The suspension was dispersed by using a vortex mixer (3 times, 30 s) as it was established to be good practice to properly disperse the components. 8 µl of the prepared suspension was then drop-casted on the previously produced silver IDE using a micropipette and covering consistently the digits. The devices were dried at 100°C for 30 min in an oven. The control PGrCuBTC 100 (carbon-graphene only) was prepared following the same procedure by dispersion only 54 mg of dry carbon-graphene materials in 1 ml of butyl acetate solvent.

2.2.3. Sensors response to humidity

To sensors were tested in different experimental setups: “under flow” using the same gas rig system as in Section **III-1**, “under vacuum” using a vacuum chamber, and in an environmental chamber.

The same gas rig system described in Section **III-1** was used to test the response of the sensors toward humidity change. To summarise, standard gas cylinders (nitrogen: 293679-L,

>99.9995%/ oxygen: 284915-V, >99.999%) were supplied by BOC (UK), connected to mass flow controllers (GFC17, Aalborg) to adjust the gas flow rate of the different lines. Solenoid valves (SCG256B404VMS, ASCO) enable the opening or closing of the lines, which then meet in the gas chamber, where the sensor is soldered on a feedthrough connected to a source meter (Keithley 6487) outside the chamber, to follow the resistance of the devices during the tests.

The main difference from the experimental setup reported in the Section **III-1** is that the ammonia line was closed, and that a derivation was installed (after the point where oxygen and the derivation of the nitrogen line meet) to install a bubbler (**Figure III-17**). The bubbler is filled with deionized water and so by adjusting the flow rate of the line passing through the bubbler ("wet line") compared to the one not passing through it ("dry line"), it is possible to vary the humidity inside the chamber. The total flow rate was kept at 100 sccm with a 4:1 v/v nitrogen to oxygen ratio to simulate air. The approximate theoretical relative humidity was estimated as the ratio of the flow rate of the lines passing through the bubbler (wet lines) and the one excluding it (dry line), so assuming 100% relative humidity (RH) for the gas exiting the bubbler. Successive dry and humid tests were conducted to investigate the sensors response and their recovery, by manually by-passing the bubbler. The tests were conducted at room temperature ca. 20-22°C. For each humidity level the response (%) of the sensors was calculated by Equation **III-2**:

$$Response\ (\%) = 100 \times \frac{R_p - R_0}{R_0} \quad \textbf{(III-2)}$$

Where R_p (Ω) is the resistance on the wet step taken on the plateau (averaged over the last 600 s of the step) and R_0 (Ω) the resistance on the previous corresponding dry step taken on the plateau. The sensors characteristics times were also calculated as follows: the recovery time is the time necessary for the sensor to recover 90% of its initial state and the response time is the time necessary to reach 90% of the response. The different estimated approximate theoretical humidity levels investigated were 30, 40, 50, 60, 70 and 80% of RH. The sensors baseline response loss (%) was calculated to evaluate the recovery of the sensors by measuring the return to the baseline after each step (comparing two successive steps) using Equation **III-3**:

$$Baseline\ response\ loss\ (\%) = 100 \times \frac{R0_{n+1} - R0_n}{R0_n} \quad \textbf{(III-3)}$$

Where $R0_n$ (Ω) is the resistance at the start of humidity input for the step n and $R0_{n+1}$(Ω) the resistance at the start of humidity input for the step n+1. Two different sensors were tested and the average is presented with its associated standard deviation.

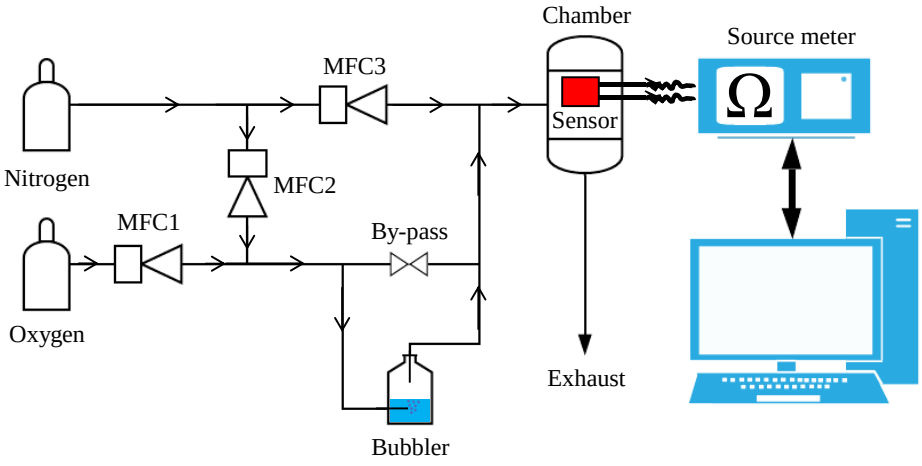

***Figure III-17**: Schematic flow chart system of the custom-built gas rig used for humidity sensing*

The electrical properties of the PGrCuBTC 21.25 and PGrCuBTC 100 sensors at different humidity level were also investigated under vacuum to exclude any influence of impurities coming from the carrier gas flow during the sensing experiments. To do this, the samples were placed in a vacuum chamber containing the probe station Janis CCR12, connected to a Keithley 2450 source meter, and the chamber was pumped down to 10^{-3} mbar overnight using a dry scroll. The humidity was set to target 0, 50 and 80 % RH by injecting Milli-Q water through a sealable vial (degassed three 3 times) connected to the vacuum chamber and measured using a 0-50 mbar pressure gauge from BOC (GK series). Two sensors of each formulation were tested at the same time in the vacuum chamber to assess reproducibility. The maximum capacity for the chamber is two sensors and the tests were done separately for PGrCuBTC 21.25 and PGrCuBTC 100. The actual RH levels measured were respectively 0 for both samples, 48.6% RH for PGrCuBTC 100 and 50.0 for PGrCuBTC 21.25, and 80.0% RH for both. At each humidity level, current/voltage curves were taken to calculate the resistance of the device with a -1 volt to 1 volt sweeping mode and 200 measurements points. Sufficient time was given for each sensor to reach an equilibrium in between the different levels which was assessed by following the resistance of the device over time. Current/voltage experiments were also recorded before and after the test in ambient conditions (38.9% RH, 23°C, at the time of measurement) to assess the influence on the sensor stability. The response of the devices under vacuum was also calculated using Equation **III-2** and the results at 0% RH as the dry step plateau. At least two different sensors were tested and averaged results are presented.

Finally, the sensors' response was also tested in a Sanyo environmental chamber (MTH-2400), while keeping the temperature at 20°C. The sensors were placed inside the chamber and connected to a Keithley 2400 source meter on the outside to measure their resistance. The resistance values were collected manually every minute. Prior to any test, the devices were put in the chamber for 15 min under the starting conditions, to equilibrate. To evaluate the humidity influence on the sensors, an increasing humidity ramp from 30 to 80% relative humidity was

performed. The sensors were kept at the desired relative humidity level for 15 min once the relative humidity was within ± 1% of the target. For one device, the relative humidity was set back at 50% at the end of the test to evaluate its recovery. Two devices of each formulations PGrCuBTC 21.25 or PGrCuBTC 100 (carbon-graphene control) were tested. Their resistance was normalised by their resistance at t=0 min and drawn against the time of the experiments. Moreover, at each relative humidity level, the normalised resistance was also averaged on each step plateau (5 last minutes of each plateau), and used to compare the two formulations. Finally, the stability of the PGrCuBTC 21.25 sensor was investigated by performing 4 successive cycles from 50 to 70% of relative humidity (and back), staying during 30 min at each humidity level once it has stabilised within ± 1% of the target.

2.3. Results and discussions

The PGrCuBTC 21.25 optimised sensor was tested for humidity sensing against different relative humidity (RH) level (30-80%) under flow in the gas rig system, and the results are summarised in **Figure III-18**. The typical evolution of the resistance for one device to step changes in humidity from 30-80% RH can be found in **Figure III-18a**, that shows the change of the electrical properties of the sensors when exposed to different humidity level. The sensors' response (%) was extracted for each step and showed a very good non-linear correlation with the humidity level (**Figure III-18b**). The observed response ranged from 13.2 to 54.2% which is significantly higher than for ammonia sensing reported in Section **III-1** (from 0.5 to 5.0%) which is probably due to the higher gas concentration (thousands of water ppm compared to tens of ppm for ammonia sensing).

The characteristic times (response and recovery) were extracted for each step and summarised in **Figure III-18c**. For the different humidity levels, the response times were measured between 15 and 20 min and the recovery times between 5 and 10 min for the PGrCuBTC 21.25 sensor selected for this study. Both were found to be independent of the RH level. The characteristic times for humidity sensing are lower compared to ammonia sensing reported in Section **III-2** where it was measured as from 10 to 25 min for the response time and 15 to 30 min for the recovery time for PGrCuBTC 21.25 (depending on the ammonia concentration). This could be explained by the larger gas concentration but the significantly lower total flow rate (100 sccm for humidity compared to 1000 sccm for ammonia) tends to suggest that the sensors' kinetics are much better for humidity sensing than for ammonia. However, the sensors' recovery was not complete after each step as the resistance of the sensors did not go back entirely to the starting baseline at the end of each step (**Figure III-18d**). The difference in the recovered resistance compared to the starting baseline was measured as a baseline response loss (%). It was found to be not dependent on the relative humidity and relatively random (between 1.9 and 4.1%). This response loss could be explained by irreversible adsorption, slower kinetics desorption mechanism, or partial permanent damage to the crystalline structure of CuBTC even though this hydrolysis supposedly happens for exposure to high humidity only[110–112].

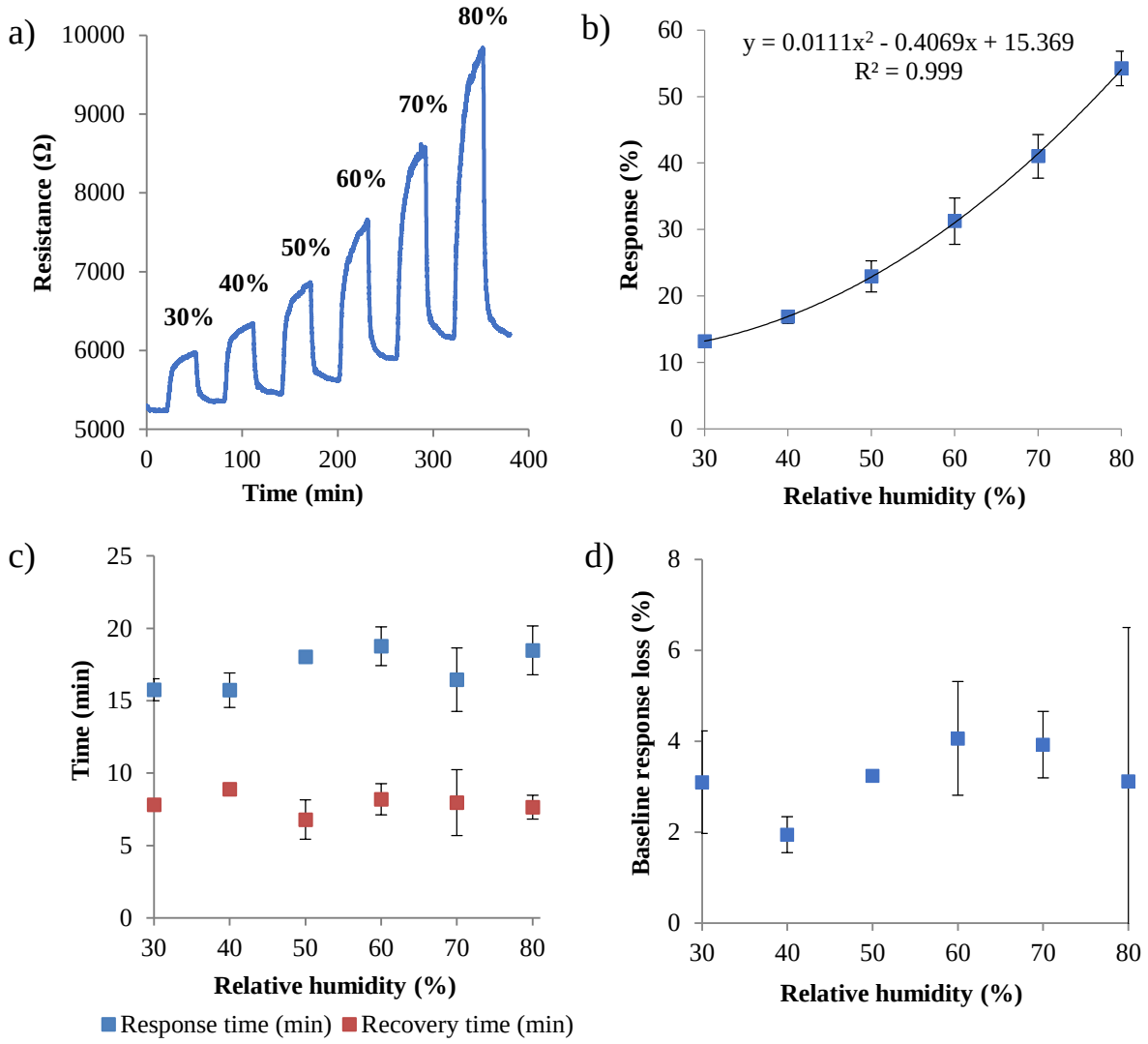

***Figure III-18**: Sensors response to under flow humidity sensing with a) typical evolution of one sensor resistance when exposed to different humidity level (30-80% relative humidity) over time, b) response (%) of the sensors extracted from each humidity level compared to humidity level, c) response time (min) and recovery time (min) for each humidity level and d) baseline response loss (%) for each humidity level*

The sensors were also tested for humidity sensing in a vacuum chamber to exclude any external influence (**Figure III-19**) and especially at 0, 50 and 80% RH. First of all, the control PGrCuBTC 100 (carbon-graphene only) showed only a slight change on its resistance (**Figure III-19a**) when exposed to 0, 50 and 80% RH, respectively 7.57 ± 0.34, 7.72 ± 0.40 and 7.86 ± 0.42 Ω. The PGrCuBTC 21.25 sensors however displayed a large variation of resistance when exposed to the different humidity levels, measured as 67440 ± 5817, 76686 ± 694 and 97728 ± 2009Ω (**Figure III-19b**). Using these values, the responses (%) at 50 and 80% RH were calculated and range from 2 to 4% and 14 to 45% respectively for PGRCuBRC 100 and PGrCuBTC 21.25 (**Figure III-19c**). Finally, the results of the tests in vacuum and under flow were compared and showed a difference of around 10% (**Figure III-19d**), which might be explained by the not

perfectly consistent humidity control in the under flow test (a possible gap between theoretical and real tested humidity).

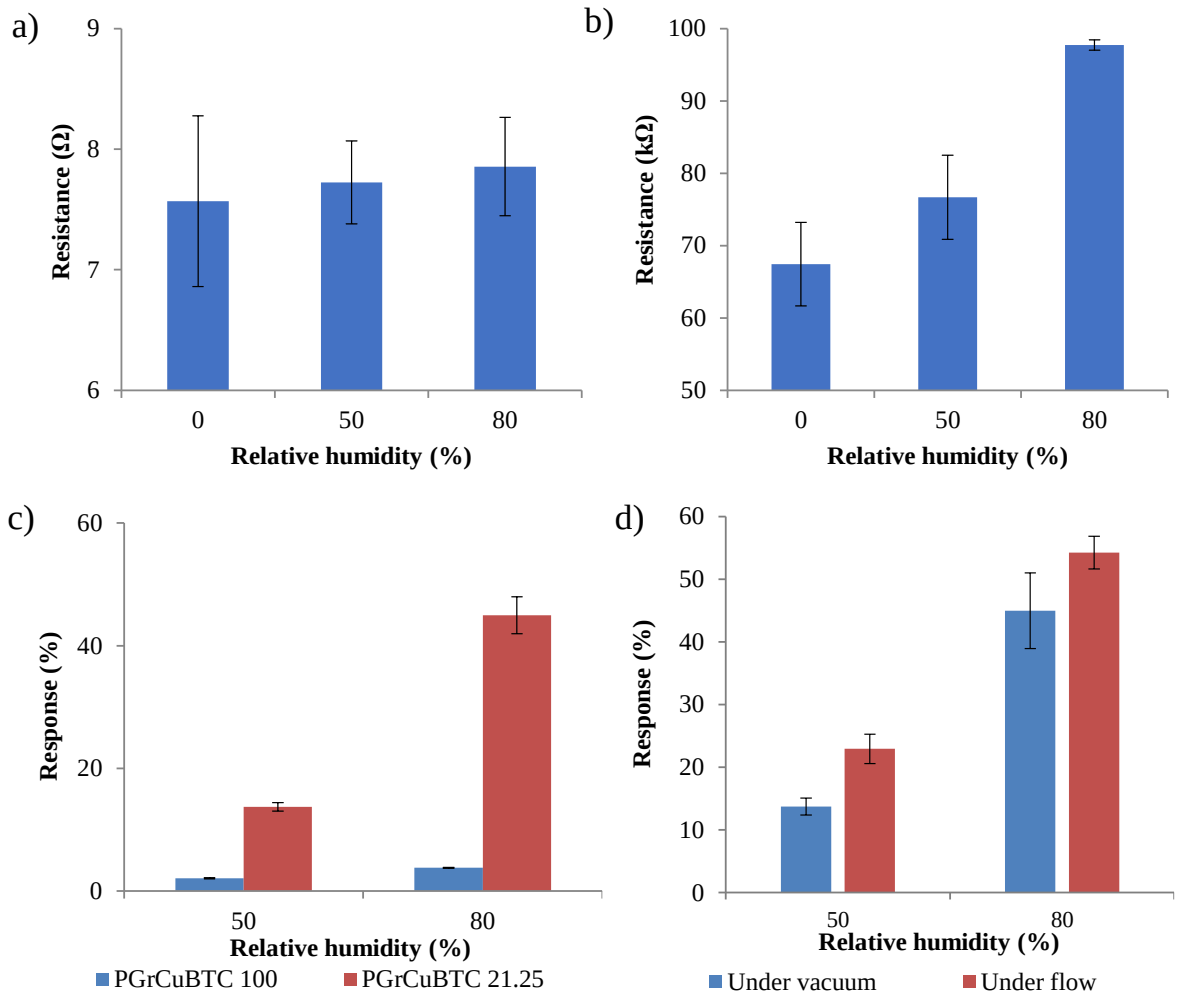

***Figure III-19**: Sensors exposure to different relative humidity level in vacuum chamber with a) PGrCuBTC 100 (graphene only) resistance evolution at 0, 50, 80% RH, b) PGrCuBTC 21.25 resistance evolution at 0, 50, 80% RH, c) calculated response (%) at 50 and 80% RH (normalized with 0% RH) for PGrCuBTC 100 and 21.25 and d) comparison of response (%) from under flow gas sensing test and in vacuum chamber test for PGrCuBTC 21.25*

Finally, the same devices were also tested in an environmental chamber, by applying an increasing RH ramp from 30 to 80%. Using this experimental setup, both PGrCuBTC 21.25 and PGrCuBTC 0 were sensitive to an increasing humidity level (**Figure III-20a** and **b**), in a reproducible manner. The recovery of one PGrCuBTC 21.25 device was also proven. However, it can be seen in **Figure III-20c**, that the overall response of the system is significantly more higher for PGrCuBTC 21.25 than for PGrCuBTC 100, proving the importance of using CuBTC MOF in the formulation. The CuBTC normalised resistance through the ramp test was found to be well correlated to the RH level (**Figure III-20c**). Finally, the stability of the PGrCuBTC 21.25 device was investigated by successive cycles from 50 to 70% RH, which showed a slight drifting in the bassline as well as a small loss in the response (**Figure III-20d**), which could be

correlated as described previously, to irreversible adsorption, slow kinetics of desorption mechanism or permanent damage to the MOF structure at these humidity levels.

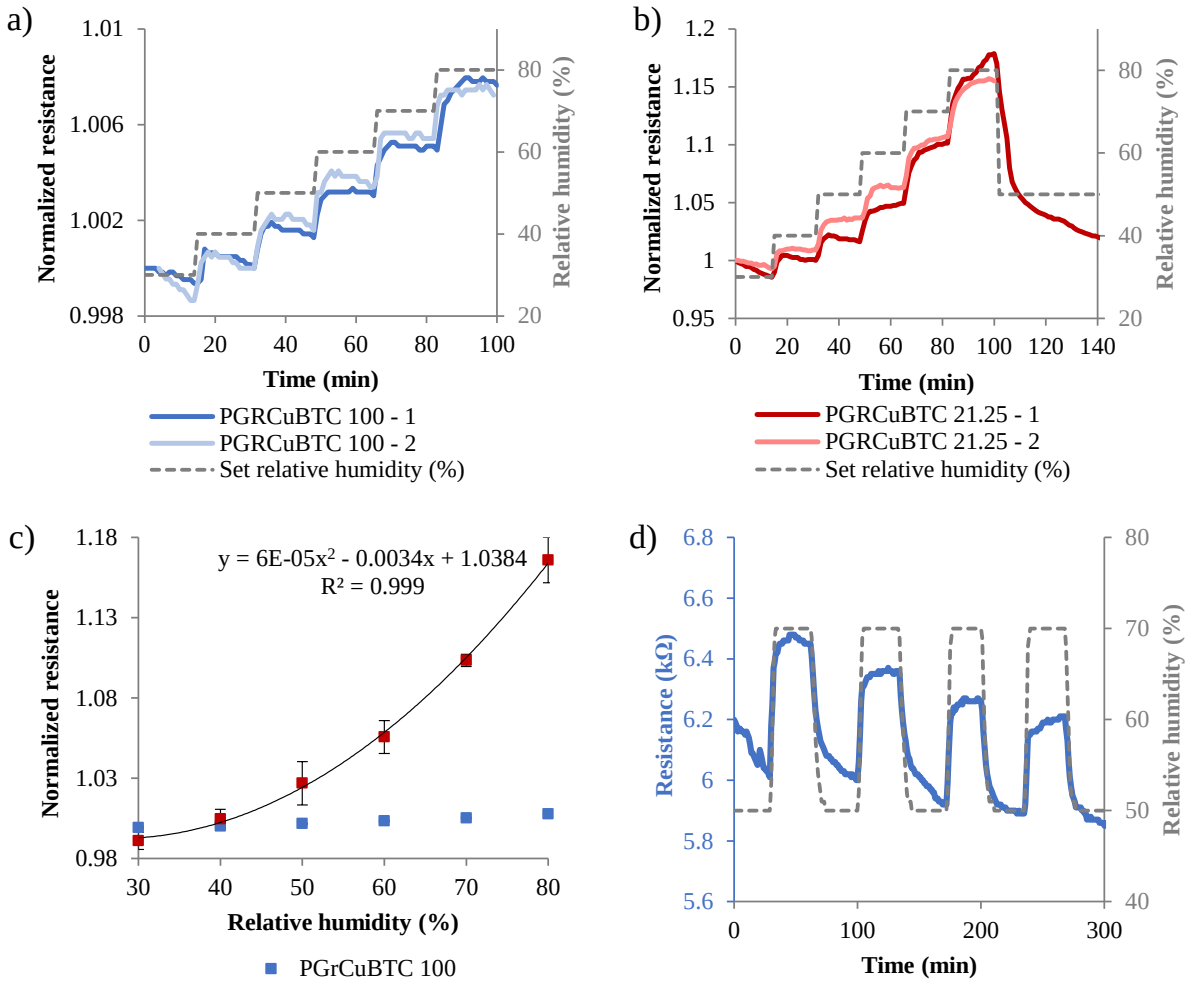

***Figure III-20**: Humidity sensing in the environmental chamber with a) increasing RH ramp test from 30 to 80% RH for PGrCuBTC 100, b) increasing RH ramp test from 30 to 80% RH for PGrCuBTC 21.25, c) extracted plateau normalized resistance vs RH (%) and d) stability investigation of PGrCuBTC 21.25 by 4 successive cycle from 50 to 70% RH and back*

The performances of the developed resistive sensors were compared to existing electrical solutions using CuBTC MOF in the literature (**Table III-15**). Most of the electrical devices are capacitive devices and their response (%) vary from 2 to 1523% at approximately 50% RH. The solution proposed in this work is in the low side of the response range and the characteristic times are higher than the one proposed in the literature review. However, the straight forward preparation of the devices by drop-casting an active mixture of commercial products on screen-printed electrodes on flexible polymeric substrate, shows the promising potential of such system.

***Table III-15**: Literature review of electrical humidity sensors based on CuBTC MOF system (GO=graphene oxide, App.=approximatively, N/A=not applicable)*

Sensor material	Sensing type	Device preparation (substrate)	Range (% RH)	Response (%, %RH)	Response/recovery times (min)	Reference
CuBTC	Capacitive	Electrochemical in-situ growth on copper parallel plate (copper)	0.08-0.4	50.0 (0.4%RH)	App. 6.0/2.9	Hosseini et al. (2019)[3]
CuBTC	Capacitive	In-situ growth on copper plate (copper)	11-84.3	49.3* (57.6%RH)	App. 0.3/0.3	Liu et al. (2011)[92]
CuBTC	Capacitive	In-situ growth on Au IDE prepared by lithography (Si wafer)	30-90	2.0 (50%RH)	N.A.	Sapsanis et al. (2015)[93]
CuBTC (+GO)	Resistive	Drop-casting on Ag IDE prepared by lithography (glass)	11-85	**1522.6 (54%RH)	App. 0.7/0.5	Zhang et al. (2018)[94]
Cu-BTC/carbon-graphene	**Resistive**	**Drop-casting suspension on screen printed Ag IDE (PET)**	**30-80**	**23.9 (50%RH)**	**App. 18.0/6.8**	**This study**

* compared to 11.3%RH as reference

** compared to 11%RH as reference. GO only sensor display a 412.9% response

2.4. Conclusion

The sensors reported in Section **III-1** and successfully applied for ammonia sensing were here tested for humidity sensing. The optimised sensor was successful in detecting and quantifying humidity in the 30 to 80% relative humidity (RH) range tested, with a very good correlation between RH (%) and response (%). The devices responses at 80%RH were as high as 54.2%, which is significantly higher than the response obtained previously for low concentration ammonia sensing. The response time and recovery time were calculated as between 15-20 and 5-10 min respectively. However, a small baseline loss was measured after each step, independently of the humidity level (between 1.9 and 4.1%). The results obtained for the same sensors under vacuum also shows the impact of CuBTC compared to carbon-graphene only reference, with a response 6.6 times higher at 50% RH and 11.8 times higher at 80% RH. This also confirms that the measured change is solely due to the humidity and not to any external factor. The tests performed in the environmental chamber also highlighted the superior performances of PGrCuBTC 21.25 against the carbon-graphene control. When the stability of the device was investigated, a small performance loss however was measured after several cycle from 50 to 70% RH and back. These results indicate that the developed humidity sensor could be successfully adapted for intelligent packaging applications.

A further investigation of the relationship between water vapour and ammonia sensing together would be interesting to link Sections **III-2** and **III-3** together. For instance, the response toward ammonia under different humidity level, as well as the response toward humidity under different ammonia level, could be researched to assess the possibility of a selective sensing under real-life applications. Moreover, the selectivity to other gas analytes, remain a critical parameter to control for an efficient and working sensors in environmental conditions.

Conclusions of Chapter III

The target of the **Chapter III** was to develop gas sensors suitable for smart packaging applications using Metal Organic Frameworks (MOFs) and conductive carbon materials. Different analytes as well as different active materials composition were tested and proved to be successful for gas sensing applications.

In the work reported in Section **III-1**, Copper benzene-1,3,5-tricarboxylate (CuBTC) MOF was formulated with different ratio of carbon-graphene conductive ink and drop-cast on screen printed silver interdigitated electrodes. The resistance of the devices was found to be highly formulation dependant (measured resistance from few ohms to tens of megaohms) and an optimal composition was established based on the compromise between electrical properties, minimal quantity of carbon-graphene and reproducibility of preparation. The surface physico-chemical properties were also investigated using a large variety of high-end characterisation techniques, including white light interferometry, X-ray diffraction, X-ray photoelectron spectroscopy, scanning electron microscopy coupled with energy dispersive X-ray analyser or atomic force microscopy, all of which proved the retained chemical and crystalline properties of the materials after formulation and deposition on the electrodes. The ammonia sensing in dry conditions was successful in the 20 to 100 ppm with a maximal response (100 ppm) of 4.6% which is 36 times higher than for the carbon-graphene reference, and the characteristic times were found to fit the packaging requirements. The sensors were proven to be stable over several cycles and the sensing mechanism was also verified by Fourier-transform infrared and Raman spectroscopic techniques.

In the work reported in section **III-2**, the sensors optimised in Section **III-1** were selected to be tested for humidity sensing and especially in the 30-80% relative humidity (RH) range. The sensors resistance was impacted by the humidity change and a very good correlation between the response (%) and the relative humidity (%) was established with a maximum response as high as 54.2% for under flow experiments at 80% RH. A small irreversible response loss was however noted after each sensing step, that could be attributed to irreversible adsorption, slow desorption kinetics or permanent damage to the MOF structure. The sensors characteristic times were found to be lower than for ammonia sensing. Moreover, experiments performed in vacuum concluded that the response was solely due to humidity sensing, but also proved the higher performance of the optimised formulation against carbon-graphene control. The interest of using CuBTC MOF in the formulation was also emphasised by the ramp tests in environmental chamber, that show a higher response compared to the carbon-graphene control. A small loss in performances was however noted in the stability tests.

References of Chapter III

1. Yaghi, O. M., Li, G. & Li, H. Selective binding and removal of guests in a microporous metal–organic framework. *Nature* **378**, 703 (1995).
2. Gangu, K. K., Maddila, S., Mukkamala, S. B. & Jonnalagadda, S. B. A review on contemporary Metal–Organic Framework materials. *Inorganica Chimica Acta* **446**, 61–74 (2016).
3. Hosseini, M. S., Zeinali, S. & Sheikhi, M. H. Fabrication of capacitive sensor based on Cu-BTC (MOF-199) nanoporous film for detection of ethanol and methanol vapors. *Sensors and Actuators B: Chemical* **230**, 9–16 (2016).
4. Wu, X., Xiong, S., Mao, Z., Hu, S. & Long, X. A Designed ZnO@ZIF-8 Core–Shell Nanorod Film as a Gas Sensor with Excellent Selectivity for H2 over CO. *Chemistry – A European Journal* **23**, 7969–7975 (2017).
5. Sel, K., Demirci, S., Ozturk, O. F., Aktas, N. & Sahiner, N. NH3 gas sensing applications of metal organic frameworks. *Microelectronic Engineering* **136**, 71–76 (2015).
6. Aubrey, M. L. *et al.* Chemiresistive Detection of Gaseous Hydrocarbons and Interrogation of Charge Transport in Cu[Ni(2,3-pyrazinedithiolate)2] by Gas Adsorption. *Journal of the American Chemical Society* (2019) doi:10.1021/jacs.9b00654.
7. DMello, M. E., Sundaram, N. G., Singh, A., Singh, A. K. & Kalidindi, S. B. An amine functionalized zirconium metal–organic framework as an effective chemiresistive sensor for acidic gases. *Chem. Commun.* **55**, 349–352 (2019).
8. Achmann, S. *et al.* Metal-Organic Frameworks for Sensing Applications in the Gas Phase. *Sensors* **9**, 1574–1589 (2009).
9. Campbell, M. G., Liu, S. F., Swager, T. M. & Dincă, M. Chemiresistive Sensor Arrays from Conductive 2D Metal–Organic Frameworks. *J. Am. Chem. Soc.* **137**, 13780–13783 (2015).
10. Tchalala, M. R. *et al.* Concurrent Sensing of CO2 and H2O from Air Using Ultramicroporous Fluorinated Metal–Organic Frameworks: Effect of Transduction Mechanism on the Sensing Performance. *ACS Appl. Mater. Interfaces* **11**, 1706–1712 (2019).
11. Sun, L., Campbell, M. G. & Dincă, M. Electrically Conductive Porous Metal–Organic Frameworks. *Angewandte Chemie International Edition* **55**, 3566–3579 (2016).
12. Zhu, L. *et al.* Metal-organic frameworks/carbon-based materials for environmental remediation: A state-of-the-art mini-review. *Journal of Environmental Management* **232**, 964–977 (2019).
13. Fardindoost, S., Hatamie, S., Zad, A. I. & Astaraei, F. R. Hydrogen sensing properties of nanocomposite graphene oxide/Co-based metal organic frameworks (Co-MOFs@GO). *Nanotechnology* **29**, 015501 (2017).
14. Jafari, N., Zeinali, S. & Shadmehr, J. Room temperature resistive gas sensor based on ZIF-8/MWCNT/AgNPs nanocomposite for VOCs detection. *J Mater Sci: Mater Electron* **30**, 12339–12350 (2019).
15. Lin, G. *et al.* Co3O4 /N-doped RGO nanocomposites derived from MOFs and their highly enhanced gas sensing performance. *Sensors and Actuators B: Chemical* **303**, 127219 (2020).
16. Ding, D. *et al.* Chemically functionalized 3D reticular graphene oxide frameworks decorated with MOF-derived Co3O4: Towards highly sensitive and selective detection to acetone. *Sensors and Actuators B: Chemical* **259**, 289–298 (2018).

17. Zhang, D., Wu, Z. & Zong, X. Metal-organic frameworks-derived zinc oxide nanopolyhedra/S, N: graphene quantum dots/polyaniline ternary nanohybrid for high-performance acetone sensing. *Sensors and Actuators B: Chemical* **288**, 232–242 (2019).
18. Zhang, D., Wu, D., Zong, X. & Yang, Z. Enhanced SO2 gas sensing properties of metal organic frameworks-derived titanium dioxide/reduced graphene oxide nanostructure. *J Mater Sci: Mater Electron* **30**, 11070–11078 (2019).
19. Travlou, N. A., Singh, K., Rodríguez-Castellón, E. & Bandosz, T. J. Cu–BTC MOF–graphene-based hybrid materials as low concentration ammonia sensors. *J. Mater. Chem. A* **3**, 11417–11429 (2015).
20. Yin, Y. *et al.* Inducement of nanoscale Cu–BTC on nanocomposite of PPy–rGO and its performance in ammonia sensing. *Materials Research Bulletin* **99**, 152–160 (2018).
21. Bhardwaj, S. K., Mohanta, G. C., Sharma, A. L., Kim, K.-H. & Deep, A. A three-phase copper MOF-graphene-polyaniline composite for effective sensing of ammonia. *Analytica Chimica Acta* **1043**, 89–97 (2018).
22. Ko, M., Aykanat, A., Smith, M. K. & Mirica, K. A. Drawing Sensors with Ball-Milled Blends of Metal-Organic Frameworks and Graphite. *Sensors* **17**, 2192 (2017).
23. Lewis, A. R., Náhlík, J., Jones, D. R. & Maffeis, T. G. G. Highly Sensitive Hydrogen Gas Sensors Based on Gold Nanoparticle Decorated Zinc Oxide Nanosheets. *Procedia Engineering* **168**, 321–324 (2016).
24. Campbell, M. G., Sheberla, D., Liu, S. F., Swager, T. M. & Dincă, M. Cu3(hexaiminotriphenylene)2: An Electrically Conductive 2D Metal–Organic Framework for Chemiresistive Sensing. *Angewandte Chemie International Edition* **54**, 4349–4352 (2015).
25. Zhou, T. *et al.* Pore size dependent gas-sensing selectivity based on ZnO@ZIF nanorod arrays. *Sensors and Actuators B: Chemical* **258**, 1099–1106 (2018).
26. Yao, M.-S. *et al.* Layer-by-Layer Assembled Conductive Metal–Organic Framework Nanofilms for Room-Temperature Chemiresistive Sensing. *Angewandte Chemie International Edition* **56**, 16510–16514 (2017).
27. Li, Y.-P., Li, S.-N., Jiang, Y.-C., Hu, M.-C. & Zhai, Q.-G. A semiconductor and fluorescence dual-mode room-temperature ammonia sensor achieved by decorating hydroquinone into a metal–organic framework. *Chem. Commun.* **54**, 9789–9792 (2018).
28. Mohan Reddy, A. J., Katari, N. K., Nagaraju, P. & Manabolu Surya, S. ZIF-8, Zn(NA) and Zn(INA) MOFs as chemical selective sensors of ammonia, formaldehyde and ethanol gases. *Materials Chemistry and Physics* **241**, 122357 (2020).
29. Yao, M.-S. *et al.* Van der Waals Heterostructured MOF-on-MOF Thin Films: Cascading Functionality to Realize Advanced Chemiresistive Sensing. *Angewandte Chemie International Edition* **58**, 14915–14919 (2019).
30. Meng, Z., Aykanat, A. & Mirica, K. A. Welding Metallophthalocyanines into Bimetallic Molecular Meshes for Ultrasensitive, Low-Power Chemiresistive Detection of Gases. *Journal of the American Chemical Society* (2018) doi:10.1021/jacs.8b11257.
31. Guo, K. *et al.* A Water-Stable Proton-Conductive Barium(II)-Organic Framework for Ammonia Sensing at High Humidity. *Inorg. Chem.* **57**, 7104–7112 (2018).
32. Liu, R. *et al.* A Highly Proton-Conductive 3D Ionic Cadmium–Organic Framework for Ammonia and Amines Impedance Sensing. *ACS Applied Materials & Interfaces* (2018) doi:10.1021/acsami.8b18891.

33. Sun, Z. *et al.* A Highly Stable Two-Dimensional Copper(II) Organic Framework for Proton Conduction and Ammonia Impedance Sensing. *Chemistry – A European Journal* **24**, 10829–10839 (2018).
34. Assen, A. H., Yassine, O., Shekhah, O., Eddaoudi, M. & Salama, K. N. MOFs for the Sensitive Detection of Ammonia: Deployment of fcu-MOF Thin Films as Effective Chemical Capacitive Sensors. *ACS Sens.* **2**, 1294–1301 (2017).
35. Hao, J.-N. & Yan, B. Simultaneous determination of indoor ammonia pollution and its biological metabolite in the human body with a recyclable nanocrystalline lanthanide-functionalized MOF. *Nanoscale* **8**, 2881–2886 (2016).
36. Zhang, J. *et al.* A luminescent metal-organic framework film fabricated on porous Al2O3 substrate for sensitive detecting ammonia. *Microporous and Mesoporous Materials* **253**, 146–150 (2017).
37. Zhang, J. *et al.* Mixed-Valence Cobalt(II/III) Metal–Organic Framework for Ammonia Sensing with Naked-Eye Color Switching. *ACS Appl. Mater. Interfaces* **10**, 27465–27471 (2018).
38. Ma, J. & Yan, B. Multi-component luminescence responsive Eu3+/Tb3+ hybrids based with metal-organic frameworks and zeolites A. *Spectrochimica Acta Part A: Molecular and Biomolecular Spectroscopy* **220**, 117107 (2019).
39. Ma, J., Zhao, L.-M., Jin, C.-Y. & Yan, B. Luminescence responsive composites of rare earth metal-organic frameworks covalently linking microsphere resin. *Dyes and Pigments* **173**, 107883 (2020).
40. Zhang, J. *et al.* Pencil-trace on printed silver interdigitated electrodes for paper-based NO2 gas sensors. *Appl. Phys. Lett.* **106**, 143101 (2015).
41. Daud, A. I., Wahid, K. A. A. & Khairul, W. M. Room-temperature operated cyano-terminated ethynylated-thiourea as a resistive-type carbon dioxide (CO2) gas sensor. *Organic Electronics* **70**, 32–41 (2019).
42. Khan, S., Lorenzelli, L. & Dahiya, R. S. Technologies for Printing Sensors and Electronics Over Large Flexible Substrates: A Review. *IEEE Sensors Journal* **15**, 3164–3185 (2015).
43. Oliveira, J., Correia, V., Castro, H., Martins, P. & Lanceros-Mendez, S. Polymer-based smart materials by printing technologies: Improving application and integration. *Additive Manufacturing* **21**, 269–283 (2018).
44. Timothy, C. Deposition of High Conductivity Low Silver Content Materials by Screen Printing. *Coatings* **5**, 172 (2015).
45. Zheng, Y., Zheng, S., Xue, H. & Pang, H. Metal-Organic Frameworks/Graphene-Based Materials: Preparations and Applications. *Advanced Functional Materials* **28**, 1804950 (2018).
46. Chui, S. S.-Y., Lo, S. M.-F., Charmant, J. P. H., Orpen, A. G. & Williams, I. D. A Chemically Functionalizable Nanoporous Material [Cu3(TMA)2(H2O)3]n. *Science* **283**, 1148–1150 (1999).
47. Chen, Y., Mu, X., Lester, E. & Wu, T. High efficiency synthesis of HKUST-1 under mild conditions with high BET surface area and CO2 uptake capacity. *Progress in Natural Science: Materials International* **28**, 584–589 (2018).
48. Al-Janabi, N. *et al.* Mapping the Cu-BTC metal–organic framework (HKUST-1) stability envelope in the presence of water vapour for CO2 adsorption from flue gases. *Chemical Engineering Journal* **281**, 669–677 (2015).

49. Li, X., Li, C., Wu, C. & Wu, K. Strategy for Highly Sensitive Electrochemical Sensing: In Situ Coupling of a Metal–Organic Framework with Ball-Mill-Exfoliated Graphene. *Analytical Chemistry* (2019) doi:10.1021/acs.analchem.9b00556.
50. Rani, R., Deep, A., Mizaikoff, B. & Singh, S. Enhanced hydrothermal stability of Cu MOF by post synthetic modification with amino acids. *Vacuum* **164**, 449–457 (2019).
51. Lin, S. *et al.* Adsorption behavior of metal–organic frameworks for methylene blue from aqueous solution. *Microporous and Mesoporous Materials* **193**, 27–34 (2014).
52. Fonseca, R. R. F., Gaspar, R. D. L., Raimundo, I. M. & Luz, P. P. Photoluminescent Tb3+-based metal-organic framework as a sensor for detection of methanol in ethanol fuel. *Journal of Rare Earths* **37**, 225–231 (2019).
53. Shi, N., Yin, G., Han, M., Jiang, L. & Xu, Z. Self-Assembly of Two Different Hierarchical Nanostructures on Either Side of an Organic Supramolecular Film in One Step. *Chemistry – A European Journal* **14**, 6255–6259 (2008).
54. Bartlam, C. *et al.* Nanoscale infrared identification and mapping of chemical functional groups on graphene. *Carbon* **139**, 317–324 (2018).
55. Dhumal, N. R., Singh, M. P., Anderson, J. A., Kiefer, J. & Kim, H. J. Molecular Interactions of a Cu-Based Metal–Organic Framework with a Confined Imidazolium-Based Ionic Liquid: A Combined Density Functional Theory and Experimental Vibrational Spectroscopy Study. *J. Phys. Chem. C* **120**, 3295–3304 (2016).
56. Al-Janabi, N. *et al.* A Facile Post-Synthetic Modification Method To Improve Hydrothermal Stability and CO_2 Selectivity of CuBTC Metal–Organic Framework. *Ind. Eng. Chem. Res.* **55**, 7941–7949 (2016).
57. Pawlyta, M., Rouzaud, J.-N. & Duber, S. Raman microspectroscopy characterization of carbon blacks: Spectral analysis and structural information. *Carbon* **84**, 479–490 (2015).
58. Malard, L. M., Pimenta, M. A., Dresselhaus, G. & Dresselhaus, M. S. Raman spectroscopy in graphene. *Physics Reports* **473**, 51–87 (2009).
59. Devadoss, A. *et al.* Ultrathin Functional Polymer Modified Graphene for Enhanced Enzymatic Electrochemical Sensing. *Biosensors* **9**, 16 (2019).
60. Shao, Y., Yin, G., Zhang, J. & Gao, Y. Comparative investigation of the resistance to electrochemical oxidation of carbon black and carbon nanotubes in aqueous sulfuric acid solution. *Electrochimica Acta* **51**, 5853–5857 (2006).
61. Stankovich, S. *et al.* Synthesis of graphene-based nanosheets via chemical reduction of exfoliated graphite oxide. *Carbon* **45**, 1558–1565 (2007).
62. Choi, S.-J., Kim, S.-J. & Kim, I.-D. Ultrafast optical reduction of graphene oxide sheets on colorless polyimide film for wearable chemical sensors. *NPG Asia Materials* **8**, e315 (2016).
63. Beard, B. C. Cellulose nitrate as a binding energy reference in N(1s) XPS studies of nitrogen-containing organic molecules. *Applied Surface Science* **45**, 221–227 (1990).
64. Kim, S.-Y., Kim, A.-R., Yoon, J. W., Kim, H.-J. & Bae, Y.-S. Creation of mesoporous defects in a microporous metal-organic framework by an acetic acid-fragmented linker co-assembly and its remarkable effects on methane uptake. *Chemical Engineering Journal* **335**, 94–100 (2018).
65. Han, S., Ciufo, R. A., Meyerson, M. L., Keitz, B. K. & Mullins, C. B. Solvent-free vacuum growth of oriented HKUST-1 thin films. *J. Mater. Chem. A* **7**, 19396–19406 (2019).
66. Sienkiewicz-Gromiuk, J., Rusinek, I., Kurach, Ł. & Rzączyńska, Z. Thermal and spectroscopic (IR, XPS) properties of lanthanide(III) benzene-1,3,5-triacetate complexes. *J Therm Anal Calorim* **126**, 327–342 (2016).

67. Moulder, J. F., Stickle, W. F., Sobol, P. E. & Bomben, K. D. *Handbook of X Ray Photoelectron Spectroscopy: A Reference Book of Standard Spectra for Identification and Interpretation of Xps Data*. (Physical Electronics, 1995).
68. Duke, A. S. *et al.* Active Sites in Copper-Based Metal–Organic Frameworks: Understanding Substrate Dynamics, Redox Processes, and Valence-Band Structure. *J. Phys. Chem. C* **119**, 27457–27466 (2015).
69. Li, X. *et al.* Novel approach for removing brominated flame retardant from aquatic environments using Cu/Fe-based metal-organic frameworks: A case of hexabromocyclododecane (HBCD). *Science of The Total Environment* **621**, 1533–1541 (2018).
70. Li, W. *et al.* Hierarchical hollow ZnO cubes constructed using self-sacrificial ZIF-8 frameworks and their enhanced benzene gas-sensing properties. *New J. Chem.* **39**, 7060–7065 (2015).
71. Li, W. *et al.* MOF-derived hierarchical hollow ZnO nanocages with enhanced low-concentration VOCs gas-sensing performance. *Sensors and Actuators B: Chemical* **225**, 158–166 (2016).
72. Han, N., Tian, Y., Wu, X. & Chen, Y. Improving humidity selectivity in formaldehyde gas sensing by a two-sensor array made of Ga-doped ZnO. *Sensors and Actuators B: Chemical* **138**, 228–235 (2009).
73. Borfecchia, E. *et al.* Insights into Adsorption of NH3 on HKUST-1 Metal–Organic Framework: A Multitechnique Approach. *J. Phys. Chem. C* **116**, 19839–19850 (2012).
74. Nijem, N., Fürsich, K., Bluhm, H., Leone, S. R. & Gilles, M. K. Ammonia Adsorption and Co-adsorption with Water in HKUST-1: Spectroscopic Evidence for Cooperative Interactions. *J. Phys. Chem. C* **119**, 24781–24788 (2015).
75. Petit, C., Mendoza, B. & Bandosz, T. J. Reactive Adsorption of Ammonia on Cu-Based MOF/Graphene Composites. *Langmuir* **26**, 15302–15309 (2010).
76. Peterson, G. W. *et al.* Ammonia Vapor Removal by Cu3(BTC)2 and Its Characterization by MAS NMR. *J. Phys. Chem. C* **113**, 13906–13917 (2009).
77. Bekyarova, E. *et al.* Mechanism of Ammonia Detection by Chemically Functionalized Single-Walled Carbon Nanotubes: In Situ Electrical and Optical Study of Gas Analyte Detection. *J. Am. Chem. Soc.* **129**, 10700–10706 (2007).
78. Farahani, H., Wagiran, R. & Hamidon, M. N. Humidity Sensors Principle, Mechanism, and Fabrication Technologies: A Comprehensive Review. *Sensors* **14**, 7881–7939 (2014).
79. Lv, C. *et al.* Recent Advances in Graphene-Based Humidity Sensors. *Nanomaterials* **9**, 422 (2019).
80. Li, Y. Temperature and humidity sensors based on luminescent metal-organic frameworks. *Polyhedron* **179**, 114413 (2020).
81. Furukawa, H., Cordova, K. E., O'Keeffe, M. & Yaghi, O. M. The Chemistry and Applications of Metal-Organic Frameworks. *Science* **341**, (2013).
82. Li, B. *et al.* Emerging Multifunctional Metal–Organic Framework Materials. *Advanced Materials* **28**, 8819–8860 (2016).
83. Li, Y. *et al.* Advances of metal–organic frameworks for gas sensing. *Polyhedron* **154**, 83–97 (2018).
84. Dantas, S., Sarkisov, L. & Neimark, A. V. Deciphering the Relations between Pore Structure and Adsorption Behavior in Metal–Organic Frameworks: Unexpected Lessons from Argon Adsorption on Copper–Benzene-1,3,5-tricarboxylate. *J. Am. Chem. Soc.* **141**, 8397–8401 (2019).

85. Schlichte, K., Kratzke, T. & Kaskel, S. Improved synthesis, thermal stability and catalytic properties of the metal-organic framework compound Cu3(BTC)2. *Microporous and Mesoporous Materials* **73**, 81–88 (2004).
86. Kosuru, L., Bouchaala, A., Jaber, N. & Younis, M. I. Humidity Detection Using Metal Organic Framework Coated on QCM. *Journal of Sensors* vol. 2016 e4902790 https://www.hindawi.com/journals/js/2016/4902790/ (2016).
87. Chappanda, Karumbaiah. N. *et al.* The quest for highly sensitive QCM humidity sensors: The coating of CNT/MOF composite sensing films as case study. *Sensors and Actuators B: Chemical* **257**, 609–619 (2018).
88. Robinson, A. L. *et al.* Ultrasensitive Humidity Detection Using Metal–Organic Framework-Coated Microsensors. *Anal. Chem.* **84**, 7043–7051 (2012).
89. Lu, G. *et al.* Fabrication of Metal-Organic Framework-Containing Silica-Colloidal Crystals for Vapor Sensing. *Advanced Materials* **23**, 4449–4452 (2011).
90. Ohira, S.-I. *et al.* A fiber optic sensor with a metal organic framework as a sensing material for trace levels of water in industrial gases. *Analytica Chimica Acta* **886**, 188–193 (2015).
91. Ullman, A. M. *et al.* Hybrid Polymer/Metal–Organic Framework Films for Colorimetric Water Sensing over a Wide Concentration Range. *ACS Appl. Mater. Interfaces* **10**, 24201–24208 (2018).
92. Liu, J. *et al.* In situ growth of continuous thin metal–organic framework film for capacitive humidity sensing. *J. Mater. Chem.* **21**, 3775–3778 (2011).
93. Sapsanis, C. *et al.* Insights on Capacitive Interdigitated Electrodes Coated with MOF Thin Films: Humidity and VOCs Sensing as a Case Study. *Sensors* **15**, 18153–18166 (2015).
94. Zhang, W., Meng, S., Wang, H. & He, Y. Metal organic frameworks enhanced graphene oxide electrode for humidity sensor. *J. Phys.: Conf. Ser.* **986**, 012013 (2018).
95. Jang, Y. J., Jung, Y. E., Kim, G. W., Lee, C. Y. & Park, Y. D. Metal–organic frameworks in a blended polythiophene hybrid film with surface-mediated vertical phase separation for the fabrication of a humidity sensor. *RSC Adv.* **9**, 529–535 (2018).
96. Gardner, D. W. *et al.* Transistor-Based Work-Function Measurement of Metal–Organic Frameworks for Ultra-Low-Power, Rationally Designed Chemical Sensors. *Chem. Eur. J.* **25**, 13176–13183 (2019).
97. Andrés, M. A. *et al.* Methanol and Humidity Capacitive Sensors Based on Thin Films of MOF Nanoparticles. *ACS Appl. Mater. Interfaces* **12**, 4155–4162 (2020).
98. Ru, C. *et al.* Effective enhancement on humidity sensing characteristics of sulfonated poly(ether ether ketone) via incorporating a novel bifunctional metal–organic–framework. *Journal of Electroanalytical Chemistry* **833**, 418–426 (2019).
99. Zhang, Y. *et al.* A novel humidity sensor based on NH2-MIL-125(Ti) metal organic framework with high responsiveness. *J Nanopart Res* **15**, 2014 (2013).
100. Seo, Y.-K. *et al.* Formation of Polyaniline-MOF Nanocomposites Using Nano-Sized Fe(III)-MOF for Humidity Sensing Application. *J Nanosci Nanotechnol* **19**, 8157–8162 (2019).
101. Weiss, A., Reimer, N., Stock, N., Tiemann, M. & Wagner, T. Screening of mixed-linker CAU-10 MOF materials for humidity sensing by impedance spectroscopy. *Microporous and Mesoporous Materials* **220**, 39–43 (2016).
102. Su, P.-G. & Lee, X.-H. Electrical and humidity-sensing properties of flexible metal-organic framework M050(Mg) and KOH/M050 and AuNPs/M050 composites films. *Sensors and Actuators B: Chemical* **269**, 110–117 (2018).

103. Yin, Y.-Y. *et al.* A 3D pillared-layer cadmium (II) metal-organic framework for chemiresistive humidity sensing with high performance. *Inorganic Chemistry Communications* **97**, 49–55 (2018).

104. Zhang, J. *et al.* High performance humidity sensor based on metal organic framework MIL-101(Cr) nanoparticles. *Journal of Alloys and Compounds* **695**, 520–525 (2017).

105. Weiss, A., Reimer, N., Stock, N., Tiemann, M. & Wagner, T. Surface-modified CAU-10 MOF materials as humidity sensors: impedance spectroscopic study on water uptake. *Phys. Chem. Chem. Phys.* **17**, 21634–21642 (2015).

106. Zhang, Y. *et al.* Humidity sensing properties of FeCl3-NH2-MIL-125(Ti) composites. *Sensors and Actuators B: Chemical* **201**, 281–285 (2014).

107. Zhang, Y. *et al.* Regulating the dissociation of LiCl and transportation of Li ions within UiO-66-NH2 framework for humidity sensing applications with superb comprehensive performances. *Journal of Alloys and Compounds* **818**, 152854 (2020).

108. Wang, D., Tan, Q., Liu, J. & Liu, Z. A stable europium metal–organic framework as a dual-functional luminescent sensor for quantitatively detecting temperature and humidity. *Dalton Trans.* **45**, 18450–18454 (2016).

109. Zhou, Z. *et al.* Antiferromagnetic Copper(II) Metal–Organic Framework Based Quartz Crystal Microbalance Sensor for Humidity. *Crystal Growth & Design* **17**, 6719–6724 (2017).

110. Terracina, A. *et al.* Multitechnique Analysis of the Hydration in Three Different Copper Paddle-Wheel Metal–Organic Frameworks. *J. Phys. Chem. C* **123**, 28219–28232 (2019).

111. Xue, W., Zhang, Z., Huang, H., Zhong, C. & Mei, D. Theoretical Insights into the Initial Hydrolytic Breakdown of HKUST-1. *J. Phys. Chem. C* **124**, 1991–2001 (2020).

112. Gul-E-Noor, F. *et al.* Effects of varying water adsorption on a Cu3(BTC)2 metal–organic framework (MOF) as studied by 1H and 13C solid-state NMR spectroscopy. *Phys. Chem. Chem. Phys.* **13**, 7783–7788 (2011).

General Conclusion and Perspectives

General Conclusion and Perspectives

This PhD project was dedicated to the development of new active and intelligent packaging material solutions. The main objective was to implement innovative micro- and nanomaterials such as nanocellulose, silver nanoparticles or Metallic Organic Frameworks into packaging materials for the development of smart and safe applications. Mainly two technologies were investigated namely antibacterial surfaces and smart gas sensors. The proof of concept of the solutions developed, as well as the characterisation of the materials used, their processing, their properties and their final performances for the desired applications were investigated.

In **Chapter I**, an extensive and complete literature review was presented concerning the field of active and intelligent packaging. The global economic, social, environmental and innovative context of the packaging field was detailed as well as the existing technologies of active and intelligent packaging both at the industrial/commercial and academic research scale. A specific focus on the materials and applications relevant to the experimental section of the work was also applied. This literature review highlighted how innovative the materials selected for these studies are. The number of scientific publications and patents associated to "Metal Organic Framework for gas sensing" and "Cellulose nanofibrils and silver nanoparticle" have indeed boomed since the start of this PhD project in 2017 (**Table 1**).

***Table 1**: Bibliometric studies of the materials used in the experimental section of the study and comparison between the start of this PhD project in 2017 and at the end in 2020. The numbers were extracted from SciFinder with the following descriptors: "Metal Organic Framework", "gas sensing"; "cellulose nanofibrils", "cellulose microfibrils", "microfibrillated cellulose", "nanofibrillated cellulose", "silver nanoparticle"*

	Publications		Patents	
	Before 2017 (1st publication)	**2017-2020**	Before 2017 (1st patent)	**2017-2020**
Cellulose nanofibrils and silver nanoparticles	28 (2007)	**48**	5 (2013)	**1**
Metal Organic Frameworks and gas sensing	191 (2008)	**406**	41 (2005)	**60**

This chapter not only showed the versatility and variety of materials, processes, and specific applications in the field, but also showed the promising capability of the materials selected for such applications: cellulose nanofibrils and silver nanowires for antibacterial packaging, and Metal Organic Framework for the development of smart gas sensors. This literature review also emphasised some challenges and research gaps which impacted the experimental strategies developed in the study. For instance, these main gaps are: the preparation of antibacterial cellulose nanofibrils and silver nanoparticles materials using a direct route (no chemical synthesis) with a high tunability and adaptability of the solution proposed (silver loading,

thickness, etc.) or using a different shape than spherical silver nanoparticles, or the implementation of Metal Organic Frameworks for packaging applications using straightforward and easy-to-produce systems. The experimental section of this work was then separated into two chapters relevant to the two different technologies that were developed.

In **Chapter II**, the antibacterial activity of materials based on cellulose nanofibrils and silver nanowires was proven. Inks made of these materials were deposited on different substrates using different processes and their active properties were assessed and optimised. In **Chapter III**, the combined use of Metal Organic Frameworks and conductive carbon-graphene materials for the preparation of gas sensors on flexible packaging materials was demonstrated. Their morphological, electrical and chemical properties were characterised as well as their gas sensing performances.

This PhD project was conducted at the interface of chemistry, material science, process engineering, and biology, making it strongly multidisciplinary. This has deeply impacted the wide variety of experiments, tests and characterisation procedures performed throughout the project. The main results obtained in **Chapters II** and **III** as well as future work perspectives are summarised in **Table 2** and **Table 3**.

Table 2**: Summary of the main results and perspectives associated to Chapter **II

Chapter **II**: Cellulose nanofibrils and silver nanowires for antibacterial packaging		
Section	Results	Perspectives
1. Cellulose nanofibrils and silver nanowires transparent coatings for the development of enhanced packaging surfaces	**Thickness-controlled** thin **coatings** on both **PET and PLA** (< 2µm) **High transparency** (75 $\%T_{550\ nm}$ for 350 nm coating) **Limited release** of active silver materials (< 0.5 ppm after 24 hours for 350 nm coating) **Strong antibacterial activity** (>90% for 350 nm coating) **Enhancement of barrier properties** (50% reduction of both oxygen and water vapour transmission rate for 350 nm coating) and **other active properties** Roll-to-roll **up-scaling** by reverse gravure process	Different substrates (paper, cardboard, glass, aluminium) Comparison with spherical silver nanoparticles Influence of cellulose nanofibrils' chemical functionalisation on antibacterial properties
2. Rheology of cellulose nanofibrils and silver nanowires for the development of screen-printed antibacterial surfaces	**Thixotropic** and **viscosity** properties are formulation dependent Screen-printing quality requires 5% wt **HPMC additive** **High antibacterial activity** (67%) and **high transparency** (73 $\%T_{550\ nm}$) is retained with HPMC addition	Impact of different additives (chitosan, starch, etc.) and solvent influence Roll-to-roll screen printing Preparation of smart labels and efficiency assessment
3. Antibacterial and barrier mode of action of cellulose nanofibrils and silver nanowires films casting systems	**Potentiometry** is not well adapted for the leaching assessment of silver ions from such matrix No or **limited Ag NWs leaching** by UV-vis spectroscopy Promising preliminary assessment of the leaching by ICP-OES shows **limited release** of silver (0.76 ppm after 1 hour) **Barrier properties** of the films are not impacted by Ag NWs	Long term leaching assessment by ICP-OES Comparison with spherical silver nanoparticles Influence of cellulose nanofibrils' chemical functionalisation on silver leaching

In **Chapter II**, cellulose nanofibrils and silver nanowires suspensions were first coated on packaging dedicated substrates (PET, PLA), using a laboratory-scale process. Different thicknesses were achieved (200-1750 nm) and the functional layers were found to be highly antibacterial both Gram-positive *S. Aureus* and Gram-negative *E. Coli*, working by contact with a minimal release of active materials. The coatings also enhanced the barrier properties of the films and displayed other active properties such as antioxidant, UV-barrier or antifog properties. The optimum system was found to be the 350 nm thick coating that reached 75 $\%T_{550\ nm}$ transparency, around 50% reduction of both oxygen and water vapor transmission rate, and the antibacterial activity superior to 90% toward both *S. Aureus* and *E. Coli*. The capability of the system to be upscaled was also proven using the reverse gravure process with retained active properties.

In the studies reported in the second section of this chapter, inks based on cellulose nanofibrils and silver nanowires were formulated using raw materials of different sources and different ratios. The rheological parameters of the inks were found to be source and formulation dependent. Inks that fit screen-printing requirements were then formulated. However, it was necessary to add at least 5% wt of hydroxypropymethyl cellulose (HPMC) additive in the ink formulation to achieve the desired print quality. The optimal formulation led to a deposited thickness measured around 600 nm, with 73 $\%T_{550\ nm}$ transparency. Moreover, a good antibacterial activity of 67% was retained, showing that the HPMC additive only slightly hindered the antibacterial properties.

In the studies reported in the last section of this chapter, larger scale cellulose nanofibrils and silver nanowires composites were prepared by film casting. The silver leaching was assessed by UV-vis spectroscopy, potentiometry and a preliminary ICP-OES study. No or limited release of Ag NWs was found proving their strong entanglement into the nanocellulose network. The potentiometric studies displayed a surprisingly high amount of silver ions released and was deemed not adequate for the assessment of silver ions leaching from the prepared materials. The preliminary assay using ICP-OES found a low release of silver ions (0.76 ppm) after 1 hour. Extrapolating this number for the coating developed in Section 1 and relying on a food product packaging scenario, led to calculations that show that the developed system could theoretically presents silver ions leaching behaviour below the European Food Safety Agency recommendation, within the tested timeframe. Finally, the barrier properties of the films were investigated, and the water vapour and oxygen transmission rate were only slightly affected by the Ag NWs compared to the good barriers of the T-CNF control.

The main perspective for this chapter would be first to study different new substrates for the coating techniques to enlarge the potential of the proposed solution for packaging applications (paper, cardboard, glass, aluminium, etc.). Then, the comparison with spherical silver nanoparticles could be conducted both in terms of antibacterial activity and silver leaching to

conclude on the superior characteristics of silver nanowires for this application, due to the physical entrapment within the cellulose nanofibrils matrix. On the same idea, it would be interesting to verify how the cellulose nanofibrils' chemical functionalisation (e.g. use of cationic CNF) impact the silver leaching and antibacterial properties. Finally, other additives and solvent could be used to optimise the screen-printing process and aim at upscaling the localised deposition process toward roll-to-roll screen printing.

In the studies reported in **Chapter III**, gas sensors were prepared by formulating copper benzene-1,3,5-tricarboxylate (CuBTC) Metal Organic Framework (MOF) along with carbon-graphene materials and drop-casting the prepared ink on screen-printed silver interdigitated electrodes.

Table 3**: Summary of the main results and perspectives associated to Chapter **III

Chapter **III**: Intelligent sensors based on Metal Organic Framework for packaging applications		
Section	Results	Perspectives
1. Ammonia sensors based on Metal Organic Framework on flexible substrate	**Straight-forward** and easy **preparation of sensors** using commercial raw materials, on **flexible substrate** by screen-printing and drop-casting Electrical properties of the devices are strongly **formulation dependant** Devices are sensitive in the **20-100 ppm range** (4.6% response at 100 ppm) **Response and recovery time** are relatively high but fit for packaging applications	Other gas targets and selectivity measurements Development of fully screen-printed sensors Influence of the conductive carbon counterpart
2. Humidity sensors based on Metal Organic Framework on flexible substrate	Optimised devices are sensitive in the **30 to 80% of relative humidity (RH) range** **Lower characteristic times** than for ammonia sensing but **higher response** (up to 54% at 80% RH)	Selectivity between humidity and ammonia Performances for ammonia sensing under humidity

In the studies reported in the first section, the devices were optimised and tested against ammonia sensing. The electrical properties of the sensors were highly formulation dependent and the resistance of the devices ranged from few ohms to hundreds of Mega-ohms. The surface morphology was also impacted by the formulation and surface chemistry was investigated using a large variety of characterisation methods. It proved the proper dispersion and the retention of physico-chemical properties for the components throughout the sensor's preparation process. The optimised device response was linear in the 20-100 ppm of ammonia range with a maximal response of 4.6% at 100 ppm. The characteristics times were slightly high but fit with packaging expectations (10-30 min for recovery time and 15-25 min for response time), the sensors were stable over several cycles and the interaction between the CuBTC and ammonia was verified using spectroscopic method to be linked with reversible adsorption on the metallic centre with partial amidation of the BTC ligand. In the studies reported in the second sub-section, the optimised formulation was tested for humidity sensing and the results showed a good correlation between the sensors response and the relative humidity for a tested range of 30-80 % relative humidity. The sensor maximal response was as high as 54.2% with lower recovery and response time than for ammonia sensing. The response of the optimised formulation was significantly higher than the carbon-graphene control, proving the interest of using CuBTC MOF for the development of these gas sensors. The sensors preparation was straight-forward, easy to implement and used commercial products making the proposed solution interesting to be adapted at an industrial level.

The main perspectives of this chapter would be to investigate further the sensing capability of the developed systems for different gas targets such as carbon dioxide or ethanol, and to check the selectivity between these different gasses. The final target would be to fully prepare sensors using only screen-printing or other high-volume continuous process such as a roll-to-roll printing process like flexography. Evaluating the influence of the conductive carbon counterpart using for instance carbon nanotubes or different type of functional graphene materials is also an interesting idea.

Finally, the perspective that is common to both **Chapter II** and **Chapter III** is to implement the developed system in real food product packaging demonstrators and test their performances in the enhancement and control of the shelf-life of such products, within the regulatory requirements of the field.

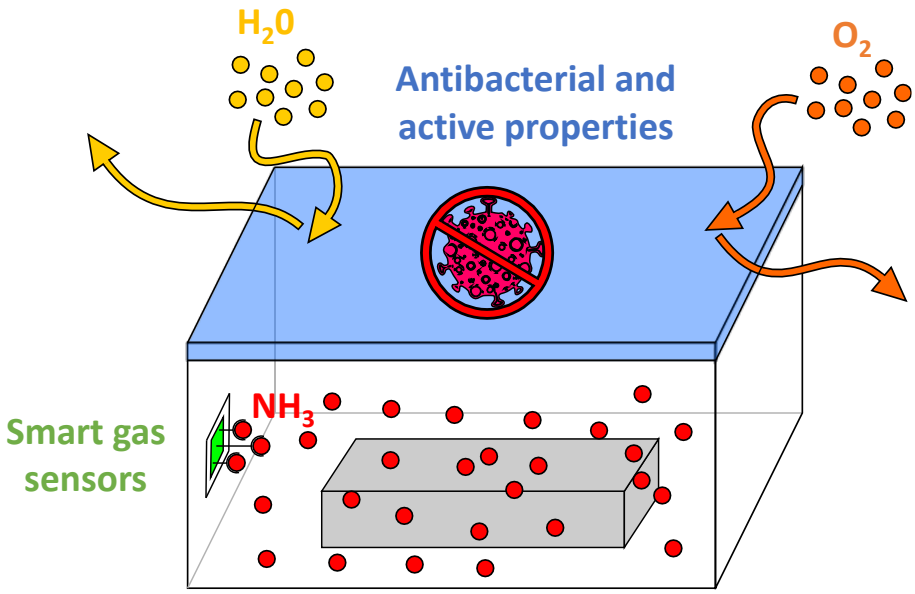

***Figure 1**: Schematic representation of the two active and intelligent packaging technologies developed in the project*

As a conclusion, this PhD project successfully developed and proved the concept of two different technologies linked to active and intelligent packaging (**Figure 1**). Transparent and antibacterial surface processing was achieved using cellulose nanofibrils and silver nanowires composites, while smart sensors were produced using Metal Organic Frameworks and conductive carbon materials as sensitive layers in sensors prepared on flexible polymer films. This paves the way for further development in the field of active and intelligent packaging using innovative micro- and nanotechnology to achieve societal and ecological targets in global reduction of food and packaging waste.

Extended French abstract

Résumé en Français

Ce résumé a pour but de synthétiser en français le travail effectué durant ce projet de thèse. Il respecte donc les différentes parties de la version complète du manuscrit rédigée en anglais, à savoir une introduction générale du contexte de la thèse, une première section dédiée à la littérature scientifique relative au travail expérimental effectué, et finalement une section décrivant les principaux résultats expérimentaux obtenus vis-à-vis des deux stratégies déployées au sein de ce projet : (i) le développement d'emballages antibactériens à base de nanofibrilles de cellulose et de nanofils d'argent d'une part, et (ii) le développement de capteurs de gaz intelligent à base de Metal Organic Frameworks et de matériaux conducteurs à base de carbone.

1. Introduction

L'accès à la nourriture, sa production ou sa conservation ou encore son transport a toujours été un enjeu majeur lié au développement de la vie humaine sur Terre. Le concept d'emballage n'est en effet pas nouveau et remonte historiquement à il y a plus de deux mille ans avec par exemple, en Chine, l'utilisation d'écorce d'arbre traitée chimiquement pour servir d'emballage flexible[1]. Depuis ce temps, le domaine de l'emballage s'est bien évidement diversifié grâce à l'explosion des échanges internationaux et de la mondialisation dans la seconde partie du 20ème siècle mais aussi grâce à certaines avancées scientifiques et technologiques majeures qui ont révolutionnées le domaine. Le secteur de l'emballage reste aujourd'hui un secteur industriel fort. La valeur globale du marché de l'industrie de l'emballage a en effet été estimée en 2019 à 917 milliards de dollars (US) et est en croissance constante avec une valeur estimée et attendue de 1050 milliards de dollars (US) en 2024, ce qui correspond à un taux de croissance annuelle de 2,8% (2019)[2].

Les emballages alimentaires représentent la plus forte part du secteur et dans ce cas précis, le rôle de l'emballage est de protéger son contenu de l'environnement extérieur, que ce soit d'un point de vue mécanique, chimique, ou encore microbien afin d'optimiser la durée de vie des denrées alimentaires. Les principaux risques pour un emballage et son produit emballé sont par exemple un choc mécanique lors des étapes diverses de la chaîne d'approvisionnement (transport, etc.), des interactions chimiques conduisant par exemple à l'oxydation ou l'absorption d'eau ou de graisse ou encore une contamination bactérienne (**Figure 1**).

Les principaux matériaux utilisés aujourd'hui pour les emballages sont le verre, l'aluminium, le papier, le carton ou encore les matériaux plastiques (**Figure 2**). Le terme de « plastiques » réfère de façon générale aux polymères synthétiques produit par polyaddition ou polycondensation. Leurs propriétés physico-chimiques remarquables ont fait d'eux des matériaux essentiels dans notre société actuelle et particulièrement dans le domaine des emballages. Les principaux emballages plastiques utilisés aujourd'hui proviennent des polymères dits « thermoplastiques » qui fondent et se ramollissent à haute température, ce qui

permet de les façonner à la forme désirée très facilement[3]. Les polymères les plus souvent utilisés dans le domaine de l'emballage sont le polypropylène (PP), le polyéthylène (PE), le polyéthylène téréphtalate (PET) ou encore le polystyrène (PS).

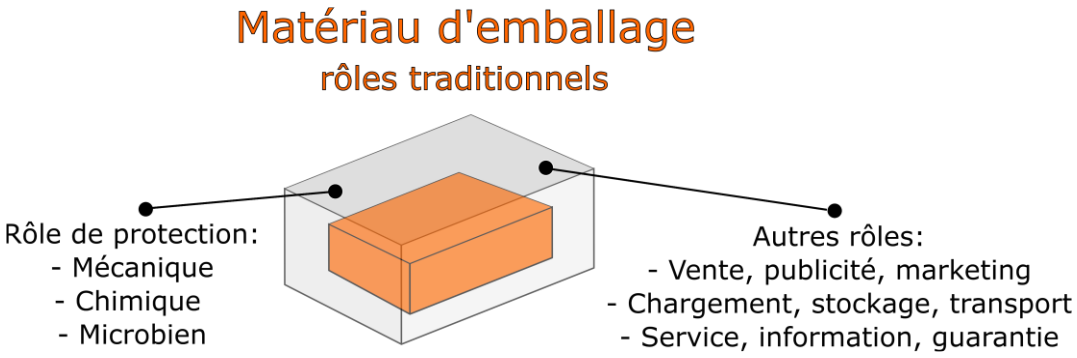

***Figure 1**: Rôles traditionnels des emballages*

Si les emballages plastiques proposent des propriétés physico-chimiques intéressantes, ils ne sont toutefois pas biodégradables dans la majorité des cas et peuvent causer d'importants dommages environnementaux. Les principales préoccupations liées à une mauvaise récupération et traitement de déchets d'emballages plastiques, sont leur dégradation en micro et nanoparticules de plastiques dans l'environnement ayant des conséquences désastreuses sut la faune et la flore marines ou terrestres[4,5]. Si les thermoplastiques sont par définition recyclables, l'utilisation de produits finis complexes, multi-matériaux et multifonctionnels rend la séparation et le recyclage difficile. Sur les 17.8 millions de tonnes de plastiques collectés après usage en Europe en 2018, 42% ont été recyclés, 33% utilisés pour récupérer de l'énergie et 18% entreposés dans des décharges[6]. Plusieurs solutions existent pour faire pencher la balance d'un côté davantage respectueux de l'environnement : un meilleur recyclage, l'utilisation de matériaux biosourcés et biodégradables ou encore une utilisation plus efficace et raisonnée des emballages.

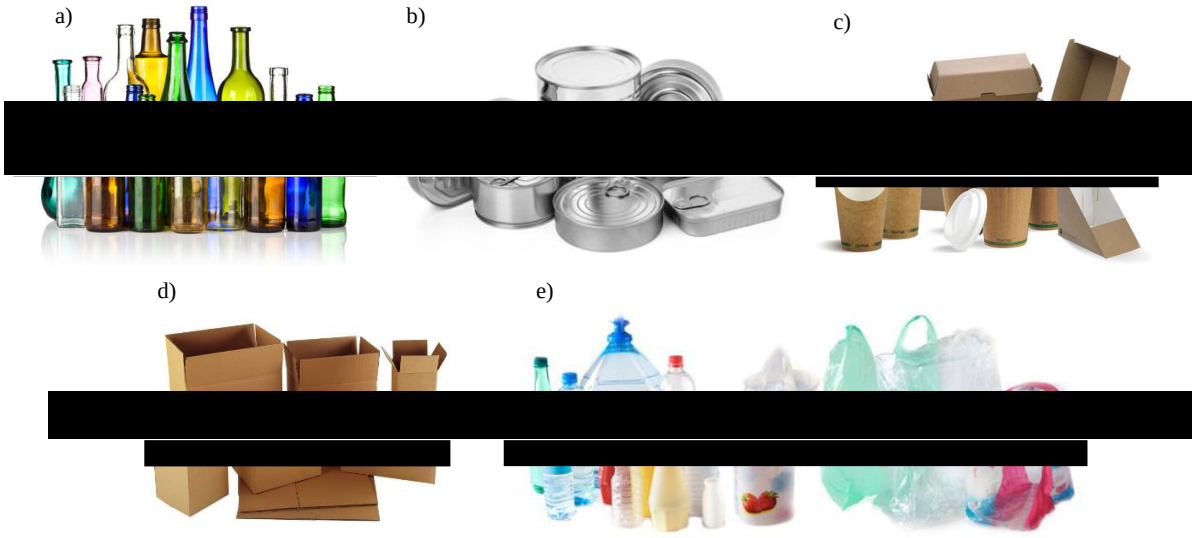

***Figure 2**: Les différents matériaux utilisés pour l'emballage avec a) le verre, b) le métal, c) le papier, d) le carton et e) le plastique. Images respectivement extraites de www.packaginginnovation.com, www.bccourier.com, www.cwpdistributors.com, www. parrs.co.uk, and www.actu-environnement.com, consulté en ligne le 22.04.20*

Un autre problème majeur de la mondialisation, et en particulier de l'explosion des échanges et des flux de marchandises, est le gaspillage alimentaire. L'Organisation des Nations Unies pour l'Alimentation et l'Agriculture estime qu'environ un tiers de la nourriture produite à l'échelle mondiale n'est pas consommée, ce qui représente 1.2 milliard de tonnes de déchets par an[7]. Cela semble particulièrement aberrant en sachant que la même organisation a estimé qu'en 2018, environ 800 millions d'êtres humains vivaient en situation de sous-nutrition critique. De plus, nourrir l'intégralité de la planète reste un défi majeur pour le futur, compte tenu de la croissance démographique mondiale qui estime que la population globale atteindra les 10 milliards de personnes en 2050[8]. Ce gaspillage alimentaire engendre aussi d'énormes impacts environnementaux et si l'on devait par exemple comparer le gaspillage alimentaire en termes d'émission de dioxyde de carbone aux différentes nations mondiales, il en prendrait la troisième place dernière la Chine et les Etats-Unis (**Figure 3**).

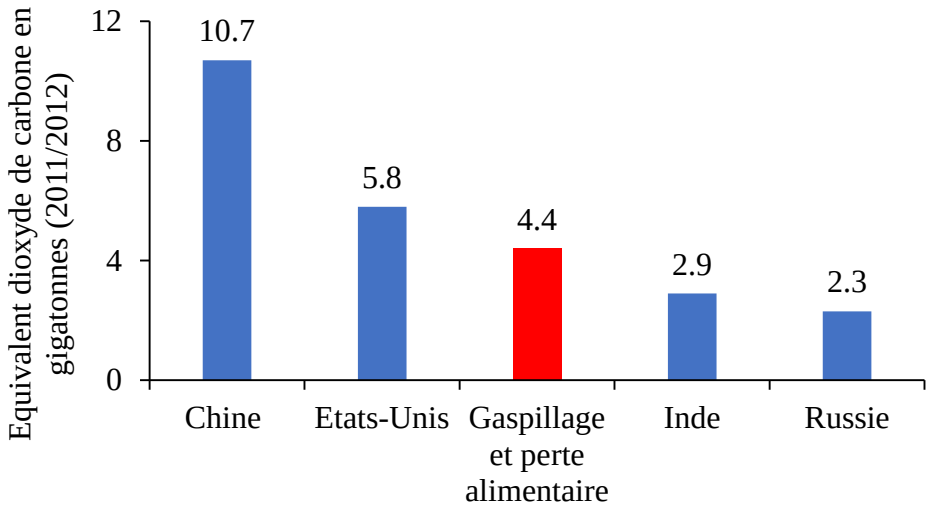

***Figure 3**: Equivalent en émission de dioxyde de carbone du gaspillage alimentaire comparé aux pays avec les plus importantes émissions à l'échelle mondiale en 2011/2012. Extrait et adapté de World Resources Institute. Creating a sustainable food future. (2019), consulté en ligne le 22.04.20*

Les emballages ne servent plus aujourd'hui de simples barrières physiques pour protéger les produits emballés. Ils ont aussi un rôle de communication, de publicité et de marketing pour les marques concernées. Certaines des dernières innovations dans le domaine comme les emballages actifs et intelligents vont encore plus loin, en ajoutant de nouvelles fonctionnalités aux emballages, et sont un moyen de combattre le gaspillage alimentaire en permettant une utilisation plus efficace et raisonnée des matériaux d'emballages (**Figure 4**). Les emballages actifs sont généralement définis comme des emballages capables de répondre à un stimulus extérieur en absorbant ou relarguant des substances actives. Ils incluent des technologies telles que les absorbeurs d'oxygène, d'humidité ou d'éthylène, les emballages antibactériens ou antioxydants ou encore des émetteurs de dioxyde de carbone. Les emballages intelligents sont eux capables de collecter, de stocker et de redistribuer des informations concernant le produit emballé ou l'emballage. Ils concernent des technologies telles que divers capteurs et indicateurs (gaz, temps/température, bactérien) mais aussi des systèmes interactifs comme la radio-identification. Ces emballages actifs et intelligent permettent soit d'augmenter la durée de vie des produits emballés, soit d'obtenir des informations sur le produit emballé. Les informations peuvent être de différentes natures et par exemple aider les différents acteurs de la chaîne d'approvisionnement pour identifier certaines étapes critiques ou dysfonctionnelles, ou encore renseigner le consommateur. En somme, ces technologies sont des outils pour optimiser les emballages aux produits emballés et aux différentes spécificités de leur chaîne d'approvisionnement, ce qui permet de lutter contre le gaspillage alimentaire et le gaspillage de matériaux d'emballages.

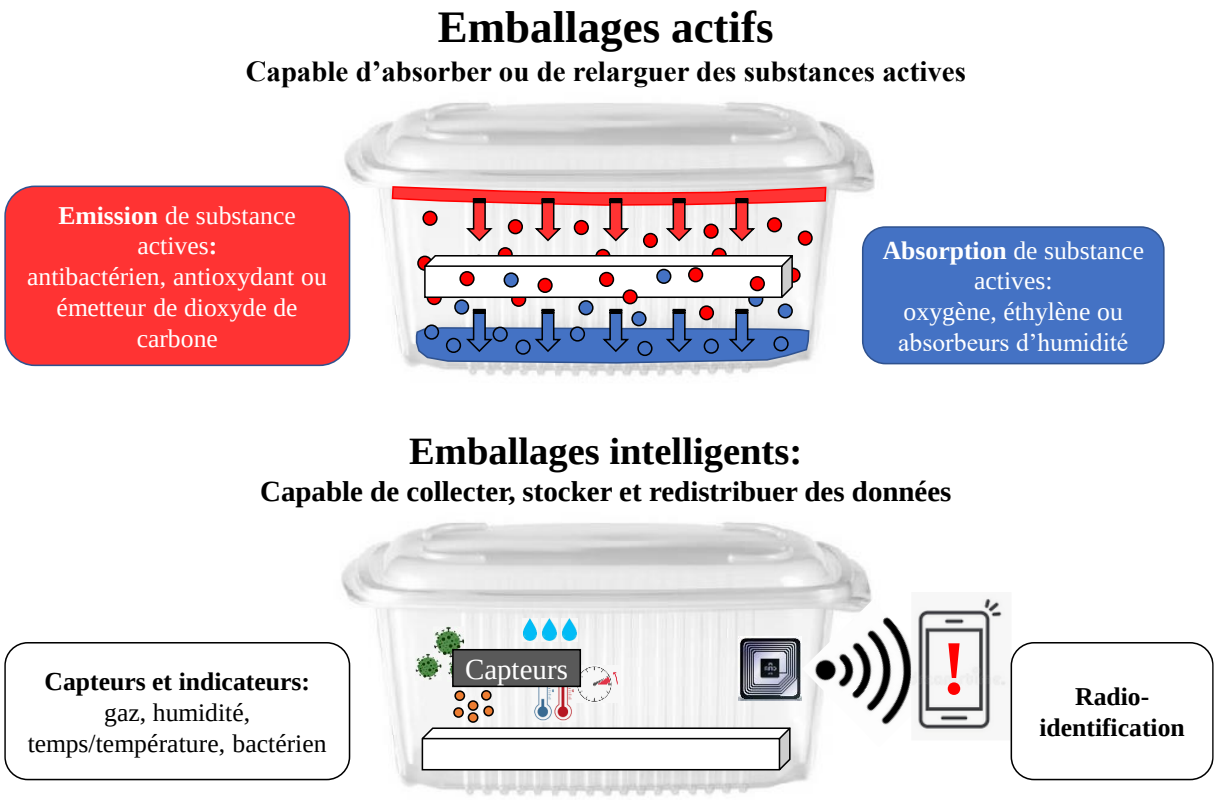

***Figure 4**: Représentation schématique des technologies liées aux emballages actifs et intelligents*

2. Description du projet et littérature associée

2.1. Description du projet

Ce projet, intitulé « Développement d'emballages antimicrobiens et intelligents » a débuté en octobre 2017 et a pour but de développer des emballages actifs et intelligents pour le domaine alimentaire et médical, en incorporant de nouveaux micro- et nanomatériaux innovants. Il s'agit d'un projet collaboratif entre le Laboratoire Génie des Procédés Papetiers (LGP2, UMR 5518) de Grenoble (France) et le Welsh Centre for Printing and Coating (WCPC) du College of Engineering de l'Université de Swansea (Royaume-Uni). Le projet a été réalisé dans le cadre d'un partenariat stratégique international entre l'Université Grenoble Alpes et l'Université de Swansea. La moitié du temps a été passé respectivement dans chaque Université et les partenaires ont été en collaboration et communication constante tout au long du projet afin d'apporter leurs compétences respectives sur les technologies liés aux emballages actifs et intelligents. Le projet repose sur le développement de deux stratégies différentes, la première dédiée au développement d'un emballage actif et en particulier antibactérien et la seconde au développement d'un emballage intelligent en en particulier incorporant des capteurs de gaz.

Dans la première stratégie, le concept a été de développer des emballages antibactériens grâce au dépôt d'une couche composée de nanofibrilles de cellulose et de nanofils d'argent. Les films d'emballage ont été fonctionnalisés par enduction sur différents substrats en utilisant différents procédés. Les propriétés actives mais aussi les propriétés naturellement liées à leur nature d'emballages (antibactérien, propriétés barrières, optiques, etc.) ont été étudiées. Ensuite, l'adaptation de la solution proposée pour un procédé d'impression sérigraphie ainsi que l'étude rhéologique des encres produites a été réalisée. Finalement, le mode d'action des propriétés antibactériennes et barrières a été investigué, en utilisant des films autoporteurs préparés par évaporation de solvent. Dans la seconde stratégie, des capteurs de gaz ont été produits sur des substrats flexibles, en utilisant des Metal Organic Frameworks comme matériaux actifs en combinaison avec des matériaux conducteurs à base de carbone,. Leurs performances ont été mesurées d'abord pour la détection et quantification d'ammoniac gazeux et ensuite en tant que capteurs d'humidité en testant plusieurs paramètres tels que l'influence de la formulation, leurs propriétés physico-chimiques de surface, le mode d'action des capteurs ainsi que leur stabilité.

Les prochaines sections s'appliquent donc à synthétiser l'état de l'art, ainsi que les parties expérimentales développées dans ce travail (**Figure 5**).

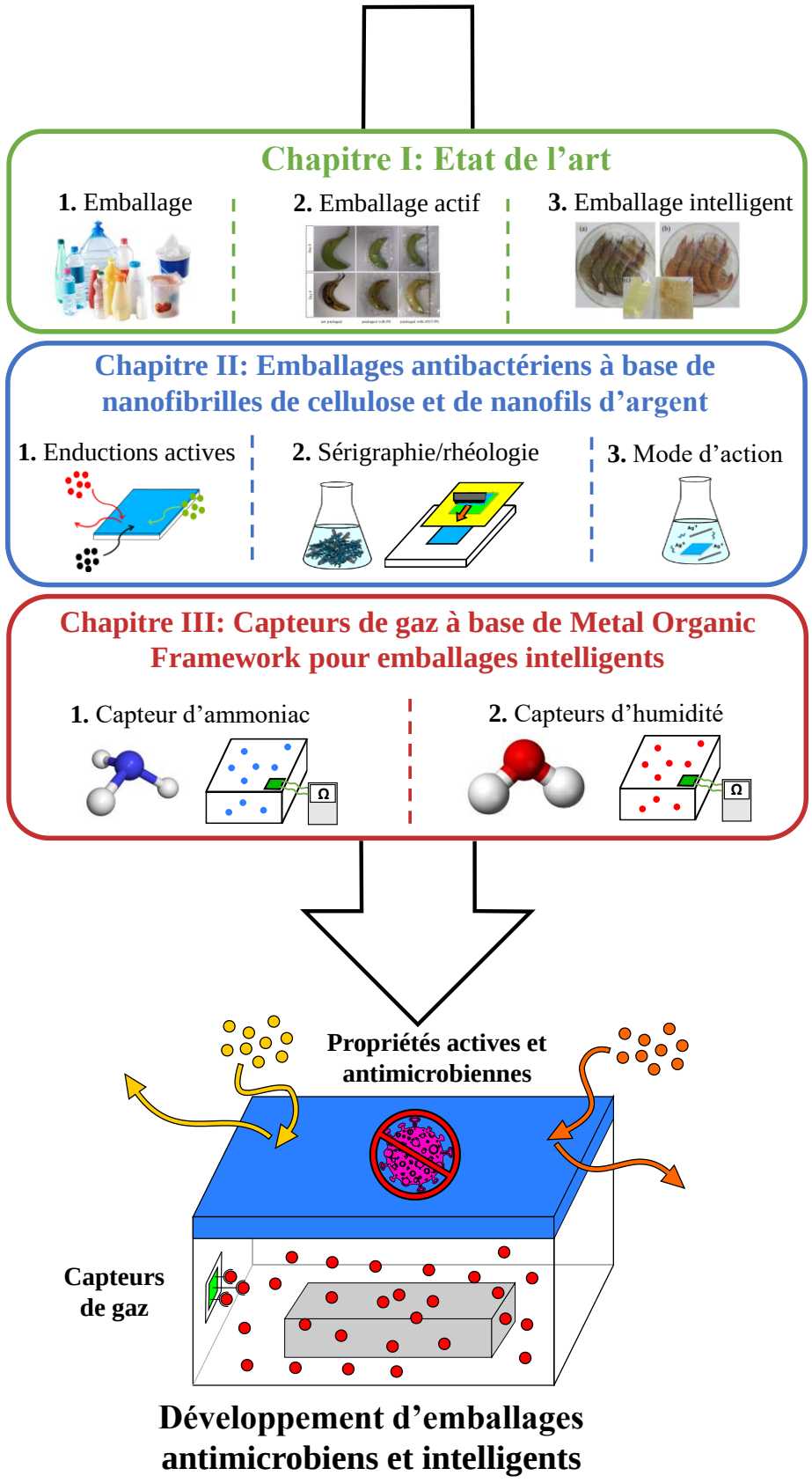

***Figure 5**: Schéma résumant l'organisation générale du projet. Les images ont respectivement été extraites et reproduites de www.actu-environnement.com (consulté le 22.04.20), de Tas et al. (2017) avec la permission de Springer Nature (Copyright 2017)[9] et de Ma et al. (2017) avec la permission d'Elsevier (Copyright 2017)[10]*

2.2. Littérature scientifique

Le concept des emballages actifs et intelligents a été détaillé précédemment dans l'introduction et cette section est particulièrement focalisée sur les technologies relatives à la partie expérimentale de la thèse à savoir les emballages antibactériens et les capteurs de gaz, ainsi que les principaux matériaux utilisés.

2.2.1. Emballages antibactériens

Le rôle des emballages antibactériens est de combattre les contaminations bactériennes afin de limiter la détérioration des produits emballés et ainsi d'augmenter leur durée de vie. Différents matériaux ont déjà été utilisés dans ce but, comme par exemple des polymères antibactériens (chitosan, polylysine), des huiles essentielles (arbre à thé, origan, citronnelle, etc.), des extraits naturels (rosin, sumac, aloe vera, etc.), des enzymes ou bactériocines (lysozyme, nisine, lacticine, etc.), des acides organiques (acide citrique, sorbique, tannique, etc.) ou encore des nanoparticules métalliques (argent, oxide de zinc, dioxyde de titane, cuivre, etc.)[11].

Les nanoparticules d'argent (Ag NPs) sont particulièrement intéressantes pour des applications d'emballages antibactériens pour différentes raisons. Tout d'abord, l'argent est un matériau relativement abordable et abondant, qui a été utilisé par différentes civilisations à travers les âges pour la préservation d'aliments et de boissons mais aussi pour la médecine et le traitement des blessures[12]. Les Ag NPs sont généralement produites par un procédé chimique qui implique la réduction de sels d'argent en utilisant des réducteurs tels que les polyols, le réactif de Tollens ou encore du borohydrure de sodium mais dont la synthèse peut aussi être catalysée par traitement ultraviolet (UV)[13]. Les propriétés finales des nanoparticule (NPs) peuvent être contrôlés par différent paramètres lors de leur synthèse comme le temps de réaction, le solvent, le précurseur (concentration, ratio), les tensioactifs, etc. Les Ag NPs présentent des propriétés antibactériennes intéressantes et sont peu sensibles au développement de résistance chez les bactéries pathogènes contrairement aux antibiotiques[14]. Leur mode d'action est complexe et n'est pas totalement élucidé par la communauté scientifique. Il est attribué à la fois aux nanoparticules elle-même mais aussi au relargage continue d'ions argent, avec différents effets notoires comme la destruction de la paroi et membrane cellulaire bactérienne, des interférences avec les protéines respiratoires, la perturbation de la réplication de l'ADN ou encore l'induction de stress oxydatif au sein de la cellule[15] (**Figure 6**).

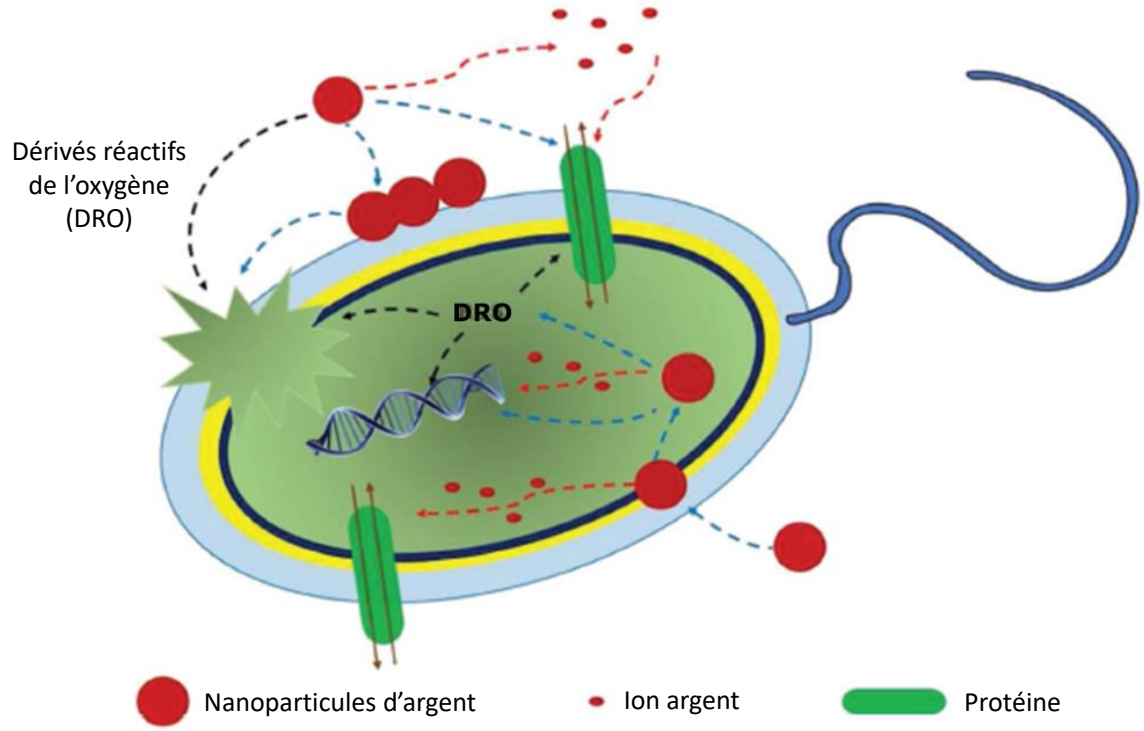

***Figure 6**: Mode d'action antibactérien des nanoparticules d'argent avec différents mécanismes proposés : accumulation sur la paroi cellulaire et pénétration au sein de la cellule, dommage sur la membrane, relargage d'ion argent ainsi que perturbation de l'ADN et autres enzymes/protéines, ou encore production de dérivés réactifs d'oxygène. Reproduit et adapté de Tang et al. (2018) avec la permission de Wiley (Copyright 2018)*[15]

Dans ce projet, des nanoparticules de forme cylindrique avec un rapport longueur/largeur très important ont été utilisés, couramment appelées nanofils d'argent. Ces nanofils d'argent (Ag NWs) utilisés dans ce projet ont été associés à des nanofibrilles de cellulose (CNF) pour préparer des composites antibactériens. La cellulose est un polymère naturel, composé de monomères de D-glucose reliés par une liaison glycosidique β-1,4. Les CNF sont des nanoparticules de cellulose produites par fibrillation mécanique d'une source cellulosique[16] (**Figure 7**). Elles sont obtenues la plupart du temps sous la forme d'une suspension aqueuse blanchâtre plus ou moins transparente. La production mondiale de CNF est en pleine expansion et a par exemple triplée entre 2015 et 2018 et de nombreux produits commerciaux incluant des CNF existent à présent sur le marché[17,18]. L'avancée industrielle de ces matériaux s'explique principalement par le développement de prétraitements chimiques et biologiques dans les années 2000 qui ont permis de réduire drastiquement la consommation énergétique nécessaire pour la production de CNF (et donc le coût de production), comme par exemple l'oxydation TEMPO ou le prétraitement enzymatique[19,20]. Cependant, il existe un grande variété possible de CNF grâce à la grande diversité de sources de cellulose, de prétraitements, de nature de fibrillation mécanique, de fonctionnalisation chimique ainsi que de post-traitements[21,22]. Les principales propriétés des CNF, outre leur biodégradabilité, biocompatibilité et caractère biosourcé, proviennent de leur taille nanométrique qui leur confère une grande surface

spécifique, un fort réseau de liaison hydrogène, ainsi qu'une grande versatilité pour effectuer des modifications chimiques[23]. Les propriétés finales obtenues dépendront également de la façon dont seront mise en forme les CNF, à savoir suspensions, couches minces, aérogels, etc.

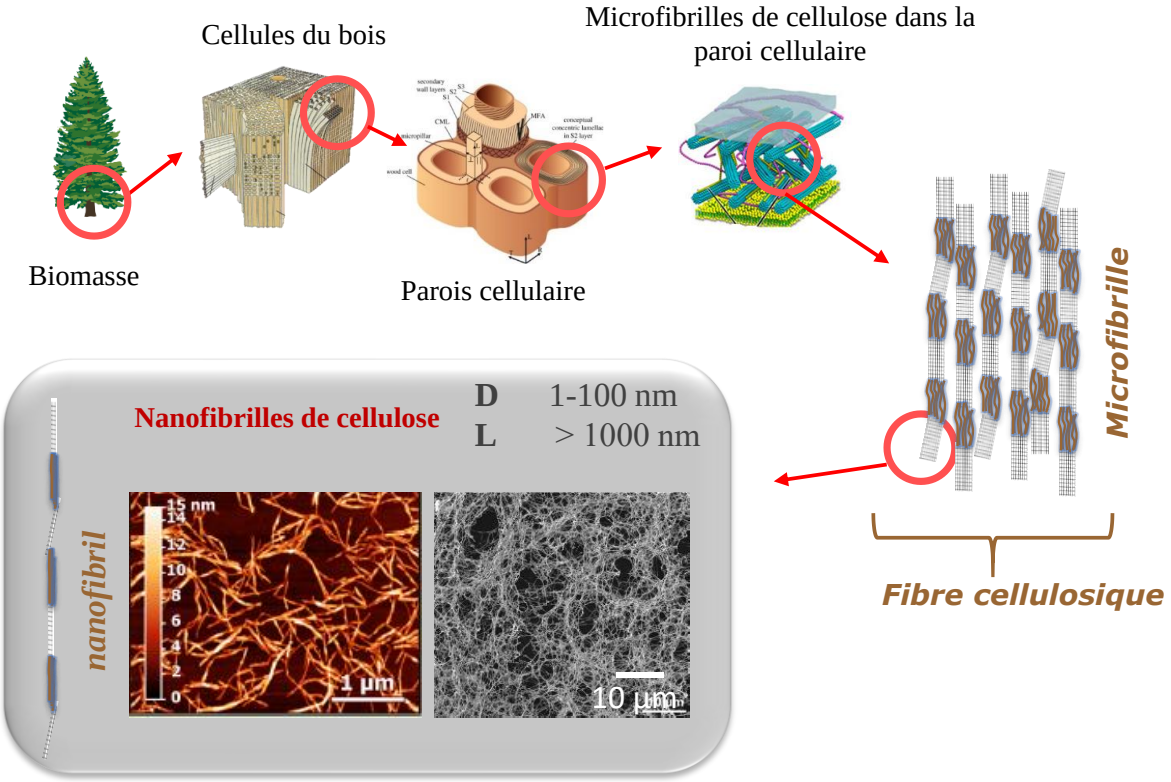

***Figure 7**: Représentation schématique de la production de nanofibrilles de cellulose. Les images microscopiques des nanofibrilles de cellulose ont été respectivement reproduites et adaptées de Grüneberger et al. (2014) avec la permission de Springer Nature (Copyright 2014)[24], et de Nechyporchuk et al. (2016) avec la permission de American Chemical Society (Copyright 2016)[25]*

Les matériaux hybrides composés de CNF et de Ag NPs ont été largement étudiés par la communauté scientifique ces 20 dernières années. De tels matériaux sont en général produits par réduction in-situ de sels d'argent en présence d'une suspension de CNF ou alors par réduction après immersion d'un matériau nanocellulosique dans une solution de sels d'argent.

Différents auteurs ont reporté la production de tels matériaux antibactériens par filtration. Par exemple, Yan et al. (2020) ont produits des supports antibactériens pour le biomédical en filtrant un mélange de CNF/Ag NPs sur des membranes en acide polylactique[26]. Li et al. (2019) ont préparés des membranes antibactériennes en utilisant des CNF modifiées par oxydation au périodate qui ont aussi servis de réducteurs lors de la synthèse des Ag NPs. Les auteurs ont montrés de bonnes propriétés antibactériennes avec un relargage faible et contrôlé d'ions argent[27]. En utilisant un système plus complexe, Xiao et al. (2013) ont préparés des films antibactériens à base de Ag NPs[28], CNF, dioxyde de titane et chitosan tandis que Bober et al. (2014) ont utilisés un système à base de Ag NPs, CNF et polypyrrole[29]. Finalement, Ramaraju et al. (2015) est sûrement le seul exemple dans la littérature de liaison covalente dans la

préparation de composites Ag NPs/CNF en stabilisant les Ag NPs par un dendrimère lié de façon covalente à des CNF ayant subi une oxydation TEMPO[30]. L'activité antibactérienne de ces films a été vérifiés par un test de zone d'inhibition contre *E. Coli* et *S. Aureus*.

La préparation de composites antibactérien à base de Ag NPs/CNF se fait aussi classiquement par évaporation de solvent. Des systèmes assez simples ont été développés impliquant un mélange de Ag NPs/CNF[31,32] ou alors plus complexe impliquant des additifs (latex, acide citrique, tannins) ou l'utilisation d'un composite époxy avec des CNF modifiés à la triéthanol amine[33–35]. Yan et al. (2016) ont quant à eux préparés des films antibactériens de façon innovantes en sprayant une solution de nitrate d'argent sur des films de CNF suivi par réduction chimique ou UV, ce qui a permis d'atteindre une concentration en argent importante dans le film (de l'ordre de 4% wt)[36].

Finalement de tels composites peuvent aussi être mis en forme autrement que sous la forme de films, avec par exemple la préparation d'aérogels[37,38], d'enduction sur du papier[39] ou encore l'utilisation directe d'une suspension à base de Ag NPs/CNF[40]. Des exemples de matériaux à base de CNF/Ag NPs sont présentés sur la **Figure 8**.

La majorité de la littérature impliquant des composites à base de Ag NPs/CNF s'applique à des matériaux préparés par évaporation de solvent ou filtration synthétisant in-situ les Ag NPs. Les méthodes proposées apparaissent difficilement envisageables pour la production à plus grande échelle. De plus, seul des Ag NPs sphériques ont été testées et très peu de références ont également investigué le relargage d'ions argent et son implication dans l'activité antibactérienne des matériaux produits.

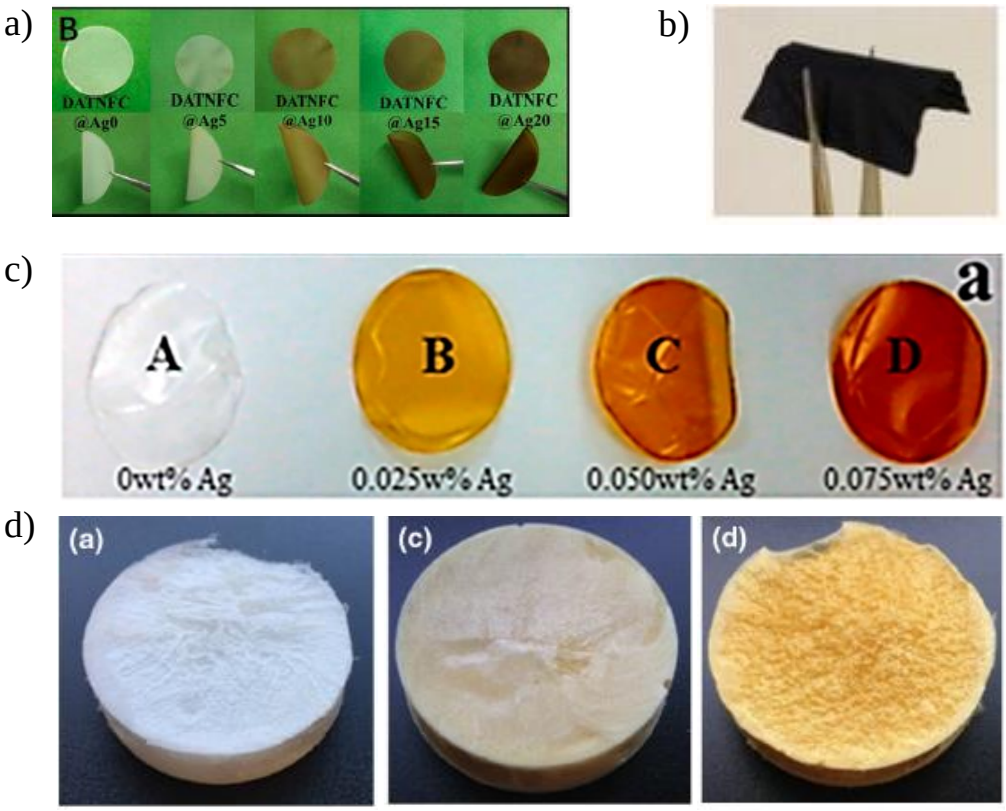

***Figure 8**: Différent exemples de matériaux antibactériens à base de Ag NPs avec a) films composés de CNF modifiées par oxydation au periodate et Ag NPs, b) films composés de CNF modifiées par oxydation au periodate, Ag NPs et polypyrrole, c) films composés de CNF modifiées par oxydation TEMPO et Ag NPs, utilisant un dendrimère à base de poly(amido amine) comme agent de réticulation et d) aérogels préparés à base de CNF (gauche), CNF/Ag NPs (milieu et droite). Les images ont été respectivement reproduites et adaptées de Li et al. (2019) avec la permission de l'American Chemical Society (Copyright 2018) pour a)[27], de Bober et al. (2014) avec la permission de l'American Chemical Society (Copyright 2014) pour b)[29], de Ramaraju et al. (2015) avec la permission de Elsevier (Copyright 2014) pour c)[30] et de Uddin et al. (2017) avec la permission de Springer Nature (Copyright 2017) pour d)[38]*

2.2.2. Capteurs de gaz

Dans les technologies des emballages intelligents, les capteurs et indicateurs sont probablement les plus utilisés. Ils permettent de donner des informations à différentes étapes de la chaîne d'approvisionnement et à ses différents acteurs, concernant un changement dans l'atmosphère interne des emballages. Ces changements peuvent par exemple être lié à la concentration gazeuse de certains analytes, comme l'oxygène, le dioxyde de carbone, la vapeur d'eau, l'ammoniac, etc. Les capteurs permettent une quantification de la concentration en analytes tandis que les indicateurs donnent une information visuelle qualitative souvent représenté par un changement de couleur ou l'apparition/disparition d'un motif (**Figure 9**). Ils peuvent s'appuyer sur différents principes physiques comme des principes électriques, optiques, électrochimiques, etc.

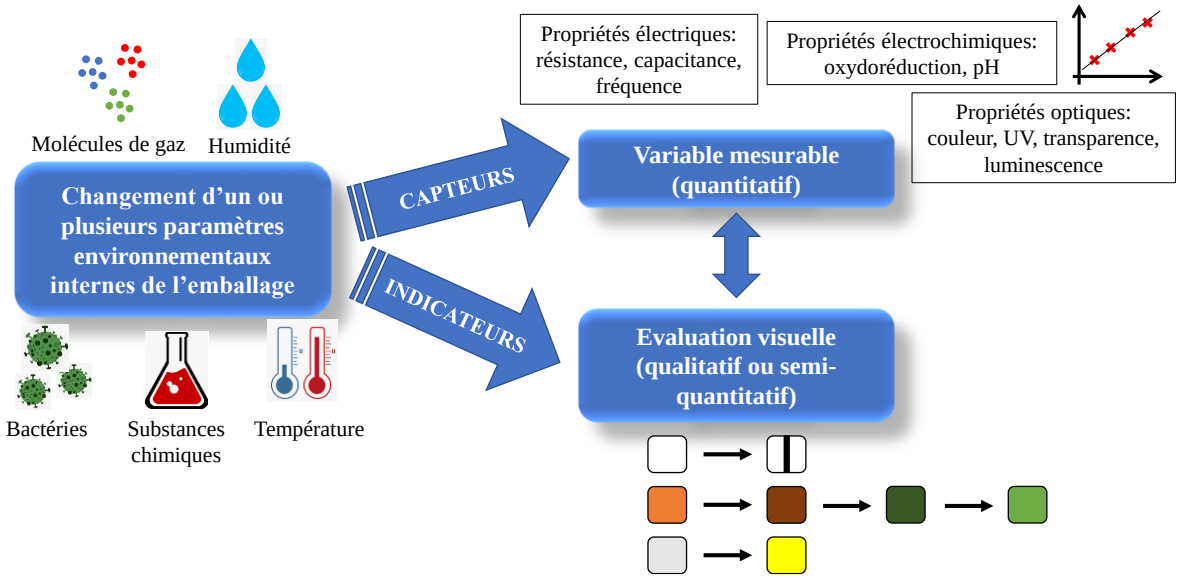

***Figure 9**: Représentation schématique des capteurs et indicateurs utilisés dans les emballages intelligents*

Mesurer le taux d'oxygène à l'intérieur des emballages est intéressant car l'oxygène peut être responsable de l'oxydation des aliments mais aussi promouvoir le développement de bactéries[11]. Les capteurs d'oxygène peuvent aussi permettre d'identifier des dysfonctionnements dans des produits emballés sous atmosphère modifiée. Ces capteurs utilisés dans le cadre d'emballages intelligents fonctionnent principalement par photoluminescence car cela consiste en une approche non destructive, réversible et adaptable à une échelle industrielle[41,42]. Différents types d'indicateurs d'oxygène ont aussi été développés, en se basant sur des systèmes d'oxydo-réduction[43–45]. Le contenu en dioxyde de carbone est aussi un indicateur intéressant à mesurer. En effet, il est souvent utilisé en partie dans les emballages à atmosphère modifiée car il réduit la croissance microbienne et augmente donc la durée de vie des produits[46]. Le principe de quantification du dioxyde de carbone est aussi principalement basé sur des système optiques[47,48] même si certains auteurs ont montrés la possibilité d'utiliser des capteurs électriques[49]. Différents types d'indicateurs de dioxyde de carbone ont aussi été développés, en utilisant principalement des techniques colorimétriques couplées à des indicateurs de pH[50–52]. Même s'il s'agit d'un paramètre important à contrôler, peu d'études ont appliqué la détection et quantification de l'humidité au domaine des emballages[53–55].

Les amines volatiles (ammoniac triméthylamine, diméthylamine) sont connues pour être des indicateurs de la dégradation d'aliments à base de poisson ou de fruits de mers[56,57]. Ces paramètres sont d'habitude contrôlés par une mesure de l'azote basique volatil total, qui est un test long et destructif. Des emballages intelligents mesurant la quantité de tels composés sont donc intéressants pour mesurer la fraîcheur et la qualité de poissons et fruits de mer emballés. Des capteurs optiques basés sur une technologie à base de vésicules de polyacétylène ainsi que de nanocristaux de cellulose et de chitosan, ont par exemple été développés par Nguyen et al.

(2019)[58]. Kuswandi et al. (2012) ont aussi préparés un capteur optique d'ammoniac en utilisant un film de polyaniline en corrélant la concentration mesurée en gaz avec la croissance de bactéries[59]. D'autres capteurs innovants ont aussi été récemment développés par Narwade et al. (2019) en utilisant une structure d'aérogel à base de nanofibrilles de cellulose et d'hydroxyapatite mais sans toutefois tester le système avec des produits alimentaires[60]. Chung et al. a aussi démontré l'utilisation d'un capteur d'ammoniac commercial couplé avec une technologie de radio-identification pour le suivi sans fil de la dégradation de la qualité de poissons frais[61]. Les indicateurs d'ammoniac sont pour la plupart basés sur des indicateurs colorés sensibles au pH[10,62–65] (**Figure 10**). Finalement, même si peu adaptés pour l'instant au domaine des emballages, une large palette de capteurs d'ammoniac sur des supports flexibles ont déjà été développés, en utilisant par exemple des matériaux à base de nanoparticules de carbone (nanotubes de carbone, graphène) ou encore de polymères conducteurs (polypyrrole, poylaniline, polythiophène)[66,67].

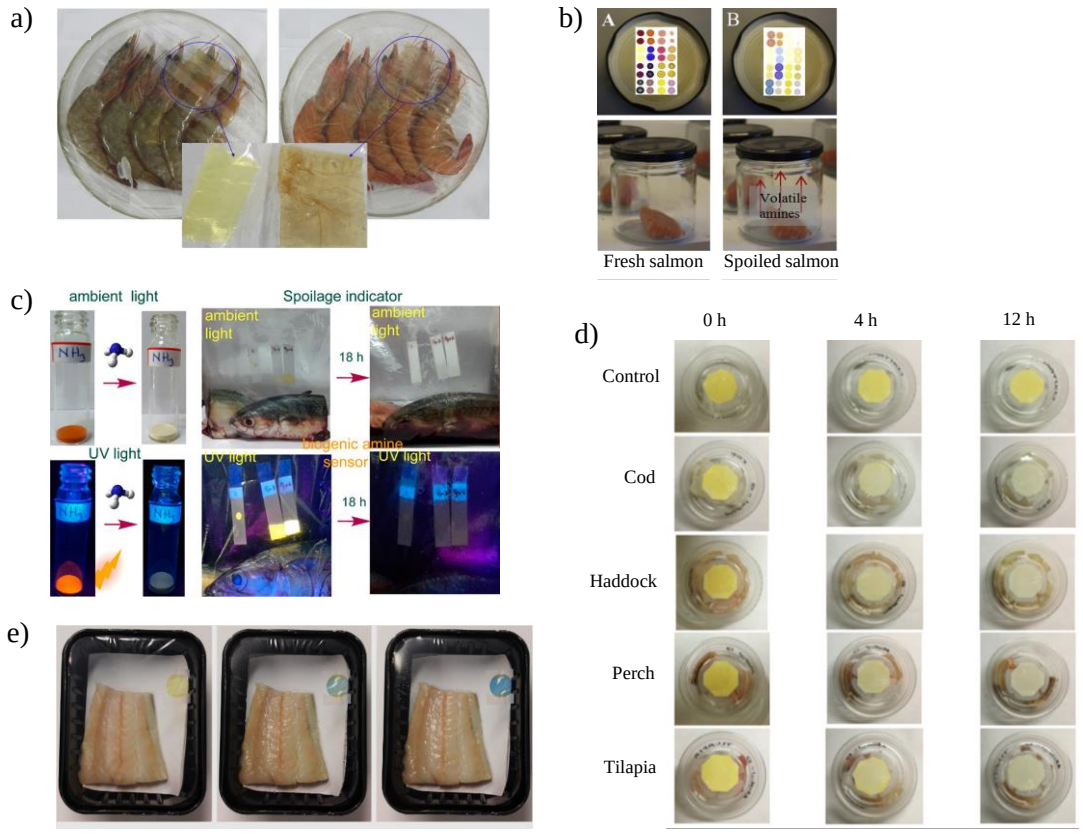

***Figure 10**: Différents indicateurs d'ammoniac et d'amines volatiles pour des emballages intelligent, avec a) un film sensible au pH à base de curcuma/gomme de tara et d'alcool polyvinylique avec changement de couleur avant (gauche) et après détérioration de l'aliment (droite), b) une étiquette sensible au pH formée de 16 différents indicateurs colorés avant (gauche) et après (droite) exposition à du saumon en décomposition, c) une étiquette fluorescente à base de sels de pyridium et changement de couleur sous lumière UV pour du poisson frais (gauche) et en décomposition (droite), d) une étiquette sensible au pH à base de quinoxaline sur du papier et changement de couleur en fonction du temps de stockage (0, 4 et 12 h) de différents poissons, et e) film sensible au pH à base de bleu de bromophénol extrudé avec du polyéthylène basse densité et changement de couleur après stockage (de gauche à droite : 0, 24 et 48 h). Images respectivement reproduites et adaptées de Ma et al. (2017) avec la*

permission de Elsevier (Copyright 2017) pour a)[10], de Morsy et al. (2016) avec la permission de Elsevier (Copyright 2015) pour b)[64], de Basavaraja et al. (2020) avec la permission de l'American Chemical Society (Copyright 2020) de c)[62], de Luo et al. (2019)[63] pour d) et de Wells et al. (2019) avec la permission de Elsevier (Copyright 2018) pour e)[65]

Dans ce projet, des Metal Organic Frameworks (MOFs) ont été utilisés pour le développement de capteurs de gaz sur des supports flexibles. Dans les différents matériaux innovants pour le développement de capteurs des gaz, les MOFs ont particulièrement suscité l'intérêt de la communauté scientifique ces 15 dernières années. Les MOFs sont des matériaux hybrides organiques-inorganiques formés par la liaison entre un centre métallique et des ligands organiques multifonctionnels, ce qui forme un réseau 3D, cristallin et poreux. Ces matériaux sont principalement synthétisés par des procédés thermiques en présence de solvants. En jouant sur la structure géométrique du centre métallique et des ligands associés, il est possible d'obtenir une large variété de MOFs différents. Un des MOFs les plus utilisés est le Cuivre benzène-1,3,5-tricarboxylate (CuBTC) découvert en 1999 par Chui et al. et qui consiste en une structure dimérique cuivre-cuivre de formule $[Cu_3(BTC)_2(H_2O)_3]_n$[68]. Les cristaux de CuBTC sont de taille micrométrique et de forme bipyramidal à base carré. A l'échelle macroscopique, CuBTC se présente sous forme de poudre de couleur bleu turquoise (hydratés) ou bleu foncé (secs) et possède une surface spécifique BET qui peut atteindre les 2000 $m^2.g^{-1}$ avec des pores principaux de 9 Å par 9 Å[69–71] (**Figure 11**). CuBTC a été étudié pour diverses applications comme pour de la séparation de gaz, des capteurs, de la catalyse, de la dépollution et plusieurs produits commerciaux existent actuellement sur le marché.

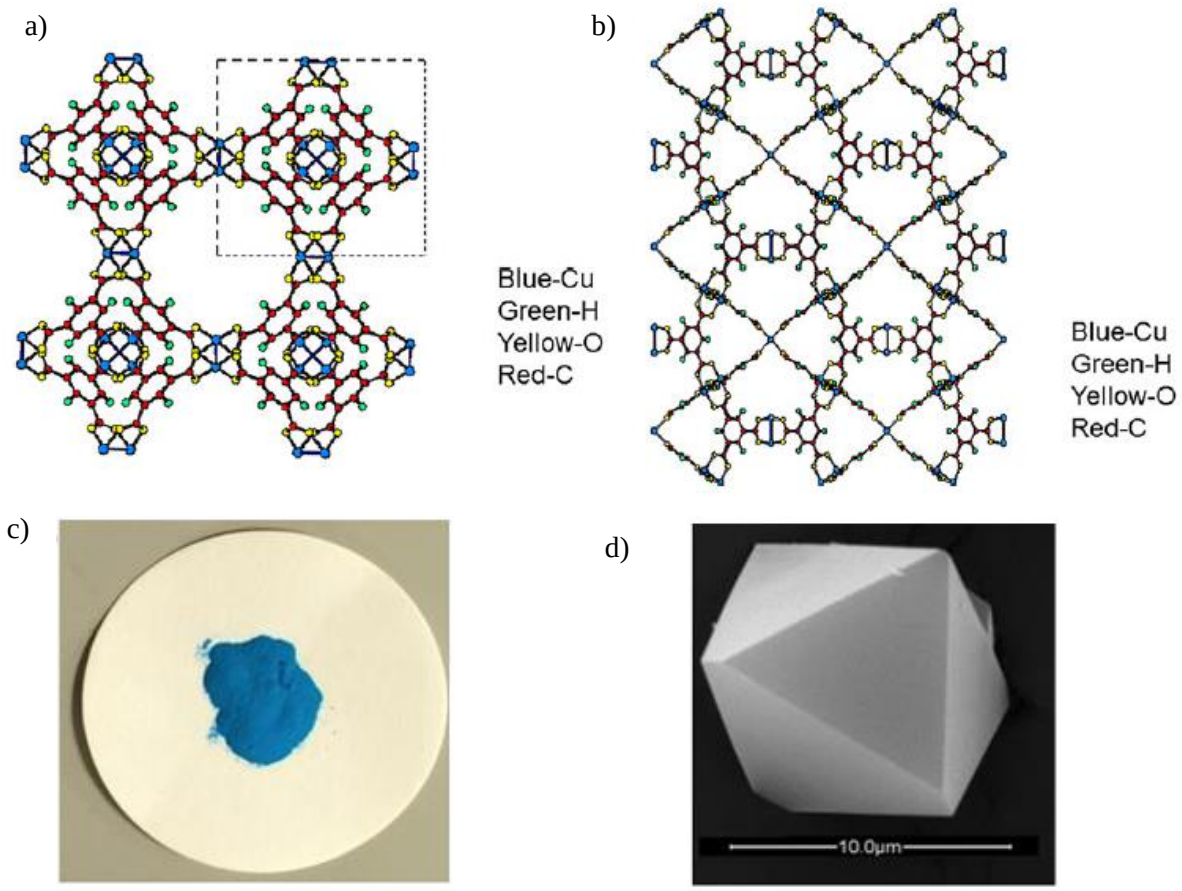

***Figure 11**: Structure cristalline du MOF CuBTC avec a) vue schématique de la structure selon l'axe [100], b) vue schématique de la structure après rotation de 45° selon l'axe [100], c) photo de l'aspect visuel et d) Microscopie Electronique à Balayage d'un cristal. Images respectivement reproduites et adaptées de Wong-Ng et al. (2015) pour a) et b)[70], Hendon et al. (2015) pour c)[71] et de Al-Janabi et al. (2016) avec la permission de l'American Chemical Society (Copyright 2016) pour d)[69]*

Même si des capteurs de gaz à base de MOFs ont largement été produits et caractérisés dans la littérature, il n'existe pas, à notre connaissance, de références les couplant avec le domaine des emballages intelligents. Les capteurs de gaz utilisant des MOFs peuvent utiliser différent concept comme des techniques mécaniques (microbalance à quartz, micro-leviers, onde acoustique de surface), optiques (interférométrie, luminescence, résonnance plasmonique de surface) ou encore électrique (capacitance, résistance, impédance). Les capteurs électriques sont principalement préparés suivant deux méthodes : soit en utilisant directement une pastille compressée de MOFs ou alors en déposant une suspension de MOFs sur des électrodes. De nombreuses références ont montrés l'efficacité de tels capteurs pour différents gaz et différents MOFs (**Table 1**) et certains exemples sont regroupés sur la **Figure 12**.

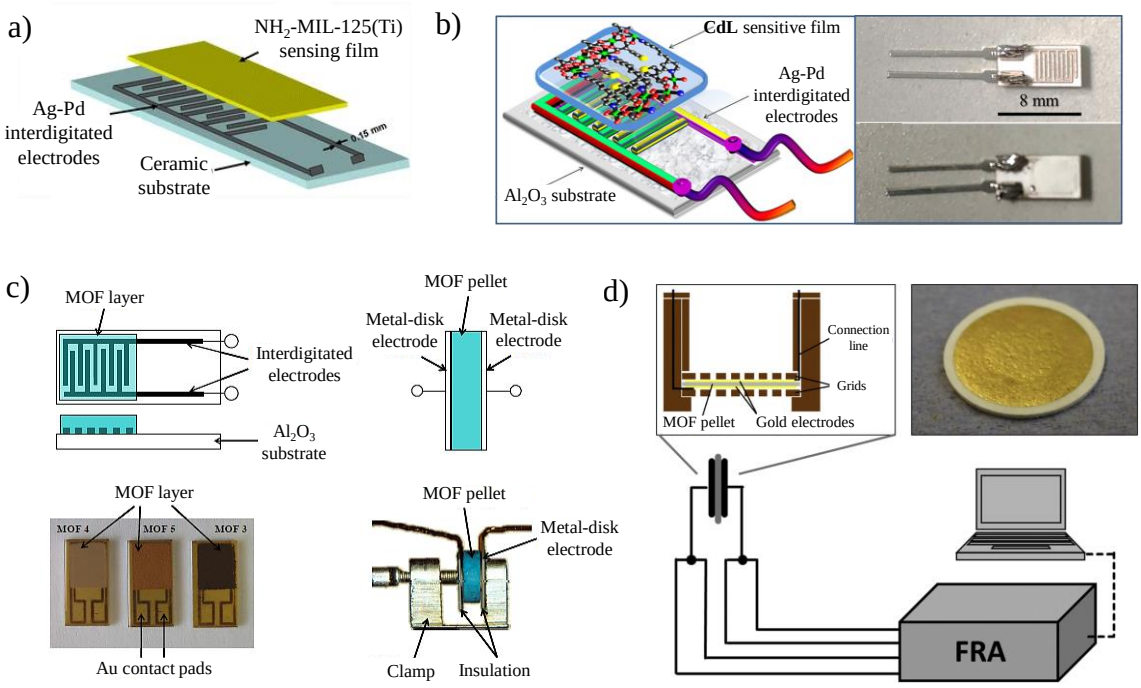

***Figure 12**: Exemples de capteurs de gaz utilisant des MOFs avec a) NH_2-MIL-125(Ti) MOF déposé sur une électrode interdigitalisée Ag-Pd pour capter l'humidité, b) représentation schématique d'un capteur d'humidité utilisant le Cd(TMA)(DPP) MOF déposé sur une électrode interdigitalisée Ag-Pd, c) capteurs fonctionnant par impédance pour la quantification de différents gaz (CO_2, O_2, NO, H_2, éthanol, propane, méthanol, et humidité) et d) capteur d'humidité utilisant une pastille de CAU-10 MOF. Images respectivement reproduites et adaptées de Zhang et al. (2013) avec la permission de Springer Nature (Copyright 2013) pour a)[72], de Yin et al. (2018) avec la permission de Elsevier (Copyright 2018) pour b)[73], de Achmann et al. (2009) pour c)[74] et de Weiss et al. (2016) avec la permission de Elsevier (Copyright 2015) pour d)[75]*

Les propriétés intrinsèques des MOFs, et en particulier leur faible conductivité électronique (souvent considérés comme des matériaux isolants pour la plupart d'entre eux) leur font souvent défauts pour des applications électroniques et c'est pourquoi il est intéressant de les coupler avec des matériaux conducteurs tels que des polymères conducteurs, des oxides métalliques ou encore des nanoparticules de carbone[76–78].

***Table 1**: Capteurs de gaz électriques utilisant des MOFs soit sous forme de pastilles soit par dépôt de suspension sur des electrodes interdigitalisés (TA = température ambiante)*

Gaz	MOF	Préparation des capteurs	Concept (Température)	Reference
CO_2	CDMOF-2	Pastille	Conductivité ionique (TA)	Gassensmith et al. (2014)[79]
CO_2	Co-MOF-74	Pastille	Conductivité (TA)	Strauss et al. (2019)[80]
Humidité	Cu_3TCPP	Pastille	Capacitance (TA)	Tian et al. (2016)[81]
Humidité	Différentes modifications de CAU-10	Pastille	Capacitance (TA)	Weiss et al (2015)[82] Weiss et al. (2016)[75]
NH_3	Trimésic acide (TMA) MOFs (Ba, Cd, Pb, and Zn)	Pastille	Conductivité (TA)	Sel et al. (2015)[83]
Hydrocarbures	$Cu[Ni(pdt)_2]$	Pastille	Résistance (TA)	Aubrey et al. (2019)[84]
SO_2, NO_2 and CO_2	NH_2-UiO-66	Pastille	Résistance (150°C)	DMello et al. (2019)[85]
Humidité	NH_2-MIL-125	Dépôts sur électrodes interdigitalisées	Impédance (TA)	Zhang et al. (2013)[72]
Humidité	Cd(TMA)(DPP)	Dépôts sur électrodes interdigitalisées	Impédance (TA)	Yin et al. (2018)[73]
NH_3	$Cu_3(HITP)_2$	Dépôts sur électrodes interdigitalisées	Conductivité (TA)	Campbell et al. (2015)[86]
NH_3	CuBTC/oxide de graphite	Dépôts sur électrodes interdigitalisées	Résistance (TA)	Travlou et al. (2015)[76]
NH_3, H_2S, NO	Metallophthalocyanines MOFs	Dépôts sur électrodes interdigitalisées	Conductance (TA)	Meng et al. (2019)[87]
NH_3, formaldéhyde, éthanol	ZIF-8, Zn(NA), Zn(INA)	Dépôts sur électrodes interdigitalisées	Résistance (TA)	Mohan Reddy et al. (2020)[88]
Formaldéhyde	ZIF-67	Dépôts sur électrodes interdigitalisées	Résistance (150°C)	Chen et al. (2014)[89]
Différent composés organiques volatiles	$Cu_3(HHTP)_2$, $Cu_3(HITP)_2$ $Ni_3(HITP)_2$	Dépôts sur électrodes interdigitalisées	Conductivité (TA)	Campbell et al. (2015)[90]
H_2	ZIF-8 (+ZnO)	Dépôts sur électrodes interdigitalisées	Résistance (125°C)	Cui et al. (2018)[91]
CO_2	AlFFIVE-1-Ni et NbOFFIVE-1-Ni	Dépôts sur électrodes interdigitalisées	Capacitance (TA)	Tchalala et al. (2019)[92]

3. Parties expérimentales

Comme décrit précédemment, deux stratégies ont été mises en œuvre dans ce projet. Tout d'abord des emballages antibactériens à base de nanofibrilles de cellulose et de nanofils d'argent ont été produits et caractérisés. Ensuite, des capteurs de gaz à base de Metal Organic Framework et de carbones conducteurs ont été développés. Ces deux sections expérimentales sont résumées ci-dessous.

3.1. Emballages antibactériens

La partie dédiée aux emballages antibactériens a été divisée en trois différentes sections dans le manuscrit. La première s'applique à prouver le concept de l'enduction d'une couche antibactérienne sur différents types de substrats et en utilisant différent procédés. Un vaste panel de propriétés actives a aussi été investiguées (barrières, UV, antioxydant, etc.). La seconde section montre la préparation de motifs antibactériens en utilisant un procédé d'impression par sérigraphie et relie propriétés rhéologiques des encres préparées avec la qualité des impressions. Finalement la dernière section s'attelle à définir le mode d'action antibactérien et des propriétés barrières des systèmes en utilisant des films autoporteurs préparés par évaporation de solvant.

3.1.1. Enductions pour le développement de surfaces d'emballages actifs

Une encre à base de nanofibrilles de cellulose oxydées par prétraitement TEMPO (T-CNF) et de nanofils d'argent (Ag NWs) (ratio environ 1 :1) à faible taux de masse (<1% wt) a été tout d'abord déposée sur des films de polyéthylène téréphtalate (PET) par un procédé d'enduction à barre. Quatre différentes épaisseurs ont été testées et les épaisseurs réelles sèches ont été mesurées par microscopie électronique à balayage avec canon à émission de champ (MEB-CEC) sur des coupes transversales. Les épaisseurs des couches produites ont respectivement été mesurées à 217 ± 27, 349 ± 52, 851 ± 79 et 1733 ± 375 nm. Les échantillons sont nommés après leurs épaisseurs mesurées (T-CNF/Ag NWs 200, T-CNF/Ag NWs 350, T-CNF/Ag NWs 850, T-CNF/Ag NWs 1750). Une bonne corrélation a aussi été prouvée entre valeur sèche mesurée et valeur humide théorique, ce qui prouve la qualité et la fiabilité du dépôt.

Les dépôts sont homogènes et présentent une haute transparence (proportionnelle à l'épaisseur déposée) (**Figure 13a**), respectivement 83,3, 75,6 et 67,3% pour T-CNF/Ag NWs 200, T-CNF/Ag NWs 350 and T-CNF/Ag NWs 850, comparé à 89,8% pour le PET de référence. Les couches déposées forment un réseau dense, organisées avec une tendance d'orientation des nanofils d'argent dans le sens de l'enduction (**Figure 13b**).

Les propriétés antibactériennes des matériaux produits ont ensuite été vérifiées. Des tests de relargage effectués par spectrométrie d'émission optique à plasma à couplage inductif (ICP-

OES) ont montrés que la quantité totale d'argent relargué après 24 h est inférieur à 0.5 ppm. Des tests de zone d'inhibition comparant T-CNF/Ag NWs et Ag NWs seuls tendent aussi à montrer que les Ag NWs sont piégés physiquement dans la matrice de T-CNF ce qui conduit à un relargage minimal voire inexistant de substances actives et un mode d'action antibactérien fonctionnant principalement par contact (**Figure 13c**). Ensuite, ces propriétés antibactériennes ont été quantifiées en utilisant la norme AATCC TM100-1998 contre une bactérie Gram-positive *Staphylococcus Aureus* et une bactérie Gram-négative *Escherichia Coli*. Les échantillons T-CNF/Ag NWs 350 and T-CNF/Ag NWs 850 montrent une activité antibactérienne similaire, respectivement 89,3% contre *E. Coli*/100% contre *S. Aureus* et 87,6 contre *E. Coli*/100% contre *S. Aureus*, ce qui montre qu'un dépôt de 350 nm est suffisant pour atteindre une activité antibactérienne supérieure à 90% (**Figure 13d**). Les surfaces obtenues ont aussi montré une légère activité antioxydante, de bonnes propriétés barrières à l'ultraviolet (UV) ainsi que des propriétés anti-condensation.

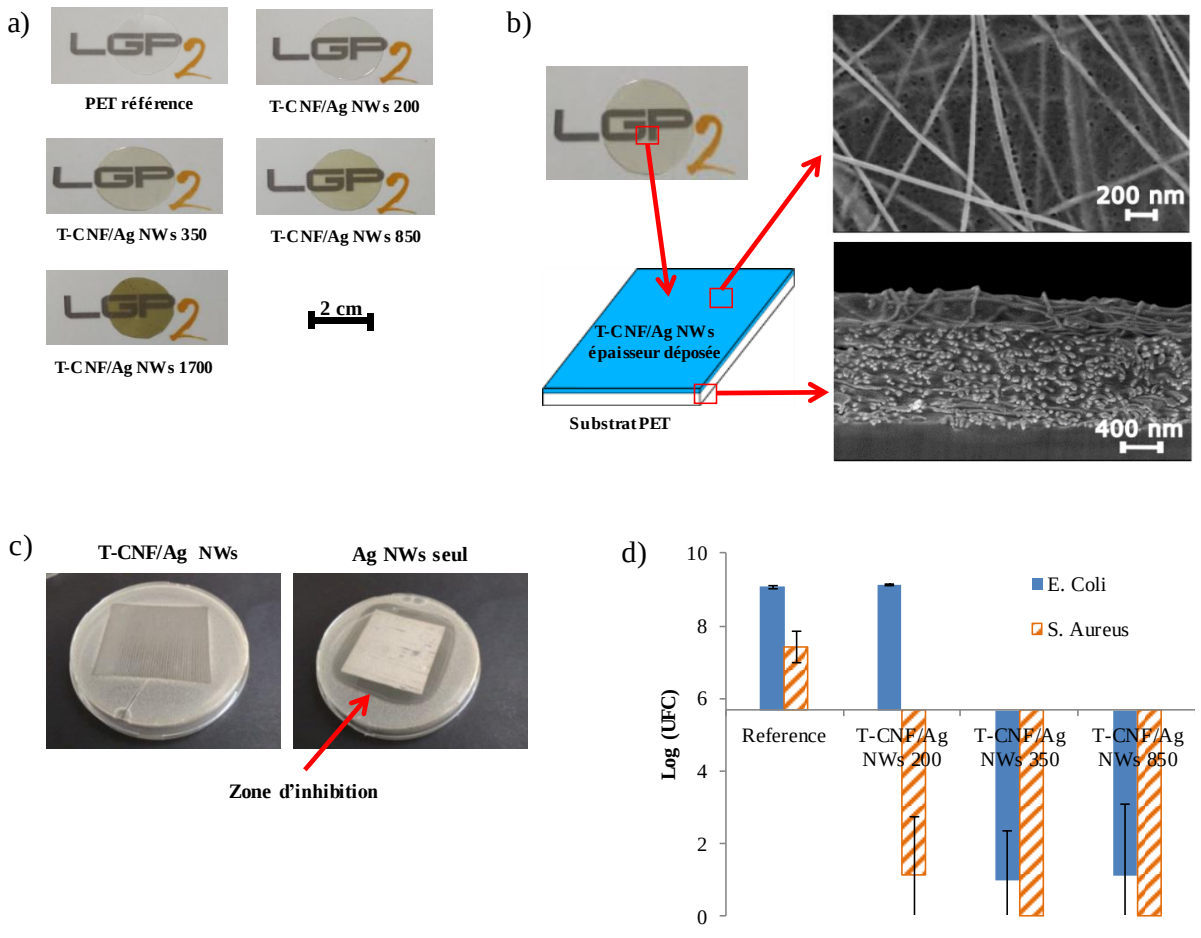

***Figure 13**: Enductions de l'encre active composée de T-CNF/Ag NWs sur du PET avec a) photos des différents films obtenus et de leur transparence, b) représentation schématique d'une couche obtenue et images MEB-CEC de la surface et coupe transversale de T-CNF/Ag NWs 850, c) zone d'inhibition contre E. Coli pour un dépôt multicouches de T-CNF/Ag NWs comparé à Ag NWs seuls et d) analyse quantitative suivant la norme AATCC TM100-1998 pour les différentes épaisseurs obtenues contre E. Coli et S. Aureus (les résultats sont exprimés en log d'unités formant des colonies)*

La même encre a ensuite été déposée sur un substrat d'origine biosourcé, l'acide polylactique (PLA). Les couches déposées sont homogènes, sans défauts, avec des épaisseurs estimées similaires aux dépôts sur le PET (par comparaison de la transparence). Les propriétés barrières des films obtenus ont été testées, en particulier les barrières à l'oxygène et à la vapeur d'eau. La réduction de taux de transmission de l'oxygène (OTR) dépend de l'épaisseur déposée et est relativement importante pour les couches les plus épaisses (90% de réduction pour T-CNF/Ag NWs 1750) mais reste cependant inférieure aux valeurs attendues dans la littérature (**Figure 14a**)[94,95]. Comme cela est attendu pour les CNF, la réduction de l'OTR dépend de l'humidité relative du test et à 80% d'humidité relative, les valeurs obtenues sont proches de celle du substrat de référence. Le taux de transmission à la vapeur d'eau est cependant amélioré par les différents dépôts (environ 50% pour chaque échantillon) (**Figure 14b**).

Finalement une encre similaire a aussi été déposé par un procédé continu de gravure inverse sur du PET. Les films obtenus sont homogènes et sans défauts (**Figure 14c**). De plus, l'activité antibactérienne des films obtenus est relativement similaire à celle obtenue à l'échelle laboratoire (comparant des épaisseurs similaires), ce qui prouve l'important potentiel d'industrialisation de la solution développée (**Figure 14d**).

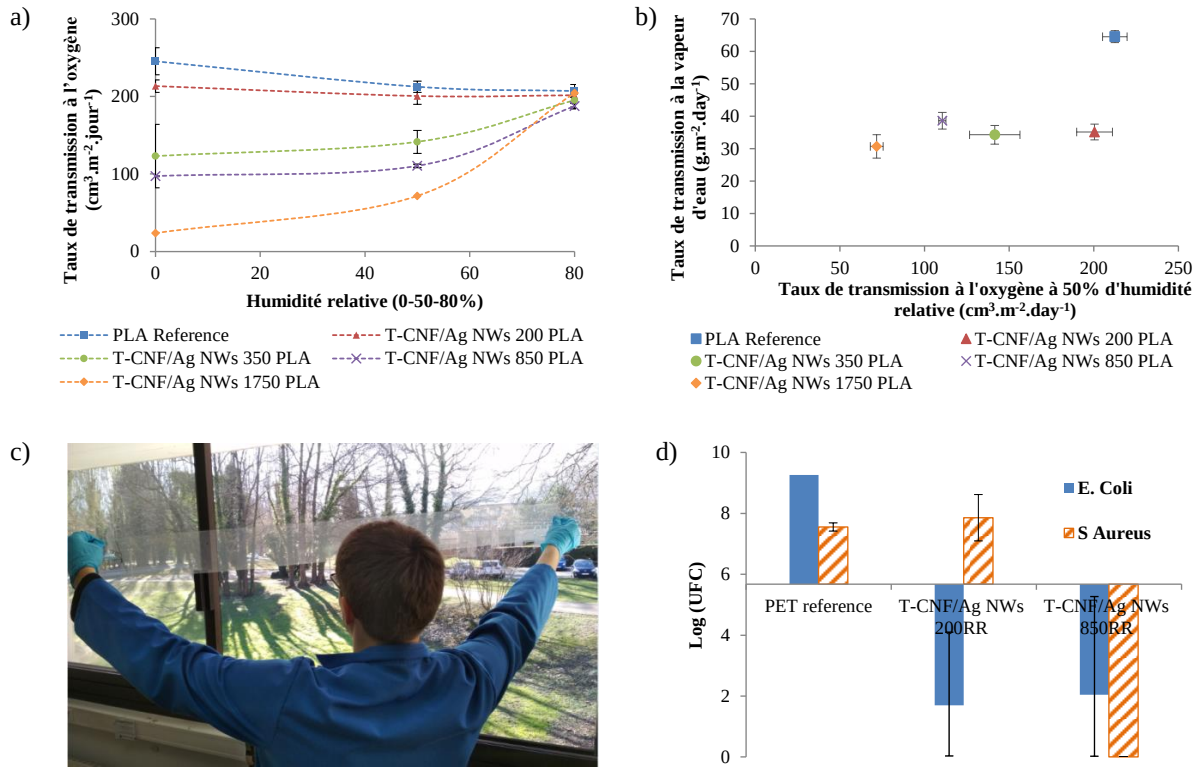

***Figure 14**: Enductions sur le PLA et propriétés barrières avec a) influence de l'humidité relative (%) sur le taux de transmission à l'oxygène ($cm^{-3}.m^{-2}.jour^{-1}$) et b) taux de transmission à la vapeur d'eau ($g.m^{-2}.day^{-1}$) en fonction du taux de transmission à l'oxygène ($cm^{-3}.m^{-2}.jour^{-1}$) à 50% d'humidité relative. Enductions en continue par le procédé de gravure inverse avec c) photo d'un exemple de film obtenu et d) activité antibactérienne des films obtenus par la norme AATCC TM100-1998 contre E. Coli et S. Aureus*

Cette section a donc montré qu'il est possible de déposer de fines couches (< 2µm) sur différents substrats (PET ou PLA) de façon contrôlée et sans défaut, par des procédés d'enduction à l'échelle laboratoire ou semi-industriel, pour obtenir des emballages antibactériens avec des propriétés barrières améliorées, mais qui ont aussi d'autres propriétés actives comme barrière à l'UV, antioxydant ou encore anti-condensation.

3.1.2. Rhéologie de nanofibrilles de cellulose et de nanofils d'argent pour impression sérigraphique.

Différentes encres à bases de T-CNF et de Ag NWs ont été formulées dans le but de préparer une encre capable d'être imprimée en sérigraphie. Dans une démarche empirique, les propriétés rhéologiques des encres ont été investiguées et corrélées à la qualité des impressions obtenues.

Tout d'abord, les courbes d'écoulement des T-CNF seules (0,5% wt), Ag NWs seuls (0,5% wt) et T-CNF/Ag NWs ensemble (1%, ratio 1 :1) montrent que les T-CNF sont prédominant dans la définition de la viscosité du système (**Figure 15a**).

Un modèle rhéologique simulant la sérigraphie a ensuite été appliqué à différents ratios de T-CNF/Ag NWs à 1% (**Figure 15b**). Ce modèle comprend une première étape à faible taux de cisaillement (2 s^{-1} – 150 s) qui modèle l'encre au repos sur l'écran, une seconde étape à fort taux de cisaillement pendant un temps court (1000 s^{-1} – 15 s) qui modèle le passage de la racle emportant l'encre à travers l'écran et une troisième étape à faible taux de cisaillement (2 s^{-1} – 150 s) qui modèle l'encre au repos sur le substrat. Il en ressort que les différents paramètres extraits de ces résultats et en particulier la viscosité de chaque étape, la récupération de la viscosité (%, ratio entre viscosité à la fin de la première et troisième étape) et les temps de récupération (temps nécessaires pour récupérer la viscosité finale) sont fortement dépendants de la composition des encres. Plus la concentration en T-CNF est importante, alors plus la viscosité est importante, plus la récupération (%) est faible et plus les temps de récupération sont importants, probablement à cause d'un système de T-CNF plus enchevêtré, plus sensible aux forces de cisaillement.

En testant des concentrations plus importantes de T-CNF, une encre T-CNF/Ag NWs 2,5% ratio 2 :1 a été sélectionnée comme adéquate pour être imprimée par sérigraphie. Cependant, les impressions réalisées avec cette encre présentent un défaut de moutonnement (**Figure 15c**). Pour pallier à ce défaut, différentes concentrations (3, 5 ou 8% wt) d'hydroxypropyl méthylcellulose (HPMC), un additif hydrosoluble dérivé de la cellulose, a été ajouté car il a été montré dans des études précédentes que cela avait un impact positif sur de tels défauts d'impression[96]. La concentration en HPMC a aussi un impact sur les propriétés rhéologiques extraites du modèle en trois étapes (**Figure 15d**). Avec l'augmentation de la concentration en HPMC, la viscosité augmente, la récupération augmente et les temps de récupération diminuent.

Les résultats obtenus ont suggéré que la formulation avec 5% d'HPMC serait adéquate pour l'impression.

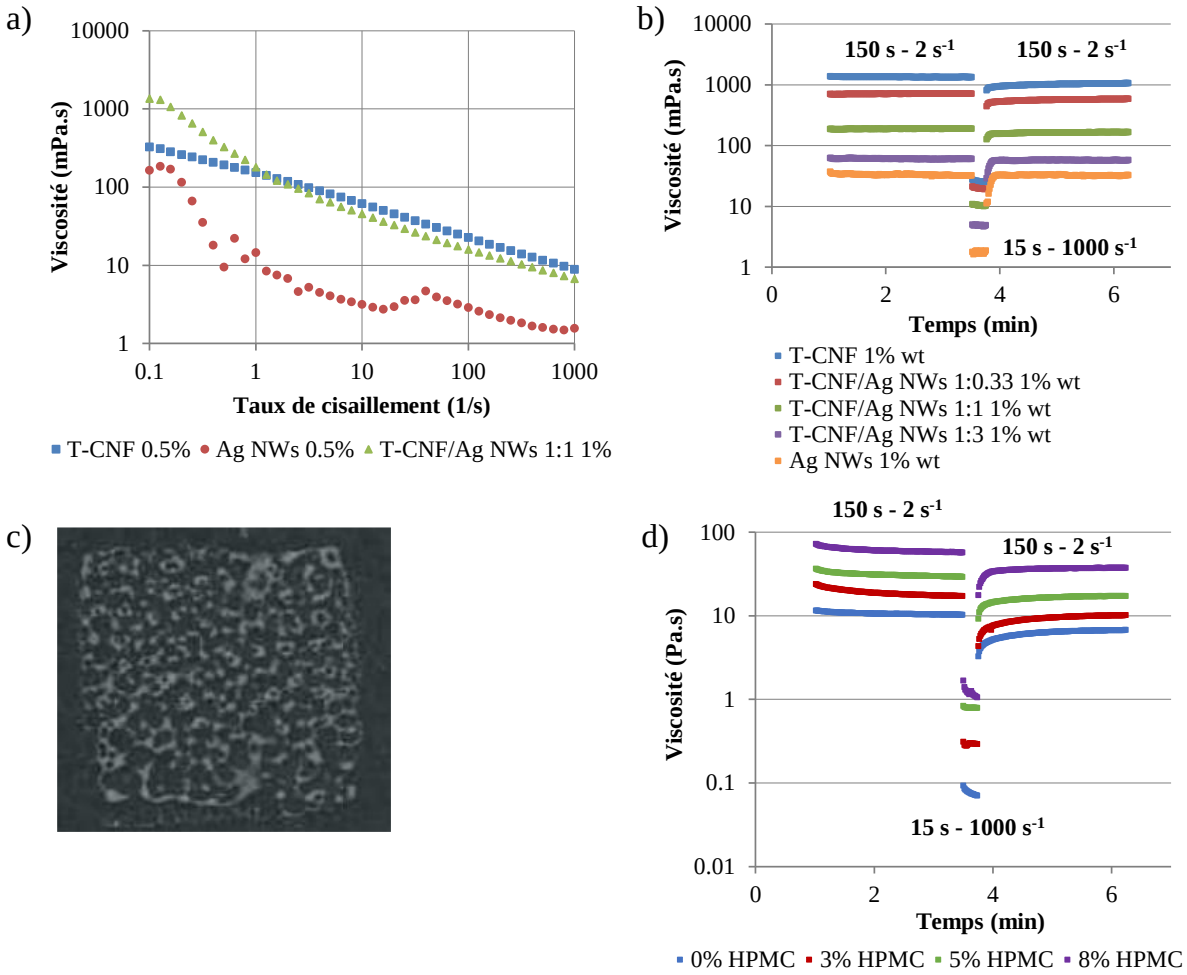

***Figure 15**: Propriétés rhéologiques des différents encres obtenues et qualité d'impression avec a) courbes d'écoulement de T-CNF à 0,5% wt, d'Ag NWs à 0,5% wt et de T-CNF/Ag NWs 1:1 à 1% wt, b) modèle rhéologique de sérigraphie en trois étapes pour différents ratios de T-CNF/Ag NWs à 1% wt., c) impression en sérigraphie d'un encre T-CNF/Ag NWs 2,5% wt 2:1 et d) modèle rhéologique de sérigraphie en trois étapes pour T-CNF/Ag NWs 2,5% wt 2:1 avec différents ajout d'HPMC comme additif (0, 3, 5 et 8%)*

Les différentes formulations avec l'HPMC ont été imprimées et il est ressort qu'ajouter de l'HPMC a un impact positif sur la qualité de l'impression à partir de 5% wt. Il y a en effet moins de défauts d'impression et l'analyse d'image des niveaux de gris des motifs imprimés montre une meilleure homogénéité. Les épaisseurs déposées valent respectivement 269, 622 et 811 nm pour 3, 5 et 8% d'HPMC. La transparence (transmittance à 550 nm) des différentes couches déposées a été mesurée entre 75,2, 73,3 et 68,0% respectivement pour 3, 5 et 8% d'HPMC comparé à 82,4% pour la formulation sans HPMC.

Finalement, les propriétés antibactériennes des impressions ont été vérifiées en utilisant la norme AATCC TM100-1998 et la formulation avec 5% wt d'HPMC présente une activité

antibactérienne de 67,4% contre *E. Coli* comparé à 81,8% sans HPMC. Cela prouve que l'ajout d'HPMC n'écrante pas totalement les propriétés antibactériennes de systèmes composés de T-CNF/Ag NWs.

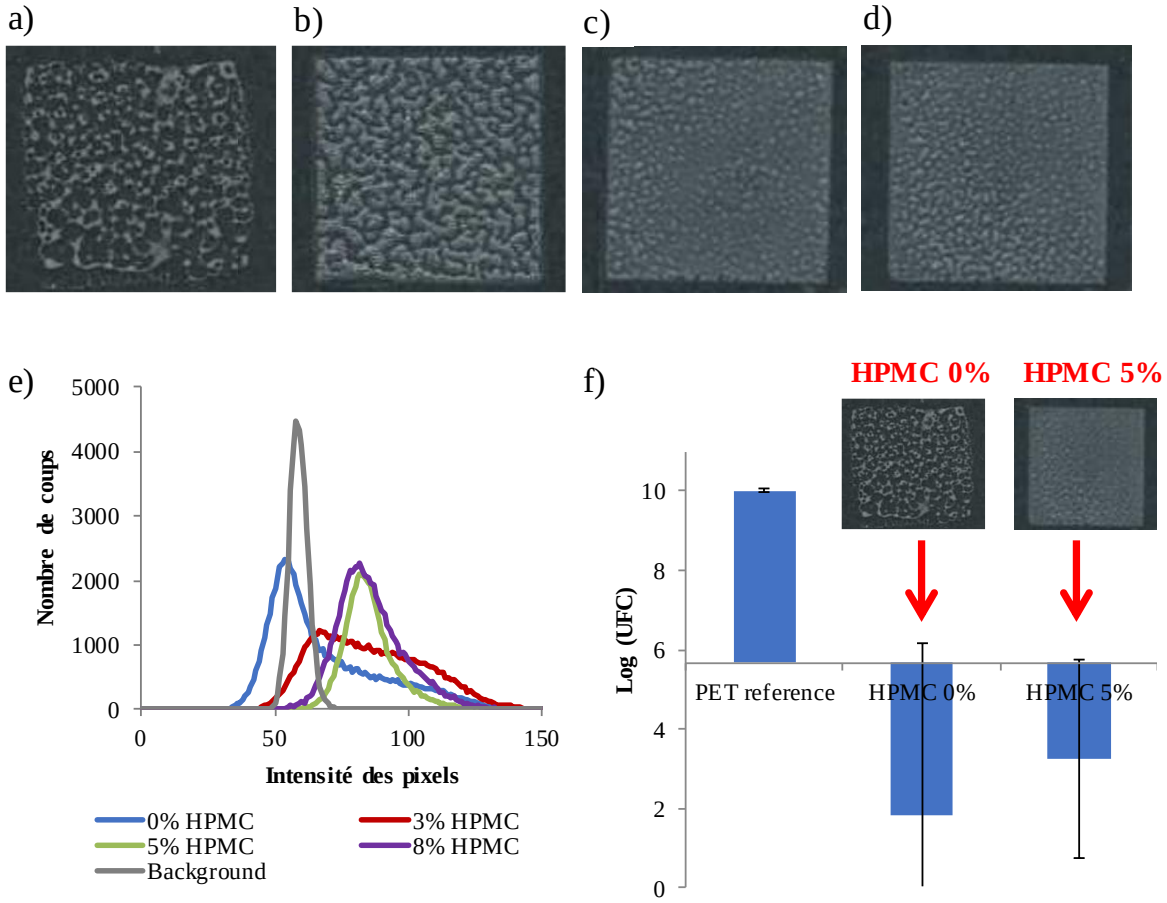

***Figure 16**: Impressions sérigraphiques des encres préparées avec a) photo du motif pour 0% HPMC, b) photo du motif pour 3% HPMC, c) photo du motif pour 5% HPMC, d) photo du motif pour 8% HPMC, e) analyse des niveaux de gris et f) contrôle des propriétés antibactériennes de HPMC 0% et HPMC 8% comparé au substrat de référence en utilisant la norme AATCC TM100-1998*

Finalement, cette section a montré qu'il est possible d'adapter la solution développée à la section précédentes pour de l'enduction, à un procédé d'impression (la sérigraphie) permettant d'envisager la production de motifs localisés tout en conservant de bonnes propriétés antibactériennes. De plus les paramètres rhéologiques des encres qui dépendent grandement de la formulation, ont été investigués pour obtenir une meilleure qualité des impressions.

3.1.3. Mode d'action antibactérien et des propriétés barrières de films préparés par évaporation de solvent

Dans cette dernière section présentant des résultats préliminaires, des films autoporteurs composés de T-CNF/Ag NWs ont été préparé par évaporation de solvent (respectivement 0,25 sec de T-CNF et 0,05 g sec d'Ag NWs par film circulaire de diamètre 8,9 cm). Les films sont

homogènes, de l'ordre de 20 µm d'épaisseur (**Figure 17a** et **b**) et ont été utilisés dans des tests de relargage afin de préciser le mode d'action antibactérien et d'éclairer leurs utilisations pour des emballages alimentaires. Tout d'abord des mesures spectroscopiques ont montrés l'absence de relargage de Ag NWs. Ensuite, le relargage d'ions argent a été mesuré par potentiométrie et en particulier après 1 heure de test (agitation à 37°C dans 10 ml d'eau déionisé), où 12.3 ppm d'ions argent relargués ont été mesurés (**Figure 17c**). Ces valeurs ont été comparé à un contrôle effectué par spectrométrie d'émission optique à plasma à couplage inductif (ICP-OES). Les valeurs du contrôle sont nettement plus faibles (0.76 ppm) (**Figure 17c**) et il a donc été supposé que la technique par potentiométrie ne soit pas pleinement adaptée à la mesure de tels échantillons. En extrapolant ces résultats aux systèmes préparés par enduction (et en particulier à l'épaisseur de 350 nm), et en considérant un emballage de 400 cm² nécessaire pour emballer un kg de nourriture, alors le relargage d'ions a été estimé à 0,011 mg/kg nourriture (pour une heure), ce qui est inférieur à la limite fixée par l'Autorité Européenne de Sécurité des Aliments (EFSA), égale à 0,05 mg/kg nourriture.

Il a aussi été montré que les Ag NWs ajoutés dans la structure des T-CNF, n'impactent pas de façon significatives les propriétés barrières des T-CNF (**Figure 17d**), et en particulier la perméabilité à la vapeur d'eau et à l'oxygène. Cette section a donc permis d'obtenir plus d'informations sur le mode d'action antibactérien et des propriétés barrières de systèmes composés de T-CNF/Ag NWs.

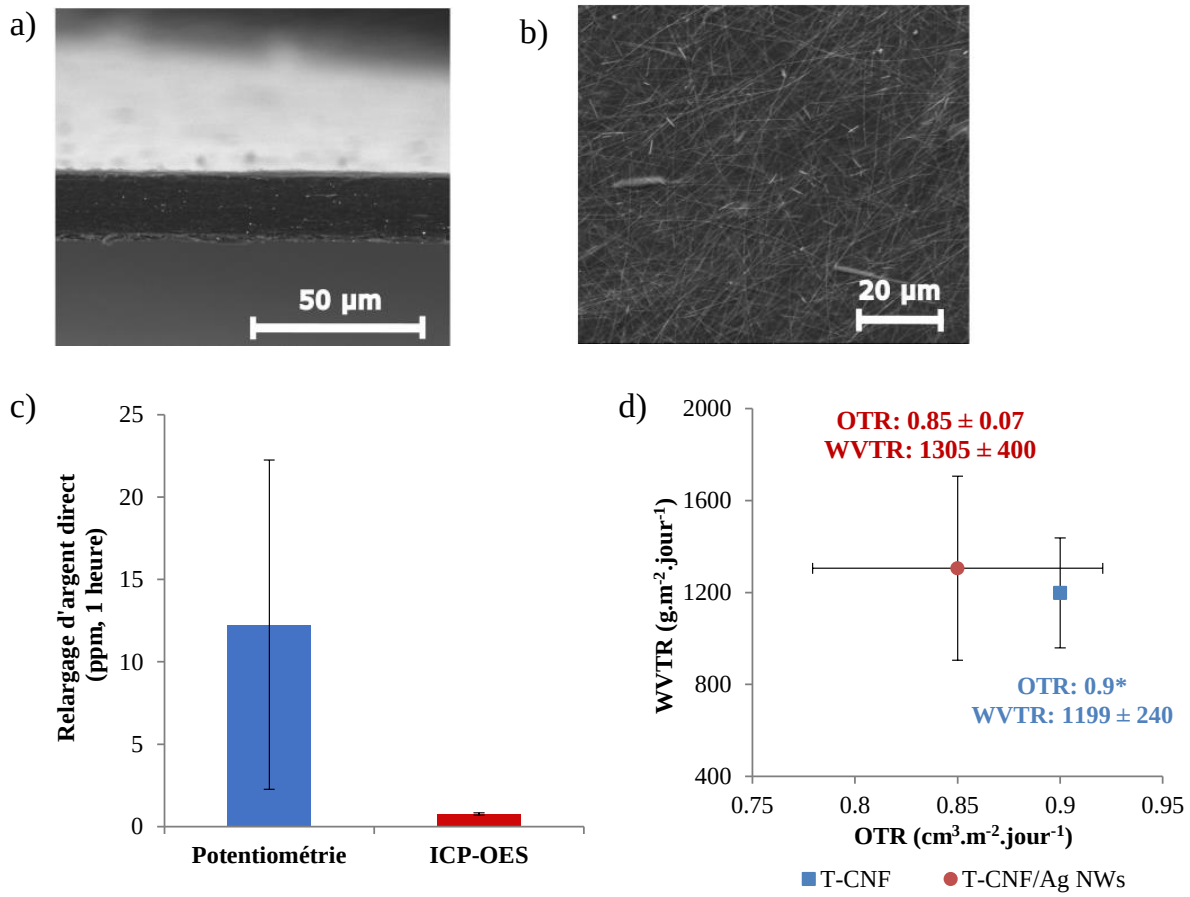

***Figure 17**: Films de T-CNF/Ag NWs et leurs caractérisations par a) Microscopie Electronique à Balayage en coupe transversale et b) Microscopie Electronique à Balayage de la surface, c) relargage d'ions argent (2 x 2 cm de film déposé dans 10 ml d'eau distillée sous agitation pendant une heure) mesuré par potentiométrie et ICP-OES et d) taux de transmission à la vapeur d'eau (OTR, $g.m^{-2}.jour^{-1}$) en fonction du taux de transmission à l'oxygène (WTR, $cm^3.m^{-2}.jour^{-1}$) à 50% d'humidité relative*

En guise de conclusion, différents matériaux à base de nanofibrilles de cellulose et de nanofils d'argent ont été produits pour des applications antibactériennes, soit par enduction (échelle laboratoire ou semi-industrielle), par impression sérigraphique ou par évaporation de solvants. Les propriétés des encres actives ainsi que des matériaux finaux ont été investigués et caractérisés.

3.2. Capteurs de gaz pour emballages intelligents

Cette stratégie a été divisée en deux sections différentes dans le manuscrit. La première est dédiée au développement de capteurs d'ammoniac. En particulier, la préparation des capteurs et l'optimisation de leurs propriétés électriques et physico-chimiques de surface, ainsi que leurs performances et leur mode d'action ont été investigués en détails. Dans la seconde partie, l'adaptation de systèmes similaires pour des applications de capteurs d'humidité a été analysée.

3.2.1. Capteurs d'ammoniac à base de Metal Organic Framework sur substrats flexibles

Des électrodes interdigitalisées en argent ont d'abord été préparées par sérigraphie sur un substrat flexible polyéthylène téréphtalate (PET) (**Figure 18a**). Des encres actives ont ensuite été formulées en mettant en suspension dans l'acétate de butyle, un mélange de Metal Organic Framework Cuivre benzène-1,3,5-tricarboxylate (CuBTC) et de matériaux conducteurs à base de carbone (carbone-graphène). Différents ratios MOF/carbone-graphène ont été préparés (en conservant une quantité toujours égale de CuBTC à 200 $mg.ml^{-1}$) et déposés sur les électrodes interdigitalisées en utilisant une micropipette. Les capteurs flexibles produits (**Figure 18b**) sont appelés en fonction de leur composition : PGrCuBTC X correspond à une composition avec X % wt de carbone-graphène. Par exemple PGrCuBTC 21.25 correspond à capteur préparé avec une encre à 200 $mg.ml^{-1}$ de CuBTC et 54 $mg.ml^{-1}$ de carbone-graphène, ce qui correspond à 21.25% wt de carbone-graphène et 78.75% wt de CuBTC. Environ 2 mg de matière sèche ont été déposés sur chaque capteur.

La morphologie des capteurs a été vérifiée par interférométrie de lumière blanche, qui montre que l'épaisseur de la couche déposée ainsi que sa rugosité surfacique diminue avec l'augmentation de la quantité de carbone-graphène dans la formulation des encres. Cela a été attribuée à une meilleure dispersion de CuBTC en présence de carbon-graphène[97]. Ces constations ont été secondées par des mesures de Microscopie à Force Atomique.

L'ajout de carbone-graphène au sein de la formulation est nécessaire pour conférer une conductivité suffisante au système afin d'être utilisé en tant que capteur résistif. La résistance des capteurs est en effet très dépendante de la formulation (**Figure 18c**). En dessous de 20% wt de carbone-graphène, les capteurs ne sont plus suffisamment conducteurs (> 50 MΩ) et au-dessus de 50% wt la résistance est égal à 6-7Ω et ne varie plus avec la concentration en carbone-graphène. En particulier, une légère variation de la composition entre 21.25-25% wt implique une importante variation de la conductivité. Le capteur PGrCuBTC 21.25 devrait avoir des performances optimales car suffisamment conducteur mais ayant le moins de carbone-graphène possible.

Les propriétés physico-chimiques des surfaces produites ont aussi été investiguées avec de la Microscopie Electronique à Balayage (MEB) qui montre l'interaction entre cristaux de CuBTC et plateaux graphitiques (**Figure 18d**). De la spectroscopie infrarouge à transformée de Fourier, de la spectroscopie Raman, de la Microanalyse X couplée au MEB, de la cristallographie aux rayons X, ainsi que de spectrométrie de photoélectrons induits par rayons X, ont prouvés la nature de chaque composé, ainsi que la bonne conservation de leurs caractéristiques à travers la préparation des capteurs (comme la cristallinité de CuBTC par exemple) et enfin la bonne dispersion des composants au sein des capteurs.

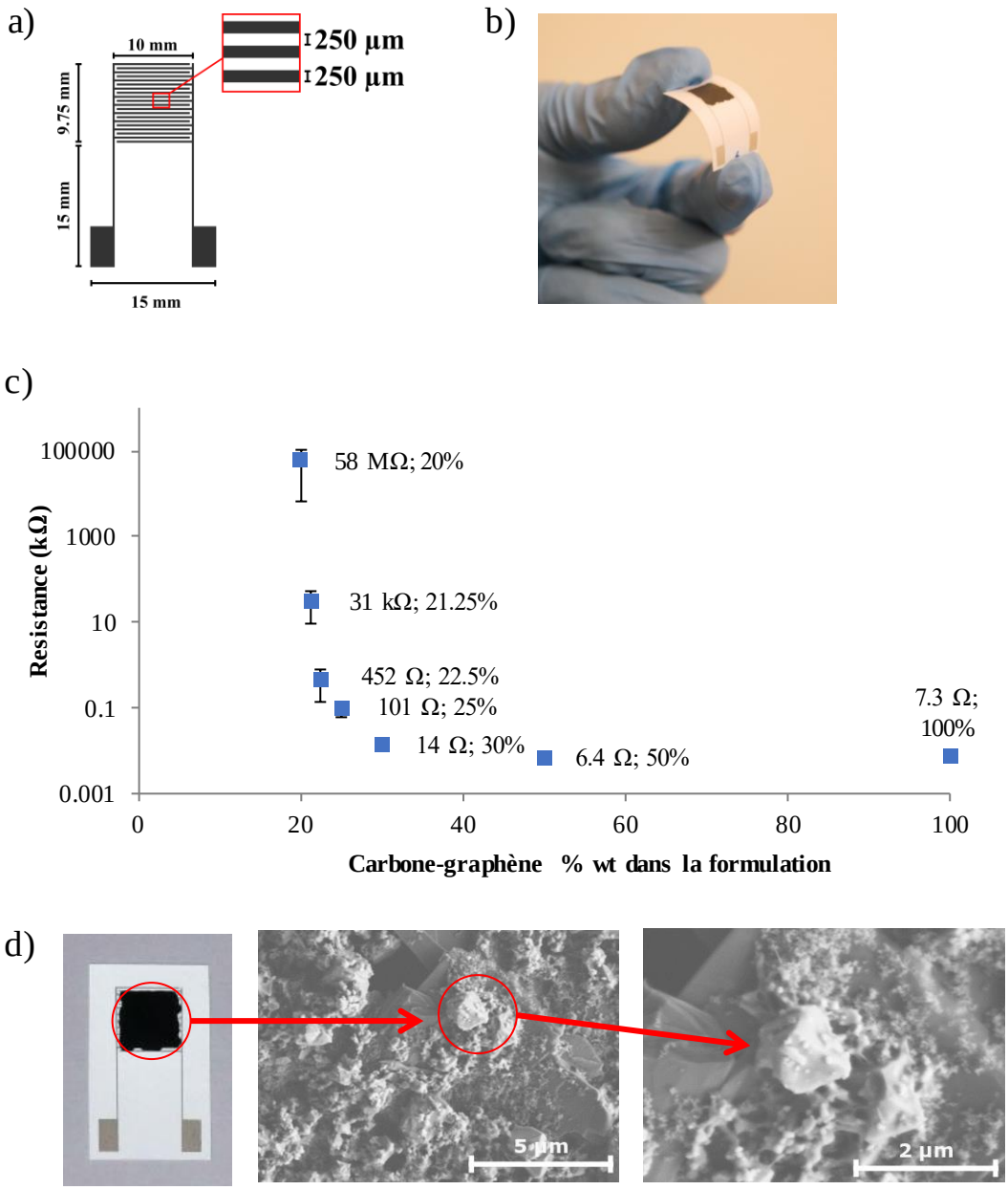

***Figure 18**: Capteurs à base de CuBTC MOF et carbone-graphène avec a) structure des électrodes interdigitalisés en argent imprimées par sérigraphie, b) photo de la flexibilité des capteurs préparés, c) résistance (Ω) en fonction de la composition des encres formulées et d) photo d'un capteur et Microscopie Electronique à Balayage de sa surface*

Les capteurs ont ensuite été exposés à différentes concentrations en ammoniac dans un équipement conçu pour atteindre avec précision des concentrations très faibles de gaz. En particulier, la résistance des capteurs a été suivie en fonction de la concentration gazeuse en ammoniac (20-100 ppm), en utilisant un mélange oxygène-azote comme gaz vecteur modélisant l'air, en conditions sèches. Les capteurs ont été soumis à plusieurs cycles successifs d'exposition à l'ammoniac suivis d'étapes de repos d'exposition au gaz vecteur seulement. Un exemple de la réponse du capteur PGrCuBTC 25 sur trouve sur la **Figure 19a** et la **Figure 19b**

recense la réponse (comparant résistance stabilisée à l'exposition pour chaque concentration d'ammoniac et résistance stabilisée de la ligne de base) extraite pour chaque type de capteurs.

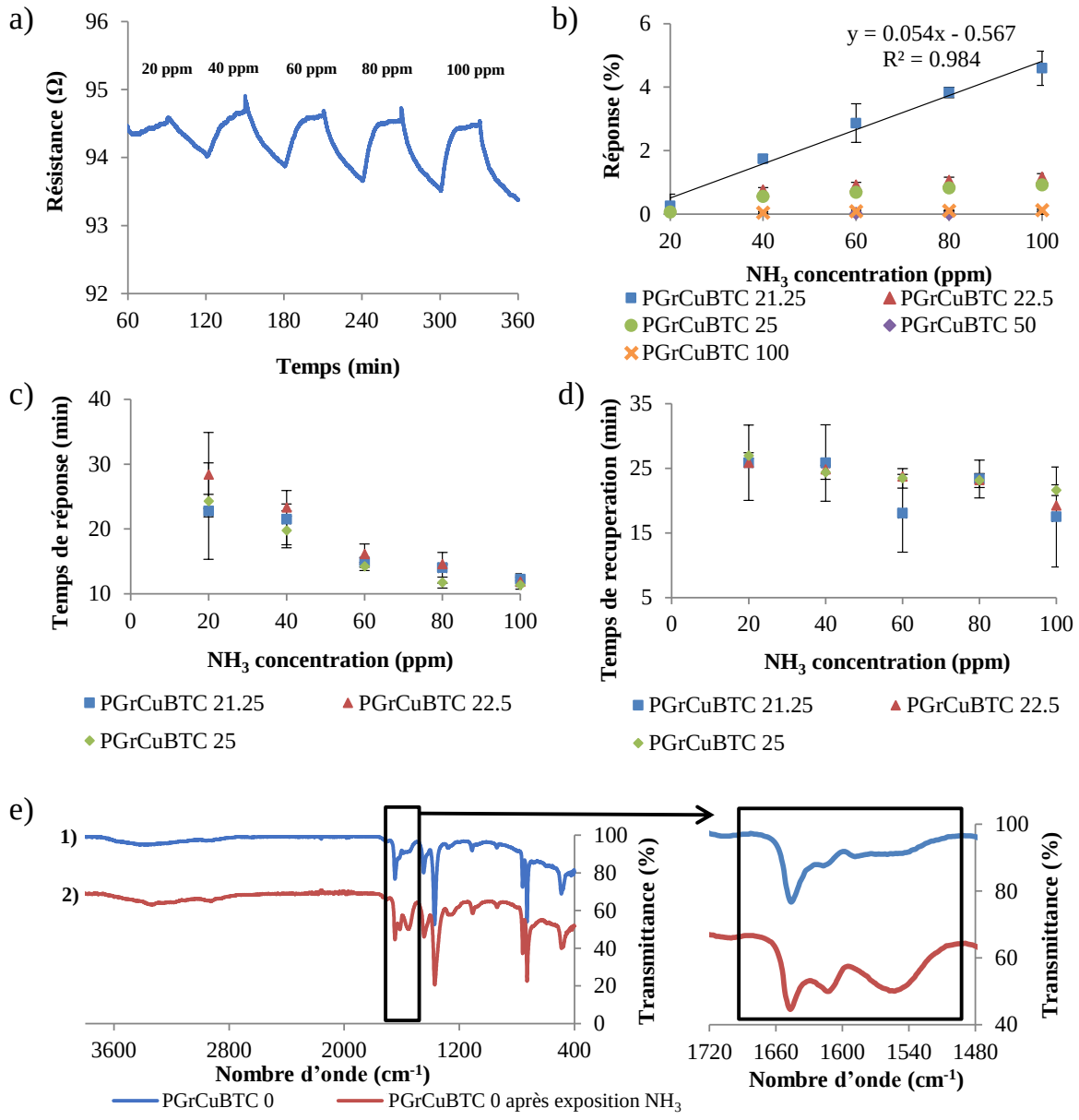

***Figure 19**: Performances des capteurs d'ammoniac préparés avec a) exemple de l'évolution de la résistance en fonction de la concentration en ammoniac (ppm) pour PGrCuBTC 25, b) réponse (%) en fonction de la concentration en ammoniac (ppm), c) temps de réponse (min) en fonction de la concentration en ammoniac (ppm), d) temps de récupération (min) en fonction de la concentration en ammoniac (ppm) et e) spectroscopie infrarouge à transformée de Fourier de PGrCuBTC 0 avant et après exposition à l'ammoniac*

Les temps de réponse (pour atteindre 90% de la valeur finale lors de l'exposition à l'ammoniac) et les temps de récupération (pour revenir à 90% de la ligne de base lorsque exposé au gaz vecteur seul) sont respectivement aux alentours de 10-30 min et 15-25 min ce qui est cohérent pour des applications de types emballages intelligents (**Figure 19c** et **d**). Comme attendu, le capteur PGrCuBTC 21.25 présente les meilleurs performances (réponse et sensitivité) ce qui

peut s'expliquer par un bon ratio entre CuBTC et carbone-graphène : un compromis entre conductivité et faible quantité de carbone-graphène pour ne pas écranter les propriétés d'adsorption de CuBTC. Finalement, le mécanisme des capteurs a été investigué en caractérisant la nature chimique de leur surface avant et après exposition à l'ammoniac avec de la spectroscopie infrarouge à transformée de Fourier (FTIR) et de la spectroscopie Raman. Les mesures de FTIR montrent pour PGrCuBTC 0 (MOF seulement), l'augmentation importante de l'intensité des pics à 1648, 1618 et 1254 cm^{-1} (**Figure 19e**). Cela semble indiquer un changement dans la coordination des ligands BTC mais qui ne correspondent pas à des ligands libres. Cela correspondrait donc plutôt une réaction entre ammoniac et BTC pour former des complexe $BTC(NH_4)_3$. L'interaction entre ammoniac et CuBTC serait donc similaire à celle proposés dans la littérature : adsorption d'ammoniac sur le centre métallique cuivre et partiale amidation des ligands BTC[98–100]. Toutefois, les techniques utilisées ne permettent pas de conclure entièrement sur le mécanisme complet des systèmes CuBTC/carbone-graphène.

Dans cette section, il a donc été montré qu'il est possible de fabriquer des capteurs d'ammoniac avec de bonnes performances, de façon contrôlée et en utilisant une méthode de préparation simple et directe avec des produits commerciaux. Ceci prouve l'intérêt de tels systèmes pour de futures applications industrielles.

3.3. Capteurs d'humidité à base de Metal Organic Framework sur substrats flexibles

La formulation PGrCuBTC 21.25, optimisée dans la section précédente, a été utilisée en tant que capteur d'humidité. Différents taux d'humidité relative (30-80%) ont été testés en effectuant des cycles successifs humide/sec avec un gaz vecteur composé d'un mélange oxygène-azote simulant l'air. La résistance des capteurs varie avec l'humidité (**Figure 20a)** et la réponse pour chaque humidité relative a été extraite des résultats obtenus et résumée sur la **Figure 20b,** qui montre une bonne corrélation entre les deux. Les réponses mesurées (13.2-54.2%) sont bien plus importantes que pour l'application en tant que capteur d'ammoniac. De plus les temps de réponse et de récupération sont respectivement de l'ordre de 15-20 et 5-10 minutes ce qui est aussi inférieur aux valeurs obtenues avec l'ammoniac (**Figure 20c**). Cependant, après chaque étape d'exposition à l'humidité, les capteurs de reviennent jamais complètement à la ligne de base, ce qui pourrait s'expliquer par une adsorption irréversible, une cinétique de désorption beaucoup plus lente ou encore une destruction partielle de la structure du MOF. Des tests effectués en chambre climatique ont aussi montrés que lors d'une rampe croissante d'humidité (30-40-50-60-70-80%), la formulation PGrCuBTC 21.25 montre une résistance normalisée bien supérieur à celle du contrôle carbone-graphène (**Figure 20d**), ce qui prouve l'intérêt d'utiliser une combinaison des deux matériaux.

Ainsi, cette section a montré que la formulation optimisée à base de Metal Organic Frameworks et carbone-graphène peut aussi être utilisée en tant que capteur d'humidité, fiable, avec une réponse relativement importante, et des temps caractéristiques cohérents avec le domaine des emballages intelligents.

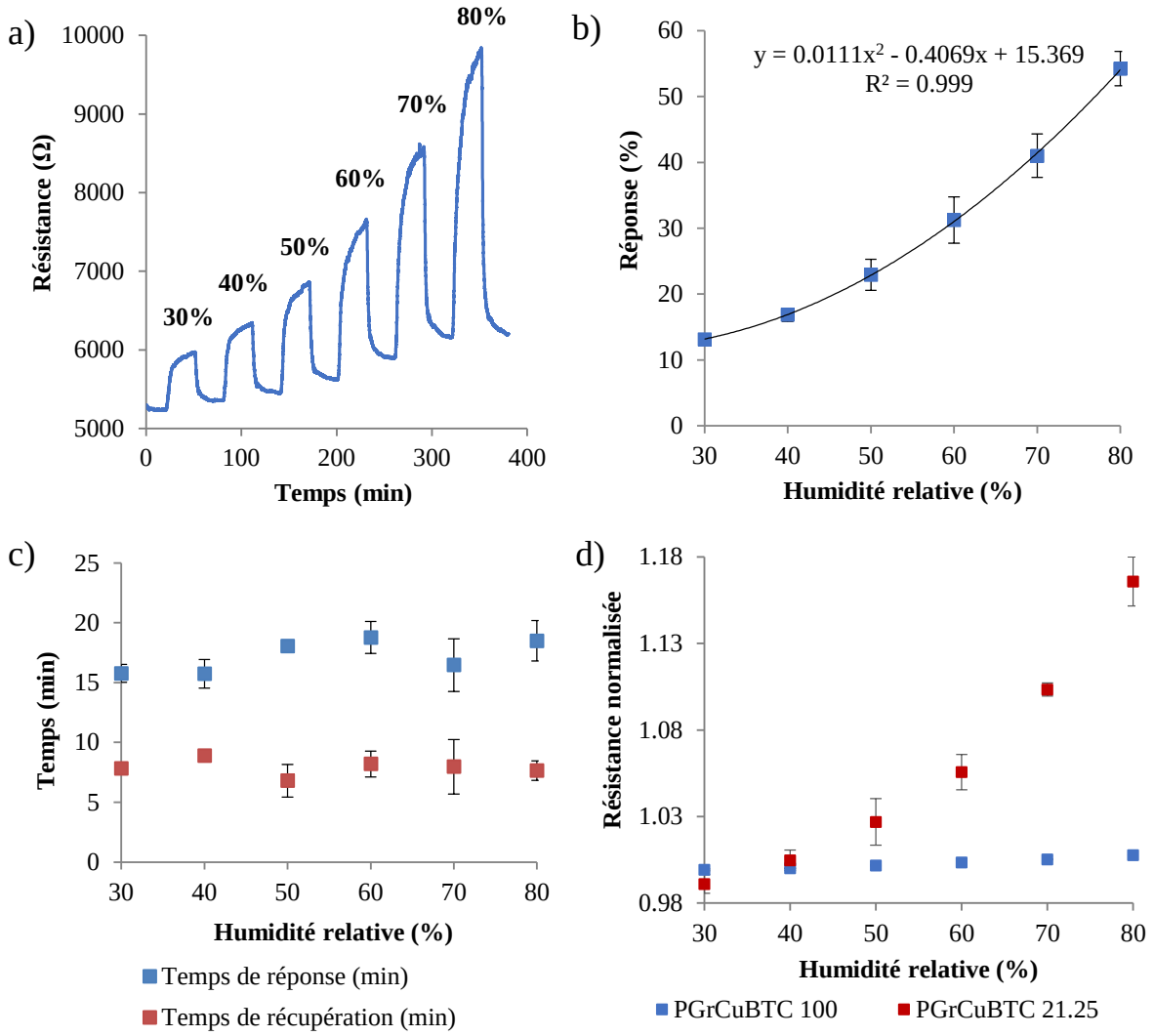

***Figure 20**: Performances de PGrCuBTC 21.25 en tant que capteurs d'humidité avec a) évolution de la résistance (Ω) à différent taux d'humidité relative (30-80%), b) réponse (%) à différent taux d'humidité relative (30-80%), c) temps de réponse et récupération (min) en fonction du taux d'humidité relative (30-80%), et d) résistance normalisée de PGrCuBTC 21.25 et PGrCuBTC 100 exposés à une rampe croissante d'humidité relative dans une enceinte climatique*

Il a donc été montré dans cette deuxième stratégie, la possibilité de produire des capteurs de gaz à base de Metal Organic Frameworks, efficaces et optimisés pour la détection et quantification d'ammoniac gazeux et d'humidité, de façon simple, directe (sans synthèse chimique compliquée) et en utilisant des produits commerciaux et des substrats flexibles. Cela est encourageant pour de futurs développements d'emballages intelligents incorporant de telles technologies.

4. Conclusion

Dans ce projet, le développement d'emballage actifs et intelligents suivant deux stratégies différentes a été démontré à travers la production et caractérisation d'emballages antibactériens et de capteurs de gaz (**Figure 21**).

La première stratégie a spécifiquement démontré la possibilité de préparer différents matériaux antibactériens utilisant une combinaison de nanofibrilles de cellulose et de nanofils d'argent. En particulier, des enductions réalisées sur différents substrats (PET, PLA) à partir de différents procédés (couchage à bar, gravure inverse) ont révélés des propriétés antibactériennes et barrières intéressantes. Grâce à un travail d'optimisation de formulation, le système a ensuite été transposée au procédé d'impression sérigraphique, ce qui permet de pouvoir générer des motifs localisés antibactériens. Finalement la préparation de films par évaporation de solvant a permis de discuter l'impact du relargage des ions argent ainsi que de montrer que l'ajout de nanofils d'argent dans la matrice de cellulose nanofibrilles n'impacte pas de façon significative leurs propriétés barrières.

La seconde stratégie a permis de montrer la possibilité de préparer des capteurs en utilisant un mélange de matériaux innovants, à savoir de Metal Organic Framework (MOF) et de carbon-graphène. La préparation des capteurs est simple, directe (ne nécessitant pas de synthèse chimique complexe), peu onéreuse et en utilisant des produits commerciaux. La formulation et la composition des encres s'est révélée être une étape critique dans la préparation des capteurs. La formulation a donc été soigneusement optimisée pour obtenir des propriétés électriques et des performances optimales. Les capteurs développés dans cette étude à base de MOF apparaissent stables, reproductibles, et efficaces pour la détection et la mesure de l'ammoniac mais aussi de l'humidité.

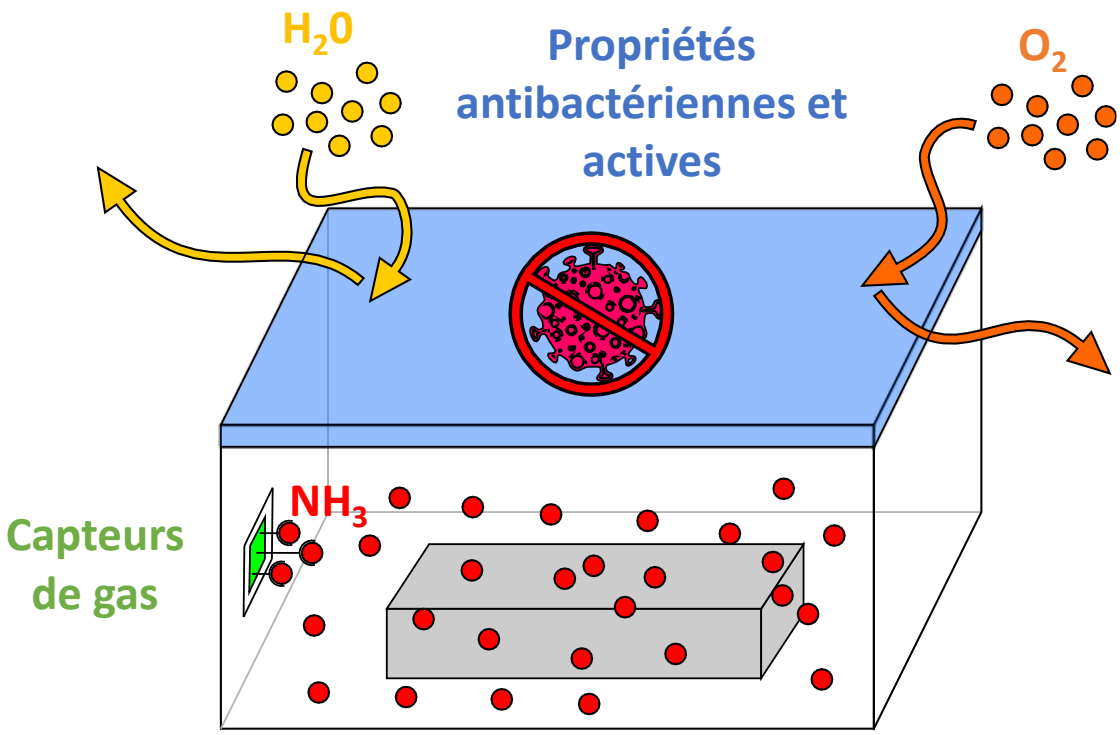

***Figure 21**: Représentation schématique des deux stratégies d'emballages actifs et intelligents développées dans le projet*

Des perspectives intéressantes pour la première stratégie serait tout d'abord d'élargir la palette de substrats possible pour le dépôt de la solution antibactérienne développée afin d'offrir une gamme plus large d'emballages antibactériens (papier, carton, aluminium, verre, etc.). Ensuite il serait intéressant de travailler plus en détails sur le relargage d'ions argent et en particulier d'investiguer en détail l'importances de la chimie de surface des nanofibrilles de cellulose sur ce relargage. De même la comparaison avec des nanoparticules d'argent de différentes morphologies (sphériques par exemple) serait intéressant. L'adaptation des encres sérigraphiques avec d'autres types d'additifs et de solvants est aussi une piste d'exploration, ainsi que l'adaptation vers d'autres procédés de dépôts.

Pour la seconde stratégie, étudier la capacité des capteurs pour détecter et quantifier d'autres gaz comme le dioxyde de carbone ou l'éthanol serait une perspective intéressante, en vérifiant de plus la sélectivité des capteurs pour chaque analyte. De plus, une perspective majeure du projet reste le développement de capteurs entièrement préparés par un procédé d'impression et en particulier la sérigraphie, même si utiliser un procédé d'impression continue comme la flexographie est aussi une piste sérieuse.

Finalement, construire un démonstrateur incluant les deux stratégies et tester son efficacité contre des produits alimentaires réels serait une étape clé pour permettre de transférer le concept vers l'industrie, et de vérifier les concepts développés dans ce projet dans le contexte législatif de l'emballage alimentaire.

References

1. Berger, K. R. A Brief History of Packaging. *1* **2003**, (2003).
2. The Future of Global Packaging to 2024. *Strategic forecasts for global packaging to 2024*.
3. Fakirov, S. *Fundamentals of Polymer Science for Engineers*. (Wiley-VCH Verlag GmbH & Co. KGaA, 2017). doi:10.1002/9783527802180.
4. Xu, B. *et al.* Microplastics in the soil environment: Occurrence, risks, interactions and fate – A review. *Critical Reviews in Environmental Science and Technology* **0**, 1–48 (2019).
5. Kögel, T., Bjorøy, Ø., Toto, B., Bienfait, A. M. & Sanden, M. Micro- and nanoplastic toxicity on aquatic life: Determining factors. *Science of The Total Environment* **709**, 136050 (2020).
6. PlasticsEurope. *Plastics - the Facts 2019*. (2019).
7. Food and Agriculture Organization of the United Nations. *State of food and agriculture 2019: moving forward on food loss and waste reduction.* (2019).
8. World Resources Institute. *Creating a sustainable food future*. (2019).
9. Tas, C. E. *et al.* Halloysite Nanotubes/Polyethylene Nanocomposites for Active Food Packaging Materials with Ethylene Scavenging and Gas Barrier Properties. *Food Bioprocess Technol* **10**, 789–798 (2017).
10. Ma, Q., Du, L. & Wang, L. Tara gum/polyvinyl alcohol-based colorimetric NH3 indicator films incorporating curcumin for intelligent packaging. *Sensors and Actuators B: Chemical* **244**, 759–766 (2017).
11. Yildirim, S. *et al.* Active Packaging Applications for Food. *Comprehensive Reviews in Food Science and Food Safety* **17**, 165–199 (2018).
12. Ebrahiminezhad, A., Raee, M. J., Manafi, Z., Sotoodeh Jahromi, A. & Ghasemi, Y. Ancient and Novel Forms of Silver in Medicine and Biomedicine. *Journal of Advanced Medical Sciences and Applied Technologies* **2**, 122–128 (2016).
13. Abbasi, E. *et al.* Silver nanoparticles: Synthesis methods, bio-applications and properties. *Critical Reviews in Microbiology* **42**, 173–180 (2016).
14. Rai, M. k., Deshmukh, S. d., Ingle, A. p. & Gade, A. k. Silver nanoparticles: the powerful nanoweapon against multidrug-resistant bacteria. *Journal of Applied Microbiology* **112**, 841–852 (2012).
15. Tang, S. & Zheng, J. Antibacterial Activity of Silver Nanoparticles: Structural Effects. *Advanced Healthcare Materials* **7**, 1701503 (2018).
16. Turbak, A. F., Snyder, F. W. & Sandberg, K. R. Microfibrillated Cellulose, a New Cellulose Product: Properties, Uses, and Commercial Potential. *J. Appl. Polym. Sci.: Appl. Polym. Symp.; (United States)* **37**, (1983).
17. Jack Miller. *Nanocellulose - State of the industry 2015*. www.tappinano.org (2015).
18. Jack Miller. *2018 - Cellulose nanomaterials production update*. www.tappinano.org (2018).
19. Pääkkö, M. *et al.* Enzymatic Hydrolysis Combined with Mechanical Shearing and High-Pressure Homogenization for Nanoscale Cellulose Fibrils and Strong Gels. *Biomacromolecules* **8**, 1934–1941 (2007).
20. Saito, T., Kimura, S., Nishiyama, Y. & Isogai, A. Cellulose Nanofibers Prepared by TEMPO-Mediated Oxidation of Native Cellulose. *Biomacromolecules* **8**, 2485–2491 (2007).

21. Nechyporchuk, O., Belgacem, M. N. & Bras, J. Production of cellulose nanofibrils: A review of recent advances. *Industrial Crops and Products* **93**, 2–25 (2016).
22. Missoum, K., Belgacem, M. N. & Bras, J. Nanofibrillated Cellulose Surface Modification: A Review. *Materials* **6**, 1745–1766 (2013).
23. Dufresne, A. *Nanocellulose: From Nature to High Performance Tailored Materials*. (Walter de Gruyter, 2013).
24. Grüneberger, F., Künniger, T., Zimmermann, T. & Arnold, M. Rheology of nanofibrillated cellulose/acrylate systems for coating applications. *Cellulose* **21**, 1313–1326 (2014).
25. Nechyporchuk, O., Belgacem, M. N. & Pignon, F. Current Progress in Rheology of Cellulose Nanofibril Suspensions. *Biomacromolecules* **17**, 2311–2320 (2016).
26. Yan, D. *et al.* Surface modified electrospun poly(lactic acid) fibrous scaffold with cellulose nanofibrils and Ag nanoparticles for ocular cell proliferation and antimicrobial application. *Materials Science and Engineering: C* **111**, 110767 (2020).
27. Li, J. *et al.* Controlled Release and Long-Term Antibacterial Activity of Dialdehyde Nanofibrillated Cellulose/Silver Nanoparticle Composites. *ACS Sustainable Chem. Eng.* **7**, 1146–1158 (2019).
28. Xiao, W., Xu, J., Liu, X., Hu, Q. & Huang, J. Antibacterial hybrid materials fabricated by nanocoating of microfibril bundles of cellulose substance with titania/ chitosan /silver-nanoparticle composite films. *Journal of Materials Chemistry B* **1**, 3477–3485 (2013).
29. Bober, P. *et al.* Biocomposites of Nanofibrillated Cellulose, Polypyrrole, and Silver Nanoparticles with Electroconductive and Antimicrobial Properties. *Biomacromolecules* **15**, 3655–3663 (2014).
30. Ramaraju, B., Imae, T. & Destaye, A. G. Ag nanoparticle-immobilized cellulose nanofibril films for environmental conservation. *Applied Catalysis A: General* **492**, 184–189 (2015).
31. Yu, Z. *et al.* Antimicrobial effect and toxicity of cellulose nanofibril/silver nanoparticle nanocomposites prepared by an ultraviolet irradiation method. *Colloids and Surfaces B: Biointerfaces* **180**, 212–220 (2019).
32. Yu, Z., Wang, W., Kong, F., Lin, M. & Mustapha, A. Cellulose nanofibril/silver nanoparticle composite as an active food packaging system and its toxicity to human colon cells. *International Journal of Biological Macromolecules* **129**, 887–894 (2019).
33. Errokh, A., Magnin, A., Putaux, J.-L. & Boufi, S. Hybrid nanocellulose decorated with silver nanoparticles as reinforcing filler with antibacterial properties. *Materials Science and Engineering: C* **105**, 110044 (2019).
34. Gogoi, B., Barua, S., Sarmah, J. K. & Karak, N. In situ synthesis of a microbial fouling resistant, nanofibrillar cellulose-hyperbranched epoxy composite for advanced coating applications. *Progress in Organic Coatings* **124**, 224–231 (2018).
35. Scatolino, M. V. *et al.* Tannin-stabilized silver nanoparticles and citric acid added associated to cellulose nanofibrils: effect on film antimicrobial properties. *SN Appl. Sci.* **1**, 1243 (2019).
36. Yan, J., Abdelgawad, A. M., El-Naggar, M. E. & Rojas, O. J. Antibacterial activity of silver nanoparticles synthesized In-situ by solution spraying onto cellulose. *Carbohydrate Polymers* **147**, 500–508 (2016).
37. Xiong, R., Lu, C., Wang, Y., Zhou, Z. & Zhang, X. Nanofibrillated cellulose as the support and reductant for the facile synthesis of Fe3O4/Ag nanocomposites with catalytic and antibacterial activity. *J. Mater. Chem. A* **1**, 14910–14918 (2013).
38. Uddin, K. M. A. *et al.* Retention of lysozyme activity by physical immobilization in nanocellulose aerogels and antibacterial effects. *Cellulose* **24**, 2837–2848 (2017).

39. Martins, N. C. T. *et al.* Electrostatic assembly of Ag nanoparticles onto nanofibrillated cellulose for antibacterial paper products. *Cellulose* **19**, 1425–1436 (2012).
40. Wang, M. S., Jiang, F., Hsieh, Y.-L. & Nitin, N. Cellulose nanofibrils improve dispersibility and stability of silver nanoparticles and induce production of bacterial extracellular polysaccharides. *J. Mater. Chem. B* **2**, 6226–6235 (2014).
41. Kelly, C. A., Cruz-Romero, M., Kerry, J. P. & Papkovsky, D. P. Assessment of Performance of the Industrial Process of Bulk Vacuum Packaging of Raw Meat with Nondestructive Optical Oxygen Sensing Systems. *Sensors* **18**, 1395 (2018).
42. Kelly, C. *et al.* Extruded phosphorescence based oxygen sensors for large-scale packaging applications. *Sensors and Actuators B: Chemical* **304**, 127357 (2020).
43. Saarinen, J. J. *et al.* Large-Scale Roll-to-Roll Patterned Oxygen Indicators for Modified Atmosphere Packages. *Packaging Technology and Science* **30**, 219–227 (2017).
44. Mihindukulasuriya, S. D. F. & Lim, L.-T. Oxygen detection using UV-activated electrospun poly(ethylene oxide) fibers encapsulated with TiO2 nanoparticles. *J Mater Sci* **48**, 5489–5498 (2013).
45. Vu, C. H. T. & Won, K. Novel water-resistant UV-activated oxygen indicator for intelligent food packaging. *Food Chemistry* **140**, 52–56 (2013).
46. Daniels, J. A., Krishnamurthi, R. & Rizvi, S. S. H. A Review of Effects of Carbon Dioxide on Microbial Growth and Food Quality. *J. Food Prot.* **48**, 532–537 (1985).
47. Borisov, S. M., Waldhier, M. Ch., Klimant, I. & Wolfbeis, O. S. Optical Carbon Dioxide Sensors Based on Silicone-Encapsulated Room-Temperature Ionic Liquids. *Chem. Mater.* **19**, 6187–6194 (2007).
48. Schutting, S. *et al.* NIR optical carbon dioxide sensors based on highly photostable dihydroxy-aza-BODIPY dyes. *J. Mater. Chem. C* **3**, 5474–5483 (2015).
49. Bibi, F., Guillaume, C., Gontard, N. & Sorli, B. Wheat gluten, a bio-polymer to monitor carbon dioxide in food packaging: Electric and dielectric characterization. *Sensors and Actuators B: Chemical* **250**, 76–84 (2017).
50. Nopwinyuwong, A., Trevanich, S. & Suppakul, P. Development of a novel colorimetric indicator label for monitoring freshness of intermediate-moisture dessert spoilage. *Talanta* **81**, 1126–1132 (2010).
51. Saliu, F. & Della Pergola, R. Carbon dioxide colorimetric indicators for food packaging application: Applicability of anthocyanin and poly-lysine mixtures. *Sensors and Actuators B: Chemical* **258**, 1117–1124 (2018).
52. Meng, X., Lee, K., Kang, T.-Y. & Ko, S. An irreversible ripeness indicator to monitor the CO2 concentration in the headspace of packaged kimchi during storage. *Food Sci Biotechnol* **24**, 91–97 (2015).
53. Le, G. T., Tran, T. V., Lee, H.-S. & Chung, W.-Y. Long-range batteryless RF sensor for monitoring the freshness of packaged vegetables. *Sensors and Actuators A: Physical* **237**, 20–28 (2016).
54. Cao, X.-T. & Chung, W.-Y. Range-extended wireless food spoilage monitoring with a high energy efficient battery-free sensor tag. *Sensors and Actuators A: Physical* **299**, 111632 (2019).
55. Tan, E. L., Ng, W. N., Shao, R., Pereles, B. D. & Ong, K. G. A Wireless, Passive Sensor for Quantifying Packaged Food Quality. *Sensors* **7**, 1747–1756 (2007).
56. LeBlanc, R. J. & Gill, T. A. Ammonia as an Objective Quality Index in Squid. *Canadian Institute of Food Science and Technology Journal* **17**, 195–201 (1984).

57. Monique, E. Volatile amines as criteria for chemical quality assessment. 22 (2005).
58. Nguyen, L. H., Naficy, S., McConchie, R., Dehghani, F. & Chandrawati, R. Polydiacetylene-based sensors to detect food spoilage at low temperatures. *J. Mater. Chem. C* **7**, 1919–1926 (2019).
59. Kuswandi, B. *et al.* A novel colorimetric food package label for fish spoilage based on polyaniline film. *Food Control* **25**, 184–189 (2012).
60. Narwade, V. N., Anjum, S. R., Kokol, V. & Khairnar, R. S. Ammonia-sensing ability of differently structured hydroxyapatite blended cellulose nanofibril composite films. *Cellulose* **26**, 3325–3337 (2019).
61. Chung, W.-Y., Le, G. T., Tran, T. V. & Nguyen, N. H. Novel proximal fish freshness monitoring using batteryless smart sensor tag. *Sensors and Actuators B: Chemical* **248**, 910–916 (2017).
62. Basavaraja, D., Thodi F. Salfeena, C., Panda, M. K. & Somappa, S. B. Rapid Visual Detection of Amines by Pyrylium Salts for Food Spoilage Taggant. *ACS Appl. Bio Mater.* **3**, 772–778 (2020).
63. Luo, X. & Lim, L.-T. Cinnamil- and Quinoxaline-Derivative Indicator Dyes for Detecting Volatile Amines in Fish Spoilage. *Molecules* **24**, 3673 (2019).
64. Morsy, M. K. *et al.* Development and validation of a colorimetric sensor array for fish spoilage monitoring. *Food Control* **60**, 346–352 (2016).
65. Wells, N., Yusufu, D. & Mills, A. Colourimetric plastic film indicator for the detection of the volatile basic nitrogen compounds associated with fish spoilage. *Talanta* **194**, 830–836 (2019).
66. Alrammouz, R., Podlecki, J., Abboud, P., Sorli, B. & Habchi, R. A review on flexible gas sensors: From materials to devices. *Sensors and Actuators A: Physical* **284**, 209–231 (2018).
67. Dai, J. *et al.* Printed gas sensors. *Chem. Soc. Rev.* **49**, 1756–1789 (2020).
68. Chui, S. S.-Y., Lo, S. M.-F., Charmant, J. P. H., Orpen, A. G. & Williams, I. D. A Chemically Functionalizable Nanoporous Material [Cu3(TMA)2(H2O)3]n. *Science* **283**, 1148–1150 (1999).
69. Al-Janabi, N. *et al.* A Facile Post-Synthetic Modification Method To Improve Hydrothermal Stability and CO_2 Selectivity of CuBTC Metal–Organic Framework. *Ind. Eng. Chem. Res.* **55**, 7941–7949 (2016).
70. Wong-Ng, W. *et al.* Reference diffraction patterns, microstructure, and pore-size distribution for the copper (II) benzene-1,3,5-tricarboxylate metal organic framework (Cu-BTC) compounds. *Powder Diffraction* **30**, 2–13 (2015).
71. Hendon, C. H. & Walsh, A. Chemical principles underpinning the performance of the metal–organic framework HKUST-1. *Chem. Sci.* **6**, 3674–3683 (2015).
72. Zhang, Y. *et al.* A novel humidity sensor based on NH2-MIL-125(Ti) metal organic framework with high responsiveness. *J Nanopart Res* **15**, 2014 (2013).
73. Yin, Y.-Y. *et al.* A 3D pillared-layer cadmium (II) metal-organic framework for chemiresistive humidity sensing with high performance. *Inorganic Chemistry Communications* **97**, 49–55 (2018).
74. Achmann, S. *et al.* Metal-Organic Frameworks for Sensing Applications in the Gas Phase. *Sensors* **9**, 1574–1589 (2009).

75. Weiss, A., Reimer, N., Stock, N., Tiemann, M. & Wagner, T. Screening of mixed-linker CAU-10 MOF materials for humidity sensing by impedance spectroscopy. *Microporous and Mesoporous Materials* **220**, 39–43 (2016).
76. Travlou, N. A., Singh, K., Rodríguez-Castellón, E. & Bandosz, T. J. Cu–BTC MOF–graphene-based hybrid materials as low concentration ammonia sensors. *J. Mater. Chem. A* **3**, 11417–11429 (2015).
77. Bhardwaj, S. K., Mohanta, G. C., Sharma, A. L., Kim, K.-H. & Deep, A. A three-phase copper MOF-graphene-polyaniline composite for effective sensing of ammonia. *Analytica Chimica Acta* **1043**, 89–97 (2018).
78. Khudiar, A. I., Elttayef, A. K., Khalaf, M. K. & Oufi, A. M. Fabrication of ZnO@ZIF-8 gas sensors for selective gas detection. *Mater. Res. Express* **6**, 126450 (2020).
79. Gassensmith, J. J. *et al.* A Metal–Organic Framework-Based Material for Electrochemical Sensing of Carbon Dioxide. *J. Am. Chem. Soc.* **136**, 8277–8282 (2014).
80. Strauss, I. *et al.* Metal–Organic Framework Co-MOF-74-Based Host–Guest Composites for Resistive Gas Sensing. *ACS Appl. Mater. Interfaces* **11**, 14175–14181 (2019).
81. Tian, M., Fu, Z.-H., Nath, B. & Yao, M.-S. Synthesis of large and uniform Cu3TCPP truncated quadrilateral nano-flake and its humidity sensing properties. *RSC Adv.* **6**, 88991–88995 (2016).
82. Weiss, A., Reimer, N., Stock, N., Tiemann, M. & Wagner, T. Surface-modified CAU-10 MOF materials as humidity sensors: impedance spectroscopic study on water uptake. *Phys. Chem. Chem. Phys.* **17**, 21634–21642 (2015).
83. Sel, K., Demirci, S., Ozturk, O. F., Aktas, N. & Sahiner, N. NH3 gas sensing applications of metal organic frameworks. *Microelectronic Engineering* **136**, 71–76 (2015).
84. Aubrey, M. L. *et al.* Chemiresistive Detection of Gaseous Hydrocarbons and Interrogation of Charge Transport in Cu[Ni(2,3-pyrazinedithiolate)2] by Gas Adsorption. *Journal of the American Chemical Society* (2019) doi:10.1021/jacs.9b00654.
85. DMello, M. E., Sundaram, N. G., Singh, A., Singh, A. K. & Kalidindi, S. B. An amine functionalized zirconium metal–organic framework as an effective chemiresistive sensor for acidic gases. *Chem. Commun.* **55**, 349–352 (2019).
86. Campbell, M. G., Sheberla, D., Liu, S. F., Swager, T. M. & Dincă, M. Cu3(hexaiminotriphenylene)2: An Electrically Conductive 2D Metal–Organic Framework for Chemiresistive Sensing. *Angewandte Chemie International Edition* **54**, 4349–4352 (2015).
87. Meng, Z., Aykanat, A. & Mirica, K. A. Welding Metallophthalocyanines into Bimetallic Molecular Meshes for Ultrasensitive, Low-Power Chemiresistive Detection of Gases. *J. Am. Chem. Soc.* **141**, 2046–2053 (2019).
88. Mohan Reddy, A. J., Katari, N. K., Nagaraju, P. & Manabolu Surya, S. ZIF-8, Zn(NA) and Zn(INA) MOFs as chemical selective sensors of ammonia, formaldehyde and ethanol gases. *Materials Chemistry and Physics* **241**, 122357 (2020).
89. Chen, E.-X., Yang, H. & Zhang, J. Zeolitic Imidazolate Framework as Formaldehyde Gas Sensor. *Inorg. Chem.* **53**, 5411–5413 (2014).
90. Campbell, M. G., Liu, S. F., Swager, T. M. & Dincă, M. Chemiresistive Sensor Arrays from Conductive 2D Metal–Organic Frameworks. *J. Am. Chem. Soc.* **137**, 13780–13783 (2015).
91. Cui, F. *et al.* Fabrication of ZIF-8 encapsulated ZnO microrods with enhanced sensing properties for H2 detection. *J Mater Sci: Mater Electron* **29**, 19697–19709 (2018).
92. Tchalala, M. R. *et al.* Concurrent Sensing of CO2 and H2O from Air Using Ultramicroporous Fluorinated Metal–Organic Frameworks: Effect of Transduction

Mechanism on the Sensing Performance. *ACS Appl. Mater. Interfaces* **11**, 1706–1712 (2019).

93. Spieser, H. *et al.* Cellulose nanofibrils and silver nanowires active coatings for the development of antibacterial packaging surfaces. *Carbohydrate Polymers* **240**, 116305 (2020).
94. Fukuzumi, H., Saito, T., Iwata, T., Kumamoto, Y. & Isogai, A. Transparent and High Gas Barrier Films of Cellulose Nanofibers Prepared by TEMPO-Mediated Oxidation. *Biomacromolecules* **10**, 162–165 (2009).
95. Wu, B. *et al.* Preparation and characteristics of TEMPO-oxidized cellulose nanofibrils from bamboo pulp and their oxygen-barrier application in PLA films. *Front. Chem. Sci. Eng.* **11**, 554–563 (2017).
96. Hoeng, F., Denneulin, A., Reverdy-Bruas, N., Krosnicki, G. & Bras, J. Rheology of cellulose nanofibrils/silver nanowires suspension for the production of transparent and conductive electrodes by screen printing. *Applied Surface Science* **394**, 160–168 (2017).
97. Zheng, Y., Zheng, S., Xue, H. & Pang, H. Metal-Organic Frameworks/Graphene-Based Materials: Preparations and Applications. *Advanced Functional Materials* **28**, 1804950 (2018).
98. Borfecchia, E. *et al.* Insights into Adsorption of NH3 on HKUST-1 Metal–Organic Framework: A Multitechnique Approach. *J. Phys. Chem. C* **116**, 19839–19850 (2012).
99. Nijem, N., Fürsich, K., Bluhm, H., Leone, S. R. & Gilles, M. K. Ammonia Adsorption and Co-adsorption with Water in HKUST-1: Spectroscopic Evidence for Cooperative Interactions. *J. Phys. Chem. C* **119**, 24781–24788 (2015).
100. Petit, C., Mendoza, B. & Bandosz, T. J. Reactive Adsorption of Ammonia on Cu-Based MOF/Graphene Composites. *Langmuir* **26**, 15302–15309 (2010).

English Abstract – Résumé en anglais

In line with the latest innovations in the packaging field, this joint project aims at implementing new and innovative micro- and nanoparticles for the development of active and intelligent packaging solutions dedicated to food and medical packaging applications. More specifically, the project combines two major developments which both falls within the scope of active and intelligent packaging. In this work, a specific focus was given to the development of an antibacterial packaging solution and to the development of smart gas sensors. The antibacterial strategy developed was based on the combination of two active materials - silver nanowires and cellulose nanofibrils - to prepare antibacterial surfaces. The formulation as an ink and the deposition processing has been deeply studied for different surface deposition processes that include coatings or screen-printing. Results showed surfaces that display strong antibacterial activity both against Gram-positive and Gram-negative bacteria, but also interesting properties for active packaging applications such as a highly retained transparency or enhanced barrier properties. Regarding the second strategy, gas sensors have been prepared using a combination of Copper benzene-1,3,5-tricarboxylate Metal Organic Framework and carbon-graphene materials, deposited on flexible screen-printed electrodes. The easy-to-produce and optimized sensors exhibit good performances toward ammonia and toward humidity sensing, proving the versatility and the great potential of such solution to be adapted for different target applications. The results of this project lead to innovative solutions that can meet the challenges raised by the packaging industry.

***Keywords**: Active and intelligent packaging, antibacterial packaging, cellulose nanofibrils, silver nanowires, smart gas sensors, metal organic framework, carbon-graphene*

French Abstract – Résumé en Français

En lien avec les dernières innovations dans le domaine des emballages, ce projet collaboratif a pour but d'implémenter de nouveaux micro- et nanomatériaux innovants pour le développement d'emballages actifs et intelligents dans le domaine alimentaire et médical. Il se focalise en particulier sur deux stratégies : le développement d'emballages antibactériens d'un côté et de capteurs de gaz de l'autre. La première stratégie est donc dédiée à l'utilisation combinée de nanofils d'argent et de nanofibrilles de cellulose pour la production de surfaces antibactériennes. La formulation d'encres ainsi que les paramètres de dépôt ont été optimisés pour différent procédés tels que l'enduction ou l'impression sérigraphique. Une forte activité antibactérienne contre des souches bactériennes Gram-positive mais aussi Gram-négative a été prouvée pour toutes les surfaces préparées. Des propriétés intéressantes relatives au domaine des emballage actifs ont aussi été démontrées telles que la conservation d'une haute transparence et l'amélioration des propriétés barrières. Dans la seconde stratégie, des capteurs de gaz ont été préparés en utilisant un mélange actif composé de Cuivre benzène-1,3,5-tricarboxylate Metal Organic Framework et de carbone-graphène, déposé sur des électrodes flexibles produites par sérigraphie. Les capteurs sont faciles à produire et ont été optimisés pour présenter de bonnes performances à la fois pour détecter et quantifier l'ammoniac gazeux mais aussi servir de capteurs d'humidité, ce qui prouve leur versatilité et leur important potentiel industriel. Ce projet a donc conduit à différentes solutions innovantes qui peuvent relever les défis de l'industrie des emballages.

***Mots-clés** : Emballages actifs et intelligents, emballages antibactérien, nanofibrilles de cellulose, nanofils d'argent, capteurs de gaz, metal organic framework, carbone-graphène*